

nature



BIODIVERSITY

What makes a species?

SATURN'S ROTATION

The variable season

TROPOSPHERIC OZONE

Down from the heights

GENOMICS ON A PHYLOGENY

Twelve *Drosophila* sequences traverse
400 million years of evolution

NATUREWIRE

Number 100
Highlight

A drop in the ocean

Wave power and other renewable-energy resources deserve carefully targeted government support.

If the world is to wean itself off fossil fuels, a wide range of alternative energy sources will have to be brought into play. The geographically dispersed nature of renewable resources, including power from solar, wind, wave, tidal and geothermal sources, underscores the need for different nations to develop viable alternatives that utilize the resources they are best placed to exploit.

But some technologies are struggling to make their mark. The harnessing of wave power, for example, has so far had mixed results. This renewable resource held considerable currency in some territories during earlier energy crises, but it has yet to make any real contribution to the global energy mix (see page 156). After the energy crises of 1974 and 1979, nations in the stormy northern Atlantic Ocean, including Britain and Norway, set up relatively modest programmes to explore wave power. But faced with assessments suggesting that the costs of wave power were unlikely to fall quickly enough to render it competitive, government backing for wave energy was all but abandoned.

Now the energy crisis is back with a bang, and numerous privately run companies around the world are testing wave-power devices, many of them developed in collaboration with university researchers. All of the designs face common obstacles. They will need to survive in a physically hostile and corrosive environment, which will sometimes subject them to forces ten or twenty times as great as those they need for normal operation. And although economies of scale will reduce the costs of wave-power plants, such reductions are likely to follow the unspectacular trajectories enjoyed by, say, builders of marine engines, rather than the spectacular leaps achieved by manufacturers of silicon chips.

These are the considerations that have, in effect, relegated wave power to a 'second tier' of renewable-energy resources that do not attract substantial public- or private-sector backing. Yet there is a strong argument, given the grim outlook for the world's energy supply, that such support should be forthcoming so that the commercial viability of

the more promising wave technologies can be examined more fully.

The London-based Carbon Trust, a company set up by the UK government to promote a low-carbon economy, has identified wave energy as one of Britain's most promising renewable resources, with the potential to provide up to 20 gigawatts of power by 2050. But the trust estimates that it could cost £2.2 billion (US\$4.6 billion) in development to reduce the cost of wave-generated electricity from current estimates of between 12p and 44p to a competitive 6p per kilowatt-hour.

That sum may seem daunting to the British government acting on its own; but in global terms, it isn't much. The Carbon Trust estimates, for example, that Denmark has so far spent £1.3 billion on the development of wind power. The Japanese government has invested at least £1 billion in solar power. And don't mention it to the nuclear lobby, but the amount of public money invested to make atomic power fit-for-purpose was orders of magnitude higher.

Both governments and private investors, of course, need assurance that any wave-power technologies they decide to support will have some worth. To gauge the potential of different designs, it can be valuable for backers of rival technologies to benchmark prototype equipment and compare it objectively with the competition.

A promising model in this regard is the European Marine Energy Centre in the Orkney Islands in Scotland, a testing site set up in 2003 that receives support from Edinburgh, London and Brussels. The centre helps private companies to test their wave-power designs. One firm, Edinburgh-based Pelamis, has already tested and improved its design at the centre, and four more are expected to do so in the next two years.

Such benchmarking can, of course, get wave energy only so far. At some stage, it will have to take its chances on the open market. But in the meantime, governments whose coastlines may be suitable for wave energy should support promising technologies to an extent that will at least allow for a firmer measure of their viability. ■

"Wave power has been relegated to a 'second tier' of renewable-energy resources."

The great divide

The gap between theory and practice remains surprisingly wide in conservation biology.

Men and women do not decide to become conservation biologists because they yearn for riches and fame, for swimming pools or caviar. They decide to become conservation biologists because they want to stop species from becoming extinct.

So it can sometimes come as a surprise for outsiders to learn how far removed the conservation biologist often is from actual efforts to save species. Most of the time, conservation biologists describe

problems, float solutions, prioritize areas and actions, and run computer models of natural ecosystems. They are cartographers of crises, producing demoralizing maps of threat and extinction. They are adept at coming up with ever-better methods of doing more with less — at least in theory (see page 152).

It generally falls to a separate and amorphous group, known as 'practitioners', to buy land, put up fences, set fires, put out fires, lobby politicians, negotiate with farmers, spray invasive weeds, poison rats and guard against poachers. These people are generally not conservation biologists: they are civil servants, environmental consultants, park managers or environmental lobbyists.

The distance between these two groups creates a sometimes-yawning 'implementation gap' between theory and practice. Conservation

biologists write and publish papers, which the practitioners seldom read. The practitioners, in turn, rarely document their actions or collate their data in forms useful to conservation biologists. Typically, practitioners make decisions based on personal experience and intuition. Their knowledge stays untapped by others — and can be impervious to fresh scientific findings.

The existence of this gap has been acknowledged, and numerous efforts are already directed at bridging it. Some publications try to bring scientific news to practitioners. William Sutherland, a conservation biologist at the University of Cambridge, UK, runs a site called ConservationEvidence.com where practitioners are encouraged to deposit reports on the outcomes of their interventions — successful or otherwise. Data from these reports can then be fed into systematic reviews of the kind being done by Andrew Pullin at Bangor University in Wales, whose Centre for Evidence-Based Conservation attempts to answer questions such as ‘are Japanese knotweed control and eradication interventions effective?’.

There have been many calls for more mid-career training of practitioners. Conservation biologists could run workshops, and squeeze in some much-needed interaction with their peers on the application side of the discipline. The need for this may sound obvious — but in

a field so cash-strapped that many conservation projects can’t even afford to assess their own effectiveness afterwards, it sometimes seems like a luxury.

Local and national governments with a stake in conservation should be encouraged to support such training as a cost-effective means of raising the efficiency of the conservation projects on their turf — an objective that constituents at both ends of the political spectrum are liable to support.

But the gap can also be bridged if conservation biologists remember to look at all of their professional activities in light of their interest — be it practical, moral, aesthetic or even humanitarian — in saving species from extinction. In essence, the more time that they can spend working with local practitioners on real conservation issues the better.

What is needed is a concerted effort by both academic scientists and practitioners to get out of their respective ruts, open up paths of communication, share information and seek ever more efficient means to a common end. ■

“What is needed is a concerted effort by both academic scientists and practitioners to get out of their respective ruts.”

Deadly consequences

Health authorities have yet to respond effectively to the combination of HIV and tuberculosis.

Tuberculosis (TB) is not only completely treatable, it is curable and controllable, and has been so for decades. So it is appalling that the disease is currently flaring up around the world in an epidemic of co-infection with HIV, which is also associated with a frightening increase in strains of TB that are resistant to existing drugs.

This week, the 38th Union World Conference on Lung Health convenes in Cape Town, South Africa. The main themes of the meeting will be the challenges of HIV–TB co-infection and multiple-drug resistance in TB.

The importance of co-infection has been emerging steadily, especially in Africa, since the early days of the AIDS pandemic. TB is now the most common opportunistic infection in HIV-positive patients starting antiretroviral therapy. Such co-infection presents particularly troubling complications for treatment: there are overlapping drug toxicities and the risk of a life-threatening inflammatory syndrome if infection status is unknown and treatment administered incorrectly.

The South African city of Tugela Ferry presents a startling example of how an HIV–TB epidemic could play out. The incidence of TB there is very high, and of some 400 multidrug-resistant cases identified since 2006, more than half were classified as extensively drug resistant, meaning that they are resistant to second-line as well as first-line drug treatments. Most of the resistant infections occur in individuals co-infected with HIV. Efforts to manage both diseases in patients may itself encourage the emergence of drug-resistant strains.

“Researchers, doctors and health-care workers need to do far more to respond to the scale of the problem that TB and co-infection with HIV presents.”

Activists and health-care workers have often sought to blame the South African government for its lax response to this crisis. But it has also been aggravated by an unfortunate historical divide in the worlds of research and health care between those addressing TB and those tackling AIDS (see *Nature* **446**, 109–110; 2007). Researchers, doctors, health-care workers and the entities that support them need to do far more to respond to the scale of the problem that TB presents, and its interconnectedness with HIV. Priorities outlined in 2004 by the World Health Organization for HIV/TB research have not been implemented adequately, according to a report released by the Forum for Collaborative HIV Research last week.

Large parts of sub-Saharan Africa are becoming subsumed by co-infection. And although the rate of infection has dropped elsewhere, many European and Asian nations still face large numbers of patients with active TB infections. A report from the US Centers for Disease Control and Prevention last month showed that the phenomenon may present a threat in the United States as well (*Morbidity and Mortality Weekly Report* **56**, 1103–1106; 2007). One-third of TB patients there didn’t know their HIV status, despite official policy that routine testing be performed on everyone with TB. And 9% of those with TB were

also HIV positive, according to the report.

The global co-infection epidemic is all the more troubling because it was potentially avoidable with better use of existing drugs. The rising incidence of drug-resistant TB is now forcing agencies in Africa and around the world to react to the scale of the problem. The list of needs is a familiar one: better delivery of existing care approaches, development of more useful diagnostics, and community-based care. But a bigger mental shift is needed in recognizing the size of the problem and its interconnectedness with the AIDS pandemic. ■

RESEARCH HIGHLIGHTS

Go with the flow

J. Geophys. Res. **112**, G04S58 (2007)

Rising temperatures could increase nitrogen and phosphorus in the waters off Siberia's coast, altering local biological productivity, a study suggests.

Rivers that drain western Siberia's peatlands (pictured, right) wash nutrients into Arctic waters, and previous work has shown that global warming could lead to more dissolved organic carbon being carried north. Karen Frey at Clark University in Worcester, Massachusetts, and her colleagues sampled 96 Siberian streams. They estimate that levels of dissolved nitrogen and phosphorus, which also make the journey north, could both increase by between about 30% and 50% by 2100.

The extra nutrients are likely to rev up photosynthetic production in the Ob' and Yenisey bays.



K. E. FREY

DEVELOPMENTAL BIOLOGY

Miracle grow

Science **318**, 772–777 (2007)

Salamanders have the phenomenal ability to regenerate a lost limb from a mound of stem cells — or 'blastema' — that forms at the wound site, but only if nerves are present. A protein called anterior gradient (AG) bypasses this requirement and offers promise for regenerative medicine.

While examining AG expression at amputation sites in *Notophthalmus viridescens*, a type of salamander, Jeremy Brookes of University College London and colleagues discovered that when there's no nerve, there's no AG. Strikingly, the introduction of AG into denervated blastemas rescued limb regeneration (pictured below), although the limbs were not fully functional.

SCIENCE



If blastemas could be engineered in mammals, propose the authors, then growth-promoting proteins such as AG could be used to trigger limb regrowth.

PALAEONTOLOGY

A predator for lunch

Proc. R. Soc. B doi:10.1098/rspb.2007.1170 (2007)

Fossil-hunters in Germany have dug up an amazing find — the oldest known example of a food chain with three links, or 'trophic levels'. The find, which dates back almost 300 million years, consists of the remains of a prehistoric fish, which was eaten by an amphibian, which in turn was gobbled up by a primitive shark.

The fossil record contains few documented predator–prey relationships, because digested remains in the gut of larger animals tend not to be preserved, explain researchers led by Jürgen Kriwet of Berlin's Natural History Museum. The fossil shark, a member of the species *Triodus sessilis* that was found near Saarbrücken in southwest Germany, actually contained the remains of two amphibian species, one of which had already feasted on a fish called *Acanthodes bronni*.

ASTRONOMY

Bigger galaxies earlier

Astrophys. J. **669**, 184–201 (2007)

Giant galaxies seem to have formed earlier than models suggest, say the authors of a new survey.

Roberto Abraham of the University of Toronto in Canada and his colleagues used images from the Gemini Deep Deep Survey and Hubble Space Telescope to study 144 galaxies between 3 billion and 6 billion years old. By examining the concentration of

starlight in each pixel of the images, the team was able to classify the galaxies by shape.

The results show that, contrary to some predictions, most of the early Universe's stars resided in large elliptical galaxies. The findings will help astronomers rethink models of galaxy formation.

NANOTECHNOLOGY

Inside story

Nature Nanotechnol. doi:10.1038/nnano.2007.347 (2007)

How toxic are carbon nanotubes? That's one of the pressing questions in assessing possible risks of nanotechnology, which has applications in medicine. But the matter is hard to study at the cellular level, because it is tricky to spot nanotubes entering cells. Unless they are fluorescently labelled, the carbon tubes are hard to distinguish from carbon-based cell structures such as membranes.

Using a combination of electron and optical microscopy, Alexandra Porter at the University of Cambridge, UK, and her team have now obtained clear evidence of single-walled nanotubes — which are only 0.6–3.5 nanometres in diameter — entering human cells. They found that, once inside cells, nanotubes accumulate in the cell cytoplasm and nucleus, where they cause cell death.

MICROBIOLOGY

RNAi on the offensive

Nature Biotechnol. doi:10.1038/nbt1352; 10.1038/nbt1359 (2007)

A new and easy way to fight plant pests using RNA interference (RNAi) has been suggested by two groups working independently.

RNA interference occurs when short

pieces of RNA are introduced into a cell, where they bind to a target RNA sequence, decreasing the expression of that sequence and of its encoded protein. Xiao-Ya Chen and colleagues at the Shanghai Institutes for Biological Sciences in China used this technique to target an enzyme in cotton bollworms that confers resistance to the cotton plant's chemical defences. When plant leaves containing a trigger RNA were fed to the cotton bollworms, the worms were unable to make as much of their defensive enzyme against the cotton toxin, and their growth was stunted.

James Roberts of Monsanto Company in Chesterfield, Missouri, led a team that took its experiments all the way to the field. The group engineered corn plants that express short RNAs targeted against an essential enzyme found in the western corn rootworm. They then allowed corn rootworm larvae to dine on engineered and non-engineered plants for three weeks, and found that the engineered plants had much less root damage (pictured below, right) than their unprotected counterparts (left).



CHEMISTRY

Green cleaver

Science **318**, 783–787 (2007)

An iron compound that can selectively break carbon–hydrogen bonds in organic compounds looks set to pave the way for easier — and greener — syntheses.

The carbon–hydrogen bond is ubiquitous in organic molecules. Breaking it open to add other chemical groups generally requires a catalyst. Often, in more complex molecules, the bond has to be made more reactive and other parts of the molecule need to be shielded from activity before the catalyst can do its job. Both these steps involve potentially toxic reagents.

Christina White and Mark Chen at the University of Illinois in Urbana have unveiled an iron catalyst that can oxidize carbon–hydrogen bonds using only hydrogen peroxide, which is relatively benign. The catalyst can target specific bonds, even in complicated molecules. For each molecule, this selectivity is based largely on the inherent reactivity of the bonds and how accessible

the bonds are to the catalyst.

GENETICS

Light release

Nature Chem.

Biol. doi:10.1038/nchembio.2007.44

(2007)

Manipulation of the genetic code has allowed researchers in San Diego, California, to produce proteins in which the amino acid serine is

'photocaged'. Changes to the genetic coding and translational mechanisms in the yeast *Saccharomyces cerevisiae* can be used to produce proteins in which an extra chemical group masks a specific serine residue, report Peter Schultz and his colleagues at the Scripps Research Institute and the Novartis Research Foundation. The masking group can later be removed by exposure to visible light.

By selectively illuminating such cells, and thus choosing when to expose the serine residues, the researchers were able to study the circumstances under which Pho4, a transcription factor, is phosphorylated. They suggest that this means of exerting fine control over protein function *in vivo* could have wide applicability, and expect in time to apply it to other amino acids and cell types.

MICROBIOLOGY

Divide and conquer

Chem. Biol. **14**, 1119–1127 (2007)

Researchers have found a new treatment that fights *Staphylococcus aureus* infections in mice by shutting down lines of communication among bacterial cells.

Antibiotic-resistant forms of *S. aureus* pose an escalating public health threat. Kim Janda and his colleagues at the Scripps Research Institute in La Jolla, California, report a new type of antibiotic: an antibody that binds to a signalling molecule *S. aureus* use to communicate with each other. This communication, known as quorum sensing, regulates the production of some proteins associated with virulence.

The antibody reduced production of one such protein, α -haemolysin, and inhibited the breaking apart of red blood cells in bacterial cultures. It also prevented *S. aureus*-induced skin lesions in mice, and fully protected mice against lethal doses of the bacterium.

JOURNAL CLUB

Brian J. Enquist
University of Arizona, Tucson,
Arizona USA

An ecologist wonders how biotic feedback matters to global-change research.

I have increasingly been drawn to the question of how the biotic world responds to climatic change. In the face of environmental change, biology responds — organisms often compensate, adapt and change the nature of their ecologies. But exactly

how important is this biological feedback to how ecosystems respond to a warmer world?

My colleagues and I have called for a need to focus on quantifying the importance of what we call the three As — acclimation, adaptation and assembly — on ecosystem-level processes such as carbon flux.

Acclimation is a plastic response by an organism to a change in the environment, whereas adaptation is the end result of natural selection in populations. Assembly is how species come to dominate a local environment and is the result of ecological interactions. We

know that all these processes are affected by changes in climate. The end result of the three As is a group of species that live in a given location and control the flow of resources and energy.

These processes operate on differing time scales and have mostly been studied in isolation. However, two fascinating papers (K. Ishikawa *et al.* *New Phytol.* **176**, 356–364; 2007, and C. Campbell *et al.* *New Phytol.* **176**, 375–389; 2007) assess the role of both acclimation processes and between-species adaptation in the responses of photosynthesis

and respiration to changing temperature. Remarkably, they find that acclimation and adaptive responses seem to compensate for temperature-driven changes in carbon flux.

Putting these two As together with how species assemble in ecological communities will probably reveal generalities in how evolutionary biology and plant-community ecology matters in global change.

Discuss these papers at <http://blogs.nature.com/nature/journalclub>

NEWS

Foreign students face extra UK security checks

The British government has quietly introduced a programme of security checks on foreign students coming to the United Kingdom for graduate studies in the sciences and engineering.

The Academic Technology Approval Scheme (ATAS) began on 1 November. It requires all graduate students from outside the European Economic Area and Switzerland to complete an online questionnaire if they intend to study any of a broad range of scientific disciplines, including biology, physics, chemistry and mathematics. The questionnaire, which includes questions about family background, must be vetted and approved by UK security agencies before students are allowed to apply for visas to enter the country. The list of disciplines includes 41 subject areas, and the government estimates that some 23,000 students will be affected.

The screenings are designed to prevent the spread of sensitive knowledge to foreign nationals, according to a spokesman for the UK Foreign & Commonwealth Office (FCO) who asked not to be identified. Sensitive fields such as nuclear physics and microbiology could easily be turned to malicious purposes, he says. "You can think of half a dozen countries where you don't want this technology getting into the wrong hands," he adds.

Some researchers expressed scepticism about the plan. The vast majority of academic research lies in the public domain, and it remains unclear

how the government will decide who should have access to "sensitive" subjects.

"This is not a very intelligent scheme," says Peter Littlewood, chair of the physics department at the University of Cambridge. "It seems unlikely to make a positive contribution to security, and for most students will be an extra hoop to jump through that will encourage them to go elsewhere."

The ATAS replaces a system of voluntary reporting by UK universities. Under that system, individual schools notified the FCO if they suspected a student of pursuing a sensitive subject for improper reasons. The government decided voluntary reporting was insufficient, according to the FCO spokesman. "The system now is going to be much more robust," he says.

It will also mean more paperwork for researchers. As part of the ATAS application, departments will have to provide a brief summary of the intended course of study. "This is something of a change as a student doesn't know [their precise topic] until after they arrive,"

says Robert Hay, academic secretary of the physics department at Cambridge. Hay adds that Cambridge is developing an online system to help students get their summaries quickly.

Critics say the screenings are unfair. "This new screening system treats international students with undue suspicion," claims Gemma Tumelty, president of Britain's National Union of Students.

"This is not an area where sane discussion prevails at the moment."

A US entry screening programme was blamed for a dip in the number of academics visiting the United States after the 11 September 2001 terror attacks.



"We might be denying opportunities for genuine students," adds Ali Alhadithi, president of the Federation of Student Islamic Societies in the UK & Ireland.

Not all researchers contacted by *Nature* were aware of the scheme, but some said they would not object to it as long as it didn't take undue time and interfere with the inflow of foreign students. "Clearly, there have been certain [security] worries with certain technologies," says Neil Ferguson, a mathematical modeller of infectious disease at Imperial College London. "If they can approve students in a week or two, then fine."

But a similar American programme that was tightened up in the wake of the terror attacks of 11 September 2001 caused significant delays. Like the ATAS, the US programme required students whose subjects appeared on a 'Technology Alert List' to undergo further screening. The system, which required screening by many US security services, quickly became overwhelmed by applicants, and in its first years, many scientists experienced delays of months.

Observers blame the delays for a dip in the number of academics visiting the United States in the ensuing years, with universities in Britain and elsewhere benefiting through increases in applications from foreign students (see *Nature* 427, 190–195; 2004). "Some of the science and engineering departments at major research universities in the United States saw a big impact," says Peggy Blumenthal, executive vice-president of the Institute of International Education, a non-profit agency based in New York that monitors the flow of international students.

Any such problems could seriously affect both the research enterprise and the financial situation at UK universities. "International students are an important source of income,"





A new UK scheme screens some foreign students before they can apply for entry visas.

says Bruce Nelson, chair of the Association of University Administrators, a higher-education group involved in the government consultation on the ATAS programme. Foreign students pay full fees of around £10,000 (US\$21,000) a year to study in Britain, Nelson says.

The US scheme is still in place, but delays have been largely ameliorated by increases in staff, automation of the system and the extension of clearances for up to four years.

The UK government has assured the university community that students will not be hit by delays, according to Dominic Scott, chief executive of the UK Council for International Student Affairs, which promotes international student mobility. The screening will be free to applicants and require no additional documentation beyond a brief summary of their studies, Scott says. Most importantly, the FCO has promised to process applicants quickly, he explains. "We are assured that the vast majority will receive their answers within seven to ten days."

But Alhadithi remains concerned that the screening system could unfairly hinder students whose primary goal is simply to improve life in their home countries. The FCO has provided little information on how it plans to distinguish the few potential security risks from the majority of hard-working students, he says. "We need more information about the triggers: what exactly is going to cause a red mark?"

"This is not an area where sane discussion prevails at the moment," Littlewood says. "We will do our best to smooth the process of recruiting foreign students while working within the rules."

Geoff Brumfiel

J. WESTRICH/ZEFA/CORBIS



HAVE YOUR SAY

Comment on any of our news stories, online.

www.nature.com/news

Excessive fat intake can throw out the body clock

The body's circadian rhythm — the internal 'clock' that regulates physiological processes — can be shifted by eating more fat, say researchers¹. This surprising finding suggests that a more complex interplay exists between the body clock and metabolism, with implications for disorders such as diabetes and obesity.

The circadian rhythm is a near-24-hour cycle that is known to be modulated by sunlight and eating schedules. Previous studies have shown that a disrupted circadian rhythm leads people to crave high-fat foods. And a study out this week shows that children who lack sleep risk being overweight². This is an issue of increasing concern as researchers attempt to elucidate the link between disturbances in circadian rhythm and health conditions such as obesity, heart disease and diabetes³.

Joseph Bass, an endocrinologist at Northwestern University in Evanston, Illinois, fed a group of male mice a diet in which 45% of the calories were derived from fat, and monitored their daily wheel-running schedule. Mice given high-fat food had 23.8-hour daily cycles, whereas the body clock in control mice, whose caloric intake included only 16% fat, was 23.6 hours long¹. The internal time change occurred before the mice had gained any weight, although the researchers did not measure changes in body-fat percentage.

"This is the first time that a paper has really shown the impact of feeding on the molecular and behavioural expression of the circadian rhythm," says Eve Van Cauter, a sleep researcher at the University of Chicago in Illinois, who was not affiliated with the study. "In a human, this would mean the person would have increased difficulties going to bed at a reasonable time," she says. "That might result in insomnia or night-eating", which further boost the risk of obesity and diabetes.

The link between circadian rhythm and metabolism is not surprising, says Bass, because the two systems share many molecular signalling pathways. The expression patterns of some genes involved in lipid metabolism change in 24-hour cycles, and several nuclear receptors that are activated by sterols regulate expression of clock-related genes⁴. In addition, mice bearing mutations in

the circadian-rhythm gene *Clock* show signs of metabolic dysregulation, including obesity and altered expression of genes involved in appetite regulation⁵.

Precisely how a fatty diet could disturb the circadian clock remains elusive, but the hunt is on. "In discovering these molecular switches that couple metabolic and circadian systems, we might actually uncover new pathways or targets to alter metabolic state," says Bass. Research has shown that the activity of two clock-regulating proteins depends on the nutrient status of the cell⁶, providing one possible molecular connection, he says.

Others note that the connection between nutrient status and clock length may be indirect. The eating habits of mice on the high-fat diet also altered — they ate more and consumed more calories during the day, when mice normally sleep. It could be that the change in eating habits, rather than a direct effect of specific nutrients, altered their body clocks, says Hitoshi Ando at Kanazawa University in Japan. Ando has studied the impact of fatty food on the body clock in female mice, but found only a minimal effect⁷. The reason for that discrepancy is unclear, he says.

Heidi Ledford

1. Kohsaka, A. *et al. Cell Metab.* **6**, 414–421 (2007).

2. Lumeng, J. C. *et al. Pediatrics* **120**, 1020–1029 (2007).

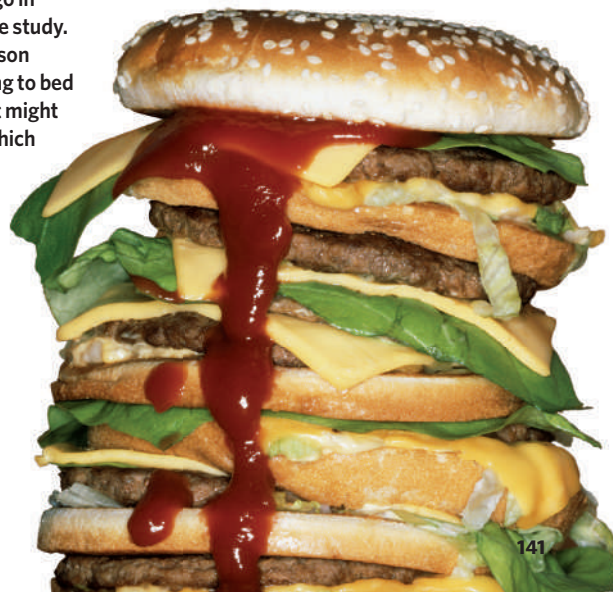
3. Pearson, H. *Nature* **443**, 261–263 (2006).

4. Yang, X. *et al. Cell* **126**, 801–810 (2006).

5. Turek, F. W. *et al. Science* **308**, 1043–1045 (2005).

6. Rutter, J., Reick, M., Wu, L. C. & McKnight, S. L. *Science* **293**, 510–514 (2001).

7. Yanagihara, H. *et al. Chronobiol. Int.* **23**, 905–914 (2006).



SPECIAL REPORT

Attack of the genomes

How many genome sequences do you need to characterize a model organism? For *Drosophila*, **Heidi Ledford** finds, a dozen is a good start.

There was a time not so long ago when sequencing a single genome was cause for celebration. If that genome was from a eukaryote, so much the better. A multicellular eukaryote? Then break out the champagne.

The bar has now been raised even higher with the publication in this issue of full genome sequences from, not one, but ten fruitfly species, to add to the two sequenced previously^{1,2}. Getting the genome sequence for one's favourite organism is still an achievement, but researchers are realizing that to truly understand how genomes function and evolve, they need points of comparison.

The *Drosophila* research community is not the only one benefiting from comparative genomics. More than 20 vertebrate genomes have been published or are being sequenced, and more are on the way, in projects often funded solely with the aim of using the sequences to improve understanding of the human genome.

Daniel Hartl, a geneticist at Harvard University who studies vineyard yeasts as well as *Drosophila*, says that he has lost count of how many yeast genomes have been sequenced. "I don't even keep track. It's like the Broad Institute sequences one of these before breakfast," he says, referring to the genomics centre in Cambridge, Massachusetts. The genomes of 22 species of yeast have been published, with another four on the way, bringing the number of sequenced fungal genomes to more than 60.

Given the plummeting price and escalating power of sequencing technology, researchers can now afford to be a little greedy. "At one stage even I thought: 'This is ridiculous, we're getting more and more genomes,'" says Greg Elgar, a vertebrate genomicist at Queen Mary, University of London. "But it really does give us new insight

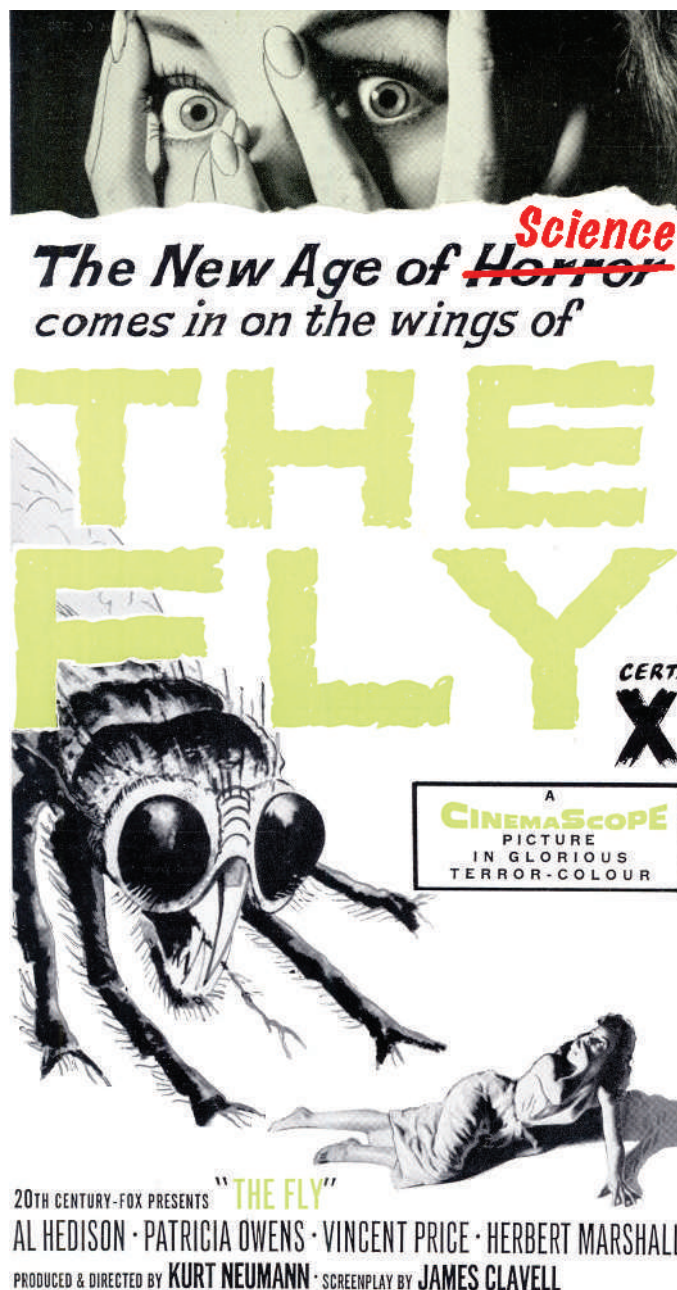
into evolutionary processes."

By placing these vast repositories of information side by side, sequence-gazers have been able to trace the evolution of genomes. It's no sleepy drama. Chromosomes fragment and rejoin in different orientations, and entire genomes

have duplicated themselves. Genes have been tossed from region to region, sometimes coming under the influence of new regulatory elements that alter the time and place of the genes' expression. These chaotic changes only begin to explain the vast phenotypic differences between related species (see 'Dew-loving all-stars'). Many of the genomic changes had been inferred from laboratory experiments and snippets of sequence, says Antonis Rokas, a geneticist at Vanderbilt University in Nashville, Tennessee, but these whole-genome studies provide the full script and confirm the story of genomic rearrangement. Nevertheless, inferring the source of the turmoil remains a challenge. "There are many different paths by which you can create a scrambled genome," says Rokas. "Identifying the most likely path is very challenging."

The immediate benefit of comparing genome sequences is the increased precision with which researchers can reveal the sequences that have been carefully preserved over time, implying that they have an important role in the organism³. Alternatively, these comparisons can pinpoint sequences that differ in just one species or a group of species. Subsequent lab experiments can determine whether and how those sequences — and not all of them are protein-coding genes — yielded a behavioural or morphological trait unique to that group, translating the genomes' most mysterious bits. "Sequences don't come with an index," says Hartl. "We don't really know what the sequences mean."

Even the relatively easy sequences to sort out — those that code for protein and are traditionally thought of as genes — can be challenging to nail down. The *Drosophila melanogaster* genome, sequenced in 2003 (ref. 4), nearly a century after Thomas Hunt





NATURE PODCAST
New lease of life for fruitfly genetics.
www.nature.com/nature/podcast

Morgan characterized his first white-eyed mutant, has a stellar reputation for 'annotation', as members of the community have supplemented computer-driven predictions with expert annotation of potential genes. Yet analysis of the 12 *Drosophila* genomes surprised observers by revealing hundreds of protein-coding genes in *D. melanogaster* that had been either misannotated or missed completely.

Still more challenging has been to determine which regions of the genome regulate when and where genes are expressed — giving the stage directions for building a living animal. Little is understood about how these regions work and evolve. When the mouse genome sequence was completed⁵, there were hopes that human regulatory sequences could be fished out by looking for all the 'conserved' non-coding sequences — that is, those that have remained unchanged over thousands of years of evolution. "One of the big surprises in the genomics community was just how hard that was," says Andrew Clark, a geneticist at Cornell University in Ithaca, New York.

The proteins that drive gene expression typically bind to small sequence motifs that can be as short as ten nucleotides. Such motifs will appear by chance many times in the genome, making it difficult to sort out those that are conserved for a purpose, especially as some regulatory elements are located thousands of nucleotides away from the genes they regulate. Regulation of gene expression can also

be affected by a gene's location in the genome, and by chemical modifications to the DNA that surrounds it.

"When the genomes started coming out, a lot of people thought they could track the regulatory code just by comparing sequences," says Nicolas Gompel, a developmental biologist at the Institute of Developmental Biology at Marseille-Luminy, France. "That would have been really nice, but unfortunately it doesn't work," he says. "You do find patterns, but they're not necessarily relevant." Large-scale projects such as ENCODE, which is designed to use comparative genomics to hunt for human regulatory sequences, and modENCODE, which aims to do the same in fruitflies and nematodes, aspire to improve these predictions.

Sometimes a little shuffling can help prediction programs to home in on regulatory sequences. When researchers compared known regulatory elements directly upstream of genes in *D. melanogaster* with the same regions in *D. pseudoobscura*, they found that short motifs of 8–10 nucleotides had been conserved, but that the order of the motifs had been jumbled. "Motifs that had been previously characterized were all scrambled," says Hartl, possibly because the tiny regions had been duplicated by chance elsewhere, leaving the original motif free to decay. Annotation programs now compare genomes and look for short sequences that have been conserved but shuffled as a hallmark of these regulatory elements.

Other researchers hope to use the *Drosophila* genomes to identify puzzling cases in which the genetic regulation of a pathway has changed, yet the output of the pathway has remained the same. Researchers have found a few isolated cases of this 'transcriptional rewiring' in yeast and *Drosophila*, leading some to speculate that it might be a trend rather than a trivial chance occurrence. Comparative sequence data are crucial for uncovering these examples, says Alexander Johnson of the University of California, San Francisco. "Most 'evo-devo' studies would miss this type of circuit change," he says, because classical studies start with the overt differences between species and work backwards.

Understanding genetic circuitry is precisely the kind of area that will benefit from *Drosophila* sequences, says Elgar, who has been studying transcriptional rewiring in vertebrates. Genomic studies require careful follow-up with wet lab experiments; *D. melanogaster* has played a starring role in experimental research for more than a century and is up to the job. "I don't work on *Drosophila* but sometimes I wish I did," Elgar says. "Now everybody's going to want to join the fly community." ■

1. *Drosophila* 12 Genomes Consortium *Nature* **450**, 203–218 (2007).
2. Stark, A. *et al.* *Nature* **450**, 219–232 (2007).
3. *Nature* **449**, 10–11 (2007).
4. Adams, M. D. *et al.* *Science* **287**, 2185–2195 (2000).
5. Mouse Genome Sequencing Consortium *Nature* **420**, 520–562 (2002).

For more on the *Drosophila* genomes see articles starting on page 183.

Dew-loving all-stars

The *Drosophila* species that have had their genomes sequenced differ quite a bit physically. Here is a small sample.



Drosophila melanogaster

Genome size: 117 million bases

Chromosomes: 4

Of interest because: This fly has redefined itself and genetics several times during the past century. Gene mapping was invented on the huge polytene chromosomes in its salivary glands. And *D. melanogaster* is the only *Drosophila* species that can be reliably manipulated by genetic engineering.



D. grimshawi

Genome size: 201 million bases

Chromosomes: 6

Of interest because: A giant among the drosophilids, this large fly's showy wings are useful for studies of development and mating behaviour. *D. grimshawi* is also used to study fruitfly evolution and population biology in its native home of Hawaii. The Hawaiian islands are host to about one-third of all *Drosophila* species.



D. mojavensis

Genome size: 193 million bases

Chromosomes: 4

Of interest because: *D. mojavensis* survives the harsh environment of the Sonoran desert in the southwestern United States by drinking the juice of toxic cacti. Despite the dry habitat, males of the species lose 2–3% of their body weight every time they ejaculate. They mate several times a day.



D. pseudoobscura

Genome size: 156 million bases

Chromosomes: 4

Of interest because: The second fruitfly genome to be sequenced, *D. pseudoobscura* was a favourite of the geneticist Theodosius Dobzhansky. He studied evolution in natural populations of the fly in the 1930s, and looked at some of the chromosomal rearrangements now evident by comparing genome sequences.

SCORECARD

**Curry**

Japanese curry-lovers can now experience the taste of space, as pouches of curry identical to those eaten on the International Space Station have gone on public sale.

**Bacon**

The World Cancer Research Fund has branded the breakfast treat as one of the top food no-nos if you want to avoid cancer.

ZOO NEWS

Dolphin danger

Conservationists want to stop children with disabilities such as autism from swimming with dolphins. Far from being therapeutic, they say the aquatic mammals' play is a danger to kids.

ON THE RECORD

“An airport with 50 million passengers and countless take-offs and landings per day is not the place for a large wild cat community.”

Pasquale DiFulco of the New York port authority explains the city's decision to round up the estimated 75 feral cats roaming JFK airport.

J. LITTLEJOHN/ALAMY



NUMBER CRUNCH

500 million people in India do not have access to toilets.

10 billion rupees

(US\$255 million) has been pledged by the Indian government to build toilets for the country's poor.

2012 is the deadline the government has set for eradicating open-air defecation.

Sources: Reuters, The Times, Mainichi Daily News



Poor follow-up hampers malaria projects

The incidence of malaria in some African countries may soon approach that of the eastern Mediterranean as a result of increased use of insecticide-treated mosquito bednets, spraying and more effective drugs. The first analyses of the effects of such interventions in the field indicate that they have had a direct and major effect on the malaria burden in Kenya and in Tanzania's Zanzibar archipelago.

However, a lack of global coordination on eradication projects and poor data evaluation are jeopardizing malaria-control programmes in the worst-affected parts of the continent. Studies of the actual impact of control programmes on public health and mortality are surprisingly few, and as a result there is a worrying paucity of data.

“The biggest flaw in current malaria-control efforts is that we need to invest more in disease surveillance systems to know the true story of what is really happening in Africa,” says Mark Grabowsky, Malaria Program Manager at the Global Fund to fight AIDS, Tuberculosis and Malaria. What's needed, says one prominent international health official who wishes to remain anonymous, is a greater international focus to put in place tools to compare data and standardize protocols. This has been achieved for diseases such as polio and measles, in which standardized data are available by district and month in Africa. There are no data of comparable quality for malaria, he says, adding that most reports of successes have been anecdotal.

One study to evaluate the success of these pro-

grammes was carried out by Bob Snow's group at the Kenya Medical Research Institute (KEMRI)-Wellcome Trust Collaborative Research Programme in Nairobi, and an international team. The researchers found that paediatric malaria admissions at hospitals on the Kenyan coast have fallen by up to 63% since 1999, as a result of interventions such as new drugs called artemisinin-based combination therapies (ACTs)¹.

Snow's group also studied about 3,500 children in 72 rural areas of Kenya and found that bednet use was linked to a 44% reduction in mortality².

Snow says he is convinced that the decreases in malaria in Kenya are a direct result of the rise in bednet coverage in the zone between 2004 and 2006 from 7% to 67% of children, and the fact that 85% of rural clinics now stock ACTs that were non-existent only a few years ago. “I think we are going through an epidemiological transition because of scaling up of intervention coverage,” says Snow, who believes that the epidemiology of malaria in many African countries is as a result shifting closer to that of the eastern Mediterranean region, where malaria incidence is at a more containable level of fewer than 10 in every 1,000, compared with 350 in every 1,000 Africans.

Data from Zanzibar, published this week by Achuyt Bhattarai at the Karolinska Institute in Stockholm and his colleagues, also show that malaria deaths dropped to one-quarter of previous levels between 2002 and 2005 after the introduction of ACTs and widened use of bed-

“We are going through an epidemiological transition.”

S. MEISEL/MAGNUM PHOTOS



TURNING BREAST-MILK INTO BRAIN FOOD
Not all children can harness the full goodness of their mother's milk.
www.nature.com/news

GETTY

nets³. Similarly encouraging preliminary data are coming in from Ethiopia, Eritrea, Mozambique, South Africa and Rwanda.

But collecting and analysing rigorous data is difficult. Snow had to ensure that his data covered a long enough period, and that his models accounted for rainfall and other factors that make teasing out the direct impact of interventions difficult.

Until now, most of the data have emerged in a fragmented way from organizations with a vested interest in the figures released. A report that has been billed as a success story, released by the United Nations Children's Fund (UNICEF) on 17 October, showed that annual global production of insecticide-treated bednets soared from 30 million nets in 2004 to 63 million nets in 2006, and orders of artemisinin jumped from 3 million doses in 2003 to 100 million in 2006.

But experts argue that such organizations often release data more for advocacy than to assess operations. The spin on the figures masks the fact that all countries are far short of the targets set by Rollback Malaria of 80% coverage of all interventions by 2010 — most have not achieved a fraction of that.

One key test will be in Zambia, in a programme launched in 2005 and funded by the Bill & Melinda Gates Foundation. It aims to reduce deaths from malaria by 75% by 2008, through a huge scale-up of bednets, drugs and house spraying. Results submitted for publication show that in households with bednets, parasite prevalence in children and anaemia in infants fell from about 20% to 13%. At the end of 2006, the project had 20% of children under bednets; 40% of households owned a net; and spraying reached 34% of targeted households. In absolute terms these are still "miserably low numbers", points out one expert, adding that the overall malaria effort falls far short of its own targets.

The few countries where progress on mortality is being reported all fall within zones in Africa that are moderate both in terms of the intensity of transmission (the number of infected mosquito bites per person) and the length of the malaria season.

No one has yet shown a reduction of malaria in countries such as the Democratic Republic of Congo and Nigeria, where transmission rates are so high that preventative measures might have little impact on mortality. These two countries alone account for around half of malaria mortality in Africa, but poor management and health systems mean that they remain laggards in implementing malaria control measures, let alone evaluating their impact. ■

Declan Butler

- Okoro, E. E. *et al. Malaria J.* (in the press).
- Fegan, G. W. *et al. Lancet* **370**, 1035–1039 (2007).
- Bhattarai, A. *et al. PLoS Med.* **4**, e309 (2007).

Committee releases shortlist of Mars landing sites

Six potential landing sites have been chosen for NASA's Mars Science Laboratory, a large rover set to assess the past habitability of sites on the planet's surface, when it lands in October 2010. The shortlist, chosen from dozens of possibilities, includes craters partly filled with sediment, an ancient flood channel and regions rich in clay minerals thought to date from an era when the martian surface was wetter than it is today. However, changes to the mission's scope mean that options that might offer excellent science could end up being dismissed as impractical.

The mission has a 'landing ellipse' roughly 20 kilometres across to account for the uncertainties involved in guiding a spacecraft over millions of kilometres to a soft landing on a windy planet. The terrain in the ellipse needs to be smooth and flat. "If you ask an engineer, they'd like to land in a Walmart parking lot," says Jack Mustard, a planetary geologist at Brown University in Providence, Rhode Island.

As originally conceived, once landed, the rover would have been able to travel well outside this ellipse to places neither smooth nor flat — the sorts of outcrop that geologists favour. But participants at last month's workshop to choose the candidate sites, hosted by NASA's Jet Propulsion Laboratory in Pasadena, California, found that sites where the rover would need to travel 10 kilometres or more to obtain samples were now being flagged as possibly problematic.

"I would have been screaming at that,"

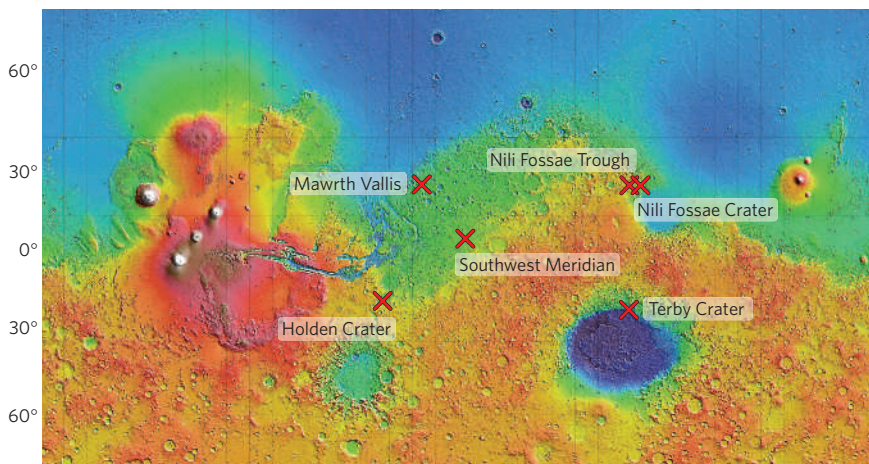
"If you ask an engineer, they'd like to land in a Walmart parking lot."

says Ken Edgett, of Malin Space Science Systems of San Diego, who is a principal investigator on the mission but was unable to attend the workshop because of the wildfires in California. "It limits your expectations," says Mustard, who favours a site in the Nili Fossae region from which the rover would be able, if all went well, to sally forth to a region of dramatic erosion that he has dubbed Monument Valley.

Changes in the way that the rover's moving parts will be lubricated raise issues for sites in the planet's southern highlands, as they reduce the rover's capabilities in winter conditions. Nevertheless, the scientists shortlisted two southern sites as worthy of further study. One of them, Holden Crater, contains what seem to be lake sediments and a delta. "It's awesome," says Mustard.

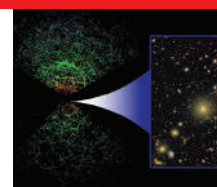
The shortlisted sites will now be scrutinized further by instruments on board NASA's Mars Reconnaissance Orbiter, which is currently circling the planet. At the same time, computer models will assess the risk of winds at the sites being strong enough to mess up the landing. It is very unlikely that all six will be considered too risky, says John Grant of the Smithsonian Institution's Center for Earth and Planetary Studies in Washington DC and co-chair of the site-selection committee. The final decision does not need to be made until nearer the launch in October 2009. ■

Oliver Morton



Mars projection with shortlisted landing sites, two of which are in the southern hemisphere.

MOLA SCIENCE TEAM



BURSTING DARK ENERGY'S BUBBLE
Mysterious force could be an 'artefact' of a void in space.
www.nature.com/news

SDSS/NASA/NSF/DOE

Peering into the heart of a black hole

Quantum mechanics might be capable of stripping bare a black hole to reveal the mysterious and unseeable 'singularity' that exists at its heart¹, say George Matsas and André da Silva of the São Paulo State University in Brazil.

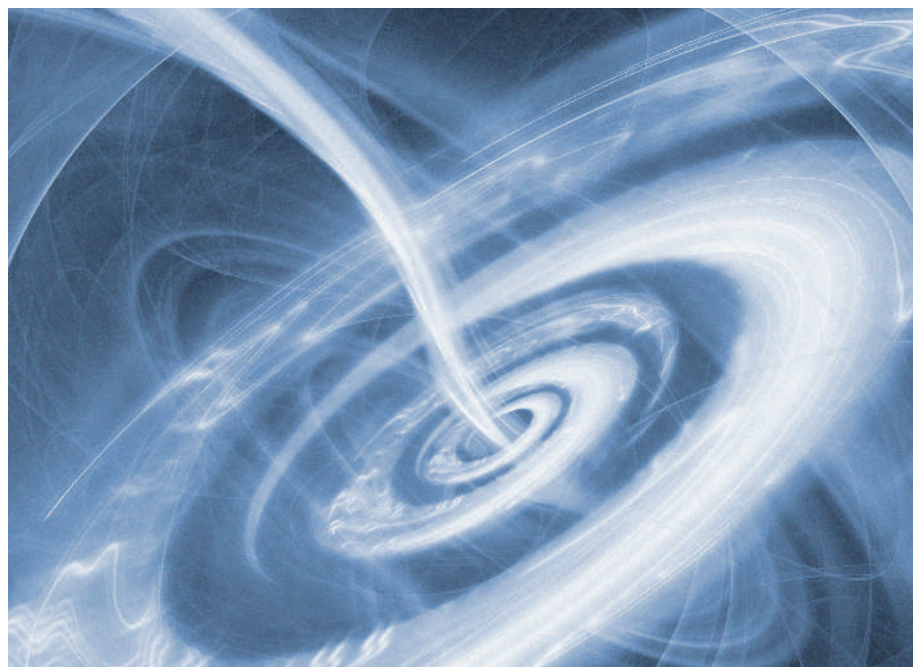
It has long been suspected that these singularities — where the known laws of physics break down — are always decorously veiled behind the 'event horizon', a boundary beyond which light cannot escape from the fearsome gravitational pull of a black hole. Theoretically, nothing within an event horizon can ever be perceived or investigated by an outside observer, because no light can escape. So the singularities remain insulated from the rest of the Universe.

This amounts to what in 1969 physicist Roger Penrose called 'cosmic censorship', whereby the laws of physics conspire to save us from having to gaze on the unthinkable. According to Einstein's general theory of relativity, in the middle of a black hole, its mass collapses in on itself to form an infinitely small, infinitely dense point, where space-time itself is punctured. Even causality — the relation of a cause and its effect — breaks down, which seems to defy not only physics but logic. "Penrose's motivation seemed to be to preserve the decorum of physics," Matsas says.

But physicists have wondered whether event horizons are ever stripped away, leaving these absurdist singularities naked. One possibility, for example, is that the event horizon might vanish if a black hole spins very fast. Light and matter might then be flung out by centrifugal force.

In September, physicists Arlie Petters of Duke University in Durham, North Carolina, and Marcus Werner of the University of Cambridge, UK, proposed that singularities stripped naked by fast rotation should be detectable by astronomers because they act as very strong 'gravitational lenses', bending the light coming from stars behind them by their distortion of space-time. Petters and Werner say that existing telescopes should have sufficient spatial resolution to spot naked singularities in the centre of our own Galaxy².

But how could a black hole spin fast enough to bare its heart? It was shown in the 1970s that a black hole's spin cannot be increased by swallowing rotating objects, because the gain in angular momentum — the momentum caused by rotation — is generally balanced by the slowing influence of the extra mass. To



M. KULYK/SPL

No light escapes the event horizon, so the infinitely dense singularity remains hidden.

transfer enough angular momentum to the hole to overspin it into nakedness, a particle would have to approach the event horizon at such a high speed and such a glancing angle (similar to stroking the side of a spinning-top) that it wouldn't get sucked inside the event horizon in the first place.

No way of creating a naked singularity has yet been discovered within the framework of the classical physics described by the theory of relativity. But in a paper published last week, Matsas and da Silva propose that quantum mechanics, which normally applies only to very small objects, could subvert cosmic censorship. An electrically charged black hole spinning fast enough to be right on the brink of losing its event horizon might be pushed over the edge by gaining angular momentum in a non-classical way, they conclude.

Quantum particles have the strange property of being able to 'tunnel' through barriers that, according to classical mechanics, they have insufficient energy to pass over or through.

So whereas classical particles with enough angular momentum to overspin a black hole can't get inside the event horizon for the reasons explained in the 1970s, Matsas and da Silva's study finds that quantum particles could tunnel inside, and send the black hole

over the brink into nakedness. "It's a neat idea," says Petters. "One issue is whether such black holes exist, or if they will remain charged long enough for us to catch one, since charged black holes tend to become neutralized."

Matsas himself cautions that the work does not necessarily mean that cosmic censorship is violated in reality, because quantum theory is known to be incomplete. The general theory of relativity that explains gravity and predicts black holes, and the theory of quantum mechanics, are known to be fundamentally incompatible, and physicists hope that they might ultimately be reconciled in a quantum theory of gravity.

Whether such a theory would rescue cosmic censorship, says Matsas, remains to be seen. But he says that "we don't see any compelling reason to preclude the existence of naked singularities in the context of quantum gravity". Such an improved theory should in fact help make sense of what naked singularities are like in the first place. "It is widely believed that quantum gravity will unveil the structure of the singularities," says Matsas, adding that they will then probably seem "quite benign to physics" rather than the monstrosities they now seem to be. ■

Philip Ball

1. Matsas, G. E. A. & da Silva, A. R. R. *Phys. Rev. Lett.* **99**, 181301 (2007).
2. Werner, M. C. & Petters, A. O. *Phys. Rev. D* **76**, 064024 (2007).

"It is widely believed that quantum gravity will unveil the structure of the singularities."

Congress to vote on open access and NIH funds

US investigators funded by the National Institutes of Health (NIH) may soon be compelled to publish only in journals that make their research papers freely available within one year of publication.

Congress is this week expected to take final votes on a bill incorporating this directive. The measure is contained in a spending bill that boosts the biomedical agency's effective budget by 3.1%, to \$29.8 billion in 2008.

President George W. Bush has vowed to veto the bill, which will fund the Department of Health and Human Services and other agencies, because it includes what he calls "irresponsible and excessive" levels of spending.

But congressional Democrats have attached to the measure an unrelated but politically popular bill funding the Department of Veterans Affairs. They hope that this will generate the two-thirds support needed in both houses of Congress to override a presidential veto.

The open-access requirement in the bill would apply only during fiscal year 2008; it would need to be renewed in yearly spending bills in the future.

Argo system makes a splash with final float

A global network of floats gauging the vital signs of the world's oceans was completed last week, with the launch of the 3,000th device.

Buoy-like floats in the Argo project periodically dive to depths of 2,000 metres, where they drift for 10 days recording temperatures, salinity and current velocity,



Floating vote: crew onboard the *Kaharoa* deploy the 3,000th device in the Argo network.

and then surface — sending the data to a satellite for transmission to a central repository (see *Nature* 415, 954–955; 2002). More than 30 nations in the Argo system will use the data to create ocean profiles, which then will be monitored for changes over time.

Eight years after deployments began, the New Zealand research vessel *Kaharoa* on 1 November dropped what were designated as the final floats at latitude 45° south in the southern Pacific Ocean.

Biomedical agency puts epigenetics on the map

The US National Institutes of Health (NIH) is set to roll out the latest highway on its 'roadmap for medical research' (see *Nature* 448, 406–407; 2007). It is seeking project proposals worth \$191 million in epigenetics.

The agency already spends about \$240 million per year on epigenetics, the study of stable, inherited genetic modifications that affect gene expression and function without altering the DNA sequence.

Several projects will be funded in the push. These include the development of 'reference' epigenomic maps; studies

Factory delay leaves flamingos in the pink

The lesser flamingos (*Phoenicopeterus minor*) of Tanzania's Lake Natron (pictured) may get a temporary reprieve from a US\$400-million soda-ash plant that was to have been built nearby. An environmental advisory committee has recommended the government block the factory's construction unless its Indian-Tanzanian developer provides more details of plans to protect the local ecosystem.

Environmentalists are up in arms over the factory because the lake is a major breeding ground for East Africa's roughly 2 million lesser flamingos and also home to a number of rare species, says Lota Melamari, chief executive of the Wildlife Conservation Society of Tanzania.

Melamari, who served on the advisory panel, says developers presented few details about how the plant would affect the lake ecosystem. "The main concern was a lack of information," he says. The government is now deciding how to handle the proposal.



C. RATIER/NHPA

SCRIPPS INST. OCEANOGRAPHY/UNIV. CALIFORNIA, SAN DIEGO

Congress to vote on open access and NIH funds

US investigators funded by the National Institutes of Health (NIH) may soon be compelled to publish only in journals that make their research papers freely available within one year of publication.

Congress is this week expected to take final votes on a bill incorporating this directive. The measure is contained in a spending bill that boosts the biomedical agency's effective budget by 3.1%, to \$29.8 billion in 2008.

President George W. Bush has vowed to veto the bill, which will fund the Department of Health and Human Services and other agencies, because it includes what he calls "irresponsible and excessive" levels of spending.

But congressional Democrats have attached to the measure an unrelated but politically popular bill funding the Department of Veterans Affairs. They hope that this will generate the two-thirds support needed in both houses of Congress to override a presidential veto.

The open-access requirement in the bill would apply only during fiscal year 2008; it would need to be renewed in yearly spending bills in the future.

Argo system makes a splash with final float

A global network of floats gauging the vital signs of the world's oceans was completed last week, with the launch of the 3,000th device.

Buoy-like floats in the Argo project periodically dive to depths of 2,000 metres, where they drift for 10 days recording temperatures, salinity and current velocity,



Floating vote: crew onboard the *Kaharoa* deploy the 3,000th device in the Argo network.

and then surface — sending the data to a satellite for transmission to a central repository (see *Nature* 415, 954–955; 2002). More than 30 nations in the Argo system will use the data to create ocean profiles, which then will be monitored for changes over time.

Eight years after deployments began, the New Zealand research vessel *Kaharoa* on 1 November dropped what were designated as the final floats at latitude 45° south in the southern Pacific Ocean.

Biomedical agency puts epigenetics on the map

The US National Institutes of Health (NIH) is set to roll out the latest highway on its 'roadmap for medical research' (see *Nature* 448, 406–407; 2007). It is seeking project proposals worth \$191 million in epigenetics.

The agency already spends about \$240 million per year on epigenetics, the study of stable, inherited genetic modifications that affect gene expression and function without altering the DNA sequence.

Several projects will be funded in the push. These include the development of 'reference' epigenomic maps; studies

Factory delay leaves flamingos in the pink

The lesser flamingos (*Phoenicopeterus minor*) of Tanzania's Lake Natron (pictured) may get a temporary reprieve from a US\$400-million soda-ash plant that was to have been built nearby. An environmental advisory committee has recommended the government block the factory's construction unless its Indian-Tanzanian developer provides more details of plans to protect the local ecosystem.

Environmentalists are up in arms over the factory because the lake is a major breeding ground for East Africa's roughly 2 million lesser flamingos and also home to a number of rare species, says Lota Melamari, chief executive of the Wildlife Conservation Society of Tanzania.

Melamari, who served on the advisory panel, says developers presented few details about how the plant would affect the lake ecosystem. "The main concern was a lack of information," he says. The government is now deciding how to handle the proposal.



C. RATIER/NHPA

SCRIPPS INST. OCEANOGRAPHY/UNIV. CALIFORNIA, SAN DIEGO

of epigenetic contributions to ageing, development and disease, and responses to environmental exposures; the discovery of new epigenetic targets; and the development of technology, data analysis and computational infrastructure. The deadline for proposals is March, and five-year funding will begin next autumn.

San Francisco gets a green natural history museum

Last week, the California Academy of Sciences received the keys to its new environmentally friendly headquarters. The building sits on the site of its historic home, which was damaged during the 1989 Loma Prieta earthquake. Nestled in scenic Golden Gate Park, in environmentally conscious San Francisco, it is in an ideal location for an ecologically inspired museum.

The new \$484-million building was designed by architect Renzo Piano and incorporates so many green design features,



Going green: a model of the California Academy of Sciences' new home.

including a green roof (pictured above) and insulation made from recycled blue jeans, that it beats the energy-use standards set by the US Department of Energy by 30%. Even the steel and rubble from the old headquarters were recycled to make other buildings and new roads.

It is also expected to be the first museum to earn the highest stamp of approval from the US Green Building Council's Leadership in Energy and Environmental Design Green Building Rating System — a nationally accepted set of benchmarks for green design.

Partnership paves way for global carbon market

A coalition of countries, US states and Canadian provinces formed a partnership last week to promote the establishment of a global carbon-trading market.

Officials billed the International Carbon Action Partnership as a central repository for sharing information among various

nations and coalitions that are adopting market-based regulations for greenhouse gases. The goal is to align the development of independent markets so that they can serve as the foundation for an integrated global market.

The European Union has a functioning carbon-trading market under the Kyoto Protocol, and the Chicago Climate Exchange, a smaller market based on voluntary emissions reductions, is operational in the United States.

The new coalition includes nine members of the European Union, the European Commission, ten US states and two Canadian provinces that are organizing two regional greenhouse-gas markets. New Zealand and Norway are also founding members.

White males maintain pole positions in US science

If you are studying science in the United States, the chances are that your mentor is a white male. And although more underrepresented minorities and women are earning degrees, fields such as chemistry and mathematics are among the worst in helping them make the leap to faculty positions, according to a report led by Donna Nelson, a chemist at the University of Oklahoma in Norman (see <http://tinyurl.com/yqwjyq>).

The department-by-department breakdown of the 100 top-spending science and engineering departments shows that some fields are more inclusive than others. In sociology, one of the best disciplines at training minorities, the percentage of blacks, Hispanics and Native Americans earning PhDs equals the percentage of assistant professors from those groups in the top 50 departments surveyed. In chemistry, by contrast, minorities earn 8.5% of PhDs — but just 3.7% of all professorships and 4.7% of assistant professorships.

For women, children and lower self-confidence may help to explain the gap, suggests a separate survey by the US National Institutes of Health of more than 1,300 postdocs (E. D. Martinez *et al.* *EMBO Rep.* 8, 977–981; 2007). Women are more likely than men to sacrifice their careers for kids, the survey found, and 60% of males versus 40% of females felt confident that they would find a faculty job after completing their postdoc.

Correction

The News Feature 'Space invaders' (*Nature* 448, 746–748; 2007) stated that Omar Yaghi was the first to design a metal-organic framework (MOF) in 1998. But in the early 1990s, before the term MOF was coined, a similarly open three-dimensional polymeric network structure linking organic ligands and metal centres had been reported (B. F. Hoskins and R. Robson *J. Am. Chem. Soc.* 112, 1546–1554; 1990).

BUSINESS

Carbon tax lite

The impact of a British tax on greenhouse-gas emissions has faded over time, as **Geoff Brumfiel** reports.

Eight years ago Gordon Brown, then Britain's chancellor of the exchequer, announced a wide-ranging 'climate levy' on industrial carbon emissions. He pledged that the levy would benefit the environment and encourage investment in cleaner technologies.

But a recent audit — one of the most far-reaching of its type in the world — suggests that the scheme's bark was worse than its bite. The widely respected National Audit Office (NAO) reported in August that nearly 90% of its estimated impact occurred even before the levy started in 2001, as firms reacted to the idea. Subsequent reductions that could be attributed to the actual tax itself were small.

"It appears that the announcement had more of an impact than the taxes," says Tim Yeo, a Conservative MP and chair of the House of Commons Environmental Audit Committee, which has an investigation of its own under way. The NAO estimated that the levy cut Britain's total annual industrial emissions of about 60 million tonnes of carbon by 3.1 million tonnes between 1999 and 2001, but by only 400,000 tonnes in subsequent years.

"I don't think the levy is doing very much," says Terry Barker, an economist at the University of Cambridge and chairman of the consultancy firm Cambridge Econometrics, which has carried out several analyses of the tax's impact for the Department of Food, Agriculture and Rural Affairs (DEFRA), which is responsible for its implementation.

Soft targets

As originally conceived, the climate levy would simply have taxed industrial users on their overall energy consumption. But the UK treasury, sensitive to charges from the Confederation of British Industry (CBI) and other lobby groups that such a tax would damage the competitiveness of UK firms, agreed to a more complex implementation that seems to have reduced its effectiveness.

Energy-intensive sectors such as brewing and bulk chemicals can win an 80% rebate on the tax if the sector as a whole is managing to meet emissions targets that they negotiate with DEFRA. For example, a 2001 agreement guaranteed brewers the rebate if they managed to cut energy use on every pint of beer produced by 9% over seven years — which they then did.



Gordon Brown's climate levy has had a modest impact on industry's carbon emissions.



According to Barker, DEFRA officials negotiating these targets lacked detailed knowledge of the sectors in question and were usually out-foxed by industry, agreeing to targets that the sectors could meet without much effort.

Matthew Farrow, head of environmental policy at the CBI, disagrees with this assessment, saying that both sides lacked information on how easily emissions cuts could be achieved. "When the agreements were first negotiated in many sectors, there wasn't much data," he says.

The NAO reports that the resulting agreements were usually modest in scope. They typically required sectors to cut their emissions per unit of production — not of total emissions. This meant that industries could increase overall emissions if production increased, and not lose their rebate. And when sector targets were renegotiated in 2004, ten sectors out of 45 renegotiated agreements with DEFRA that exempted them from 80% of the levy as long as they met a 2010 target that turned out to be actually above their reported 2004 emissions, when those figures became available.

As a result, the agreements part of the levy has fallen short of its goals, according to the NAO. It was supposed to deliver a 2.9-million-tonne annual reduction in carbon emissions by 2010, but a revised estimate now puts this

figure at 1.9 million tonnes. By contrast, it is estimated that rising energy prices and other factors will deliver a total of 2.4 million tonnes of annual reductions by 2010.

According to the NAO, the impact of the levy on sectors excluded from agreements, such as retail and banking, is hard to gauge as they are not required to report their emissions.

Environmentalists say that even the full levy of 0.44 pence on a kilowatt-hour of electricity — less than 10% of the cost of the energy — is too small to make a difference. "The fact is that it didn't significantly hit the bottom line,"

says Mike Childs, head of campaigns at environmental group Friends of the Earth in London.

Nevertheless, many believe the levy has had a positive impact. It forced many sectors to look at their consumption, says Paul Ekins, head of the environmental

group at the Policy Studies Institute, a London-based think-tank. "Boards will have demanded reports on energy use, probably for the first time in their lives," he says. And despite being critical of the tax, Childs and others still see the levy as a useful starting point for Britain — and an example for other countries.

The UK government has announced that it will extend both the levy and the sector agreements until 2017. But Yeo says that his committee, when it reports next month, may advocate the renegotiation of these agreements to give the climate levy some much-needed teeth. ■

"It appears that the announcement had more of an impact than the taxes."

— Tim Yeo



WHAT TO LET GO

Not all species can be saved from extinction. **Emma Marris** talks to conservation biologists about prioritization and triage.

Richard Cowling was playing with maps of South Africa on a computer screen when he had his epiphany. He was designing a conservation plan for the Cape Floristic Region, or fynbos, an arid landscape of shrubs and flowers that contains some 9,000 species, many unique to the area. Some of these, such as the mandala-like sunset blooms of the protea flowers, are spectacular. Some — like the geometric tortoises, whose fetching shells help them hide from baboons and secretary birds — are seriously endangered. Cowling, a conservation biologist at Nelson Mandela Metropolitan University in Port Elizabeth, was working on defining a set of reserves that would maximize the chances of conserving all those species. The project was so large that it would end up as a series of 16 papers by 36 authors that occupied all 297 pages of *Biological Conservation's* July–August 2003 issue. And it was also, Cowling realized as he stared at the screen, “sheer nonsense”.

“I had to click on a couple of grid squares and the project would be complete,” Cowling says. “And it dawned on me: complete for whom? There was no way that this reserve would ever happen. It had to be linked to some social realities on the ground.”

In the preface to his 1981 book, *Extinction*¹, Paul Ehrlich, a biologist at Stanford University

in California, provided a powerful parable for conservation biology: the story of the rivet popper. A passenger inspecting the plane he is about to fly in notices someone popping rivets out of the wings. When challenged, the rivet popper says that the passenger shouldn't worry because not all the rivets are necessary. For Ehrlich the rivets represent species and the rivet popper represents humanity, indifferent to the looming danger of ecosystem collapse and the end of the natural processes that supply raw materials of life such as clean water, wild food, carbon sequestration and climate regulation. In the apocalyptic style for which he has become famous, Ehrlich predicted that continuing to pop the rivets of ecosystems would lead to “a crumbling of post-industrial society”. He demanded that the rivet popping be stopped.

There aren't many, if any, conservation biologists who would disagree with that conclusion. In principle. The problem is that they don't have the resources to back up such ambition in practice. Spending on conservation by major international and non-governmental organizations has been estimated at around US\$2 billion a year². Given constrained resources, the biologists have to set priorities. “Triage” is a dirty word in some conservation circles, but like many dirty words, it describes

something common. Whether they admit it or not, conservationists have long had to make decisions about what to save.

As more and more admit it, open discussion about how the decisions are best made — by concentrating on particular species, or particular places, or absolute costs, or any other criterion — becomes possible. Whichever criteria come into play, one thing remains constant. The decisions have to be made quickly. In the bloody business of conservation biology, the longer you pause to reorder your list, the more species will become extinct.

Superfluous species

Perhaps the most controversial basis for triage is redundancy — prioritizing those species that provide a unique and necessary function to the ecosystem they live in and letting go of those that are functionally redundant. It might seem sensible to lose a few rivets around the plane's over-engineered windows if that saves the rivets actually holding the wings to the fuselage. This idea was raised in the early 1990s by Brian Walker of the Australian Commonwealth Scientific and Industrial Research Organization³. “Regrettable as it might be,” he wrote, “it is most likely that global biodiversity concerns will ultimately reduce to a cost–benefit analysis. Without knowledge of redundancy,

M. HARVEY/NHPA

or more broadly, the relationship between the levels of biodiversity and ecosystem function, we cannot estimate either the costs or the benefits."

The majority opinion among conservation biologists today is that they still understand too little about ecosystem functions to say for sure which species are the 'load-bearing' ones whose presence keeps a complex, multi-tiered ecosystem from collapsing into some worst case dull scenario of rats, roaches and invasive grass. "We are so fundamentally ignorant," says Norman Myers, a fellow of the University of Oxford, UK, and adjunct professor at Duke University in Durham, North Carolina. "We cannot afford, by a long, long way, to say which species are dispensable." Andrew Balmford, a conservation biologist at the University of Cambridge, UK, tends to agree: spotting key species is "an interesting exercise intellectually ... but by the time we've figured it out the forest will have gone anyway".

Save the genes

Not everyone is quite so convinced the problem is ineluctable. "I think there are a lot of systems where we know more than we think," says Reed Noss, a conservation biologist at the University of Central Florida in Orlando. "If you can get naturalists to open up and talk about what they know, we can at least generate some testable hypothesis and do some manipulation if we have time." Kent Redford, head scientist at the New York-based Wildlife Conservation Society, agrees, up to a point. "Our big problem is that we have been raised to believe that unless you have complete information you cannot make recommendations, and I think that is something we are going to be put on trial for by our children. It's baloney." But his belief that science might make this sort of prioritization possible doesn't mean he approves of it. "I don't care if something is redundant," he says, "I want to save it for all these other reasons."

Perhaps aware of the resistance that functional prioritization might encounter, Walker's forthright paper suggested a complementary approach: taxonomic distinctiveness³. This turns out to be less contentious; although there are no organizations dedicated to sorting the load-bearing species from the non-load-bearing, there is at least one that dedicates its resources to saving the mammals that are phylogenetically distinct. The EDGE programme — its initials stand for evolutionarily distinct and globally endangered — of the Zoological

Society of London argues for giving priority to endangered species of mammals that are far out on their own on the tree of life, without close relatives.

The EDGE scheme gives each species a score derived from its position on a phylogenetic tree. A lone species out on a long branch gets a higher score because it is the sole bearer of genes that represent a very long period of evolution. Take the three-toed sloths, which parted company with the rest of the sloths some 15 million years ago. "There are two species of three-toed sloth that only diverged 1 million years ago. If one went extinct, we would lose 1 million years, but if we lose both, we lose 15 million years," says Nick Isaac, a research fellow at the Zoological Society who helps to run the EDGE programme⁴.

"You could make an analogy with art," says Isaac. "You are in a spaceship leaving Earth with three paintings. Do you take three Rembrandts, or do you take one Rembrandt, one Leonardo and one Picasso?" The group's top five targets for funding — which at this point amounts to paying for a student in the countries where the animals live to study their conservation — are the Yangtze River dolphin (*Lipotes vexillifer*), the long-beaked echidna (*Zaglossus bruijnii*) of New Guinea, the riverine rabbit (*Bunolagus monticularis*) of the Karoo desert in South Africa, the Cuban solenodon (*Solenodon*

cubanus) and its cousin, the Hispaniolan solenodon (*Solenodon paradoxus*). Similar to each other, but distinct from anything else, the solenodons merit two slots. Conservation favourites such as tigers, pandas and gorillas are noticeably absent from the list.

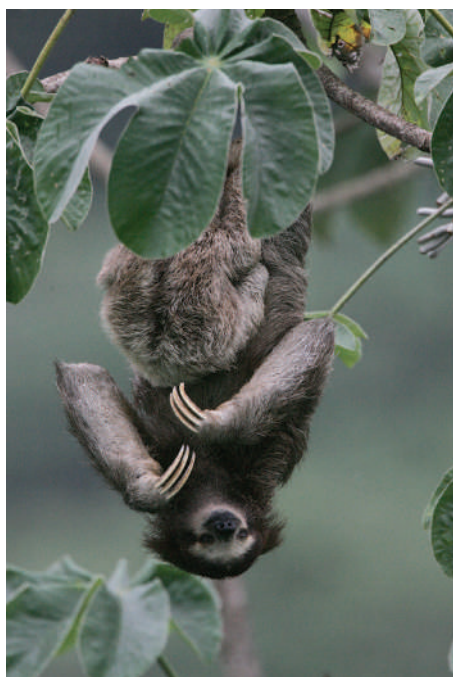
There are variations on this theme floating about. Redford suggests that when a species is identified as endangered, a priority list of populations within the species should be drawn up based on genetic diversity. And a biologist who considers his idea a little too hot to put his name to suggests putting species that have future evolutionary potential at the top of the list. This means prioritizing current species according to their capacity for future speciation. Big, long-lived species face inherent disadvantages under this idea: such a list would have little room for elephants or whales. Or redwoods.

Battle of the maps

A much more popular alternative to prioritizing species is prioritizing areas. There is less need to know how the ecosystem works — just identify an area of interest and try to preserve it in its entirety.

The first such scheme to gain real influence was Myers' hotspot map, which has been published in several incarnations since its inception⁵ in 1988. The original version, which prioritized tropical forests above all other places, was persuasive enough for Conservation International, headquartered in Arlington, Virginia, and the MacArthur Foundation, based in Chicago,

"I don't care if something is redundant. I want to save it for all these other reasons."
— Kent Redford



Two species of three-toed sloth — 15 million years of evolution.

Illinois, to adopt it as a framework for their efforts. But like all prioritizing, it had its critics: "I was told it was immoral, that all species are equal," Myers recalls.

The criteria he has used to define the hotspots are, Myers freely admits, somewhat arbitrary, and have evolved over time. In the 2000 version an area makes the grade if it contains at least 0.5%, or 1,500, of the world's 300,000 plant species as endemics — that is, species that are seen nowhere else — and has lost 70% or more of its primary vegetation⁶. In this iteration the Brazilian cerrado, the fynbos and other mixed grasslands joined the forests.

Myers' hotspot map set a trend: it is now practically compulsory for every conservation organization to have its own priority map. The Cape Floristic Region received its journal-filling loving-care from Cowling and his peers in part because it had made it onto so many of these prioritization lists. As well as being an accredited hotspot under Myers's scheme it had also made it into conservation group WWF's 'Global 200' scheme. Birds found nowhere else, such as the protea canary and the orange-breasted sunbird, had propelled the area onto Birdlife International's Endemic Bird Areas list⁷.

Priority actions

The fynbos demonstrates the extent to which maps will agree about things, which raises the question of why there should be so many. "It has been a not terribly profitable exercise over the last ten years to have such a proliferation of schemes that are basically very similar," says Georgina Mace, who runs the Centre for Population Biology at Imperial College in London, UK. "They act as sort of branding for the organizations. It still surprises me that the big conservation organizations have not gotten together under a single banner, like Make Poverty History."

At the same time, partisans can detect — and defend, debate and disparage — various differences in approach. "We have been arguing, or certainly jockeying, to present one piece of science as more legitimate or stronger than another," says Jon Hoekstra, a senior scientist at the Nature Conservancy in Seattle, Washington. These squabbles are framed to suggest that there is one right answer — one most valid way to prioritize areas.

But different starting assumptions and different goals mean that many of the schemes are not directly comparable. "We have to remember that they reflect the philosophical decisions made at the beginning," says Hoekstra.

The approach that currently enjoys perhaps the highest level of acclaim, at least scientifically, is that taken by Hugh Possingham of the University of Queensland, in Brisbane, Australia. His one goal is maximizing number of species conserved, and he loathes scoring systems. Instead he uses algorithms that measure real-world costs against benefits in terms of species number, and the resulting papers, colleagues say, are in a league of their own⁸.

In his latest work he compares different actions in different places with each other, which is more complex than one might think. Land prices vary around the world, as does species richness. Many investments have diminishing returns over time: once a large chunk of one ecosystem is protected, turning a bit more into a park won't save many additional species. On the other hand, some interventions begin to pay off seriously only after a certain investment threshold is reached. "If you were trying to get all the rats off an island, unless you invest enough to get them all off, you might as well not even bother," explains Possingham. On top of all this is the problem that data on costs are infamously scanty — so much so that many earlier analyses just used land area as a

proxy, an astonishing simplification.

"In a sense, it is just about good problem definition," says Possingham. "If you don't do that right, you head down these scoring paths. The people who make them just have a feeling of which facts are important, and they throw them in." Possingham tries to be as rigorous as possible, and sometimes that means not everything gets saved. "A lot of people get upset with that. It basically says some regions aren't working at all. They are too expensive, the threats are too huge, or there are not enough species in them."

Mount Lofty's short straw

Consider, for example, the Mount Lofty woodlands of Australia, where eucalyptus trees shelter rare orchids (pictured), spiny echidnas and cockatoos. Surely it is worth preserving them from the invasive predators such as foxes and cats that threaten them? But in a trade-off between spending on the Mount Lofty ranges and on the montane regions of the fynbos, Possingham's algorithms give the money to the fynbos — among other regional investments. The Australian woodlands get nothing, despite the fact that Possingham, an avid birder, would bitterly regret losing part of the original range of the endangered regent honeyeater (*Xanthomyza phrygia*); he's particularly keen on honeyeaters.

Putting this sort of insight into practice is not simple. Most Australian money isn't transferable to South Africa, any more than money given to preserve pandas can be spent on solenodons. But some of those who administer the sliver that is fungible — people at the World Bank, the Global Environmental Facility and other large foundations — are taking an interest in Possingham's approach. Peter Kareiva, the head scientist of the Nature Conservancy, is one of many researchers who has been co-authoring papers with Possingham on such return-on-investment models of conservation⁹; a few years ago, as it happens, he rubbished the whole idea of hotspots in *American Scientist*¹⁰.

Balmford, too, is excited about these approaches. "Possingham's new techniques on setting priorities dynamically, allowing you to shift from one to another, are really exciting," he says. The difficulty is getting them adopted by managers and decision-makers on the ground. "We have got to get away from conservation scientists handing down ideas from on-high to practitioners and expecting them to be received gratefully. It has got to be through examples, and from realizing from their peers that those things make sense."

This is the dreaded implementation gap, in

"I was told it was immoral, that all species are equal."
— Norman Myers



which theory ignores practice and practice ignores theory. In the end, it may not matter which prioritization scheme is most scientifically defensible. What matters is that the people carrying out a scheme feel that it makes sense and will save species. On this pragmatic basis, many schemes shouldn't even be considered for implementation, says Hoekstra — including some of his own work. “I wrote this crisis eco-regions paper. It gives some real interesting perspective on the world. It highlights the crisis in temperate grasslands. But I don't think it is as useful to look at the map I generated to decide where to work; you could end up trying to restore something that is lost.”

Armchair scientists

“So much of this stuff is done by well-meaning people sitting as it were in their armchairs,” says Stuart Pimm, a conservationist at Duke University. Pimm recently eschewed the priority list for his own expertise and invested in some land in the Amazon he knew was ripe for conservation. “You have to do what you think you can do. It is going to be based on imperfect information and it is going to be very, very strongly conditioned by local politics and economic and social conditions,” he says.

Pimm aside, the armchair approach can seem deeply entrenched. Redford points out the perennial problem of papers that follow pages of science with a cursory command, “that deadly last paragraph that begins ‘managers should’”. For Noss, one solution is educating those managers. “We need a system that can provide mid-career training to people who are going to be working in land-management agencies, ocean-management institutions, and in environmental consultancies. Otherwise they are going to keep using these more outdated and less defensible approaches to prioritization.”

For an on-the-ground conservationist, such as Stuart Cowell, project coordinator with Bush Heritage Australia, the many different schemes have been influential, but not immediately applicable. “We haven't taken those approaches off the shelf,” he says. Bush Heritage buys land with conservation value, but unlike the ideal maps on paper, some land is never going to come up for sale. What Cowell and his colleagues are asking themselves, he says, is: “Is there a benefit to an organization spending the time and resources in doing this sort of prioritization, which looks good in theory but perhaps does not take us as far as just some good expert knowledge?”

There are some small successes. Possingham

“We cannot afford, by a long, long way, to say which species are dispensable.”
— Andrew Balmford



Preserving the Mount Lofty ranges might not be as cost effective as spending on conservation elsewhere, despite the charms of its endangered orchids (opposite).

has had some luck impressing government bureaucrats with the rigour of his analyses; some spending decisions in Australia have been made on the back of his work. And South Africa has had real success in bridging the implementation gap. “The US and European style is that the scientists write it and hope someone picks it up, but the South Africans are trying to get the people who are going to implement it to help with the priorities,” says Redford.

The messy reality

Since his conversion experience over the digital maps of the fynbos, Cowling has been one of those attempting to build the input of decision-makers and local people into his schemes from day one. “The plans [I've worked on] were done not because they appealed to anyone's curiosity in an academic sense but because they were needed,” he explains. He's more interested in determining the possible than mapping the ideal. “Through the process of negotiation [with stakeholders] you end up with a series of projects, and funding is sought.” And sometimes that which is sought is actually found.

Cowling says that getting all conservation biologists to do their prioritization work with both feet on the ground “will require a substantial change in how researchers operate”. “Getting involved in the slushy stuff takes time. The kind of research is not likely to appear in the pages of high impact journals. You might get it into the pages of *Ecology and Society*,” he says. But his work is not going unrecognized,

whatever its impact factor; Balmford singles Cowling out for praise as someone “not just concerned with getting the algorithm to get the best bang for the buck, but with the more messy, more real, more interesting reality”.

There is no reason why, in theory, one could not include the slushy stuff of real life as inputs in a prioritization scheme. “People say that this mathematical approach can't account for anything, but it can,” says Possingham. “The question is, can you put it in with a plausible number?” Imagine a platonic scheme in which one could include the intransigence of a particular politician, the likelihood of a coup in a certain country, the relative value of the US dollar, the effect of eco-fatigue among the donating public, and the looming spectre of climate change, each quantified and slotted into equations (along with values representing their uncertainty, of course). Such a marvel might give you the best tactics. But it would be no help in setting fundamental goals for future conservation — a subject on which unanimity seems about as likely as a full recovery for the Yangtze River dolphin. ■

Emma Marris writes for *Nature* from Columbia, Missouri.

1. Ehrlich, P. R. & Ehrlich, A. *Extinction: the causes and consequences of the disappearance of species* (Random House, London, 1981).
2. Halpern, B. S. *et al.* *Conserv. Biol.* **20**, 56–64 (2006).
3. Walker, B. H. *Conserv. Biol.* **6**, 18–23 (1992).
4. Isaac, N. J. B., Turvey, S. T., Collen, B., Waterman, C. & Baillie, J. E. M. *PLoS ONE* **2**, e296 (2007).
5. Myers, N. *Environmentalist* **8**, 1–20 (1988).
6. Myers, N. *et al.* *Nature* **403**, 853–858 (2000).
7. Brooks, T. M. *et al.* *Science* **313**, 58–61 (2006).
8. Wilson, K. A. *et al.* *PLoS Biol.* **5**, e223 (2007).
9. Murdoch, W. *et al.* *Biol. Conserv.* **139**, 375–388 (2007).
10. Kareiva, P. & Marvier, M. *Am. Sci.* **91**, 344–351 (2003).

See Editorial, page 135.

P. FAKLER / ALAMY

TO CATCH A WAVE

Ocean wave energy is trying to break into the renewable-energy market, but many challenges remain. **Ewen Callaway** reports.

The North Sea is not known for calm days, and neither is its inlet called Nissum Bredning, 300 kilometres northwest of Copenhagen. On a typical afternoon, windsurfers skate across the grey-green water while birds seem to hover, frozen, in mid-air. Along the horizon stretch rows of giant white windmills, their long blades whirring in the gusts.

"There's really some good action today," Per Steenstrup shouts over the gust as a mix of sea water and rain pelts his face. Steenstrup, an engineer from Copenhagen, is 200 metres offshore, aboard a steel platform with 20 large floats on each side lined up like oars on a Viking ship. A knee-high wave washes under the platform, and the floats move up and down a dozen centimetres in quick succession.

Steenstrup opens the door to a small prefabricated structure on the platform, and suddenly a mechanical roar rises above the noise of the wind and sea. "It's a 40-piston engine running on waves," he yells. In the control room next door to the turbine, Steenstrup peers at

a computer that keeps an instantaneous pulse on the Wavestar, as the platform is called. "At the moment, the output of power is around 800 watts," he says — enough to run a large-screen plasma television.

The wind turbines on the horizon, for their part, are components in a well-established system that produces 41 megawatts of wind power. That's enough on some days to power the entire agriculture-dense region.

Yet Steenstrup and dozens like him think that power harvested from ocean waves will one day be competitive with other methods for extracting energy from the physical environment such as wind, solar and hydroelectric. Wave energy is applicable only in a few regions of the world, and uses technologies that, for the most part, remain unproven. But given the scale of the energy challenge facing the world, supporters say that wave energy could supply enough electricity to make it part of a green-energy portfolio.

The European Ocean Energy Association in Brussels, for instance, estimates that the global resource for wave energy lies between 1 and 10 terawatts; the world currently produces about 13 terawatts from all sources. Others see a more realistic number of 0.2 terawatts, or less, coming from wave energy; that's still three times the current installed capacity for wind power worldwide.

Whether wave energy becomes economical depends heavily on a new round of open-ocean tests that are under way from Portugal to Wales to Oregon. Engineers and entrepreneurs are field-testing machines that until now have been scale models in water tanks. Few are looking for profits; they just want to see if the technologies can produce a consistent amount of power from the ocean. Success could attract funds from investors, industry and utilities; failure could set the field back years.

"A lot is riding on how well the first sets of large-scale devices work," says Tom Thorpe of the consultancy firm Oxford Oceanics in Grove, UK, which advises prospective wave-energy investors and developers. "They've got to be either successful or, if they fail, there has to be a good reason why."

"Wave energy is where wind was 25 years ago."
— Alla Weinstein

Blowing in the wind

Wave energy's most obvious parallel — and, perhaps, competitor — is wind energy. "We are where wind was 25 years ago," says Alla Weinstein, director of ocean energy at Finavera Renewables in Vancouver, Canada. Finavera's prototype, the Aqua Buoy, sank off the coast of Oregon last month after operating for two months and before it was scheduled to be taken out of the water later this month. A quarter of a century ago, world capacity for wind energy was around 90 megawatts. But that was a nine-fold jump from just two years previously, and today countries such as Denmark and Germany get more than a tenth of their power from wind — although it still accounts for just 1% of energy produced worldwide.

Global figures for the power that waves produce are hard to pin down, as most projects are still in the testing phase. But when the industry's leading company, Pelamis in Edinburgh, Scotland, gets a new project online in Portugal — as is expected within weeks — that will add

The Wavestar project harnesses power from the oceans around Denmark.



K. E. JENSEN/WSE

2.25 megawatts from three machines. And wave-energy proponents think that the growth could be exponential after that.

Waves offer several improvements over wind, although they are trickier to harvest. Wind is notoriously fickle; when gusts fail, utility companies have to deliver power to their customers from other sources. Waves can be fickle too, but are easier to predict, says George Hagerman, an engineer at Virginia Tech's Advanced Research Institute in Arlington, who forecasts wave-energy days in advance using weather satellites. Knowing when waves are coming and how big they will be can save utilities money by cutting down on the power they need to keep ready in reserve, he says.

Water is not only more reliable than wind; it is also 800 times the density of air. Aboard the Wavestar, it's not a hard concept to grasp. "This is a big guy," Steenstrup says, eyeing an approaching metre-high curl like a surfer would. It hits head-on, and sea foam gushes over the floats. The steel platform shudders, even though it's anchored to the seabed by concrete piles.

Like other renewable energies, wave power works better in some locations than others. It takes more than just a shore to harness the power of waves. Because of the planet's prevailing winds, the best spots are on the west coast of continents in the mid-latitudes of the Northern Hemisphere, or on the east coast in the Southern Hemisphere. Not coincidentally, most wave-energy tests are being installed in those spots in the North Atlantic and North Pacific oceans.

Some of the strongest waves hit the Orkney Islands in Scotland, where the European Marine Energy Centre has established a wave-energy test site two kilometres offshore. The centre, which receives both government money and private funding, offers developers steady waves and easy connection to electricity grids to field-test machines. Pelamis began testing a 750-kilowatt wave machine there in 2004, although it is now gone. Four other manufacturers plan to join the site in the next two years. In the Southern Hemisphere, Australia-based Oceanlinx has been testing a 600-kilowatt machine off Port Kembla, New South Wales, since 2005, and is working on a larger, 2-megawatt model.

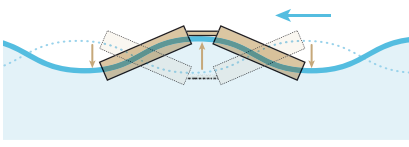
In such places, wave energy could provide an alternative source of renewable energy to the usual standbys of wind and solar. Given recent government mandates to increase the power generated from renewable-energy sources — the European Union is aiming for 20% from renewables, and California 33%, by 2020 — wave power could be another much-needed option. The targets are aggressive enough that all options could be needed, says Dan Kammen, director of a renewable-energy laboratory at the University of California, Berkeley.

THE POWER OF WAVES

Engineers have developed at least six main types of machine to harvest the mechanical power of waves. Field tests currently under way should reveal which of these will ultimately be practical.

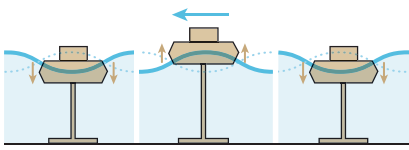
Attenuator

This floating device effectively 'rides' the waves, flexing as they pass.



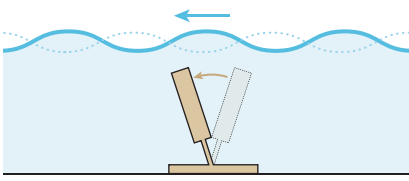
Point absorber

This float absorbs wave energy from all directions as it bobs up and down.



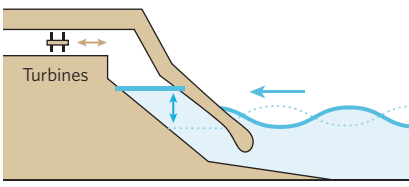
Oscillating wave surge converter

The tethered arm acts as a pendulum in response to wave surges.



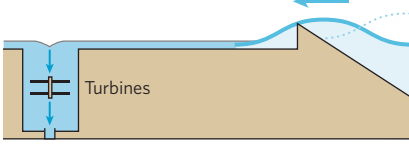
Oscillating water column

As the water level goes up and down, a column of air is compressed and decompressed, powering a turbine.



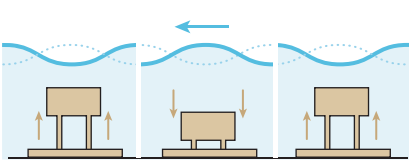
Overtopping device

Collecting water from waves in a reservoir, this device powers a turbine as the captured water drains away.



Submerged pressure differential

As this device responds to the waves, a pressure differential is set up inside it, which is used to pump fluid and so generate electricity.



Some energy companies and industrial giants are already starting to take notice. At a September conference in Porto, Portugal, representatives from the national utilities of France, Denmark and Portugal attended the usually science-focused meeting. In California, the utility behemoth Pacific Gas and Electric has sought permission to establish wave-energy test sites off the coast of northern California. And in 2005, the hydroelectric firm Voith Siemens in Heidenheim, Germany, purchased Wavegen, a Scottish developer.

Patents and promises

For much of its 200-year history, wave energy has been flush with ideas but short on results. In 1799, French engineer Pierre Girard and his son filed the first patent to harness power from waves. Never constructed, the device was to work by linking the bobbing of moored ships to heavy machinery ashore via a plank and fulcrum. Through the nineteenth and twentieth centuries, patents trickled out of inventors' workshops, but no machine ever produced enough power to gain widespread use.

Wave energy's supporters began moving out of garages and into government ministries in the early 1970s. The embargo imposed by the Organization of the Petroleum Exporting Countries (OPEC) propelled the price of crude oil from \$7 in 1970 to \$38 by 1974. Many countries saw independence from Middle East oil in renewables, beefing up their research into wind and solar energy. When it came to ways to get energy from the sea, the United States mounted an ultimately unsuccessful effort to capture thermal energy from oceans by exploiting the temperature difference between deep and surface water (see 'Energy from the sea, overleaf'). Meanwhile, Britain led the way in wave energy.

In 1974, the UK government commissioned academia and industry to draw up plans for how the country could bring wave power into the mainstream. The first prototypes for wave-energy machines were "hopelessly uneconomic", says Thorpe. The plans called for massive machines that cost more than \$100 million each to generate 2,000 megawatts of electricity — roughly the output of the nuclear and oil-powered plants they were designed to replace. No rationales were given as to how such a technological leap would be made, says Thorpe. None of the proposed plants was ever built.

A 1983 progress report effectively ended Britain's foray into wave energy, saying that the technology was unproven and too costly. Developers felt betrayed by the criticism, prompting the government to commission Thorpe to repeat the review; yet he came to a similarly dim conclusion in 1992.

As wind energy took off in the 1980s, wave

energy went back to its roots, in university laboratories and inventors' workshops. Lessons learned from the early failures and from offshore oil rigs would guide the designs of a new generation of machines.

Currently, at least 50 wave-energy projects are in development, with more appearing every year. Analysts divide the machines into more than half a dozen breeds (see graphic), each with a different trick to turn waves into electricity. Pelamis' resembles a giant snake with three segments that shimmy back and forth. Oceanlinx's looks like a giant steel bagpipe that's played by a rising and falling water column. And Finavera's are oversized buoys that use waves to drive hydraulic pumps.

Such heterogeneity is natural for a field in its early days — but within a decade the various designs should shake out into those that are practical and those that aren't, says analyst Roger Bedard of the Electric Power Research Institute, a think-tank based in Palo Alto, California. "It's still anybody's game."

Thorpe is more sceptical. "There are lots and lots of ideas out there and hundreds and hundreds of patents," he says. "Some of these actually defy the laws of physics, many of them will not be technically viable, even more of them would not be economically attractive — and we are left with very, very few designs that I think have a chance, on a 10- to 15-year timescale, of becoming economic."

Even now, the most promising designs can be washed under by the smallest technical glitch.

A short drive from Steenstrup's Wavestar rests a competing project: 237 tonnes of crimson-painted steel and concrete dotted with barnacles. Curled up onshore, the Wave Dragon resembles a giant piece of playground equipment, its steep, curved walls sloping up to a large concrete bed with an opening at its centre. When operating, the Wave Dragon floats in open water; waves gush over its wall and into a hole, where they power a turbine.

Many see the machine as one of the industry's leading prospects. Installed in Nissum Bredning in 2003, the 20-kilowatt device ran for 20,000 hours, says Lars Christensen, a developer in Wave Dragon's Copenhagen office. But the machine has been ashore since early this year after a rusted screw put it out of commission. The screw, it turned out, should have been made of stainless steel. And Finavera's Aqua Buoy was apparently sunk by a pump that failed to remove water once the device started leaking.

Trial by error

Such minor errors underscore the difficulty of engineering devices to withstand the demands of the open ocean. Waves come in all shapes and sizes, and most devices are designed to run on average ones. Yet to last years without regular maintenance, they must withstand swells twenty times more powerful. To counter such storms, many of the new machines are

moored loosely to the ocean floor, allowing them to better absorb a pummelling. "The ocean is really going to beat these things up," says Hagerman. "They need to be out there for a few years to demonstrate that they can survive."

In 1988, a severe storm destroyed a 600-kilowatt pilot plant made by Kvaerner Brug, a Norwegian firm. The shore-based machine — one of the few built in the 1980s — produced power for just three years, and the company later abandoned wave energy. Not to be

deterred, Wave Dragon plans to install an even larger model next year in Wales, where the waves dwarf those in Denmark.

Although technical hurdles could torpedo any one machine, engineering alone is unlikely to sink the whole field, says Thorpe.

He sees greater challenges in the potential costs of developing and delivering wave energy in the face of competition from traditional and other renewable sources. "Technically it will work," he says. "Getting the cost down is a significant challenge, and I think some of them are going to be successful — but not that many."

The UK-based Carbon Trust has estimated that wave power costs between 25 and 91 US cents per kilowatt-hour. Investing some £2.2 billion (US\$4.6 billion) could bring the cost down to 12 cents per kilowatt-hour, it estimates, although that will depend on cost-cutting

"A lot is riding on how well the first sets of large-scale devices work."

— Tom Thorpe

Energy from the sea

Waves are just one way to extract power from the oceans; at least three other technologies attempt to harvest electricity from the sea.

Tidal power, captured from the tides as they rise and ebb, is a resource estimated at 91 gigawatts, according to a report from the UK consulting firm AEA.

In the United States, most of the tidal resource is in Alaska, far from populations and energy infrastructure. Other sites, such as San Francisco Bay in California, aren't ideal because of competition with shipping lanes. "Under the Golden Gate Bridge," says Roger Bedard of the Electric Power Research Institute in Palo Alto, California, "it ain't going to happen." Still, at least one firm has managed to make tidal energy work in a densely populated area.

Since 2006, Verdant Power has worked to extract about 1,000 kilowatt-hours per day from the tidal flows in New York City's East River, although the turbines are now under repair (pictured).

More projects are under way in Europe. France has kept its 240-megawatt La Rance tidal-energy plant in operation since the 1960s. New tidal technologies use turbines powered by beefed-up propellers that spin as the tides rise and fall. But in the French plant, the tides pump water behind a barrier. The 'dam' is then released to create power.

Such designs have not gained widespread use mainly because of environmental concerns.

The sea's largest cache of energy is thermal, with an estimated resource of 1.1 terawatts. The

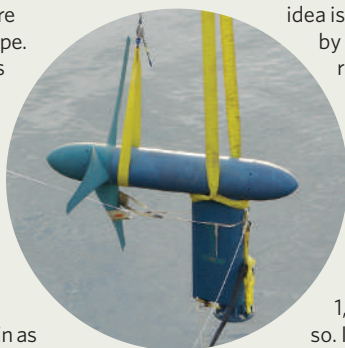
idea is to get electricity by tapping into the roughly 20 °C temperature difference between the surface water in tropical waters and that pumped from depths of 1,000 metres or so. In the 1970s, the

United States invested heavily in such thermal energy; several small plants generating up to 50 kilowatts were built in

Hawaii, although funding dried up in the mid-1990s. Lockheed Martin is now exploring the possibility of building new plants in conjunction with the US Navy.

Finally, the chemical difference between fresh water and sea water holds energy in the form of a salinity gradient that can create water pressure and run a turbine. The global salinity resource is estimated at 220 gigawatts, but the technology to tap this source has lagged behind the others. Statkraft, a Norwegian firm, has now opened a laboratory in Trondheim to look into it. The largest technical barrier seems to be the membrane that maintains a salt concentration between salt water and fresh, according to AEA.

E.C.





Sea snake: Pelamis has been testing its 750-kilowatt wave machine in the Orkney Islands in Scotland.

innovations that will make or break the field. Wind energy, however, can cost as little as 4 cents per kilowatt-hour. The price of solar energy varies with location, but averages around 19 cents per kilowatt-hour for utility installations.

Desperate to diversify their energy supplies and narrow the gap between wave energy and other sources of power, European governments have started to offer subsidies and grants. The Portuguese government pays developers 32.5 cents for every kilowatt-hour they put on the grid. It uses the same strategy to support other renewable sources. In Britain, the Marine Renewables Deployment Fund will give out up to £50 million to push devices to field-testing and commercialization. The United States offers no specific support to wave energy, but a bill to provide \$50 million in funding per year for five years has been introduced in Congress by Representative Darlene Hooley (Democrat, Oregon).

Unsurprisingly, many developers complain that governments haven't been generous enough towards the field. According to a report from the UK consulting firm AEA, the members of the International Energy Agency, which includes nearly every country investing in wave power, spent just 0.3% of their renewable-energy budgets on ocean energy between 1974 and 2004. That's equivalent to US\$800 million adjusted for inflation.

So some private investors have opened their wallets. Nearly three-quarters of Wavestar's recent funding round came from private investors such as the chief executive of Danish industrial giant Danfoss, and several wave-

energy start-ups are publicly traded. Yet Thorpe worries that backers will flee if the field doesn't return money quickly. And with so many firms competing for attention and few side-by-side comparisons available, investors could throw their money at doomed projects. "A lot of people have invested in wave energy without taking a serious look at the economics," he says.

Energy companies with outdated power grids could also dash the hopes of wave-energy supporters. Designed to handle large, centrally located power plants, many utility company networks are unprepared for the dispersed



Bobbing buoys: Finavera's Aqua Buoy used to harvest energy from the waves near Oregon.

nature of renewable energies. "Historically, their role in this was to say 'over my dead body,'" says Thorpe. "The last thing they wanted was a wave-energy device on their network." In some countries, such as the United Kingdom, power infrastructure is minimal in the remote coastlands with the biggest waves. The situation is better in Portugal, which boasts an extensive grid up and down its coast, which wave-energy developers could theoretically plug into.

Go with the flow

Although most environmentalists see wave energy as a valuable green alternative to fossil fuel, opposition has emerged from groups that compete for the ocean. In Oregon, local fishermen wary of being pushed out of waters they have fished for decades initially opposed test projects proposed by Finavera and other developers. "There's no law that says that renewable power supersedes renewable food," says Terry Thompson, a county commissioner in Newport, Oregon, and a retired crab fisherman. After Thompson brokered discussions between Finavera and his county's \$100-million fishing industry, the firm installed its Aqua Buoy out of the way of fishing grounds. Yet Thompson worries about what might happen when companies move from tests to full-scale wave farms.

Surfers have also aired concerns over efforts to cut into waves before they've ridden them. In Oregon, a non-profit advocacy group, the Surfrider Foundation, has filed a complaint with the US government over Oceanlinx's plans to build a wave farm off its coast. And in Cornwall, UK, surfers have complained about a wave-energy farm that is under discussion for instalment off the coast. But, as with fishing, wise planning could side-step any conflicts with surfers, especially in hotspots such as Hawaii. "I wouldn't put it in the north shore of O'ahu," jokes Christensen. "That would be suicidal."

Back in Nisum Bredning, though, the wind-surfers and gulls remain unperturbed, and Steenstrup's most pressing concern is funding. To make the leap to commercialization, the Danish engineer needs to build a Wavestar five times larger than the platform his hopes now rest on. The first prototype will cost \$11 million, he says.

Waves will continue to crash on the shores of Nisum Bredning, Oregon and Portugal no matter what happens in the new round of tests. It should soon be clear whether the technology aimed at moving wave energy forwards can keep the concept afloat.

Ewen Callaway is an intern in Nature's Washington DC office.

See Editorial, page 135.

Time: research necessities make it hard to keep track

SIR — Plans to impose effort-reporting on scientists, as mentioned in your Editorial ‘On the paper trail’ and News story ‘Researchers criticized for poor time-keeping’ (*Nature* **449**, 508 and 512–513; 2007), will be difficult to implement. In practice, it is almost impossible to give an accurate estimate of effort, because scientists are rarely off the job, even when asleep. If they are not actually doing a particular task, they are planning the next, or puzzling over the most recent observation. How should that time be counted? In most research, the edges of a project are only known indistinctly. So in many cases it is difficult to know when one has wandered from one project to another or into an unfunded area.

The definition of ‘100% effort’ causes another problem. This metric tends to be based on a 40-hour week, but not many funded scientists can afford to do so little work — 80 hours (200% effort?) is more common. Also, in these days of tight budgets, how should the project director account for the time spent on writing and revising new grant applications? Under the current funding system, a very large fraction of time is spent on this activity.

Finally, it must be recognized that bootstrapping a new project with the funds of an existing project is built into the system. If there is no venture capital available, new grants have to be built on the backs of existing ones. After all, that’s how they got funded in the first place. When was the last time a new proposal was funded in the absence of any preliminary data?

There may be some abuse in very large labs with multiple sources of funding. Filling in the blanks on applications and enforcing appropriate effort reports should be the norm. But please don’t reduce the time available for research still further by making researchers account for every moment.

Robert J. O’Connell

Brudnick Neuropsychiatric Research Institute,
303 Belmont Street, Worcester,
Massachusetts 01604, USA

Time: accounting problems caused by Caltech system

SIR — You report on a National Science Foundation (NSF) audit of Caltech’s accounting system in your News story ‘Researchers criticized for poor time-keeping’ (*Nature* **449**, 512–513; 2007). The audit cited accounting deficiencies, in particular the handling of professorial effort as “voluntary committed cost sharing” as opposed to “voluntary uncommitted cost sharing”.

Although faculty and staff were following the Caltech accounting practices that were in place at the time, your News story states that researchers “failed to report this to Caltech’s payroll system”. In fact, we did not have that option because of the deficiencies in the system. The audit report did state that “Caltech’s responses, once implemented, should address our audit recommendations”.

Although the NSF report discusses interviews and facts related to several principal investigators and their grants, it does not name individuals. Even though the report does not refer to me by name, your News story associates information in the report with me personally. The NSF auditor, Joyce Werking, incorrectly recorded my statements about my time allocation in the report. The statements about me in your article are erroneous, taken out of context and unfair to me. Although *Nature* did attempt to contact me during the week before going to press, I was away at the time and unable to respond.

Certainly, Caltech and other universities should increase their efforts to align their accounting practices with agency regulations. Also, NSF should improve its methods for gathering and accurately reporting information. And *Nature* could have presented a more informed, responsible and balanced view.

Robert D. McKeown

Department of Physics, Mail Code 106-38,
California Institute of Technology, Pasadena,
California 91125, USA

Turkish science suffers as government vies with law

SIR — Praise for the present Turkish government’s work in fostering good science, in your Editorial ‘Turkey’s transformation’ (*Nature* **449**, 116; 2007), reads to my eyes like a cruel joke in the face of what is really going on in the country. It is true that the current government has increased the budget placed at the disposal of Tubitak, the main research agency under government control. It did so, however, by slashing the budgets of the independent universities.

Tubitak’s new administration was appointed in a manner that was decreed illegal by the Turkish courts. As a result, the Turkish Higher Education Council advised the universities not to have any dealings or communication with Tubitak, because of the legal status of its administration. Therefore, no Turkish scientist can legally use a penny of the increased research budget. That some do use it, in violation of the law, is an act of desperation, because few other sources are left that can be used to sustain research and support students. For example, I had already had two projects accepted when the present

administration was unlawfully appointed but I withdrew them immediately; since then I have had no interaction with Tubitak.

The bad health of Turkish science is further demonstrated by the party-political appointments made by the government within organizations such as the Geological Survey and the Atomic Energy Commission, as well as many senior and junior academic posts, which are not made on the basis of scientific merit. Many of these appointments are being challenged in the courts. Another source of serious headache for Turkish science is the minister of education’s sympathy for ‘intelligent design’, and the way that evolution is taught in our country.

A. M. Celâl Sengör

Istanbul Technical University,
Eurasia Institute of Earth Sciences and
Department of Geology, Faculty of Mines,
34469 Istanbul, Turkey

Explorers’ challenge sunk by Arctic warming

SIR — The so-called Northwest passage (between the Pacific and the Atlantic) has become fully navigable, as mentioned in your News story ‘Arctic melt opens Northwest passage’ (*Nature* **449**, 267; 2007). It is worth recalling that when Roald Amundsen led an east–west expedition through the Northwest passage on the ship *Gjøa*, it took him two and a half years to reach Gjøahaven (now called Gjoa Haven) in mid-August 1905. He wrote in his diary: “The North West Passage was done. My boyhood dream — at that moment it was accomplished. A strange feeling welled up in my throat; I was somewhat overstrained and worn — it was weakness in me — but I felt tears in my eyes.”

In June 1940, the Royal Canadian Mounted Police vessel *St Roch* left Vancouver to sail the passage from west to east. It docked at Halifax on 11 October 1942. In 1944, the *St Roch* returned to Vancouver by a more northerly route, cutting the time down to just 86 days. More recently, icebreakers and ice-strengthened ships have on occasion traversed the route. But by the end of the 2007 melt season, a standard ocean-going vessel could have sailed smoothly through, proof indeed that the Arctic summer ice is rapidly diminishing.

A. J. (Tom) van Loon

Geological Institute, Adam Mickiewicz University,
Maków Polnych 16, 61-606 Poznań, Poland

Contributions to Correspondence may be submitted to correspondence@nature.com. Published contributions are edited. Science publishing issues of interest to authors are regularly featured at Nautilus (<http://blogs.nature.com/nautilus>), where we welcome comments and debate.

COMMENTARY

Rules of engagement

Is there an inherent conflict between public debate and free scientific inquiry? **Patrick L. Taylor** argues that earning public trust is essential to defending scientific freedoms.

Public engagement in scientific research has gone viral. Today, public consultation is invoked for subjects as diverse as war veterans' responses to genomic research, responsible nanotechnology and the use of animal transplants in humans. It has also gone global, as demonstrated by the just-completed consultation on research using animal-human hybrid embryos by Britain's Human Fertilisation and Embryology Authority (HFEA), and the Singapore government's plan to consult on hybrid research and oocyte donation later this year. As groups of citizens mobilize and blog on science issues — from patenting to public health and drug development — it is time to reconsider the ground rules for public debates on science.

Public engagement today can directly affect research. It has gone beyond debating controversial social impacts of applied science and technology such as should this nuclear power plant be built or that pesticide be approved. It now delves into research methods that are unique to the laboratory, such as somatic-cell nuclear transfer and hybrids.

Sceptical scientists fear that scientific means and ends might be determined by referendum, and that public debate will irrationally restrict free scientific inquiry. The occasional shrillness of public comment, or its seeming ignorance of scientific facts, can trouble scientists who are weary of the politics and misunderstandings they see plaguing important research; it can lead researchers to question the value of public engagement.

Some would prefer policies to be decided by government bodies alone. In other words, yes, the public has a right to decide whether it would fund a new atom bomb, but no, the public has no legitimate stake in limiting scientific freedom and professional judgment about research aims and methods. Yes, the public has a right to deliberate on certain aspects of scientific policy, but through government representatives, to ensure that public ignorance is disarmed, and scientists can advise government on scientific fact.



In the public mind there is no such thing as 'pure' science.

This position is mistaken. It was legislative bodies and government executives that acted so irrationally in the Terri Schiavo case, in which a Florida woman in a vegetative state became the subject of politicized battles. Three US surgeon-generals have testified about presidential tampering with science policy. And although fears of the politicization of science are easily overblown, the time may come — perhaps it is here already — when direct public involvement may be the best protection against politicians who are selectively unfriendly to scientific freedoms.

Public involvement is inevitable, whether invited or not. Sheila Jasanoff of Harvard University in Cambridge, Massachusetts,

has shown¹, in her comparative political study of biotechnology in the United Kingdom, Europe and North America, that where public engagement is insufficiently available formally, it will occur informally, through public protest; market choices, such as consumer rejection of genetically modified foods; or new political structures, such as environmental movements.

So the question is not whether public involvement should occur. The questions are how, with what impact, in what areas, and with what level of trust and precision? Some forms of engagement, as in California's launch of stem-cell funding, have been successful: the engagement produced a social consensus sufficient for action, based on reasonably evaluated truths, which supported legitimate scientific work. Other forms have been less successful, increasing scientists' frustration and public distrust. How should public engagement proceed, to be productive, credible and precise?

Undermining ourselves

We should start by recognizing where we in research organizations — scientists, administrators, lawyers, ethicists — harm public trust and engagement, through discrediting our own and others' ability to be persuasive participants.

When scientists advise governments, or publish, they often demand that the public, peers and editors treat them as disinterested, when in fact — in simple financial terms that the public understands — they are not. Scientists are surprised when the public discounts their

views. On advisory committees, some scientists want to be funded by interested companies, yet they want to be publicly perceived as uniquely disinterested. No matter how much we believe this, we cannot force the public to accept a combination that ordinary experience convinces them is suspect. Some lawyers and public figures polarize through exaggeration, whereas some ethicists' credibility

"Nearly half of the public feared the slippery slope of what scientists might do next."

is sacrificed to sophistication and inaccessible arguments. Together, such 'experts' convince the public that we cannot be trusted to arrive at a reliable consensus rooted in shared societal values, common sense and public intuitions.

We know a lot about what the public fears from science and expects from responsible policy, and what forms of dialogue are effective. The HFEA consultation teaches us², again, what research surveys have taught us before³⁻⁵. If in framing consultations we ignore that knowledge, we suggest that responsible self-regulation, and concerns about unforeseen consequences, social impact and disinterestedness, have not occurred to us. Instead, we must explicitly address the prevailing perception that "scientific research does not pay enough attention to moral values"⁶ and recognize that trust and character, as much as subject expertise, are critical to being persuasive.

The best sort of public consultation is flexible, including deliberative methods, surveys and interactions validated by social scientists. But even these methods can lead to frustrating outcomes. The HFEA consultation delivered what scientists wanted: UK licences for hybrid research will be considered on a case-by-case basis.

On the broad question of the desirability of creating chimaeras, the consultation process admitted that its attempts at public engagement "were unsuccessful, as the public are reluctant to form a committed view without understanding the full context of the research proposals". Queried generally about whether licences should be granted, nearly half of the public feared the slippery slope of what scientists might do next, and nearly half had concerns about meddling with nature. Many, it appeared, felt "far removed" from biomedical research.

Question further

The HFEA rightly used a combination of approaches, including representative opinion polls, deliberative sessions, written consultations and public meetings. But what if one went beyond asking the public open-ended questions about which types of embryo research are personally acceptable, or what types of licences should be given?

Open-ended questions do elicit important responses, but imagine asking additional questions that demonstrate the questioner's awareness of known public concerns, such as the needs to provide careful oversight, to be sensitive to runaway consequences and to offer precise alternatives based on the best professional judgment about solutions to reassure public fears. Asking, without conditions, whether

licences should be granted is less precise than asking for public reaction to delineated alternatives. I believe that, if such reactions had been sought, more of the public would have endorsed the HFEA's ultimate decision to conduct case-by-case reviews.

In thinking long-term about public engagement — by which I mean a range of activities, not just direct consultation — here is what I think we should do.

First, when soliciting public engagement, we must be clear what the public is being asked to contribute. We should invite perceptions of how society and quality of life will be affected under alternative scenarios, yet avoid relying solely on open-ended questions uninformed by potential



Public debate is no longer limited to the immediate effects of research.

solutions. In seeking to understand public perceptions and engage in open exploration of complex issues, engagement must build public confidence. This confidence will come with the knowledge that unexpected consequences and personal and social effects will be considered and transparently addressed, because this is where the public believes we fail.

If we ask question that are too conclusory — such as whether a power plant should be built next door — to a public unaware of how its concerns might actually be addressed, we

"Scientists should abandon the head-in-sand hope, in this Internet age, that we can return to some golden era of politically insulated scientific seclusion."

underestimate the public, and it will respond by underestimating scientists' good sense and good faith. A request for public input should distinguish factual points established by scientific methods and validated data from public

interpretation of the meaning of those facts and goals. It should exchange ideas on the way that scientific objectives and solutions to public concerns can best be married. Collective deliberation is essential. Just before her death, the celebrated biologist Anne McLaren succinctly said this: "Education of the public is not enough ... Let us aim for an informed dialogue, and let us hope that the media

will do their best to make sure that nothing is 'lost in translation'."

Second, we ought to encourage the public to share in understanding the wonder of scientific developments. Physicists have done this much better than biologists, thoroughly engaging the public in mysteries of space and time. Life scientists do some of this, around ecology, evolution, health and hopes for promised cures, but not enough. We need to do much more, engaging people's imaginations in what development, genetics, molecular biology and physiology mean for knowledge, community and our world-view. There is a new world discovered every day in the biosciences, and we are not taking full advantage of the part that public imagination and fascination can play in supporting natural science for its own sake.

Maintain our neutrality

Third, we need to respect and actively support the neutrality, credibility and independence of bodies of scientific expertise, particularly advisory committees and academic journals. This means preserving the credibility of individual scientists, as well as that of the independence of journals and committees, by increasing transparency and avoiding personal conflicts of interest. It also means limiting ourselves to honest criticism, and ensuring that debates about scientific reporting in the media remain focused on objective scientific review of data and conclusions, rather than descending into partisan attacks. We need to challenge more consistently the erroneous statements made by politicians of what is scientifically known, especially through unflagging public responses by scientific and professional societies.

Fourth, we must be continuously creative in public engagement. The whirlwind of scientific and biotechnological change must be met with complementary engagement, in which people's need to know and evaluate can be grounded in intelligent understanding of possible solutions to their concerns. Scientists should abandon the head-in-sand hope, in this Internet age, that we can return to some golden era of politically insulated scientific seclusion. Abandoning real public engagement is not ending it. It is abandoning it to the very forces scientists fear. ■

Patrick L. Taylor is at Children's Hospital Boston and Harvard Medical School, Boston, Massachusetts 02115, USA.

1. Jasanoff, S. *Designs on Nature: Science and Democracy in Europe and the United States* (Princeton Univ. Press, New Jersey, 2005).
2. www.hfea.gov.uk/docs/2007-09-05_Authority_Paper_Hybrids_and_Chimeras_Findings_of_the_Consultation_396.pdf
3. www.ipsos-mori.com/polls/2004/pdf/ost.pdf
4. www.vcu.edu/lifesci/images2/lis_survey_2006_report.pdf
5. www.wellcome.ac.uk/assets/wtx032159.pdf
6. www.nsf.gov/statistics/seind06/c7/c7c.htm

COMMENTARY

Benchmarks for ageing studies

The hopes for improving human health during ageing are largely based on studies with animal models. But **Linda Partridge** and **David Gems** ask if we are learning the right lessons from ageing research.

Ageing is complex. Diverse molecular and cellular damage accumulates over time, causing functional failure in different tissues. The process can seem to be intractable to experimental analysis or medical intervention — a pessimistic view overturned by the discovery of genetic mutations that can extend healthy lifespan in laboratory model organisms¹. Perhaps even more surprising, these genetic effects seem to be conserved over large evolutionary distances, because mutations in related genes can extend lifespan in the yeast *Saccharomyces cerevisiae*, the nematode worm *Caenorhabditis elegans*, the fruitfly *Drosophila melanogaster* and the mouse^{2,3}.

Thus, despite their very different physiology and lifestyles, the simpler and shorter-lived yeast, worm and fruitfly can be used to help understand mammalian ageing. Mutations that extend lifespan can also reduce the impact of ageing-related diseases, including cancer, cardiovascular disease and neurodegeneration¹. This raises the prospect that a single, underlying ageing process may act as a common risk factor for multiple diseases. Drugs that slow down ageing could therefore reduce the impact of many of the ageing-related diseases simultaneously.

Yet the biology of ageing is a young field with emerging pitfalls (see table, page 167). Genetic mutations that increase longevity will generate exciting headlines, but experimental findings are only as good as the experimental design. For example, neglect of genetic background effects can lead to misleading or hard-to-interpret results⁴. If researchers are rescuing a lab strain from the effects of a disadvantageous environment or genetic background, then we may be learning less about human ageing than we think. It is critical to learn the right lessons from this work if the field is to flourish and provide real insights into human ageing.

The model-organism approach has already told us much about other processes, such as development, immunity and behavioural traits. But compared to many developmental traits, such as the number of eyes or limbs, lifespan is more sensitive to the genetic make-up of different strains and to the environment. For instance, a mutation always occurs in a genetic background — the rest of the genome — and in some cases lifespan differences vanish when



WELLCOME IMAGES

The lifespan of model organisms (such as fruitflies) is affected by the lab environment.

the background is made identical in mutants and controls⁴. Often, organisms of the same strain, but from different laboratories, actually differ in lifespan. A goal of longevity research is to identify gene products that control lifespan and that could be good drug targets; however, reported effects of drugs on lifespan are themselves not always reproducible⁵.

Understanding the reasons for all this variability is a key challenge for the field. We need to investigate the robustness and repeatability of findings, to better control experimental variables and to establish some benchmarks for experimental work on lifespan.

One immediate problem for measurements of lifespan is that death can be a surprisingly slippery endpoint. When measuring population lifespan, it is critical to discriminate between accidental and ageing-related deaths, and to exclude the former, which can be tricky. Flies can meet with accidental death from sticky food products and worms can die prematurely when young worms hatch inside their parent and devour it from within.

Identifying the cause of death is therefore a somewhat subjective process, vulnerable to potential bias. So it is wise to work in 'blind' conditions — ignorant of the identity of the experimental treatment and according to stated criteria. Different observers should be

able to obtain similar results. For mice, animals can be excluded from a study for veterinary reasons, and this should also be done according to a standard set of criteria, and reported in the literature. Such precautions might seem obvious, but they are routinely overlooked.

Variance within strains

The most pervasive problem in lifespan research is the presence of uncontrolled genetic differences between strains under study. Substantial natural genetic variation can exist across the genome among different individuals and strains. A mutant gene arose, at some point, in a single individual. That individual had a particular genetic background, which will be passed to progeny along with the mutant gene.

To detect the influence of a specific mutant gene on lifespan, it is essential to place it in a genome that is otherwise identical to that of the strain used as the control. This is best done by repeatedly crossing carriers of the mutation with a standard genetic strain (Fig. 1, overleaf). In flies and mice it is often necessary to bring two different mutations together to produce the desired gene expression, thereby also crossing the two genetic backgrounds in which the mutations reside. This will introduce uncontrolled genetic variation unless both strains have been previously backcrossed to the same control, and hence have the same genetic

"Ultimately, the findings of ageing research need confirmation in humans."

background as each other. For mice, where new mutants are usually introduced into a mixed genetic background for technical reasons, it can take years of backcrossing to establish the mutation in the control strain.

An unfortunate and under-appreciated fact is that backcrossed strains can diverge genetically from each other quite rapidly. Spontaneous mutations occur regularly, causing gradual genetic divergence between strains. In addition, the presence of a mutation can lower reproductive success, so that natural selection acts on genetic variation elsewhere in the genome, causing it to diverge, often rapidly, from the genome of the control strain. The effects of a mutation can therefore lessen with time. For example, the yellow mutation in *Drosophila* makes the fruitfly a golden colour and also greatly impairs the courtship behaviour of male fruitflies. Female fruitflies from long-standing yellow stocks are more receptive to the courtship of yellow males, presumably because natural selection has acted to prevent the females from failing to mate.

Strains can also diverge genetically in the lab because low numbers of individuals lead to inbreeding. This allows natural harmful genetic variants to become more common, resulting in lowered survival and fertility. This is particularly problematic whenever inbred strains are crossed with each other, for instance to produce targeted changes of gene expression, because hybrid offspring typically have a longer lifespan than their parents. Thus, one should not assume that strains that were backcrossed several generations ago have remained genetically homogeneous; regular backcrossing is required to achieve this.

An imperfect world

Genetic divergence between strains over time is also problematic when it comes to comparing results from different laboratories. In a perfect world, laboratories would all use genetically identical strains to ensure direct comparability of results and to eliminate uncontrolled sources of genetic variation. However, the reality is that laboratory stocks can differ substantially in lifespan, even when ostensibly from the same strain. For instance, the *C. elegans* strain N2, originally isolated from mushroom compost, is treated as the wild-type by convention. Yet a comparison of 'N2' strains from different laboratories revealed median lifespans ranging from 12 to 17 days⁵. This problem can be partly addressed by freezing strains that are not in use, to minimize divergence, but this is a major weakness of using *Drosophila*, for which attempted methods of cryo-preservation have been largely unsuccessful. To improve repeatability in fruitfly studies, laboratories may therefore need to share strains immediately before undertaking measurements.

The variable longevity of strains raises a question that also applies to human ageing. What constitutes a 'normal' lifespan? In the N2 worm study described above, only the longest-

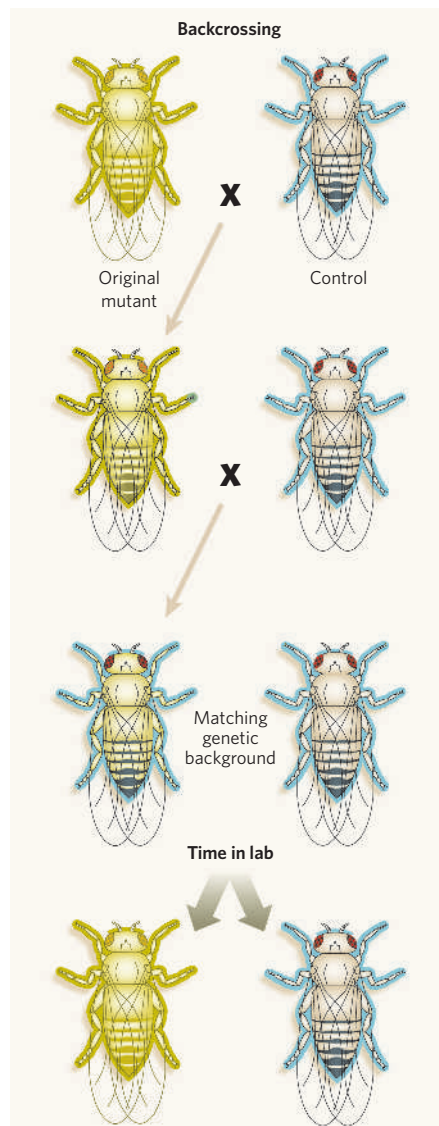


Figure 1 | Backcrossing model organisms. Repeatedly backcrossing mutants with controls will prevent genetic divergence and create individuals with identical genetic backgrounds.

lived of the laboratory strains had a lifespan resembling that of wild strains⁶; the rest had accumulated life-shortening mutations during laboratory culture. This shortening of lifespan in lab strains is also seen in *Drosophila*⁷. The results for mice are less clear-cut, but suggestive of slower-maturing lab strains⁸. An additional problem with mice is that inbreeding can shorten lifespan, and the standard lab stock are deliberately inbred to produce genetic uniformity within strains. This problem can be avoided by the use of mice that are the product of a standard cross between multiple strains, which produces a standard but outbred mouse⁹. For the invertebrates, backcrossing to wild strains and the use of husbandry methods that maintain wild-type lifespans could help avoid declines in lifespan in the laboratory.

More indirectly, genetic variation among strains can cause them to respond differently to mutations and to lab conditions. It is important to understand whether this genetic varia-

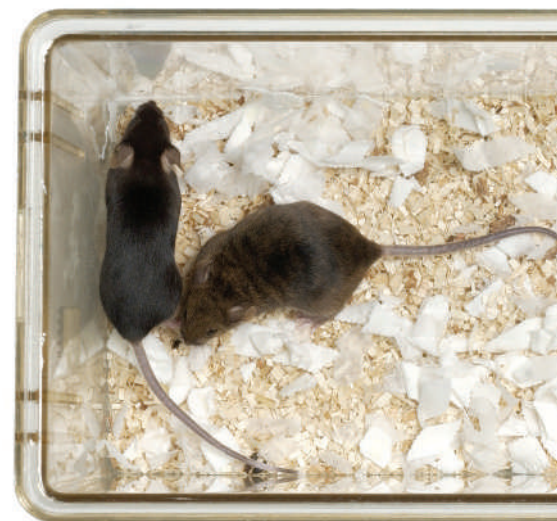
tion is essentially normal, and if so, whether it is part of natural ageing processes, or instead the result of some laboratory artefact. For instance, in most strains of yeast, over-expression of the *SIR2* gene extends lifespan, but one strain is completely unresponsive¹⁰, for reasons that are not understood.

In other cases the interpretation is clearer. A meta-analysis of studies of *Drosophila* in which genes encoding antioxidants had been over-expressed showed a clear pattern: the lifespan-extending effects were greatest in experiments with the shortest-lived control strains, with no effect seen with the longest-lived controls¹¹. These data suggest that over-expression of the antioxidant gene restored normal lifespan in strains whose lifespan had been shortened by laboratory culture. Similarly, dietary restriction can produce substantial increases in mean and maximum lifespan in laboratory-adapted rodents. But a recent study found no increase in mean lifespan in wild-derived mice, which had longer lifespans and lower food intake — although there was a small increase in maximum lifespan and a decreased incidence of tumours¹². Disentangling the effects of natural genetic variation from the effects of laboratory culture is an important task for the future.

External variation

Environmental sources of variation are equally problematic. Laboratory environments are in some ways more benign and in others more dangerous than those in nature. Study conditions can cause the outcome to vary, and understanding this source of variation is hugely important for applying results from model organisms to humans. For example, the impact of natural enemies, including pathogens, is greatly reduced in the lab, and there is a superabundance of food and little opportunity for exercise.

Food can sometimes be harmful. *C. elegans* is generally fed on another model organism, the bacterium *Escherichia coli*. However, in nature the worm eats soil microbes, such as slime moulds, and *E. coli* has been shown to be mildly



EXPERIMENTAL FACTORS AFFECTING LIFESPAN STUDIES

Factors affecting lifespan	Yeast	<i>C. elegans</i>	<i>Drosophila</i>	Mouse
Subjective decisions about age at death	Problems assessing if mother cell divided once or twice	Premature deaths e.g. caused by rupture of uterus	Accidental death caused by sticking to food products	Variable veterinary criteria for excluding mice
Genetic background can affect lifespan	Strains differ in lifespan	Lifespan shorter in some lab strains than in wild strains	Strains differ in lifespan. Flies cannot be frozen	Strains differ in lifespan
Reduced lifespan through inbreeding	Unknown	Not applicable. Worms are self-fertilizing hermaphrodites	Shorter lifespan for inbred offspring; longer lifespan for subsequent hybrids	Shorter lifespan for inbred offspring; longer lifespan for subsequent hybrids
Genetic adaptation to laboratory conditions	Unknown	Unknown	Lifespan shortens during lab culture	Some evidence that lab strains are shorter-lived
Laboratory environment	Variations in nutrient supply can affect lifespan	Bacterial food supply can be pathogenic and vary between laboratories	Variation in food supplies or recipes and use of mixed-sex populations	Variations in bedding, food supplies and husbandry can affect lifespan

KEY: ■ Moderate problem ■ Significant problem ■ Important problem. Weightings reflect our impressions of the extent to which these factors have posed potential or actual problems for existing studies.

pathogenic to *C. elegans*. If the worms are fed a different bacterium, *Bacillus subtilis*, which is arguably more similar to the natural bacterial diet of the worms, their lifespan is extended and they respond less strongly to life-extending mutations¹³. At least some of the increase in lifespan seen following dietary restriction in worms could therefore result from reduced exposure to food pathogens. Some laboratories use 'disabled' bacteria that are alive but cannot divide, to avoid this complication.

Reproductive behaviour can also affect lifespan. In *Drosophila*, the presence of males can greatly shorten the lifespan of females and vice versa. It is thus important that any mating regime is standardized when measuring lifespan, unless mating effects are specifically being studied, and the simplest way to achieve this is to work with the sexes separately.

Given these many factors, we recommend that environmental variables are clearly specified when describing methods, and wherever possible, procedures should be standardized, both during the rearing of strains and the measurement of their lifespan. We should also be aware that variables that seem unimportant to researchers may still affect the experimental subjects. For example, mice are highly sensitive to smell and to noise, which will vary between

laboratories and are difficult to control.

Ultimately, the findings of ageing research need confirmation in humans. The main goal of studies with model organisms is to generate hypotheses about the mechanisms of human ageing. Humans in many industrialized societies have some similarities to laboratory model organisms. They are largely freed from the burden of infectious diseases, they are surrounded by a superabundance of food, many of them take little exercise and they voluntarily restrict their reproductive rate. Unlike laboratory model organisms, they have not yet undergone many generations of adaptation to this regime. So, rather than studying only lab-adapted strains, wild strains of model organisms examined under laboratory conditions may provide one relevant comparison to human ageing. For mice, which are likely to undergo considerable stress during adaptation, work under controlled, but semi-natural, conditions could be revealing.

Working on humans

Work has also started in human populations on genetic associations with lifespan, ageing-related diseases and other late-life traits. Studying the genetic basis of lifespan in humans presents some peculiar challenges beyond those normally associated with determining the genetic basis of complex traits. The characteristics of older people, by definition, do not become apparent until they are old. By that time, many of the obvious control groups (siblings, spouses) are no longer available for study. The accumulation of environmental exposures during a long life — including the pre-natal environment — could be important, but unknown, factors in determining late-life health and survival. The genetic composition of populations in specific geographic areas can also change with time through immigration, resulting in a mixture of sub-populations with multiple genetic differences, making careful choice of control groups essential.

Studies of twins, combined with long-term studies of the health of individuals, offer one way of circumventing some of these

difficulties. They have shown that genetic influence on mortality before the age of 60 is small and increases after that age, with genetic differences accounting for about 25% of the variation in lifespan¹⁴. This natural genetic variation is comparable to what has been observed in model organisms. But we know that in some animal studies we can get a doubling of lifespan from a mutation in a single gene, and there may

therefore be untapped potential for modifying healthy lifespan in humans.

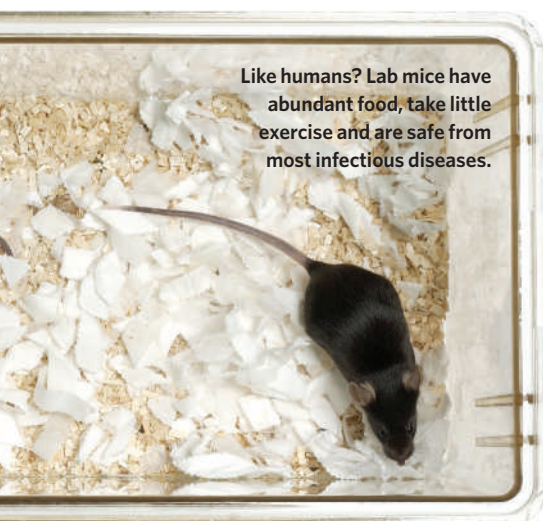
As the research field of genetic effects on ageing and lifespan starts to mature, the pitfalls and their remedies are becoming apparent. Aside from the need to make new discoveries, the key future challenges are to understand sources of variation, deliver robust and repeatable findings and to make the studies of model organisms as relevant as possible to humans. Understanding sources of variation is challenging, but once understood in context, they will enrich our knowledge of the complex process of ageing.

Linda Partridge and David Gems are at the Centre for Research on Ageing, Department of Biology, University College London, The Darwin Building, Gower Street, London WC1E 6BT, UK.

1. Kenyon, C. *Cell* **120**, 449–460 (2005).
2. Piper, M. D. W., Selman, C., McElwee, J. J. & Partridge, L. *Drug Discov. Today: Dis. Mod.* **2**, 249–256 (2005).
3. Smith, E. D., Kennedy, B. K. & Kaerberlein, M. *Mech. Ageing Dev.* **128**, 106–111 (2007).
4. Toivonen, J. M. et al. *PLoS Genet.* **3**, e95 (2007).
5. Bass, T. M., Weinkove, D., Houthoofd, K., Gems, D. & Partridge, L. *Mech. Ageing Dev.* **128**, 546–552 (2007).
6. Gems, D. & Riddle, D. L. *J. Gerontol. A* **55**, B215–B219 (2000).
7. Sgró, C. M. & Partridge, L. *Am. Nat.* **156**, 341–353 (2000).
8. Miller, R. A., Harper, J. M., Dysko, R. C., Durkee, S. J. & Austad, S. N. *Exp. Biol. Med.* **227**, 500–508 (2002).
9. Miller, R. A. & Nadon, N. L. *J. Gerontol. A* **55**, B117–B123 (2000).
10. Kaerberlein, M., Kirkland, K. T., Fields, S. & Kennedy, B. K. *PLoS Biol.* **2**, E296 (2004).
11. Orr, W. C. & Sohal, R. S. *Exp. Gerontol.* **38**, 227–230 (2003).
12. Harper, J. M., Leathers, C. W. & Austad, S. N. *Aging Cell* **5**, 441–449 (2006).
13. Garsin, D. A. et al. *Science* **300**, 1921 (2003).
14. Christensen, K., Johnson, T. E. & Vaupel, J. W. *Nature Rev. Genet.* **7**, 436–448 (2006).

Acknowledgements We thank Brian Kennedy, Richard A. Miller and Scott D. Pletcher for helpful comments.

WELLCOME IMAGES



BOOKS & ARTS

The twentieth century in a nutshell

A sad and salutary tale of success, commerce, hubris, razzmatazz and scientific heroism.

American Chestnut: The Life, Death, and Rebirth of a Perfect Tree

by Susan Freinkel

University of California Press: 2007.

294 pp. \$27.50, £16.95

Colin Tudge

Prominent among the many riches that successive waves of human beings discovered in North America was *Castanea dentata*, the American chestnut. This tree could be relied on to produce an enormous crop of edible nuts every year, unlike the oak and beech. It was also huge — more than 5 metres in diameter — and, although not as strong as oak or as pretty as walnut, it supplied timber for anything from telegraph poles to coffins and even, at a pinch, for pianos. The tannin in the wood stopped it rotting or could be extracted to treat leather, leaving fibre for making paper.

The American chestnut grew abundantly. It was said that a squirrel could jump from chestnut to chestnut without touching the ground, all the way from Georgia to Maine. And, as Susan Freinkel remarks in *American Chestnut*, it “would pass over 1,094 places along the way with ‘chestnut’ in their names”. In the Appalachian mountains, the tree’s main stronghold, it supported an entire economy and culture. People ate the nuts and let their pigs and cattle loose to feed on them. They sent trains full of nuts and timber to the eastern cities. Ten million wild turkeys gorged on the Appalachian chestnuts. And the trees supported the now-extinct passenger pigeon — so numerous in the late nineteenth century that single flocks took several hours to pass overhead.

Unfortunately, European Americans from the early nineteenth century onwards have tried to improve on the native chestnut. They introduced other species of *Castanea* that had bigger and fleshier nuts. Former US President Thomas Jefferson favoured the European species; others went for Asian types. And with the Asian trees came the blight. These trees were resistant, but the American species was not. The fungus was originally identified as the genus *Cytospora*, then reascribed to *Diaporthe*, then to *Endothia*. In 1978 it wound up in *Cryphonectria*, where it remains as *Cryphonectria parasitica*.

The first signs of disease appeared in 1904 in what is now the Bronx Zoo: dying leaves, then canker, then death. The Bordeaux fungicide mixture that had worked so well in French vineyards was of no use. By 1908 the disease was out of hand, and by 1911 it had spread to more than ten states. One of these, Pennsylvania, created a ‘firewall’ by destroying all of its chestnuts in an unsuccessful attempt to contain the disease, spending \$275,000 (about \$5 million in today’s money) and inflicting much misery. They may even have signed



The American chestnut was wiped out by fungus.

the American chestnut’s death warrant by wiping out those trees that might have founded a resistant generation. By the end of the 1920s, the wild trees had all but gone.

Ever since, various enthusiasts and professional institutions have been trying to stage a chestnut come-back by means of three strategies. One is conventional breeding — crossing native American and resistant Asian trees to combine the best of both, or backcrossing resistant hybrids with pure Americans to produce second-generation hybrids that are 75% American and 25% Asian, hoping that the Asian contribution includes the genes for resistance. Hypovirulence is another approach,

infecting the blight fungus with a virus (discovered by chance in Italy) that greatly reduces its vigour, so that even American trees recover from its attacks. Blight-ridden American trees have been saved by infecting the active fungus with virus-ridden fungus. The third approach is to use genetic engineering to introduce genes for blight resistance — including synthetic ones. This is difficult because chestnuts — in contrast to, say, poplars — grow poorly in culture. Like the giant panda, these trees seemingly resist the efforts of conservationists.

The story of the American chestnut encapsulates the history of the twentieth century. We began the century with a tree that could do everything, and all we had to do was to treat it with respect. Instead, the entrepreneurs undertook an exercise in hubris, trying to improve on the unimprovable with sublime disregard for the complexity of nature. Then came the political razzmatazz: much posturing and rhetoric, and significant consignments of public money — all well intended but, in the end, horribly misguided. It would have been better to have done nothing (which is difficult for politicians). Then there have been decades of scientific enterprise by heroic individuals, some of whom sacrificed careers and income for chestnut breeding.

The result? To celebrate Arbor Day in 2005, President George W. Bush planted a hybrid chestnut outside the White House that was 75% American; it may have enough resistance to fend off blight but probably not the genetic wherewithal to grow to American size. The president told us that planting trees “is good for the economy and good for the environment”.

Latest reports indicate that the White House tree is not thriving.

American Chestnut is a parable for our time: a sad and salutary tale, beautifully told by US science journalist Susan Freinkel. Parables lend themselves to different interpretations. Freinkel says, “The American chestnut, successfully restored, would confirm that we have the power to make things right.” A potentially dangerous conclusion, as only with large slices of luck do we get away with our excesses. The lesson to be learned from this majestic tree, I suggest, is that we should aim to leave well alone. ■

Colin Tudge is the author of *The Secret Life of Trees* and *Feeding People is Easy*.

DK LIMITED/CORBIS

TELEVISION

Dover trial documentary screens

Judgment Day: Intelligent Design on Trial
produced by NOVA & Vulcan Productions
for PBS

broadcast on 13 November on PBS

Adam Rutherford

Conflict between religion and science has rarely been of more concern. Whereas the rhetoric of Richard Dawkins, Sam Harris and others has little measurable effect, the outcome of a juryless trial in a two-bit Pennsylvania town in 2005 had a profound impact on how science is taught throughout the United States, and beyond. The parents of 11 pupils at the only high school in Dover launched a legal challenge to prevent the teaching of intelligent design as an alternative to evolution by natural selection. There followed thefts, fires, death threats, a media sensation and a robust verdict.

Hot on the heels of several books chronicling *Kitzmiller vs Dover*, comes *Judgment Day*, a rigorous television documentary from the producers of the prestigious science series *Nova*. This two-hour montage of interviews and reconstructions, to be shown on the Public Broadcasting Service (PBS) in the United States, features all the main players, bar one. Michael Behe, inventor of the specious meme “irreducible complexity” and guiding light of the intelligent-design movement, refused to participate. His testimony — the cornerstone of the defence — revealed a definition of science so loose that it includes astrology.

Herein lies the dramatic challenge of retelling this important story. The feebleness of the

intelligent-design case, and the overwhelming strength of the prosecution in systematically deconstructing it, render the verdict clear just minutes into the programme. The makers of *Judgment Day* inject tension with eyewitness accounts from the people of Dover, and home-video footage of raucous school board meetings shows how passionate and divided this small community became. It works: it is inspiring to hear parents and educators, such as Sunday school and physics teacher Bryan Rehm, recount how they refused to be steam-rolled into bringing religion into the science classroom.

Judgment Day gracefully avoids ridiculing intelligent design for the pseudo-intellectual fundamentalist fig-leaf that it is, by simply showing how the protagonists shot themselves in the foot. They plead for the teaching of “alternative theories” to strengthen children’s education (the misguided sentiment picked up by President Bush). But subpoenaed drafts of a textbook that promoted intelligent design reveal that the word ‘creationists’ was simply replaced with ‘design proponents’. In one instance, this alteration was made so hastily it caused the misprint ‘design proponentsists’, satirized by the prosecution as the transitional verbal fossil linking creationism to intelligent design.

At times in this overlong show, one feels almost sorry for the intelligent-design team, they’re so inept. And then you remember that its champions take comments from scientists out of context and even lied under oath.

The judge at the centre of the dispute, John E. Jones III, is the hero of the piece. When this republican lutheran, appointed by the commander-in-chief himself, was assigned to the case, the pro-evolution lobby feared they had been dealt an unsympathetic ear. Happily, the measured, dry-witted Jones was fascinated by the comprehensive scientific case for darwinian evolution. He handed down a damning judgment that intelligent design is not science, and that its teaching is a violation of the cherished First Amendment. As a result, *Time* magazine rightly put him in their 2006 list of the world’s 100 most influential people.

Intelligent design has not gone away. Next February, cinemas will be showing the pro-intelligent-design film *Expelled: No Intelligence Allowed*, written by comedian Ben Stein. Richard Dawkins, prominent anti-creationist blogger P. Z. Myers, and others claim the producers duped them into appearing.

But the *Kitzmiller vs Dover* verdict, matched this September with the outlawing of intelligent design in the UK national curriculum, marked the official neutering of this unpleasant, sneaky movement in much of the western world. *Judgment Day* is just the sort of thoughtful programming that celebrates how sensible people — faithful and otherwise — can use science and reason to combat fundamentalism.

Adam Rutherford is podcast producer for *Nature*.

For more information on the documentary, see www.pbs.org/wgbh/nova/id/



Judge Jones's
damning verdict
neutered the
intelligent-design
movement.

NOVA/PBS

NIBSC/SPL



Escherichia coli bacteria and the skull of Phineas Gage, whose injury profoundly altered his personality: do model organisms, case histories and computer simulations have interesting similarities?

Comparing modes of inquiry

Science Without Laws: Model Systems, Cases, Exemplary Narratives

edited by Angela N. H. Creager, Elizabeth Lunbeck & M. Norton Wise
Duke University Press: 2007. 287 pp.
\$22.95

Carlos Martínez del Río

What do fruitflies, computer simulations and the daydreams of a psychoanalysis patient have in common? A lot, according to the editors of *Science Without Laws*. This essay collection contends that there is telling overlap between model organisms, mathematical models and exemplary narratives — such as the accounts of patients beloved by neurologist Oliver Sacks. As the economist and historian Mary Morgan argues, all these model systems that scientists use to explore the world are themselves objects to be inquired into, as well as being objects with which to inquire. So much so, indeed, that philosophers have begun to discover and catalogue them, as in this book. Model systems are, in effect, the species in the tangled bank of science today.

Science Without Laws has three sections: biology, simulations and the human sciences. Each chapter analyses an exemplar and illustrates its value as a model. The word 'model' is construed much more broadly here than in other similar books, such as Ronald Giere's *Science Without Laws* (University of Chicago Press) or Mary Morgan and Margaret Morrison's *Models as Mediators: Perspectives on*

Natural and Social Science (Cambridge University Press) both published in 1999.

The collection thus reflects on science's elaborately constructed descriptors and test beds, and tries to discern their dependence on each other. Morgan's superb chapter on the prisoner's dilemma in game theory illustrates how a model can, in symbiosis with economic narratives, shake the theoretical principles of a discipline — much as an invasive species can disrupt an ecosystem. In an otherwise very nice chapter, Josiah Ober attempts to find analogies between Athenian democracy and laboratory mice. Not surprisingly, this is more of a stretch.

With the exception of the book's beginning and end, there is little cross-fertilization between chapters. This lack of exchange is a pity, as we shall probably learn the most about how we know by creating a comparative natural history of modes of inquiry. An opportunity is missed, for instance, for interplay among the chapters on model organisms in biology and on simulations in geology and atmospheric science. Naomi Oreskes and Amy Dahan Dalmedico emphasize how scientific practices in atmospheric science shape and are shaped by scientists interacting with each other and with their patrons. Similarly, the study of the nematode worm *Caenorhabditis elegans*, the plant *Arabidopsis*, the bacterium *Escherichia coli* and the like have led to huge changes in the workings of biologists and in the expectations of their governments and corporate financiers.

But the fact that modes of inquiry evolve in a sociological theatre is largely absent in the essays on flies and worms.

There is also a gulf between the biology and simulations sections and the one on the human sciences. These last chapters weaken the opportunity for a theme that could unify *Science Without Laws*. Discussing worms, Jane Albert Hubbard makes the point that the genealogical structure of life allows model organisms to act both as individually interesting cases and as sources for general inferences and implications. In contrast, the chapters that conclude the book suggest that such a flexible role is more difficult for the case studies of psychoanalysis and history. In her afterword, Morgan is too generous in seeing a hint of exemplarity in John Forrester's detailed account of the trials of a psychoanalytical patient and in Carlo Ginzburg's pocket history of a failed Dutch merchant.

Taxonomists are either lumpers or splitters. The authors of this book are lumpers: they seek commonalities. But the diversity of science also requires judicious splitting. Our experience of trying to use the ways of a single scientific discipline, such as physics, as a template for correct thinking suggests that forcing too much epistemological common ground can be unwise. ■

Carlos Martínez del Río is professor of zoology and physiology at the University of Wyoming, Laramie, Wyoming 82071, USA. His latest book is *Physiological Ecology*.

H. DAMASIO ET AL. SCIENCE 264, 1102–1105 (1994), REPRINTED WITH PERMISSION OF AAAS

Dance of the forest

Biome

choreographed by Jodi Lamask
premieres on 10 November in La
Gran Via, San Salvador

Michael Hopkin

To a literalist, dance is a celebration of the human body. Of course, it can also allude to other organisms — even, in the case of San Francisco-based choreographer Jodi Lamask, to the relationships between them. *Biome*, a new work by Lamask's company Capacitor, has its premiere in San Salvador this week. Like her previous pieces, it began with research scientists — here including the tropical-tree ecologist Nalini Nadkarni — sharing their insights.

The result, Lamask stresses, does not attempt to convey scientific concepts; it uses the ideas as a jumping-off point. Audience members pre-occupied with looking for metaphors will find themselves frustrated. The goal, says Lamask, is to “draw attention to open spaces and the importance of pristine biomes”.



Ecological phenomena are strongly referenced in the show's preview film, shot in the Monteverde cloud forest of Costa Rica and screened at this year's meeting of the Ecological Society of America in San Jose, California. A naked dancer unfurls herself towards the Sun, capturing with uncanny precision the jerky grace of a plant in a time-lapse movie.

Another creeps, vine-like, up a huge tree; yet more lithe bodies cram themselves into a hollow trunk, like a colony of fungal parasites. “Both artists and scientists are working to show what's really there,” says Lamask.

Engaging with the biological community is a change of direction for Capacitor. Her previous shows *Digging in the Dark* and *Within Outer Spaces* were inspired by geology and astrophysics. With performances at universities, theatres, nightclubs, schools, corporate events and fringe festivals, the company has reached a large number of people. The new show will add a shopping mall in Central America to that list.

Capacitor's next piece, called *Urban Canopies*, premieres in December 2008 at the opening of the new California Academy of Sciences building in Golden Gate Park.

Michael Hopkin is a senior news reporter for *Nature*.

View the preview at www.capacitor.org

MELINDASTROM PHOTOGRAPHY

EXHIBITION

Demonic deeds in symbiotic art

Colin Martin

“Science and natural history museums have increasingly become places of theatrical spectacle — venues for display in which negotiations for the meanings of objects take place,” says Bergit Arends, curator of contemporary arts at London's Natural History Museum. The museum's spectacular hall, designed by Victorian architect Alfred Waterhouse, has certainly provided the public with its fair share of spatial drama since it opened in 1881. Now the evolving function of the museum is marked by a resident artist's exhibition.

Tessa Farmer got her inspiration for *Little Savages* from insects of the order Hymenoptera, which includes ants, bees, wasps and sawflies. She was captivated by the parasitic wasps, perceiving their similarity with the malevolent fairy creatures she has assembled from insect fragments over the past decade. Her exhibition has three parts: a sculptural intervention based on a stuffed fox; six beautifully observed pencil drawings of entomological subjects; and an animated film,

An Insidious Intrusion, in which demonic insect-fairies spear an unfortunate stag beetle with porcupine spines before sawing it into lifeless fragments.

Attacked from all sides, the fox has on its shoulders a bird grasping an insect in its beak, and what seems to be a crustacean clinging to its lower back. Swarms of insects hover around it: its ears are filled with larvae, pupae or wasp nests

hang from its abdomen, beetles infest its flank, and its matted brush resembles a wasp's nest made out of wool. On a finer scale, a parasitic fairy forces a ruby-tailed wasp to lay its eggs in the fox's nose, while another with similar intent attempts to abseil into its mouth (pictured).

“Looking at parts of the collection with Tessa has made me think of it more as a treasure trove,”

says Gavin Broad, curator of Hymenoptera, in an endearingly frank account of his obsessive working life as an entomological taxonomist, “Tessa's fairies seem just as real as ‘my’ wasps.”

Farmer's work imaginatively reinforces how the museum's entomological fieldwork has evolved from its nineteenth-century preoccupation with collecting insect specimens for pinning or pickling — it now has 28 million — into an institution that is research-driven and focused on how insect communities interact ecologically.

“In the institutional ecology of the museum, artists and scientists can develop a relationship of mutual benefit,” concludes Arends. “The role of artists is to disrupt engrained perceptions for the benefit of the museum, to change its course, and to reveal new knowledge in the process.”

Colin Martin is a London-based science writer.

Little Savages is at the Natural History Museum in London until 27 January 2008.



T. FARMER

Time to pick the fly's brain

Drosophila transformed developmental genetics and cell biology. Now the fruitfly is poised to help biologists decipher how the brain works.

Claude Desplan

One afternoon in 1997, a colleague called me into his office to announce that *Drosophila* research was all washed up. The fruitfly had amassed fantastic successes as a model system for developmental biology. In less than a decade, biologists had used it to map the genetic and molecular network that governs organism development. Now my colleague thought that, having served its purpose, *Drosophila* must be about to reclaim its status as the odd little creature obscure scientists used to manipulate genetic characters. How wrong he was.

In the early 1980s, basic research exploded. Working on *Drosophila* was valued as a way to understand phenomena believed to be unique to flies, such as weird body deformations. If the *Drosophila* pioneers believed that their work might have broader relevance, they could not have dreamed of its awesome implications.

A huge breakthrough came in 1984 with the discovery of the homeobox, the Rosetta Stone of developmental biology. This piece of DNA is shared by the genes that govern body pattern. Mutations in these 'homeotic' genes cause body parts to transform into one another — a leg grows where an antenna should be, four wings develop instead of two, and so on. This homeobox sequence was soon found to have similar functions in mice, humans and indeed most animals.

The discovery transformed vertebrate developmental biology. Biologists identified the molecules underlying what had been abstract concepts, such as morphogenetic gradients — rising or falling amounts of a single protein that direct the development of different body parts. To the surprise of most, it became clear that *Drosophila* use the same developmental genes as vertebrates. For more than ten years, there was formidable excitement as each new fly gene clarified how a mouse embryo develops, an organ forms or what causes a human mutation.

Things went so fast that by the late 1990s it seemed that the fruitfly had reached its full potential for answering

big questions, and that developmental biology should be left to those working on vertebrates. By then, fly scientists had made great advances that relied more on clever tricks and a century of genetics than on expensive equipment. A few drosophilists defected to plants or zebrafish in an attempt to adapt these techniques, but the fly stalwarts kept going.

By the start of the new millennium, immensely powerful methods, such as the ability to generate a single mutant cell in an otherwise normal organism, helped solve the major challenge of the time: understanding how cells communicate.

pathways that recognize and then fight bacterial, fungal or viral infections without relying on previous encounters with the pathogen. The same molecules and pathways were later shown to have similar roles in humans, which led to the revival of innate immunity, a field with far-reaching applications in medicine.

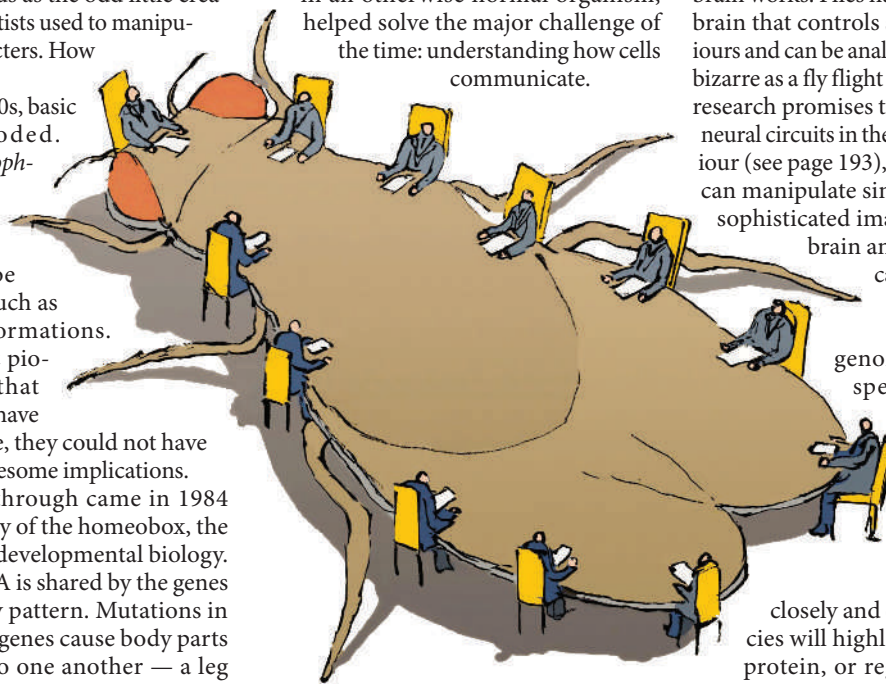
What can *Drosophila* still deliver that will change biology again? The time is ripe to use these tiny creatures to understand the biggest challenge in biology: how the brain works. Flies have a relatively simple brain that controls sophisticated behaviours and can be analysed with machines as bizarre as a fly flight simulator. *Drosophila* research promises to solve how complex neural circuits in the brain mediate behaviour (see page 193), now that researchers can manipulate single neurons and use sophisticated imaging of the working brain and electrophysiological techniques.

This issue of *Nature* reports the whole-genome sequences of 12 species of *Drosophila*, which will allow the organism that can be manipulated so exquisitely to have the best annotated genome. Comparing the genomes of closely and distantly related species will highlight which parts of a protein, or regions of DNA, have been conserved during evolution, and so are likely to have a function. This will offer a way to decipher the grammar of regulatory DNA, which has so far proved elusive.

Powerful genetic tools, genomic advances and beautiful imaging of the tiny structure of a fly brain or embryonic tissue have kept fruitfly research booming for more than two decades. By enabling us to pose biological questions in an *in vivo* context, the fly is an ideal subject for integrating molecular or cellular processes in the biology of the whole organism. *Drosophila* research is thriving and should live up to our hopes for many decades to come.

Claude Desplan is in the Department of Biology at New York University, 1009 Silver Center, 100 Washington Square East, New York, New York 10003, USA.

For further reading see www.nature.com/nature.



Most molecular cascades that bring a signal from the cell surface to the nucleus where it can change the fate of a cell were discovered in flies. Their function was then further analysed in cultured mammalian cells.

In fact, the entire field of cell biology benefited tremendously from work in *Drosophila*. Logic says processes that concern single cells should be probed in yeast or cultured mammalian cells. But the fly oocyte and embryo proved to be ideal test beds for studying events of the single cell. A purely mechanistic description of molecular interactions was superseded by an understanding of how coordinated events take place in the context of a whole organism.

Immunity is another area in which *Drosophila* had a surprisingly big role. Findings in flies uncovered the molecular

J. KAPUSTA

ESSAY

A timely harvest

The public should be consulted on contentious research and development early enough for their opinions to influence the course of science and policy-making.

Pierre-Benoit Joly and Arie Rip

Public engagement in emerging science and technology is thriving, particularly in the United Kingdom. Recent initiatives such as 'Nanodialogues', organized by the think-tank Demos, suggest that citizen juries, dialogue exercises and interactive public understanding projects can be fruitful for scientists and members of the public. Over two years, the Nanodialogues series allowed members of the public to join scientists in discussions on regulation, research funding, development and corporate innovation of nanotechnologies. Such enterprises may foster mutual understanding, but they can struggle to make a difference to research or to policy-making.

Governments and research institutions generally fail to respond to the outcomes of public engagement exercises, perhaps because the outcomes are often too late and too vague on concrete strategies to move forward. We've learnt that it is better to engage the public 'midstream', at a point in the research process when it is possible to incorporate their opinions into research orientation and policy-making.

The French National Institute of Agronomic Research (INRA) used such an approach to focus on research into and field trials of genetically modified vines. In 2001, INRA had to decide whether to run field trials of a genetically modified vine that is potentially resistant to a disease-causing virus. INRA's research director for plant sciences, Guy Riba, voiced the opinion of most researchers: "Surely scientists have a responsibility to carry out these experiments with a view to the future, even in the face of current public opposition?"

INRA met strong opposition to the trials because of the cultural significance of wine in France. A group of wine producers, including some prestigious châteaux, had signed a petition in June 2000 calling for a moratorium on the use of genetic modification techniques in wine production, and joined forces to create the non-governmental organization Terre et Vin du Monde (Land and Wine of the World).

In response, INRA asked a group of social scientists who specialize in science

and technology studies to organize a public consultation, in which we took leading roles. Our goal was to produce a public report to be taken into account in decision-making at INRA.

Our working group comprised 14 people, including members of the public, wine growers and researchers. It had seven days of intensive discussions over a six-month period in 2002. The set of recommendations it produced was made freely

not for commercial purposes; that a local committee would be in charge of monitoring the experiment; and that INRA would commit to exploring alternative ways to fight viruses. Appropriately, it was not a smooth process, either during deliberation within the group, or in implementing the agreement.

Researchers at INRA criticized the public consultation process for its power to reduce the freedom of research. Non-governmental organizations claimed that INRA was manipulating public opinion through the exercise. These tensions are an unavoidable part of the process.

Three important lessons emerged from the exercise. First, midstream engagement is not a recipe for wide social agreement and acceptance. Rather, it improves the robustness of decisions by taking into account the diversity of world views and interests. Second, it stimulates institutional learning. Third, the process can produce research and development options not previously considered. This is of particular value if directors of public research are truly committed to generating beneficial sociotechnical innovation.

Public consultations in science and technology should be undertaken at a point early enough in the development process when it is still feasible to change course. The nanotechnology world often refers to 'the lessons to be learned from genetic modification' — the main one is timely, considered public engagement. ■ Pierre-Benoit Joly is director of research at INRA, 65 Boulevard de Brandebourg, F-94205 Ivry, France, and director of the TSV (Social and Political Transformations related to Life Sciences) research unit. Arie Rip is emeritus professor of philosophy of science and technology at the University of Twente in Enschede, the Netherlands, and leads a programme on social and ethical aspects of nanotechnology.

For more essays and information see <http://nature.com/nature/focus/scipol/index.html>.

Correction

In the Essay 'Big lessons for a healthy future' (*Nature* **449**, 791–792; 2007) the conversion of £45.5 billion should have read US\$93 billion, not million.



D. PARKINS

NEWS & VIEWS

QUANTUM INFORMATION

Reality check

Liesbeth Venema

It will be a long experimental haul before the great potential of quantum effects can routinely be exploited for technological ends. A sense of practical purpose among researchers will encourage progress.

When the citizens of Geneva cast their votes in the Swiss federal elections on 21 October, they could be confident that their ballots were safe — thanks to the rules of quantum mechanics. The poll results were sent down an optical fibre from the counting station to a government data centre, and their integrity was safeguarded by a quantum encryption key transmitted through the same fibre. Such a key promises to be 100% secure. It is composed of a stream of single photons that each take a random, unpredictable polarization state, and any attempts at tampering or eavesdropping will be noticed by the sender and receiver.

Quantum cryptography was high on the agenda at a meeting* last month on quantum information technology. Whether or not the exercise in Geneva was genuinely motivated by security concerns, it demonstrates, as a first public deployment of quantum cryptography, that the technique is ready to enter the commercial market for data encryption (G. Ribordy, id Quantique, Geneva; J. Dubois, Senetas, Melbourne). But a recurring theme of the meeting was the pressing requirement to identify other areas of practical application for quantum-information systems.

Another major prospect is quantum computing. Quantum computers will not simply be faster versions of the computers we have today. Rather, they will carry out tasks that are hard to tackle with any classical approach: for example, factoring large numbers and searching databases. Algorithms for such tasks have been available for more than a decade, and it is realizing the hardware that remains the main barrier to progress.

The building-block of a quantum computer is the qubit, a versatile version of the conventional bit. Like its classical counterpart, a qubit has two well-defined levels, '0' and '1'. But it also has the curious property that it can be in both states at the same time, occupying them with a certain probability. This phenomenon, known as 'superposition', in principle offers a powerful way to perform calculations because several logic operations can be carried out

simultaneously. Another useful property of qubits is that they can be entangled — that is, their states can be prepared so that they are correlated to each other, even though each is unknown. For example, if one qubit happens to be in level 0 the other one will occupy level 1, and vice versa. The exact outcome becomes fixed as soon as either of the two is measured.

A wide range of qubit designs — based on atoms, ions, electrons, photons and even superconducting currents — was highlighted at the meeting. In most cases, at least two qubits can now be connected so that some sort of logic operation can be carried out. In one of the most advanced approaches, in which qubits take the form of ions trapped in an electromagnetic field, up to eight qubits have been entangled with each other. A new experimental development is the construction of a so-called Toffoli logic gate with ion qubits (R. Blatt, Univ. Innsbruck). Toffoli gates are a familiar concept in classical computation, but are the subject of renewed interest because they may offer a solution to error correction, a crucial consideration for quantum computers. However, they require three inputs and are therefore more difficult to realize than the two-qubit logic gates demonstrated so far.

The main problem with qubits is that their quantum states are fragile, and quickly leak away into the environment. This raises the scaling issue. Coupling just a few qubits together seems feasible. But as an increasing number of them are connected, more quantum leaks occur, so that information is quickly lost. Part of the solution may lie in using photons, relatively robust quantum entities, to channel quantum information between remote qubits, and experimental work is under way to construct such optical quantum connections. Instead of building a computer of say, 5,000 qubits, a more realistic goal may be to optically connect 1,000 quantum registers of just five qubits — one for storage, one for communication and three auxiliary qubits to ensure fault tolerance (A. Sørensen, Niels Bohr Inst., Copenhagen)¹.

Small-scale quantum computers, designed to carry out a specific task, could be just a few years away. But a take-home message from the meeting was that more immediate applications of quantum technologies are urgently required to keep industrial partners interested (T. Spiller, Hewlett-Packard, Bristol). The 'killer application' for quantum information is not yet known, and more practical ideas need to be generated to kick-start a new market². It is sobering to realize that the inventors of the transistor did not foresee the huge integrated-circuit industry that would develop; their first

"The 'killer application' for quantum information is not yet known, and more practical ideas need to be generated to kick-start a new market."

idea for a useful application of transistors was in hearing aids. What we need to bootstrap quantum-information technology, says Spiller, are quantum hearing aids.

When it comes to near-future technological applications, quantum communication, and quantum cryptography in particular, seems to be the best bet. The record distance over which a quantum key has been transmitted, both through an optical fibre and through free space, is about 150 km. But if quantum-communication technology is to be widely developed, it will be necessary to improve efficiency. At the meeting there was much talk of 'quantum repeaters' — pieces of hardware that can temporarily store and release photons without losing their quantum states, and that are seen as essential for the effective distribution of quantum information over large networks and distances. The experimental challenge to construct quantum repeaters is probably on a par with the challenge to generate practical qubits. So far, quantum memories, the basic element of a quantum repeater, have been made from ensembles of cold gaseous atoms. But a solid-state form will eventually be required: atomic ensembles of rare-earth ions, inserted in a nonlinear optical waveguide, are among the first candidates to be investigated (M. Staudt, Univ. Geneva)³.

The quantum future looks bright, although it will take a sustained experimental push before basic effects such as entanglement, inherent randomness and superposition can be exploited

*QIPC 2007: International Conference on Quantum Information Processing and Communication, 15–19 October 2007, Barcelona, Spain.

in real devices (practical or otherwise). But although quantum mechanics has been one of the most successful theories of the past century, nobody can confidently claim to understand why it works so well; for instance, how two entangled particles seem to communicate with each other at a distance, without any interaction, is beyond anybody's comprehension. There is a nagging feeling that we are missing something. A quantum-information industry may indeed

be just around the corner, but its underlying principles remain largely mysterious. ■

Liesbeth Venema is a senior editor at *Nature*.
e-mail: l.venema@nature.com

1. Jiang, L., Taylor, J. M., Sorensen, A. S. & Lukin, M. D. preprint at <http://arxiv.org/abs/quant-ph/0703029> (2007).
2. Spiller, T. P. & Munro, W. J. *J. Phys. Condens. Matter* **18**, V1-V10 (2006).
3. Staudt, M. U. *et al. Phys. Rev. Lett.* **99**, 173602 (2007).

COMPUTATIONAL BIOLOGY

Protein predictions

Eleanor J. Dodson

Predicting the three-dimensional structure of a protein from its amino-acid sequence is a dauntingly complex task. But with colossal computer power and knowledge of other structures, it can be done.

Fifty years have passed since the Nobel-prizewinning discovery that the amino-acid sequence of a protein determines its three-dimensional structure¹ — yet computational biologists are still unable to predict the shape of a protein from its sequence. Given that there are many more protein sequences available than structures, and that protein shape is crucial for understanding cellular and physiological processes, a method for predicting such structures is vital. The paper by Qian *et al.*² (page 259 of this issue), in which the structure of a protein containing 112 amino acids is accurately predicted, thus represents a real breakthrough*. The authors' model was sufficiently accurate to act as the starting point in the X-ray structure determination of the protein.

Most structural information on proteins is derived from X-ray and nuclear magnetic resonance (NMR) experiments. These have revealed the general characteristics of proteins — for example, sequence motifs that form secondary structural elements such as helices and sheets. Such elements are organized to generate the overall protein architecture, mainly as a result of internal interactions between hydrophobic amino-acid side chains buried within the structure.

The shape of a protein corresponds to the lowest-energy conformation of that molecule and reflects the combined properties of the constituent amino acids. Low-energy conformations arise when the 'backbone' peptide chain is tightly packed into secondary structural features. Such packing exploits both the hydrogen-bonding of amino-acid side chains to each other and the energetically favourable, compact patterns that arise from hydrophobic interactions. Several crucial

side-chain interactions are almost always found in certain structural elements of proteins, but in general there is no simple correlation between amino-acid sequence and protein structure; quite different sequences can adopt very similar folds.

Once a protein structure is known, it is fairly easy to see the atomic interactions that underpin it. But it is much harder to take an amino-acid sequence and work out the optimal interactions that determine how it will fold. First, it is necessary to quantify the energy contributions from various types of

interaction. The effects of molecular conformations on these contributions must then be assessed. But even a relatively small protein can have a bewilderingly large number of possible conformations. Although some progress has been made towards devising a structural prediction method, crystallographers have so far had no reason to worry about their job security.

The field was greatly stimulated by a network set up in 1994 to provide a critical assessment of structure prediction (CASP)³. The main goal of the CASP network is "to obtain an in-depth and objective assessment of our current abilities and inabilities in the area of protein structure prediction"⁴. Every two years the organizers provide the amino-acid sequences of a set of proteins for which undisclosed crystal structures exist. Modellers are challenged to predict structures for the proteins, and these are then assessed against the crystallographic results. The assessors use various scoring systems, but the most rigorous test is the one used by Qian *et al.*² to test their own models — can the prediction be used in 'molecular replacement' searches⁵ that allow the raw data from X-ray diffraction studies to be related to the structure of the compound being investigated? Normally, a previously determined structure of a protein with a similar amino-acid sequence is used for this purpose.

Qian and colleagues' models² passed the molecular-replacement test with flying colours (Fig. 1): one of the authors' *ab initio* predictions was used successfully as a molecular-replacement model. Furthermore, the authors used their method to refine ten NMR models of protein structures, yielding results that were in better agreement with X-ray data than the original models. And finally, they were able to improve the molecular-replacement scores of several models that started from protein structures distantly related to that of the target protein. This gives the lie to the old crystallographers' adage that computational modelling is a time-consuming way to make a poor model worse.

The authors used a program called Rosetta to make their structural predictions. The program begins by mapping fragments of the sequence under review against existing information from previously determined structures, to identify likely structural motifs. It then constructs many rough, low-resolution models from these fragments and tests them against energy criteria (which are dominated by hydrophobic interactions). In this way, a large set of possible low-energy conformations is identified, one of which is likely to be that adopted by the protein.

At the next stage, the energy profile of every atom in the protein is incorporated into the low-energy models. Rosetta explores a huge range of randomly generated side-chain and backbone conformations, again calculating their effects on molecular energy. The resulting energy 'landscape' can vary dramatically — for example, small shifts of a single atom can make or break a hydrogen bond.

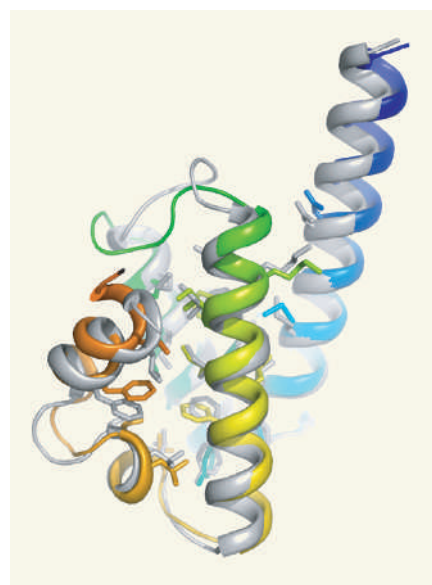


Figure 1 | Model test. Qian *et al.*² have developed a computational method for predicting the three-dimensional structure of a protein from its amino-acid sequence. Here, their predicted structure (grey) of a protein is overlaid with the experimentally determined crystal structure (shown in colour) of that protein. The agreement between the two is excellent, with the amino-acid side chains overlapping particularly well.

*This article and the paper concerned² were published online on 14 October 2007.

The whole procedure is iterative — solutions are repeatedly assessed, the lowest-energy models are clustered to identify common features and then further effort is concentrated on more variable regions. Rosetta also analyses peptide sequences found in analogous proteins from species of organisms other than that of the target sequence, as such proteins are expected to have similar three-dimensional structures to the target molecule. The whole process is terminated when conformations are identified that have significantly lower energies than the average energy of the protein.

The algorithms used in Rosetta are sophisticated, and the computing resources required to carry out the calculations, to keep track of results and to plan future strategies, are awesome. The authors therefore used a procedure called Rosetta@home⁶, which distributes the calculations across a network of home computers — more than 70,000 in June 2006 — whose owners allow the program access to their idle machines.

There is still much to be done. Cynics might mutter that one success doesn't prove that Qian and colleagues' method² is truly general, and

that it should be assessed further using known structures. Nevertheless, this approach demonstrates real progress in several respects: the use of enormous computational power; the exploitation of known three-dimensional structures; the development of powerful search algorithms that relate those structures to new sequences; and the steadily improving tactics used to determine low-energy conformations of molecules. The benefits will be seen in structure-based drug design and in improved models for crystallographic calculations. And in the future, this method might provide structural information about intractable molecules that are difficult to study experimentally. ■

Eleanor J. Dodson is at the York Structural Biology Laboratory, Department of Chemistry, University of York, Heslington, York YO10 5YW, UK. e-mail: e.dodson@ysbl.york.ac.uk

1. Sela, M., White, F. H. Jr & Anfinsen, C. B. *Science* **125**, 691–692 (1957).
2. Qian, B. et al. *Nature* **450**, 259–264 (2007).
3. Moulton, J. *Phil. Trans. R. Soc. Lond. B* **361**, 453–458 (2006).
4. <http://predictioncenter.org>
5. McCoy, A. J., Grosse-Kunstleve, R. W., Storoni, L. C. & Read, R. J. *Acta Crystallogr. D* **61**, 458–464 (2005).
6. Das, R. et al. *Proteins* doi:10.1002/prot.21636 (2007).

MATERIALS SCIENCE

Magnetic blue

Jeroen van den Brink and Alberto F. Morpurgo

A commonly used blue dye is more than just a pretty colour. This material and its relatives are semiconductors, and their magnetic properties can be controlled by engineering their crystal structure.

Organic compounds are rarely magnetic, but metal phthalocyanine (MPc) materials are notable exceptions to this rule. Reporting in *Advanced Materials*, Heutz et al.¹ now show that the magnetism of MPcs can be controlled. By changing the crystal structure of an MPc film, the authors switched the material from being in a magnetically ordered state to a non-magnetic one. This approach might provide a method for customizing the magnetism of molecular materials.

MPcs are flat molecules that take the shape of a four-leaf clover. They consist of an outer ring, formed from nitrogen, carbon and hydrogen atoms, with a metal atom bound at the centre (Fig. 1). The first molecule of this class was discovered at the beginning of the twentieth century, and had a copper atom in the middle. Because of its brilliant blue colour, the compound was immediately seized upon for use in paints and dyes. The hue also inspired the name 'phthalocyanine', which was taken from the Greek-derived words for rock oil (naphtha) and blue (cyan).

Since then, more than 70 MPcs have been synthesized, each with a different central atom or group of atoms. The properties of these

compounds vary widely. For example, simply attaching chlorine atoms to the aromatic rings in copper phthalocyanine (CuPc) modifies the electronic absorption spectrum of the molecules. This process is used to add subtle green tones to blue paint. No great conceptual leap is required to see that similar structural modifications to MPcs could result in compounds with other interesting properties.

In fact, chemists have long known how versatile MPcs can be. Apart from their common use as dyes in the textile and paper industry, they can also act as catalysts, and they have even been investigated as anticancer agents. But perhaps their most interesting characteristics are their magnetic and electronic properties. If a transition-metal atom is placed in the centre of the ring, MPcs carry a magnetic moment because of the particle spin of the transition-metal atom. The spin value varies depending on the metal used, so that MPcs can be thought of as nanomagnets, the magnetic strength of which can be controlled at a molecular level.

Physicists are only just starting to explore systematically the full potential of MPc-based compounds. The leitmotif of this work is the addition of electrons to the materials to probe

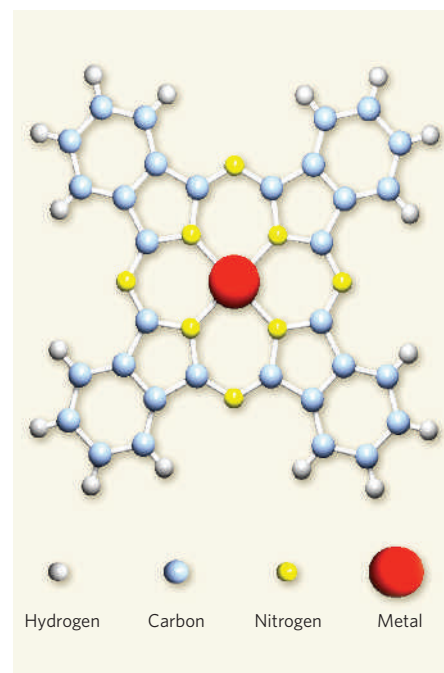


Figure 1 | Structure of metal phthalocyanines. Metal phthalocyanines are a class of molecule that comprises an organic, four-leaf-clover structure with a metal at the centre. Heutz et al.¹ show that the magnetic state of films of these molecules can be switched by controlling their crystalline structure.

changes in their electrical and magnetic properties. Of particular interest is the unexpectedly large number of electrons that can be hosted by MPcs — up to four or five on a single molecule. The resulting charge density can be tuned by adding electron-donating atoms (such as lithium, potassium or rubidium) to the materials. This 'electron-doping' technique has also been used on buckminsterfullerene (C₆₀), the famous football-shaped carbon molecule that has been a fertile playground for condensed-matter physicists for almost two decades.

The latest experiments on MPcs have produced some surprises. These compounds are usually semiconductors, but several MPc films turn into metallic conductors when electron-doped with potassium atoms². The variation of conductance with the amount of potassium incorporated into the films provides information about which molecular orbitals the donated electrons occupy in each MPc (ref. 3). Other experiments reveal that the magnetic properties of manganese-containing MPcs can be tuned by varying the concentration of lithium dopants⁴.

The big idea behind all this work is that it should be possible to engineer the electronic properties of solids by chemical actions at a molecular level. This proposal is certainly not new. But researchers who have attempted this in the past have almost invariably been confronted with a harsh reality: small molecular modifications made to tune the bulk electronic properties of a solid often cause drastic changes to the packing of the molecules in that solid. Such changes to the crystal packing cannot usually

be controlled, and can easily eclipse any chemically induced changes to the electronic properties. In most cases, this has prevented systematic progress. MPCs, however, are different from other compounds; in most MPC crystals, the molecules are packed in a similar way, so that structural effects are less likely to be a problem.

Heutz *et al.*¹ now show that not only do the crystal structures of MPCs create fewer problems, but they may also be turned to advantage. The authors controlled the crystal form of thin MPC films by growing them on different substrates; this allowed them to exploit the fact that the interaction between the magnetic moments of neighbouring molecules depends on the relative orientation of those molecules. On one of the substrates, the orientation of the molecules in the film is such that the interaction between magnetic moments vanishes. In this case, the MPC nanomagnets point in random directions and do not create a net magnetic moment. But on a different substrate, the molecules were slightly rotated with respect to their previous orientation. This is enough to switch on the magnetic interaction between the molecules. In other words, the authors engineered the macroscopic ordering of the nanomagnets by controlling the crystal form of the material.

The authors' findings¹ are the latest in a growing body of work that explores the unique properties of MPCs. It is now clear that these compounds display a rich interplay of electronic, magnetic and structural properties, with potential technological relevance. Stimulated by this experimental activity, theorists have also started to investigate electron-doped MPCs, and have made some startling predictions. For example, they propose that, under appropriate conditions, these systems may become superconductors at high temperatures⁵, adding to the already impressive roll-call of MPC properties.

It is always difficult to predict how any field of research will develop. But it is clear that multifunctional MPCs are potential building-blocks for future materials. We would not be surprised if physicists soon start to approach their colleagues in chemistry and materials-science departments asking for a greater variety of well-characterized MPC compounds. At present, MPC materials may just be the toys of blue-skies researchers. But once they make it out of the playground, they could become invaluable. ■

Jeroen van den Brink is at the Instituut-Lorentz for Theoretical Physics, Leiden University, Postbus 9506, 2300 RA Leiden, the Netherlands. Alberto F. Morpurgo is at the Kavli Institute of Nanoscience, Delft University of Technology, Postbus 5, 2600 AA Delft, the Netherlands. e-mails: brink@ilorentz.org; a.morpurgo@tnw.tudelft.nl

PLANETARY SCIENCE

A twist on periodicity at Saturn

Margaret Galland Kivelson

Saturn's nominal rotation period is timed by a 'radio clock' that counts bursts of emissions controlled by the planet's magnetic field. Buffeting by the solar wind may explain the clock's irregularities.

Einstein showed us that measurements of time made in systems moving at different speeds will not agree. What would he have thought of a clock whose ticking depends on how fast the solar wind — a gas of charged particles, or plasma, constantly flowing outwards from the Sun — is blowing? Yet that is what, on page 265 of this issue, Zarka and colleagues¹ tell us is the case for the radio-emission clock that has been used to infer Saturn's rotation period.

Time-keeping on planets is linked to their orbital periods ('years') and their rotation periods ('days'). Strangely, it is not straightforward to determine the rotation periods of the gas-giant planets: Jupiter, Saturn, Neptune and Uranus. These planets lack solid surfaces with features to track as the planet rotates. Images of the gas giants allow one to track clouds, but their motions are not precisely tied to the rotation of the interior. How, then, do we establish rotation rates?

A particularly fruitful approach has been to monitor the intensity of radio-frequency

emissions from sources close to the planet. Such emissions arise in a planet's magnetosphere, the region of space dominated by its magnetic field (Fig. 1), and their intensity depends on the angle between the observer and the magnetic field at the source. If the planet's internally generated magnetic field is asymmetric about its spin axis, the direction of the field at the source will seem to nod up and down as the planet spins, and the intensity of the observed emissions will vary with the rotation period. The planetary rotation rates of Jupiter², Neptune and Uranus have been identified in this way.

Saturn emits radio signals modulated at a period of about 10.75 hours. This period has been used to define the period of rotation of the interior³, but it has proved hard to understand why the radio power varies periodically because the best available measurements fail to detect any asymmetry of the internal magnetic field⁴. Possibly even more puzzling is the recognition that the period of the modulation is not fixed. The first hints of that, initially greeted

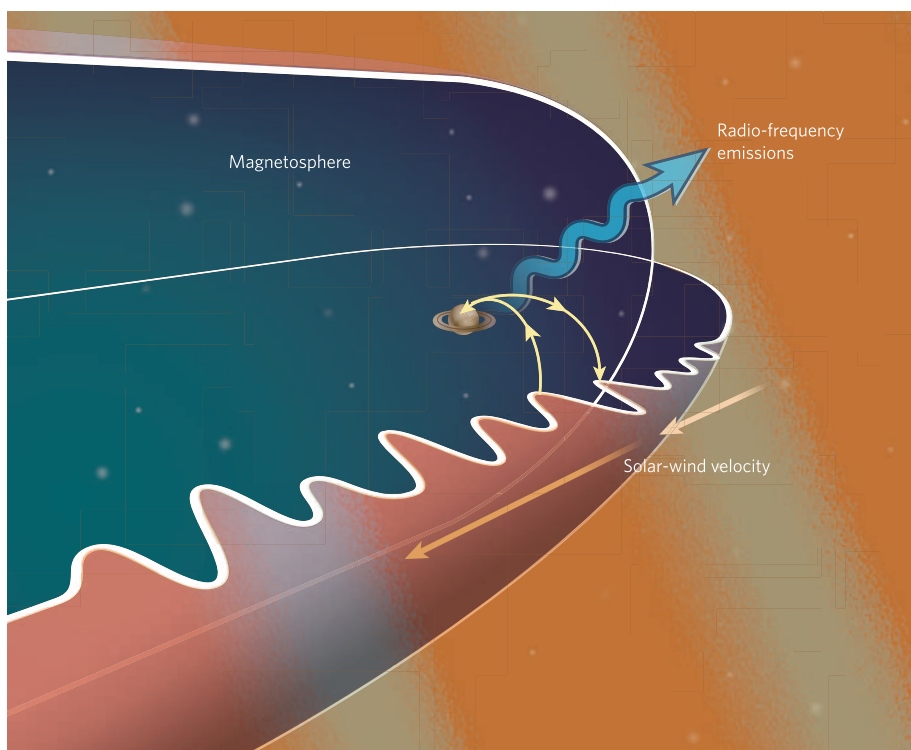


Figure 1 | Generation of radio emissions at Saturn. Saturn's magnetosphere is embedded in the solar wind, here shown as flowing away from the Sun at speeds that increase and decrease periodically (the faster-flowing portions are depicted in dark orange). Radio emissions are produced where electrical current flows into Saturn's auroral ionosphere. Zarka *et al.*¹ show that the power of the radio emissions is modulated periodically, and that the period varies with the speed of the solar wind, possibly because the currents are generated by wave-like disturbances at shifting locations along the magnetospheric boundary.

1. Heutz, S. *et al.* *Adv. Mater.* doi:10.1002/adma.200701458 (2007).
2. Craciun, M. F. *et al.* *Adv. Mater.* **18**, 320–324 (2006).
3. Craciun, M. F., Rogge, S. & Morpurgo, A. F. *J. Am. Chem. Soc.* **127**, 12210–12211 (2005).
4. Taguchi, Y. *et al.* *J. Am. Chem. Soc.* **128**, 3313–3323 (2006).
5. Tosatti, E., Fabrizio, M., Tóbi, J. & Santoro, G. E. *Phys. Rev. Lett.* **93**, 117002 (2004).

with some scepticism, came from measurements made by the Ulysses spacecraft⁵. More recently, observations by the Cassini orbiter have confirmed that the period changes by as much as 1% or so in months to years⁶.

So, today, we know that the radio power is periodically modulated but we do not understand why. And we know that the radio period drifts too rapidly to be consistent with changes in the rotation period of the deep interior of a massive spinning planet. Other types of analysis give an estimate of the rotation rate of the deep interior that is distinctly shorter than the shortest period inferred from the radio clock⁷. Thus, it seems likely that the radio clock responds to processes in the planet's upper atmosphere and magnetosphere. Explanations of the varying period of the radio clock have appealed to changing conditions that are either external to Saturn's magnetosphere (such as the speed of the solar wind⁸) or internal to it (such as the mass injected from the vapour plume of Saturn's small moon, Enceladus⁹). But evidence that such effects cause the observed drift in the period has been sketchy.

Zarka *et al.*¹ use roughly three years of Cassini radio-wave data to provide compelling support for the hypothesis that external effects contribute to the modulation of the radio period. They find that the total power within a defined range of radio frequencies integrated over a full Saturn rotation period of 10.75 hours fluctuates on timescales of about 20–30 days. The properties of the solar wind are known to fluctuate at the solar rotation period of 25 days, and also to show trends over longer timescales. Zarka *et al.* find that cross-correlations with the speed of the solar wind are high, especially when Cassini's colatitude (the difference between its latitude and 90°) remains relatively constant, relative to Saturn's spin axis. The correlations with other properties of the solar wind (such as dynamic pressure) are weak.

Given evidence that the source of the radio emissions seems to be localized in the morning to noon sector⁸, it was previously proposed⁹ that changes in the period of the radio clock would occur if the source location shifts with changing solar-wind velocity. Such shifts could arise (and vary systematically with solar-wind velocity) if the emissions are triggered where the magnetospheric boundary becomes unstable through the growth of a phenomenon known as Kelvin–Helmholtz waves (the equivalent for magnetized plasma of wave-breaking when high winds blow over water). This interpretation remains speculative: the new results do not establish a mechanism for the changing periodicity. But the knowledge that the radio period is modulated by the speed of the solar wind should help in the quest for a more complete understanding.

Many planetary scientists expected Saturn's magnetosphere to be a bloated but rather boring analogue of Earth's. The data being collected by Cassini continue to belie this

expectation. Ten years after its launch from Earth, the mission continues its fruitful exploration of a planetary system that is dramatically different from any previously investigated. ■

Margaret Galland Kivelson is at the Institute of Geophysics and Planetary Physics, University of California, Los Angeles, 6843 Slichter Hall, Los Angeles, California 90095-1567, USA.
e-mail: mkivelson@igpp.ucla.edu

1. Zarka, P., Lamy, L., Cecconi, B., Prangé, R. & Rucker, H. O. *Nature* **450**, 265–267 (2007).

2. Riddle, A. C. & Warwick, J. W. *Icarus* **27**, 457–459 (1976).
3. Desch, M. D. & Kaiser, M. L. *Geophys. Res. Lett.* **8**, 253–256 (1981).
4. Giampieri, G., Dougherty, M. K., Smith, E. J. & Russell, C. T. *Nature* **441**, 62–64 (2006).
5. Galopeau, P. H. M. & Lecacheux, A. *J. Geophys. Res.* **105**, 13089–13102 (2000).
6. Gurnett, D. A. *et al. Science* **316**, 442–445 (2007).
7. Anderson, J. D. & Schubert, G. *Science* **317**, 1384–1387 (2007).
8. Galopeau, P. H. M., Zarka, P. & Le Quéau, D. *J. Geophys. Res.* **100**, 26397–26410 (1995).
9. Cecconi, B. & Zarka, P. *J. Geophys. Res.* **110**, A12203, doi:10.1029/2005JA011085 (2005).

FISHERIES

Nets versus nature

David O. Conover

The life-histories of pike adjust quickly to shifts in the opposing forces of fishing and natural selection. Such rapid changes suggest that evolutionary dynamics must be incorporated into fisheries management.

People like to catch big fish, sometimes so much so that fish sizes overall become greatly diminished. According to one view, the continual removal of large fish from a population sets the stage for rapid, undesirable evolutionary changes, including slower growth, earlier adult maturation and permanently smaller size^{1,2}. This occurs because removing the largest fish directly opposes natural selection, which tends to favour large size.

What happens when these two forces simultaneously oppose one another? Can evolution respond quickly enough to track changes in fishing selection, or does natural selection counteract it? Writing in *Proceedings of the National Academy of Sciences*³, Eric Edeline and colleagues illustrate the outcome of this dynamic tug-of-war between the forces of natural selection and fishing selection.

Until now, the theory underlying the management of fisheries has been based on ecological models that predict how the productivity of an exploited population changes in relation to its density, and the age and size at which fish are caught. The goal is to ensure a maximal but sustainable catch in perpetuity. Current management approaches do not take into account the potential for evolutionary change in response to fishing.

Why is evolution important to fisheries management? It could be argued that fishing merely adds an additional predator to the ecosystem. But from the fish's point of view, humans turn the rules of engagement completely upside down. Most natural predators attack smaller fish more frequently than larger fish. The bigger a fish gets, the lower its mortality (Fig. 1). Hence, growing fast early in life is a good strategy. Moreover, because big fish produce many more offspring than small fish, delaying maturation to larger size also

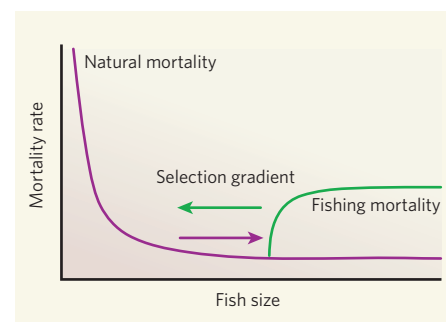


Figure 1 | The darwinian struggle between natural selection and fishing selection. The graph depicts the contrast between mortality rates as a function of fish size in the absence and presence of mortality due to fishing. Natural rates of mortality decline dramatically with increasing size early in life, until reaching a low level for the remainder of life (purple). Fishing greatly increases the mortality of large fish (green). Arrows represent the direction of selection on body size in the absence (purple arrow) and presence of fishing (green arrow).

increases fitness — that is, the likelihood that one's genes will be passed on to future generations. By causing greatly increased mortality at large sizes, fishing selects for fish that grow slowly and mature at small sizes. Numerous other physiological, behavioural and reproductive traits likewise evolve that can lower fitness⁴. Taken to its extreme, many generations of intense size-selective fishing could in theory cause the evolution of a population of runts.

The introduction of darwinian principles into fisheries science has been controversial^{5,6}. Some have argued that adequate proof of evolutionary changes caused by fishing has not been demonstrated. That would require changes in traits such as growth rate to be shown to have a genetic basis. This is extremely difficult to do

in the wild because environmental and genetic influences are confounded, although new statistical methods have enabled the evolution of certain traits (such as size at maturity) to be revealed⁷. Lab experiments, in which environmental conditions are standardized, can demonstrate genetic change⁸ but have been criticized for not representing real fisheries in the wild⁹.

Edeline *et al.*³ now enter the fray. They took advantage of a unique 50-year time series of data on growth rates of pike (*Esox lucius*) in Lake Windermere in northwest England. This lake was fished for centuries until 1921, when the net fisheries were closed. Net fishing did not reopen until 1944. Each year from 1944 onwards, biologists tracked the age and growth of individual pike landed in the fishery by measuring the annual rings that form in certain bones, much like reading the rings in a tree trunk. They also tagged and recaptured pike, providing estimates of population size and mortality.

These highly detailed data enabled the authors to show in an earlier paper⁹ that fishing did indeed remove the larger, faster-growing fish whereas natural sources of mortality did the opposite. Hence, they hypothesized that the sudden resurgence of fishing in 1944 should cause an evolutionary decline in growth rate followed later by an increase as the fishery waned over the 50 years. After using statistical models to account for the effect of a suite of confounding environmental factors, the temporal trend in growth rate closely tracked the predicted pattern. Several twists and turns in growth trajectory seemed to coincide with episodes of excessively high fishing and with the large-scale death of perch (a prime food source for pike) in 1976. In addition, changes occurred in the level of reproductive investment by young females that were also as predicted from evolutionary theory. The authors conclude that evolutionary responses to the opposing forces of fishing and natural selection must be accounted for in managing fisheries.

Critics will contend that consistency with the predictions of evolution is not proof that the changes observed were in fact genetic. The responses are probably far too rapid to be entirely evolutionary as opposed to ecological in origin. With only one population under study, any interpretation of this sequence of growth changes contains an element of story-telling. Perhaps the changes in growth rate fit the predictions of evolution purely by coincidence.

Yet this is one of the most data-rich and comprehensive analyses of fishery-induced evolution ever published. Together with strong evidence also emerging from a variety of other harvested species^{7,10–12}, the likelihood that all such studies are erroneous is becoming vanishingly small. Moreover, Edeline and colleagues' approach provides fresh incentive and the methodology to test for evolutionary change in the many other long-term data sets of age and growth that exist for heavily fished species. ■

David O. Conover is in the School of Marine and Atmospheric Sciences, Stony Brook University, Stony Brook, New York 11794-5000, USA. e-mail: dconover@notes.cc.sunysb.edu

1. Law, R. *ICES J. Mar. Sci.* **57**, 659–668 (2000).
2. Stokes, T. K., McGlade, J. M. & Law, R. *The Exploitation of Evolving Resources* (Springer, Berlin, 1993).
3. Edeline, E. *et al. Proc. Natl Acad. Sci. USA* **104**, 15799–15804 (2007).
4. Walsh, M. R., Munch, S. B., Chiba, S. & Conover, D. O.

Ecol. Lett. **9**, 142–148 (2006).

5. Hilborn, R. *Fisheries* **31**, 554–555 (2006).
6. Conover, D. O. & Munch, S. B. *Fisheries* **32**, 90–91 (2007).
7. Olsen, E. M. *et al. Nature* **428**, 932–935 (2004).
8. Conover, D. O. & Munch, S. B. *Science* **297**, 94–96 (2002).
9. Carlson, S. M. *et al. Ecol. Lett.* **10**, 512–521 (2007).
10. Haugen, T. O. & Vøllestad, L. A. *Genetica* **112–113**, 475–491 (2001).
11. Swain, D. P., Sinclair, A. F. & Hanson, J. M. *Proc. R. Soc. Lond. B* **274**, 1015–1022 (2007).
12. Coltman, D. W. *et al. Nature* **426**, 655–658 (2003).

DEVELOPMENTAL BIOLOGY

The power of blood

Paige Snider and Simon J. Conway

Compared with the masterpiece crafted by nature, even Leonardo da Vinci's anatomical drawings of the cardiovascular system seem primitive. In creating this system, nature seems to use blood flow as its paintbrush.

More than a century ago, Thoma noted¹ that blood vessels carrying a high volume enlarge, whereas those with low flow regress. Since then, significant evidence has accumulated to suggest that the mechanical force created by blood flow affects gene expression in the developing embryo^{2,3}. But how does blood flow contribute to shaping a functional vascular architecture, when vessel identity and developmental patterning are genetically predetermined? On page 285 of this issue, Yashiro *et al.*⁴ take a step towards solving this puzzle by showing that an interplay between haemodynamics (the dynamics of blood flow) and genetic factors mediates cardiovascular development.

Among the most common congenital birth defects are abnormalities in the growth and development of the cardiovascular system; in particular, anomalies in the asymmetric remodelling of a transient structure known as the branchial arch artery apparatus that occurs in 6–7-week-old human embryos⁵. Mammals have five branchial arches, each of which contains an arch artery (numbered 1–4 and 6). Blood flows out of the heart via branchial arch arteries to circulate throughout the embryo. Although the arterial system initially forms symmetrically (Fig. 1a), in the mature organism, the left fourth and sixth arch arteries persist and give rise to the aortic arch and pulmonary trunk, whereas the right fourth and sixth arch arteries regress (Fig. 1b). This results in the asymmetric development of the great vessels of the ventricular outflow tract⁶, which forms part of the left and right ventricles.

A likely candidate for directing asymmetric development was the transcription factor Pitx2, which is the product of the only gene known to be asymmetrically expressed in the embryonic tissue that generates the branchial arch^{6–9}. Moreover, Pitx2 is induced by Nodal, a signalling molecule that regulates the initial establishment of left–right patterning in the embryo⁶.

But the overall mechanisms — or genetic pathways — that govern asymmetric development of the artery arches remained elusive.

In search of an answer, Yashiro *et al.*⁴ used mutant mice that do not express physiologically significant levels of Pitx2 in the left side of their ventricular outflow tract. The authors found that this mutation prevents normal rotational movement of the outflow tract, which is essential for remodelling of the right sixth arch artery into a long, narrow vessel with reduced blood flow. Consequently, they observed that in about half of the mutant mice the right sixth arch artery persists in its initial morphology.

This finding led Yashiro and colleagues to propose that, in normal mice, reduced blood flow through the right sixth arch artery leads to its regression. To test this hypothesis, they performed a clever microsurgical procedure to 'tie off' the left sixth arch artery, thereby reducing blood flow through it (Fig. 1c). They reasoned that if this treatment causes unexpected regression of the left sixth arch artery, then haemodynamics has a pivotal role in the asymmetric development of the arterial system. They found that microsurgical ligation of this artery does result in its regression, and that the usually regressing right sixth arch artery — which after ligation receives normal levels of blood — persists.

The authors went on to show that another factor that contributes to normal arch-artery remodelling is the asymmetric expression of vascular growth factors such as PDGF and VEGF, because inhibition of these factors results in the loss of both the left and right sixth arch arteries. Remarkably, they find that only the sixth arch arteries are sensitive to growth-factor-mediated signalling pathways, as the remodelling of the fourth arch artery was not affected by inhibition of these factors' receptors.

Although sixth arch arteries depend on Pitx2 for their normal, asymmetrical remodelling⁹,

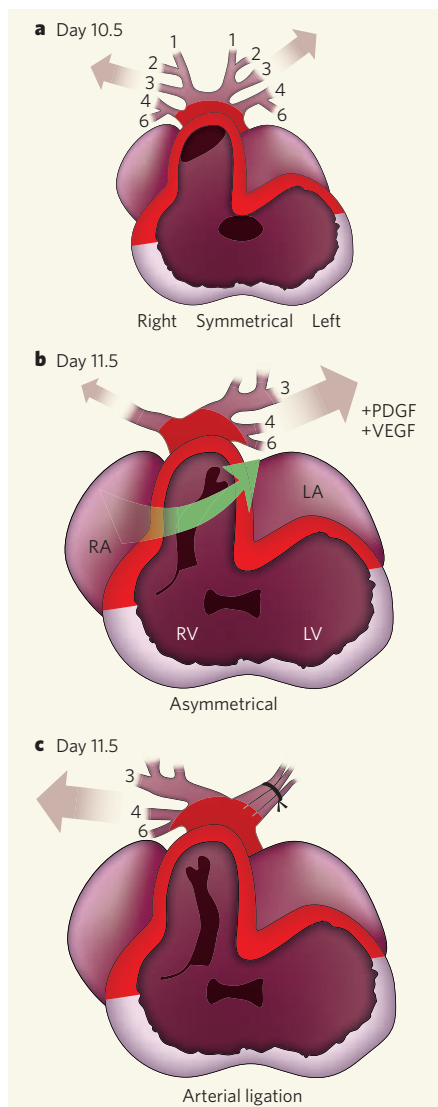


Figure 1 | Blood flow shapes the great arteries. **a**, The heart of a 10.5-day-old mouse embryo (the equivalent of 30-day-old human embryo) shows symmetrical development of branchial arch arteries (1–4 and 6); at this stage, equivalent amounts of blood flow through all of these arteries. **b**, By embryonic day 11.5 (the equivalent of day 35 in human embryos), these arch arteries have undergone asymmetrical remodelling. Consequently, the right fourth and sixth arch arteries regress, and the left fourth and sixth arch arteries persist to become the aortic artery and pulmonary trunk. At this stage, blood predominantly flows through the left arch arteries; this follows the rotation and realignment of the outflow tract (green arrow), and is concomitant with increased expression of the growth factors PDGF and VEGF. **c**, To test whether blood flow determines asymmetrical remodelling of the branchial arch arteries, Yashiro *et al.*⁴ surgically ligated the left arch arteries in 11.5-day-old mouse embryos, thereby preventing normal blood flow through them. This led to abnormal regression of the left sixth arch artery and the parallel development of the right arteries, into which blood flow was not obstructed. The anterior-heart-derived cells⁸ are shown in red and blood flow is indicated by pink arrows. LA, left atrium; LV, left ventricle; RA, right atrium; RV, right ventricle.

Yashiro *et al.* found to their surprise that *Pitx2* is not expressed in any of the cells that surround these arteries. Instead, this transcription factor is known¹⁰ to be expressed in the anterior heart, where it orchestrates rotation of the outflow tract^{8,9}. Given that the anterior heart requires the action of the growth factor Fgf8 (ref. 10), and that mouse embryos lacking *Pitx2* express abnormal levels of Fgf8 (ref. 11), it will be interesting to determine whether Fgf8 is another mediator of arch-artery regression.

Earlier work has demonstrated that several other mouse mutants that show defects in arch-artery laterality do not have either a deficiency in the Nodal–*Pitx2* signalling pathway or abnormal rotation of the outflow tract⁵. To reconcile these observations with those of Yashiro and colleagues, it is necessary to find out what other mechanisms underlie abnormal remodelling of the arch arteries and whether there is a common molecular pathway responsible for causing these congenital heart defects.

It also remains to be seen whether the cardiovascular abnormalities in the mutant mice studied by Yashiro *et al.* are due to a direct effect of haemodynamics. This is because a general reduction in cardiac output and blood flow could cause an overall decrease in shear-stress-responsive vascular growth factors, which might, in turn, result in the regression of certain vessels. Other questions that need to be addressed include whether direct manipulation of the outflow-tract rotation would affect arch-artery remodelling, and why the sixth arch artery is particularly sensitive to haemodynamics.

Nonetheless, Yashiro and colleagues' results provide a useful model for converting physical forces into genetic information — that is, the maintenance by haemodynamics of the expression of vessel-stabilization factors (such as PDGF and VEGF) that shape the asymmetrical cardiovascular system of mammals. It is also exciting that these researchers have successfully manipulated embryonic blood flow — a technically challenging task — to carry out genetic analysis. ■

Paige Snider and Simon J. Conway are in the Cardiovascular Development Group, Herman B. Wells Center for Pediatric Research, Indiana University School of Medicine, Indianapolis, Indiana 46202-5120, USA.
e-mail: siconway@iupui.edu

1. Thoma, R. *Untersuchungen über die Histogenese und Histomechanik des Gefäßsystems* (Ferdinand Enke, Stuttgart, 1893).
2. Groenendijk, B. C. W. *et al. Circ. Res.* **96**, 1291–1298 (2005).
3. Jones, E. A. V., le Noble, F. & Eichmann, A. *Physiology* **21**, 388–395 (2006).
4. Yashiro, K., Shiratori, H. & Hamada, H. *Nature* **450**, 285–288 (2007).
5. Snider, P., Olaopa, M., Firulli, A. B. & Conway, S. J. *ScientificWorldJournal* **7**, 1090–1113 (2007).
6. Meno, C. *et al. Cell* **94**, 287–297 (1998).
7. Ryan, A. K. *et al. Nature* **394**, 545–551 (1998).
8. Ai, D. *et al. Dev. Biol.* **296**, 437–449 (2006).
9. Liu, C. *et al. Development* **129**, 5081–5091 (2002).
10. Ilagan, R. *et al. Development* **133**, 2435–2445 (2006).
11. Lu, M.-F., Pressman, C., Dyer, R., Johnson, R. L. & Martin, J. F. *Nature* **401**, 276–278 (1999).



50 YEARS AGO

On the morning of November 3, the U.S.S.R. announced from Moscow the launching of the second artificial Earth satellite — about a month after the launching, on October 4, of the first ... For the first time in history, a living mammal from the Earth is travelling in an Earth satellite, for the second one is carrying a dog: at the time of writing it was “calm and behaving normally” according to Russian reports ... The launching of the second satellite is staggering enough in itself; but some Russian scientists have stated that it is hoped that the dog will return alive. They claim to have solved the immensely difficult ‘re-entry’ problem; that is, the safe passage through the atmosphere in spite of the great heat generated through friction. This possibility will be watched with the keenest interest. The greatest peril which the animal is facing is the absence, or considerable reduction in strength, of gravity; also it is conceivable that cosmic rays at that height may have a fatal effect on the nervous system.

From *Nature* 9 November 1957.

100 YEARS AGO

No-one more fully understands the danger of indiscriminately using a questionnaire than Dr. J. G. Frazer, who is publishing through the Cambridge University Press his “Questions on the Customs, Beliefs, and Languages of Savages” ... They are intended, not so much to be put directly to the savage, as to indicate to the inquirer in the field those subjects upon which students at home desire information. Leading questions should be avoided, as they tempt the savage to give answers which he thinks will be acceptable. The savage should be encouraged to talk in his usual vague way until he has exhausted his information for the time, when a question judiciously asked may jog his memory.

From *Nature* 7 November 1907.

50 & 100 YEARS AGO

OBITUARY

Wolfgang K. H. Panofsky (1919–2007)

Physicist, and passionate and influential advocate of arms control.

Wolfgang Panofsky — ‘Pief’ to his friends and colleagues — died of a heart attack on 24 September at his home in Los Altos, California. He was admired worldwide as a great physicist and the founding director of the Stanford Linear Accelerator Center. But beyond that, he earned universal respect for his humanity and integrity, and for the perseverance with which he fought to achieve the goals that he greatly valued.

Panofsky was born in Berlin in 1919, and was raised in Hamburg until 1934, when his father, the eminent art historian Erwin Panofsky, was dismissed from his professorship at the university because he was Jewish. Realizing that their lives were at risk as well as their careers, the Panofsky family sailed to the United States, settling in Princeton, New Jersey. The young Panofsky entered Princeton University at the age of 15, graduating in 1938 with a major in physics, and moved on to the California Institute of Technology in Pasadena for his graduate studies. He received his PhD in 1942 after completing his dissertation based on research in the laboratory of Jesse W. DuMond, whose daughter, Adele, he married the same year.

Although officially an enemy alien, Panofsky was granted clearance to work on the atom bomb and other military projects during the Second World War. In 1945 he was recruited by Luis Alvarez to the Radiation Laboratory at the University of California, Berkeley, where he remained for the next six years. These were fruitful years of research in elementary particle physics for Panofsky. Working with several colleagues at the accelerators at the Radiation Lab, he made important measurements of the properties of π mesons (pions, mediators of the strong nuclear force). Most notably, in collaboration with Jack Steinberger, he confirmed the existence of the elusive neutral pion and discovered its decay into two γ -rays.

The early 1950s were a time of security witch-hunts and congressional investigations into communist subversion in the United States. Panofsky objected on principle when a loyalty oath was imposed on the faculty at the University of California. Although willing to sign this oath, which was later invalidated by the courts and thrown out, he felt that it made the situation there intolerable and moved to Stanford University in 1951 as a professor of physics. He also assumed directorship of Stanford's High Energy Physics Laboratory, which had an electron linear accelerator that he developed into a powerful research tool.

The outstanding productivity of that facility stimulated a proposal to build a

two-mile linear accelerator. The result was the Stanford Linear Accelerator Center (SLAC), with Panofsky serving as director from its authorization in 1961 until 1984. A measure of his leadership and SLAC's success are the three Nobel prizes for discoveries that were made there — the quark structure of protons and neutrons; the J/ψ meson whose constituents are the charmed quarks; and the heavy τ lepton. Panofsky also supported major advances in accelerator technology, including the development and exploitation of electron–positron storage rings and colliders.

As a teacher, Panofsky was renowned for his excellent lectures, his patience and his accessibility. He created the same open, collegial relationship with students that he nurtured at SLAC for the entire staff, top to bottom. On the wider stage, he was committed to supporting international collaboration in science, and to advancing the cause of arms control and peace in a world in which nuclear weapons of enormously devastating potential were proliferating.

He pursued those efforts with great vigour, whether at Pugwash disarmament meetings, participating in official government or National Academy of Sciences conferences and working panels, or through his wide network of personal contacts. He fostered bonds of cooperation in the belief that they were of great importance even beyond their value to science. He saw improving the mutual understanding and trust between otherwise estranged communities in countries with confrontational relationships, particularly in the Soviet Union and China, as steps towards reducing the misunderstandings that could trigger a nuclear holocaust.

Panofsky's commitment to international cooperation in high-energy physics started as far back as the 1950s, including serving on the high-energy physics subcommittee of the International Union of Pure and Applied Physics. It continued to the end of his life, with his work as an adviser for the scientific programme at China's Institute of High Energy Physics in Beijing. He took special interest in the Beijing Electron/Positron Collider, which SLAC strongly supported.

As a White House science adviser during the administrations of presidents Dwight D. Eisenhower and John F. Kennedy, Panofsky's technical contributions were instrumental in the negotiation between the United States and the Soviet Union that led, in 1963, to



P. GINTER/SCIENCE FACTION/GETTY

the Limited Test Ban Treaty that prohibited all except underground nuclear explosive tests. Throughout his life, he fought for a Comprehensive Test Ban Treaty, and against the decision to deploy ballistic-missile defences, on the grounds of their technical limitations and ineffectiveness against massive attacks.

In 1977, his prominence in arms control drew the attention of *Playboy* magazine. The article pointed out that “He is 5-feet, 2-inches tall, weighs 150 pounds, neither smokes nor drinks, and is manifestly, painfully indifferent to clothes” — but that, as a “key figure in the Strangelove business”, he had helped the US government avoid pitfalls it might otherwise have stumbled into.

Panofsky received just about every honour that science, academia and a national government can bestow. His awards included the National Medal of Science and the Enrico Fermi Award from the US government. His many contributions to scientific collaborations were recognized by his election as an honorary member of the leading scientific societies in the United Kingdom, France, Russia and China.

Pief spent the last day of his life in his office at SLAC, writing and arguing for arms control, and looking forward to the publication of his informal autobiography, *Panofsky on Physics, Politics, and Peace: Pief Remembers*, which appeared the following week. He is survived by his wife Adele DuMond Panofsky, 5 children and 11 grandchildren.

Sidney D. Drell

Sidney D. Drell is professor emeritus of the Stanford Linear Accelerator Center, Stanford University, Menlo Park, California 94025, USA, and a senior fellow of the university's Hoover Institution.

e-mail: drell@slac.stanford.edu



Cover illustration

The centrepiece of this landmark collection of papers is the publication of newly sequenced genomes for ten *Drosophila* species, which are compared with the two previously known. On the cover are anaesthetized individuals of all 12 species. (Image by Andrew G Clark, Cornell University.)

GENOME LABOURS BEAR FRUIT

Approximately 100 years ago now, the fruit fly *Drosophila* was first bred at Harvard for use in laboratory research. These stocks led to experiments establishing many early tenets of classical genetics. Hard-core *Drosophila* researchers can even trace their own 'pedigree' based on their relationship to Thomas Hunt Morgan, the father of fruit-fly genetics.

In 2007, *Drosophila* is one the most Internet-savvy laboratory organisms, with extensive databases devoted to genetics, genomics, taxonomy, breeding and mail ordering. Several Nobel Prizes have been based in part or in total on work in flies. Flies have even been sent on the space shuttle to study immune system function. The genome of the most familiar species, *Drosophila melanogaster*, was the test case for 'whole-genome shotgun sequencing', which opened the doors to the era of organismal genome sequencing.

The community has not rested on these laurels, and now marries the pre-eminent position of the fly in evolutionary biology with cutting-edge genomics by studying 12 completed *Drosophila* genomes at once. *Nature* is honoured to publish two Articles detailing the sequence and analysis, allowing the description of 'evolutionary signatures' on functional elements throughout the genomes. To capture the scope of this achievement and celebrate the fruit fly as a model organism in basic research, we have also asked researchers to explore the past, present and future of *Drosophila* in many diverse areas of biology — from physiology and cell biology to neural circuits and gene expression. Size doesn't matter: these tiny fruit flies are once again poised to take on the world.

Chris Gunter, Senior Editor
Francesca Cesari, Associate Editor
Deepa Nath, Senior Editor
I-Han Chou, Senior Editor
Alex Eccleston, Senior Editor
Ritu Dhand, Chief Biology Editor

NEWS AND VIEWS

- 184 Evolutionary genomics: Come fly with us**
 E Birney

PROGRESS

- 186 *Drosophila* and the genetics of the internal milieu**
 P Leopold & N Perrimon
- 189 Orchestrating size and shape during morphogenesis**
 T Lecuit & L Le Goff

REVIEWS

- 193 Into the mind of a fly**
 L B Vosshall
- 198 Imaging *Drosophila* gene activation and polymerase pausing *in vivo***
 J T Lis

ARTICLES

- 203 Evolution of genes and genomes on the *Drosophila* phylogeny**
Drosophila 12 Genomes Consortium
- 219 Discovery of functional elements in 12 *Drosophila* genomes using evolutionary signatures**
 A Stark *et al.*

LETTERS

- 233 Constraint and turnover in sex-biased gene expression in the genus *Drosophila***
 Y Zhang, D Sturgill, M Parisi, S Kumar & B Oliver
- 238 Demasculinization of X chromosomes in the *Drosophila* genus**
 D Sturgill, Y Zhang, M Parisi & B Oliver

NEWS & VIEWS

EVOLUTIONARY GENOMICS

Come fly with us

Ewan Birney

The genomes of 12 fly species have been analysed comparatively. Why should we care? Because sequences that have resisted the selective forces of evolution from fly to human must have functional significance.

Geneticists and molecular biologists have always had a soft spot for the fruitfly *Drosophila melanogaster*, for this innocuous organism is continually providing insights into the biology of multicellular organisms. But in the 1990s, when the nematode worm *Caenorhabditis elegans* became the life and soul of the genomics party, and we humans were always the guests of honour, flies were in danger of being left off the guest list.

This started to change when Celera Genomics¹ sequenced the genome of *D. melanogaster* as a trial, before tackling the genomes of larger species. Now, in the era of evolutionary genomics, the sequencing of 10, and comparative analysis of 12, fly species — reported in this issue^{2,3} and elsewhere in more than 40 companion papers — means that flies have overtaken other species to become a favourite organism of genomicists too.

Every aspect of an organism emerges and persists through evolution. Consequently, researchers have always used evolutionary analysis to understand genomes, in particular to identify protein-coding genes that are conserved between organisms. But evolutionary processes can be studied far more effectively than by merely cataloguing the gene content of a genome. Specifically, researchers can investigate two complementary evolutionary aspects: negative selection and positive selection. Stark *et al.*² (page 219) study negative selection, or the presence of functional genomic elements that, despite having undergone many random mutational events, have not changed in function (Fig. 1a). By contrast, the *Drosophila* 12 Genomes Consortium (Clark and colleagues, page 203)³ investigate positive selection, or the acquisition of new functions in different species (Fig. 1b).

The remarkable diversity of fruitfly species makes them ideal organisms for such comparative analysis. Consequently, the authors studied closely related species such as *D. simulans* (pictured) and *D. sechellia* (which have a genetic distance equivalent to that between humans and closely related primates), as well as more distant drosophilids such as *D. grimshawi*. This is one of the many exotic Hawaiian species, and is physically 100 times bigger than

its normal laboratory cousins, with a genetic distance between them equivalent to that between humans and lizards.

To discover functional elements and to refine our understanding of elements already known, Stark *et al.*² draw on most of our current knowledge of these elements, and use nature's own repertoire of mutations and selection. They consider all known classes of functional element — from the well-understood protein-coding genes to the more elusive motifs that regulate gene expression. These analyses allowed the authors to identify incorrect biological information ascribed to specific genomic sequences of *D. melanogaster*.

Stark and colleagues identify several evolutionarily conserved elements embedded in continuous sequences of coding DNA. These include stop codons (three-nucleotide sequences that signal termination of a protein sequence) and frameshift mutations, which throw the coding sequence out of step. It is hard to imagine that such gene structures — in which, for example, stop codons transcribed into messenger RNAs are ignored by the protein-translation machinery — are compatible with the normal rules of translation. So these findings strongly indicate the existence of additional, as yet unknown, mechanisms for the pre-translational processing of mRNAs, or alternative modes of translation.

MicroRNAs are short sequences of naturally occurring, single-stranded RNA that regulate gene expression. The authors next investigated genes for non-coding RNA sequences, such as microRNAs, and identify new microRNA sequences, thereby expanding the list of these regulatory sequences in *D. melanogaster* from 74 to 101.

Regulatory motifs are another type of functional element Stark *et al.* studied. The authors

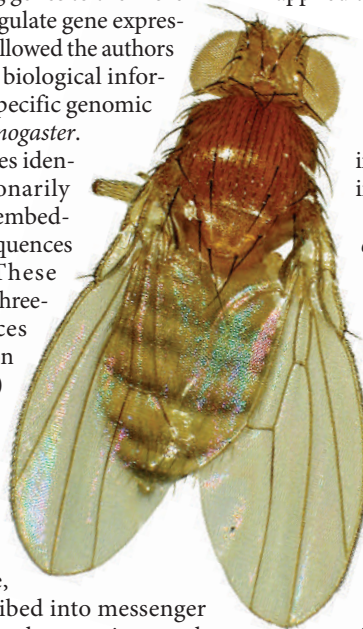
provide both an extensive 'dictionary' of such motifs and, for the first time in a genome-wide manner for an organism, a set of instances in which such motifs are putatively functional. Using genomics to identify cases of regulatory-motif activity is, indeed, an exciting new approach, and uses what the authors call 'branch length score'. This method takes into account the alignment and sequencing errors that are common in real data, and it can be applied to the whole of a phylogenetic tree.

Stark *et al.* carefully assess different statistical aspects of their method, providing a goldmine of functional elements that can be confidently used by molecular biologists studying flies and by laboratories interested in gene regulation.

Compared with the work of Stark *et al.*, Clark and colleagues' findings³ on aspects of positive selection are of less direct use to molecular biologists working on *D. melanogaster*. Instead, their results provide for the first time a comprehensive set of genome-wide insights into how organisms arise during evolution. Statistically, the authors' analysis is not as powerful as that of Stark and colleagues. But this is not surprising, because their aim was to understand positive selection, which occurs in a non-continuous manner across the different

Drosophila lineages, whereas the negative selection studied by Stark *et al.* is relatively constant and can easily be aggregated across the entire data set (Fig. 1).

Nevertheless, Clark and colleagues provide valuable insights into the evolution of *Drosophila* species. For example, by comparing the genomes of 12 drosophilid species, 10 of which they have sequenced and present in this issue, they show that, on both large and small scales, genomic rearrangements are extremely common in these genomes. They also find that about a third of the genes have undergone positive selection through mutations that affect the position of at least one amino acid. This suggests that positive selection



S. J. CASTREZANA

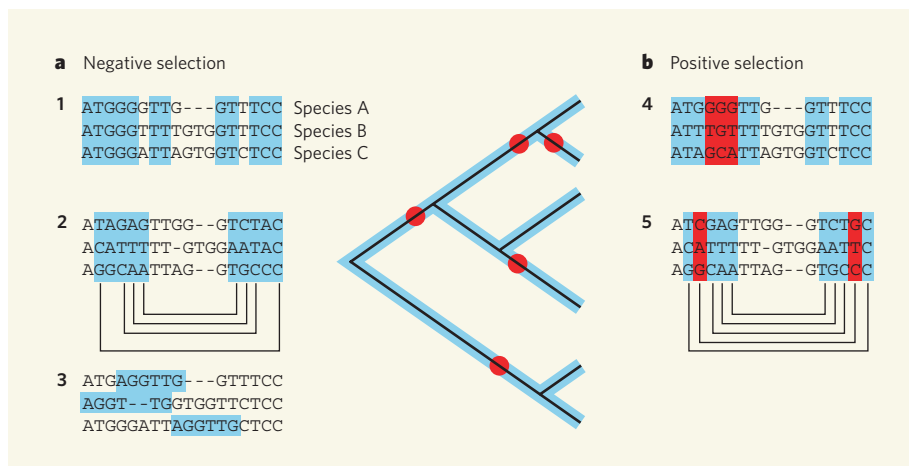


Figure 1 | Two types of evolutionary selection. **a**, For their analysis, Stark *et al.*² studied negative selection (blue), in which specific bases (from the four possible ones, A, T, C and G) remain roughly constant across the genomes of all lineages to ensure the conservation of functional genomic elements. Such an analysis uses three main methods: identifying conserved protein-coding sequences (1); identifying conserved paired bases in non-coding RNA genes (2); and identifying conserved specific motifs in the locale of the alignment (3). **b**, By contrast, Clark and colleagues³ searched for cases of positive selection (red), which results in modification of specific bases in different species, leading to the acquisition of new functions. Two main methods are used to study positive selection: identifying fast-evolving codons embedded in a set of negatively selected codons (4), and searching for fast-evolving base pairs in the context of a non-coding RNA structure (5). The central tree, which indicates the phylogeny of the species (not all branches are shown), highlights the fact that, whereas negative selection is relatively continuous, positive selection is intermittent. Black lines in 2 and 5 show base pairing in the secondary structure. So although the positions paired may not show conservation on each blue column, the paired positions maintain a valid base pair.

occurs across many genes in a genome.

Codon-usage bias is the selective use by an organism of certain codons from a pool of codons that all specify a given amino acid, and it varies between different organisms. Clark and colleagues discover that, compared with other drosophilids, one species, *D. willistoni*, shows substantially reduced codon-usage bias.

The authors also show that genes encoding proteins involved in olfaction and immunity — the usual suspects for positive selection among protein-coding genes — have evolved faster than the rest of the genome. Rapid evolution was also seen in genes that regulate specific aspects of *Drosophila* physiology, such as insecticide resistance. During its long association with humans, *Drosophila* has endured radical changes to its environment, ranging from the introduction of insecticides to the transfer of species through human migration. We can therefore probably expect many interesting studies attempting to correlate genomic changes with such events in the fly's evolutionary history.

What are the broader implications of the findings of these two studies^{2,3}, particularly for further study of the human genome? In the case of negative selection, the evolutionary-genomics approach taken by Stark *et al.* clearly provides impressive insights into functional elements that are conserved across a clade (a group of related organisms). The proposed Mammalian Genome Project⁴, which is well under way, is likely to have roughly the same statistical power as Stark and colleagues' data

set. This would mean that we have a collection of powerful exploratory methods that can be applied to large-scale genomic analysis in mammals, and that are complementary to experimental techniques. In theory, there should be no qualitative difference in generating results for the *Drosophila* and mammalian clades using these methods. Nonetheless, the larger size of mammalian genomes, and the fact that there are potentially more fluctuations in the rate of neutral evolution, both across the genome of one species and between genomes of different species, may pose some interesting problems to be overcome.

Researchers are concerned that data obtained using methods based on evolutionary-genomic analysis do not entirely overlap with those obtained through experimental discovery methods, such as ChIP-chip and ChIP-seq, which generate comprehensive *in vivo* maps of transcription-factor binding sites and other functional DNA elements. In particular, these experimental techniques often define a set of elements that are not identified as conserved by the sensitive criteria of evolutionary-genomic analysis. As discussed previously⁵ and by Stark *et al.*, this mismatch seems to be consistent across species and analyses performed by different laboratories. So it probably reflects our lack of understanding of how seemingly neutral evolutionary processes give rise to new, biochemically active elements before selection kicks in, rather than the existence of a large portion of lineage-specific elements, or defects in the methods used.

The analysis of positive selection by Clark

and colleagues³ is undoubtedly the broadest and most detailed investigation performed in any clade of multicellular organisms. Their study emphasizes the fact that, to understand differences between species, and thus how evolution leads to adaptive changes, we must improve the methods we use, and look at larger data sets and a broader range of species. This argument favours both sequencing the genomes of more species — now a realistic prospect given the advent of radically cheaper sequencing technologies — and determined efforts to carry out experimental studies on other members of each clade. Such studies are essential to any attempts to correlate sequence changes with changes in functional elements, and so test any new methods developed.

For the drosophilids, the next phase should entail sequencing the genomes of yet more fruitflies and other members of the order Diptera, thereby adding to the sequenced genomes of the drosophilids discussed here and their distant cousins, mosquitoes^{6,7}. Moreover, more sequences should be generated at the population level — that is, we should sequence several individuals of the same species to gather the raw material for classical population-genetic analysis, which can be used for comparison with evolutionary data. Attempts to generate such resources are well under way for some drosophilid species. Finally, concerted efforts to obtain new experimental results in other species, beyond the experimental workhorse *D. melanogaster*, are needed for comparison with data obtained through evolutionary analysis.

Clark and colleagues' findings suggest that, to understand the fascinating adaptive changes among primates, including those unique to humans, we probably need to sequence the genome of every extant primate (and, where possible, any extinct primates with recoverable DNA), using optimal sequencing strategies to obtain both population-level data and accurate genome sequences. Basic molecular-biological studies on cell lines from selected primate species will also be needed to correlate sequence changes with changes in functional elements.

Returning to the present, the data presented and analysed by Stark *et al.*² and Clark and colleagues³ provide the first significant example of the power of evolutionary genomics, which will be a central research theme for the next decade. It also means that genomicists can finally join their geneticist and molecular-biologist colleagues in the fruitfly fan club.

Ewan Birney is at the European Bioinformatics Institute, Wellcome Trust Genome Campus, Hinxton, Cambridge CB10 1SD, UK.
e-mail: birney@ebi.ac.uk

1. Adam, M. D. *et al.* *Science* **287**, 2185–2195 (2000).

2. Stark, A. *et al.* *Nature* **450**, 219–232 (2007).

3. *Drosophila* 12 Genomes Consortium *Nature* **450**, 203–218 (2007).

4. www.broad.mit.edu/mammals

5. The ENCODE Project Consortium *Nature* **447**, 799–816 (2007).

6. Holt, R. A. *et al.* *Science* **298**, 129–149 (2002).

7. Nene, V. *et al.* *Science* **316**, 1718–1723 (2007).

PROGRESS

Drosophila and the genetics of the internal milieu

Pierre Leopold¹ & Norbert Perrimon²

'Homeostasis', from the Greek words for 'same' and 'steady', refers to ways in which the body acts to maintain a stable internal environment despite perturbations. Recent studies in *Drosophila* exemplify the conservation of regulatory mechanisms involved in metabolic homeostasis. These new findings underscore the use of *Drosophila* as a model for the study of various human disorders.

In 1865, Claude Bernard, in his *Introduction to the Study of Experimental Medicine*, proposed the concept of the 'internal milieu', later referred to as 'homeostasis' in 1932 by Walter Cannon. Homeostasis is one of the most remarkable properties of complex systems that permit organisms to function effectively in a broad range of environmental conditions and allow survival against fluctuations such as temperature, salinity, acidity and nutrients. The kidney, for example, contributes to homeostasis by maintaining salt and ion levels in the blood, regulating the excretion of urea, reabsorbing substances into the blood and regulating blood water levels. Homeostasis depends on the dynamic action and interaction of a number of sensors to adapt to ever-changing environmental conditions, and on hundreds of positive and negative feedback mechanisms.

In recent years, and perhaps surprisingly, we have learned, mostly from genetic studies of physiological responses in *Drosophila*, that many parallels exist between invertebrate and mammalian homeostasis. As exemplified by the seminal studies of Vincent Wigglesworth¹, insects have historically been long-standing models in physiology as a result of their technical advantages such as short life cycles, large populations and the possibility of simple surgical procedures. In the past, however, interest in their physiology was driven mostly by intellectual fascination with their diverse physiological adaptations to virtually every habitat on Earth, as well as by potential applications for pest control. Here we review several recent findings that establish *Drosophila* as an emerging model for mammalian physiology.

Metabolic homeostasis

Drosophila and all other higher organisms constantly adapt their energy needs to nutritional status through metabolic regulation; that is, sugar and lipid homeostasis. The emerging picture in the fly is that of a simpler and well-balanced integrated system between various organs, each with distinct physiological roles in maintaining energy homeostasis (Fig. 1). *Drosophila* has a less complex genome than vertebrates and has little gene redundancy. For example, flies have a unique insulin receptor that mediates all functions that have so far been attributed to insulin-like peptides. Sugar levels are maintained by neurosecretory cells located in the brain and ring gland (together forming a bipartite '*Drosophila* pancreas') that secrete insulin and adipokinetic hormone (AKH, the insect glucagon) into the open haemolymph (the '*Drosophila* blood')^{2–5} (reviewed in refs 6–8). Excess sugar is stored in the form of glycogen that accumulates both

in muscles and in the fat body (the '*Drosophila* liver'). On stimulation by AKH, the fat-body glycogen phosphorylase is activated and sugar (trehalose in insects) is released into the haemolymph. The fat body also acts as the storage place for fat and thus is reminiscent of the 'white fat' of vertebrates. A recent series of studies illustrate the convergences in the control of lipid metabolism between flies and mammals. When food is scarce, fat is released from the fat body into the haemolymph and is then captured by the oenocytes (the fly 'hepatocytes') for energy production⁹. In both systems, information on energy shortage is relayed by lipolytic hormones, which activate a pathway dependent on cyclic-AMP-dependent protein kinase that leads to the activation of specific lipases at the surface of intracellular lipid droplets. However, in flies the specific role of these lipases is still unclear: both adipose triglyceride lipase (*ATGL*) knockout mice and *brummer* (the *ATGL* orthologue in flies) mutant flies are obese as a result of an impairment of lipid mobilization^{10,11}.

Genetic ablations have had major roles in deciphering the elaborate crosstalk between the various sensor tissues and their responsive organs. For example, ablation of insulin-producing cells leads to diabetic flies and, conversely, flies in which AKH-producing cells have been ablated have low levels of circulating sugars^{3,12}. Further, proper mobilization of fat from the fat body is perturbed in the absence of oenocytes—an interaction reminiscent of the crosstalk between hepatocytes and adipocytes in humans^{9,13}. Additional

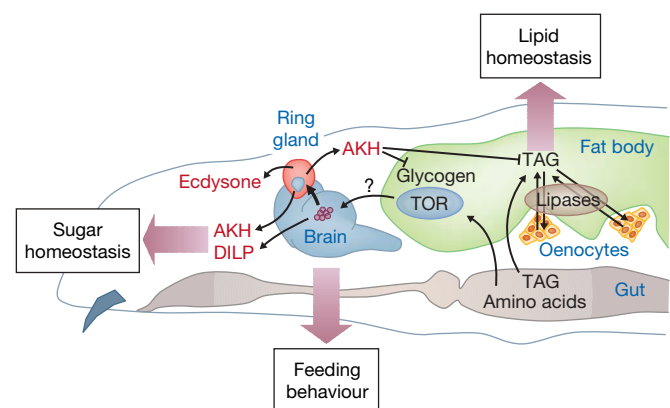


Figure 1 | Interactions between the various organs involved in metabolic homeostasis in a *Drosophila* larva. Hormone names are shown in red, tissue names in blue. DILP, *Drosophila* insulin-like peptides; TAG, triacylglycerol.

¹University of Nice-Sophia Antipolis/CNRS UMR6543, Parc Valrose, 06108 Nice cedex 2, France. ²Department of Genetics and Howard Hughes Medical Institute, Harvard Medical School, 77 Avenue Louis Pasteur, Boston, Massachusetts 02115, USA.

insights have been obtained from the use of drugs such as sulphonylurea (glyburide or tolbutamide), currently used in the treatment for type 2 diabetes as activators of insulin secretion by pancreatic beta cells¹⁴. *Drosophila* larvae fed with sulphonylurea show increased sugar levels, suggesting that AKH-expressing cells in the fly use a conserved mechanism for coupling circulating sugars to glucagon and AKH release⁴.

An important notion emerging from studies in the fly is that all tissues in the organism might not be exposed or equally sensitive to variations in nutritional conditions. The fat body, in particular, seems to be a unique metabolic sensor because it has a pivotal function in buffering nutritional information for the entire animal^{15–17}. For example, in conditions of amino-acid restriction, the conserved TOR pathway in fat cells functions as an energy sensor that induces a remote and systemic inhibition of insulin/insulin-like growth factor signalling, leading to a general decrease in growth during larval development¹⁶.

Cross-regulation between tissues for the control of insulin signalling is reminiscent of recent observations in mammals related to insulin resistance, which leads to obesity and type 2 diabetes, two components of a highly prevalent and complex disorder called the metabolic syndrome^{18,19}. Whether *Drosophila* is a good model for dissecting the basic molecular and genetic mechanisms of this disorder is still uncertain; however, the first example of insulin-resistant flies has emerged recently. Teleman *et al.*²⁰ showed that flies that do not express the microRNA-encoding gene *miR-278* in the fat body are lean and have elevated levels of sugar in the haemolymph, despite high expression levels of insulin. Further, whereas injection of insulin into wild-type larvae provoked an activation of the insulin pathway in fat cells, this response was abrogated in *miR-278* mutant animals, indicating that the 'lean fly' phenotype is associated with insulin resistance in the fat body²⁰. These findings are reminiscent of the decreased fat-pad mass observed in the fat-specific insulin receptor knockout model in the mouse²¹. Thus, as in mammals, insulin signalling in *Drosophila* regulates patterns of energy storage in fat and other tissues, and disruption of this process by insulin resistance leads to important lipid disorders.

Interaction between metabolism and other processes

In addition to progress in our understanding of the logic of metabolic homeostasis in the fly, important advances are being made in our knowledge of the complex interactions between metabolism and growth, ageing or behaviour. For relevant reviews in the *Drosophila* literature see refs 22–25. How organisms adapt their growth programme to changes in energy needs and status, and how hormonal systems such as insulin and steroid hormones interact with metabolic regulation, are areas of particular interest for future research. In particular, functional interactions recently identified between insulin and the steroid hormone ecdysone^{26,27} suggest that fly steroids also participate in metabolic control. Further, in adult flies a decrease in metabolic rates resulting from dietary restriction or decreased insulin signalling results in extension of the normal lifespan (reviewed in refs 23, 24). The mechanism by which dietary restriction controls lifespan is unclear, but metabolic studies in this short-lived model system will undoubtedly contribute to an explanation of the control of ageing by nutrition.

Finally, several complex behaviours are modulated by metabolic conditions. Feeding behaviour is regulated by two major intermingled controls: the homeostatic and the hedonic systems²⁸. Homeostatic regulation of feeding ensures that circulating nutrient levels are sensed, which in turn directly regulates feeding activity. Work on *Drosophila* and studies on the mouse recently showed that a TOR-dependent molecular sensor for amino acids exists in specific brain cells (hypothalamic cells in the mouse; neuroendocrine cells in *Drosophila*). These cells sense variations in circulating amino-acid levels and in turn regulate feeding^{29,30}. Understanding the circuits that transmit these neuroendocrine signals is of prime interest for

the study of eating disorders and are beginning to be studied in *Drosophila*²⁵.

Concluding remarks

The goal of this review is to provide a selective overview of recent progress in studies of metabolic homeostasis in *Drosophila*. Through the examples cited, it is clear that many questions will be answered in the next few years. For example, studies will decipher the specific crosstalk between various larval and adult tissues for the control of energy homeostasis. Characterization of mutants associated with insulin resistance is likely to provide insights into the mechanisms of insulin response and its disruption. In addition, *Drosophila* has great potential as a model system in which to study the balance between lipid storage and lipolysis, a process whose disruption in humans leads to obesity or type 2 diabetes.

In flies, the characterization of homeostatic regulatory mechanisms is facilitated by the smaller number of homeostatic constants and, of course, the ever-improving arsenal of available genetic tools. Genetic screens have already identified new components of metabolic regulatory networks (such as *meltd*, a new modulator of FOXO and TSC2 activity³¹), whose function can now be tested in mammals. Genome-wide RNA-mediated interference (RNAi) screens, both in tissue culture cells³² and *in vivo*³³, provide unique tools for the study of metabolic regulations. In particular, *in vivo* RNAi, allowing the activity of a specific pathway to be reduced in a given tissue, should showcase *Drosophila* as a model for metabolic disorders. These *Drosophila* models should prove to be very powerful for drug screening, to determine modes of drug action, and to identify drug targets. Finally, a better characterization of *Drosophila* metabolites will benefit the continuing work to understand experimental perturbations of the 'internal milieu'.

1. Wigglesworth, V. B. *Principles of Insect Physiology* (Chapman & Hall, London, 1972).
2. Brogiolo, W. *et al.* An evolutionarily conserved function of the *Drosophila* insulin receptor and insulin-like peptides in growth control. *Curr. Biol.* **11**, 213–221 (2001).
3. Rulifson, E. J., Kim, S. K. & Nusse, R. Ablation of insulin-producing neurons in flies: growth and diabetic phenotypes. *Science* **296**, 1118–1120 (2002).
4. Kim, S. K. & Rulifson, E. J. Conserved mechanisms of glucose sensing and regulation by *Drosophila* corpora cardiaca cells. *Nature* **431**, 316–320 (2004).
5. Lee, G. & Park, J. H. Hemolymph sugar homeostasis and starvation-induced hyperactivity affected by genetic manipulations of the adipokinetic hormone-encoding gene in *Drosophila melanogaster*. *Genetics* **167**, 311–323 (2004).
6. Gade, G., Hoffmann, K. H. & Spring, J. H. Hormonal regulation in insects: facts, gaps, and future directions. *Physiol. Rev.* **77**, 963–1032 (1997).
7. Wu, Q. & Brown, M. R. Signaling and function of insulin-like peptides in insects. *Annu. Rev. Entomol.* **51**, 1–24 (2006).
8. Geminard, C. *et al.* Control of metabolism and growth through insulin-like peptides in *Drosophila*. *Diabetes* **55** (Suppl. 2), S5–S8 (2006).
9. Gutierrez, E., Wiggins, D., Fielding, B. & Gould, A. P. Specialized hepatocyte-like cells regulate *Drosophila* lipid metabolism. *Nature* **445**, 275–280 (2007).
10. Gronke, S. *et al.* Brummer lipase is an evolutionary conserved fat storage regulator in *Drosophila*. *Cell Metab.* **1**, 323–330 (2005).
11. Haemmerle, G. *et al.* Defective lipolysis and altered energy metabolism in mice lacking adipose triglyceride lipase. *Science* **312**, 734–737 (2006).
12. Broughton, S. J. *et al.* Longer lifespan, altered metabolism, and stress resistance in *Drosophila* from ablation of cells making insulin-like ligands. *Proc. Natl Acad. Sci. USA* **102**, 3105–3110 (2005).
13. Oike, Y., Akao, M., Kubota, Y. & Suda, T. Angiotensin-like proteins: potential new targets for metabolic syndrome therapy. *Trends Mol. Med.* **11**, 473–479 (2005).
14. Nagashima, K. *et al.* Sulphonylurea and non-sulphonylurea hypoglycemic agents: pharmacological properties and tissue selectivity. *Diabetes Res. Clin. Pract.* **66** (Suppl 1), S75–S78 (2004).
15. Britton, J. S. & Edgar, B. A. Environmental control of the cell cycle in *Drosophila*: nutrition activates mitotic and endoreplicative cells by distinct mechanisms. *Development* **125**, 2149–2158 (1998).
16. Colombani, J. *et al.* A nutrient sensor mechanism controls *Drosophila* growth. *Cell* **114**, 739–749 (2003).
17. Zinke, I., Kirchner, C., Chao, L. C., Tetzlaff, M. T. & Pankratz, M. J. Suppression of food intake and growth by amino acids in *Drosophila*: the role of *pumpless*, a fat body expressed gene with homology to vertebrate glycine cleavage system. *Development* **126**, 5275–5284 (1999).
18. Petersen, K. F. *et al.* Inaugural article: The role of skeletal muscle insulin resistance in the pathogenesis of the metabolic syndrome. *Proc. Natl Acad. Sci. USA* **104**, 12587–12594 (2007).

19. Grundy, S. M. Metabolic syndrome: a multiplex cardiovascular risk factor. *J. Clin. Endocrinol. Metab.* **92**, 399–404 (2007).
20. Teleman, A. A., Maitra, S. & Cohen, S. M. *Drosophila* lacking microRNA miR-278 are defective in energy homeostasis. *Genes Dev.* **20**, 417–422 (2006).
21. Kitamura, T., Kahn, C. R. & Accili, D. Insulin receptor knockout mice. *Annu. Rev. Physiol.* **65**, 313–332 (2003).
22. Edgar, B. A. How flies get their size: genetics meets physiology. *Nature Rev. Genet.* **7**, 907–916 (2006).
23. Giannakou, M. E. & Partridge, L. Role of insulin-like signalling in *Drosophila* lifespan. *Trends Biochem. Sci.* **32**, 180–188 (2007).
24. Tatar, M. Diet restriction in *Drosophila melanogaster*. Design and analysis. *Interdiscipl. Top. Gerontol.* **35**, 115–136 (2007).
25. Melcher, C., Bader, R. & Pankratz, M. J. Amino acids, taste circuits, and feeding behavior in *Drosophila*: towards understanding the psychology of feeding in flies and man. *J. Endocrinol.* **192**, 467–472 (2007).
26. Colombani, J. *et al.* Antagonistic actions of ecdysone and insulins determine final size in *Drosophila*. *Science* **310**, 667–670 (2005).
27. Mirth, C. Ecdysteroid control of metamorphosis in the differentiating adult leg structures of *Drosophila melanogaster*. *Dev. Biol.* **278**, 163–174 (2005).
28. Saper, C. B., Chou, T. C. & Elmquist, J. K. The need to feed: homeostatic and hedonic control of eating. *Neuron* **36**, 199–211 (2002).
29. Wu, Q., Zhang, Y., Xu, J. & Shen, P. Regulation of hunger-driven behaviors by neural ribosomal S6 kinase in *Drosophila*. *Proc. Natl Acad. Sci. USA* **102**, 13289–13294 (2005).
30. Cota, D. *et al.* Hypothalamic mTOR signaling regulates food intake. *Science* **312**, 927–930 (2006).
31. Teleman, A. A., Chen, Y. W. & Cohen, S. M. *Drosophila* Melted modulates FOXO and TOR activity. *Dev. Cell* **9**, 271–281 (2005).
32. Perrimon, N. & Mathey-Prevot, B. Applications of high-throughput RNA interference screens to problems in cell and developmental biology. *Genetics* **175**, 7–16 (2007).
33. Dietzl, G. *et al.* A genome-wide transgenic RNAi library for conditional gene inactivation in *Drosophila*. *Nature* **448**, 151–156 (2007).

Acknowledgements We thank Liz Perkins for comments on the manuscript. Work in the Perrimon laboratory is supported by the Howard Hughes Medical Institute and the NIH, and in the Leopold laboratory by INSERM, the CNRS, the Agence Nationale de la Recherche and the Fondation pour la Recherche Médicale.

Author Information Reprints and permissions information is available at www.nature.com/reprints. Correspondence should be addressed to P.L. (leopold@unice.fr) or N.P. (perrimon@receptor.med.harvard.edu).

PROGRESS

Orchestrating size and shape during morphogenesis

Thomas Lecuit^{1,2} & Loïc Le Goff^{1,2}

Living organisms exhibit tremendous diversity, evident in the large repertoire of forms and considerable size range. Scientists have discovered that conserved mechanisms control the development of all organisms. *Drosophila* has proved to be a particularly powerful model system with which to identify the signalling pathways that organize tissue patterns. More recently, much has been learned about the control of tissue growth, tissue shape and their coordination at the cellular and tissue levels. New models integrate how specific signals and mechanical forces shape tissues and may also control their size.

Questions such as how can groups of cells make up organized tissues, organs and bodies, how can development produce organisms with reproducible morphological patterns, and what mechanisms underlie the diversity of organ size and shape (Fig. 1) have haunted scientists for over a century. From the early observations of embryology to the quantitative models of systems biology, important discoveries marked the long history of morphogenesis.

Drosophila has proven to be a powerful system with which to elucidate the molecular mechanisms of morphogenesis, identifying the signals that pattern the body plan and characterizing cell mechanics and dynamics underling tissue remodelling. A principal challenge is to understand within a single mechanistic framework how these patterning signals and cellular responses—such as cell division and cell shape changes—are coordinated in tissue growth and tissue remodelling.

The size and shape of genetically marked clones of cells reflect in miniature the size and shape of the tissue they belong to. Cell division, cell death, cell shape changes and cell rearrangements are the building blocks on which tissues are shaped and organs are made (Fig. 2). The orchestration of these elementary processes depends on a constraining genetic programme operating on cell behaviour: for instance, a specific set of signalling molecules, growth factors, promote cell divisions and tissue size, whereas other proteins control the orientation of cell divisions, oriented cell rearrangements and so on, and hence tissue shape. A surveillance mechanism orchestrates proper tissue size and shape and involves reciprocal interactions between the cell and tissue scales. When a group of cells dies, compensatory mechanisms controlled at the tissue level ensure that the proper tissue size and shape are not compromised.

The aim of this review is to highlight recent important findings on the mechanisms of tissue growth and shape and to encapsulate them

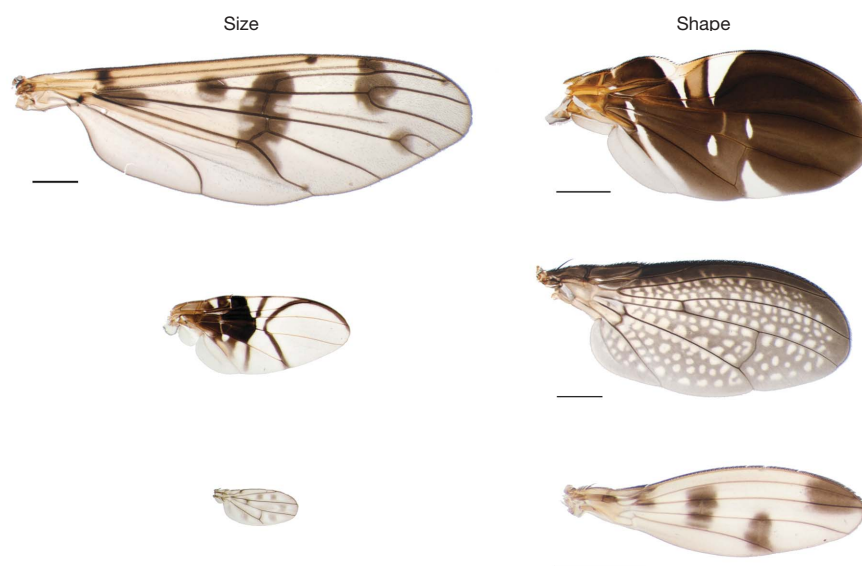


Figure 1 | Diversity of size and shape of organs during morphogenesis. Wings of dipterans illustrate marked differences in the size and shape of organs. Variations in wing length can almost reach tenfold (left). The

width-to-length ratio can also vary significantly (right). Scale bar, 1 mm. (Images are courtesy of N. Gompel and B. Prud'homme.)

¹Université de la Méditerranée, Institut de Biologie du Développement de Marseille Luminy (IBDML), ²CNRS, UMR6216, Campus de Luminy case 907, 13288 Marseille Cedex 09, France.

in a single framework of morphogenesis. We first focus on how cell division and cell death control tissue growth. We then detail how the mechanics of cell shape and division underlie tissue shape. Finally, we discuss how feedback mechanisms may orchestrate tissue size and shape.

Tissue growth: to die, to survive, to divide

Tissue growth can be best studied in the *Drosophila* developing adult tissues called imaginal discs. Imaginal discs are epithelial layers growing from about 40 cells to 50,000 cells in 4 days of continued divisions. Although this massive increase in cell number and tissue mass is under organismal control as far as the provision of the necessary energy input is concerned, the control of tissue size is intrinsic to the disc. Proper tissue size is not reached by counting cells: changes in cell size often yield compensatory modifications in cell number, thereby maintaining tissue size^{1,2}. This suggests that tissue dimensions (size or mass) may be measured.

Cell competition and apoptosis. Tissue-level control of tissue size is manifest in the process of cell competition discovered 30 yr ago^{3,4}, whereby faster growing cells can out-compete slow-growing cells (Fig. 2c). For example, wild-type clones can take over entire compartments initially occupied by slow-growing cells heterozygous for the *Minute (M)* mutations in genes encoding ribosomal proteins. Myc is another major regulator of cell competition, with as little as twofold changes in Myc expression being enough to trigger overgrowth of cells and competition with surrounding wild-type cells^{5,6}. The cellular mechanisms underlying competition are only starting to be unravelled. To some extent, fast cells may compete with slow cells for limited amount of survival signals provided by the transforming growth factor (TGF)- β /BMP (bone morphogenetic protein)

molecule Decapentaplegic (Dpp)⁷. There is no consensus, however, on the exact importance of Dpp in the competition process^{5,6}. Competition also involves apoptotic elimination of the slow cells and their engulfment by the fast-growing cells⁸. The stress-response pathway mediated by Jun N-terminal kinase (JNK)⁷ and the pro-apoptotic genes *hid* (also called *Wrinkled*) and *rpr*^{5,6} were shown to be involved in the apoptosis of the out-competed cells. The link between cell competition and tissue size is manifest in the following set of experiments: uniform expression of *myc*, where no competition occurs, causes tissue overgrowth, whereas mosaic expression of *myc*, which triggers competition, leaves size unchanged, indicating that the out-competed cells buffer the overgrowth of *myc*-overexpressing cells. Consistent with this, mosaic expression of *myc* results in tissue overgrowth when cell competition is reduced by blocking apoptosis. Another notable observation indicates that cell competition in a wild-type tissue buffers variations in tissue size⁵.

Control of cell division. Control of tissue size also involves a regulation of cell division. Two remarkable properties of cell division in imaginal discs are that it is random but uniform across the discs and that it ceases uniformly when correct disc proportions are attained. Two models have been proposed to explain scale invariance in growing tissues. One model emphasizes the role of local communications between cells with different positional values to drive intercalary growth⁹. These communications could be mediated by the cell adhesion molecule Fat, an activator of the Hippo pathway that controls cell proliferation (reviewed in ref. 10). Alternatively, long-range signalling by extracellular morphogens is viewed as the principal determinant of growth¹¹. Morphogens are molecules that form gradients of concentration from a source and activate different target genes at different concentration thresholds. The morphogen Dpp controls tissue pattern^{12,13} and tissue growth^{14,15}. Day and Lawrence¹¹ proposed that the slope of the gradient promotes cell division above a certain threshold. Provided that the addition of new cells decreases the slope of the gradient, growth would arrest when the gradient becomes too shallow (Fig. 2). Consistent with this, it was elegantly shown that cell division is transiently induced in regions where the slope of the Dpp gradient is experimentally modified¹⁶. Several observations, however, contradict a simple formulation of this model: (1) uniform Dpp expression causes overgrowth; (2) the assumption that the Dpp ligand gradient scales with the tissue is not experimentally supported^{17,18}; (3) the model fails to account for uniform cell division in the tissue. Thus, additional mechanisms will be required to explain fully the control of tissue size. As detailed below, the mechanical constraints imposed by tissue growth on local cell division can also be considered in parallel with signalling.

Whereas an increase in cell number drives tissue growth, tissue shape involves changes in cell positions controlled by cell rearrangements and the orientation of cell division.

Tissue shape: orienting cell division and movements

Spatial control of cell divisions. A number of mechanisms have been proposed for tissue elongation. It was suggested a long time ago that polarized cell divisions might be important for morphogenesis in *Drosophila*¹⁹ (Fig. 1a, b). However, the major role of polarized cell rearrangements during cell intercalation in vertebrates and invertebrates (see below) overshadowed this mechanism. As a result, experimental evidence that polarized cell division also has an essential role in plant and animal morphogenesis only accumulated recently^{20–26}, with striking examples in *Antirrhinum* petal morphogenesis²¹ and zebrafish neurulation²⁴. In *Drosophila* too, polarized cell divisions occur and participate in tissue morphogenesis. A detailed analysis of *Drosophila* imaginal discs showed, for example, that clones of cells grow anisotropically along the axis of tissue growth because cell divisions are biased along the proximal/distal axis²². Elongation of *Drosophila* embryonic epithelia is also controlled to some extent by oriented cell divisions²⁶.

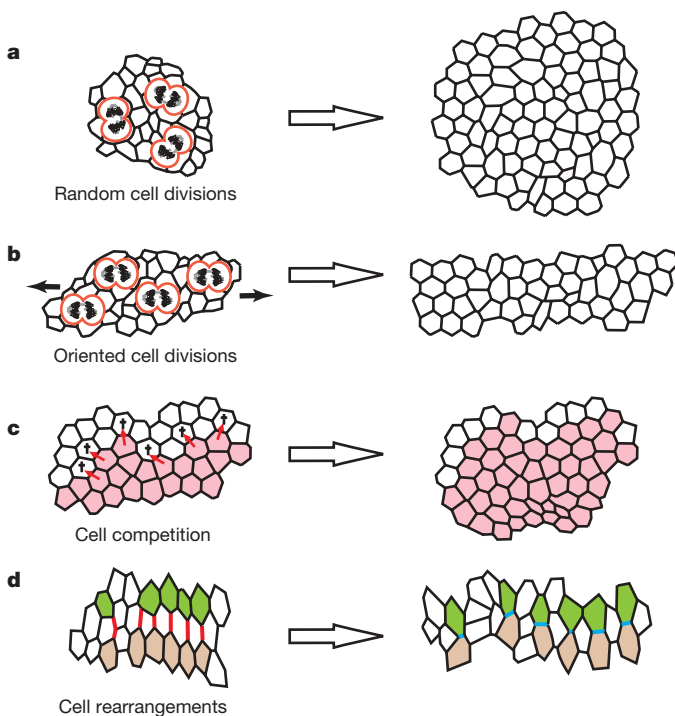


Figure 2 | Cellular mechanisms of tissue size and shape. **a**, Tissue proliferation and the increase in tissue mass are driven by continuous cell divisions (outlined in red). **b**, Oriented cell divisions, here along the horizontal axis, cause the elongated growth of the clone and of the organ. **c**, Cell competition is the process by which a fast-growing population (red) out-competes a slow-growing one (white). Out-competed cells die by apoptosis (cross symbol). This process is implicated in tissue size regulation. **d**, Cell rearrangements such as intercalation drive tissue elongation and affect tissue shape. Here the red interfaces shrink and new horizontal interfaces (blue) are formed, producing an exchange in cell neighbours.

What controls the orientation of cell division? Several components of the planar cell polarity pathway (PCP)—that orient other processes such as hairs and cilia—have been implicated. For instance, the cell adhesion molecules *Dachsous* and *Fat*, which orient PCP signalling, are required in the *Drosophila* wing²². However, core components of PCP signalling (for example, *Dishevelled*, *Frizzled*) have not been implicated in polarized cell division in the *Drosophila* wing. Note, however, that *Frizzled* controls orientation of the mitotic spindle during division of the sensory organ precursor in the *Drosophila* notum²⁷. Moreover, PCP signalling controls polarized cell divisions in vertebrates. The search for signals controlling oriented cell divisions is thus still ongoing in *Drosophila* and other organisms.

Cell division and cell shape. Changes in cell shape have also been proposed to drive tissue extension. In an epithelial layer cells adopt characteristic polygonal shapes dictated largely by the interplay between adhesion and cortical tension²⁸. Cell adhesion mediated by cadherins tends to increase cell contacts whereas cortical tension exerted by the actomyosin network reduces them. This is remarkably illustrated in post-mitotic tissues, such as the pupal *Drosophila* retina, where differential adhesion mediated by E- and N-cadherin controls the shape of cone cells²⁹. In pupae, wing cells remodel their irregular contacts to produce a highly ordered hexagonal tiling by a mechanism implicating E-cadherin trafficking and PCP signalling³⁰. In remodelling epithelia, cells may change shape markedly. Epithelial cell elongation accompanies several tissue extension processes such as *Drosophila* dorsal closure³¹ and imaginal discs evagination³². The underlying mechanisms remain unclear.

What is the effect of cell division on cell shape? During division epithelial cells exhibit a rounder (less polygonal) morphology, but live imaging has shown that cell contacts are not remodelled and daughter cells remain in contact³³. This explains the old observation that clones remain compact in imaginal discs. Defects in the even distribution of E-cadherin after cell division lead to a disruption of cell contacts and to cell scattering³⁴. Remarkably few constraints on the process of cell division (such as the production of two new vertices at each round of mitosis) conspire to produce a single topological equilibrium with a majority of hexagons^{33,35}, without assumptions on the mechanics of cell shape²⁸. Heterogeneities in the rate of cell division locally affect the distribution of cell shape.

Thus, the shape of cells in a growing tissue is influenced by cell surface mechanics and by local cell division rates.

Cell rearrangements and intercalation. Another major mechanism driving tissue extension is cell intercalation, whereby cells change position by remodelling their adhesive contacts. The evagination of pupal imaginal wing and leg discs, for instance, was proposed early on to stem from changes in the organization of cell contacts³². Intercalation has been carefully studied during elongation of the embryo, called germ-band elongation^{36,37} (Fig. 2d). In this system, contacts between antero-posterior neighbours shrink (Fig. 2d, red) and new contacts are formed at a perpendicular axis (Fig. 2d, blue). This process does not depend on external forces exerted at tissue boundaries, but on the local increase in cortical tension imposed by the enrichment of Myosin-II at shrinking junctions³⁶. Adhesion is also probably downregulated, as *Bazooka* (also called *Par-3*)³⁸—a determinant of E-cadherin stabilization^{39,40}—and E-cadherin³⁷ are downregulated in shrinking junctions. Planar junction remodelling and intercalation are controlled by embryonic polarity^{36,38,41}. Surprisingly, the non-canonical Wnt PCP pathway is not required for cell intercalation during germ-band extension. The signals orienting cell rearrangements remain elusive.

The proper shaping of a growing organ thus requires that, as new cells are formed, their relative positions be controlled. This is achieved by regulation of the cell division orientation and of cell rearrangements. Cell division itself and cell mechanics thus underlie important aspects of tissue shaping. A complete understanding of the coordination of tissue size and shape must integrate the regulation of tissue growth by signalling pathways with the mechanics and dynamics of morphogenesis at the cellular level.

Feedback mechanisms coordinating size and shape

Cell division and cell growth drive tissue expansion. Yet, attaining the proper tissue size and shape does not simply rely on cell counting. Thus, a tissue-intrinsic property informs, in return, dividing cells about their division rate, growth or eventual death. Such a feedback mechanism is required to understand growth arrest and tissue shape. Stochastic fluctuations or persistent variations in growth rate could produce changes of an internal variable (for example, pressure or *Dpp* activity) that would, in return, affect growth rate. An inhibitory negative feedback signal can have a stabilizing effect, smoothening fluctuations and providing the system with a dynamic control to ensure homogeneous growth.

What mechanisms could generate a feedback? Two plausible alternatives have been proposed. Local regulation of the morphogen-ligand or activity gradient might be a way. Regions of enhanced growth could locally reduce the slope of the *Dpp* gradient, and hence feed back on growth (Fig. 3a). Quantitative analysis of the

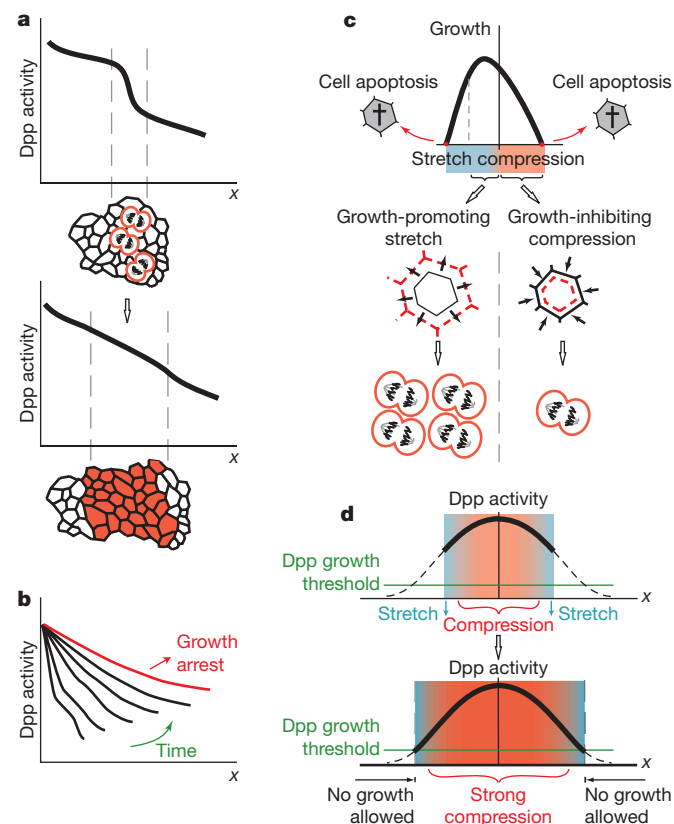


Figure 3 | Models of size control by feedback. **a, b**, Gradient model. **a**, A spatial gradient in *Dpp* signalling controls growth by promoting cell divisions. A local increase in the slope of the gradient (between dashed lines) would locally stimulate increased proliferation (outlined in red in the schematic diagram of epithelium), resulting (below) in the insertion of new cells and tissue expansion. The model proposes that growth changes the local slope of the gradient and thereby feeds back on the activity profile of the morphogen gradient. **b**, Evolution of the morphogen activity (not necessarily the ligand) gradient profile: as the tissue grows, the *Dpp* activity gradient scales with the tissue. Growth arrest is triggered when the gradient becomes too flat. **c, d**, Mechanical feedback model. **c**, Growth is proposed to be influenced by mechanical forces, with compression (in red) inhibiting cell division and mild stretch (blue) promoting it. Above extreme stretch or compression, cells die by apoptosis. This mechanical feedback explains uniform cell divisions in a growing tissue. **d**, The combination of this mechanical feedback and the graded growth-promoting function of the *Dpp* gradient above a threshold value (green) explains uniform growth and homogeneous growth arrest. Cells at the periphery stop dividing when, as a result of growth, they fall below this threshold *Dpp* activity. Simultaneously, cells in the centre no longer divide because of the increased compression (dark red) imposed onto them by cell division arrest at the periphery. *x* indicates spatial coordinates.

establishment of the Dpp ligand gradient^{18,42,43} showed that it forms on short timescales (minutes) not commensurate with the long timescales (hours) of tissue growth, consistent with the fact that the ligand gradient does not scale with the tissue¹⁷. However, the activity gradient (monitored by phosphorylated Mad or expression of target genes) is clearly influenced by the local tissue growth⁴³. Further tests of this model will thus require a better characterization of the temporal lag between ligand and activity gradients and of the effect of growth on the latter.

The interplay between cell mechanics and the cell cycle^{44,45} is another potential way to provide dynamic regulation of tissue growth, as recently suggested in the *Drosophila* ovary⁴⁶. Indeed, an inhibition of growth by mechanical compression (and stimulation by stretch, Fig. 3c) would provide a negative feedback to repress heterogeneities of growth. Using quantitative modelling, Shraiman proposed that mechanical feedback could account for the uniformity of cell division⁴⁷. Moreover, combining mechanical feedback with the growth-promoting function of a non-scaling Dpp gradient predicts growth arrest and scale invariance^{17,48} (Fig. 3d).

This opens up new perspectives and prompts a better integration of the cellular and signalling aspects of morphogenesis in fly and other organisms. A better understanding of the causal relationships between growth and activity gradient dynamics will be important to probe further how morphogens orchestrate size and shape. Whether morphogens also control cell division orientation and cell rearrangements remains an open and major question to investigate. It will also be important to test the mechanical feedback model: do stretch and compression influence cell division and survival? Do fields of forces constrain tissue growth in parallel with growth factors? This mechanical feedback could have other implications on organ shape. It could orient cell division—as was suggested in plants⁴⁹—or cell rearrangements. These important discoveries in *Drosophila* should prompt further studies testing how they apply to size and shape control in mammals.

- Neufeld, T. P., de la Cruz, A. F., Johnston, L. A. & Edgar, B. A. Coordination of growth and cell division in the *Drosophila* wing. *Cell* **93**, 1183–1193 (1998).
- Weigmann, K., Cohen, S. M. & Lehner, C. F. Cell cycle progression, growth and patterning in imaginal discs despite inhibition of cell division after inactivation of *Drosophila* Cdc2 kinase. *Development* **124**, 3555–3563 (1997).
- Morata, G. & Ripoll, P. Minutes: mutants of *Drosophila* autonomously affecting cell division rate. *Dev. Biol.* **42**, 211–221 (1975).
- Simpson, P. & Morata, G. Differential mitotic rates and patterns of growth in compartments in the *Drosophila* wing. *Dev. Biol.* **85**, 299–308 (1981).
- de la Cova, C., Abril, M., Bellosta, P., Gallant, P. & Johnston, L. A. *Drosophila* myc regulates organ size by inducing cell competition. *Cell* **117**, 107–116 (2004).
- Moreno, E. & Basler, K. dMyc transforms cells into super-competitors. *Cell* **117**, 117–129 (2004).
- Moreno, E., Basler, K. & Morata, G. Cells compete for decapentaplegic survival factor to prevent apoptosis in *Drosophila* wing development. *Nature* **416**, 755–759 (2002).
- Li, W. & Baker, N. E. Engulfment is required for cell competition. *Cell* **129**, 1215–1225 (2007).
- Garcia-Bellido, A., Cortes, F. & Milan, M. Cell interactions in the control of size in *Drosophila* wings. *Proc. Natl Acad. Sci. USA* **91**, 10222–10226 (1994).
- Saucedo, L. J. & Edgar, B. A. Filling out the Hippo pathway. *Nature Rev. Mol. Cell Biol.* **8**, 613–621 (2007).
- Day, S. J. & Lawrence, P. A. Measuring dimensions: the regulation of size and shape. *Development* **127**, 2977–2987 (2000).
- Lecuit, T. et al. Two distinct mechanisms for long-range patterning by Decapentaplegic in the *Drosophila* wing. *Nature* **381**, 387–393 (1996).
- Nellen, D., Burke, R., Struhl, G. & Basler, K. Direct and long-range action of a DPP morphogen gradient. *Cell* **85**, 357–368 (1996).
- Burke, R. & Basler, K. Dpp receptors are autonomously required for cell proliferation in the entire developing *Drosophila* wing. *Development* **122**, 2261–2269 (1996).
- Martin-Castellanos, C. & Edgar, B. A. A characterization of the effects of Dpp signaling on cell growth and proliferation in the *Drosophila* wing. *Development* **129**, 1003–1013 (2002).
- Rogulja, D. & Irvine, K. D. Regulation of cell proliferation by a morphogen gradient. *Cell* **123**, 449–461 (2005).
- Hufnagel, L., Teleman, A. A., Rouault, H., Cohen, S. M. & Shraiman, B. I. On the mechanism of wing size determination in fly development. *Proc. Natl Acad. Sci. USA* **104**, 3835–3840 (2007).
- Kicheva, A. et al. Kinetics of morphogen gradient formation. *Science* **315**, 521–525 (2007).
- Bryant, P. J. & Schneiderman, H. A. Cell lineage, growth, and determination in the imaginal leg discs of *Drosophila melanogaster*. *Dev. Biol.* **20**, 263–290 (1969).
- Reddy, G. V., Heisler, M. G., Ehrhardt, D. W. & Meyerowitz, E. M. Real-time lineage analysis reveals oriented cell divisions associated with morphogenesis at the shoot apex of *Arabidopsis thaliana*. *Development* **131**, 4225–4237 (2004).
- Rolland-Lagan, A. G., Bangham, J. A. & Coen, E. Growth dynamics underlying petal shape and asymmetry. *Nature* **422**, 161–163 (2003).
- Baena-Lopez, L. A., Baonza, A. & Garcia-Bellido, A. The orientation of cell divisions determines the shape of *Drosophila* organs. *Curr. Biol.* **15**, 1640–1644 (2005).
- Ciruna, B., Jenny, A., Lee, D., Mlodzik, M. & Schier, A. F. Planar cell polarity signalling couples cell division and morphogenesis during neurulation. *Nature* **439**, 220–224 (2006).
- Concha, M. L. & Adams, R. J. Oriented cell divisions and cellular morphogenesis in the zebrafish gastrula and neurula: a time-lapse analysis. *Development* **125**, 983–994 (1998).
- Gong, Y., Mo, C. & Fraser, S. E. Planar cell polarity signalling controls cell division orientation during zebrafish gastrulation. *Nature* **430**, 689–693 (2004).
- da Silva, S. M. & Vincent, J. P. Oriented cell divisions in the extending germband of *Drosophila*. *Development* **134**, 3049–3054 (2007).
- Gho, M. & Schweisguth, F. Frizzled signalling controls orientation of asymmetric sense organ precursor cell divisions in *Drosophila*. *Nature* **393**, 178–181 (1998).
- Lecuit, T. & Lenne, P. F. Cell surface mechanics and the control of cell shape, tissue patterns and morphogenesis. *Nature Rev. Mol. Cell Biol.* **8**, 633–644 (2007).
- Hayashi, T. & Carthew, R. W. Surface mechanics mediate pattern formation in the developing retina. *Nature* **431**, 647–652 (2004).
- Classen, A. K., Anderson, K. I., Marois, E. & Eaton, S. Hexagonal packing of *Drosophila* wing epithelial cells by the planar cell polarity pathway. *Dev. Cell* **9**, 805–817 (2005).
- Kaltschmidt, J. A. et al. Planar polarity and actin dynamics in the epidermis of *Drosophila*. *Nature Cell Biol.* **4**, 937–944 (2002).
- Fristrom, D. The mechanism of evagination of imaginal discs of *Drosophila melanogaster*. III. Evidence for cell rearrangement. *Dev. Biol.* **54**, 163–171 (1976).
- Gibson, M. C., Patel, A. B., Nagpal, R. & Perrimon, N. The emergence of geometric order in proliferating metazoan epithelia. *Nature* **442**, 1038–1041 (2006).
- Knox, A. L. & Brown, N. H. Rap1 GTPase regulation of adherens junction positioning and cell adhesion. *Science* **295**, 1285–1288 (2002).
- Cowan, R. & Morris, V. B. Division rules for polygonal cells. *J. Theor. Biol.* **131**, 33–42 (1988).
- Bertet, C., Sulak, L. & Lecuit, T. Myosin-dependent junction remodelling controls planar cell intercalation and axis elongation. *Nature* **429**, 667–671 (2004).
- Blankenship, J. T., Backovic, S. T., Sanny, J. S., Weitz, O. & Zallen, J. A. Multicellular rosette formation links planar cell polarity to tissue morphogenesis. *Dev. Cell* **11**, 459–470 (2006).
- Zallen, J. A. & Wieschaus, E. Patterned gene expression directs bipolar planar polarity in *Drosophila*. *Dev. Cell* **6**, 343–355 (2004).
- Harris, T. J. & Peifer, M. Adherens junction-dependent and -independent steps in the establishment of epithelial cell polarity in *Drosophila*. *J. Cell Biol.* **167**, 135–147 (2004).
- Pilot, F., Philippe, J. M., Lemmers, C. & Lecuit, T. Spatial control of actin organization at adherens junctions by a synaptotagmin-like protein Btsz. *Nature* **442**, 580–584 (2006).
- Irvine, K. D. & Wieschaus, E. Cell intercalation during *Drosophila* germband extension and its regulation by pair-rule segmentation genes. *Development* **120**, 827–841 (1994).
- Entchev, E. V., Schwabedissen, A. & Gonzalez-Gaitan, M. Gradient formation of the TGF- β homolog Dpp. *Cell* **103**, 981–991 (2000).
- Teleman, A. A. & Cohen, S. M. Dpp gradient formation in the *Drosophila* wing imaginal disc. *Cell* **103**, 971–980 (2000).
- Chen, C. S., Mrksich, M., Huang, S., Whitesides, G. M. & Ingber, D. E. Geometric control of cell life and death. *Science* **276**, 1425–1428 (1997).
- Nelson, C. M. et al. Emergent patterns of growth controlled by multicellular form and mechanics. *Proc. Natl Acad. Sci. USA* **102**, 11594–11599 (2005).
- Wang, Y. & Riechmann, V. The role of the actomyosin cytoskeleton in coordination of tissue growth during *Drosophila* oogenesis. *Curr. Biol.* **17**, 1349–1355 (2007).
- Shraiman, B. I. Mechanical feedback as a possible regulator of tissue growth. *Proc. Natl Acad. Sci. USA* **102**, 3318–3323 (2005).
- Aegerter-Wilmsen, T., Aegerter, C. M., Hafen, E. & Basler, K. Model for the regulation of size in the wing imaginal disc of *Drosophila*. *Mech. Dev.* **124**, 318–326 (2007).
- Lynch, T. M. & Lintilhac, P. M. Mechanical signals in plant development: a new method for single cell studies. *Dev. Biol.* **181**, 246–256 (1997).

Acknowledgements We thank Pierre Golstein and Steve Cohen for suggestions that improved the manuscript. The Lecuit lab is supported by the CNRS, Agence Nationale de la Recherche and Association pour la recherche contre le cancer.

Author Information Reprints and permissions information is available at www.nature.com/reprints. Correspondence should be addressed to T.L. (lecuit@ibdm.univ-mrs.fr).

Into the mind of a fly

Leslie B. Vosshall¹

Where do animal behaviours come from and are they controlled by genes? This is the fundamental question posed by the field of neurogenetics. Pioneering work from the 1960s in Seymour Benzer's laboratory demonstrated for the first time that *Drosophila melanogaster* fruitflies could be mutated to obtain animals with insomnia, learning disabilities and homosexual courtship behaviours.

Forty years ago, the field of *Drosophila* neurogenetics (defined in Box 1) was born in Seymour Benzer's laboratory at Caltech¹. In the mid-1960s, Benzer made an abrupt and orthogonal turn from his early ground-breaking work defining the fine structure of the gene in bacteriophage² to the heretical idea that single genes could control behaviour in complex animals. A paper appearing in the September 1967 issue of *Proc. Natl Acad. Sci.* presented the first evidence that mutant flies defective in phototaxis behaviour, or locomotor responses to light, could be identified¹. The premise of neurogenetics—widely disbelieved at the time—was that complex behaviours such as the ability to learn and remember, the internal biological rhythms of the body, and courtship and sexuality could all be under genetic control.

Drosophila melanogaster as an experimental organism has contributed much to contemporary neurobiology. The first cloning of a structural gene for a potassium channel was achieved by Benzer's trainees, Yuh Nung Jan and Lily Jan, when they isolated the gene corresponding to the *shaker* (*sh*) mutant³. The founding member of the now enormous *transient receptor potential* (*trp*) ion channel family had its origins as a fly mutant defective in light-evoked retinal electrophysiology⁴. Vertebrate and invertebrate TRP channels have since turned up in biological processes as diverse as the sensation of odours, tastes, pungent compounds such as wasabi, capsaicin and menthol, cold, heat, touch and hearing, among others (reviewed in ref. 5). Beginning in the late 1960s, William Pak amassed a large collection of mutants defective in visual signal transduction, such as the *neither inactivation nor afterpotential* (*nina*) mutants⁶. This genetic dissection of phototransduction in *Drosophila* enabled later molecular analysis of the molecules underlying visual signal transduction in the laboratories of Pak, Gerald Rubin, Charles Zuker and others (reviewed in ref. 7).

The cloning of *sh* and *trp* are excellent examples of the power of neurogenetics. Both arose from genetic screens designed to test the hypothesis that studying shaky flies or flies with altered retinal physiology would lead to interesting insights into neural function. The tools of this discipline are simple and require only a suitable behavioural paradigm (three are shown in Fig. 1), a means to make flies with mutations in single genes, and standard molecular genetic techniques to progress from a mutant phenotype to a genotype.

This Review article will discuss how the revolution started by Benzer and his students in 1967 has spread to many fields of neurobiological investigation in *Drosophila*, from whence it jumped to mice, zebrafish and other species, including humans. Here I will focus specifically on three original discoveries in *Drosophila* neurogenetics and behaviour—biological rhythms, sexual courtship and chemoreception—and how these have blossomed in the last 40 yr.

The genetics of circadian rhythms in the fly

Flies, like all other animals and plants on earth, have a daily routine in synchrony with the rhythms of the Sun and Earth. Like humans, flies tend to wake up around dawn, enjoy a siesta in the afternoon, and are largely inactive after nightfall⁸. The biological rhythm in locomotor activity recurs on a roughly 24 h cycle, hence it is termed a circadian (*circa diem*—around a day) rhythm. This modulation of locomotor behaviour is driven by external environmental rhythms, but can also persist in flies raised for generations in the dark⁹.

Ronald Konopka in Benzer's laboratory provided the first evidence that the biological clock was under genetic control and could be broken by mutagenesis¹⁰. In an elegant and simple screen for flies with altered hatching and locomotor rhythms, using activity-monitoring devices such as those in Fig. 1b, Konopka and Benzer

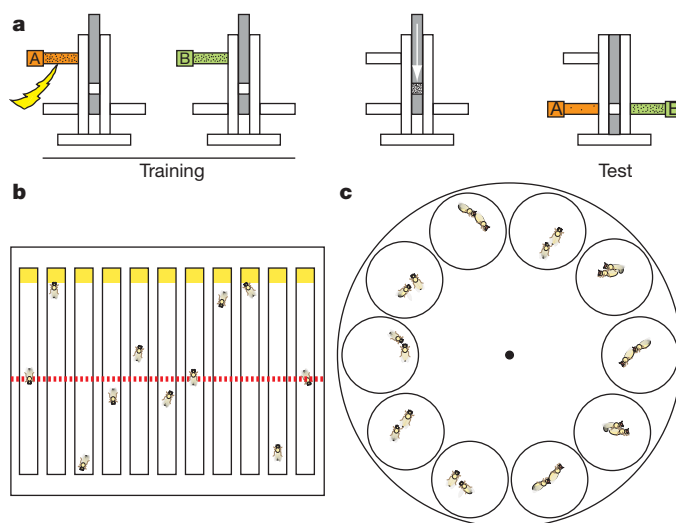


Figure 1 | A diversity of behaviour paradigms is used to measure *Drosophila* behaviour in the laboratory. **a**, The olfactory T-maze is used for Pavlovian olfactory conditioning^{40,64}. Flies are trained to associate odour A (orange) with electric shock (left). During testing, these flies avoid odour A (right). The assay is carried out with reciprocal training, such that only one half of the paradigm is depicted here. Flies are depicted as small black dots. **b**, Circadian-activity monitors measure locomotor activity of individual flies using an infrared beam (red dotted line)¹⁰. An external computer tracks the number of times the fly breaks the beam, allowing continual monitoring of fly locomotor activity over a period of weeks. **c**, The courtship wheel permits the observation of up to 10 fly couples in which the male engages in such stereotyped sexual activity as the following: genital licking, wing vibration to produce a species-specific song, and copulation. Graphic in **a** is adapted from figure 1 of ref. 65 with permission from Elsevier (copyright 2004).

¹Laboratory of Neurogenetics and Behaviour, The Rockefeller University 1230 York Avenue, Box 63 New York, New York 10065, USA.

Box 1 | The subject

Neurogenetics merges concepts and techniques from neurobiology and genetics to study the genetic basis of behaviour and neural function. By generating and studying mutant animals that exhibit abnormal behaviour, mistakes in neural wiring, or anomalies in the structure or function of neurons, neurogeneticists can track down the genes responsible for these phenotypes, thereby understanding the function of the genes in producing a normal brain and its associated behaviours. In 1967, Seymour Benzer suggested that neurogenetics could act as a 'microsurgical tool' to study the brain:

"Thus, use of mutation as a microsurgical tool could conceivably lead to the identification of the various transmitters, about which little is presently known. The counter-current procedure is obviously adaptable to a wide range of stimuli, such as gravity, odour, sound and special visual patterns, thus lending itself to the isolation of many kinds of behavioural mutants, including ones in which the wiring pattern of the nervous system is affected. Furthermore, as preliminary experiments have shown, the speed of the procedure permits its use in the study of short-term modifications of behavior."¹¹

isolated three different mutant alleles of the same gene, called *period* (*per*). *per⁰* flies are insomniac, *per^s* flies live a short day, and *per^L* flies a long day¹⁰. An amazing parallel with humans was uncovered with the recent identification of mutations in a human *period* homologue (*PER2*) as the genetic culprit behind the *per^s*-like phenotype in familial advanced sleep-phase syndrome¹¹.

How a single gene could both be necessary for the clock but also set its running speed remained a mystery until the age of molecular cloning and the isolation of other clock genes. The groups of Michael Rosbash and Jeffrey Hall, and the group of Michael Young cloned *per* in 1984 (refs 12, 13). Both *per* messenger RNA and PER protein were subsequently shown to cycle with a circadian rhythm, and show a rhythmic nuclear accumulation, prompting a model in which PER acts as a feedback suppressor to control the clock¹⁴. *per* turned out to be just the tip of an enormous iceberg of clock genes, clock accessory genes, and clock-controlled genes. The present model for the *Drosophila* clock includes a host of core clock components that include a positive transcriptional feedback loop (*Clock* (*Clk*), *cycle* (*cyc*) and *vri* (*vri*)), a negative transcriptional feedback loop (*per* and *timeless* (*tim*)), and factors that modulate the light-regulated accumulation and output of the core clock genes (*double-time* (*dbt*; also known as discs overgrown or *dco*), *shaggy* (*sgg*), *cryptochrome* (*cry*), *Pigment-dispersing factor* (*Pdf*) and others; reviewed in ref. 8). Some recent surprises in the clock field include a somewhat mysterious cytoplasmic timing mechanism that regulates the delay in nuclear accumulation of period and timeless¹⁵, as well as the discovery that the clock protein has chromatin-remodelling activity¹⁶.

Homologues of many of the core clock genes have been identified in vertebrates, further validating the fly as a model for circadian biology. Microarray studies by Young¹⁷ and others have identified several hundred genes under circadian control, the analysis of which promises to provide an integrated view of how the physiology of the entire organism is synchronized to the daily rhythms of the planet.

fruitless and its power to shape sexual behaviour

Copulation in *Drosophila* is preceded by an intricate series of sexually dimorphic pre-copulatory courtship behaviours between the male and female fly¹⁸ (Fig. 1c). Benzer's trainees Hall and Yoshiki Hotta (Box 2) used genetic mosaic analysis to define portions of the central nervous system required for male courtship behaviour^{19,20} and genes that governed heterosexual behaviour²¹. One gene named *fruitless* (*fru*), identified in 1963 by K. S. Gill and cloned over 30 yr later by Daisuke Yamamoto²²—and separately by the group effort of Hall, Bruce Baker and Barbara Taylor²³—is now known to be a master regulator of sexuality in the fly^{23,24}. The transcription factor encoded by the *fru* gene is expressed in a subset of central, peripheral, sensory and motor neurons in the adult fly, which are likely to comprise a

circuit controlling sexually dimorphic behaviour^{25–27}. Mutant *fru* males show homosexual courtship behaviour in which large groups form chains of males courting each other. In a remarkable experiment, Barry Dickson showed recently that male courtship behaviour directed at females can be induced in chromosomally female flies simply by expressing the male-specific isoform of *fru* in the female brain²⁴. Recent work in the mouse from Catherine Dulac's group suggests a similar underlying latency in the female mouse to exhibit male behaviours on manipulation of a single gene²⁸. A major goal in this field is to define the molecular targets of *fru* and define the neural circuits that drive both male and female sexual behaviours.

Olfactory communication in the fly

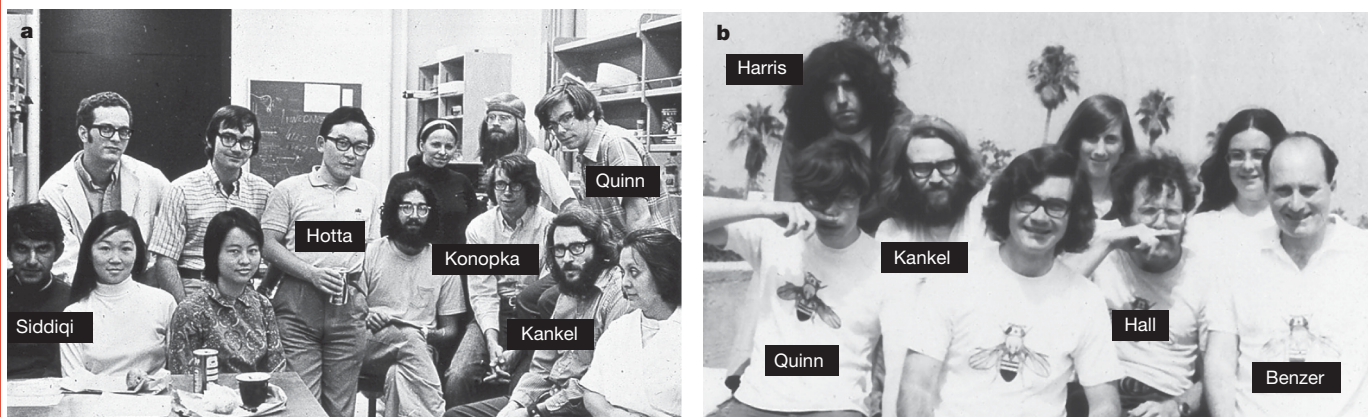
Fruitflies are strongly attracted to the smell of vinegar, yeast, rotting fruit and to each other. The genetic basis of this chemosensory behaviour was first studied by Obaid Siddiqi, a Benzer trainee (Box 2). Mutants defective in the olfactory T-maze, using the device in Fig. 1a but omitting electric shock, as well as other olfactory behaviour paradigms were collected throughout the 1980s by Siddiqi²⁹, and later by John Carlson³⁰, and others. One of the Carlson mutants, *acj6*, proved to be a key transcription factor necessary for the regulation of a subset of odorant receptor genes³¹. The availability of the genome sequence of *Drosophila melanogaster* opened this system to rapid molecular analysis by Carlson, Dean Smith, Liquan Luo, Dickson, Richard Axel and a number of former Axel trainees, resulting in the complete description of the sequence and expression of all 62 odorant receptors and 68 taste receptors (reviewed in ref. 32), the complete map of connectivity of primary olfactory centres^{33,34}, an initial view of how primary olfactory information is mapped in the higher brain^{35,36}, and a comprehensive survey of ligand tuning of a majority of the odorant receptors³⁷, including those tuned to pheromones^{38,39}. A major effort in this growing field is to understand the underlying central mechanisms by which a fly discriminates among all the odours it is able to detect and how the circuitry underlying pheromone perception leads to stereotyped behaviours.

A myriad of other complex behaviours

Beyond these brief examples from the original neurogenetic studies to emerge from the Benzer laboratory, many other behaviours have been productively dissected with genetic and behavioural tools in *Drosophila*. The seminal work of William Quinn, William Harris and Benzer (Box 2) demonstrating that flies can be conditioned to avoid an odour paired with shock (Fig. 1a)⁴⁰, was followed by the identification of a series of mutant flies that either could not learn this task or rapidly forgot it (reviewed in ref. 41). Subsequent genetic analysis by Quinn, Ronald Davis, Tim Tully and others produced the provocative finding that many learning and memory defective mutations in the fly affect the cyclic AMP pathway (reviewed in ref. 41), the same signalling pathway implicated in conditioned behaviours in *Aplysia* and the mouse^{42,43}. Subsequent genetic screens for learning mutants by Tully and others, in one case combined with microarray analysis, produced a host of other candidate memory genes, including several involved in local control of mRNA translation⁴⁴.

The cloning of the *dunce* (*dnc*) gene⁴⁵ and its enrichment in a part of the fly brain called the mushroom body⁴⁶ allowed the field to move from the genetic to the cellular level. Davis, Martin Heisenberg and others carried out a series of genetic and ablation studies strongly implicating this olfactory processing centre in the fly as the seat of memory^{47,48}. Current work in the field is zeroing in on how fly-brain microcircuitry processes paired odour and shock input⁴⁹, how the circuitry is modulated by conditioning⁵⁰, and how the processes of learning and retrieval of memories are compartmentalized⁵¹. Neurogenetics has also enabled scientists to localize memory to smaller and smaller areas of the fly brain. A particularly elegant recent example comes from Heisenberg, Li Liu and co-workers, who localized circuits that learn certain visual features to two groups of

Box 2 | The people



Box 2 Figure | The birth of neurogenetics in the Benzer laboratory at Caltech. **a, Benzer laboratory at Caltech, November 1971.** Front row (left to right): O. Siddiqi; research technicians, Y.-H. Jing and J.-Y. Yu; M. Deniro; R. Konopka; D. Kankel; and laboratory manager, E. Eichenberger. Back row (left to right): T. Hanson, D. Edgington, Y. Hotta, J. Lewis, P. Christensen and W. Quinn. **b, Benzer laboratory at Caltech, around 1972.** Front row (left to right): W. Quinn, D. Edgington, J. Hall, S. Benzer. Back row (left to right): W. Harris, D. Kankel and research technicians, J. Gorn and B. Butler. Photos courtesy of S. Benzer, Caltech.

Career paths of selected Benzer laboratory members (interested readers can learn more about the history of neurogenetics and the Benzer laboratory by consulting J. Weiner's celebrated book⁶⁵):

- Seymour Benzer: still active and scientifically prolific at the age of 86 as the James Griffin Boswell Professor of Neuroscience, Emeritus (active) at Caltech. In recent years, his group has studied longevity, brain degeneration, fear, and feeding behaviours in *Drosophila*.
- Jeffrey Hall: Professor at Brandeis University, who was inducted into the US National Academy of Sciences in 2003 for his comprehensive work on the neurogenetics of circadian, courtship and social behaviours in *Drosophila*.
- William Harris: fellow of the Royal Society and Head of the Neuroscience Department at the University of Cambridge, UK, with a group working on the molecular embryogenesis of the vertebrate visual system.
- Yoshiki Hotta: Director of the National Institute of Genetics in Japan, Hotta went on to a prominent career in *Drosophila* neural development.
- Douglas Kankel: Professor at Yale University investigating the neurogenetics of visual and nervous system development in *Drosophila*.
- Ronald Konopka: Continued to work on biological clocks at Clarkson University before retiring from science.
- William Quinn: Professor in the Department of Brain and Cognitive Sciences at Massachusetts Institute of Technology has continued his seminal work on learning and memory in *Drosophila*.
- Obaid Siddiqi: founding Director of the TIFR National Centre for Biological Sciences at Bangalore and inducted in 2003 as a foreign member of the US National Academy of Sciences, Siddiqi pioneered the field of behaviour genetics of *Drosophila* olfaction after leaving the Benzer laboratory.

neurons in a structure called the fan-shaped body⁵². Although the small size of *Drosophila* central-brain neurons has hindered electrophysiological access, recent work from Rachel Wilson and Gilles Laurent suggests that this barrier is not insurmountable⁵³, and a more detailed functional analysis of memory at the level of single mushroom-bodies seems likely.

Ulrike Heberlein has turned the fly into a genetic model for alcohol intoxication, demonstrating that flies exhibit progressive and eerily human-like responses to acute alcohol exposure: first, they become hyperexcitable, then they lose coordination, and finally they pass out⁵⁴. Some of the same cAMP pathway genes required for learning and memory affect a fly's sensitivity to alcohol⁵⁵.

Both Edward Kravitz, who studies aggression in lobster, and Ralph Greenspan have recently turned their attention to fly aggression. Flies, both male and female, exhibit aggressive behaviours, with males fighting other males in the presence of a female and females jousting with females over food resources⁵⁶. Kravitz has shown that fighting style differs between the sexes and is controlled by *fru* (ref. 57). Multi-generational selection for aggressive or docile strains has been achieved by Greenspan, and such strains have been analysed by whole-genome microarray to identify a large number of genes, the expression of which is modulated differentially in aggressive strains⁵⁸. These genes will provide avenues for future investigation into the genetic basis of aggression.

A behavioural paradigm recently pioneered by Roland Strauss is that of gap-crossing (Fig. 2). Flies are presented with gaps of varying widths, from narrow and easy to cross to unbreachable chasms, and make sophisticated estimations of which gaps can be reasonably crossed⁵⁹. This goal-directed climbing behaviour is useful to dissect

motor planning and coordination, and to identify the circuits in the fly brain that estimate distance, but could, in principle, also lead to mutants with altered appetite for risk. It is conceivable that both risk-averse flies, capable of crossing a gap but choosing not to, and reckless flies, those choosing to cross impossibly wide gaps, could be identified through genetic screens.

Unlike the classic eusocial insects such as ants and bees, flies are not typically known for their group dynamics. This view has been changing somewhat on closer behavioural investigation, which has revealed some surprising evidence of social interactions in *Drosophila*. For instance, Joel Levine and Hall have shown that circadian rhythms can be phase-shifted by the odour of flies living in another time zone or flies of another genotype⁶⁰. Hubert Amrein showed that normal circadian locomotor activity of a male is drastically affected by the presence of a female⁶¹. These experiments hint at as yet unknown volatile chemical substances produced by other flies and detected by the olfactory system, and suggest that social interactions shape group interactions in the fly. In fact there is a growing trend to monitor *Drosophila* behaviour in more natural and enriched contextual environments that mimic those they might encounter in the real world. For instance, Levine has been observing fly social interactions in groups in the presence of food (Fig. 3). Free from the constraints of courting a single female in an austere Plexiglas chamber, as is the norm for observing courtship behaviour (Fig. 1c), *Drosophila* males in group situations seem to engage in complex group sex that combines foreplay, copulation and feeding behaviours (Fig. 3). It will be interesting to study the regulation and modulation of such group social behaviours and the importance of context in regulating them.



Figure 2 | Goal-oriented behaviour is measured in a gap-climbing paradigm, in which the fly estimates the width of the gap and judges if it seems feasible to cross. Photo by S. Pick, kindly provided by R. Strauss. Reprinted from ref. 59 with permission from Elsevier (copyright 2005).

A related example of a behaviour that emerges in groups is the innate avoidance that flies show for an empty tube previously occupied by flies that experienced stress. Avoidance by naive flies of tubes previously occupied by shaken flies was first noticed by Benzer in 1967 (ref. 1), and subsequently investigated by Greg Suh, working with the Benzer laboratory and the groups of David Anderson and Axel, as an innate olfactory avoidance of a *Drosophila* stress odor, dSO (ref. 62). This robust behaviour, resulting from the recognition and avoidance of the smell of a fellow fly in trouble, will be useful in future studies of the circuitry of anxiety, stress and innate fear.

Concluding remarks

Significant advances in our understanding of the biological clock, sensory systems, learning and memory, sexual courtship and many other behaviours have been made through neurogenetic research in *Drosophila*. With these successes behind us, some adventurous *Drosophila* neurogeneticists are moving beyond these original neurogenetics questions, which may in hindsight represent the low-hanging fruit—robust behaviours amenable to investigation in laboratory-based behavioural paradigms. It now seems possible to approach in the fly more complex behaviours and even emotions, the neurobiological basis of which are not well understood at the genetic or functional level in any animal: sociality, common sense, altruism, empathy, frustration, motivation, hatred, jealousy, peer pressure, and so on. The only a priori limitation to studying any of these traits is the belief that flies can show such emotions and the design of a plausible behavioural paradigm to measure them.

This Progress article accompanies the release of complete genomes of eleven additional *Drosophila* species (*D. ananassae*, *D. erecta*, *D. grimshawi*, *D. mojavensis*, *D. pseudoobscura*, *D. simulans*, *D. virilis*, *D. yakuba*, *D. persimilis*, *D. sechellia*, *D. willistoni*), with vastly different ecologies and lifestyles to *Drosophila melanogaster*. What will be the impact of these additional *Drosophila* genomes on neurogenetics and behaviour research? Such information may begin to provide clues to differences in pheromonal communication and species recognition among these flies, some of which occupy overlapping ecological niches and need to pay careful attention to which species they are courting. A second area of interest will be in food preference and how

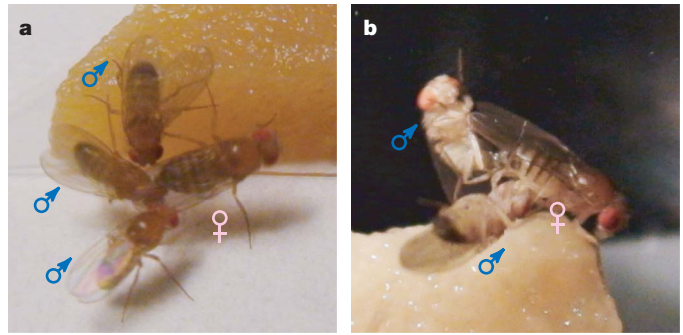


Figure 3 | The contextual courtship assay measures sexual behaviour under more naturalistic conditions in group situations on food. **a**, Three males courting a single virgin female near a wedge of food. **b**, Male with forelegs raised high copulates with a female, while another male, on his back, touches and licks her abdomen. This occurs on top of a wedge of food. Note that the female's right foreleg stretches out across the surface of the food as does the left foreleg of the male beneath her. Such sexual behaviour is affected by the presence or absence of food in the assay. Gustatory receptors on the tarsi, the part of the foreleg in contact with the sweet food, are in a good position to sample food and may play a mechanistic role in this sexual interaction. Photo by N. Stepek and J.-C. Billeter, kindly provided by J. D. Levine, Univ. of Toronto, Mississauga.

this might be influenced by the evolution of smell and taste receptors. Are there functional differences in chemosensory reception of a fly with omnivorous taste as compared to a fly species with more specialized tastes? Hints that such phenomena are both existent and genetically tractable come from recent work in Bill Hansson's group, which found that the Seychelles island species *D. sechellia* has an olfactory system specialized to sense its preferred food, the Noni fruit⁶³.

The little vinegar fly *Drosophila melanogaster*, along with its sister species, promises to reveal many more surprises about how the nervous system produces complex behaviours in the next 40 yr.

1. Benzer, S. Behavioral mutants of *Drosophila* isolated by countercurrent distribution. *Proc. Natl Acad. Sci. USA* **58**, 1112–1119 (1967).
2. Benzer, S. Fine Structure of a genetic region in bacteriophage. *Proc. Natl Acad. Sci. USA* **41**, 344–354 (1955).
3. Papazian, D. M., Schwarz, T. L., Tempel, B. L., Jan, Y. N. & Jan, L. Y. Cloning of genomic and complementary DNA from *Shaker*, a putative potassium channel gene from *Drosophila*. *Science* **237**, 749–753 (1987).
4. Cosens, D. J. & Manning, A. Abnormal electroretinogram from a *Drosophila* mutant. *Nature* **224**, 285–287 (1969).
5. Montell, C. The TRP superfamily of cation channels. *Sci. STKE* **2005**, re3 (2005).
6. Pak, W. L., Grossfield, J. & Arnold, K. S. Mutants of the visual pathway of *Drosophila melanogaster*. *Nature* **227**, 518–520 (1970).
7. Smith, D. P., Stamnes, M. A. & Zuker, C. S. Signal transduction in the visual system of *Drosophila*. *Annu. Rev. Cell Biol.* **7**, 161–190 (1991).
8. Hardin, P. E. The circadian timekeeping system of *Drosophila*. *Curr. Biol.* **15**, R714–R722 (2005).
9. Sehgal, A., Price, J. & Young, M. W. Ontogeny of a biological clock in *Drosophila melanogaster*. *Proc. Natl Acad. Sci. USA* **89**, 1423–1427 (1992).
10. Konopka, R. J. & Benzer, S. Clock mutants of *Drosophila melanogaster*. *Proc. Natl Acad. Sci. USA* **68**, 2112–2116 (1971).
11. Toh, K. L. et al. An hPer2 phosphorylation site mutation in familial advanced sleep phase syndrome. *Science* **291**, 1040–1043 (2001).
12. Bargiello, T. A., Jackson, F. R. & Young, M. W. Restoration of circadian behavioural rhythms by gene transfer in *Drosophila*. *Nature* **312**, 752–754 (1984).
13. Zehring, W. A. et al. P-element transformation with *period* locus DNA restores rhythmicity to mutant, arrhythmic *Drosophila melanogaster*. *Cell* **39**, 369–376 (1984).
14. Hardin, P. E., Hall, J. C. & Rosbash, M. Feedback of the *Drosophila* period gene product on circadian cycling of its messenger RNA levels. *Nature* **343**, 536–540 (1990).
15. Meyer, P., Saez, L. & Young, M. W. PER–TIM interactions in living *Drosophila* cells: an interval timer for the circadian clock. *Science* **311**, 226–229 (2006).
16. Doi, M., Hirayama, J. & Sassone-Corsi, P. Circadian regulator CLOCK is a histone acetyltransferase. *Cell* **125**, 497–508 (2006).
17. Claridge-Chang, A. et al. Circadian regulation of gene expression systems in the *Drosophila* head. *Neuron* **32**, 657–671 (2001).
18. Greenspan, R. J. & Ferveur, J. F. Courtship in *Drosophila*. *Annu. Rev. Genet.* **34**, 205–232 (2000).

19. Hotta, Y. & Benzer, S. Courtship in *Drosophila* mosaics: sex-specific foci for sequential action patterns. *Proc. Natl Acad. Sci. USA* **73**, 4154–4158 (1976).
20. Hall, J. C. Control of male reproductive behavior by the central nervous system of *Drosophila*: dissection of a courtship pathway by genetic mosaics. *Genetics* **92**, 437–457 (1979).
21. Hall, J. C. Courtship among males due to a male-sterile mutation in *Drosophila melanogaster*. *Behav. Genet.* **8**, 124–141 (1978).
22. Ito, H. *et al.* Sexual orientation in *Drosophila* is altered by the *satori* mutation in the sex-determination gene *fruitless* that encodes a zinc finger protein with a BTB domain. *Proc. Natl Acad. Sci. USA* **93**, 9687–9692 (1996).
23. Ryner, L. C. *et al.* Control of male sexual behavior and sexual orientation in *Drosophila* by the *fruitless* gene. *Cell* **87**, 1079–1089 (1996).
24. Demir, E. & Dickson, B. J. *fruitless* specifies male courtship behavior in *Drosophila*. *Cell* **121**, 785–794 (2005).
25. Kimura, K., Ote, M., Tazawa, T. & Yamamoto, D. *Fruitless* specifies sexually dimorphic neural circuitry in the *Drosophila* brain. *Nature* **438**, 229–233 (2005).
26. Manoli, D. S. *et al.* Male-specific *fruitless* specifies the neural substrates of *Drosophila* courtship behaviour. *Nature* **436**, 395–400 (2005).
27. Stockinger, P., Kvitsiani, D., Rotkopf, S., Tirian, L. & Dickson, B. J. Neural circuitry that governs *Drosophila* male courtship behavior. *Cell* **121**, 795–807 (2005).
28. Kimchi, T., Xu, J. & Dulac, C. A functional circuit underlying male sexual behaviour in the female mouse brain. *Nature* **448**, 1009–1014 (2007).
29. Ayyub, C., Paranjape, J., Rodrigues, V. & Siddiqi, O. Genetics of olfactory behavior in *Drosophila melanogaster*. *J. Neurogenet.* **6**, 243–262 (1990).
30. Carlson, J. Olfaction in *Drosophila*: genetic and molecular analysis. *Trends Neurosci.* **14**, 520–524 (1991).
31. Clyne, P. J. *et al.* The odor specificities of a subset of olfactory receptor neurons are governed by *Acj6*, a POU-domain transcription factor. *Neuron* **22**, 339–347 (1999).
32. Vosshall, L. B. & Stocker, R. F. Molecular architecture of smell and taste in *Drosophila*. *Annu. Rev. Neurosci.* **30**, 505–533 (2007).
33. Couto, A., Alenius, M. & Dickson, B. J. Molecular, anatomical, and functional organization of the *Drosophila* olfactory system. *Curr. Biol.* **15**, 1535–1547 (2005).
34. Fishilevich, E. & Vosshall, L. B. Genetic and functional subdivision of the *Drosophila* antennal lobe. *Curr. Biol.* **15**, 1548–1553 (2005).
35. Lin, H. H., Lai, J. S., Chin, A. L., Chen, Y. C. & Chiang, A. S. A map of olfactory representation in the *Drosophila* mushroom body. *Cell* **128**, 1205–1217 (2007).
36. Jefferis, G. S. *et al.* Comprehensive maps of *Drosophila* higher olfactory centers: spatially segregated fruit and pheromone representation. *Cell* **128**, 1187–1203 (2007).
37. Hallem, E. A. & Carlson, J. R. Coding of odors by a receptor repertoire. *Cell* **125**, 143–160 (2006).
38. van der Goes van Naters, W. & Carlson, J. R. Receptors and neurons for fly odors in *Drosophila*. *Curr. Biol.* **17**, 606–612 (2007).
39. Kurtovic, A., Widmer, A. & Dickson, B. J. A single class of olfactory neurons mediates behavioural responses to a *Drosophila* sex pheromone. *Nature* **446**, 542–546 (2007).
40. Quinn, W. G., Harris, W. A. & Benzer, S. Conditioned behavior in *Drosophila melanogaster*. *Proc. Natl Acad. Sci. USA* **71**, 708–712 (1974).
41. Davis, R. L. Olfactory memory formation in *Drosophila*: from molecular to systems neuroscience. *Annu. Rev. Neurosci.* **28**, 275–302 (2005).
42. Bourchuladze, R. *et al.* Deficient long-term memory in mice with a targeted mutation of the cAMP-responsive element-binding protein. *Cell* **79**, 59–68 (1994).
43. Schacher, S., Castellucci, V. F. & Kandel, E. R. cAMP evokes long-term facilitation in *Aplysia* sensory neurons that requires new protein synthesis. *Science* **240**, 1667–1669 (1988).
44. Dubnau, J. *et al.* The *staufen/pumilio* pathway is involved in *Drosophila* long-term memory. *Curr. Biol.* **13**, 286–296 (2003).
45. Byers, D., Davis, R. L. & Kiger, J. A. Jr. Defect in cyclic AMP phosphodiesterase due to the *dunce* mutation of learning in *Drosophila melanogaster*. *Nature* **289**, 79–81 (1981).
46. Nighorn, A., Healy, M. J. & Davis, R. L. The cyclic AMP phosphodiesterase encoded by the *Drosophila dunce* gene is concentrated in the mushroom body neuropil. *Neuron* **6**, 455–467 (1991).
47. Heisenberg, M., Borst, A., Wagner, S. & Byers, D. *Drosophila* mushroom body mutants are deficient in olfactory learning. *J. Neurogenet.* **2**, 1–30 (1985).
48. Han, P. L., Levin, L. R., Reed, R. R. & Davis, R. L. Preferential expression of the *Drosophila rutabaga* gene in mushroom bodies, neural centers for learning in insects. *Neuron* **9**, 619–627 (1992).
49. Yu, D., Keene, A. C., Srivatsan, A., Waddell, S. & Davis, R. L. *Drosophila* DPM neurons form a delayed and branch-specific memory trace after olfactory classical conditioning. *Cell* **123**, 945–957 (2005).
50. Yu, D., Ponomarev, A. & Davis, R. L. Altered representation of the spatial code for odors after olfactory classical conditioning; memory trace formation by synaptic recruitment. *Neuron* **42**, 437–449 (2004).
51. Krashes, M. J., Keene, A. C., Leung, B., Armstrong, J. D. & Waddell, S. Sequential use of mushroom body neuron subsets during *Drosophila* odor memory processing. *Neuron* **53**, 103–115 (2007).
52. Liu, G. *et al.* Distinct memory traces for two visual features in the *Drosophila* brain. *Nature* **439**, 551–556 (2006).
53. Wilson, R. I., Turner, G. C. & Laurent, G. Transformation of olfactory representations in the *Drosophila* antennal lobe. *Science* **303**, 366–370 (2004).
54. Wolf, F. W., Rodan, A. R., Tsai, L. T. & Heberlein, U. High-resolution analysis of ethanol-induced locomotor stimulation in *Drosophila*. *J. Neurosci.* **22**, 11035–11044 (2002).
55. Moore, M. S. *et al.* Ethanol intoxication in *Drosophila*: Genetic and pharmacological evidence for regulation by the cAMP signaling pathway. *Cell* **93**, 997–1007 (1998).
56. Chen, S., Lee, A. Y., Bowens, N. M., Huber, R. & Kravitz, E. A. Fighting fruit flies: a model system for the study of aggression. *Proc. Natl Acad. Sci. USA* **99**, 5664–5668 (2002).
57. Vrontou, E., Nilsen, S. P., Demir, E., Kravitz, E. A. & Dickson, B. J. *fruitless* regulates aggression and dominance in *Drosophila*. *Nature Neurosci.* **9**, 1469–1471 (2006).
58. Dierick, H. A. & Greenspan, R. J. Molecular analysis of flies selected for aggressive behavior. *Nature Genet.* **38**, 1023–1031 (2006).
59. Pick, S. & Strauss, R. Goal-driven behavioral adaptations in gap-climbing *Drosophila*. *Curr. Biol.* **15**, 1473–1478 (2005).
60. Levine, J. D., Funes, P., Dowse, H. B. & Hall, J. C. Resetting the circadian clock by social experience in *Drosophila melanogaster*. *Science* **298**, 2010–2012 (2002).
61. Fujii, S., Krishnan, P., Hardin, P. & Amrein, H. Nocturnal male sex drive in *Drosophila*. *Curr. Biol.* **17**, 244–251 (2007).
62. Suh, G. S. *et al.* A single population of olfactory sensory neurons mediates an innate avoidance behaviour in *Drosophila*. *Nature* **431**, 854–859 (2004).
63. Dekker, T., Ibba, I., Siju, K. P., Stensmyr, M. C. & Hansson, B. S. Olfactory shifts parallel superspecialism for toxic fruit in *Drosophila melanogaster* sibling, *D. sechellia*. *Curr. Biol.* **16**, 101–109 (2006).
64. Tully, T. & Quinn, W. G. Classical conditioning and retention in normal and mutant *Drosophila melanogaster*. *J. Comp. Physiol.* **157**, 263–277 (1985).
65. Gerber, B., Tanimoto, H. & Heisenberg, M. Classical conditioning and retention in normal and mutant *Drosophila melanogaster*. *Curr. Opin. Neurobiol.* **14**, 737–744 (2004).
66. Weiner, J. Time, Love, Memory: A Great Biologist and His Quest for the Origins of Behavior (Alfred A. Knopf, Inc., New York, 1999).

Acknowledgements Work in the author's laboratory is supported by the NIH, FNIH and the Gates Foundation, and the Irma T. Hirsch Trust. I apologise to the many excellent *Drosophila* neurogeneticists whose work was not discussed here due to space constraints.

Author Information Reprints and permissions information is available at www.nature.com/reprints. Correspondence should be addressed to L.B.V. (leslie@mail.rockefeller.edu).

REVIEWS

Imaging *Drosophila* gene activation and polymerase pausing *in vivo*

John T. Lis¹

Since the early 1960s, imaging studies of *Drosophila* sp. polytene chromosomes have provided unique views of gene transcription *in vivo*. The dramatic changes in chromatin structure that accompany gene activation can be visualized as chromosome puffs. Now, live-cell imaging techniques coupled with protein–DNA crosslinking assays on a genome-wide scale allow more detailed mechanistic questions to be addressed and are prompting the re-evaluation of models of transcription regulation in both *Drosophila* and mammals.

Determining the complete genome sequence of humans, *Drosophila* and other model higher eukaryotes was an important step in cataloguing the complete code that programmes the development and maintenance of multicellular organisms. A critical challenge that remains is to determine in molecular terms how this code is read and regulated in higher eukaryotes¹. The regulation of transcription of the genome is a major mode by which an organism controls both its homeostasis and development. This regulation is executed mainly through the interactions of a plethora of transcription factor proteins and RNAs with each other and with DNA and associated histones². These interactions then dictate when, where, and to what level specific genes are transcribed. Although biochemical and genetic approaches have identified many of the macromolecular players and their activities, a mechanistic understanding of how they operate in gene regulation can be guided and tested by direct imaging of these molecular interactions and the resulting biochemical processes in living cells.

Two developments in the imaging of transcription factors at specific endogenous gene loci *in vivo* are providing new views of transcription mechanisms and regulation. One, currently specific to *Drosophila*, makes use of state-of-the-art optics combined with the natural amplification of signals in tissue containing polytene chromosomes, allowing investigation of molecular interactions and dynamics at specific loci in real time in living nuclei³. The other, although having a history in *Drosophila*^{4–6}, is species-general and uses crosslinking *in vivo*—that is, chromatin immunoprecipitation (ChIP) assays and variants thereof—to produce a ‘molecular image’ of specific protein interactions and chromatin modifications with particular DNA sequences in the genome⁷. Here I describe how these optical and molecular imaging approaches are providing new insights into transcription and the rate-limiting steps in its regulation in multicellular organisms. In particular, recent genome-wide ChIP assays in *Drosophila*^{8,9} and mammals¹⁰ support a paradigm shift in gene regulation by indicating that control of transcription elongation by RNA polymerase II (Pol II) in a promoter-proximal pausing model (Box 1), rather than control of the recruitment or initiation of Pol II, is the rate-limiting step for a large fraction of highly regulated genes.

Early insights from spread polytene nuclei

Over the past several decades, *Drosophila* has provided extraordinary views of chromosome structure and gene regulation. Simple phase

microscopy of fixed and spread polytene nuclei provided early *Drosophila* geneticists with a high-resolution view of interphase chromosomes and a physical framework for their genetic maps¹¹. This allowed genes to be positioned relative to the characteristic band and interband patterns seen along the lengths of each chromosome (Fig. 1). Particularly striking are the changes in polytene chromosome structure that occur when genes become transcriptionally activated¹². High levels of transcription activation result in the decondensation of chromatin at specific genetic loci to form interbands and, in some cases, large distended chromosome puffs. These puffs provide cytological landmarks along each chromosome that come and go during the course of development, with each new set of puffs appearing, and old puffs disappearing, in response to waves of activation and repression of gene transcription (Fig. 1)¹².

Environmental signals also activate the transcription of sets of genes, the activity of which can be observed as chromosomal puffs. The initial discovery in 1962 of the rapidly and highly activated heat shock response was not made by biochemists observing the induction of new messenger RNAs and proteins, but rather by a cytologist who was impressed by a striking new puffing pattern¹³. These observations of dramatic changes in cytology (Fig. 2) foreshadowed the changes in the molecular composition and dynamics of genes that would be uncovered by many laboratories in the decades that followed².

The genes that underlie these heat-shock-activated chromosomal puffs form a frequently used model for investigating mechanisms of gene activation and the accompanying changes in chromatin and chromosome structure. The staining of polytene chromosomes with antibodies to specific transcription factors¹⁴ allowed these factors to

Box 1 | Pausing and stalling

Here we use the term ‘paused RNA polymerase II (Pol II)’ to link to historical origins and because of properties in nuclear run-on assays²² and relationships to some features of prokaryotic pausing that have been extensively characterized⁴⁰. However, the more general term of ‘stalled’ is also very useful^{8,9}, especially because these populations of promoter-proximal Pol II will probably contain an equilibrium mix of both paused and arrested Pol II²⁹. Nuclear run-on assays are a key technique used to define the state of Pol II. The assays are performed in isolated nuclei and allow elongationally competent Pol II to extend existing RNA chains with labelled nucleotide; this nascent RNA can be identified and quantified by hybridization to specific genomic sequences.

¹Molecular Biology and Genetics, 416 Biotechnology Building, Cornell University, Ithaca, New York 14853, USA.

be visualized at these readily inducible loci and, more globally, over the entire genome. The molecular composition and chromatin architecture of these loci, and the changes triggered by the activation of these genes, have often proven to be general features of other developmentally activated loci¹⁵.

Live-cell imaging during gene activation

The ability to attach green fluorescent protein (GFP) and related fluorescent tags on chromosomal proteins has added a vital temporal dimension to the analysis of protein–DNA and protein–protein interactions in nuclei and on chromosomes. Expression of GFP-tagged proteins in mammalian cell lines allows the dynamics of transcription factors and chromatin components to be examined in nuclei in real time^{16,17}. Fluorescence recovery after photobleaching (FRAP) experiments additionally reveal the dynamics of a nuclear protein within an arbitrarily chosen nuclear region¹⁸, or at a specific transgenic locus containing tandemly repeated genes¹⁶. Examination of specific, native gene loci requires more sensitivity and higher-resolution views of interphase nuclei. The giant interphase nuclei of *Drosophila* polytene tissue provide both the sensitivity and effective resolution to detect signals from specific chromosomal loci³.

The advent of new optical-sectioning capabilities added further power to the imaging of intact nuclei. Computational deconvolution methods were used initially with wide-field microscopy to optically section *Drosophila* polytene nuclei¹⁹. Confocal, spinning disk and multi-photon microscopy further enhanced sectioning capabilities, with multi-photon microscopy being particularly effective in minimizing photodamage and providing high effective-resolution of thick biological specimens³. By applying these approaches to

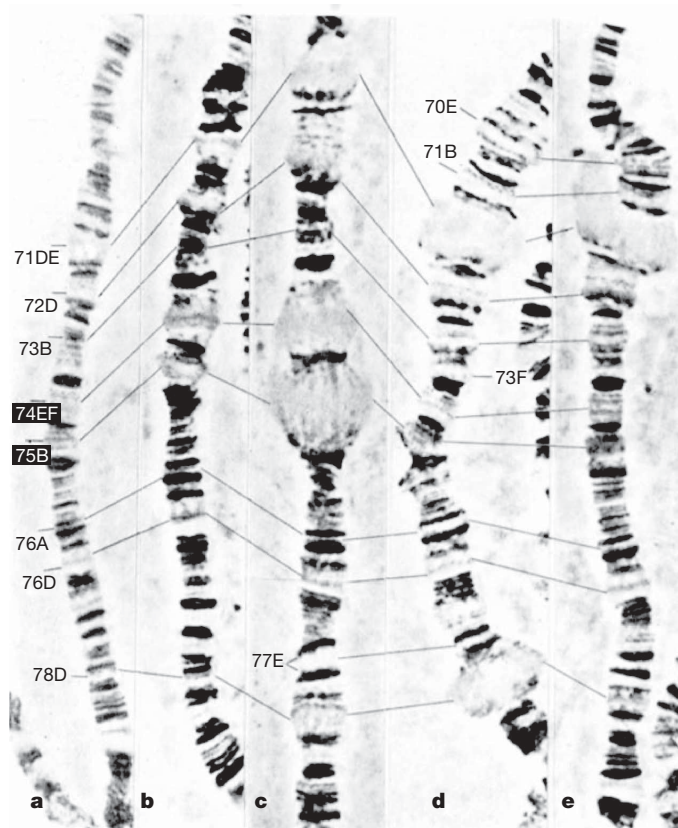


Figure 1 | Puffing patterns on chromosome 3L during *Drosophila* larval development. The chromosomes in a–e were isolated from progressively later developmental stages of third instar larvae. The light-staining distended puffs represent regions of high transcription activity. As developmental genes are turned on and off, the puffs appear and disappear. Reproduced with kind permission of Springer Science and Business Media from ref. 12.

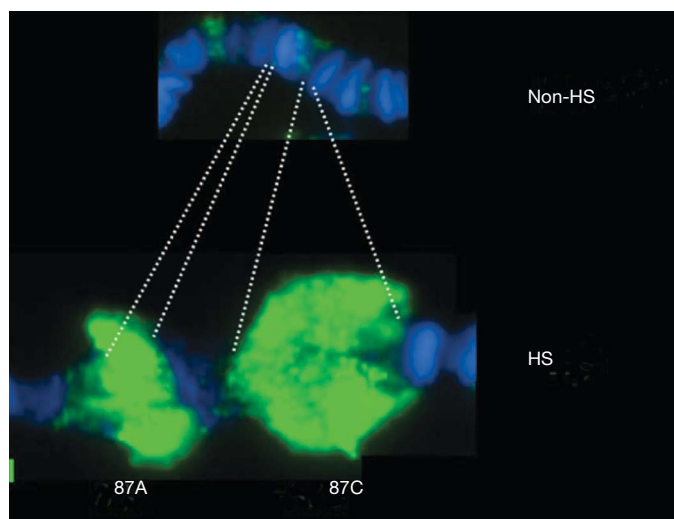


Figure 2 | Heat-shock-induced puffing at major heat shock loci 87A and C. Displayed is a small segment of fixed chromosome 3 before (top) and after (bottom) heat shock. Chromosomes are stained for DNA (Hoeschst dye; blue) and for Pol II (green)²⁹. HS, heat shock.

Drosophila polytene nuclei, it is possible to observe protein interactions with specific endogenous genetic loci in real time (Fig. 3). This was invaluable in directly tracking heat shock transcriptional activator (HSF) movement from nucleoplasm to specific heat shock gene loci (*Hsp70*), and for demonstrating that activated HSF remains bound in a non-exchanging state for many dozens of cycles of transcription³. These optical strategies should prove to be critical in exploring challenging mechanistic questions concerning transcription regulation, as discussed later.

Molecular imaging of proteins on genes *in vivo*

As a complement to the microscopic views of nuclear protein distributions on polytene chromosomes, molecular approaches using protein–DNA crosslinking and immunoprecipitation of protein–DNA complexes (ultraviolet (UV)-ChIP and formaldehyde-ChIP) were developed in the mid-1980s to provide higher-resolution images of the molecular architecture of proteins and genes *in vivo*^{4–6}. Applying these methods both before and during the time course of gene activation identified the timing and location of numerous protein interactions at high resolution (~200 base pairs). The immediate, synchronous and robust heat shock response allows the heat shock genes to be examined before, and in the seconds that follow, stimulation, such that changes in chromatin and factor recruitment can be followed as a wave that passes along the length of these transcription units²⁰. Additionally, the role of particular factors in these processes can be readily assessed using existing mutants or inhibitory drugs or by RNA interference knock-down strategies².

An early and surprising finding, seen initially by UV-ChIP²¹, was that *Drosophila* heat shock genes had a polymerase associated with

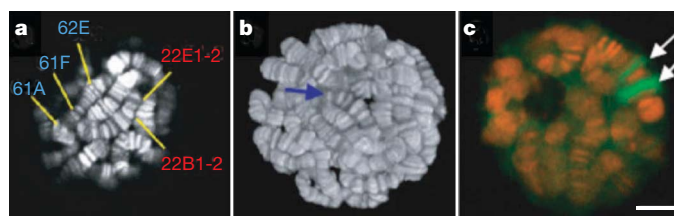


Figure 3 | Two-photon image of living salivary gland nuclei. DAPI (4,6-diamidino-2-phenylindole)-stained DNA of a single nuclear section (a), a three-dimensional reconstructed nucleus (b), and GFP–Pol II at heat shock puffs (c; Pol II, green)³.

their promoters before activation, and that this associated Pol II was engaged in transcription and competent for elongation as determined by nuclear run-on assays (Box 1)²². These findings seemed to contradict the widely held view that the recruitment of Pol II or the initiation of transcription was the rate-limiting step in gene activation. Additional support for the existence and characterization of the nature of this Pol II complex came from the mapping of promoter melting with KMnO_4 (ref. 23), which revealed melted DNA in the regions of heat shock genes residing 20–50 base pairs downstream of the transcription start sites. Also, the isolation and sizing of the chain-terminated run-on transcripts²⁴ provided near-nucleotide-resolution mapping of pause sites to this same region, as two peaks separated by 10 base pairs. Interestingly, the RNAs are progressively more 5'-capped as they progress through the pause region, suggesting that capping occurs as soon as the RNA emerges from Pol II.

Two protein complexes—DRB sensitivity-inducing factor (DSIF; made up of *spt4* and *Spt5*) and negative elongation factor (NELF; made up of five subunits)—were found to cooperate to repress transcription elongation *in vitro*²⁵, and their negative effects could be overcome by P-TEFb (made up of *Cdk9* and *CycT*) kinase²⁶. Using ChIP assays, both DSIF and NELF were found to be located along with paused Pol II in the promoter-proximal regions of uninduced heat shock genes (Fig. 4)^{2,27}. The P-TEFb kinase is recruited to active genes where it overcomes the negative effects through its kinase activity, which can phosphorylate DSIF, NELF and Ser 2 residues of the carboxy-terminal domain of the largest subunit of Pol II^{2,26}. Interestingly, P-TEFb recruitment to heat shock genes depends on the heat shock activator HSF, but HSF does not seem to bind directly to P-TEFb¹⁵. Some, but not all, activators have been shown to interact with P-TEFb, so other mechanisms of P-TEFb recruitment need to be considered²⁶. The transition into productive elongation seems to correlate with the loss of NELF from the promoter²⁷. In contrast, DSIF remains associated with productively elongating Pol II and is thought to have a positive role after escape from the pause^{2,28}. Paused polymerases are susceptible to backtracking, and the presence of

elongation factor TFIIS at the pause region *in vivo* in *Drosophila* may stimulate the intrinsic RNA cleavage activity of Pol II to create a new RNA 3' end in the active site, and thereby maintain a population of elongationally competent complexes²⁹.

Defining a Pol II as 'promoter paused'

The presence of a peak of Pol II at the promoter is not sufficient to identify a Pol II as paused. Although such a distribution is indicative of Pol II promoter recruitment not being rate limiting in transcription, this Pol II could be in a pre-initiation complex or at some other post-recruitment step that precedes pausing. Additional criteria need to be applied³⁰. Nuclear run-on assays can demonstrate that the detected Pol II is transcriptionally engaged, particularly if performed in the presence of Sarkosyl or high salt, which blocks new initiation and seems to remove barriers to elongation²². The isolation and sizing of intentionally terminated run-on RNAs show, at near-nucleotide-resolution, the location of the paused RNAs *in vivo*, and have the additional benefit of determining the capping signature, which in the cases examined is absent from the earliest pause sites, but is nearly complete by position +30 (ref. 24). Promoter-melting assays using KMnO_4 can be performed on intact cells for short periods (30 s) to provide a snapshot of the reactivity of T residues, the hyper-reactivity of which is indicative of Pol II-melted DNA²³. Whereas these melted residues tend to cluster in the region of 20–50 base pairs and highly correlate with paused Pol II, the pattern of reactivity can be influenced by other proteins either protecting or altering the reactivity of T residues. Additional signatures can be detected by ChIP assays and include the presence of NELF, and Ser 5- but not Ser 2-phosphorylated carboxy-terminal domain of the largest subunit (RpII215) of Pol II^{20,27}.

How general is paused Pol II?

Pol II paused on promoters was regarded initially as a feature of the heat shock genes and a few other rapidly responsive genes. A small set of randomly chosen *Drosophila* genes also seemed to have paused Pol II, as assessed by UV-ChIP and nuclear run-on assays³¹, though not at the full occupancy (1 Pol II per promoter) seen for *Hsp70* (ref. 30). Additionally, evidence supporting some form of elongational control in specific vertebrate genes has existed since the early 1980s, for example, greater nuclear run-on signals from 5' portions than 3' regions of chicken β -globin³². Similar data for mammalian *c-Myc* and *c-Fos* were augmented with *in vitro* studies that suggested initially a termination control further downstream, but more thorough characterizations *in vivo* showed these genes to have properties like those of *Drosophila Hsp70* paused Pol II^{33,34}.

More recently, genome-wide ChIP analyses of Pol II in human cells showed Pol II peaks in the promoter regions of a large fraction of genes³⁵, and a study in human stem cells and differentiated cells showed that the majority of genes have peaks of Pol II that seem to have undergone transcription initiation, on the basis of their pattern of histone H3K4 trimethylation (a modification linked to active promoters) and the production of short 5' transcripts¹⁰. Interestingly, many of these genes are not producing mature transcripts^{1,10}. Very recent genome-wide studies in *Drosophila* have revealed that many genes have peaks of paused Pol II, including important regulatory genes of early *Drosophila* development^{8,9}. Numbers of promoters with paused Pol II in *Drosophila*, as defined by exhibiting additional signatures of paused Pol II such as NELF occupancy and promoter melting^{8,9}, are estimated conservatively to be about 20% of all genes that have any associated Pol II.

Is this mechanism of elongation control used only for the estimated 20% of genes in *Drosophila*^{7,8}, and >50% (estimated by different criteria) in human stem cells, or is pausing a still more universal step on the pathway of transcription of most genes? The inhibition of P-TEFb kinase, (a kinase which is critical for Pol II escape from pausing into productive elongation), can lead to an

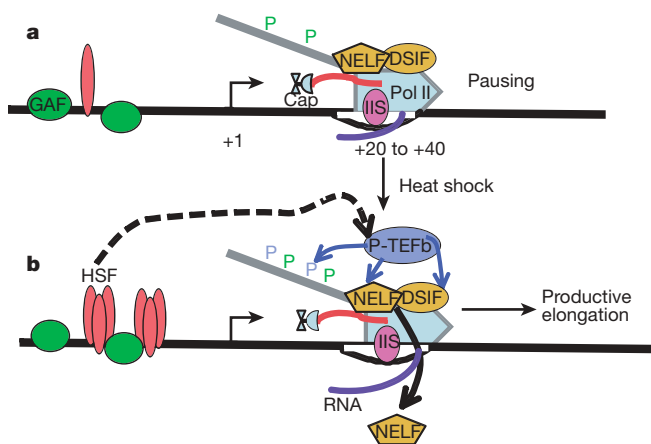


Figure 4 | Minimal model of Pol II pausing at *Hsp70* genes before and after heat shock. For a more complete description of factors associated with heat shock genes see the more comprehensive review². **a**, Prior to heat-shock, paused Pol II, which is partially phosphorylated at Ser 5 residues (green P) of the carboxy-terminal domain, is in a complex with DSIF and NELF complexes and occupies a region between 20–40 base pairs downstream of the start site of *Hsp70*. GAF is a sequence-specific binding factor that is present before activation. **b**, HSF is the key activator protein that trimerizes and binds with high affinity to its DNA elements in response to heat shock. Both DSIF and TFIIS (IIS) are part of both the paused and the fully competent Pol II elongation complexes. P-TEFb is the kinase that is critical for the maturation of paused Pol II into a productive elongation product, and it phosphorylates DSIF, NELF and the Ser 2 residues (blue P) of the carboxy-terminal domain of Pol II²⁶.

80% reduction of Pol II transcription³⁶, indicating that these steps may be pervasive, though not necessarily rate limiting, under the particular cellular conditions examined.

Questions and future prospects

What are the proteins and RNAs that set up and maintain paused Pol II, and what is the mechanism used to achieve this? In *Drosophila*, GAGA factor (GAF; also known as Trl) is bound before heat shock induction and seems to be critical for setting up the pause on *Hsp70* (refs 37 and 38). However, many, but not all, genes showing paused Pol II have associated GAF, and GAF homologues are not obvious in mammals. Is there a class of transcription factors with GAF-like function, and how do they function mechanistically? Although NELF and DSIF are major players, their depletion leads to neither a complete loss of paused Pol II nor high constitutive expression. Do other factors, and perhaps inherent features of Pol II and the underlying DNA or RNA sequence, also participate in this process? Can we devise other genome-wide approaches that allow characterization of paused Pol II RNAs at nucleotide-resolution and thereby improve the search for global sequence elements?

How dynamic is the promoter-proximal paused Pol II? The paused Pol II has been described by some as performing abortive transcription, meaning that Pol II undergoes termination before completing a full-length transcript. An extreme version of this view posits that the paused Pol II is terminated and replaced with productive Pol II following gene activation. However, there is no evidence *in vivo* that abortive transcription is a necessary property of these paused Pol II molecules. Clearly, there are cases in which Pol II does abort transcription early in the process of transcription in eukaryotes, for example, HIV transcription. However, these short HIV transcripts are terminated downstream of the HIV pause region and these termination events are dictated by mechanisms distinct from pausing³⁹. In the case of *Drosophila Hsp70*, short transcripts do not accumulate, although some fraction of transcripts fail to efficiently elongate in run-on assays and are likely to be back-tracked and arrested. However, TFIIS is also present at the promoter and may allow these arrested Pol II complexes to be in dynamic equilibrium with elongationally competent paused complexes^{2,29}. For some genes, Pol II shows only fractional promoter occupancy—less than one Pol II per promoter. Does that reflect only a fraction of the cells having a poised promoter and thus an active or activatable gene? Or does this variation in occupancy reflect differences in the relative rates with which Pol II enters and escapes from the pause region? Both of these steps may be influenced by the spectrum of regulatory proteins bound to enhancer and promoter regions. These difficult questions concerning molecular dynamics at native gene loci should be addressable with the improved optical approaches discussed above, and with carefully developed *in vitro* systems that recapitulate all of the *in vivo* landmarks of these Pol II complexes.

How do activator proteins interface with paused Pol II to influence its escape to productive elongation? Clearly the P-TEFb kinase is a critical executor of the activation signal, and its presence and ability to phosphorylate components of the paused Pol II complex are critical for stimulating productive elongation²⁶. In some cases, activators are known to interact with P-TEFb, at least in simple pull-down or co-immunoprecipitation assays²⁶; however, in other cases, activators show no detectable affinity for P-TEFb¹⁵, and other existing mechanisms²⁶, or novel mechanisms yet to be discovered, allow activators to communicate with P-TEFb.

In summary, the pervasiveness of paused Pol II is causing the re-evaluation of the long-held textbook view of transcription and its regulation. For decades, the major mechanism of gene regulation in higher eukaryotes was thought to reside at the level of either recruitment of Pol II to promoters or transcription initiation. In light of genome-wide data^{7–10}, a post-recruitment and early elongation mechanism needs to be considered as a major mode of regulation in higher eukaryotes. *Drosophila* has been a useful model system for

past characterization of this regulation and its unique and shared features hold great promise for its role in addressing these outstanding questions.

1. ENCODE Project Consortium. Identification and analysis of functional elements in 1% of the human genome by the ENCODE pilot project. *Nature* **447**, 799–816 (2007).
2. Saunders, A., Core, L. J. & Lis, J. T. Breaking barriers to transcription elongation. *Nature Rev. Mol. Cell Biol.* **7**, 557–567 (2006).
3. Yao, J., Munson, K. M., Webb, W. W. & Lis, J. T. Dynamics of heat shock factor association with native gene loci in living cells. *Nature* **442**, 1050–1053 (2006).
4. Gilmour, D. S. & Lis, J. T. *In vivo* interactions of RNA polymerase II with genes of *Drosophila melanogaster*. *Mol. Cell. Biol.* **5**, 2009–2018 (1985).
5. Solomon, M. J., Larsen, P. L. & Varshavsky, A. Mapping protein–DNA interactions *in vivo* with formaldehyde: evidence that histone H4 is retained on a highly transcribed gene. *Cell* **53**, 937–947 (1988).
6. Orlando, V. & Paro, R. Mapping Polycomb-repressed domains in the bithorax complex using *in vivo* formaldehyde cross-linked chromatin. *Cell* **75**, 1187–1198 (1993).
7. Ren, B. *et al.* Genome-wide location and function of DNA binding proteins. *Science* **290**, 2306–2309 (2000).
8. Zeitlinger, J. *et al.* A polymerase stalling at developmental control genes in the *Drosophila* embryo. *Nature Genet.* (in the press).
9. Muse, *et al.* RNA polymerase is poised for activation across the genome. *Nature Genet.* (in the press).
10. Guenther, M. G., Levine, S. S., Boyer, L. A., Jaenisch, R. & Young, R. A. A chromatin landmark and transcription initiation at most promoters in human cells. *Cell* **130**, 77–88 (2007).
11. Bridges, C. B. Salivary chromosome maps with a key to the banding of the chromosome of *Drosophila melanogaster*. *J. Hered.* **26**, 60–64 (1935).
12. Ashburner, M. in *Developmental studies on giant chromosomes*, (ed. W. Beermann) 101–151 (Springer, New York, 1972).
13. Ritossa, F. A new puffing pattern induced by temperature shock and DNP in *Drosophila*. *Experientia* **18**, 571–573 (1962).
14. Silver, L. M. & Elgin, S. C. Production and characterization of antisera against three individual NHC proteins; a case of a generally distributed NHC protein. *Chromosoma* **68**, 101–114 (1978).
15. Lis, J. T., Mason, P., Peng, J., Price, D. H. & Werner, J. P-TEFb kinase recruitment and function at heat shock loci. *Genes Dev.* **14**, 792–803 (2000).
16. Hager, G. L., Elbi, C. & Becker, M. Protein dynamics in the nuclear compartment. *Curr. Opin. Genet. Dev.* **12**, 137–141 (2002).
17. Janicki, S. M. *et al.* From silencing to gene expression: real-time analysis in single cells. *Cell* **116**, 683–698 (2004).
18. Kimura, H., Sugaya, K. & Cook, P. R. The transcription cycle of RNA polymerase II in living cells. *J. Cell Biol.* **159**, 777–782 (2002).
19. Mathog, D., Hochstrasser, M., Gruenbaum, Y., Saumweber, H. & Sedat, J. Characteristic folding pattern of polytene chromosomes in *Drosophila* salivary gland nuclei. *Nature* **308**, 414–421 (1984).
20. Boehm, A. K., Saunders, A., Werner, J. & Lis, J. T. Transcription factor and polymerase recruitment, modification, and movement on *dhsp70* *in vivo* in the minutes following heat shock. *Mol. Cell. Biol.* **23**, 7628–7637 (2003).
21. Gilmour, D. S. & Lis, J. T. RNA polymerase II interacts with the promoter region of the noninduced *hsp70* gene in *Drosophila melanogaster* cells. *Mol. Cell. Biol.* **6**, 3984–3989 (1986).
22. Rougvie, A. E. & Lis, J. T. The RNA polymerase II molecule at the 5' end of the uninduced *hsp70* gene of *D. melanogaster* is transcriptionally engaged. *Cell* **54**, 795–804 (1988).
23. Giardina, C., Perez-Riba, M. & Lis, J. T. Promoter melting and TFIID complexes on *Drosophila* genes *in vivo*. *Genes Dev.* **6**, 2190–2200 (1992).
24. Rasmussen, E. B. & Lis, J. T. *In vivo* transcriptional pausing and cap formation on three *Drosophila* heat shock genes. *Proc. Natl Acad. Sci. USA* **90**, 7923–7927 (1993).
25. Yamaguchi, Y. *et al.* NELF, a multisubunit complex containing RD, cooperates with DSIF to repress RNA polymerase II elongation. *Cell* **97**, 41–51 (1999).
26. Peterlin, B. M. & Price, D. H. Controlling the elongation phase of transcription with P-TEFb. *Mol. Cell* **23**, 297–305 (2006).
27. Wu, C. H. *et al.* NELF and DSIF cause promoter proximal pausing on the *hsp70* promoter in *Drosophila*. *Genes Dev.* **17**, 1402–1414 (2003).
28. Zhu, W. *et al.* DSIF contributes to transcriptional activation by DNA-binding activators by preventing pausing during transcription elongation. *Nucleic Acids Res.* **35**, 4064–4075 (2007).
29. Adelman, K. *et al.* Efficient release from promoter-proximal stall sites requires transcript cleavage factor TFIIS. *Mol. Cell* **17**, 103–112 (2005).
30. Lis, J. Promoter-associated pausing in promoter architecture and postinitiation transcriptional regulation. *Cold Spring Harb. Symp. Quant. Biol.* **63**, 347–356 (1998).
31. Rougvie, A. E. & Lis, J. T. Postinitiation transcriptional control in *Drosophila melanogaster*. *Mol. Cell. Biol.* **10**, 6041–6045 (1990).

32. Gariglio, P., Bellard, M. & Chambon, P. Clustering of RNA polymerase B molecules in the 5' moiety of the adult β -globin gene of hen erythrocytes. *Nucleic Acids Res.* **9**, 2589–2598 (1981).
 33. Krumm, A., Meulia, T., Brunvand, M. & Groudine, M. The block to transcriptional elongation within the human c-myc gene is determined in the promoter-proximal region. *Genes Dev.* **6**, 2201–2213 (1992).
 34. Albert, T. *et al.* Nucleosomal structures of c-myc promoters with transcriptionally engaged RNA polymerase II. *Mol. Cell. Biol.* **17**, 4363–4371 (1997).
 35. Kim, T. H. *et al.* A high-resolution map of active promoters in the human genome. *Nature* **436**, 876–880 (2005).
 36. Chao, S. H. & Price, D. H. Flavopiridol inactivates P-TEFb and blocks most RNA polymerase II transcription *in vivo*. *J. Biol. Chem.* **276**, 31793–31799 (2001).
 37. Lee, H., Kraus, K. W., Wolfner, M. F. & Lis, J. T. DNA sequence requirements for generating paused polymerase at the start of *hsp70*. *Genes Dev.* **6**, 284–295 (1992).
 38. Wang, Y. V., Tang, H. & Gilmour, D. S. Identification *in vivo* of different rate-limiting steps associated with transcriptional activators in the presence and absence of a GAGA element. *Mol. Cell. Biol.* **25**, 3543–3552 (2005).
 39. Henderson, A. J. & Gilmour, D. S. Transcription termination factor Pcf11 limits the processivity of Pol II on an HIV provirus to repress gene expression. *Genes Dev.* **21**, 1609–1614 (2007).
 40. Ring, B. Z., Yarnell, W. S. & Roberts, J. W. Function of *E. coli* RNA polymerase sigma factor sigma 70 in promoter-proximal pausing. *Cell* **86**, 485–493 (1996).
- Acknowledgements** I thank J. Werner for generating the immunofluorescence images used in Fig. 2, and M. Hamblin, D. Gilmour, K. Adelman and my laboratory members for helpful comments on the manuscript. This work was supported by an NIH grant.
- Author Information** Reprints and permissions information is available at www.nature.com/reprints. Correspondence and requests for materials should be addressed to D.L. (jtl10@cornell.edu).

Evolution of genes and genomes on the *Drosophila* phylogeny

Drosophila 12 Genomes Consortium*

Comparative analysis of multiple genomes in a phylogenetic framework dramatically improves the precision and sensitivity of evolutionary inference, producing more robust results than single-genome analyses can provide. The genomes of 12 *Drosophila* species, ten of which are presented here for the first time (*sechellia*, *simulans*, *yakuba*, *erecta*, *ananassae*, *persimilis*, *willistoni*, *mojavensis*, *virilis* and *grimshawi*), illustrate how rates and patterns of sequence divergence across taxa can illuminate evolutionary processes on a genomic scale. These genome sequences augment the formidable genetic tools that have made *Drosophila melanogaster* a pre-eminent model for animal genetics, and will further catalyse fundamental research on mechanisms of development, cell biology, genetics, disease, neurobiology, behaviour, physiology and evolution. Despite remarkable similarities among these *Drosophila* species, we identified many putatively non-neutral changes in protein-coding genes, non-coding RNA genes, and cis-regulatory regions. These may prove to underlie differences in the ecology and behaviour of these diverse species.

As one might expect from a genus with species living in deserts, in the tropics, on chains of volcanic islands and, often, commensally with humans, *Drosophila* species vary considerably in their morphology, ecology and behaviour¹. Species in this genus span a wide range of global distributions: the 12 sequenced species originate from Africa, Asia, the Americas and the Pacific Islands, and also include cosmopolitan species that have colonized the planet (*D. melanogaster* and *D. simulans*) as well as closely related species that live on single islands (*D. sechellia*)². A variety of behavioural strategies is also encompassed by the sequenced species, ranging in feeding habit from generalist, such as *D. ananassae*, to specialist, such as *D. sechellia*, which feeds on the fruit of a single plant species.

Despite this wealth of phenotypic diversity, *Drosophila* species share a distinctive body plan and life cycle. Although only *D. melanogaster* has been extensively characterized, it seems that the most important aspects of the cellular, molecular and developmental biology of these species are well conserved. Thus, in addition to providing an extensive resource for the study of the relationship between sequence and phenotypic diversity, the genomes of these species provide an excellent model for studying how conserved functions are maintained in the face of sequence divergence. These genome sequences provide an unprecedented dataset to contrast genome structure, genome content, and evolutionary dynamics across the well-defined phylogeny of the sequenced species (Fig. 1).

Genome assembly, annotation and alignment

Genome sequencing and assembly. We used the previously published sequence and updated assemblies for two *Drosophila* species, *D. melanogaster*^{3,4} (release 4) and *D. pseudoobscura*⁵ (release 2), and generated DNA sequence data for 10 additional *Drosophila* genomes by whole-genome shotgun sequencing^{6,7}. These species were chosen to span a wide variety of evolutionary distances, from closely related pairs such as *D. sechellia*/*D. simulans* and *D. persimilis*/*D. pseudoobscura* to the distantly related species of the *Drosophila* and *Sophophora* subgenera. Whereas the time to the most recent common ancestor of the sequenced species may seem small on an evolutionary timescale, the evolutionary divergence spanned by the genus *Drosophila* exceeds

that of the entire mammalian radiation when generation time is taken into account, as discussed further in ref. 8. We sequenced seven of the new species (*D. yakuba*, *D. erecta*, *D. ananassae*, *D. willistoni*, *D. virilis*, *D. mojavensis* and *D. grimshawi*) to deep coverage (8.4× to 11.0×) to produce high quality draft sequences. We sequenced two species, *D. sechellia* and *D. persimilis*, to intermediate coverage (4.9× and 4.1×, respectively) under the assumption that the availability of a sister species sequenced to high coverage would obviate the need for deep sequencing without sacrificing draft genome quality. Finally, seven inbred strains of *D. simulans* were sequenced to low coverage (2.9× coverage from *w*⁵⁰¹ and ~1× coverage of six other strains) to provide population variation data⁹. Further details of the sequencing strategy can be found in Table 1, Supplementary Table 1 and section 1 in Supplementary Information.

We generated an initial draft assembly for each species using one of three different whole-genome shotgun assembly programs (Table 1). For *D. ananassae*, *D. erecta*, *D. grimshawi*, *D. mojavensis*, *D. virilis* and *D. willistoni*, we also generated secondary assemblies; reconciliation of these with the primary assemblies resulted in a 7–30% decrease in the estimated number of misassembled regions and a 12–23% increase in the N50 contig size¹⁰ (Supplementary Table 2). For *D. yakuba*, we generated 52,000 targeted reads across low-quality regions and gaps to improve the assembly. This doubled the mean contig and scaffold sizes and increased the total fraction of high quality bases (quality score (Q) > 40) from 96.5% to 98.5%. We improved the initial 2.9× *D. simulans* *w*⁵⁰¹ whole-genome shotgun assembly by filling assembly gaps with contigs and unplaced reads from the ~1× assemblies of the six other *D. simulans* strains, generating a 'mosaic' assembly (Supplementary Table 3). This integration markedly improved the *D. simulans* assembly: the N50 contig size of the mosaic assembly, for instance, is more than twice that of the initial *w*⁵⁰¹ assembly (17 kb versus 7 kb).

Finally, one advantage of sequencing genomes of multiple closely related species is that these evolutionary relationships can be exploited to dramatically improve assemblies. *D. yakuba* and *D. simulans* contigs and scaffolds were ordered and oriented using pairwise alignment to the well-validated *D. melanogaster* genome

*A list of participants and affiliations appears at the end of the paper.

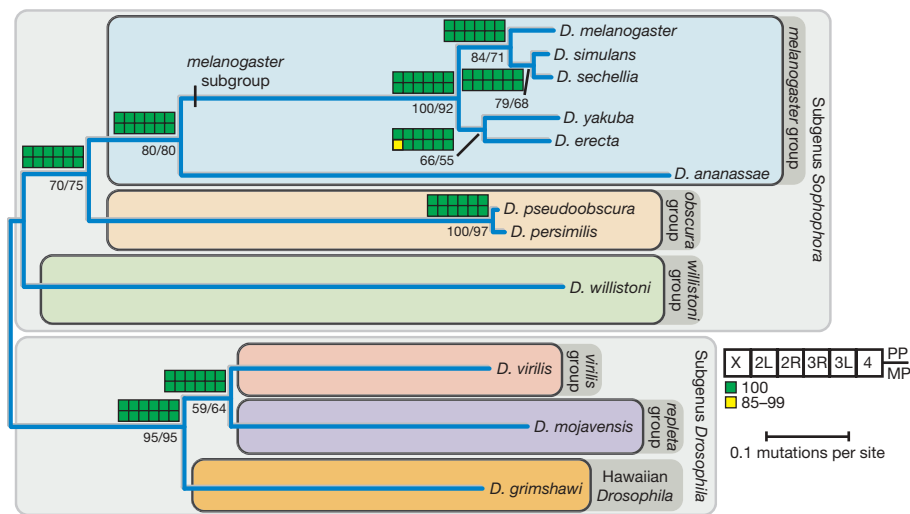


Figure 1 | Phylogram of the 12 sequenced species of *Drosophila*. Phylogram derived using pairwise genomic mutation distances and the neighbour-joining method^{152,153}. Numbers below nodes indicate the per cent of genes supporting a given relationship, based on evolutionary distances estimated from fourfold-degenerate sites (left of solidus) and second codon positions (right of solidus). Coloured blocks indicate support from bayesian

(posterior probability (PP), upper blocks) and maximum parsimony (MP; bootstrap values, lower blocks) analyses of data partitioned by chromosome arm. Branch lengths indicate the number of mutations per site (at fourfold-degenerate sites) using the ordinary least squares method. See ref. 154 for a discussion of the uncertainties in the *D. yakuba*/*D. erecta* clade.

sequence (Supplementary Information section 2). Likewise, the 4–5× *D. persimilis* and *D. sechellia* assemblies were improved by assisted assembly using the sister species (*D. pseudoobscura* and *D. simulans*, respectively) to validate both alignments between reads and linkage information. For the remaining species, comparative syntenic information, and in some cases linkage information, were also used to pinpoint locations of probable genome mis-assembly, to assign assembly scaffolds to chromosome arms and to infer their order and orientation along euchromatic chromosome arms, supplementing experimental analysis based on known markers (A. Bhutkar, S. Russo, S. Schaeffer, T. F. Smith and W. M. Gelbart, personal communication) (Supplementary Information section 2).

The mitochondrial (mt)DNA of *D. melanogaster*, *D. sechellia*, *D. simulans* (siII), *D. mauritiana* (maII) and *D. yakuba* have been previously sequenced^{11,12}. For the remaining species (except *D. pseudoobscura*, the DNA from which was prepared from embryonic nuclei), we were able to assemble full mitochondrial genomes, excluding the A+T-rich control region (Supplementary Information section 2)¹³. In addition, the genome sequences of three *Wolbachia* endosymbionts (*Wolbachia wSim*, *Wolbachia wAna* and *Wolbachia wWil*) were assembled from trace archives, in *D. simulans*, *D. ananassae* and *D. willistoni*, respectively¹⁴. All of the genome sequences described here are available in FlyBase (www.flybase.org) and GenBank (www.ncbi.nlm.nih.gov) (Supplementary Tables 4 and 5).

Repeat and transposable element annotation. Repetitive DNA sequences such as transposable elements pose challenges for

whole-genome shotgun assembly and annotation. Because the best approach to transposable element discovery and identification is still an active and unresolved research question, we used several repeat libraries and computational strategies to estimate the transposable element/repeat content of the 12 *Drosophila* genome assemblies (Supplementary Information section 3). Previously curated transposable element libraries in *D. melanogaster* provided the starting point for our analysis; to limit the effects of ascertainment bias, we also developed *de novo* repeat libraries using PILER-DF^{15,16} and ReAS¹⁷. We used four transposable element/repeat detection methods (RepeatMasker, BLASTER-TX, RepeatRunner and CompTE) in conjunction with these transposable element libraries to identify repetitive elements in non-*melanogaster* species. We assessed the accuracy of each method by calibration with the estimated 5.5% transposable element content in the *D. melanogaster* genome, which is based on a high-resolution transposable element annotation¹⁸ (Supplementary Fig. 1). On the basis of our results, we suggest a hybrid strategy for new genome sequences, employing translated BLAST with general transposable element libraries and RepeatMasker with species-specific ReAS libraries to estimate the upper and lower bound on transposable element content.

Protein-coding gene annotation. We annotated protein-coding sequences in the 11 non-*melanogaster* genomes, using four different *de novo* gene predictors (GeneID¹⁹, SNAP²⁰, N-SCAN²¹ and CONTRAST²²); three homology-based predictors that transfer annotations from *D. melanogaster* (GeneWise²³, Exonerate²⁴, GeneMapper²⁵); and one predictor that combined *de novo* and homology-based evidence (Gnomon²⁶). These gene prediction sets

Table 1 | A summary of sequencing and assembly properties of each new genome

Final assembly	Genome centre	Q20 coverage (×)	Assembly size (Mb)	No. of contigs ≥2 kb	N50 contig ≥2 kb (kb)	Per cent of base pairs with quality >Q40
<i>D. simulans</i>	WUGSC*	2.9	137.8	10,843	17	90.3
<i>D. sechellia</i>	Broad†	4.9	166.6	9,713	43	90.6
<i>D. yakuba</i>	WUGSC*	9.1	165.7	6,344	125	98.5
<i>D. erecta</i>	Agencourt†	10.6	152.7	3,283	458	99.2
<i>D. ananassae</i>	Agencourt†	8.9	231.0	8,155	113	98.5
<i>D. persimilis</i>	Broad†	4.1	188.4	14,547	20	93.3
<i>D. willistoni</i>	JCVI‡	8.4	235.5	6,652	197	97.4
<i>D. virilis</i>	Agencourt†	8.0	206.0	5,327	136	98.7
<i>D. mojavensis</i>	Agencourt†	8.2	193.8	5,734	132	98.6
<i>D. grimshawi</i>	Agencourt†	7.9	200.5	9,632	114	97.1

Contigs, contiguous sequences not interrupted by gaps; N50, the largest length L such that 50% of all nucleotides are contained in contigs of size ≥L. The Q20 coverage of contigs is based on the number of assembled reads, average Q20 readlength and the assembled size excluding gaps. Assemblers used: *PCAP6, †ARACHNE4.5 and ‡Celerator Assembler 7.

Table 2 | A summary of annotated features across all 12 genomes

	Protein-coding gene annotations			Non-coding RNA annotations				Repeat coverage (%) [*]	Genome size (Mb; assembly [†] /flow cytometry [‡])
	Total no. of protein-coding genes (per cent with <i>D. melanogaster</i> homologue)	Coding sequence/intron (Mb)	tRNA (pseudo)	snoRNA	miRNA	rRNA (5.8S + 5S)	snRNA		
<i>D. melanogaster</i>	13,733 (100%)	38.9/21.8	297 (4)	250	78	101	28	5.35	118/200
<i>D. simulans</i>	15,983 (80.0%)	45.8/19.6	268 (2)	246	70	72	32	2.73	111/162
<i>D. sechellia</i>	16,884 (81.2%)	47.9/21.9	312 (13)	242	78	133	30	3.67	115/171
<i>D. yakuba</i>	16,423 (82.5%)	50.8/22.9	380 (52)	255	80	55	37	12.04	127/190
<i>D. erecta</i>	15,324 (86.4%)	49.1/22.0	286 (2)	252	81	101	38	6.97	134/135
<i>D. ananassae</i>	15,276 (83.0%)	57.3/22.3	472 (165)	194	76	134	29	24.93	176/217
<i>D. pseudoobscura</i>	16,363 (78.2%)	49.7/24.0	295 (1)	203	73	55	31	2.76	127/193
<i>D. persimilis</i>	17,325 (72.6%)	54.0/21.9	306 (1)	199	75	80	31	8.47	138/193
<i>D. willistoni</i>	15,816 (78.8%)	65.4/23.5	484 (164)	216	77	76	37	15.57	187/222
<i>D. virilis</i>	14,680 (82.7%)	57.9/21.7	279 (2)	165	74	294	31	13.96	172/364
<i>D. mojavensis</i>	14,849 (80.8%)	57.8/21.9	267 (3)	139	71	74	30	8.92	161/130
<i>D. grimshawi</i>	15,270 (81.3%)	54.9/22.5	261 (1)	154	82	70	32	2.84	138/231

^{*} Repeat coverage calculated as the fraction of scaffolds >200 kb covered by repeats, estimated as the midpoint between BLASTER-tx + PILER and RepeatMasker + ReAS (Supplementary Information section 3). [†] Total genome size estimated as the sum of base pairs in genomic scaffold >200,000 bp. [‡] Genome size estimates based on flow cytometry³⁸.

were combined using GLEAN, a gene model combiner that chooses the most probable combination of start, stop, donor and acceptor sites from the input predictions^{27,28}. All analyses reported here, unless otherwise noted, relied on a reconciled consensus set of predicted gene models—the GLEAN-R set (Table 2, and Supplementary Information section 4.1).

Quality of gene models. As the first step in assessing the quality of the GLEAN-R gene models, we used expression data from microarray experiments on adult flies, with arrays custom-designed for *D. simulans*, *D. yakuba*, *D. ananassae*, *D. pseudoobscura*, *D. virilis* and *D. mojavensis*²⁹ (GEO series GSE6640; Supplementary Information section 4.2). We detected expression significantly above negative controls (false-discovery-rate-corrected Mann–Whitney U (MWU) $P < 0.001$) for 77–93% of assayed GLEAN-R models, representing 50–68% of the total GLEAN-R predictions in each species (Supplementary Table 6). Evolutionarily conserved gene models are much more likely to be expressed than lineage-specific ones (Fig. 2). Although these data cannot confirm the detailed structure of gene models, they do suggest that the majority of GLEAN-R models contain sequence that is part of a poly-adenylated transcript. Approximately 20% of transcription in *D. melanogaster* seems to be unassociated with protein-coding genes³⁰, and our microarray experiments fail to detect conditionally expressed genes. Thus,

transcript abundance cannot conclusively establish the presence or absence of a protein-coding gene. Nonetheless, we believe these expression data increase our confidence in the reliability of the GLEAN-R models, particularly those supported by homology evidence (Fig. 2).

Because the GLEAN-R gene models were built using assemblies that were not repeat masked, it is likely that some proportion of gene models are false positives corresponding to coding sequences of transposable elements. We used RepeatMasker with *de novo* ReAS libraries and PFAM structural annotations of the GLEAN-R gene set to flag potentially transposable element-contaminated gene models (Supplementary Information section 4.2). These procedures suggest that 5.6–32.3% of gene models in non-*melanogaster* species correspond to protein-coding content derived from transposable elements (Supplementary Table 7); these transposable element-contaminated gene models are almost exclusively confined to gene predictions without strong homology support (Fig. 2). Transposable element-contaminated gene models are excluded from the final gene prediction set used for subsequent analysis, unless otherwise noted.

Homology assignment. Two independent approaches were used to assign orthology and paralogy relationships among euchromatic *D. melanogaster* gene models and GLEAN-R predictions. The first approach was a fuzzy reciprocal BLAST (FRB) algorithm, which is an

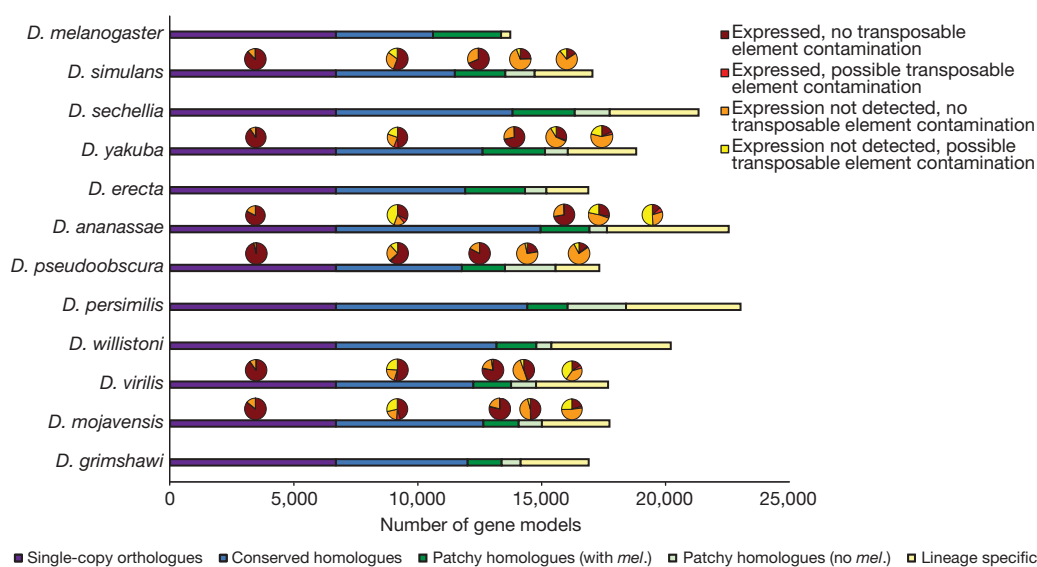


Figure 2 | Gene models in 12 *Drosophila* genomes. Number of gene models that fall into one of five homology classes: single-copy orthologues in all species (single-copy orthologues), conserved in all species as orthologues or paralogues (conserved homologues), a *D. melanogaster* homologue, but not found in all species (patchy homologues with *mel.*), conserved in at least two

species but without a *D. melanogaster* homologue (patchy homologues, no *mel.*), and found only in a single lineage (lineage specific). For those species with expression data²⁹, pie charts indicate the fraction of genes in each homology class that fall into one of four evidence classes (see text for details).

extension of the reciprocal BLAST method³¹ applicable to multiple species simultaneously (Supplementary Information section 5.1). Because the FRB algorithm does not integrate syntenic information, we also used a second approach based on Synpipe (Supplementary Information section 5.2), a tool for synteny-aided orthology assignment³². To generate a reconciled set of homology calls, pairwise Synpipe calls (between each species and *D. melanogaster*) were mapped to GLEAN-R models, filtered to retain only 1:1 relationships, and added to the FRB calls when they did not conflict and were non-redundant. This reconciled FRB + Synpipe set of homology calls forms the basis of our subsequent analyses. There were 8,563 genes with single-copy orthologues in the *melanogaster* group and 6,698 genes with single-copy orthologues in all 12 species; similar numbers of genes were also obtained with an independent approach³³. Most single-copy orthologues are expressed and are free from potential transposable element contamination, suggesting that the reconciled orthologue set contains robust and high-quality gene models (Fig. 2).

Validation of homology calls. Because both the FRB algorithm and Synpipe rely on BLAST-based methods to infer similarities, rapidly evolving genes may be overlooked. Moreover, assembly gaps and poor-quality sequence may lead to erroneous inferences of gene loss. To validate putative gene absences, we used a synteny-based GeneWise pipeline to find potentially missed homologues of *D. melanogaster* proteins (Supplementary Information section 5.4). Of the 21,928 cases in which a *D. melanogaster* gene was absent from another species in the initial homology call set, we identified plausible homologues for 13,265 (60.5%), confirmed 4,546 (20.7%) as genuine absences, and were unable to resolve 4,117 (18.8%). Because this approach is conservative and only confirms strongly supported absences, we are probably underestimating the number of genuine absences.

Coding gene alignment and filtering. Investigating the molecular evolution of orthologous and paralogous genes requires accurate multi-species alignments. Initial amino acid alignments were generated using TCOFFEE³⁴ and converted to nucleotide alignments (Supplementary Table 8). To reduce biases in downstream analyses, a simple computational screen was developed to identify and mask problematic regions of each alignment (Supplementary Information section 6). Overall, 2.8% of bases were masked in the *melanogaster* group alignments, and 3.0% of bases were masked in the full 12 species alignments, representing 8.5% and 13.8% of alignment columns, respectively. The vast majority of masked bases are masked in no more than one species (Supplementary Fig. 3), suggesting that the masking procedure is not simply eliminating rapidly evolving regions of the genome. We find an appreciably higher frequency of masked bases in lower-quality *D. simulans* and *D. sechellia* assemblies, compared to the more divergent (from *D. melanogaster*) but higher-quality *D. erecta* and *D. yakuba* assemblies, suggesting a higher error rate in accurately predicting and aligning gene models in lower-quality assemblies (Supplementary Information section 6 and Supplementary Fig. 3). We used masked versions of the alignments, including only the longest *D. melanogaster* transcripts for all subsequent analysis unless otherwise noted.

Annotation of non-coding (nc)RNA genes. Using *de novo* and homology-based approaches we annotated over 9,000 ncRNA genes from recognized ncRNA classes (Table 2, and Supplementary Information section 7). In contrast to the large number of predictions observed for many ncRNA families in vertebrates (due in part to large numbers of ncRNA pseudogenes^{35,36}), the number of ncRNA genes per family predicted by RFAM and tRNAscan in *Drosophila* is relatively low (Table 2). This suggests that ncRNA pseudogenes are largely absent from *Drosophila* genomes, which is consistent with the low number of protein-coding pseudogenes in *Drosophila*³⁷. The relatively low numbers of some classes of ncRNA genes (for example, small nucleolar (sno)RNAs) in the *Drosophila* subgenus are likely to be an artefact of rapid rates of evolution in these types

of genes and the limitation of the homology-based methods used to annotate distantly related species.

Evolution of genome structure

Coarse-level similarities among Drosophilids. At a coarse level, genome structure is well conserved across the 12 sequenced species. Total genome size estimated by flow cytometry varies less than three-fold across the phylogeny, ranging from 130 Mb (*D. mojavensis*) to 364 Mb (*D. virilis*)³⁸ (Table 2), in contrast to the order of magnitude difference between *Drosophila* and mammals. Total protein-coding sequence ranges from 38.9 Mb in *D. melanogaster* to 65.4 Mb in *D. willistoni*. Intronic DNA content is also largely conserved, ranging from 19.6 Mb in *D. simulans* to 24.0 Mb in *D. pseudoobscura* (Table 2). This contrasts dramatically with transposable element-derived genomic DNA content, which varies considerably across genomes (Table 2) and correlates significantly with euchromatic genome size (estimated as the summed length of contigs > 200 kb) (Kendall's $\tau = 0.70$, $P = 0.0016$).

To investigate overall conservation of genome architecture at an intermediate scale, we analysed synteny relationships across species using Synpipe³² (Supplementary Information section 9.1). Synteny block size and average number of genes per block varies across the phylogeny as expected, with the number of blocks increasing and the average size of blocks decreasing with increasing evolutionary distance from *D. melanogaster* (A. Bhutkar, S. Russo, T. F. Smith and W. M. Gelbart, personal communication) (Supplementary Fig. 4). We inferred 112 syntenic blocks between *D. melanogaster* and *D. sechellia* (with an average of 122 genes per block), compared to 1,406 syntenic blocks between *D. melanogaster* and *D. grimshawi* (with an average of 8 genes per block). On average, 66% of each genome assembly was covered by syntenic blocks, ranging from 68% in *D. sechellia* to 58% in *D. grimshawi*.

Similarity across genomes is largely recapitulated at the level of individual genes, with roughly comparable numbers of predicted protein-coding genes across the 12 species (Table 2). The majority of predicted genes in each species have homologues in *D. melanogaster* (Table 2, Supplementary Table 9). Moreover, most of the 13,733 protein-coding genes in *D. melanogaster* are conserved across the entire phylogeny: 77% have identifiable homologues in all 12 genomes, 62% can be identified as single-copy orthologues in the six genomes of the *melanogaster* group and 49% can be identified as single-copy orthologues in all 12 genomes. The number of functional non-coding RNA genes predicted in each *Drosophila* genome is also largely conserved, ranging from 584 in *D. mojavensis* to 908 in *D. ananassae* (Table 2).

There are several possible explanations for the observed interspecific variation in gene content. First, approximately 700 *D. melanogaster* gene models have been newly annotated since the FlyBase Release 4.3 annotations used in the current study, reducing the discrepancy between *D. melanogaster* and the other sequenced genomes in this study. Second, because low-coverage genomes tend to have more predicted gene models, we suspect that artefactual duplication of genomic segments due to assembly errors inflates the number of predicted genes in some species. Finally, the non-*melanogaster* species have many more predicted lineage-specific genes than *D. melanogaster*, and it is possible that some of these are artefactual. In the absence of experimental evidence, it is difficult to distinguish genuine lineage-specific genes from putative artefacts. Future experimental work will be required to fully disentangle the causes of interspecific variation in gene number.

Abundant genome rearrangements during Drosophila evolution.

To study the structural relationships among genomes on a finer scale, we analysed gene-level synteny between species pairs. These synteny maps allowed us to infer the history and locations of fixed genomic rearrangements between species. Although *Drosophila* species vary in their number of chromosomes, there are six fundamental chromosome arms common to all species. For ease of denoting

chromosomal homology, these six arms are referred to as 'Muller elements' after Hermann J. Muller, and are denoted A–F. Although most pairs of orthologous genes are found on the same Muller element, there is extensive gene shuffling within Muller elements between even moderately diverged genomes (Fig. 3, and Supplementary Information section 9.1).

Previous analysis has revealed heterogeneity in rearrangement rates among close relatives: careful inspection of 29 inversions that differentiate the chromosomes of *D. melanogaster* and *D. yakuba* revealed that 28 were fixed in the lineage leading to *D. yakuba*, and only one was fixed on the lineage leading to *D. melanogaster*³⁹. Rearrangement rates are also heterogeneous across the genome among the 12 species: simulations reject a random-breakage model, which assumes that all sites are free to break in inversion events, but fail to reject a model of coldspots and hotspots for breakpoints (S. Schaeffer, personal communication). Furthermore, inversions seem to have played important roles in the process of speciation in at least some of these taxa⁴⁰.

One particularly striking example of the dynamic nature of genome micro-structure in *Drosophila* is the homeotic *homeobox* (*Hox*) gene cluster(s)⁴¹. *Hox* genes typically occur in genomic clusters, and this clustering is conserved across many vertebrate and invertebrate taxa, suggesting a functional role for the precise and collinear arrangement of these genes. However, several cluster splits have been previously identified in *Drosophila*^{42,43}, and the 12 *Drosophila* genome sequences provide additional evidence against the functional importance of *Hox* gene clustering in *Drosophila*. There are seven different gene arrangements found across 13 *Drosophila* species (the 12 sequenced genomes and *D. buzzatii*), with no species retaining the inferred ancestral gene order⁴⁴. It thus seems that, in *Drosophila*, *Hox* genes do not require clustering to maintain proper function, and are a powerful illustration of the dynamism of genome structure across the sequenced genomes.

Transposable element evolution. Mobile, repetitive transposable element sequences are a particularly dynamic component of eukaryotic genomes. Transposable element/repeat content (in scaffolds >200 kb) varies by over an order of magnitude across the genus, ranging from ~2.7% in *D. simulans* and *D. grimshawi* to ~25% in *D. ananassae* (Table 2, and Supplementary Fig. 1). These data support the lower euchromatic transposable element content in *D. simulans* relative to *D. melanogaster*⁴⁵, and reveal that euchromatic transposable element/repeat content is generally similar within the *melanogaster* subgroup. Within the *Drosophila* subgenus,

D. grimshawi has the lowest transposable element/repeat content, possibly relating to its ecological status as an island endemic, which may minimize the chance for horizontal transfer of transposable element families. Finally, the highest levels of transposable element/repeat content are found in *D. ananassae* and *D. willistoni*. These species also have the highest numbers of pseudo-transfer (t)RNA genes (Table 2), indicating a potential relationship between pseudo-tRNA genesis and repetitive DNA, as has been established in the mouse genome³⁶.

Different classes of transposable elements can vary in abundance owing to a variety of host factors, motivating an analysis of the intragenomic ecology of transposable elements in the 12 genomes. In *D. melanogaster*, long terminal repeat (LTR) retrotransposons have the highest abundance, followed by LINE (long interspersed nuclear element)-like retrotransposons and terminal inverted repeat (TIR) DNA-based transposons¹⁸. An unbiased, conservative approach (Supplementary Information section 3) for estimating the rank order abundance of major transposable element classes suggests that these abundance trends are conserved across the entire genus (Supplementary Fig. 5). Two exceptions are an increased abundance of TIR elements in *D. erecta* and a decreased abundance of LTR elements in *D. pseudoobscura*; the latter observation may represent an assembly artefact because the sister species *D. persimilis* shows typical LTR abundance. Given that individual instances of transposable element repeats and transposable element families themselves are not conserved across the genus, the stability of abundance trends for different classes of transposable elements is striking and suggests common mechanisms for host–transposable element co-evolution in *Drosophila*.

Although comprehensive analysis of the structural and evolutionary relationships among families of transposable elements in the 12 genomes remains a major challenge for *Drosophila* genomics, some initial insights can be gleaned from analysis of particularly well-characterized transposable element families. Previous analysis has shown variable dynamics for the most abundant transposable element family (*DINE-1*)⁴⁶ in the *D. melanogaster* genome^{18,47}: although inactive in *D. melanogaster*⁴⁸, *DINE-1* has experienced a recent transpositional burst in *D. yakuba*⁴⁹. Our analysis confirms that this element is highly abundant in all of the other sequenced genomes of *Drosophila*, but is not found outside of Diptera^{50,51}. Moreover, the inferred phylogenetic relationship of *DINE-1* paralogues from several *Drosophila* species suggests vertical transmission as the major mechanism for *DINE-1* propagation. Likewise, analysis of the *Galileo*

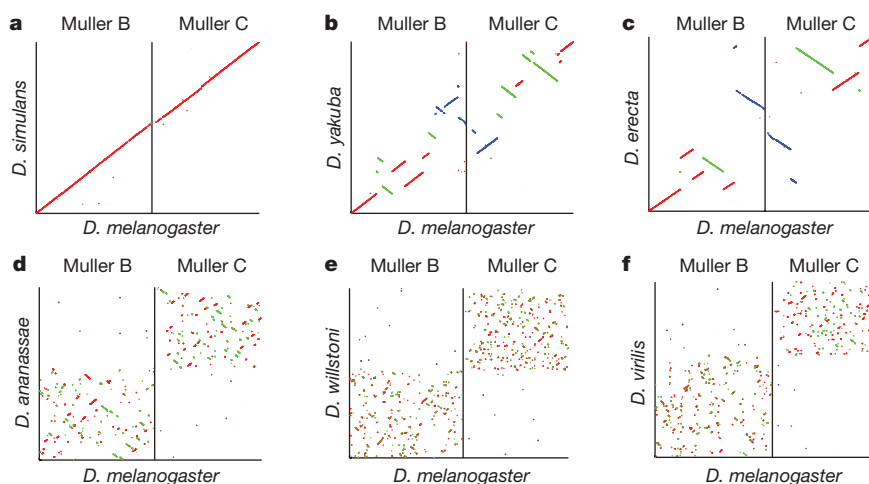


Figure 3 | Synteny plots for Muller elements B and C with respect to *D. melanogaster* gene order. The horizontal axis shows *D. melanogaster* gene order for Muller elements B and C, and the vertical axis maps homologous locations^{32,155} in individual species (a–f in increasing evolutionary distance from *D. melanogaster*). Left to right on the x axis is

from telomere to centromere for Muller element B, followed by Muller element C from centromere to telomere. Red and green lines represent syntenic segments in the same or reverse orientation along the chromosome relative to *D. melanogaster*, respectively. Blue segments show gene transposition of genes from one element to the other.

and 1360 transposons reveals a widespread but discontinuous phylogenetic distribution for both families, notably with both families absent in the geographically isolated Hawaiian species, *D. grimshawi*⁵². These results are consistent with an ancient origin of the *Galileo* and 1360 families in the genus and subsequent horizontal transfer and/or loss in some lineages.

The use of these 12 genomes also facilitated the discovery of transposable element lineages not yet documented in *Drosophila*, specifically the P instability factor (PIF) superfamily of DNA transposons. Our analysis indicates that there are four distinct lineages of this transposon in *Drosophila*, and that this element has indeed colonized many of the sequenced genomes⁵³. This superfamily is particularly intriguing given that PIF-transposase-like genes have been implicated in the origin of at least seven different genes during the *Drosophila* radiation⁵³, suggesting that not only do transposable elements affect the evolution of genome structure, but that their domestication can play a part in the emergence of novel genes.

D. melanogaster maintains its telomeres by occasional targeted transposition of three telomere-specific non-LTR retrotransposons (*HeT-A*, *TART* and *TAHRE*) to chromosome ends^{54,55} and not by the more common mechanism of telomerase-generated G-rich repeats⁵⁶. Multiple telomeric retrotransposons have originated within the genus, where they now maintain telomeres, and recurrent loss of most of the ORF2 from telomeric retrotransposons (for example, *TAHRE*) has given rise to half-telomeric-retrotransposons (for example, *HeT-A*) during *Drosophila* evolution⁵⁷. The phylogenetic relationship among these telomeric elements is congruent with the species phylogeny, suggesting that they have been vertically transmitted from a common ancestor⁵⁷.

ncRNA gene family evolution. Using ncRNA gene annotations across the 12-species phylogeny, we inferred patterns of gene copy number evolution in several ncRNA families. Transfer RNA genes are the most abundant family of ncRNA genes in all 12 genomes, with 297 tRNAs in *D. melanogaster* and 261–484 tRNA genes in the other species (Table 2). Each genome encodes a single selenocysteine tRNA, with the exception of *D. willistoni*, which seems to lack this gene (R. Guigo, personal communication). Elevated tRNA gene counts in *D. ananassae* and *D. willistoni* are explained almost entirely by pseudo-tRNA gene predictions. We infer from the lack of pseudo-tRNAs in most *Drosophila* species, and from similar numbers of tRNAs obtained from an analysis of the chicken genome ($n = 280$)⁵⁸, that the minimal metazoan tRNA set is encoded by ~300 genes, in contrast to previous estimates of 497 in human and 659 in *Caenorhabditis elegans*^{59,60}. Similar numbers of snoRNAs are predicted in the *D. melanogaster* subgroup ($n = 242$ –255), in which sequence similarity is high enough for annotation by homology, with fewer snoRNAs ($n = 194$ –216) annotated in more distant members of the *Sophophora* subgenus, and even fewer snoRNAs ($n = 139$ –165) predicted in the *Drosophila* subgenus, in which annotation by homology becomes much more difficult.

Of 78 previously reported micro (mi)RNA genes, 71 (91%) are highly conserved across the entire genus, with the remaining seven genes (*mir-2b-1*, -289, -303, -310, -311, -312 and -313) restricted to the subgenus *Sophophora* (Supplementary Information section 7.2). All the species contain similar numbers of spliceosomal snRNA genes (Table 2), including at least one copy each of the four U12-dependent (minor) spliceosomal RNAs, despite evidence for birth and death of these genes and the absence of stable subtypes⁶¹. The unusual, lineage-specific expansion in size of U11 snRNA, previously described in *Drosophila*^{61,62}, is even more extreme in *D. willistoni*. We annotated 99 copies of the 5S ribosomal (r)RNA gene in a cluster in *D. melanogaster*, and between 13 and 73 partial 5S rRNA genes in clusters in the other genomes. Finally, we identified members of several other classes of ncRNA genes, including the RNA components of the RNase P (1 per genome) and the signal recognition particle (SRP) RNA complexes (1–3 per genome), suggesting that these functional RNAs are involved in similar biological processes throughout the

genus. We were only able to locate the *roX* (RNA on X)^{63,64} genes involved in dosage compensation using nucleotide homology in the *melanogaster* subgroup, although analyses incorporating structural information have identified *roX* genes in other members of the genus⁶⁵.

We investigated the evolution of rRNA genes in the 12 sequenced genomes, using trace archives to locate sequence variants within the transcribed portions of these genes. This analysis revealed moderate levels of variation that are not distributed evenly across the rRNA genes, with fewest variants in conserved core coding regions, more variants in coding expansion regions, and higher still variant abundances in non-coding regions. The level and distribution of sequence variation in rRNA genes are suggestive of concerted evolution, in which recombination events uniformly distribute variants throughout the rDNA loci, and selection dictates the frequency to which variants can expand⁶⁶.

Protein-coding gene family evolution. For a general perspective on how the protein-coding composition of these 12 genomes has changed, we examined gene family expansions and contractions in the 11,434 gene families (including those of size one in each species) predicted to be present in the most recent common ancestor of the two subgenera. We applied a maximum likelihood model of gene gain and loss⁶⁷ to estimate rates of gene turnover. This analysis suggests that gene families expand or contract at a rate of 0.0012 gains and losses per gene per million years, or roughly one fixed gene gain/loss across the genome every 60,000 yr⁶⁸. Many gene families (4,692 or 41.0%) changed in size in at least one species, and 342 families showed significantly elevated ($P < 0.0001$) rates of gene gain and loss compared to the genomic average, indicating that non-neutral processes may play a part in gene family evolution. Twenty-two families exhibit rapid copy number evolution along the branch leading to *D. melanogaster* (eighteen contractions and four expansions; Supplementary Table 10). The most common Gene Ontology (GO) terms among families with elevated rates of gain/loss include 'defence response', 'protein binding', 'zinc ion binding', 'proteolysis', and 'trypsin activity'. Interestingly, genes involved in 'defence response' and 'proteolysis' also show high rates of protein evolution (see below). We also found heterogeneity in overall rates of gene gain and loss across lineages, although much of this variation could result from interspecific differences in assembly quality⁶⁸.

Lineage-specific genes. The vast majority of *D. melanogaster* proteins that can be unambiguously assigned a homology pattern (Supplementary Information section 5) are inferred to be ancestrally present at the genus root (11,348/11,644, or 97.5%). Of the 296 non-ancestrally present genes, 252 are either *Sophophora*-specific, or have a complicated pattern of homology requiring more than one gain and/or loss on the phylogeny, and are not discussed further. The remaining 44 proteins include 14 present in the *melanogaster* group, 23 present only in the *melanogaster* subgroup, 3 unique to the *melanogaster* species complex, and 4 found in *D. melanogaster* only. Because we restricted this analysis to unambiguous homologues of high-confidence protein-coding genes in *D. melanogaster*⁸, we are probably undercounting the number of genes that have arisen *de novo* in any particular lineage. However, ancestrally heterochromatic genes that are currently euchromatic in *D. melanogaster* may spuriously seem to be lineage-specific.

The 44 lineage-specific genes (Supplementary Table 11) differ from ancestrally present genes in several ways. They have a shorter median predicted protein length (lineage-specific median 177 amino acids, other median 421 amino acids, MWU, $P = 3.6 \times 10^{-13}$), are more likely to be intronless (Fisher's exact test (FET), $P = 6.2 \times 10^{-6}$), and are more likely to be located in the intron of another gene on the opposite strand (FET, $P = 3.5 \times 10^{-4}$). In addition, 18 of these 44 genes are testis- or accessory-gland-specific in *D. melanogaster*, a significantly greater fraction than is found in the ancestral set (FET, $P = 1.25 \times 10^{-4}$). This is consistent with previous observations that novel genes are often testis-specific in *Drosophila*^{69–73} and

expression studies on seven of the species show that species-restricted genes are more likely to exhibit male-biased expression²⁹. Further, these genes are significantly more tissue-specific in expression (as measured by τ ; ref. 74) (MWU , $P = 9.6 \times 10^{-6}$), and this pattern is not solely driven by genes with testis-specific expression patterns.

Protein-coding gene evolution

Positive selection and selective constraints in *Drosophila* genomes.

To study the molecular evolution of protein-coding genes, we estimated rates of synonymous and non-synonymous substitution in 8,510 single-copy orthologues within the six *melanogaster* group species using PAML⁷⁵ (Supplementary Information section 11.1); synonymous site saturation prevents analysis of more divergent comparisons. We investigate only single-copy orthologues because when paralogues are included, alignments become increasingly problematic. Rates of amino acid divergence for single-copy orthologues in all 12 species were also calculated; these results are largely consistent with the analysis of non-synonymous divergence in the *melanogaster* group, and are not discussed further.

To understand global patterns of divergence and constraint across functional classes of genes, we examined the distributions of ω ($=d_N/d_S$, the ratio of non-synonymous to synonymous divergence) across Gene Ontology categories (GO)⁷⁶, excluding GO

annotations based solely on electronic support (Supplementary Information section 11.2). Most functional categories of genes are strongly constrained, with median estimates of ω much less than one. In general, functionally similar genes are similarly constrained: 31.8% of GO categories have significantly lower variance in ω than expected (q -value true-positive test⁷⁷). Only 11% of GO categories had statistically significantly elevated ω (relative to the median of all genes with GO annotations) at a 5% false-discovery rate (FDR), suggesting either positive selection or a reduction in selective constraint. The GO categories with elevated ω include the biological process terms 'defence response', 'proteolysis', 'DNA metabolic process' and 'response to biotic stimulus'; the molecular function terms 'transcription factor activity', 'peptidase activity', 'receptor binding', 'odorant binding', 'DNA binding', 'receptor activity' and 'G-protein-coupled receptor activity'; and the cellular location term 'extracellular' (Fig. 4, and Supplementary Table 12). Similar results are obtained when d_N is compared across GO categories, suggesting that in most cases differences in ω among GO categories is driven by amino acid rather than synonymous site substitutions. The two exceptions are the molecular function terms 'transcription factor activity' and 'DNA binding activity', for which we observe significantly decelerated d_S (FDR = 7.2×10^{-4} for both; Supplementary Information section 11.2) and no significant differences in d_N .

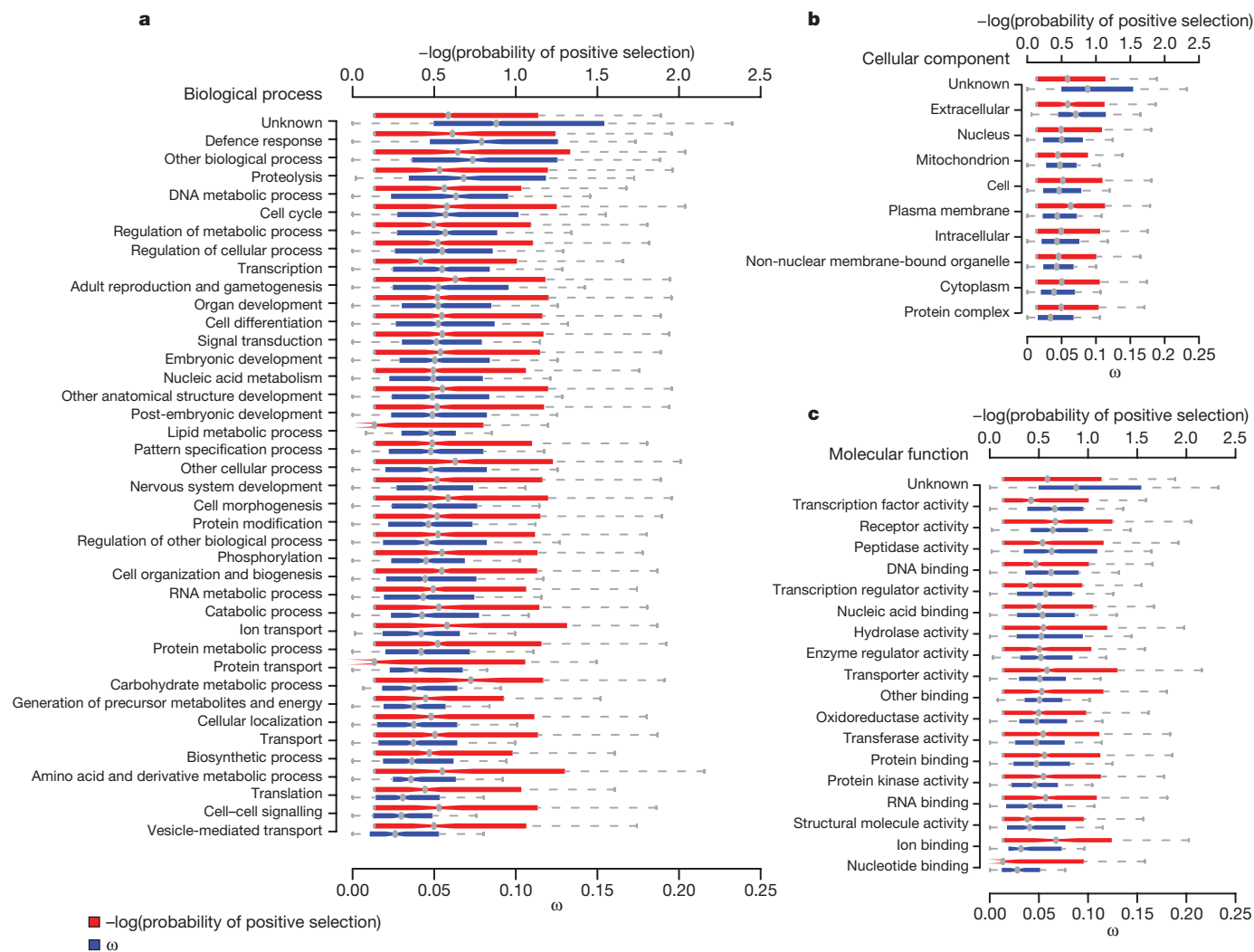


Figure 4 | Patterns of constraint and positive selection among GO terms. Distribution of average ω per gene and the negative \log_{10} of the probability of positive selection (Supplementary Information section 11.2) for genes annotated with: **a**, biological process GO terms; **b**, cellular component GO terms; and **c**, molecular function GO terms. Only GO terms with 200 or more

genes annotated are plotted. See Supplementary Table 12 for median values and significance. Note that most genes evolve under evolutionary constraint at most of their sites, leading to low values of ω ; even genes that experience positive selection do not typically have an average ω across all codons that exceeds one.

To distinguish possible positive selection from relaxed constraint, we tested explicitly for genes that have a subset of codons with signatures of positive selection, using codon-based likelihood models of molecular evolution, implemented in PAML^{78,79} (Supplementary Information section 11.1). Although this test is typically regarded as a conservative test for positive selection, it may be confounded by selection at synonymous sites. However, selection at synonymous sites (that is, codon bias, see below) is quite weak. Moreover, variability in ω presented here tends to reflect variability in d_N . We therefore believe that it is appropriate to treat synonymous sites as nearly neutral and sites with $\omega > 1$ as consistent with positive selection. Despite a number of functional categories with evidence for elevated ω , 'helicase activity' is the only functional category significantly more likely to be positively selected (permutation test, $P = 2 \times 10^{-4}$, FDR = 0.007; Supplementary Table 12); the biological significance of this finding merits further investigation. Furthermore, within each GO class, there is greater dispersion among genes in their probability of positive selection than in their estimate of ω (MWU one-tailed, $P = 0.011$; Supplementary Information section 11.1), suggesting that although functionally similar genes share patterns of constraint, they do not necessarily show similar patterns of positive selection (Fig. 4).

Interestingly, protein-coding genes with no annotated ('unknown') function in the GO database seem to be less constrained (permutation test, $P < 1 \times 10^{-4}$, FDR = 0.006)⁸⁰ and to have on average lower P -values for the test of positive selection than genes with annotated functions (permutation test, $P = 0.001$, FDR = 0.058). It is unlikely that this observation results entirely from an over-representation of mis-annotated or non-protein-coding genes in the 'unknown' functional class, because this finding is robust to the removal of all *D. melanogaster* genes predicted to be non-protein-coding in ref. 8. The bias in the way biological function is ascribed to genes (to laboratory-induced, easily scorable functions) leaves open the possibility that unannotated biological functions may have an important role in evolution. Indeed, genes with characterized mutant alleles in FlyBase evolve significantly more slowly than other genes (median $\omega_{\text{with alleles}} = 0.0525$ and $\omega_{\text{without alleles}} = 0.0701$; MWU, $P < 1 \times 10^{-16}$).

Previous work has suggested that a substantial fraction of non-synonymous substitutions in *Drosophila* were fixed through positive selection^{81–85}. We estimate that 33.1% of single-copy orthologues in the *melanogaster* group have experienced positive selection on at least a subset of codons (q -value true-positive tests⁷⁷) (Supplementary Information section 11.1). This may be an underestimate, because we have only examined single-copy orthologues, owing to difficulties in producing accurate alignments of paralogues by automated methods. On the basis of the 878 genes inferred to have experienced positive selection with high confidence (FDR < 10%), we estimated that an average of 2% of codons in positively selected genes have $\omega > 1$. Thus, several lines of evidence, based on different methodologies, suggest that patterns of amino acid fixation in *Drosophila* genomes have been shaped extensively by positive selection.

The presence of functional domains within a protein may lead to heterogeneity in patterns of constraint and adaptation along its length. Among genes inferred to be evolving by positive selection at a 10% FDR, 63.7% (q -value true-positive tests⁷⁷) show evidence for spatial clustering of positively selected codons (Supplementary Information section 11.2). Spatial heterogeneity in constraint is further supported by contrasting ω for codons inside versus outside defined InterPro domains (genes lacking InterPro domains are treated as 'outside' a defined InterPro domain). Codons within InterPro domains were significantly more conserved than codons outside InterPro domains (median ω : 0.062 InterPro domains, 0.084 outside InterPro domains; MWU, $P < 2.2 \times 10^{-16}$; Supplementary Information section 11.2). Similarly, there were significantly more positively selected codons outside of InterPro domains than inside domains (FET $P < 2.2 \times 10^{-16}$), suggesting that in addition to

being more constrained, codons in protein domains are less likely to be targets of positive selection (Supplementary Fig. 6).

Factors affecting the rate of protein evolution in *Drosophila*. The sequenced genomes of the *melanogaster* group provide unprecedented statistical power to identify factors affecting rates of protein evolution. Previous analyses have suggested that although the level of gene expression consistently seems to be a major determinant of variation in rates of evolution among proteins^{86,87}, other factors probably play a significant, if perhaps minor, part^{88–91}. In *Drosophila*, although highly expressed genes do evolve more slowly, breadth of expression across tissues, gene essentiality and intron number all also independently correlate with rates of protein evolution, suggesting that the additional complexities of multicellular organisms are important factors in modulating rates of protein evolution⁷⁸. The presence of repetitive amino acid sequences has a role as well: non-repeat regions in proteins containing repeats evolve faster and show more evidence for positive selection than genes lacking repeats⁹².

These data also provide a unique opportunity to examine the impact of chromosomal location on evolutionary rates. Population genetic theory predicts that for new recessive mutations, both purifying and positive selection will be more efficient on the X chromosome given its hemizyosity in males⁹³. In contrast, the lack of recombination on the small, mainly heterochromatic dot chromosome^{94,95} is expected to reduce the efficacy of selection⁹⁶. Because codon bias, or the unequal usage of synonymous codons in protein-coding sequences, reflects weak but pervasive selection, it is a sensitive metric for evaluating the efficacy of purifying selection. Consistent with expectation, in all 12 species, we find significantly elevated levels of codon bias on the X chromosome and significantly reduced levels of codon bias on the dot chromosome⁹⁷. Furthermore, X-chromosome-linked genes are marginally over-represented within the set of positively selected genes in the *melanogaster* group (FET, $P = 0.055$), which is consistent with increased rates of adaptive substitution on this chromosome. This analysis suggests that chromosomal context also serves to modulate rates of molecular evolution in protein-coding genes.

To examine further the impact of genomic location on protein evolution, we examined the subset of genes that have moved within or between chromosome arms^{32,98}. Genes inferred to have moved between Muller elements have a significantly higher rate of protein evolution than genes inferred to have moved within a Muller element (MWU, $P = 1.32 \times 10^{-14}$) and genes that have maintained their genomic position (MWU, $P = 0.008$) (Supplementary Fig. 7). Interestingly, genes that move within Muller elements have a significantly lower rate of protein evolution than those for which genomic locations have been maintained (MWU, $P = 3.85 \times 10^{-14}$). It remains unclear whether these differences reflect underlying biases in the types of genes that move inter- versus intra-chromosomally, or whether they are due to *in situ* patterns of evolution in novel genomic contexts.

Codon bias. Codon bias is thought to enhance the efficiency and/or accuracy of translation^{99–101} and seems to be maintained by mutation–selection–drift balance^{101–104}. Across the 12 *Drosophila* genomes, there is more codon bias in the *Sophophora* subgenus than in the *Drosophila* subgenus, and a previously noted^{105–109} striking reduction in codon bias in *D. willistoni*^{110,111} (Fig. 5). However, with only minor exceptions, codon preferences for each amino acid seem to be conserved across 11 of the 12 species. The striking exception is *D. willistoni*, in which codon usage for 6 of 18 redundant amino acids has diverged (Fig. 5). Mutation alone is not sufficient to explain codon-usage bias in *D. willistoni*, which is suggestive of a lineage-specific shift in codon preferences^{111,112}. We found evidence for a lineage-specific genomic reduction in codon bias in *D. melanogaster* (Fig. 5), as has been suggested previously^{113–119}. In addition, maximum-likelihood estimation of the strength of selection on synonymous sites in 8,510 *melanogaster* group single-copy orthologues revealed a marked reduction in the number of genes under selection

for increased codon bias in *D. melanogaster* relative to its sister species *D. sechellia*¹²⁰.

Evolution of genes associated with ecology and reproduction. Given the ecological and environmental diversity encompassed by the 12 *Drosophila* species, we examined the evolution of genes and gene families associated with ecology and reproduction. Specifically, we selected genes with roles in chemoreception, detoxification/metabolism, immunity/defence, and sex/reproduction for more detailed study.

Chemoreception. *Drosophila* species have complex olfactory and gustatory systems used to identify food sources, hazards and mates, which depend on odorant-binding proteins, and olfactory/odorant and gustatory receptors (*Ors* and *Gr*s). The *D. melanogaster* genome has approximately 60 *Ors*, 60 *Gr*s and 50 odorant-binding protein genes. Despite overall conservation of gene number across the 12 species and widespread evidence for purifying selection within the *melanogaster* group, there is evidence that a subset of *Or* and *Gr* genes experiences positive selection^{121–123}. Furthermore, clear lineage-specific differences are detectable between generalist and specialist species within the *melanogaster* subgroup. First, the two independently evolved specialists (*D. sechellia* and *D. erecta*) are losing *Gr* genes approximately five times more rapidly than the generalist species^{121,124}. We believe this result is robust to sequence quality, because all pseudogenes and deletions were verified by direct re-sequencing and synteny-based orthologue searches, respectively. Generalists are expected to encounter the most diverse set of tastants and seem to have maintained the greatest diversity of gustatory receptors. Second, *Or* and *Gr* genes that remain intact in *D. sechellia* and *D. erecta* evolve significantly more rapidly along these two lineages ($\omega = 0.1556$ for *Ors* and 0.1874 for *Gr*s) than along the generalist lineages ($\omega = 0.1049$ for *Ors* and 0.1658 for *Gr*s; paired Wilcoxon, $P = 0.0003$ and 0.003, respectively¹²⁴). There is some evidence that odorant-binding protein genes also evolve significantly faster in specialists compared to generalists¹²². This elevated ω reflects a trend observed throughout the genomes of the two specialists and is likely to result, at least in part, from demographic phenomena. However, the difference between specialist and generalist ω for *Or/Gr* genes (0.0292) is significantly greater than the difference for genes across the genome (0.0091; MWU, $P = 0.0052$)¹²¹, suggesting a change in selective regime. Moreover, the observation that elevated ω as well as accelerated gene loss disproportionately affect groups of *Or* and *Gr* genes that respond to specific chemical ligands and/or are expressed during specific life stages suggests that rapid evolution at *Or/Gr* loci in specialists is related to the ecological shifts these species have sustained¹²¹.

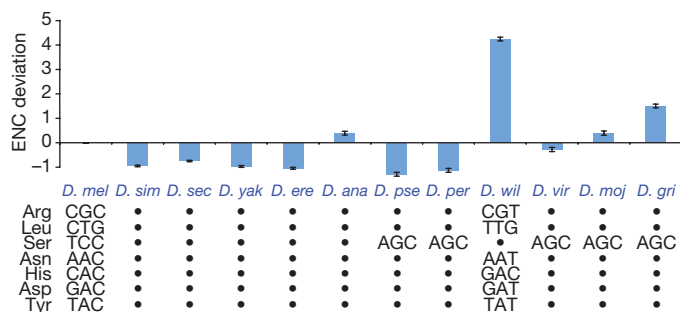


Figure 5 | Deviations in codon bias from *D. melanogaster* in 11 *Drosophila* species. The upper panel depicts differences in ENC (effective number of codons) between *D. melanogaster* and the 11 non-*melanogaster* species, calculated on a gene-by-gene basis. Note that increasing levels of ENC indicates a decrease in codon bias. The *Sophophora* subgenus in general has higher levels of codon bias than the *Drosophila* subgenus with the exception of *D. willistoni*, which shows a dramatic reduction in codon bias. The lower panel shows the 7 codons for which preference changes across the 12 *Drosophila* species. A dot indicates identical codon preference to *D. melanogaster*; otherwise the preferred codon is indicated.

Detoxification/metabolism. The larval food sources for many *Drosophila* species contain a cocktail of toxic compounds, and consequently *Drosophila* genomes encode a wide variety of detoxification proteins. These include members of the cytochrome P450 (P450), carboxyl/choline-esterase (CCE) and glutathione S-transferase (GST) multigene families, all of which also have critical roles in resistance to insecticides^{125–127}. Among the P450s, the five enzymes associated with insecticide resistance are highly dynamic across the phylogeny, with 24 duplication events and 4 loss events since the last common ancestor of the genus, which is in striking contrast to genes with known developmental roles, eight of which are present as a single copy in all 12 species (C. Robin, personal communication). As with chemoreceptors, specialists seem to lose detoxification genes at a faster rate than generalists. For instance, *D. sechellia* has lost the most P450 genes; these 14 losses comprise almost one-third of all P450 loss events (Supplementary Table 13) (C. Robin, personal communication). Positive selection has been implicated in detoxification-gene evolution as well, because a search for positive selection among GSTs identified the parallel evolution of a radical glycine to lysine amino acid change in GSTD1, an enzyme known to degrade DDT¹²⁸. Finally, although metabolic enzymes in general are highly constrained (median $\omega = 0.045$ for enzymes, 0.066 for non-enzymes; MWU, $P = 5.7 \times 10^{-24}$), enzymes involved in xenobiotic metabolism evolve significantly faster than other enzymes (median $\omega = 0.05$ for the xenobiotic group versus $\omega = 0.045$ overall, two-tailed permutation test, $P = 0.0110$; A. J. Greenberg, personal communication).

Metazoans deal with excess selenium in the diet by sequestration in selenoproteins, which incorporate the rare amino acid selenocysteine (Sec) at sites specified by the TGA codon. The recoding of the normally terminating signal TGA as a Sec codon is mediated by the selenocystein insertion sequence (SECIS), a secondary structure in the 3' UTR of selenoprotein messenger RNAs. All animals examined so far have selenoproteins; three have been identified in *D. melanogaster* (SELG, SELM and SPS2^{129,130}). Interestingly, although the three known *melanogaster* selenoproteins are all present in the genomes of the other *Drosophila* species, in *D. willistoni* the TGA Sec codons have been substituted by cysteine codons (TGT/TGC). Consistent with this finding, analysis of the seven genes implicated to date in selenoprotein synthesis including the Sec-specific tRNA suggests that most of these genes are absent in *D. willistoni* (R. Guigo, personal communication). *D. willistoni* thus seems to be the first animal known to lack selenoproteins. If correct, this observation is all the more remarkable given the ubiquity of selenoproteins and the selenoprotein biosynthesis machinery in metazoans, the toxicity of excess selenium, and the protection from oxidative stress mediated by selenoproteins. However, it remains possible that this species encodes selenoproteins in a different way, and this represents an exciting avenue of future research.

Immunity/defence. *Drosophila*, like all insects, possesses an innate immune system with many components analogous to the innate immune pathways of mammals, although it lacks an antibody-mediated adaptive immune system¹³¹. Immune system genes often evolve rapidly and adaptively, driven by selection pressures from pathogens and parasites^{132–134}. The genus *Drosophila* is no exception: immune system genes evolve more rapidly than non-immune genes, showing both high total divergence rates and specific signs of positive selection¹³⁵. In particular, 29% of receptor genes involved in phagocytosis seem to evolve under positive selection, suggesting that molecular co-evolution between *Drosophila* pattern recognition receptors and pathogen antigens is driving adaptation in the immune system¹³⁵. Somewhat surprisingly, genes encoding effector proteins such as antimicrobial peptides are far less likely to exhibit adaptive sequence evolution. Only 5% of effector genes (and no antimicrobial peptides) show evidence of adaptive evolution, compared to 10% of genes genome-wide. Instead, effector genes seem to evolve by rapid duplication and deletion. Whereas 49% of genes genome-wide, 63%

of genes involved in pathogen recognition and 81% of genes implicated in immune-related signal transduction can be found as single-copy orthologues in all 12 species, only 40% of effector genes exist as single-copy orthologues across the genus ($\chi^2 = 41.13$, $P = 2.53 \times 10^{-8}$), suggesting rapid radiation of effector protein classes along particular lineages¹³⁵. Thus, much of the *Drosophila* immune system seems to evolve rapidly, although the mode of evolution varies across immune-gene functional classes.

Sex/reproduction. Genes encoding sex- and reproduction-related proteins are subject to a wide array of selective forces, including sexual conflict, sperm competition and cryptic female choice, and to the extent that these selective forces are of evolutionary consequence, this should lead to rapid evolution in these genes¹³⁶ (for an overview see refs 137, 138). The analysis of 2,505 sex- and reproduction-related genes within the *melanogaster* group indicated that male sex- and reproduction-related genes evolve more rapidly at the protein level than genes not involved in sex or reproduction or than female sex- and reproduction-related genes (Supplementary Fig. 8). Positive selection seems to be at least partially responsible for these patterns, because genes involved in spermatogenesis have significantly stronger evidence for positive selection than do non-spermatogenesis genes (permutation test, $P = 0.0053$). Similarly, genes that encode components of seminal fluid have significantly stronger evidence for positive selection than 'non-sex' genes¹³⁹. Moreover, protein-coding genes involved in male reproduction, especially seminal fluid and testis genes, are particularly likely to be lost or gained across *Drosophila* species^{29,139}.

Evolutionary forces in the mitochondrial genome. Functional elements in mtDNA are strongly conserved, as expected: tRNAs are relatively more conserved than the mtDNA overall (average pairwise nucleotide distance = 0.055 substitutions per site for tRNAs versus 0.125 substitutions per site overall). We observe a deficit of substitutions occurring in the stem regions of the stem-loop structure in tRNAs, consistent with strong selective pressure to maintain RNA secondary structure, and there is a strong signature of purifying selection in protein-coding genes¹³. However, despite their shared role in aerobic respiration, there is marked heterogeneity in the rates of amino acid divergence between the oxidative phosphorylation enzyme complexes across the 12 species (NADH dehydrogenase, $0.059 > \text{ATPase}$, $0.042 > \text{CytB}$, $0.037 > \text{cytochrome oxidase}$, 0.020 ; mean pairwise d_N), which contrasts with the relative homogeneity in synonymous substitution rates. A model with distinct substitution rates for each enzyme complex rather than a single rate provides a significantly better fit to the data ($P < 0.0001$), suggesting complex-specific selective effects of mitochondrial mutations¹³.

Non-coding sequence evolution

ncRNA sequence evolution. The availability of complete sequence from 12 *Drosophila* genomes, combined with the tractability of RNA structure predictions, offers the exciting opportunity to connect patterns of sequence evolution directly with structural and functional constraints at the molecular level. We tested models of RNA evolution focusing on specific ncRNA gene classes in addition to inferring patterns of sequence evolution using more general datasets that are based on predicted intronic RNA structures.

The exquisite simplicity of miRNAs and their shared stem-loop structure makes these ncRNAs particularly amenable to evolutionary analysis. Most miRNAs are highly conserved within the *Drosophila* genus: for the 71 previously described miRNA genes inferred to be present in the common ancestor of these 12 species, mature miRNA sequences are nearly invariant. However, we do find a small number of substitutions and a single deletion in mature miRNA sequences (Supplementary Table 14), which may have functional consequences for miRNA–target interactions and may ultimately help identify targets through sequence covariation. Pre-miRNA sequences are also highly conserved, evolving at about 10% of the rate of synonymous sites.

To link patterns of evolution with structural constraints, we inferred ancestral pre-miRNA sequences and deduced secondary structures at each ancestral node on the phylogeny (Supplementary Information section 12.1). Although conserved miRNA genes show little structural change (little change in free energy), the five *melanogaster* group-specific miRNA genes (*miR-303* and the *mir-310/311/312/313* cluster) have undergone numerous changes across the entire pre-miRNA sequence, including the ordinarily invariant mature miRNA. Patterns of polymorphism and divergence in these lineage-specific miRNA genes, including a high frequency of derived mutations, are suggestive of positive selection¹⁴⁰. Although lineage-specific miRNAs may evolve under less constraint because they have fewer target transcripts in the genome, it is also possible that recent integration into regulatory networks causes accelerated rates of miRNA evolution.

We further investigated patterns of sequence evolution for the subset of 38 conserved pre-miRNAs with mature miRNA sequences at their 3' end by calculating evolutionary rates in distinct site classes (Fig. 6, and Supplementary Information section 12.2). Outside the mature miRNA and its complementary sequence, loops had the highest rate of evolution, followed by unpaired sites, with paired sites having the lowest rate of evolution. Inside the mature miRNA, unpaired sites evolve more slowly than paired sites, whereas the opposite is true for the sequence complementary to the mature miRNA. Surprisingly, a large fraction of unpaired bulges or internal loops in the mature miRNA seem to be conserved—a pattern which may have implications for models of miRNA biogenesis and the degree of mismatch allowed in miRNA–target prediction methods. Overall these results support the qualitative model proposed in ref. 141 for the canonical progression of miRNA evolution, and show that functional constraints on the miRNA itself supersede structural constraints imposed by maintenance of the hairpin-loop.

To assess constraint on stem regions of RNA structures more generally, we compared substitution rates in stems (*S*) to those in nominally unconstrained loop regions (*L*) in a wide variety of ncRNAs (Supplementary Information section 12.3). We estimated substitution rates using a maximum likelihood framework, and compared the observed *L/S* ratio with the average *L/S* ratio estimated from published secondary structures in RFAM, which we normalized to 1.0. *L/S* ratios for *Drosophila* ncRNA families range from a highly constrained 2.57 for the nuclear RNase P family to 0.56 for the 5S ribosomal RNA (Supplementary Table 15).

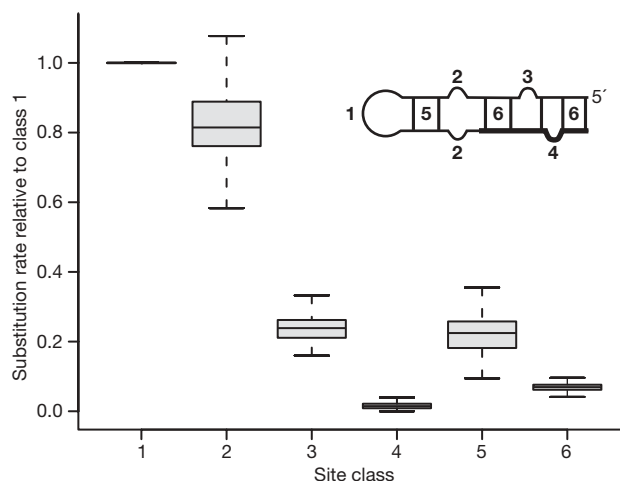


Figure 6 | Substitution rate of site classes within miRNAs. Bootstrap distributions of miRNA substitution rates. Structural alignments of miRNA precursor hairpins were partitioned into six site-classes (inset): (1) hairpin loops; unpaired sites (2) outside, (3) in the complementary region of, and (4) inside the miRNA; and base pairs (5) adjacent to and (6) involving the miRNA. Whiskers show approximate 95% confidence intervals for median differences, boxes show interquartile range.

Finally, we predicted a set of conserved intronic RNA structures and analysed patterns of compensatory nucleotide substitution in *D. melanogaster*, *D. yakuba*, *D. ananassae*, *D. pseudoobscura*, *D. virilis* and *D. mojavensis* (Supplementary Information section 13). Signatures of compensatory evolution in RNA helices are detected as covarying nucleotide sites or 'covariations' (that is, two Watson–Crick bases that interact in species A replaced by a different Watson–Crick pair in species B). The number of covariations (per base pair of a helix) depends on the physical distance between the interacting nucleotides (Supplementary Fig. 9), as has been observed for the RNA helices in the *Drosophila bicoid* 3' UTR region¹⁴². Short-range pairings exhibit a higher average number of covariations with a larger variance among helices than longer-range pairings. The decrease in rate of covariation with increasing distance may be explained by physical properties of a helix, which may impose selective constraints on the evolution of covarying nucleotides within a helix. Alternatively, if individual mutations at each locus are deleterious but compensated by mutations at a second locus, given sufficiently strong selection against the first deleterious mutation these epistatic fitness interactions could generate the observed distance effect¹⁴³.

Evolution of *cis*-regulatory DNAs. Comparative analyses of *cis*-regulatory sequences may provide insights into the evolutionary forces acting on regulatory components of genes, shed light on the constraints of the *cis*-regulatory code and aid in annotation of new regulatory sequences. Here we rely on two recently compiled databases, and present results comparing *cis*-regulatory modules¹⁴⁴ and transcription factor binding sites (derived from DNase I footprints)¹⁴⁵ between *D. melanogaster* and *D. simulans* (Supplementary Information section 8). We estimated mean selective constraint (*C*, the fraction of mutations removed by natural selection) relative to the 'fastest evolving intron' sites at the 5' end of short introns, which represent putatively unconstrained neutral standards (Supplementary Information section 8.2)¹⁴⁶. Note that this approach ignores the contribution of positively selected sites, potentially underestimating the fraction of functionally relevant sites¹⁴⁷.

Consistent with previous findings, *Drosophila cis*-regulatory sequences are highly constrained^{148,149}. Mean constraint within *cis*-regulatory modules is 0.643 (95% bootstrap confidence interval = 0.621–0.662) and within footprints is 0.692 (0.655–0.723), both of which are significantly higher than mean constraint in non-coding DNA overall (0.555 (0.546–0.563)) and significantly lower than constraint at non-degenerate coding sites (0.862 (0.856–0.868)) and ncRNA genes (0.864 (0.846–0.880)) (Supplementary Fig. 10). The high level of constraint in *cis*-regulatory sequences also extends into flanking sequences, only declining to constraint levels typical of non-coding DNA 40 bp away. This is consistent with previous findings that transcription factor binding sites tend to be found in larger blocks of constraint that cluster to form *cis*-regulatory modules¹⁵⁰. To understand selective constraints on nucleotides within *cis*-regulatory sequences that have direct contact with transcription factors, we estimated the selective constraint for the best match to position weight matrices within each footprint¹⁵¹; core motifs in transcription-factor-binding sites have a mean constraint of 0.773 (0.729–0.814), significantly greater than the mean for the footprints as a whole, and approaching the level of constraint found at non-degenerate coding sites and in ncRNA genes (Supplementary Fig. 10).

We next examined the variation in selective constraint across *cis*-regulatory sequences. Surprisingly, we find no evidence that selective constraint is correlated with predicted transcription-factor-binding strength (estimated as the position weight matrix score *P*-value) (Spearman's $r = 0.0681$, $P = 0.0609$). We observe significant variation in constraint both among target genes (Kruskal–Wallis tests, footprints, $P < 0.0001$; and position weight matrix matches within footprints, $P = 0.0023$) and among chromosomes (*cis*-regulatory modules, $P = 0.0186$; footprints, $P = 0.0388$; and position weight

matrix matches within footprints, $P = 0.0108$; Supplementary Table 16).

Discussion and conclusion

Each new genome sequence affords novel opportunities for comparative genomic inference. What makes the analysis of these 12 *Drosophila* genomes special is the ability to place every one of these genomic comparisons on a phylogeny with a taxon separation that is ideal for asking a wealth of questions about evolutionary patterns and processes. It is without question that this phylogenomic approach places additional burdens on bioinformatics efforts, multiplying the amount of data many-fold, requiring extra care in generating multi-species alignments, and accommodating the reality that not all genome sequences have the same degree of sequencing or assembly accuracy. These difficulties notwithstanding, phylogenomics has extraordinary advantages not only for the analyses that are possible, but also for the ability to produce high-quality assemblies and accurate annotations of functional features in a genome by using closely related genomes as guides. The use of multi-species orthology provides especially convincing evidence in support of particular gene models, not only for protein-coding genes, but also for miRNA and other ncRNA genes.

Many attributes of the genomes of *Drosophila* are remarkably conserved across species. Overall genome size, number of genes, distribution of transposable element classes, and patterns of codon usage are all very similar across these 12 genomes, although *D. willistoni* is an exceptional outlier by several criteria, including its unusually skewed codon usage, increased transposable element content and potential lack of selenoproteins. At a finer scale, the number of structural changes and rearrangements is much larger; for example, there are several different rearrangements of genes in the *Hox* cluster found in these *Drosophila* species.

The vast majority of multigene families are found in all 12 genomes, although gene family size seems to be highly dynamic: almost half of all gene families change in size on at least one lineage, and a noticeable fraction shows rapid and lineage-specific expansions and contractions. Particularly notable are cases consistent with adaptive hypotheses, such as the loss of *Gr* genes in ecological specialists and the lineage-specific expansions of antimicrobial peptides and other immune effectors. All species were found to have novel genes not seen in other species. Although lineage-specific genes are challenging to verify computationally, we can confirm at least 44 protein-coding genes unique to the *melanogaster* group, and these proteins have very different properties from ancestral proteins. Similarly, although the relative abundance of transposable element subclasses across these genomes does not differ dramatically, total genomic transposable element content varies substantially among species, and several instances of lineage-specific transposable elements were discovered.

There is considerable variation among protein-coding genes in rates of evolution and patterns of positive selection. Functionally similar proteins tend to evolve at similar rates, although variation in genomic features such as gene expression level, as well as chromosomal location, are also associated with variation in evolutionary rate among proteins. Whereas broad functional classes do not seem to share patterns of positive selection, and although very few GO categories show excesses of positive selection, a number of genes involved in interactions with the environment and in sex and reproduction do show signatures of adaptive evolution. It thus seems likely that adaptation to changing environments, as well as sexual selection, shape the evolution of protein-coding genes.

Annotation of ncRNA genes across all 12 species allows comprehensive analysis of the evolutionary divergence of these genes. MicroRNA genes in particular are more conserved than protein-coding genes with respect to their primary DNA sequence, and the substitutions that do occur often have compensatory changes such that the average estimated free energy of the folding structures remains remarkably constant across the phylogeny. Surprisingly,

mismatches in miRNAs seem to be highly conserved, which may impact models of miRNA biogenesis and target recognition. Lineage-restricted miRNAs, however, have considerably elevated rates of change, suggesting either reduced constraint due to novel miRNAs having fewer targets, or adaptive evolution of evolutionarily young miRNAs.

Virtually any question about the function of genome features in *Drosophila* is now empowered by being embedded in the context of this 12 species phylogeny, allowing an analysis of the ways by which evolution has tuned myriad biological processes across the hundreds of millions of years spanned in total by this phylogeny. The analyses presented herein have generated more questions than they have answered, and these results represent a small fraction of that which is possible. Because much of this rich and extraordinary comparative genomic dataset remains to be explored, we believe that these 12 *Drosophila* genome sequences will serve as a powerful tool for glean-ing further insight into genetic, developmental, regulatory and evolutionary processes.

METHODS

The full methods for this paper are described in Supplementary Information. Here, we describe the datasets generated by this project and their availability.

Genomic sequence. Scaffolds and assemblies for all genomic sequence generated by this project are available from GenBank (Supplementary Tables 4 and 5), and FlyBase (ftp://ftp.flybase.net/12_species_analysis/). Genome browsers are available from UCSC (<http://genome.ucsc.edu/cgi-bin/hgGateway?hgsid=98180333&clade=insect&org=0&db=0>) and Flybase (<http://flybase.org/cgi-bin/gbrowse/dmel/>). BLAST search of these genomes is available at FlyBase (<http://flybase.org/blast>).

Predicted gene models. Consensus gene predictions for the 11 non-*melanogaster* species, produced by combining several different GLEAN runs that weight homology evidence more or less strongly, are available from FlyBase as GFF files for each species (ftp://ftp.flybase.net/12_species_analysis/). These gene models can also be accessed from the Genome Browser in FlyBase (Gbrowse; <http://flybase.org/cgi-bin/gbrowse/dmel/>). Predictions of non-protein-coding genes are also available in GFF format for each species, from FlyBase (ftp://ftp.flybase.net/12_species_analysis/).

Homology. Multiway homology assignments are available from FlyBase (ftp://ftp.flybase.net/12_species_analysis/), and also in the Genome Browser (Gbrowse).

Alignments. All alignment sets produced are available in FASTA format from FlyBase (ftp://ftp.flybase.net/12_species_analysis/).

PAML parameters. Output from PAML models for the alignments of single copy orthologues in the *melanogaster* group, including the *q*-value for the test for positive selection, are available from FlyBase (ftp://ftp.flybase.net/12_species_analysis/).

Received 19 July; accepted 5 October 2007.

- Markow, T. A. & O'Grady, P. M. *Drosophila* biology in the genomic age. *Genetics* doi:10.1534/genetics.107.074112 (in the press).
- Powell, J. R. *Progress and Prospects in Evolutionary Biology: The Drosophila Model* (Oxford Univ. Press, Oxford, 1997).
- Adams, M. D. *et al.* The genome sequence of *Drosophila melanogaster*. *Science* **287**, 2185–2195 (2000).
- Celniker, S. E. *et al.* Finishing a whole-genome shotgun: release 3 of the *Drosophila melanogaster* euchromatic genome sequence. *Genome Biol.* **3**, research0079.1–0079.14 (2002).
- Richards, S. *et al.* Comparative genome sequencing of *Drosophila pseudoobscura*: chromosomal, gene, and *cis*-element evolution. *Genome Res.* **15**, 1–18 (2005).
- Myers, E. W. *et al.* A whole-genome assembly of *Drosophila*. *Science* **287**, 2196–2204 (2000).
- Fleischmann, R. D. *et al.* Whole-genome random sequencing and assembly of *Haemophilus influenzae* Rd. *Science* **269**, 496–512 (1995).
- Stark *et al.* Discovery of functional elements in 12 *Drosophila* genomes using evolutionary signatures. *Nature* doi:10.1038/nature06340 (this issue).
- Begun, D. J. *et al.* Population genomics: whole-genome analysis of polymorphism and divergence in *Drosophila simulans*. *PLoS Biol.* **5**, e310, doi:10.1371/journal.pbio.0050310 (2007).
- Zimin, A. V., Smith, D. R., Sutton, G. & Yorke, J. A. Assembly reconciliation. *Bioinformatics* (in the press).
- Clary, D. O. & Wolstenholme, D. R. The mitochondrial DNA molecule of *Drosophila yakuba*: nucleotide sequence, gene organization, and genetic code. *J. Mol. Evol.* **22**, 252–271 (1985).

- Ballard, J. W. When one is not enough: introgression of mitochondrial DNA in *Drosophila*. *Mol. Biol. Evol.* **17**, 1126–1130 (2000).
- Montooth, K. L., Abt, D. N., Hoffman, J. & Rand, D. M. Evolution of the mitochondrial DNA across twelve species of *Drosophila*. *Mol. Biol. Evol.* (submitted).
- Salzberg, S. *et al.* Serendipitous discovery of *Wolbachia* genomes in multiple *Drosophila* species. *Genome Biol.* **6**, R23 (2005).
- Edgar, R. C. & Myers, E. W. PILER: identification and classification of genomic repeats. *Bioinformatics* **21**, i152–i158 (2005).
- Smith, C. D. *et al.* Improved repeat identification and masking in Diptera. *Gene* **389**, 1–9 (2007).
- Li, Q. *et al.* ReAS: Recovery of ancestral sequences for transposable elements from the unassembled reads of a whole shotgun. *PLoS Comput. Biol.* **1**, e43 (2005).
- Bergman, C. M., Quesneville, H., Anxolabehere, D. & Ashburner, M. Recurrent insertion and duplication generate networks of transposable element sequences in the *Drosophila melanogaster* genome. *Genome Biol.* **7**, R112 (2006).
- Guigo, R., Knudsen, S., Drake, N. & Smith, T. Prediction of gene structure. *J. Mol. Biol.* **226**, 141–157 (1992).
- Korf, I. Gene finding in novel genomes. *BMC Bioinformatics* **5**, 59 (2004).
- Gross, S. S. & Brent, M. R. Using multiple alignments to improve gene prediction. *J. Comput. Biol.* **13**, 379–393 (2006).
- Gross, S. S., Do, C. B. & Batzoglou, S. in *BCATS 2005 Symposium Proc.* **82** (2005).
- Birney, E., Clamp, M. & Durbin, R. GeneWise and Genomewise. *Genome Res.* **14**, 988–995 (2004).
- Slater, G. & Birney, E. Automated generation of heuristics for biological sequence comparison. *BMC Bioinformatics* **6**, 31 (2005).
- Chatterji, S. & Pachter, L. Reference based annotation with GeneMapper. *Genome Biol.* **7**, R29 (2006).
- Souvorov, A. *et al.* in *NCBI News Fall/Winter, NIH Publication No. 04-3272* (eds Benson, D. & Wheeler, D.) (2006).
- Honeybee Genome Sequencing Consortium. Insights into social insects from the genome of the honeybee *Apis mellifera*. *Nature* **443**, 931–949 (2006).
- Elsik, C. G. *et al.* Creating a honey bee consensus gene set. *Genome Biol.* **8**, R13 (2007).
- Zhang, Y., Sturgill, D., Parisi, M., Kumar, S. & Oliver, B. Constraint and turnover in sex-biased gene expression in the genus *Drosophila*. *Nature* doi:10.1038/nature06323 (this issue).
- Manak, J. R. *et al.* Biological function of unannotated transcription during the early development of *Drosophila melanogaster*. *Nature Genet.* **38**, 1151–1158 (2006).
- Tatusov, R. L., Koonin, E. V. & Lipman, D. J. A genomic perspective on protein families. *Science* **278**, 631–637 (1997).
- Bhutkar, A., Russo, S., Smith, T. F. & Gelbart, W. M. Techniques for multi-genome synteny analysis to overcome assembly limitations. *Genome Informatics* **17**, 152–161 (2006).
- Heger, A. & Ponting, C. Evolutionary rate analyses of orthologues and paralogues from twelve *Drosophila* genomes. doi:10.1101/gr6249707 *Genome Res.* (in the press).
- Notredame, C., Higgins, D. G. & Heringa, J. T-Coffee: A novel method for fast and accurate multiple sequence alignment. *J. Mol. Biol.* **302**, 205–217 (2000).
- Rat Genome Sequencing Project Consortium. Genome sequence of the Brown Norway rat yields insights into mammalian evolution. *Nature* **428**, 493–521 (2004).
- Waterston, R. H. *et al.* Initial sequencing and comparative analysis of the mouse genome. *Nature* **420**, 520–562 (2002).
- Harrison, P. M., Milburn, D., Zhang, Z., Bertone, P. & Gerstein, M. Identification of pseudogenes in the *Drosophila melanogaster* genome. *Nucleic Acids Res.* **31**, 1033–1037 (2003).
- Bosco, G., Campbell, P., Leiva-Neto, J. & Markow, T. Analysis of *Drosophila* species genome size and satellite DNA content reveals significant differences among strains as well as between species. *Genetics* doi:10.1534/Genetics107.075069 (in the press).
- Ranz, J. *et al.* Principles of genome evolution in the *Drosophila melanogaster* species group. *PLoS Biol.* **5**, e152, doi:10.1371/journal.pbio.0050152 (2007).
- Noor, M. A. F., Garfield, D. A., Schaeffer, S. W. & Machado, C. A. Divergence between the *Drosophila pseudoobscura* and *D. persimilis* genome sequences in relation to chromosomal inversions. *Genetics* doi:10.1534/genetics.107.070672 (in the press).
- Lewis, E. B. A gene complex controlling segmentation in *Drosophila*. *Nature* **276**, 565–570 (1978).
- Negre, B., Ranz, J. M., Casals, F., Caceres, M. & Ruiz, A. A new split of the *Hox* gene complex in *Drosophila*: relocation and evolution of the gene labial. *Mol. Biol. Evol.* **20**, 2042–2054 (2003).
- Von Allmen, G. *et al.* Splits in fruitfly *Hox* gene complexes. *Nature* **380**, 116 (1996).
- Negre, B. & Ruiz, A. HOM-C evolution in *Drosophila*: is there a need for *Hox* gene clustering? *Trends Genet.* **23**, 55–59 (2007).
- Dowsett, A. P. & Young, M. W. Differing levels of dispersed repetitive DNA among closely related species of *Drosophila*. *Proc. Natl Acad. Sci.* **79**, 4570–4574 (1982).
- Kapitonov, V. V. & Jurka, J. DNAREP1_DM. (Repbase Update Release 3.4, 1999).
- Kapitonov, V. V. & Jurka, J. Molecular paleontology of transposable elements in the *Drosophila melanogaster* genome. *Proc. Natl Acad. Sci. USA* **100**, 6569–6574 (2003).

48. Singh, N. D., Arndt, P. F. & Petrov, D. A. Genomic heterogeneity of background substitutional patterns in *Drosophila melanogaster*. *Genetics* **169**, 709–722 (2004).
49. Yang, H.-P., Hung, T.-L., You, T.-L. & Yang, T.-H. Genomewide comparative analysis of the highly abundant transposable element *DINE-1* suggests a recent transpositional burst in *Drosophila yakuba*. *Genetics* **173**, 189–196 (2006).
50. Yang, H.-P. & Barbash, D. Abundant and species-specific miniature inverted-repeat transposable elements in 12 *Drosophila* genomes. *Genome Biol.* (submitted).
51. Wilder, J. & Hollocher, H. Mobile elements and the genesis of microsatellites in dipterans. *Mol. Biol. Evol.* **18**, 384–392 (2001).
52. Marzo, M., Puig, M. & Ruiz, A. The foldback-like element *Galileo* belongs to the P superfamily of DNA transposons and is widespread within the genus *Drosophila*. *Proc. Natl Acad. Sci. USA* (submitted).
53. Casola, C., Lawing, A., Betran, E. & Feschotte, C. PIF-like transposons are common in *Drosophila* and have been repeatedly domesticated to generate new host genes. *Mol. Biol. Evol.* **24**, 1872–1888 (2007).
54. Abad, J. P. et al. Genomic analysis of *Drosophila melanogaster* telomeres: full-length copies of *HeT-A* and *TART* elements at telomeres. *Mol. Biol. Evol.* **21**, 1613–1619 (2004).
55. Abad, J. P. et al. *TAHRE*, a novel telomeric retrotransposon from *Drosophila melanogaster*, reveals the origin of *Drosophila* telomeres. *Mol. Biol. Evol.* **21**, 1620–1624 (2004).
56. Blackburn, E. H. Telomerases. *Annu. Rev. Biochem.* **61**, 113–129 (1992).
57. Villasante, A. et al. *Drosophila* telomeric retrotransposons derived from an ancestral element that as recruited to replace telomerase. *Genome Res.* (in the press).
58. International Chicken Genome Sequencing Consortium. Sequence and comparative analysis of the chicken genome provide unique perspectives on vertebrate evolution. *Nature* **432**, 695–716 (2004).
59. Lander, E. S. et al. Initial sequencing and analysis of the human genome. *Nature* **409**, 860–921 (2001).
60. C. elegans Sequencing Consortium. Genome sequence of the nematode *C. elegans*: a platform for investigating biology. *Science* **282**, 2012–2018 (1998).
61. Mount, S. M., Gotea, V., Lin, C. F., Hernandez, K. & Makalowski, W. Spliceosomal small nuclear RNA genes in 11 insect genomes. *RNA* **13**, 5–14 (2007).
62. Schneider, C., Will, C. L., Brosius, J., Frilander, M. J. & Luhrmann, R. Identification of an evolutionarily divergent U1 small nuclear ribonucleoprotein particle in *Drosophila*. *Proc. Natl Acad. Sci. USA* **101**, 9584–9589 (2004).
63. Deng, X. & Meller, V. H. Non-coding RNA in fly dosage compensation. *Trends Biochem. Sci.* **31**, 526–532 (2006).
64. Amrien, H. & Axel, R. Genes expressed in neurons of adult male *Drosophila*. *Cell* **88**, 459–469 (1997).
65. Park, S.-W. et al. An evolutionarily conserved domain of roX2 RNA is sufficient for induction of H4-Lys16 acetylation on the *Drosophila* X chromosome. *Genetics* (in the press).
66. Stage, D. E. & Eickbush, T. H. Sequence variation within the rRNA gene loci of 12 *Drosophila* species. *Genome Res.* (in the press).
67. Hahn, M. W., De Bie, T., Stajich, J. E., Nguyen, C. & Cristianini, N. Estimating the tempo and mode of gene family evolution from comparative genomic data. *Genome Res.* **15**, 1153–1160 (2005).
68. Hahn, M. W., Han, M. V. & Han, S.-G. Gene family evolution across 12 *Drosophila* genomes. *PLoS Biol.* **3**, e197 (2007).
69. Levine, M. T., Jones, C. D., Kern, A. D., Lindfors, H. A. & Begun, D. J. Novel genes derived from noncoding DNA in *Drosophila melanogaster* are frequently X-linked and exhibit testis-biased expression. *Proc. Natl Acad. Sci. USA* **103**, 9935–9939 (2006).
70. Ponce, R. & Hartl, D. L. The evolution of the novel *Sdic* gene cluster in *Drosophila melanogaster*. *Gene* **376**, 174–183 (2006).
71. Arguello, J. R., Chen, Y., Tang, S., Wang, W. & Long, M. Origination of an X-linked testes chimeric gene by illegitimate recombination in *Drosophila*. *PLoS Genet.* **2**, e77 (2006).
72. Begun, D. J., Lindfors, H. A., Thompson, M. E. & Holloway, A. K. Recently evolved genes identified from *Drosophila yakuba* and *D. erecta* accessory gland expressed sequence tags. *Genetics* **172**, 1675–1681 (2006).
73. Betran, E., Thornton, K. & Long, M. Retrospect new genes out of the X in *Drosophila*. *Genome Res.* **12**, 1854–1859 (2002).
74. Yanai, I. et al. Genome-wide midrange transcription profiles reveal expression level relationships in human tissue specification. *Bioinformatics* **21**, 650–659 (2005).
75. Yang, Z. PAML: a program package for phylogenetic analysis by maximum likelihood. *Comput. Appl. Biosci.* **13**, 555–556 (1997).
76. The Gene Ontology Consortium. Gene Ontology: tool for the unification of biology. *Nature Genet.* **25**, 25–29 (2000).
77. Storey, J. D. A direct approach to false discovery rates. *J. R. Stat. Soc. B* **64**, 479–498 (2002).
78. Larracuente, A. M. et al. Evolution of protein-coding genes in *Drosophila*. *Trends Genet.* (submitted).
79. Yang, Z., Nielsen, R., Goldman, N. & Pedersen, A. M. Codon-substitution models for heterogeneous selection pressure at amino acid sites. *Genetics* **155**, 431–449 (2000).
80. Bergman, C. M. et al. Assessing the impact of comparative genomic sequence data on the functional annotation of the *Drosophila* genome. *Genome Biol.* **3**, research0086.1–0086.20 (2002).
81. Bierne, N. & Eyre Walker, A. C. The genomic rate of adaptive amino acid substitution in *Drosophila*. *Mol. Biol. Evol.* **21**, 1350–1360 (2004).
82. Sawyer, S. A., Kulathinal, R. J., Bustamante, C. D. & Hartl, D. L. Bayesian analysis suggests that most amino acid replacements in *Drosophila* are driven by positive selection. *J. Mol. Evol.* **57** (suppl. 1), S154–S164 (2003).
83. Sawyer, S. A., Parsch, J., Zhang, Z. & Hartl, D. L. Prevalence of positive selection among nearly neutral amino acid replacements in *Drosophila*. *Proc. Natl Acad. Sci. USA* **104**, 6504–6510 (2007).
84. Smith, N. G. & Eyre-Walker, A. Adaptive protein evolution in *Drosophila*. *Nature* **415**, 1022–1024 (2002).
85. Welch, J. J. Estimating the genomewide rate of adaptive protein evolution in *Drosophila*. *Genetics* **173**, 821–837 (2006).
86. Drummond, D. A., Bloom, J. D., Adami, C., Wilke, C. O. & Arnold, F. H. Why highly expressed proteins evolve slowly. *Proc. Natl Acad. Sci. USA* **102**, 14338–14343 (2005).
87. Drummond, D. A., Raval, A. & Wilke, C. O. A single determinant dominates the rate of yeast protein evolution. *Mol. Biol. Evol.* **23**, 327–337 (2006).
88. Pal, C., Papp, B. & Hurst, L. D. Highly expressed genes in yeast evolve slowly. *Genetics* **158**, 927–931 (2001).
89. Pal, C., Papp, B. & Lercher, M. J. An integrated view of protein evolution. *Nature Rev. Genet.* **7**, 337–348 (2006).
90. Wall, D. P. et al. Functional genomic analysis of the rates of protein evolution. *Proc. Natl Acad. Sci. USA* **102**, 5483–5488 (2005).
91. Rocha, E. P. The quest for the universals of protein evolution. *Trends Genet.* **22**, 412–416 (2006).
92. Huntley, M. A. & Clark, A. G. Evolutionary analysis of amino acid repeats across the genomes of 12 *Drosophila* species. *Mol. Biol. Evol.* (in the press).
93. Charlesworth, B., Coyne, J. A. & Barton, N. H. The relative rates of evolution of sex chromosomes and autosomes. *Am. Nat.* **130**, 113–146 (1987).
94. Larsson, J. & Meller, V. H. Dosage compensation, the origin and the afterlife of sex chromosomes. *Chromosome Res.* **14**, 417–431 (2006).
95. Riddle, N. C. & Elgin, S. C. The dot chromosome of *Drosophila*: insights into chromatin states and their change over evolutionary time. *Chromosome Res.* **14**, 405–416 (2006).
96. Gordo, I. & Charlesworth, B. Genetic linkage and molecular evolution. *Curr. Biol.* **11**, R684–R686 (2001).
97. Singh, N. D., Larracuente, A. M. & Clark, A. G. Contrasting the efficacy of selection on the X and autosomes in *Drosophila*. *Mol. Biol. Evol.* (submitted).
98. Bhutkar, A., Russo, S. M., Smith, T. F. & Gelbart, W. M. Genome scale analysis of positionally relocated genes. *Genome Res.* (in the press).
99. Akashi, H. & Eyre-Walker, A. Translational selection and molecular evolution. *Curr. Opin. Genet. Dev.* **8**, 688–693 (1998).
100. Akashi, H., Kliman, R. M. & Eyre-Walker, A. Mutation pressure, natural selection, and the evolution of base composition in *Drosophila*. *Genetica (Dordrecht)* **102–103**, 49–60 (1998).
101. Bulmer, M. The selection–mutation–drift theory of synonymous codon usage. *Genetics* **129**, 897–908 (1991).
102. McVean, G. A. T. & Charlesworth, B. A population genetic model for the evolution of synonymous codon usage: Patterns and predictions. *Genet. Res.* **74**, 145–158 (1999).
103. Sharp, P. M. & Li, W. H. An evolutionary perspective on synonymous codon usage in unicellular organisms. *J. Mol. Evol.* **24**, 28–38 (1986).
104. Akashi, H. & Schaeffer, S. V. Natural selection and the frequency distributions of “silent” DNA polymorphism in *Drosophila*. *Genetics* **146**, 295–307 (1997).
105. Powell, J. R., Sezzi, E., Moriyama, E. N., Gleason, J. M. & Cacccone, A. Analysis of a shift in codon usage in *Drosophila*. *J. Mol. Evol.* **57**, S214–S225 (2003).
106. Anderson, C. L., Carew, E. A. & Powell, J. R. Evolution of the *Adh* locus in the *Drosophila willistoni* group: The loss of an intron, and shift in codon usage. *Mol. Biol. Evol.* **10**, 605–618 (1993).
107. Rodriguez-Trelles, F., Tarrio, R. & Ayala, F. J. Switch in codon bias and increased rates of amino acid substitution in the *Drosophila saltans* species group. *Genetics* **153**, 339–350 (1999).
108. Rodriguez-Trelles, F., Tarrio, R. & Ayala, F. J. Evidence for a high ancestral GC content in *Drosophila*. *Mol. Biol. Evol.* **17**, 1710–1717 (2000).
109. Rodriguez-Trelles, F., Tarrio, R. & Ayala, F. J. Fluctuating mutation bias and the evolution of base composition in *Drosophila*. *J. Mol. Evol.* **50**, 1–10 (2000).
110. Heger, A. & Ponting, C. Variable strength of translational selection among twelve *Drosophila* species. *Genetics* (in the press).
111. Vicario, S., Moriyama, E. N. & Powell, J. R. Codon Usage in Twelve Species of *Drosophila*. *BMC Evol. Biol.* (submitted).
112. Singh, N. D., Arndt, P. F. & Petrov, D. A. Minor shift in background substitutional patterns in the *Drosophila saltans* and *willistoni* lineages is insufficient to explain GC content of coding sequences. *BMC Biol.* **4**, 10.1186/1741-7007-4-37 (2006).
113. Akashi, H. Inferring weak selection from patterns of polymorphism and divergence at “silent” sites in *Drosophila* DNA. *Genetics* **139**, 1067–1076 (1995).
114. Akashi, H. Molecular evolution between *Drosophila melanogaster* and *D. simulans*: reduced codon bias, faster rates of amino acid substitution, and larger proteins in *D. melanogaster*. *Genetics* **144**, 1297–1307 (1996).

115. Akashi, H. *et al.* Molecular evolution in the *Drosophila melanogaster* species subgroup: Frequent parameter fluctuations on the timescale of molecular divergence. *Genetics* **172**, 1711–1726 (2006).
116. Bauer DuMont, V., Fay, J. C., Calabrese, P. P. & Aquadro, C. F. DNA variability and divergence at the *Notch* locus in *Drosophila melanogaster* and *D. simulans*: a case of accelerated synonymous site divergence. *Genetics* **167**, 171–185 (2004).
117. McVean, G. A. & Vieira, J. The evolution of codon preferences in *Drosophila*: a maximum-likelihood approach to parameter estimation and hypothesis testing. *J. Mol. Evol.* **49**, 63–75 (1999).
118. Nielsen, R., Bauer DuMont, V., Hubisz, M. J. & Aquadro, C. F. Maximum likelihood estimation of ancestral codon usage bias parameters in *Drosophila*. *Mol. Biol. Evol.* **24**, 228–235 (2007).
119. Begun, D. J. The frequency distribution of nucleotide variation in *Drosophila simulans*. *Mol. Biol. Evol.* **18**, 1343–1352 (2001).
120. Singh, N. S., Bauer DuMont, V. L., Hubisz, M. J., Nielsen, R. & Aquadro, C. F. Patterns of mutation and selection at synonymous sites in *Drosophila*. *Mol. Biol. Evol.* doi:10.1093/mbevm196 (in the press).
121. McBride, C. S. & Arguello, J. R. Five *Drosophila* genomes reveal non-neutral evolution and the signature of host specialization in the chemoreceptor superfamily. *Genetics* (in the press).
122. Vieira, F. G., Sanchez-Gracia, A. & Rozas, J. Comparative genomic analysis of the odorant-binding protein family in 12 *Drosophila* genomes: Purifying selection and birth-and-death evolution. *Genome Biol.* **8**, 235 (2007).
123. Gardiner, A., Barker, D., Butlin, R. K., Jordan, W. C. & Ritchie, M. G. *Drosophila* chemoreceptor evolution: Selection, specialisation and genome size. *Genome Biol.* (submitted).
124. McBride, C. S. Rapid evolution of smell and taste receptor genes during host specialization in *Drosophila sechellia*. *Proc. Natl Acad. Sci. USA* **104**, 4996–5001 (2007).
125. Ranson, H. *et al.* Evolution of supergene families associated with insecticide resistance. *Science* **298**, 179–181 (2002).
126. Tijet, N., Helvig, C. & Feyereisen, R. The cytochrome P450 gene superfamily in *Drosophila melanogaster*. *Gene* **262**, 189–198 (2001).
127. Claudianos, C. *et al.* A deficit of detoxification enzymes: pesticide sensitivity and environmental response in the honeybee. *Insect Mol. Biol.* **15**, 615–636 (2006).
128. Low, W. L. *et al.* Molecular evolution of glutathione S-transferases in the genus *Drosophila*. *Genetics* (in the press).
129. Castellano, S. *et al.* *In silico* identification of novel selenoproteins in the *Drosophila melanogaster* genome. *EMBO Rep.* **2**, 697–702 (2001).
130. Martin-Romero, F. J. *et al.* Selenium metabolism in *Drosophila*: selenoproteins, selenoprotein mRNA expression, fertility, and mortality. *J. Biol. Chem.* **276**, 29798–29804 (2001).
131. Lemaître, B. & Hoffmann, J. The host defense of *Drosophila melanogaster*. *Annu. Rev. Immunol.* **25**, 697–743 (2007).
132. Hughes, A. L. & Nei, M. Pattern of nucleotide substitution at major histocompatibility complex class I loci reveals overdominant selection. *Nature* **335**, 167–170 (1988).
133. Murphy, P. M. Molecular mimicry and the generation of host defense protein diversity. *Cell* **72**, 823–826 (1993).
134. Schlenke, T. A. & Begun, D. J. Natural selection drives *Drosophila* immune system evolution. *Genetics* **164**, 1471–1480 (2003).
135. Sackton, T. B. *et al.* The evolution of the innate immune system across *Drosophila*. *Nature Genet.* (submitted).
136. Civetta, A. & Singh, R. S. High divergence of reproductive tract proteins and their association with postzygotic reproductive isolation in *Drosophila melanogaster* and *Drosophila virilis* group species. *J. Mol. Evol.* **41**, 1085–1095 (1995).
137. Civetta, A. Shall we dance or shall we fight? Using DNA sequence data to untangle controversies surrounding sexual selection. *Genome* **46**, 925–929 (2003).
138. Clark, N. L., Aagard, J. E. & Swanson, W. J. Evolution of reproductive proteins from animals and plants. *Reproduction* **131**, 11–22 (2006).
139. Haerty, W. *et al.* Evolution in the fast lane: rapidly evolving sex- and reproduction-related genes in *Drosophila* species. *Genetics* (in the press).
140. Lu, J. *et al.* Adaptive evolution of newly-emerged microRNA genes in *Drosophila*. *Mol. Biol. Evol.* (submitted).
141. Lai, E. C., Tomanack, P., Williams, R. W. & Rubin, G. M. Computational identification of *Drosophila* microRNA genes. *Genome Biol.* **4**, R42 (2003).
142. Parsch, J., Braverman, J. M. & Stephan, W. Comparative sequence analysis and patterns of covariation in RNA secondary structures. *Genetics* **154**, 909–921 (2000).
143. Stephan, W. The rate of compensatory evolution. *Genetics* **144**, 419–426 (1996).
144. Gallo, S. M., Li, L., Hu, Z. & Halfon, M. S. REDfly: a Regulatory Element Database for *Drosophila*. *Bioinformatics* **22**, 381–383 (2006).
145. Bergman, C. M., Carlson, J. W. & Celniker, S. E. *Drosophila* DNase I footprint database: a systematic genome annotation of transcription factor binding sites in the fruitfly, *Drosophila melanogaster*. *Bioinformatics* **21**, 1747–1749 (2005).
146. Halligan, D. L. & Keightley, P. D. Ubiquitous selective constraints in the *Drosophila* genome revealed by a genome-wide interspecies comparison. *Genome Res.* **16**, 875–884 (2006).
147. Andolfatto, P. Adaptive evolution of non-coding DNA in *Drosophila*. *Nature* **437**, 1149–1152 (2005).
148. Bird, C. P., Stranger, B. E. & Dermitzakis, E. T. Functional variation and evolution of non-coding DNA. *Curr. Opin. Genet. Dev.* **16**, 559–564 (2006).
149. Wittkopp, P. J. Evolution of *cis*-regulatory sequence and function in Diptera. *Heredity* **97**, 139–147 (2006).
150. Ludwig, M. Z., Patel, N. H. & Kreitman, M. Functional analysis of *eve stripe 2* enhancer evolution in *Drosophila*. *Development* **125**, 949–958 (1998).
151. Down, A. T. A., Bergman, C. M., Su, J. & Hubbard, T. J. P. Large scale discovery of promoter motifs in *Drosophila melanogaster*. *PLoS Comput. Biol.* **3**, e7 (2007).
152. Tamura, K., Subramanian, S. & Kumar, S. Temporal patterns of fruit fly (*Drosophila*) evolution revealed by mutation clocks. *Mol. Biol. Evol.* **21**, 36–44 (2004).
153. Kumar, S., Tamura, K. & Nei, M. MEGA3: Integrated software for molecular evolutionary genetics analysis and sequence alignment. *Brief. Bioinform.* **5**, 150–163 (2004).
154. Pollard, D. A., Iyer, V. N., Moses, A. M. & Eisen, M. B. Widespread discordance of gene trees with species tree in *Drosophila*: evidence for incomplete lineage sorting. *PLoS Genet.* **2**, e173 (2006).
155. Bhutkar, A., Gelbart, W. M. & Smith, T. F. Inferring genome-scale rearrangement phylogeny and ancestral gene order: A *Drosophila* case study. *Genome Biol.* (in the press).

Supplementary Information is linked to the online version of the paper at www.nature.com/nature.

Acknowledgements Agencourt Bioscience Corporation, The Broad Institute of MIT and Harvard and the Washington University Genome Sequencing Center were supported by grants and contracts from the National Human Genome Research Institute (NHGRI). T.C. Kaufman acknowledges support from the Indian Genomics Initiative.

Author Contributions The laboratory groups of A. G. Clark (including A. M. Larracuent, T. B. Sackton, and N. D. Singh) and Michael B. Eisen (including V. N. Iyer and D. A. Pollard) played the part of coordinating the primary writing and editing of the manuscript with the considerable help of D. R. Smith, C. M. Bergman, W. M. Gelbart, B. Oliver, T. A. Markow, T. C. Kaufman and M. Kellis. D. R. Smith served as primary coordinator for the assemblies. The remaining authors contributed either through their efforts in sequence production, assembly and annotation, or in the analysis of specific topics that served as the focus of more than 40 companion papers.

Author Information Reprints and permissions information is available at www.nature.com/reprints. Correspondence and requests for materials should be addressed to A.G.C. (ac347@cornell.edu), M.B.E. (mbeisen@lbl.gov), D.R.S. (douglas.smith@agencourt.com), C.M.B. (casey.bergman@manchester.ac.uk), W.G. (gelbart@morgan.harvard.edu), B.O. (oliver@helix.nih.gov), T.A.M. (tmarkow@public.arl.arizona.edu), T.C.K. (kaufman@indiana.edu), M.K. (manoli@mit.edu), V.N.I. (venky@berkeley.edu), T.B.S. (tbs7@cornell.edu), A.M.L. (aml69@cornell.edu), D.A.P. (daniellapollard@alum.bowdoin.edu), N.D.S. (nds25@cornell.edu), or collectively to 12flies@morgan.harvard.edu.

***Drosophila* 12 Genomes Consortium**

Project Leaders Andrew G. Clark¹, Michael B. Eisen^{2,3}, Douglas R. Smith⁴, Casey M. Bergman⁵, Brian Oliver⁶, Therese A. Markow⁷, Thomas C. Kaufman⁸, Manolis Kellis^{9,10} & William Gelbart^{11,12}

Annotation Coordination Venky N. Iyer¹³ & Daniel A. Pollard¹⁴

Analysis/Writing Coordination Timothy B. Sackton^{1,15}, Amanda M. Larracuent¹ & Nadia D. Singh¹

Sequencing, Assembly, Annotation and Analysis Contributors Jose P. Abad¹⁶, Dawn N. Abt¹⁷, Boris Adryan¹⁸, Montserrat Aguade¹⁹, Hiroshi Akashi²⁰, Wyatt W. Anderson²¹, Charles F. Aquadro¹, David H. Ardell²², Roman Arguello²³, Carlo G. Artieri²⁴, Daniel A. Barbash¹, Daniel Barker²⁵, Paolo Barsanti²⁶, Phil Batterham²⁷, Serafim Batzoglou²⁸, Dave Begun²⁹, Arjun Bhutkar^{11,30}, Enrico Blanco³¹, Stephanie A. Bosak⁴, Robert K. Bradley³², Adrienne D. Brand⁴, Michael R. Brent³³, Angela N. Brooks¹³, Randall H. Brown³³, Roger K. Butlin³⁴, Corrado Caggese²⁶, Brian R. Calvi³⁵, A. Bernardo de Carvalho³⁶, Anat Caspi³², Sergio Castrezana³⁷, Susan E. Celniker², Jean L. Chang¹⁰, Charles Chapple³¹, Sourav Chatterji^{38,39}, Asif Chinwalla⁴⁰, Alberto Civetta⁴¹, Sandra W. Clifton⁴⁰, Josep M. Comeron⁴², James C. Costello⁴³, Jerry A. Coyne²³, Jennifer Daub⁴⁴, Robert G. David⁴, Arthur L. Delcher⁴⁵, Kim Delehaunty⁴⁰, Chuong B. Do²⁸, Heather Ebling⁴, Kevin Edwards⁴⁶, Thomas Eickbush⁴⁷, Jay D. Evans⁴⁸, Alan Filipitski⁴⁹, Sven Findeiß^{49,50}, Eva Freyhult²², Lucinda Fulton⁴⁰, Robert Fulton⁴⁰, Ana C. L. Garcia⁵¹, Anastasia Gardiner²⁵, David A. Garfield⁵², Barry E. Garvin⁴, Greg Gibson⁵³, Don Gilbert⁸, Sante Gnerre¹⁰, Jennifer Godfrey⁴⁰, Robert Good²⁷, Valer Gotea²⁰, Brenton Gravely⁵⁴, Anthony J. Greenberg¹, Sam Griffiths-Jones^{5,44}, Samuel Gross²⁸, Roderic Guigo^{31,55}, Erik A. Gustafson⁴, Wilfried Haerty²⁴, Matthew W. Hahn^{8,43}, Daniel L. Halligan⁵⁶, Aaron L. Halpern⁵⁷, Gillian M. Halter²⁰, Mira V. Han⁴³, Andreas Heger^{58,59}, LaDeana Hillier⁴⁰, Angie S. Hinrichs⁶⁰, Ian Holmes³², Roger A. Hoskins², Melissa J. Hubisz⁶¹, Dan Hultmark⁶², Melanie A. Huntley¹, David B. Jaffe¹⁰, Santosh Jagadeeshan²⁴, William R. Jeck⁶³, Justin Johnson⁵⁷, Corbin D. Jones⁶³, William C. Jordan⁶⁴, Gary H. Karpen^{13,65}, Eiko Kataoka⁶⁶, Peter D. Keightley⁵⁶, Pouya Kheradpour⁹, Ewen F. Kirkness⁵⁷, Leonardo B. Koerich³⁶, Karsten Kristiansen⁶⁷, Dave

Kudrna⁶⁸, Rob J. Kulathinal⁶⁹, Sudhir Kumar^{49,70}, Roberta Kwok⁸, Eric Lander¹⁰, Charles H. Langley²⁹, Richard Lapointe⁷¹, Brian P. Lazzaro⁷², So-Jeong Lee⁶⁸, Lisa Levesque⁴¹, Ruiqiang Li^{67,73}, Chiao-Feng Lin²⁰, Michael F. Lin^{9,10}, Kerstin Lindblad-Toh¹⁰, Ana Llopart⁴², Manyuan Long²³, Lloyd Low²⁷, Elena Lozovsky⁶⁹, Jian Lu²³, Meizhong Luo⁶⁸, Carlos A. Machado⁷, Wojciech Makalowski²⁰, Mar Marzocchi⁷⁴, Muneo Matsuda⁶⁶, Luciano Matzkin⁷, Bryant McAllister⁴², Carolyn S. McBride²⁹, Brendan McKernan⁷, Kevin McKernan⁴, Maria Mendez-Lago⁶¹, Patrick Minx⁴⁰, Michael U. Mollenhauer²⁰, Kristi Montooth¹⁷, Stephen M. Mount^{45,75}, Xu Mu²⁰, Eugene Myers⁷⁶, Barbara Negre⁷⁷, Stuart Newfield⁷⁰, Rasmus Nielsen⁷⁸, Mohamed A. F. Noor⁵², Patrick O'Grady⁷¹, Lior Pachter³⁸, Montserrat Papaceit¹⁹, Matthew J. Parisi⁴, Michael Parisi⁶, Leopold Parts⁹, Jakob S. Pedersen^{60,79}, Graziano Pesole⁸⁰, Adam M. Phillippy⁴⁵, Chris P. Ponting^{58,59}, Mihai Pop⁴⁵, Damiano Porcelli²⁶, Jeffrey R. Powell⁸¹, Sonja Prohaska^{49,82}, Kim Pruitt⁸³, Marta Puig⁷⁴, Hadi Quesneville⁸⁴, Kristipati Ravi Ram¹, David Rand¹⁷, Matthew D. Rasmussen⁹⁵, Laura K. Reed⁵³, Robert Reenan⁸⁵, Amy Reily⁴⁰, Karin A. Remington⁵⁷, Tania T. Rieger⁸⁶, Michael G. Ritchie²⁵, Charles Robin²⁷, Yu-Hui Rogers⁵⁷, Claudia Rohde⁸⁷, Julio Rozas¹⁹, Marc J. Rubinfeld⁴, Alfredo Ruiz⁷⁴, Susan Russo^{11,12}, Steven L. Salzberg⁴⁵, Alejandro Sanchez-Gracia^{19,88}, David J. Saranga⁴, Hajime Sato⁶⁶, Stephen W. Schaeffer²⁰, Michael C. Schatz⁴⁵, Todd Schlenke⁸⁹, Russell Schwartz²⁰, Carmen Segarra¹⁹, Rama S. Singh²⁴, Laura Sirot¹, Marina Sirot⁹¹, Nicholas B. Sisneros⁶⁸, Chris D. Smith^{65,92}, Temple F. Smith³⁰, John Spieth⁴⁰, Deborah E. Stage⁴⁷, Alexander Stark^{9,10}, Wolfgang Stephan⁹³, Robert L. Strausberg⁵⁷, Sebastian Strempe⁹³, David Sturgill⁶, Granger Sutton⁵⁷, Granger G. Sutton⁵⁷, Wei Tao⁴, Sarah Teichmann¹⁸, Yoshihiko N. Tobari⁹⁴, Yoshihiko Tomimura⁹⁵, Jason M. Toslas⁴, Vera L. S. Valente⁵¹, Eli Venter⁵⁷, J. Craig Venter⁵⁷, Saverio Vicario⁸¹, Filipe G. Vieira¹⁹, Albert J. Vilella^{19,96}, Alfredo Villasante¹⁶, Brian Walenz⁵⁷, Jun Wang^{67,73}, Marvin Wasserman⁹⁷, Thomas Watts⁷, Derek Wilson¹⁸, Richard K. Wilson⁴⁰, Rod A. Wing⁶⁸, Mariana F. Wolfner¹, Alex Wong¹, Gane Ka-Shu Wong^{73,98}, Chung-I Wu²³, Gabriel Wu³², Daisuke Yamamoto⁹⁹, Hsiao-Pei Yang¹, Shiaw-Pyng Yang⁴⁰, James A. Yorke¹⁰⁰, Kiyohito Yoshida¹⁰¹, Evgeny Zdobnov¹⁰², Peili Zhang^{11,12}, Yu Zhang⁶, Aleksey V. Zimin¹⁰⁰, Broad Institute Genome Sequencing Platform* & Broad Institute Whole Genome Assembly Team*

¹Department of Molecular Biology and Genetics, Cornell University, Ithaca, New York 14853, USA. ²Life Sciences Division, Lawrence Berkeley National Laboratory, Berkeley, California 94720, USA. ³Center for Integrative Genomics, Department of Molecular and Cell Biology, University of California at Berkeley, Berkeley, California 94720, USA. ⁴Agencourt Bioscience Corporation, Beverly, Massachusetts 01915, USA. ⁵Faculty of Life Sciences, University of Manchester, Manchester M13 9PT, UK. ⁶Laboratory of Cellular and Developmental Biology, National Institutes of Health, Bethesda, Maryland 20892, USA. ⁷Department of Ecology and Evolutionary Biology, University of Arizona, Tucson, Arizona 85721, USA. ⁸Department of Biology, Indiana University, Bloomington, Indiana 47405, USA. ⁹Computer Science and Artificial Intelligence Laboratory, Cambridge, Massachusetts 02139, USA. ¹⁰Broad Institute of MIT and Harvard, 7 Cambridge Center, Cambridge, Massachusetts 02142, USA. ¹¹Department of Molecular and Cellular Biology, Harvard University, Cambridge, Massachusetts 02138, USA. ¹²FlyBase, The Biological Laboratories, Harvard University, Cambridge, Massachusetts 02138, USA. ¹³Department of Molecular and Cell Biology, University of California at Berkeley, Berkeley, California 94720, USA. ¹⁴Biophysics Graduate Group, University of California at Berkeley, Berkeley, California 94720, USA. ¹⁵Field of Ecology and Evolutionary Biology, Cornell University, Ithaca, New York 14853, USA. ¹⁶Centro de Biología Molecular Severo Ochoa, Universidad Autónoma de Madrid, Madrid 28049, Spain. ¹⁷Department of Ecology and Evolutionary Biology, Brown University, Providence, Rhode Island 02912, USA. ¹⁸Structural Studies Division, MRC Laboratory of Molecular Biology, Cambridge CB2 2QH, UK. ¹⁹Departament de Genètica, Universitat de Barcelona, Barcelona 08071, Spain. ²⁰Department of Biology, Pennsylvania State University, University Park, Pennsylvania 16802, USA. ²¹Department of Genetics, University of Georgia, Athens, Georgia 30602, USA. ²²Linnaeus Centre for Bioinformatics, Uppsala Universitet, Uppsala, SE-75124, Sweden. ²³Department of Ecology and Evolution, University of Chicago, Chicago, Illinois 60637, USA. ²⁴Department of Biology, McMaster University, Hamilton, Ontario, L8S 4K1, Canada. ²⁵School of Biology, University of St. Andrews, Fife KY16 9TH, UK. ²⁶Dipartimento di Genetica e Microbiologia dell'Università di Bari, Bari, 70126, Italy. ²⁷Department of Genetics, University of Melbourne, Melbourne 3010, Australia. ²⁸Computer Science Department, Stanford University, Stanford, California 94305, USA. ²⁹Section of Evolution and Ecology and Center for Population Biology, University of California at Davis, Davis, California 95616, USA. ³⁰BioMolecular Engineering Research Center, Boston University, Boston, Massachusetts 02215, USA. ³¹Research Group in Biomedical Informatics, Institut Municipal d'Investigació Mèdica, Universitat Pompeu Fabra, Barcelona 08003, Catalonia, Spain. ³²Department of Bioengineering, University of California at Berkeley, Berkeley, California 94720, USA. ³³Laboratory for Computational Genomics, Washington University, St. Louis, Missouri 63108, USA. ³⁴Animal and Plant Sciences, The University of Sheffield, Sheffield S10 2TN, UK. ³⁵Department of Biology, Syracuse University, Syracuse, New York 13244, USA. ³⁶Departamento de Genética, Universidade Federal do Rio de Janeiro, Rio de Janeiro 21944-970, Brazil. ³⁷Tucson Stock Center, Tucson, Arizona 85721, USA. ³⁸Department of Mathematics, University of California at Berkeley, Berkeley, California 94720, USA. ³⁹Genome Center, University of California at Davis, Davis, California 95616, USA. ⁴⁰Genome Sequencing Center, Washington University School of Medicine, St. Louis, Missouri 63108, USA. ⁴¹Department of Biology, University of Winnipeg, Winnipeg, Manitoba R3B 2E9, Canada. ⁴²Department of Biological Sciences, University of Iowa, Iowa City, Iowa 52242, USA. ⁴³School of Informatics, Indiana University, Bloomington, Indiana 47405, USA. ⁴⁴Wellcome Trust Sanger Institute, Wellcome Trust Genome Campus, Hinxton, Cambridge CB10 1SA, UK. ⁴⁵Center for Bioinformatics and Computational Biology,

University of Maryland, College Park, Maryland 20742, USA. ⁴⁶Department of Biological Sciences, Illinois State University, Normal, Illinois 61790, USA. ⁴⁷Department of Biology, University of Rochester, Rochester, New York 14627, USA. ⁴⁸Bee Research Lab, USDA-ARS, Beltsville, Maryland 20705, USA. ⁴⁹Center for Evolutionary Functional Genomics, Biodesign Institute, Arizona State University, Tempe, Arizona 85287, USA. ⁵⁰Department of Computer Science, University of Leipzig, Leipzig 04107, Germany. ⁵¹Departamento de Genética, Universidade Federal do Rio Grande do Sul, Porto Alegre/RS 68011, Brazil. ⁵²Department of Biology, Duke University, Durham, New Carolina 27708, USA. ⁵³Department of Genetics, North Carolina State University, Raleigh, North Carolina 27695, USA. ⁵⁴Health Center, University of Connecticut, Farmington, Connecticut 06030, USA. ⁵⁵Center of Genomic Regulation, Barcelona 8003, Catalonia, Spain. ⁵⁶Institute of Evolutionary Biology, University of Edinburgh, Edinburgh EH9 3JT, UK. ⁵⁷J. Craig Venter Institute, Rockville, Maryland 20850, USA. ⁵⁸MRC Functional Genetics Unit, University of Oxford, Oxford OX1 3QX, UK. ⁵⁹Department of Physiology, Anatomy and Genetics, University of Oxford, Oxford OX1 3QX, UK. ⁶⁰Center for Biomolecular Science and Engineering, University of California at Santa Cruz, Santa Cruz, California 95064, USA. ⁶¹Department of Human Genetics, University of Chicago, Chicago, Illinois 60637, USA. ⁶²Umeå Center for Molecular Pathogenesis, Umeå University, Umeå SE-90187, Sweden. ⁶³Department of Biology and Carolina Center for Genome Sciences, The University of North Carolina at Chapel Hill, Chapel Hill, North Carolina 27599, USA. ⁶⁴Institute of Zoology, Regent's Park, London NW1 4RY, UK. ⁶⁵Drosophila Heterochromatin Genome Project, Department of Genome and Computational Biology, Lawrence Berkeley National Laboratory, Berkeley, California 94720, USA. ⁶⁶Kyoto University, School of Medicine, Mitaka, Tokyo 181-8611, Japan. ⁶⁷Department of Biochemistry and Molecular Biology, University of Southern Denmark, Odense M DK-5230, Denmark. ⁶⁸Arizona Genomics Institute, Department of Plant Sciences and BIO5, University of Arizona, Tucson, Arizona 85721, USA. ⁶⁹Department of Organismic and Evolutionary Biology, Harvard University, Cambridge, Massachusetts 02138, USA. ⁷⁰School of Life Sciences, Arizona State University, Tempe, Arizona 85287, USA. ⁷¹Department of Environmental Science, Policy and Management, University of California at Berkeley, Berkeley, California 94720, USA. ⁷²Department of Entomology, Cornell University, Ithaca, New York 14853, USA. ⁷³Beijing Genomics Institute at Shenzhen, Shenzhen 518083, China. ⁷⁴Departament Genètica i Microbiologia, Universitat Autònoma de Barcelona, Bellaterra 08193, Spain. ⁷⁵Department of Cell Biology and Molecular Genetics, University of Maryland, College Park, Maryland 20742, USA. ⁷⁶Janelia Farm Research Campus, Howard Hughes Medical Institute, Ashburn, Virginia 20147-2408, USA. ⁷⁷Department of Zoology, University of Cambridge, Cambridge, CB2 3EJ, UK. ⁷⁸Institute of Biology, University of Copenhagen, DK-2100 Copenhagen Ø, Denmark. ⁷⁹Bioinformatics Centre, Department of Molecular Biology, University of Copenhagen, DK-2200 Copenhagen N, Denmark. ⁸⁰Dipartimento di Biochimica e Biologia Molecolare, Università di Bari and Istituto Tecnologie Biomediche del Consiglio Nazionale delle Ricerche, Bari 70126, Italy. ⁸¹Department of Ecology and Evolutionary Biology, Yale University, New Haven, Connecticut 06520, USA. ⁸²Department of Biomedical Informatics, Arizona State University, Tempe, Arizona 85287, USA. ⁸³National Center for Biotechnology Information, National Institutes of Health, Bethesda, Maryland 20894, USA. ⁸⁴Bioinformatics and Genomics Laboratory, Institut Jacques Monod, Paris, 75251, France. ⁸⁵Department of Molecular Biology, Cell Biology and Biochemistry, Brown University, Providence, Rhode Island 02912, USA. ⁸⁶Departamento de Genética, Centro de Ciências Biológicas, Universidade Federal de Pernambuco, Recife/PE 68011, Brazil. ⁸⁷Centro Acadêmico de Vitória, Universidade Federal de Pernambuco, Vitória de Santo Antão/PE, Brazil. ⁸⁸Cajal Institute, CSIC, Madrid 28002, Spain. ⁸⁹Department of Biology, Emory University, Atlanta, Georgia 30322, USA. ⁹⁰Department of Biological Sciences, Carnegie Mellon University, Pittsburgh, Pennsylvania 15213, USA. ⁹¹Biomedical Informatics, Stanford University, Stanford, California 94305, USA. ⁹²Department of Biology, San Francisco State University, San Francisco, California 94132, USA. ⁹³Department of Biology, University of Munich, 82152 Planegg-Martinsried, Germany. ⁹⁴Institute of Evolutionary Biology, Setagaya-ku, Tokyo 158-0098, Japan. ⁹⁵Shiba Gakuken, Minato-ku, Tokyo 105-0011, Japan. ⁹⁶European Bioinformatics Institute, Hinxton, CB10 1SD, UK. ⁹⁷Department of Biology, City University of New York at Queens, Flushing, New York 11367, USA. ⁹⁸Department of Biological Sciences and Department of Medicine, University of Alberta, Edmonton, Alberta T6G 2E9, Canada. ⁹⁹Department of Developmental Biology and Neurosciences, Tohoku University, Sendai 980-8578, Japan. ¹⁰⁰Institute for Physical Science and Technology, University of Maryland, College Park, Maryland 20742, USA. ¹⁰¹Hokkaido University, EESBIO, Sapporo, Hokkaido 060-0810, Japan. ¹⁰²Faculty of Medicine, Université de Genève, Geneva CH-1211, Switzerland.

*Broad Institute Genome Sequencing Platform Jennifer Baldwin¹⁰, Amr Abdouellail¹⁰, Jamal Abdulkadir¹⁰, Adal Abebe¹⁰, Briki Abera¹⁰, Justin Abreu¹⁰, St Christophe Acer¹⁰, Lynne Aftuck¹⁰, Allen Alexander¹⁰, Peter An¹⁰, Erica Anderson¹⁰, Scott Anderson¹⁰, Harindra Arachi¹⁰, Marc Azer¹⁰, Pasang Bachantsang¹⁰, Andrew Barry¹⁰, Tashi Bayul¹⁰, Aaron Berlin¹⁰, Daniel Bessette¹⁰, Toby Bloom¹⁰, Jason Blye¹⁰, Leonid Boguslavskiy¹⁰, Claude Bonnet¹⁰, Boris Boukhgalter¹⁰, Imane Bourzgui¹⁰, Adam Brown¹⁰, Patrick Cahill¹⁰, Sheridon Channer¹⁰, Yama Cheshatsang¹⁰, Lisa Chuda¹⁰, Mieke Citroen¹⁰, Alville Collymore¹⁰, Patrick Cooke¹⁰, Maura Costello¹⁰, Katie D'Aco¹⁰, Riza Daza¹⁰, Georgius De Haan¹⁰, Stuart DeGray¹⁰, Christina DeMaso¹⁰, Norbu Dhargay¹⁰, Kimberly Dooley¹⁰, Erin Dooley¹⁰, Misselle Doricent¹⁰, Passang Dorje¹⁰, Kunsang Dorjee¹⁰, Alan Dupes¹⁰, Richard Elong¹⁰, Jill Falk¹⁰, Abderrahim Farina¹⁰, Susan Faro¹⁰, Diallo Ferguson¹⁰, Sheila Fisher¹⁰, Chelsea D. Foley¹⁰, Alicia Franke¹⁰, Dennis Friedrich¹⁰, Loryn Gadbois¹⁰, Gary Gearin¹⁰, Christina R. Gearin¹⁰, Georgia Giannoukos¹⁰, Tina Goode¹⁰, Joseph Graham¹⁰, Edward Grandbois¹⁰, Sharleen Grewal¹⁰, Kunsang Gyaltsen¹⁰, Nabil Hafez¹⁰, Birhane Hagos¹⁰, Jennifer Hall¹⁰, Charlotte Henson¹⁰, Andrew Hollinger¹⁰, Tracey Honan¹⁰, Monika D. Huard¹⁰, Leanne Hughes¹⁰, Brian Hurhula¹⁰, M. Erii Husby¹⁰, Asha Kamat¹⁰, Ben Kanga¹⁰,

Seva Kashin¹⁰, Dmitry Khazanovich¹⁰, Peter Kisner¹⁰, Krista Lance¹⁰, Marcia Lara¹⁰, William Lee¹⁰, Niall Lennon¹⁰, Frances Letendre¹⁰, Rosie LeVine¹⁰, Alex Lipovsky¹⁰, Xiaohong Liu¹⁰, Jinlei Liu¹⁰, Shangtao Liu¹⁰, Tashi Lokyitsang¹⁰, Yeshe Lokyitsang¹⁰, Rakela Lubonja¹⁰, Annie Lui¹⁰, Pen MacDonald¹⁰, Vasilisa Magnisalis¹⁰, Kebede Maru¹⁰, Charles Matthews¹⁰, William McCusker¹⁰, Susan McDonough¹⁰, Teena Mehta¹⁰, James Meldrim¹⁰, Louis Meneus¹⁰, Oana Mihai¹⁰, Atanas Mihalev¹⁰, Tanya Mihova¹⁰, Rachel Mittelman¹⁰, Valentine Mlenga¹⁰, Anna Montmayeur¹⁰, Leonidas Mulrain¹⁰, Adam Navidi¹⁰, Jerome Naylor¹⁰, Tamrat Negash¹⁰, Thu Nguyen¹⁰, Nga Nguyen¹⁰, Robert Nicol¹⁰, Choe Norbu¹⁰, Nyima Norbu¹⁰, Nathaniel Novod¹⁰, Barry O'Neill¹⁰, Sahal Osman¹⁰, Eva Markiewicz¹⁰, Otero L. Oyono¹⁰, Christopher Patti¹⁰, Pema Phunkhang¹⁰, Fritz Pierre¹⁰, Margaret Priest¹⁰, Sujaa Raghuraman¹⁰, Filip Rege¹⁰, Rebecca Reyes¹⁰,

Cecil Rise¹⁰, Peter Rogov¹⁰, Keenan Ross¹⁰, Elizabeth Ryan¹⁰, Sampath Settipalli¹⁰, Terry Shea¹⁰, Ngawang Sherpa¹⁰, Lu Shi¹⁰, Diana Shih¹⁰, Todd Sparrow¹⁰, Jessica Spaulding¹⁰, John Stalker¹⁰, Nicole Stange-Thomann¹⁰, Sharon Stavropoulos¹⁰, Catherine Stone¹⁰, Christopher Strader¹⁰, Senait Tesfaye¹⁰, Talene Thomson¹⁰, Yama Thoulutsang¹⁰, Dawa Thoulutsang¹⁰, Kerri Topham¹⁰, Ira Topping¹⁰, Tsamla Tsamla¹⁰, Helen Vassiliev¹⁰, Andy Vo¹⁰, Tsering Wangchuk¹⁰, Tsering Wangdi¹⁰, Michael Weiand¹⁰, Jane Wilkinson¹⁰, Adam Wilson¹⁰, Shailendra Yadav¹⁰, Geneva Young¹⁰, Qing Yu¹⁰, Lisa Zembek¹⁰, Danni Zhong¹⁰, Andrew Zimmer¹⁰ & Zac Zwirko¹⁰ **Broad Institute Whole Genome Assembly Team** David B. Jaffe¹⁰, Pablo Alvarez¹⁰, Will Brockman¹⁰, Jonathan Butler¹⁰, CheeWhye Chin¹⁰, Sante Gnerre¹⁰, Manfred Grabherr¹⁰, Michael Kleber¹⁰, Evan Mauceli¹⁰ & Iain MacCallum¹⁰

Discovery of functional elements in 12 *Drosophila* genomes using evolutionary signatures

Alexander Stark^{1,2*}, Michael F. Lin^{1,2*}, Pouya Kheradpour^{2*}, Jakob S. Pedersen^{3,4*}, Leopold Parts^{5,6}, Joseph W. Carlson⁷, Madeline A. Crosby⁸, Matthew D. Rasmussen², Sushmita Roy⁹, Ameya N. Deoras², J. Graham Ruby^{10,11}, Julius Brenneke¹², Harvard FlyBase curators[†], Berkeley *Drosophila* Genome Project[†], Emily Hodges¹², Angie S. Hinrichs⁴, Anat Caspi¹³, Benedict Paten^{4,5,14}, Seung-Won Park¹⁵, Mira V. Han¹⁶, Morgan L. Maeder¹⁷, Benjamin J. Polansky¹⁷, Bryanne E. Robson¹⁷, Stein Aerts^{18,19}, Jacques van Helden²⁰, Bassem Hassan^{18,19}, Donald G. Gilbert²¹, Deborah A. Eastman¹⁷, Michael Rice²², Michael Weir²³, Matthew W. Hahn¹⁶, Yongkyu Park¹⁵, Colin N. Dewey²⁴, Lior Pachter^{25,26}, W. James Kent⁴, David Haussler⁴, Eric C. Lai²⁷, David P. Bartel^{10,11}, Gregory J. Hannon¹², Thomas C. Kaufman²¹, Michael B. Eisen^{28,29}, Andrew G. Clark³⁰, Douglas Smith³¹, Susan E. Celniker⁷, William M. Gelbart^{8,32} & Manolis Kellis^{1,2}

Sequencing of multiple related species followed by comparative genomics analysis constitutes a powerful approach for the systematic understanding of any genome. Here, we use the genomes of 12 *Drosophila* species for the *de novo* discovery of functional elements in the fly. Each type of functional element shows characteristic patterns of change, or 'evolutionary signatures', dictated by its precise selective constraints. Such signatures enable recognition of new protein-coding genes and exons, spurious and incorrect gene annotations, and numerous unusual gene structures, including abundant stop-codon readthrough. Similarly, we predict non-protein-coding RNA genes and structures, and new microRNA (miRNA) genes. We provide evidence of miRNA processing and functionality from both hairpin arms and both DNA strands. We identify several classes of pre- and post-transcriptional regulatory motifs, and predict individual motif instances with high confidence. We also study how discovery power scales with the divergence and number of species compared, and we provide general guidelines for comparative studies.

The sequencing of the human genome and the genomes of dozens of other metazoan species has intensified the need for systematic methods to extract biological information directly from DNA sequence. Comparative genomics has emerged as a powerful methodology for this endeavour^{1,2}. Comparison of few (two–four) closely related genomes has proven successful for the discovery of protein-coding genes^{3–5}, RNA genes^{6,7}, miRNA genes^{8–11} and catalogues of regulatory elements^{3,4,12–14}. The resolution and discovery power of these studies

should increase with the number of genomes^{15–20}, in principle enabling the systematic discovery of all conserved functional elements.

The fruitfly *Drosophila melanogaster* is an ideal system for developing and evaluating comparative genomics methodologies. Over the past century, *Drosophila* has been a pioneering model in which many of the basic principles governing animal development and population biology were established²¹. In the past decade, the genome sequence of *D. melanogaster* provided one of the first systematic views

¹The Broad Institute, Massachusetts Institute of Technology and Harvard University, Cambridge, Massachusetts 02140, USA. ²Computer Science and Artificial Intelligence Laboratory, MIT, Cambridge, Massachusetts 02139, USA. ³The Bioinformatics Centre, Department of Molecular Biology, University of Copenhagen, Ole Maaloes Vej 5, 2200 Copenhagen N, Denmark. ⁴Center for Biomolecular Science and Engineering, University of California, Santa Cruz, California 95064, USA. ⁵Wellcome Trust Sanger Institute, Wellcome Trust Genome Campus, Hinxton, Cambridge CB10 1SA, UK. ⁶Institute of Computer Science, University of Tartu, Estonia. ⁷BDGP, LBNL, 1 Cyclotron Road MS 64-0119, Berkeley, California 94720, USA. ⁸FlyBase, The Biological Laboratories, Harvard University, 16 Divinity Avenue, Cambridge, Massachusetts 02138, USA. ⁹Department of Computer Science, University of New Mexico, Albuquerque, New Mexico 87131, USA. ¹⁰Department of Biology, MIT, Cambridge, Massachusetts 02139, USA. ¹¹Whitehead Institute, Cambridge, Massachusetts 02142, USA. ¹²Cold Spring Harbor Laboratory, Watson School of Biological Sciences, 1 Bungtown Road, Cold Spring Harbor, New York 11724, USA. ¹³University of California, San Francisco/University of California, Berkeley Joint Graduate Group in Bioengineering, Berkeley, California 97210, USA. ¹⁴EMBL Nucleotide Sequence Submissions, European Bioinformatics Institute, Wellcome Trust Genome Campus, Hinxton, Cambridge CB10 1SD, UK. ¹⁵Department of Cell Biology and Molecular Medicine, G-629, MSB, 185 South Orange Avenue, UMDNJ-New Jersey Medical School, Newark, New Jersey 07103, USA. ¹⁶Department of Biology and School of Informatics, Indiana University, Indiana 47405, USA. ¹⁷Department of Biology, Connecticut College, New London, Connecticut 06320, USA. ¹⁸Laboratory of Neurogenetics, Department of Molecular and Developmental Genetics, VIB, 3000 Leuven, Belgium. ¹⁹Department of Human Genetics, K. U. Leuven School of Medicine, 3000 Leuven, Belgium. ²⁰Department de Biologie Moléculaire, Université Libre de Bruxelles, 1050 Brussels, Belgium. ²¹Department of Biology, Indiana University, Bloomington, Indiana 47405, USA. ²²Department of Mathematics and Computer Science, Wesleyan University, Middletown, Connecticut 06459, USA. ²³Biology Department, Wesleyan University Middletown, Connecticut 06459, USA. ²⁴Department of Biostatistics and Medical Informatics, University of Wisconsin-Madison, Madison, Wisconsin 53706, USA. ²⁵Department of Mathematics, University of California at Berkeley, Berkeley, California 94720, USA. ²⁶Department of Computer Science, University of California at Berkeley, Berkeley, California 94720, USA. ²⁷Department of Developmental Biology, Memorial Sloan-Kettering Cancer Center, New York, New York 10021, USA. ²⁸Graduate Group in Biophysics, Department of Molecular and Cell Biology, and Center for Integrative Genomics, University of California, Berkeley, California 94720, USA. ²⁹Lawrence Berkeley National Laboratory, Life Sciences Division, Berkeley, California 94720, USA. ³⁰Department of Molecular Biology and Genetics, Cornell University, Ithaca, New York 14853, USA. ³¹Agencourt Bioscience Corporation, 500 Cummings Center, Suite 2450, Beverly, Massachusetts 01915, USA. ³²The Department of Molecular and Cellular Biology, Harvard University, Cambridge, Massachusetts 02138, USA.

*These authors contributed equally to this work.

†Lists of participants and affiliations appear at the end of the paper.

of a metazoan genome²², and the ongoing effort by the FlyBase and Berkeley Drosophila Genome Project (BDGP) groups established a systematic high-quality genome annotation^{23–25}. Moreover, the fruit-fly benefits from extensive experimental resources^{26–28}, which enable novel functional elements to be systematically tested and used in the evaluation of genetic screens^{29,30}.

The fly research community has sequenced, assembled and annotated the genomes of 12 *Drosophila* species^{22,31,32} at a range of evolutionary distances from *D. melanogaster* (Fig. 1a, b). The analysis of these genomes was organized around two complementary aims. The first, described in an accompanying paper³², was to understand the evolution of genes and chromosomes on the *Drosophila* phylogeny, and how it relates to speciation and adaptation. The second goal, described here, was to develop general comparative methodologies to discover and refine functional elements in *D. melanogaster* using the 12 genomes, and to investigate the scaling of discovery power and its implications for studies in vertebrates (Fig. 1c).

Here, we report genome-wide alignments of the 12 species (Supplementary Information 1), and the systematic discovery of euchromatic functional elements in the *D. melanogaster* genome. We predict and refine thousands of protein-coding exons, RNA genes and structures, miRNAs, pre- and post-transcriptional regulatory motifs and regulatory targets. We validate many of these elements using complementary DNA (cDNA) sequencing, human curation, small RNA sequencing, and correlation with experimentally supported transcription factor and miRNA targets. In addition, our analysis leads to several specific biological findings, listed below.

● We predict 123 novel polycistronic transcripts, 149 genes with apparent stop-codon readthrough and several candidate programmed

frameshifts, with potential roles in regulation, localization and function of the corresponding protein products.

● We make available the first systematic prediction of general RNA genes and structures (non-coding RNAs (ncRNAs)) in *Drosophila*, including several structures probably involved in translational regulation and adenosine-to-inosine RNA editing (A-to-I editing).

● We present comparative and experimental evidence that some miRNA loci yield multiple functional products, from both hairpin arms or from both DNA strands, thereby increasing the versatility and complexity of miRNA-mediated regulation.

● We provide further comparative evidence for miRNA targeting in protein-coding exons.

● We report an initial network of pre- and post-transcriptional regulatory targets in *Drosophila* on the basis of individual high-confidence motif occurrences.

Comparative genomics and evolutionary signatures. Although multiple closely related genomes provide sufficient neutral divergence for recognition of functional regions in stretches of highly conserved nucleotides^{16,17,33}, measures of nucleotide conservation alone do not distinguish between different types of functional elements. Moreover, functional elements that tolerate abundant 'silent' mutations, such as protein-coding exons and many regulatory motifs, might not be detected when searching on the basis of strong nucleotide conservation.

Across many genomes spanning larger evolutionary distances, the information in the patterns of sequence change reveals evolutionary signatures (Fig. 2) that can be used for systematic genome annotation. Protein-coding regions show highly constrained codon substitution frequencies³⁴ and insertions and deletions that are heavily

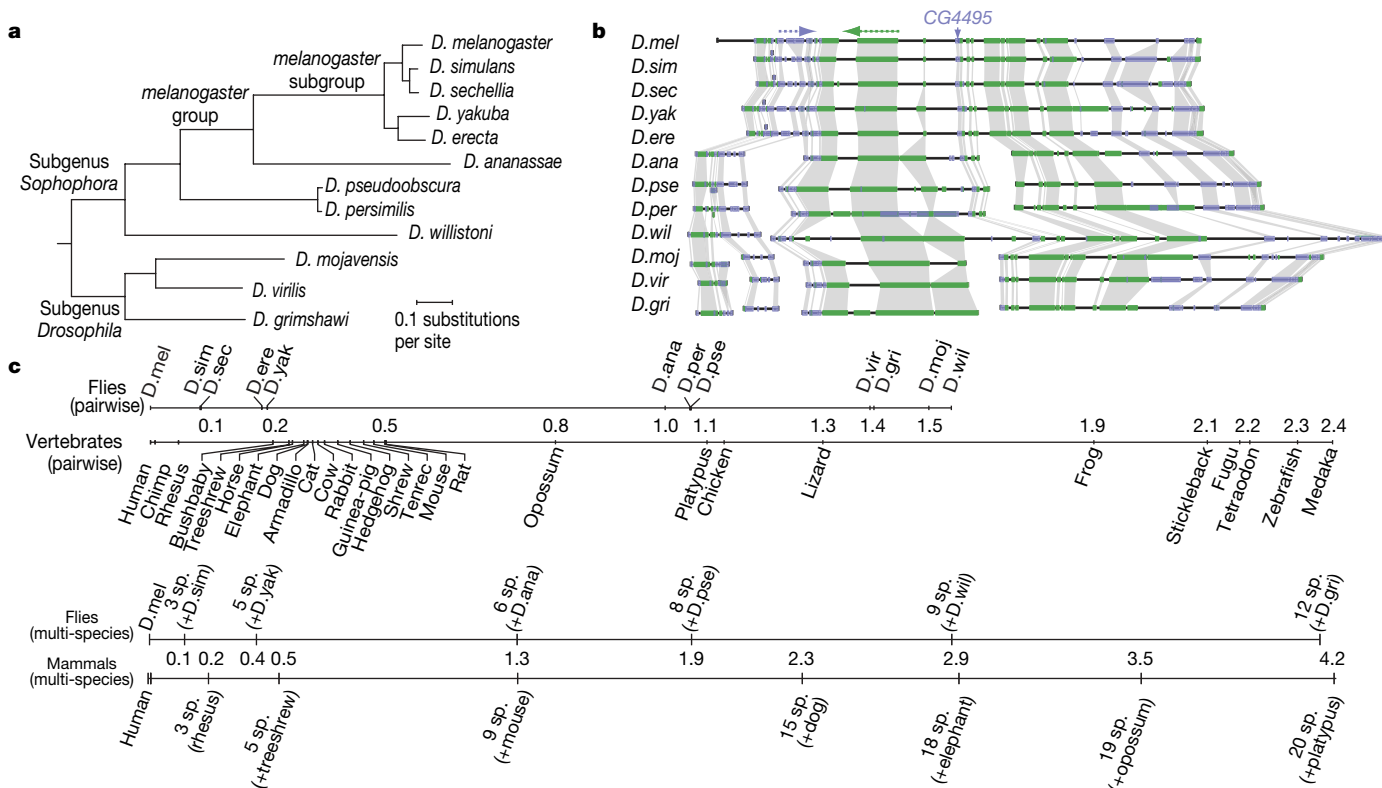


Figure 1 | Phylogeny and alignment of 12 *Drosophila* species.

a, Phylogenetic tree relating the 12 *Drosophila* species, estimated from fourfold degenerate sites (Supplementary Methods 1). The 12 species span a total branch length of 4.13 substitutions per neutral site. **b**, Gene order conservation for a 0.45-Mb region of chromosome 2L centred on CG4495, for which we predict a new exon (Fig. 3a), and spanning 35 genes. Colour represents the direction of transcription. Boxes represent full gene models.

Individual exons and introns are not shown. **c**, Comparison of evolutionary distances spanned by fly and vertebrate trees. Pairwise and multi-species distances (in substitutions per fourfold degenerate site) are shown from *D. melanogaster* and from human as reference genomes. Note that species with longer branches (for example, mouse) show higher pairwise distances, not always reflecting the order of divergence. Multi-species distances include all species within a phylogenetic clade.

biased to be multiples of three³ (Fig. 2a). RNA genes and structures tolerate substitutions that preserve base pairing^{35,36} (Fig. 2b). MicroRNA hairpins show a characteristic conservation profile with high conservation in the stem and mutations in loop regions^{10,11} (Fig. 2c). Finally, regulatory motifs are marked by high levels of genome-wide conservation^{3,4,12–14}, and post-transcriptional motifs show strand-biased conservation¹² (Fig. 2d, e).

We find that these signatures can be much more precise for genome annotation than the overall level of nucleotide conservation (for example, Fig. 3a).

Revisiting the protein-coding gene catalogue

The annotation of protein-coding genes remains difficult in metazoan genomes owing to short exons and complex gene structures

with abundant alternative splicing. Comparative information has improved computational gene predictors⁵, but their accuracy still falls far short of well-studied gene catalogues such as the FlyBase annotation, which combines computational gene prediction³⁷, high-throughput experimental data^{38–42} and extensive manual curation²³. Recognizing this, we set out not only to produce an independent computational annotation of protein-coding genes in the fly genome, but also to assess and refine its already high-quality annotations⁴³.

Our analyses of *D. melanogaster* coding genes are based on two independent evolutionary signatures unique to protein-coding regions (Fig. 2a): (1) reading frame conservation (RFC)³, which observes the tendency of nucleotide insertions and deletions to preserve the codon reading frame; and (2) codon substitution frequencies

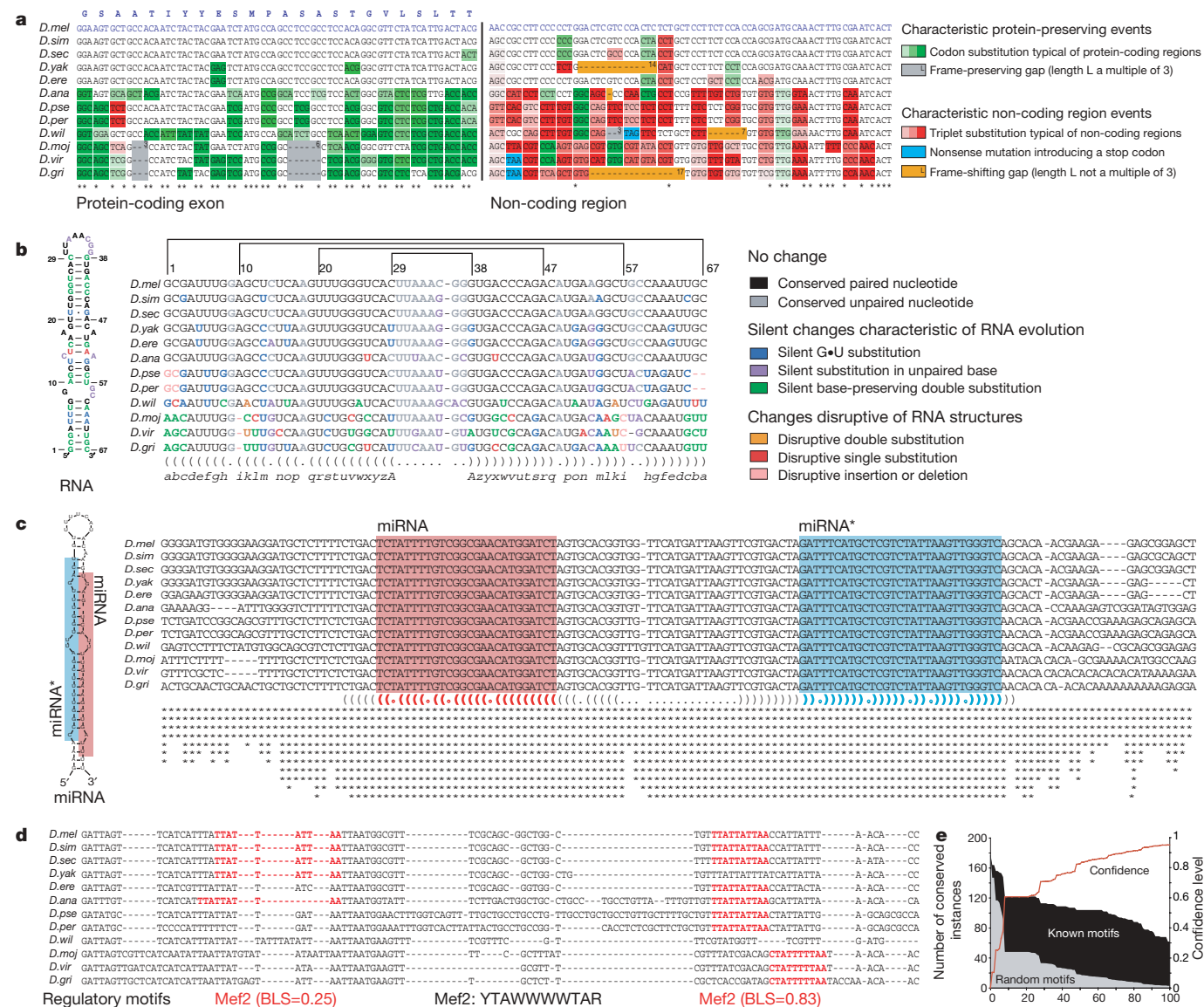


Figure 2 | Distinct evolutionary signatures for diverse classes of functional elements. **a**, Protein-coding genes tolerate mutations that preserve the amino-acid translation, leading to abundant conservative codon substitutions (green). Insertions and deletions are largely constrained to be a multiple of three (grey). In contrast, non-coding regions show abundant non-conservative triplet substitutions (red), nonsense mutations (blue) and frame-shifting insertions and deletions (orange). **b**, RNA genes tolerate mutations that preserve the secondary structure (for example, single substitutions involving G•U base pairs and compensatory changes) and exclude structure-disrupting mutations. Matching parentheses and matching letters of the alphabet indicate paired bases. **c**, MicroRNA genes, in

contrast, generally do not show changes in stem regions, but tolerate substitutions in loop regions and flanking unpaired regions, leading to a distinctive conservation profile. Asterisks denote the number of informant species matching the *melanogaster* sequence at each position. **d**, Regulatory motifs tolerate local movement and nucleotide substitutions consistent with their degeneracy patterns, and show increased conservation across the phylogenetic tree, measured as the branch length score (BLS; Supplementary Methods 5a). **e**, Increasing BLS thresholds select for instances of known motifs (black) at increasing confidence (red), as the number of conserved instances of control motifs (grey) drops significantly faster.

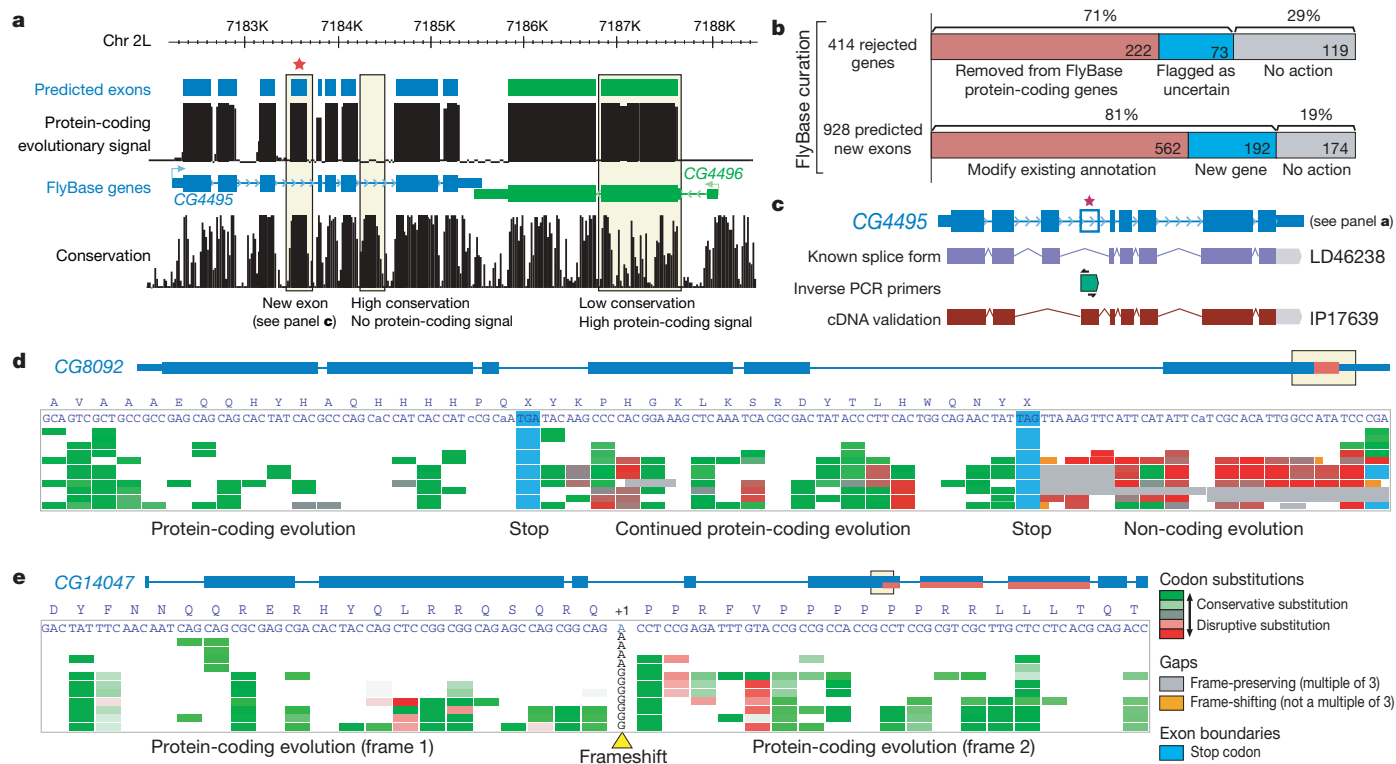


Figure 3 | Revisiting the protein-coding gene catalogue and revealing unusual gene structures. **a**, Protein-coding evolutionary signatures correlate with annotated protein-coding exons more precisely than the overall conservation level (phastCons track³³), for example excluding highly conserved yet non-coding elements. Asterisk denotes new predicted exon, which we validate with cDNA sequencing (see panel **c**). The height of the black tracks indicates protein-coding potential according to evolutionary signatures (top) and overall sequence conservation (bottom). Blue and green boxes indicate predicted coding exons (top) and the current FlyBase annotation (bottom). The region shown represents the central 6 kb of Fig. 1b,

rendered by the UCSC genome browser¹²⁶. **b**, Results of FlyBase curation of 414 genes rejected by evolutionary signatures (Table 1), and 928 predicted new exons. **c**, Experimental validation of predicted new exon from panel **a**. Inverse PCR with primers in the predicted exon (green) results in a full-length cDNA clone, confirming the predicted exon and revealing a new alternative splice form for CG4495. **d**, Protein-coding evolution continues downstream of a conserved stop codon in 149 genes, suggesting translational readthrough. **e**, Codon-based evolutionary signatures (CSF score) abruptly shift from one reading frame to another within a protein-coding exon, suggesting a conserved, 'programmed' frameshift.

(CSF, see Supplementary Methods 2a), which observes mutational biases towards synonymous codon substitutions and conservative amino acid changes, similar to the non-synonymous/synonymous substitution ratio K_A/K_S ³⁴ and other methods^{44–46}.

Assessing and refining existing gene annotations. We first assessed the 13,733 euchromatic genes in FlyBase⁴⁷ release 4.3. Using the above measures, we defined tests that 'confirmed' genes supported by the evolutionary evidence, 'rejected' genes inconsistent with protein-coding selection, or 'abstained' for genes that were not aligned or with ambiguous comparative evidence (Supplementary Methods 2a). Of the 4,711 genes with descriptive names, we confirmed 97%, rejected 1% and abstained for 2%, whereas the same criteria applied to 15,000 random non-coding regions ≥ 300 nucleotides rejected 99% of candidates and confirmed virtually none (Table 1). Together, these results illustrate the high sensitivity and specificity of our criteria.

Applying the same criteria to the 9,022 genes lacking a descriptive name (genes designated only by a CG identifier, referred to hereafter as CGid-only genes), our tests accepted 87%, rejected 5% (414 genes) and abstained for 8%. This provides strong evidence that most CGid-only genes encode proteins, but also suggests that they may be less

constrained^{20,32} and/or may include incorrect annotations. Indeed, on manual review, 222 (54%) of the 414 rejected CGid-only genes were re-categorized as non-protein-coding or deleted (of which 55 were due to genomically primed clones), 73 (18%) were flagged as being of uncertain quality, and the remaining 119 (29%) were kept unchanged (Fig. 3b). Some of these are probably rapidly evolving protein-coding genes, but others may also prove to be non-protein-coding genes or spurious; in fact, none of these had any functional gene ontology (GO) annotation⁴⁸.

In addition, we proposed specific corrections and adjustments to hundreds of existing transcript models, including translation start site adjustments (Supplementary Fig. 2b), alternative splice boundaries (Supplementary Fig. 2b), recent nonsense mutations (Supplementary Fig. 2c) and alternative translational reading frames⁴³.

Identifying new genes and exons. To predict new protein-coding exons, we integrated our metrics into a probabilistic algorithm that determines an optimal segmentation of the genome into protein-coding and non-coding regions (Fig. 3a) on the basis of whole-genome sequence alignments of the 12 fly species (Supplementary

Table 1 | Assessment of FlyBase euchromatic protein-coding gene annotations

Regions evaluated	Total	Confirm	Abstain	Reject*
Named genes	4,711	4,566 (96.9%)	105 (2.2%)	40 (0.8%)
CGid-only genes	9,022	7,879 (87.3%)	729 (8.1%)	414 (4.6%)
Non-coding regions†	15,564	3 (0.0%)	131 (0.8%)	15,430 (99.1%)

* A minority of rejected genes are false rejections; see Fig. 3b and text for details.

† Regions ≥ 300 nucleotides in length randomly chosen from the non-coding part of the genome (see Supplementary Methods 2a).

Methods 2a). Our genome-wide search predicted 1,193 new protein-coding exons, mostly in euchromatic regions annotated as intergenic (43%), intronic (26%), or 5'/3' untranslated region (UTR; 23%) in FlyBase annotation release 4.3.

We manually reviewed 928 of these predictions according to FlyBase standards²³ (Supplementary Methods 2a), leading to 142 new gene models (incorporating 192 predictions) and 438 revised gene models (incorporating 562 predictions) (Fig. 3b). In parallel, we tested 184 predictions (126 intergenic, 58 intronic) by directed cDNA sequencing using inverse polymerase chain reaction (inverse PCR) of circularized full-length clones^{49–51} (Fig. 3c), which validated 120 targeted predictions (65%) and an additional 42 predictions not directly targeted but contained within the recovered transcripts. Predictions in intergenic regions yielded 88 full-length cDNAs, providing evidence for 50 new genes and modification of 39 gene models. Predictions within introns of existing annotations yielded 32 full-length cDNAs, of which only 18 (56%) represent new splice variants of the surrounding gene, whereas the remaining 14 revealed nested or interleaved gene structures. This provides additional evidence that such complex gene structures are not rare in *Drosophila*²³.

Overall, 83% of the 948 predicted exons that we assessed by manual curation or cDNA sequencing were incorporated into FlyBase, resulting in 150 new genes and modifications to hundreds of existing gene models. Finally, the 245 predictions that we did not assess were in non-coding regions of existing transcript models, or were already included in FlyBase independent of our study. In an independent analysis⁵², we predicted 98 new genes on the basis of inferred homology to predicted genes in the informant species³², of which 63% matched the above predictions.

Discovering unusual features of protein-coding genes. Our analysis also predicted an abundance of unusual protein-coding genes that call for follow-up experimental investigation. First, we found open reading frames with clear protein-coding signatures and conserved start and stop sites on the transcribed strand of annotated UTRs, indicative of polycistronic transcripts^{23,53,54}. These include 73% of 115 annotated dicistronic transcripts and 135 new candidate cistrons of 123 genes (Supplementary Fig. 2b).

Second, we predicted that 149 genes undergo stop codon readthrough, with protein-coding selection continuing past a deeply conserved stop codon (Fig. 3d), in some cases for hundreds of amino acids. It is unlikely that these genes are selenoproteins, as they appear to lack SECIS elements

that direct selenocysteine recoding^{55–58}. Other mechanisms may instead be at work, such as regulation of ribosomal release factors⁵⁹, A-to-I editing^{39,60,61}, alternative splicing, or other less-characterized mechanisms⁶². In fact, these genes are significantly enriched in neuronal proteins ($P = 10^{-4}$), which frequently undergo A-to-I editing⁶³.

Third, we found four genes in which CSF signatures abruptly shift from one reading frame to another in the absence of nearby intron–exon boundaries or insertions and deletions (Fig. 3e). These are suggestive of conserved ‘programmed’ frameshifts⁶⁴, which are thought to be rare in eukaryotes.

Overall, our results affected over 10% of protein-coding genes, and will be available in future releases of FlyBase. They also suggest that several types of unusual protein-coding gene structure may be more prevalent in the fly than previously appreciated.

RNA genes and structures

Several comparative approaches to RNA gene identification have been developed^{6,7,65} that recognize their characteristic properties: compensatory double substitutions of paired nucleotides (for example, A•U↔C•G), structure-preserving single-nucleotide mutations involving G•U base pairs (G•U↔G•C and G•U↔A•U), and few nucleotide substitutions disrupting functional base pairs (Fig. 2b). To predict new structures, we applied EvoFold⁷ in highly conserved segments of the 12 *Drosophila* species and focused on high-stringency candidates with strong support by compensatory changes (Supplementary Methods 4).

Our search led to 394 predictions, recovering 68 known RNA structures (primarily transfer RNA genes) in 0.02% of the genome (570-fold enrichment). The novel candidates consisted of 177 structures in intergenic regions (54%), 103 in introns (32%), 36 in 3' UTRs (11%) and 10 in 5' UTRs (3%). In addition, we predicted 200 structures in protein-coding regions (Supplementary Methods 3). Notably, 75% of 3' UTR structures and 80% of 5' UTR structures were predicted on the transcribed strand, suggesting that they are frequently part of the messenger RNA. In contrast, only 47% of intronic structures are on the transcribed strand, suggesting that they are largely independent of the surrounding genes.

Known and novel types of RNA genes. Of the 177 predicted intergenic structures, 30 were detected in a tiling-array expression study⁴². This fraction (17%) is significantly above that for all conserved intergenic regions (12%, $P = 0.007$), but lower than that of known

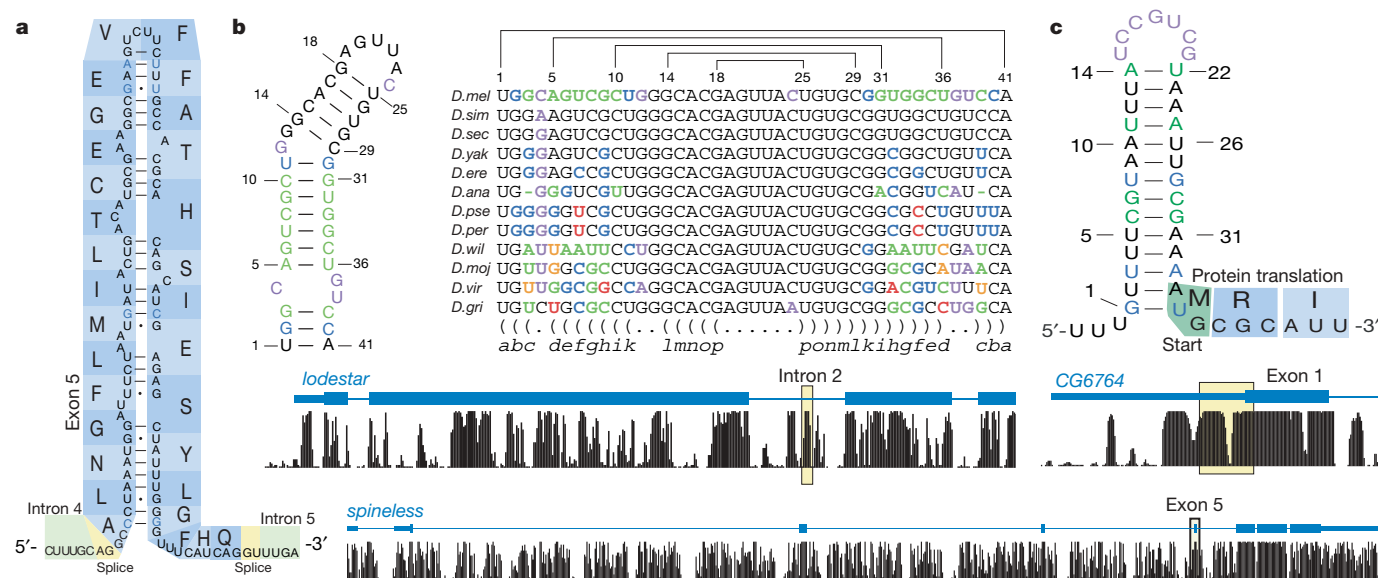


Figure 4 | Novel RNA structures. **a**, New exonic RNA structure spanning 78 of 90 nucleotides of *spineless* exon 5. **b**, New intronic RNA structure in *lodestar* shows 11 compensatory substitutions and 10 silent G•U substitutions, providing strong evidence of structural selection (colours as in

Fig. 2b). **c**, New 5' UTR structure that overlaps the translation start site of *CG6764*, the fly orthologue of yeast ribosomal protein *RPL24*, suggesting a potential role in translational regulation. **a–c**, Structure shown corresponds to shaded region in the gene model.

intergenic ncRNAs (21%), suggesting that these candidates may be of lower abundance, temporally or spatially constrained, or might include false positives. Two predictions were expressed throughout development, one extending the annotation of a previously reported but uncharacterized ncRNA⁶⁶ and the other probably representing a novel type of ncRNA. The predictions also included nine novel H/ACA-box small nucleolar RNA candidates in introns of ribosomal genes, known to frequently contain small nucleolar RNAs that guide post-transcriptional base modifications of ncRNAs⁶⁷.

Likely A-to-I editing structures. Many of the 48 intronic candidates on the transcribed strand and many of the 200 hairpins in coding sequence are probably involved in A-to-I editing or post-transcriptional regulation (Fig. 4a). Hairpins in coding sequence were associated with 11 of the 157 known editing sites (120-fold enrichment) and both intronic and coding-sequence hairpins showed a strong enrichment for ion-channel genes (6%, $P = 0.007$ and 10%, $P = 2 \times 10^{-12}$, respectively), known to be frequent editing targets. Editing is known to occur at multiple sites in the same gene⁶³, and we find an additional 10 hairpins in known editing targets, as well as 40 additional hairpins clustered in 18 genes not previously known to be edited (for example *huntingtin*⁶⁸, which harbours four predicted hairpins, more than any other gene). Intronic predictions also showed the highest abundance of compensatory substitutions: for example, *Resistant to dieldrin* (Fig. 2b) contained a 26-base-pair (bp) intronic hairpin flanked by exons known to be edited⁶⁹ with a striking 16 compensatory changes, *lodestar* showed one hairpin with 11 compensatory changes, and *Inverted repeat-binding protein* showed one hairpin with 10 compensatory substitutions (Fig. 4b).

Likely regulatory UTR structures. We predicted 38 structures in 3' UTRs, a density twofold higher than the genomic average, whereas fewer than 10 such examples are currently known⁷⁰. A considerable fraction of these lies in regulatory genes (14 out of 38; $P = 10^{-4}$), including several transcriptional regulators (for example, *cas*, *spen* and *Alh*), the tyrosine phosphatase *PTP-ER* and the translation initiation factor *eIF3-S8*. This suggests that many regulatory genes may themselves be regulated post-transcriptionally through these structures.

3' UTR structures were also enriched for genes involved in mRNA localization (3 out of 38, $P = 2.7 \times 10^{-4}$), including *oo18 RNA-binding protein* (*orb*) and *staufen* (*stau*), both of which contain double-stranded RNA-binding domains, are involved in axis specification during oogenesis, and interact with the mRNA of maternal effect protein *oskar*. The hairpin in *orb* is known to be important for mRNA transport and localization⁷¹, whereas the highly similar *stau* hairpin has not been previously described to our knowledge.

The ten structures found in 5' UTRs probably contain binding sites for factors that regulate translation. For example, the fly homologue of yeast ribosomal protein *RPL24* contains a hairpin structure overlapping its start codon (Fig. 4c). This is interesting in light of high conservation upstream of the start codon in yeast ribosomal proteins^{3,4}, and findings that ribosomal proteins bind to their mRNAs and control translation in prokaryotes^{72,73}.

Conserved RNA structures in roX2 recruit MSL. In an independent study⁷⁴, we searched for conserved regions in the non-coding *roX1* and *roX2* (RNA on the X) genes to gain insights into their function. Both RNAs are components of the MSL (Male-specific lethal) complex and are crucial for dosage compensation in male flies, inducing lysine 16 acetylation of histone H4, leading to upregulation of hundreds of genes on the X chromosome⁷⁵. We identified several stem-loop structures with repeated sequence motifs (for example, GUUNUACG), and found that tandem repeats of one of these were sufficient to recruit MSL complexes to the X chromosome and to induce acetylation of lysine 16 of histone H4. Although this structure could not fully rescue roX-deficient males, our results suggest that it mediates MSL recruitment during roX2-dependent chromatin modification and dosage compensation, illustrating the power of evolutionary evidence for directing experimental studies.

Prediction and characterization of miRNA genes

Focusing on specific classes of RNA genes markedly increases the accuracy of RNA gene prediction, reviewed in refs 35, 76 and illustrated here for *Drosophila* miRNA genes. The common biogenesis and function of miRNAs⁷⁷ lead to evolutionary and structural signatures (Fig. 2c) that can be used for their systematic *de novo* discovery⁸⁻¹¹. Using such signatures in the 12 fly genomes (Supplementary Methods 4a, b), we predicted 101 miRNAs⁷⁸ (Supplementary Table 4d), which include 60 of the 74 verified Rfam miRNAs (81%), while spanning less than 0.006% of the fly genome (13,500-fold nucleotide enrichment).

Comparison of our predictions with high-throughput sequencing data of short RNA libraries from different stages and tissues of *D. melanogaster*^{78,79} revealed that 84 of the 101 predictions (83%), including 24 of the 41 novel predictions (59%), were authentic miRNA genes (Fig. 5a and Supplementary Table 4d). An independent computational method⁷⁹ had 20 of its 45 novel predictions validated when used across six *Drosophila* species. Additional candidates may represent genuine miRNAs whose temporal or spatial expression pattern does not overlap with the surveyed libraries.

Several of the validated miRNAs were on the transcribed strand of introns or clustered with other miRNAs. For example, *mir-11* and *mir-998* (the vertebrate homologue of which, *mir-29*, has been implicated in cancer⁸⁰) were both found in the last intron of *E2f*, and might be involved in cell-cycle regulation (Fig. 5b). Notably, two predictions overlapped exons of previously annotated protein-coding genes that were independently rejected above (Fig. 5c), providing an explanation for the previously observed transcripts of these annotations and highlighting the importance of specific signatures for genome annotation.

High-throughput sequencing data discovered an additional 50 miRNAs not found computationally^{79,81}, thereby illustrating the limitations of purely computational approaches. Some of these had precursor structures not seen previously for animal miRNAs, including unusually long hairpins⁷⁹ and hairpins corresponding to short introns (mirtrons)^{81,82}. The remaining were often less broadly conserved or showed unusual conservation properties.

Signatures for mature miRNA annotation. The exact position of 5' cleavage of mature miRNAs is important, because it dictates the core of the target recognition sequence⁸³⁻⁸⁵. This leads to unique structural and evolutionary signatures, including direct signals, present at the 5' cleavage site, and indirect signals, stemming from the relationship of miRNAs with their target genes (Supplementary Methods 4a, c). Combined into a computational framework⁷⁸, these signatures predicted the exact start position in 47 of the 60 cloned Rfam miRNAs (78%), and were within 1 bp in 51 cases (85%). The method disagreed with the previous annotation in 9 of the 14 Rfam miRNAs that were not previously cloned, of which 6 were confirmed by sequencing reads^{78,79}, leading to marked changes in the inferred target spectrum (Fig. 5d). Prediction accuracy was significantly lower (41% exact, 61% within 1 nucleotide) for novel miRNAs, which, however, also showed less accurate processing *in vivo*^{78,79}.

New insights into miRNA function and biogenesis. We predicted targets for all conserved miRNAs identified by high-throughput sequencing⁷⁹ searching for conserved matches to the seed region (similar to ref. 86) evaluated using the branch length score (Supplementary Methods 5a), a new scoring scheme described below. Whereas the resulting miRNA targeting network changed substantially⁷⁹, we found that the novel and revised miRNAs shared many of their predicted targets with previously known miRNAs, resulting in a denser network with increased potential for combinatorial regulation^{78,79}.

For ten miRNA hairpins, the mature miRNA and the corresponding miRNA star sequence (miRNA*, the small RNA from the opposite arm of the hairpin) both appeared to be functional: both reached high computational scores and were frequently sequenced^{78,79}, often exceeding the abundance of many mature miRNAs (Supplementary Table 4e). The Hox miRNA *mir-10* showed a particularly striking example of a functional star sequence (Fig. 5e): both arms showed

abundant reads, high scores and highly conserved Hox gene targets^{78,79}, suggesting a key role in Hox regulation.

In addition, for 20 miRNA loci, the anti-sense strand also folded into a high-scoring hairpin suggestive of a functional miRNA⁷⁸ (Supplementary Table 4f). Indeed, sequencing reads confirmed that four of these anti-sense hairpins are processed into small RNAs *in vivo*⁷⁹. Thus, a single genomic miRNA locus may produce up to four miRNAs, each with distinct targets.

Regulatory motif discovery and characterization

Regulatory motifs recognized by proteins and RNAs to control gene expression have been difficult to identify due to their short length,

their many weakly specified positions, and the varying distances at which they can act^{87,88}. Recent studies have shown that comparative genomics of a small number of species can be used for motif discovery^{3,4,12–14}, on the basis of hundreds of conserved instances across the genome (Fig. 2d). Many related genomes should lead to increased discovery power, but also pose new challenges, arising from sequencing, assembly, or alignment artefacts, and from movement or loss of motif instances in individual species.

To account for the unique properties of regulatory motifs, we developed a phylogenetic framework to assess the conservation of each motif instance across many genomes⁸⁹. Briefly, we searched for motif instances in each of the aligned genomes, and based on the set

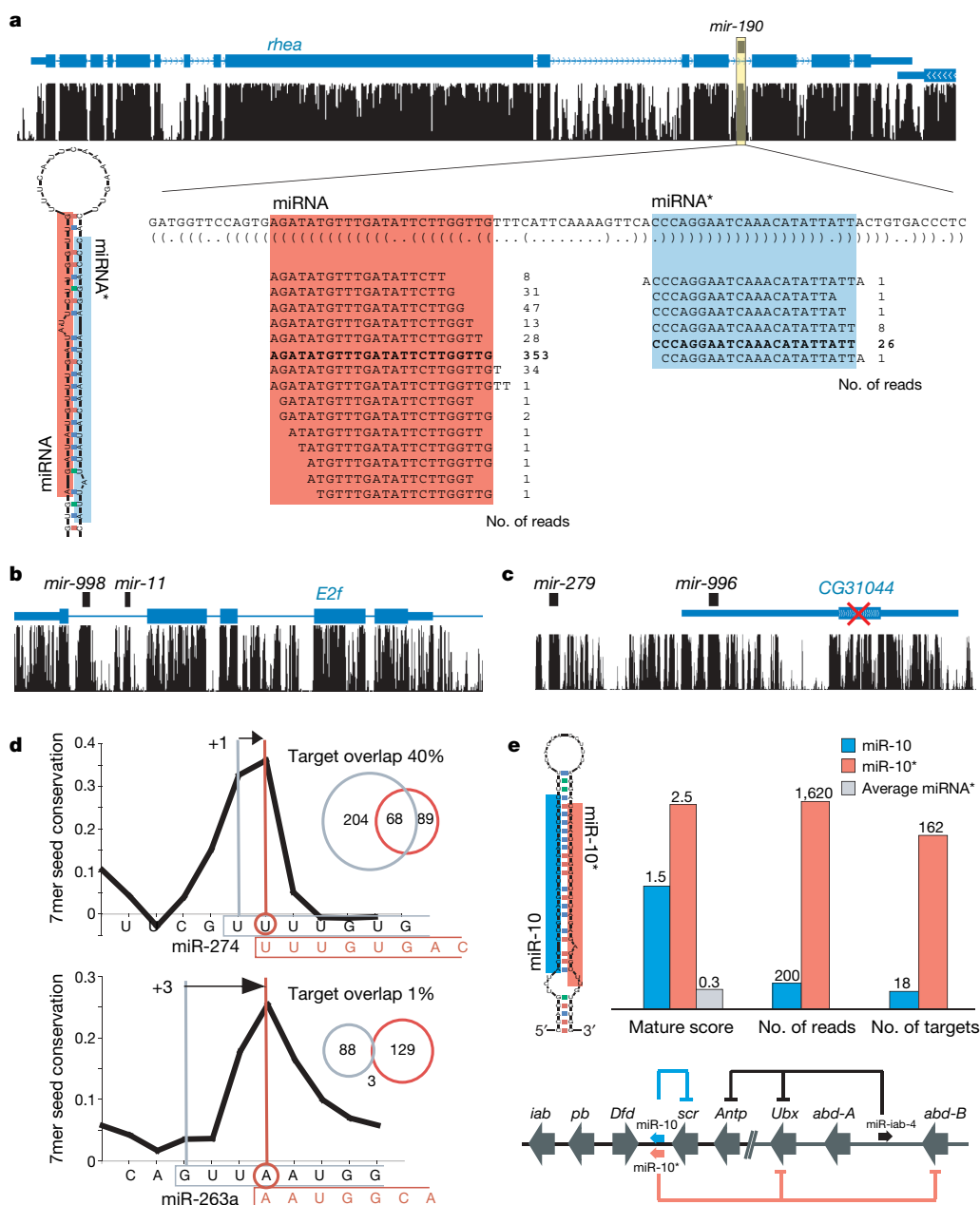


Figure 5 | MicroRNA gene identification and functional implications.

a, New predicted miRNA (*mir-190*) and its validation by sequencing reads. Total read counts for mature miRNA (red) and miRNA* (blue) show a characteristic pattern of processing indicative of miRNAs. Highlighted regions indicate most abundant processing products. **b**, Example of clustered known (*mir-11*) and new (*mir-998*) miRNAs in the intron of cell-cycle regulator *E2f*. **c**, Example of a new miRNA (*mir-996*) in the transcript of a spurious gene. *CG31044* was rejected by our protein-coding analysis, its

transcript probably representing the precursor of *mir-996*, with no protein-coding function. **d**, Revisions to the 5' end of miR-274 and miR-263a are proposed on the basis of evolutionary evidence (for example, 7mer seed conservation; black curve) and confirmed by sequencing reads. Changes at the 5' end of more than one nucleotide results in marked changes to the predicted target spectra (venn diagrams). **e**, Evidence from evolutionary signals (mature score), sequencing reads and target predictions suggests that both miR-10 and miR-10* are functional, each targeting distinct Hox genes.

of species that contained them, we evaluated the total branch length over which the *D. melanogaster* motif instance appears to be conserved (Supplementary Methods 5a, b), which we call the branch length score (BLS). We used BLS for the discovery of novel motifs (this section) and for the prediction of individual functional motif instances (next section).

Predicted motifs recover known regulators. To discover motifs, we estimated the conservation level of candidate sequence patterns with a motif excess conservation (MEC) score compared to overall conservation levels in promoters, UTRs, introns, protein-coding exons and intergenic regions (Supplementary Methods 5a).

Our search in regions with roles in pre-transcriptional regulation resulted in 145 distinct motifs (Table 2), obtained by collapsing variants across 83 motifs discovered in promoters, 35 in enhancers, 20 in 5' UTRs, 35 in core promoters, 30 in introns and 84 in the remaining intergenic regions. Motifs discovered in each region showed similar properties and large overlap: 66 (46%) were discovered independently in at least two regions and 40 (28%) in at least three, consistent with shared regulatory elements in these regions⁹⁰.

The 145 discovered motifs match 40 (46%) of the 87 known transcription factors in *Drosophila* (Supplementary Table 5c) compared to 8% expected at random ($P = 1 \times 10^{-20}$). Several of the non-discovered known motifs are involved in early anterior–posterior segmentation of the embryo, consistent with reports that they are largely non-conserved⁹¹; indeed, 74% of these did not exceed the conservation expected by chance in promoter regions. Other

non-discovered motifs often lacked characteristics expected for transcription factor motifs, suggesting that some may be spurious: 49% were unusually long (>10 nucleotides) compared to 23% of recovered ones, and showed only one or a few total instances genome-wide, suggestive of individual regulatory sites rather than motifs.

Tissue-specific and functional enrichment of novel motifs. The discovered motifs showed strong signals with respect to embryonic expression patterns (Fig. 6a). Overall, 75 (52%) were either enriched or depleted in genes expressed in at least one tissue, compared to 59% of known motifs and 3% of random controls. Motif depletion may represent either specific repressors for individual tissues, or activators excluded from these tissues. Motif depletion was found more generally in ubiquitously expressed genes (30% of discovered and 34% of known motifs compared with 1% expected at random), similar to findings for *in vivo* binding sites⁹², and probably reflecting less complex regulation. We also found significant motif enrichment in groups of genetically interacting genes (collected by FlyBase) that often function in common developmental contexts or signalling pathways, genes of metabolic pathways (Kyoto Encyclopedia of Genes and Genomes, KEGG⁹³), and genes with shared functions (GO).

In total, 68% of discovered and 70% of known motifs were enriched or depleted in one of the functional categories (14% random). Noteworthy examples include motif ME93 (GCAACA), which was more highly enriched in neuroblasts ($P = 4 \times 10^{-12}$) than either of the two well-known regulators of neuroblast development, *prospero* and *asense* ($P = 4 \times 10^{-5}$ and 2×10^{-7} , respectively). Similarly,

Table 2 | Pre-transcriptional motifs

Name	Motif consensus	MEC	MCS	Region*	Known transcription factor†	Multiplicity score‡	ImaGO enrichment§	ImaGO score§
ME1	GTCACGTD	0.448	45.41	PIG	–	–	–	–
ME2	AWNTGGGTCA	0.393	26.97	PIG	Hr46	–	Oesophagus (13–16)	4.52
ME3	BCATAAATYA	0.369	36.02	PCEIG	Caudal	–	Ubiquitous (13–16)	–6.22
ME4	HAATTAYGCRH	0.365	32.71	PCE5IG	Engrailed	–	–	–
ME5	STATAWAWR	0.358	24.31	C	TATA	–	Ventral nerve cord (13–16)	–5.1
ME6	VATTWGCAT	0.356	44.06	PE5IG	–	3.73	Ubiquitous (11–12)	–7.15
ME7	BYAATTARH	0.338	15.45	PCE5IG	Engrailed	7.08	Ubiquitous (11–12)	–10.26
ME8	HRTCAATCA	0.338	42.32	PIG	–	–	Dorsal pharyngeal muscle PR (11–12)	–4.15
ME9	TGACANNNNNNTGACA	0.336	9	G	–	–	–	–
ME10	RCGTGNNNNNGCAT	0.329	15.94	PIG	–	–	–	–
ME11	MATTAAWNATGCR	0.324	12.43	PIG	acj6	–	Tracheal PR (11–12)	4.11
ME12	TTAATGATG	0.32	20.31	PG	–	–	–	–
ME13	WTGACANBT	0.318	63.45	PE5IG	–	4.14	Ubiquitous (13–16)	–3.97
ME14	YGACMTTGA	0.313	27.06	PIG	–	–	Midgut (13–16)	4.32
ME15	AATTRNNNNCAATT	0.309	21.17	PG	–	–	–	–
ME16	TGACGTCAT	0.304	12.24	PC5IG	CrebA	–	–	–
ME17	MAATTNAATT	0.304	51.57	PE5IG	–	–	Ubiquitous (11–12)	–6.66
ME18	MRYTTCCGY	0.304	39.04	PEIG	Dorsal	–	Ubiquitous (11–12)	–4.4
ME19	MATTRRCACNY	0.303	25.24	PIG	–	–	–	–
ME20	YTAATGAVS	0.298	44.5	PEIG	–	–	Foregut PR (11–12)	4.19
ME21	TAATTRANNTTATG	0.294	8.67	G	–	–	–	–
ME22	WAATGCGCNT	0.291	18.17	G	–	–	–	–
ME23	MATTWRTCA	0.288	46.25	PEIG	–	–	Dorsal epidermis PR (11–12)	4.4
ME24	YAATTWNRGCG	0.287	30.91	PG	–	4.27	Ubiquitous (11–12)	–4.79
ME25	TTAYGTAA	0.283	13.06	S	Giant	–	Midgut (13–16)	5.32
ME26	YCGGTHAATTR	0.283	13.61	PEG	–	–	–	–
ME27	AATTRYGWCA	0.28	22.85	PEIG	–	–	Pericardial cell (13–16)	4.1
ME28	GCGCATGH	0.28	30.17	PCEG	–	–	Ventral nerve cord PR (11–12)	5.75
ME29	WAATCARCGC	0.275	13.82	G	–	–	–	–
ME30	AATTAANNNNNCATNA	0.271	16.44	G	Antennapedia	–	–	–
ME31	GCGTSAAA	0.271	29.95	PG	–	–	–	–
ME32	YCGGYRTCAWT	0.269	12.87	G	–	–	–	–
ME33	GCGTTGAYA	0.269	15.1	PG	–	–	–	–
ME34	AAATKKCATTA	0.266	14.04	PG	–	–	–	–
ME35	RACASCTGY	0.266	28.38	PCEG	Scute	–	Ventral sensory complex SA (11–12)	4.08
ME36	TGTCATTG	0.265	12.65	PG	–	–	Tracheal system (13–16)	4.56
ME37	WAATKNNNNNCRGCGY	0.261	23.34	PEG	–	–	–	–
ME38	CASGTAR	0.261	9.24	PEG	Single-minded	4.58	Ventral epidermis PR (11–12)	7.41
ME39	WCACGTGC	0.26	10.54	PCE5IG	Enhancer of split	–	–	–
ME40	CATTANNNNWAATT	0.259	19.02	G	–	–	–	–

The top 40 of 145 are shown. MEC, motif excess conservation; MCS, motif conservation score. See Supplementary Table 5c for the full table.

* Region where the motif was found: P, promoter; C, core promoter; E, enhancers; 5, 5' UTR; I, intron; G, intergenic genome.

† The known transcription factor motif matching the consensus sequence.

‡ A multiplicity score is reported for motifs with many repeated occurrences.

§ Tissue where motif is most strongly enriched or depleted, and corresponding score (positive, enrichment; negative, depletion). PR, primordium; SA, specific anlage.

motifs ME89 (CACRCAC), ME11 (MATTAAWNATGCR) and ME117 (MAAMNNCAA) were highly enriched in malpighian tubule ($P = 4 \times 10^{-7}$), trachea ($P = 4 \times 10^{-5}$) and surface glia (6×10^{-7}), respectively, in each case ranking above motifs for factors known to be important in these tissues (Supplementary Table 5c). These presumably correspond to as-yet-unknown regulators for these tissues. **Exclusion, clustering and positional constraints.** A large number of motifs were depleted in coding sequence (57% of discovered versus 57% of known and 10% of random motifs, $P = 3 \times 10^{-18}$) and in 3' UTRs (30% versus 22% and 0%, $P = 4 \times 10^{-11}$), suggesting specific exclusion similar to *in vivo* binding⁹².

Many of the intergenic or intronic instances occurred in clusters, a property of motifs that has been used to identify enhancer elements^{91,94–96}. We assessed increased conservation of motifs when found near other instances of the same motif (whether conserved or not, to correct for regional conservation biases), and found significant multiplicity for 19% of the discovered motifs (compared to 24% of known and 4% of random motifs).

In addition, 15 of the discovered motifs (10%) were significantly enriched near transcription start sites (compared to 14% of known and 1% of random motifs). Several were enriched at precise positions and preferred orientations (Fig. 6b), including close matches to several known core promoter motifs involved in transcription

initiation⁹⁷. For example, ME5 (STATAWAWR), which matches the TATA-box motif, displayed a sharp peak on the transcribed strand, 27 nucleotides upstream of the transcription start site. Similarly, ME120 (TCAGTT), corresponding to the known initiator motif (Inr) strongly peaked directly on the transcription start site, and ME54 (RCGYRCGY), which matches a known downstream promoter element (DPE), peaked 30 nucleotides downstream of the transcription start site.

Regulatory motifs involved in post-transcriptional regulation. We also used BLS/MEC to discover motifs involved in post-transcriptional regulation, and developed methods to distinguish motifs acting at the DNA level, motifs acting at the RNA level and motifs stemming from protein-coding codon biases (Supplementary Methods 5a). Motifs acting post-transcriptionally at the RNA level generally showed highly asymmetric conservation¹², as functional instances can only occur on the transcribed strand. Indeed, 71 of 90 motifs (79%) discovered in 3' UTRs showed strand-specific conservation (compared with only 3% of 5' UTR motifs and 5% of intron motifs, suggesting that these act primarily in pre-transcriptional regulation).

Overall, 33 motifs discovered in 3' UTRs were complementary to the 5' end of Rfam miRNAs, recovering 72% of known miRNAs (68% of 5' unique miRNA families). An additional 21 motifs matched to 5' ends of novel miRNAs predicted above, of which 12

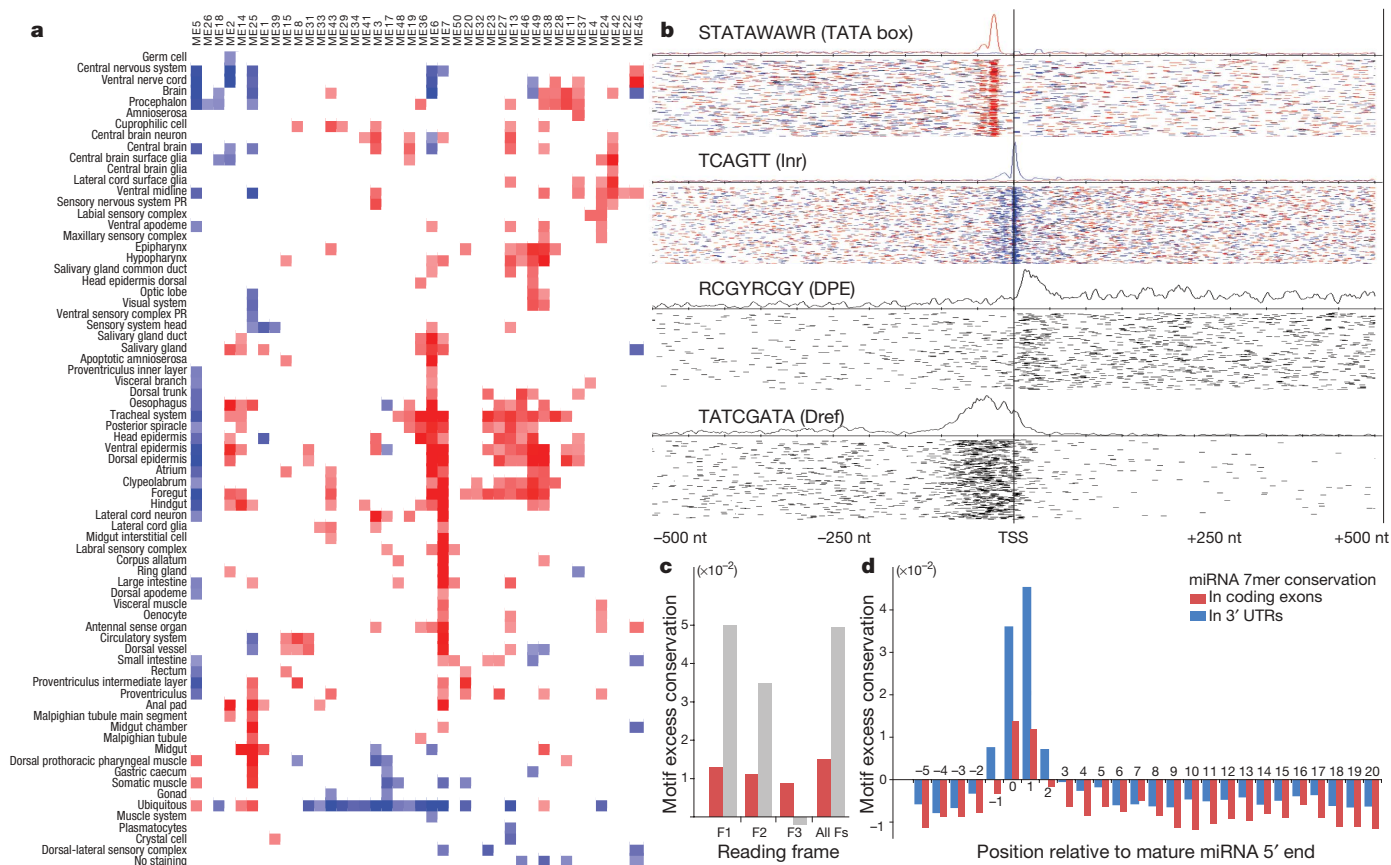


Figure 6 | Regulatory motif discovery. **a**, Discovered motifs show enrichment (red) or depletion (blue) in genes expressed in a given tissue (log colour range from $P = 10^{-5}$ enrichment to $P = 10^{-5}$ depletion). Bi-clustering reveals groups of motifs with similar tissue enrichment and groups of tissues with similar motif content. Full matrix and randomized control is shown in Supplementary Fig. 6d. **b**, Positional bias of discovered motifs relative to transcription start sites (TSS). Peaks with highly specific distances from the transcription start site (for example, first three plots) are characteristic of core promoter elements, and broad peaks (for example, fourth plot) are characteristic of transcription factors. For non-palindromic motifs, colours indicate forward-strand (red) and reverse-strand (blue) instances. Curves denote the density of all instances and individual segments

denote individual motif instances, summed across groups of 50 genes (each line). **c**, Coding regions show reading-frame-invariant conservation for miRNA motifs (red) and reading-frame-biased conservation for protein motifs (grey). MEC scores are evaluated for each of the three reading frame offsets (F1–F3) and also without frame correction (all Fs). Plots show average MEC for all miRNA motifs and 500 top-scoring protein-coding motifs (based on MEC without frame correction). **d**, Motif excess conservation (MEC) of 7mer complements at different offsets with respect to miRNA 5' end, averaged across all Rfam miRNAs. MEC scores evaluated in protein-coding regions and 3' UTRs show a highly similar profile (correlation coefficient 0.96), suggesting similar evolutionary constraints.

were validated experimentally^{78,79}, and 3 motifs matched uniquely to miRNA star sequences, all of which were abundantly expressed *in vivo* (Supplementary Table 4e).

We found 33 additional motifs in 3' UTRs that were apparently not associated with miRNAs. MO40 (TGTANWTW) closely matches the Puf-family Pumilio motif⁹⁸. MO32 (AATAAA) corresponds to the polyadenylation signal and displays both very strong conservation and a sharply defined distance preference with respect to the end of the annotated 3' UTR ($P = 10^{-69}$). Finally, several motifs (for example, MO24 = TAATTAT; MO94 = TTATTTT) are variants of known AU-rich elements, which are known to mediate mRNA instability and degradation⁹⁹.

MicroRNA targeting in protein-coding regions. Protein-coding regions can also harbour functional regulatory motifs, such as exonic splicing regulatory elements¹⁰⁰. However, motif conservation is difficult to assess within protein-coding regions because of the overlapping selective pressures. Indeed, the most highly conserved nucleotide sequence patterns of length seven (7mers) in coding sequence showed strong reading-frame-biased conservation, suggesting that they reflect protein-coding constraints rather than regulatory roles at the DNA or RNA level (Fig. 6c).

MicroRNA motifs, which function at the RNA level, instead showed high conservation in all three reading frames, suggesting that they are specifically selected within coding regions for their RNA-level function. Indeed, previous studies have shown that miRNA motifs in coding regions are preferentially conserved in vertebrates⁸⁶, that they can lead to repression in experimental assays^{101,102}, and that they are avoided in genes co-expressed with the miRNA¹⁰³. Frame-invariant conservation allows us to demonstrate the coding-region targeting of individual miRNAs, and also enables the *de novo* discovery of miRNA motifs in coding regions. Using frame-invariant conservation, we recovered 11 miRNA motifs within the top 20 coding-region motifs (Supplementary Table 5g), whereas using overall conservation required several hundred candidates to recover 11 miRNA motifs.

Moreover, 7mers complementary to different positions in the mature miRNA show a distinctive conservation pattern indicative of functional targeting in coding regions (Fig. 6d) and similar to that found in 3' UTRs^{12,83} (correlation coefficient 0.96). Finally, 6mers complementary to miRNA 5' ends were depleted in coding exons of

anti-target genes (Supplementary Fig. 5f), similar to findings for these genes' 3' UTRs^{103,104}. Overall, these results, together with findings in vertebrates^{86,101–103}, suggest that important miRNA targets have been overlooked by many target prediction methods¹⁰⁵ that have traditionally focused exclusively on 3' UTR sequences.

Prediction of individual regulator binding sites

Previous methods for regulatory motif discovery^{3,4,12–14} integrated conservation information over hundreds of motif instances across the genome, leading to an exceedingly clear signal for motif discovery even if many of these instances are only marginally conserved. In contrast, the reliable identification of individual motif instances has been hampered by lack of neutral divergence and would require many related genomes^{15–19}. In the absence of such data, previous studies have relied on motif clustering^{91,94–96} or other sequence characteristics¹⁰⁶ to predict regulatory targets or regions.

With the availability of the 12 fly genomes, we inferred high-confidence instances of regulatory motifs by mapping the BLS of each motif instance to a confidence value (Supplementary Methods 5a). This value represents the probability that a motif instance is functional, on the basis of the conservation level of appropriate control motifs evaluated in the same type of region (promoter, 3' UTR, coding, and so on). Because the number of conserved instances decreases much more rapidly for control motifs than for real motifs, the many genomes allowed us to reach high confidence values for many transcription factors and miRNAs, even at relatively modest BLS thresholds (Fig. 2e).

Conserved motif instances identify functional *in vivo* targets. We found that increasing confidence levels selected for functional instances for both transcription factor and miRNA motifs: the normalized fraction of transcription factor motif instances within promoter regions rose from 20% to 90%; that of miRNA motif instances within 3' UTRs rose from 20% to 90%; and the fraction of miRNA motif instances on the transcribed strand of 3' UTRs rose from 50% (uniform) to 100% (Fig. 7a); in each case selecting the regions and strands where the motifs are known to be functional.

We further assessed how predicted motif instances compared with *in vivo* targets in promoter regions, defined experimentally (without comparative information). We used a set of high-confidence direct CrebA targets¹⁰⁷ and three genome-wide chromatin

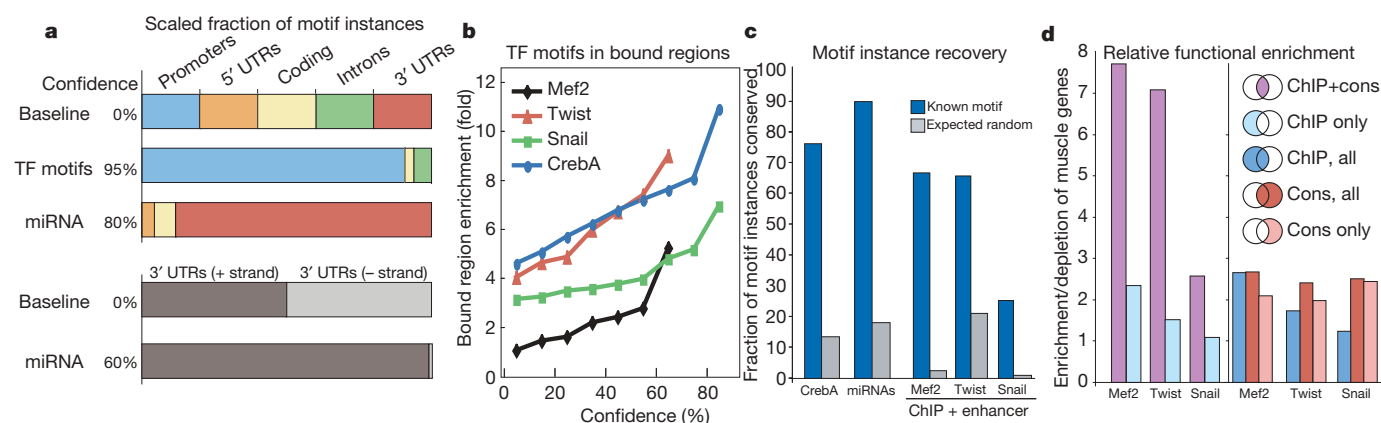


Figure 7 | Identification of individual motif instances. **a**, Increasing confidence levels select for motif instances in regions they are known to be functional: conserved transcription factor (TF) motifs enrich for promoters; miRNA motifs for 3' UTRs, and specifically the transcribed strand. Regions are normalized for their overall length, measured by the number of motif instances without conservation (0% confidence baseline). **b**, Increasing confidence levels select for transcription factor motif instances with experimental support for each factor tested. **c**, The high fraction of experimentally supported motif instances that are recovered at 60% confidence for transcription factors and 80% confidence for miRNAs illustrates the high sensitivity of the BLS approach. **d**, Comparison of

chromatin immunoprecipitation (ChIP) and conservation in their ability to identify functional motif instances. Motif instances that are both ChIP-bound and conserved (purple) show the strongest functional enrichment in muscle genes for Mef2 and Twist (depletion for Snail), whereas motif instances derived by ChIP alone (light blue) show substantially reduced enrichment levels. Comparing the enrichment of all instances recovered by ChIP (blue) and all instances recovered by conservation (red) suggests that the two approaches perform comparably. Even the sites recovered by conservation alone outside bound regions (pink) show enrichment levels comparable to ChIP, suggesting that they are also functional.

immunoprecipitation (ChIP) data sets for Snail, Mef2 and Twist^{92,108,109}, and in each case found that the enrichment between conserved motif instances and known *in vivo* regions increased sharply for increasing confidence values (Fig. 7b).

We also found that a large fraction of motif instances in experimentally determined target regions was conserved (Fig. 7c): 76% of motif instances in direct CreBA targets and 90% of motif instances in experimentally supported miRNA targets^{104,110} were recovered at 60% confidence. Although many of the miRNA targets stem from comparative predictions and are expected to be well conserved, their high recovery rate illustrates the increased sensitivity of the BLS measure compared to perfect conservation (Supplementary Fig. 7d). Similar results were found for motifs in known enhancers that were determined to be bound by ChIP ('ChIP-bound'): 65% of Mef2 motifs, 65% of Snail motifs and 25% of Twist motifs were conserved (Fig. 7c).

ChIP-determined and conservation-determined targets show similar enrichment. To determine whether ChIP-bound motifs that lack conservation are biologically meaningful, we studied their enrichment in muscle gene promoters. We found that motifs that were both bound and evolutionarily conserved showed very strong correlation with muscle genes for all three factors: Mef2 showed eightfold enrichment, Twist showed sevenfold enrichment and Snail, a mesodermal repressor, showed threefold depletion for muscle genes. However, when only non-conserved sites were considered, the correlation dropped significantly to 1–2-fold for all three factors, suggesting that non-conserved ChIP-bound sites may be of decreased biological significance (Fig. 7d).

We also used the correlation with muscle genes to compare ChIP-on-chip and evolutionary conservation as two complementary methods for target identification (Fig. 7d). We found that the enrichment of conservation-inferred targets was consistently higher than the enrichment of ChIP-inferred targets for each of the three factors. Finally, we assessed the functional significance of motif instances that were only found by the conservation approach, specifically excluding those in ChIP-bound regions, and found that these were also enriched in the same functional categories as ChIP-bound sites with comparable or higher functional correlations (Fig. 7d). This suggests that the additional conserved instances are indeed functional, probably reflecting the higher coverage of conservation-based approaches, which are not restricted to the experimental conditions surveyed, or that they may be bound *in vivo* yet missed by ChIP-on-chip technology^{111,112}.

In an independent study¹¹³ we compared several strategies for the prediction of motif instances and *cis*-regulatory modules and found that using the 12 fly genomes led to substantial improvements. In another study, we reported the recovery of conserved motifs for

several known regulators, including *Suppressor of Hairless*, in genes of the *Enhancer of split* complex¹¹⁴.

A regulatory network of *D. melanogaster* at 60% confidence. Having established the accuracy of conserved motif instances, we present an initial regulatory network for *D. melanogaster* at 60% confidence (Supplementary Fig. 5i), containing 46,525 regulatory connections between 67 transcription factors and 8,287 genes, and 3,662 connections between 81 cloned miRNAs (clustered in 49 families with unique seed sequences) and 2,003 genes.

The distribution of predicted sites per target gene is highly non-uniform and indicative of varying levels of regulatory control. Genes with the highest number of sites appeared to be enriched in morphogenesis, organogenesis, neurogenesis and a variety of tissues, whereas ubiquitously expressed genes and maternal genes with housekeeping functions had the fewest sites¹⁰⁴. Interestingly, transcription factors appeared to be more heavily targeted than other genes, both by transcription factors (10 sites versus 5.5 on average, $P = 10^{-15}$) and by miRNAs (2.3 versus 1.8 miRNAs, $P = 5 \times 10^{-5}$). Moreover, genes with many transcription factor sites also had many miRNA sites, and conversely, genes with few transcription factor sites also had few miRNA sites ($P = 10^{-4}$ and $P = 7 \times 10^{-3}$, respectively).

Several of the predicted regulatory connections have independent experimental support (Supplementary Table 5h), including direct regulation of *achaete* by Hairy¹¹⁵, of *giant* by Bicoid¹¹⁶, of *Enhancer of split* complex genes by Suppressor of Hairless¹¹⁷, and of *bagpipe* by Tinman (known to cooperate in mesoderm induction and heart specification¹¹⁸). More generally, when tissue-specific expression data were available, we found that on average 46% of all targets were co-expressed with their factor in at least one tissue (Supplementary Fig. 5i), which is significantly higher than expected by chance ($P = 2 \times 10^{-3}$).

Scaling of comparative genomics power

Theoretical considerations and pilot studies on selected genomic regions showed that the discovery power of comparative methods scales with the number and phylogenetic distance of the species compared^{16–20,46,119,120}. We extended these analyses by investigating the scaling of genome-wide discovery power using evolutionary signatures for each class of functional elements (Fig. 8), on the basis of the recovery of known elements using different subsets of informant species (at a fixed stringency).

We found that recovery consistently increased with the total number of informant species, and that multi-species comparisons outperformed pairwise comparisons within the same phylogenetic clade. When we examined subsets of informants with similar total branch length (for example, several close species versus one distant species),

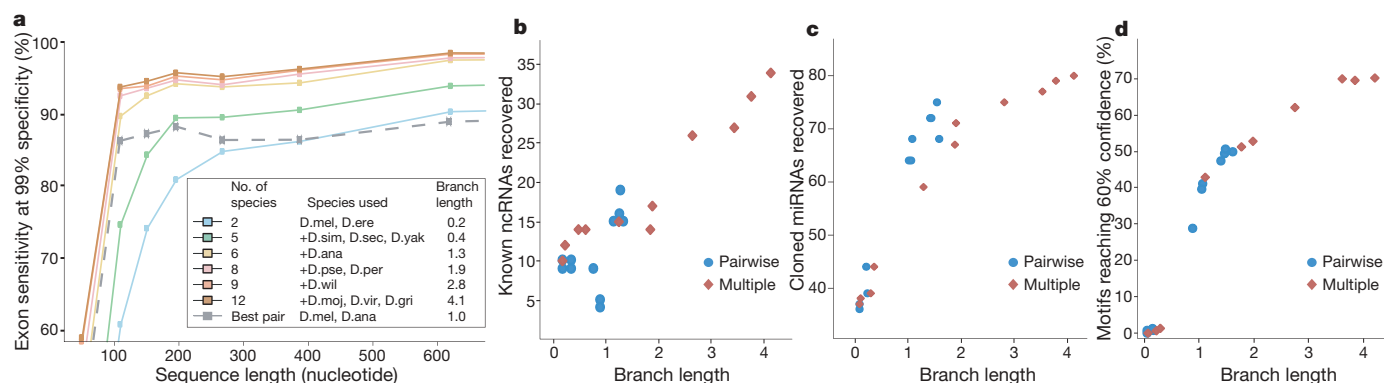


Figure 8 | Scaling of discovery power with the number and distance of informant species. **a**, Discriminatory power of CSF protein-coding evolutionary metric for varying exon lengths and using different numbers of informant species. Sensitivity is shown for known exons at a fixed false-positive rate based on random non-coding regions. Mean length is shown for each exon length quantile. Multi-species comparisons increase discovery

power, especially among short exons. **b**, Recovery of known ncRNAs (among the top 100 predictions) for pairwise (blue) and multi-species (red) comparisons. **c**, Recovery of cloned miRNAs (among the top 100 predictions). **d**, Recovery of transcription factor and miRNA motifs with instances at 60% confidence.

multi-species comparisons sometimes performed better (protein-coding exons, ncRNAs), comparably (motifs), or worse (miRNAs) than pairwise comparisons. This complex relationship between total branch length and actual discovery power probably reflects imperfect genome assemblies/alignments, characteristics of each class of functional elements, and the specific methods we used. For example, ncRNA discovery probably benefits from observing more compensatory changes across more genomes, whereas miRNA discovery may be more sensitive to artefacts in low-coverage genomes, given the expected high conservation of miRNA arms.

As expected, longer elements were easier to discover than shorter elements. Long protein-coding exons (>300 nucleotides) were recovered at very high rates even with few species at close distances (leaving little room for improvement with additional species). In contrast, more informant species and larger distances were crucial for recovering short exons, miRNAs and regulatory motifs.

Notably, the optimal evolutionary distance for pairwise comparisons to *D. melanogaster* also seemed to depend on element length: for long protein-coding exons, the best pairwise informant was the closely related *D. erecta*, for exons of intermediate lengths *D. ananassae*, and for the shortest exons the distant *D. willistoni* (Supplementary Table 7a). Distant species were also optimal for other classes of short elements (ncRNAs, miRNAs and motifs, Fig. 8b–d). This suggests that a small number of species at close evolutionary distances may generally allow the discovery of long elements, possibly including clade-specific elements, whereas short clade-specific elements may not be reliably detectable without many genomes at close distances.

Finally, we investigated the effect of alignment choice on our results (Supplementary Fig. 8). We found high similarity between different alignment strategies for longer elements (>93% agreement for exons), whereas shorter elements showed larger discrepancies between alignments (81% and 59% agreement for miRNA and motif instances, respectively).

Although factors such as genome size, repeat density, pseudogene abundance and physiological differences might confound a simple analogy to the vertebrate phylogeny based on neutral branch length (Fig. 1c), our results suggest that comparisons spanning marsupials, birds and reptiles may prove surprisingly useful for biological signal discovery in the human genome.

Discussion

Our results demonstrate the potential of comparative genomics for the systematic characterization of functional elements in a complete genome. Even in a species as intensely studied as *D. melanogaster*, our methods predicted several thousand new functional elements, including protein-coding genes and exons, novel RNA genes and structures, miRNA genes, regulatory motifs, and regulator targets. Our novel predictions have overwhelming statistical support, often surpassing that of known functional elements, and are additionally supported by experimental evidence in hundreds of cases. The common underlying methodology in this study has been the recognition of specific evolutionary signatures associated with each class of functional elements, which can be much more informative for genome annotation than overall measures of nucleotide conservation. These signatures are general and are immediately relevant to the analysis of the human genome and more generally of any species.

In addition to the many new elements, we gained specific biological insights and formulated hypotheses that we hope will guide follow-up experiments. We found 149 genes with potential translational readthrough, showing protein-like evolution downstream of a highly conserved stop codon, and possibly encoding additional protein domains or peptides specific to certain developmental contexts. We also found several candidate programmed frameshifts, which might be part of regulatory circuits (as for *ODC/Oda*⁶⁴) or help expand the diversity of protein products generated from one mRNA, similar to their role in prokaryotes¹²¹. We also presented evidence of miRNA processing from both arms of a miRNA hairpin

and from both DNA strands of a miRNA locus in some cases, potentially leading to as many as four functional miRNAs per locus. As miRNA/miRNA* pairs are expressed from a single precursor and thus co-regulated, whereas sense/anti-sense pairs are expressed from distinct promoters, the use of both arms or both strands provides compelling general building blocks for higher-level miRNA-mediated regulation.

The newly discovered elements did not dramatically increase the total number of annotated nucleotides. Known and predicted elements explain 42% of nucleotides in phastCons elements³³, compared to 35.5% for previous annotations (Supplementary Fig. 6), an 18% increase (mostly owing to conserved motif instances). The remaining phastCons elements and independent estimates based on transcriptional activity⁴² would suggest that a much higher fraction of the genome may be functional (Supplementary Fig. 6). Although it is possible that these estimates are artificially high and that we are in fact converging on a complete annotation of the fly genome, they might instead indicate that much remains to be discovered, which may require the recognition of as-yet-unknown classes of functional elements with distinct evolutionary signatures.

Our results also allowed us to compare and contrast evolutionary and experimental methods for the recovery of functional elements, particularly for the identification of regulator targets. We found that comparative genomics resulted in many functionally meaningful sites for transcription factors Mef2, Twist and Snail outside ChIP-bound regions, probably representing targets from diverse conditions not surveyed experimentally. Similarly, ChIP resulted in many additional sites outside those recovered by comparative genomics: some of these may have been replaced by functionally equivalent non-orthologous sequence, rendering them apparently non-conserved in sequence alignments^{122–124}; others may have species- or lineage-specific roles, thus lacking sufficient signal for their comparative detection; finally, some bound sites may be biochemically active yet selectively neutral¹²⁵. It is worth noting, however, that ChIP-bound motifs that were not conserved showed decreased enrichment in muscle/mesoderm development where the factors are known to act, suggesting that potential lineage-specific roles may lie outside the regulators' conserved functions. To resolve these questions, comparative genomics studies would benefit greatly from experimental studies in several related species in parallel.

Overall, comparative genomics and species-specific experimental studies provide complementary approaches to biological signal discovery. Comparative studies help pinpoint evolutionarily selected functional elements across diverse conditions, whereas experimental studies reveal stage- and tissue-specific information, as well as species-specific sites. Ultimately, their integration is a necessary step towards a comprehensive understanding of animal genomes.

METHODS SUMMARY

The Methods are described in Supplementary Information, with more details found in the cited companion papers for each section. The sections of the Supplementary Methods are arranged in the same order as the manuscript to facilitate cross-referencing, with an index on the first page to aid navigation.

Received 21 July; accepted 4 October 2007.

1. Miller, W., Makova, K. D., Nekrutenko, A. & Hardison, R. C. Comparative genomics. *Annu. Rev. Genomics Hum. Genet.* **5**, 15–56 (2004).
2. Ureta-Vidal, A., Ettwiller, L. & Birney, E. Comparative genomics: genome-wide analysis in metazoan eukaryotes. *Nature Rev. Genet.* **4**, 251–262 (2003).
3. Kellis, M. *et al.* Sequencing and comparison of yeast species to identify genes and regulatory elements. *Nature* **423**, 241–254 (2003).
4. Cliften, P. *et al.* Finding functional features in *Saccharomyces* genomes by phylogenetic footprinting. *Science* **301**, 71–76 (2003).
5. Brent, M. R. Genome annotation past, present, and future: how to define an ORF at each locus. *Genome Res.* **15**, 1777–1786 (2005).
6. Washietl, S., Hofacker, I. L. & Stadler, P. F. Fast and reliable prediction of noncoding RNAs. *Proc. Natl Acad. Sci. USA* **102**, 2454–2459 (2005).
7. Pedersen, J. S. *et al.* Identification and classification of conserved RNA secondary structures in the human genome. *PLoS Comput. Biol.* **2**, e33 (2006).

8. Lim, L. P. *et al.* The microRNAs of *Caenorhabditis elegans*. *Genes Dev.* **17**, 991–1008 (2003).
9. Lim, L. P. *et al.* Vertebrate microRNA genes. *Science* **299**, 1540 (2003).
10. Lai, E. C., Tomancak, P., Williams, R. W. & Rubin, G. M. Computational identification of *Drosophila* microRNA genes. *Genome Biol.* **4**, R42 (2003).
11. Berezikov, E. *et al.* Phylogenetic shadowing and computational identification of human microRNA genes. *Cell* **120**, 21–24 (2005).
12. Xie, X. *et al.* Systematic discovery of regulatory motifs in human promoters and 3' UTRs by comparison of several mammals. *Nature* **434**, 338–345 (2005).
13. Ettwiller, L. *et al.* The discovery, positioning and verification of a set of transcription-associated motifs in vertebrates. *Genome Biol.* **6**, R104 (2005).
14. Chan, C. S., Elemento, O. & Tavazoie, S. Revealing posttranscriptional regulatory elements through network-level conservation. *PLoS Comput. Biol.* **1**, e69 (2005).
15. Boffelli, D. *et al.* Phylogenetic shadowing of primate sequences to find functional regions of the human genome. *Science* **299**, 1391–1394 (2003).
16. Cooper, G. M. *et al.* Distribution and intensity of constraint in mammalian genomic sequence. *Genome Res.* **15**, 901–913 (2005).
17. Margulies, E. H., Blanchette, M., Haussler, D. & Green, E. D. Identification and characterization of multi-species conserved sequences. *Genome Res.* **13**, 2507–2518 (2003).
18. Thomas, J. W. *et al.* Comparative analyses of multi-species sequences from targeted genomic regions. *Nature* **424**, 788–793 (2003).
19. Eddy, S. R. A model of the statistical power of comparative genome sequence analysis. *PLoS Biol.* **3**, e10 (2005).
20. Bergman, C. M. *et al.* Assessing the impact of comparative genomic sequence data on the functional annotation of the *Drosophila* genome. *Genome Biol.* **3**, RESEARCH0086 (2002).
21. Rubin, G. M. & Lewis, E. B. A brief history of *Drosophila*'s contributions to genome research. *Science* **287**, 2216–2218 (2000).
22. Adams, M. D. *et al.* The genome sequence of *Drosophila melanogaster*. *Science* **287**, 2185–2195 (2000).
23. Misra, S. *et al.* Annotation of the *Drosophila melanogaster* euchromatic genome: a systematic review. *Genome Biol.* **3**, RESEARCH0083 (2002).
24. Celniker, S. E. & Rubin, G. M. The *Drosophila melanogaster* genome. *Annu. Rev. Genomics Hum. Genet.* **4**, 89–117 (2003).
25. Ashburner, M. & Bergman, C. M. *Drosophila melanogaster*: a case study of a model genome sequence and its consequences. *Genome Res.* **15**, 1661–1667 (2005).
26. Matthews, K. A., Kaufman, T. C. & Gelbart, W. M. Research resources for *Drosophila*: the expanding universe. *Nature Rev. Genet.* **6**, 179–193 (2005).
27. Venken, K. J., He, Y., Hoskins, R. A. & Bellen, H. J. P[acman]: a BAC transgenic platform for targeted insertion of large DNA fragments in *D. melanogaster*. *Science* **314**, 1747–1751 (2006).
28. Dietzl, G. *et al.* A genome-wide transgenic RNAi library for conditional gene inactivation in *Drosophila*. *Nature* **448**, 151–156 (2007).
29. Spradling, A. C. *et al.* The Berkeley *Drosophila* Genome Project gene disruption project: Single P-element insertions mutating 25% of vital *Drosophila* genes. *Genetics* **153**, 135–177 (1999).
30. St Johnston, D. The art and design of genetic screens: *Drosophila melanogaster*. *Nature Rev. Genet.* **3**, 176–188 (2002).
31. Richards, S. *et al.* Comparative genome sequencing of *Drosophila pseudoobscura*: chromosomal, gene, and cis-element evolution. *Genome Res.* **15**, 1–18 (2005).
32. *Drosophila* 12 Genomes Consortium. Evolution of genes and genomes on the *Drosophila* phylogeny. *Nature* doi:10.1038/nature06341 (this issue) (2007).
33. Siepel, A. *et al.* Evolutionarily conserved elements in vertebrate, insect, worm, and yeast genomes. *Genome Res.* **15**, 1034–1050 (2005).
34. Nekrutenko, A., Makova, K. D. & Li, W. H. The K_A/K_S ratio test for assessing the protein-coding potential of genomic regions: an empirical and simulation study. *Genome Res.* **12**, 198–202 (2002).
35. Eddy, S. R. Computational genomics of noncoding RNA genes. *Cell* **109**, 137–140 (2002).
36. Bompfuenewerer, A. F. *et al.* Evolutionary patterns of non-coding RNAs. *Theor. Biosci.* **123**, 301–369 (2004).
37. Reese, M. G. *et al.* Genome annotation assessment in *Drosophila melanogaster*. *Genome Res.* **10**, 483–501 (2000).
38. Rubin, G. M. *et al.* A *Drosophila* complementary DNA resource. *Science* **287**, 2222–2224 (2000).
39. Stapleton, M. *et al.* A *Drosophila* full-length cDNA resource. *Genome Biol.* **3**, RESEARCH0080 (2002).
40. Hild, M. *et al.* An integrated gene annotation and transcriptional profiling approach towards the full gene content of the *Drosophila* genome. *Genome Biol.* **5**, R3 (2003).
41. Yandell, M. *et al.* A computational and experimental approach to validating annotations and gene predictions in the *Drosophila melanogaster* genome. *Proc. Natl Acad. Sci. USA* **102**, 1566–1571 (2005).
42. Manak, J. R. *et al.* Biological function of unannotated transcription during the early development of *Drosophila melanogaster*. *Nature Genet.* **38**, 1151–1158 (2006).
43. Lin, M. F. *et al.* Revisiting the protein-coding gene catalog of *Drosophila melanogaster* using twelve fly genomes. *Genome Res.* doi:10.1101/gr.6679507 (in the press).
44. Yang, Z. & Bielawski, J. P. Statistical methods for detecting molecular adaptation. *Trends Ecol. Evol.* **15**, 496–503 (2000).
45. Mignone, F., Grillo, G., Liuni, S. & Pesole, G. Computational identification of protein coding potential of conserved sequence tags through cross-species evolutionary analysis. *Nucleic Acids Res.* **31**, 4639–4645 (2003).
46. Zhang, L., Pavlovic, V., Cantor, C. R. & Kasif, S. Human-mouse gene identification by comparative evidence integration and evolutionary analysis. *Genome Res.* **13** (6A), 1190–1202 (2003).
47. Crosby, M. A. *et al.* FlyBase: genomes by the dozen. *Nucleic Acids Res.* **35** (Database issue) D486–D491 (2007).
48. Ashburner, M. *et al.* Gene ontology: tool for the unification of biology. The Gene Ontology Consortium. *Nature Genet.* **25**, 25–29 (2000).
49. Ochman, H., Ajioka, J. W., Garza, D. & Hartl, D. L. Inverse polymerase chain reaction. *Bio/Technology* **8**, 759–760 (1990).
50. Hoskins, R. A. *et al.* Rapid and efficient cDNA library screening by self-ligation of inverse PCR products (SLIP). *Nucleic Acids Res.* **33**, e185 (2005).
51. Wan, K. H. *et al.* High-throughput plasmid cDNA library screening. *Nature Protocols* **1**, 624–632 (2006).
52. Hahn, M. W., Han, M. V. & Han, S.-G. Gene family evolution across 12 *Drosophila* genomes. *PLoS Genet* **3**, e197 (2007).
53. Andrews, J. *et al.* The stoned locus of *Drosophila melanogaster* produces a dicistronic transcript and encodes two distinct polypeptides. *Genetics* **143**, 1699–1711 (1996).
54. Brogna, S. & Ashburner, M. The Adh-related gene of *Drosophila melanogaster* is expressed as a functional dicistronic messenger RNA: multigenic transcription in higher organisms. *EMBO J.* **16**, 2023–2031 (1997).
55. Hatfield, D. L. & Gladyshev, V. N. How selenium has altered our understanding of the genetic code. *Mol. Cell. Biol.* **22**, 3565–3576 (2002).
56. Kryukov, G. V. *et al.* Characterization of mammalian selenoproteomes. *Science* **300**, 1439–1443 (2003).
57. Copeland, P. R. Regulation of gene expression by stop codon recoding: selenocysteine. *Gene* **312**, 17–25 (2003).
58. Castellano, S. *et al.* In silico identification of novel selenoproteins in the *Drosophila melanogaster* genome. *EMBO Rep.* **2**, 697–702 (2001).
59. von der Haar, T. & Tuite, M. F. Regulated translational bypass of stop codons in yeast. *Trends Microbiol.* **15**, 78–86 (2007).
60. Luo, G. X. *et al.* A specific base transition occurs on replicating hepatitis delta virus RNA. *J. Virol.* **64**, 1021–1027 (1990).
61. Casey, J. L. & Gerin, J. L. Hepatitis D virus RNA editing: specific modification of adenosine in the antigenomic RNA. *J. Virol.* **69**, 7593–7600 (1995).
62. Steneberg, P. *et al.* Translational readthrough in the hdc mRNA generates a novel branching inhibitor in the *Drosophila* trachea. *Genes Dev.* **12**, 956–967 (1998).
63. Bass, B. L. RNA editing by adenosine deaminases that act on RNA. *Annu. Rev. Biochem.* **71**, 817–846 (2002).
64. Ivanov, I. P. *et al.* The *Drosophila* gene for antizyme requires ribosomal frameshifting for expression and contains an intronic gene for snRNP Sm D3 on the opposite strand. *Mol. Cell. Biol.* **18**, 1553–1561 (1998).
65. Eddy, S. R. Non-coding RNA genes and the modern RNA world. *Nature Rev. Genet.* **2**, 919–929 (2001).
66. Yuan, G. *et al.* RNomics in *Drosophila melanogaster*: identification of 66 candidates for novel non-messenger RNAs. *Nucleic Acids Res.* **31**, 2495–2507 (2003).
67. Lestrade, L. & Weber, M. J. snoRNA-LBME-db, a comprehensive database of human H/ACA and C/D box snoRNAs. *Nucleic Acids Res.* **34** (Database issue), D158–D162 (2006).
68. Bier, E. *Drosophila*, the golden bug, emerges as a tool for human genetics. *Nature Rev. Genet.* **6**, 9–23 (2005).
69. Hoopengardner, B., Bhalla, T., Staber, C. & Reenan, R. Nervous system targets of RNA editing identified by comparative genomics. *Science* **301**, 832–836 (2003).
70. Mignone, F. *et al.* UTRdb and UTRsite: a collection of sequences and regulatory motifs of the untranslated regions of eukaryotic mRNAs. *Nucleic Acids Res.* **33** (Database issue), D141–D146 (2005).
71. Cohen, R. S., Zhang, S. & Dollar, G. L. The positional, structural, and sequence requirements of the *Drosophila* TLS RNA localization element. *RNA* **11**, 1017–1029 (2005).
72. Allemand, F. *et al.* *Escherichia coli* ribosomal protein L20 binds as a single monomer to its own mRNA bearing two potential binding sites. *Nucleic Acids Res.* **35**, 3016–3031 (2007).
73. Okumura, T., Matsumoto, A., Tanimura, T. & Murakami, R. An endoderm-specific GATA factor gene, dGATAe, is required for the terminal differentiation of the *Drosophila* endoderm. *Dev. Biol.* **278**, 576–586 (2005).
74. Park, S. W. *et al.* An evolutionarily conserved domain of roX2 RNA is sufficient for induction of H4-Lys16 acetylation on the *Drosophila* X chromosome. *Genetics* (in the press).
75. Park, Y. & Kuroda, M. I. Epigenetic aspects of X-chromosome dosage compensation. *Science* **293**, 1083–1085 (2001).
76. Berezikov, E., Cuppen, E. & Plasterk, R. H. Approaches to microRNA discovery. *Nature Genet.* **38** (Suppl 1), S2–S7 (2006).
77. Bartel, D. P. MicroRNAs: genomics, biogenesis, mechanism, and function. *Cell* **116**, 281–297 (2004).
78. Stark, A. *et al.* Systematic discovery and characterization of fly microRNAs using 12 *Drosophila* genomes. *Genome Res.* doi:10.1101/gr.6593807 (in the press).
79. Ruby, J. G. *et al.* Evolution, biogenesis, expression, and target predictions of a substantially expanded set of *Drosophila* microRNAs. *Genome Res.* doi:10.1101/gr.6597907 (in the press).
80. Pekarsky, Y. *et al.* Tcl1 expression in chronic lymphocytic leukemia is regulated by miR-29 and miR-181. *Cancer Res.* **66**, 11590–11593 (2006).
81. Ruby, J. G., Jan, C. H. & Bartel, D. P. Intronic microRNA precursors that bypass Drosha processing. *Nature* **448**, 83–86 (2007).

82. Okamura, K. *et al.* The mirtron pathway generates microRNA-class regulatory RNAs in *Drosophila*. *Cell* **130**, 89–100 (2007).
83. Lewis, B. P. *et al.* Prediction of mammalian microRNA targets. *Cell* **115**, 787–798 (2003).
84. Stark, A., Brennecke, J., Russell, R. B. & Cohen, S. M. Identification of *Drosophila* microRNA targets. *PLoS Biol.* **1**, E60 (2003).
85. Lai, E. C. Micro RNAs are complementary to 3' UTR sequence motifs that mediate negative post-transcriptional regulation. *Nature Genet.* **30**, 363–364 (2002).
86. Lewis, B. P., Burge, C. B. & Bartel, D. P. Conserved seed pairing, often flanked by adenosines, indicates that thousands of human genes are microRNA targets. *Cell* **120**, 15–20 (2005).
87. Tompa, M. Identifying functional elements by comparative DNA sequence analysis. *Genome Res.* **11**, 1143–1144 (2001).
88. Stormo, G. D. DNA binding sites: representation and discovery. *Bioinformatics* **16**, 16–23 (2000).
89. Kheradpour, P., Stark, A., Roy, S. & Kellis, M. Reliable prediction of regulator targets using 12 *Drosophila* genomes. *Genome Res.* doi:10.1101/gr.7090407 (in the press).
90. Stathopoulos, A. & Levine, M. Genomic regulatory networks and animal development. *Dev. Cell* **9**, 449–462 (2005).
91. Schroeder, M. D. *et al.* Transcriptional control in the segmentation gene network of *Drosophila*. *PLoS Biol.* **2**, e271 (2004).
92. Zeitlinger, J. *et al.* Whole-genome ChIP-chip analysis of Dorsal, Twist, and Snail suggests integration of diverse patterning processes in the *Drosophila* embryo. *Genes Dev.* **21**, 385–390 (2007).
93. Kanehisa, M. *et al.* The KEGG resource for deciphering the genome. *Nucleic Acids Res.* **32** (Database issue) D277–D280 (2004).
94. Berman, B. P. *et al.* Exploiting transcription factor binding site clustering to identify cis-regulatory modules involved in pattern formation in the *Drosophila* genome. *Proc. Natl Acad. Sci. USA* **99**, 757–762 (2002).
95. Markstein, M. *et al.* A regulatory code for neurogenic gene expression in the *Drosophila* embryo. *Development* **131**, 2387–2394 (2004).
96. Philippakis, A. A. *et al.* Expression-guided *in silico* evaluation of candidate cis regulatory codes for *Drosophila* muscle founder cells. *PLoS Comput. Biol.* **2**, e53 (2006).
97. Smale, S. T. & Kadonaga, J. T. The RNA polymerase II core promoter. *Annu. Rev. Biochem.* **72**, 449–479 (2003).
98. Gerber, A. P. *et al.* Genome-wide identification of mRNAs associated with the translational regulator PUMILIO in *Drosophila melanogaster*. *Proc. Natl Acad. Sci. USA* **103**, 4487–4492 (2006).
99. Zubiaga, A. M., Belasco, J. G. & Greenberg, M. E. The nonamer UUAUUUAUU is the key AU-rich sequence motif that mediates mRNA degradation. *Mol. Cell. Biol.* **15**, 2219–2230 (1995).
100. Fairbrother, W. G., Yeh, R. F., Sharp, P. A. & Burge, C. B. Predictive identification of exonic splicing enhancers in human genes. *Science* **297**, 1007–1013 (2002).
101. Kloosterman, W. P., Wienholds, E., Ketting, R. F. & Plasterk, R. H. Substrate requirements for let-7 function in the developing zebrafish embryo. *Nucleic Acids Res.* **32**, 6284–6291 (2004).
102. Grimson, A. *et al.* MicroRNA targeting specificity in mammals: determinants beyond seed pairing. *Mol. Cell* **27**, 91–105 (2007).
103. Farh, K. K. *et al.* The widespread impact of mammalian MicroRNAs on mRNA repression and evolution. *Science* **310**, 1817–1821 (2005).
104. Stark, A. *et al.* Animal microRNAs confer robustness to gene expression and have a significant impact on 3' UTR evolution. *Cell* **123**, 1133–1146 (2005).
105. Rajewsky, N. microRNA target predictions in animals. *Nature Genet.* **38** (suppl. 1), S8–S13 (2006).
106. Elnitski, L. *et al.* Distinguishing regulatory DNA from neutral sites. *Genome Res.* **13**, 64–72 (2003).
107. Abrams, E. W. & Andrew, D. J. CrebA regulates secretory activity in the *Drosophila* salivary gland and epidermis. *Development* **132**, 2743–2758 (2005).
108. Sandmann, T. *et al.* A temporal map of transcription factor activity: mef2 directly regulates target genes at all stages of muscle development. *Dev. Cell* **10**, 797–807 (2006).
109. Sandmann, T. *et al.* A core transcriptional network for early mesoderm development in *Drosophila melanogaster*. *Genes Dev.* **21**, 436–449 (2007).
110. Sethupathy, P., Corda, B. & Hatzigeorgiou, A. G. TarBase: A comprehensive database of experimentally supported animal microRNA targets. *RNA* **12**, 192–197 (2006).
111. Lee, T. I. *et al.* Control of developmental regulators by Polycomb in human embryonic stem cells. *Cell* **125**, 301–313 (2006).
112. Boyer, L. A. *et al.* Core transcriptional regulatory circuitry in human embryonic stem cells. *Cell* **122**, 947–956 (2005).
113. Aerts, S., van Helden, J., Sand, O. & Hassan, B. Fine-tuning enhancer models to predict transcriptional targets across multiple genomes. *PLoS ONE* **2** (11), e1115 (2007).
114. Maeder, M., Polansky, B., Robson, B. & Eastman, D. Phylogenetic footprinting analysis in the upstream regulatory regions of the *Drosophila* Enhancer of split genes. *Genetics* (in the press).
115. Van Doren, M. *et al.* Negative regulation of proneural gene activity: hairy is a direct transcriptional repressor of achaete. *Genes Dev.* **8**, 2729–2742 (1994).
116. Kraut, R. & Levine, M. Spatial regulation of the gap gene giant during *Drosophila* development. *Development* **111**, 601–609 (1991).
117. Bailey, A. M. & Posakony, J. W. Suppressor of hairless directly activates transcription of enhancer of split complex genes in response to Notch receptor activity. *Genes Dev.* **9**, 2609–2622 (1995).
118. Yin, Z. & Frasch, M. Regulation and function of tinman during dorsal mesoderm induction and heart specification in *Drosophila*. *Dev. Genet.* **22**, 187–200 (1998).
119. Margulies, E. H. *et al.* An initial strategy for the systematic identification of functional elements in the human genome by low-redundancy comparative sequencing. *Proc. Natl Acad. Sci. USA* **102**, 4795–4800 (2005).
120. Margulies, E. H., Chen, C. W. & Green, E. D. Differences between pair-wise and multi-sequence alignment methods affect vertebrate genome comparisons. *Trends Genet.* **22**, 187–193 (2006).
121. Farabaugh, P. J. Programmed translational frameshifting. *Annu. Rev. Genet.* **30**, 507–528 (1996).
122. Odom, D. T. *et al.* Tissue-specific transcriptional regulation has diverged significantly between human and mouse. *Nature Genet.* **39**, 730–732 (2007).
123. Ludwig, M. Z. & Kreitman, M. Evolutionary dynamics of the enhancer region of even-skipped in *Drosophila*. *Mol. Biol. Evol.* **12**, 1002–1011 (1995).
124. Ludwig, M. Z. *et al.* Functional evolution of a cis-regulatory module. *PLoS Biol.* **3**, e93 (2005).
125. The ENCODE Project Consortium. Identification and analysis of functional elements in 1% of the human genome by the ENCODE pilot project. *Nature* **447**, 799–816 (2007).
126. Kent, W. J. *et al.* The human genome browser at UCSC. *Genome Res.* **12**, 996–1006 (2002).

Supplementary Information is linked to the online version of the paper at www.nature.com/nature.

Acknowledgements We thank the National Human Genome Research Institute (NHGRI) for continued support. A.S. was supported in part by the Schering AG/Ernst Schering Foundation and in part by the Human Frontier Science Program Organization (HFSPO). P.K. was supported in part by a National Science Foundation Graduate Research Fellowship. J.S.P. thanks B. Raney and R. Baertsch, and the Danish Medical Research Council and the National Cancer Institute for support. J.B. thanks the Schering AG/Ernst Schering Foundation for a postdoctoral fellowship. L.Parts thanks J. Vilo. S.R. was supported by a HHMI-NIH/NIBIB Interfaces Training Grant and thanks T. Lane and M. Werner-Washburne. D.H., D.P.B., G.J.H. and T.C.K. are Investigators of the Howard Hughes Medical Institute, and B.P., J.G.R., E.H. and J.B. are affiliated with these investigators. J.W.C. and S.E.C. were supported by the NHGRI. M.K. was supported by start-up funds from the MIT Electrical Engineering and Computer Science Laboratory, the Broad Institute of MIT and Harvard, and the MIT Computer Science and Artificial Intelligence Laboratory, and by the Distinguished Alumnus (1964) Career Development Professorship.

Author Contributions Organizing committee: Manolis Kellis, William Gelbart, Doug Smith, Andrew G. Clark, Michael E. Eisen, Thomas C. Kaufman; protein-coding gene prediction: Michael F. Lin, Amey N. Deoras, Mira V. Han, Matthew W. Hahn, Donald G. Gilbert, Michael Weir, Michael Rice, Manolis Kellis; manual curation of protein-coding genes: Madeline A. Crosby, Harvard FlyBase curators, William M. Gelbart; validation of protein-coding genes: Joseph W. Carlson, Berkeley *Drosophila* Genome Project, Susan E. Celniker; non-coding RNA gene prediction: Jakob S. Pedersen, David Haussler, Yongkyu Park, Seung-Won Park, Manolis Kellis; microRNA gene prediction: Alexander Stark, Pouya Kheradpour, Leopold Parts, Manolis Kellis; microRNA cloning and sequencing: Julius Brennecke, Emily Hodges, Gregory J. Hannon; microRNA target prediction: Alexander Stark, J. Graham Ruby, Manolis Kellis, Eric C. Lai, David P. Bartel; motif identification: Alexander Stark, Pouya Kheradpour, Manolis Kellis; motif instance prediction: Alexander Stark, Pouya Kheradpour, Sushmita Roy, Morgan L. Maeder, Benjamin J. Polansky, Bryanne E. Robson, Deborah A. Eastman, Stein Aerts, Bassem Hassan, Jacques van Helden, Manolis Kellis; genome alignments: Angie S. Hinrichs, W. James Kent, Anat Caspi, Lior Pachter, Colin N. Dewey, Benedict Paten; phylogeny and branch length estimation: Matthew D. Rasmussen, Manolis Kellis; final manuscript preparation: Alexander Stark, Michael F. Lin, Pouya Kheradpour, Jakob Pedersen, Manolis Kellis.

Author Information Reprints and permissions information is available at www.nature.com/reprints. Correspondence and requests for materials should be addressed to M.K. (manoli@mit.edu).

Harvard FlyBase curators Madeline A. Crosby¹, Beverley B. Matthews¹, Andrew J. Schroeder¹, L. Sian Gramates¹, Susan E. St Pierre¹, Margaret Roark¹, Kenneth L. Wiley Jr¹, Rob J. Kulathinal¹, Peili Zhang¹, Kyl V. Myrick¹, Jerry V. Antone¹ & William M. Gelbart¹

Berkeley *Drosophila* Genome Project Joseph W. Carlson², Charles Yu², Soo Park², Kenneth H. Wan² & Susan E. Celniker²

¹FlyBase, The Biological Laboratories, Harvard University, 16 Divinity Avenue, Cambridge, Massachusetts 02138, USA. ²BDGP, LBNL, 1 Cyclotron Road MS 64-0119, Berkeley, California 94720, USA.

Constraint and turnover in sex-biased gene expression in the genus *Drosophila*

Yu Zhang^{1*}, David Sturgill^{1*}, Michael Parisi^{1†}, Sudhir Kumar² & Brian Oliver¹

Both genome content and deployment contribute to phenotypic differences between species^{1–5}. Sex is the most important difference between individuals in a species and has long been posited to be rapidly evolving. Indeed, in the *Drosophila* genus, traits such as sperm length, genitalia, and gonad size are the most obvious differences between species⁶. Comparative analysis of sex-biased expression should deepen our understanding of the relationship between genome content and deployment during evolution. Using existing^{7,8} and newly assembled genomes⁹, we designed species-specific microarrays to examine sex-biased expression of orthologues and species-restricted genes in *D. melanogaster*, *D. simulans*, *D. yakuba*, *D. ananassae*, *D. pseudoobscura*, *D. virilis* and *D. mojavensis*. We show that averaged sex-biased expression changes accumulate monotonically over time within the genus. However, different genes contribute to expression variance within species groups compared to between groups. We observed greater turnover of species-restricted genes with male-biased expression, indicating that gene formation and extinction may play a significant part in species differences. Genes with male-biased expression also show the greatest expression and DNA sequence divergence. This higher divergence and turnover of genes with male-biased expression may be due to high transcription rates in the male germline, greater functional pleiotropy of genes expressed in females, and/or sexual competition.

There are numerous case studies demonstrating that orthologues with sex-biased function diverge more rapidly than genes with non-biased function¹⁰. To determine systematically the relative contributions of gene content and expression divergence to sexual differences, we sampled sex-biased expression within the *Drosophila* genus using species-specific microarrays designed for the closely related *D. melanogaster*, *D. simulans* and *D. yakuba* group (common ancestor, 10–13 million years ago), and for the more distantly related *D. ananassae*, *D. pseudoobscura*, *D. virilis* and *D. mojavensis* (common ancestor, 40–65 million years ago) (Supplementary Table 1). The species-specific platform eliminated confounding effects of sequence divergence on hybridization and allowed us to assay the expression of lineage-restricted genes.

Previous work has demonstrated that sex-biased expression in *D. melanogaster* adults is substantial, primarily owing to gametogenesis¹⁰. This seems to be characteristic for the genus (Fig. 1, and Supplementary Fig. 1). Generally, we observed greater male-biased expression (~7–14% of the transcriptome) relative to female-biased expression (~3–9% of the transcriptome), at a significance value of

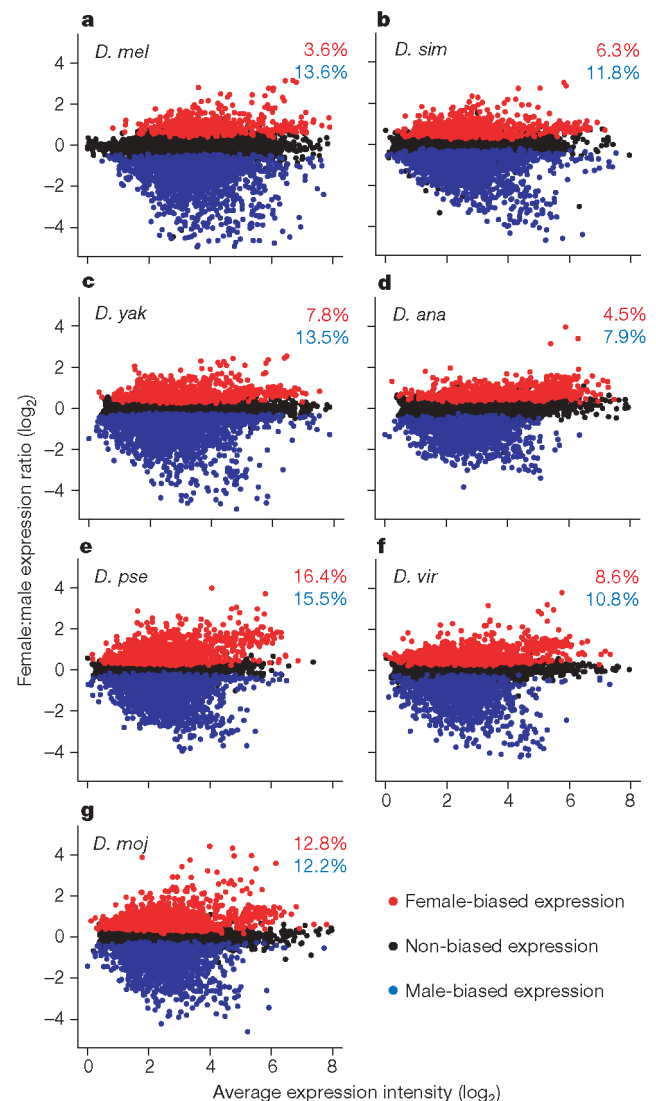


Figure 1 | Sex-biased expression in *Drosophila* species. **a–g**, Sex-biased female:male expression ratio (\log_2) versus average expression intensity (\log_2) plots for each *Drosophila* species. Expression intensities are arbitrary, where zero represents the minimum value. Values for genes with significant ($P \leq 0.01$, false-discovery-rate-corrected Mann–Whitney test) female-biased, male-biased and non-biased expression are shown. The per cent of genes with female-biased or male-biased expression is inset in each panel. *D. melanogaster*, *D. mel*; *D. simulans*, *D. sim*; *D. yakuba*, *D. yak*; *D. ananassae*, *D. ana*; *D. pseudoobscura*, *D. pse*; *D. virilis*, *D. vir*; and *D. mojavensis*, *D. moj*.

¹Laboratory of Cellular and Developmental Biology, National Institute of Diabetes and Digestive and Kidney Diseases, National Institutes of Health, Department of Health and Human Services, Bethesda, Maryland 20892, USA. ²Center for Evolutionary Functional Genomics, Biodesign Institute, Arizona State University, Tempe, Arizona 85287, USA. †Present address: Department of Biology, University of Pennsylvania, Pennsylvania 19104, USA.

*These authors contributed equally to this work.

$P \leq 0.01$ (Mann–Whitney, false-discovery-rate-corrected). The exceptions were *D. pseudoobscura* (~16% female- and male-biased expression) and *D. mojavensis* (~12% female- and male-biased expression). Additionally, the magnitude of male-biased expression was generally greater than the female-biased expression—the average \log_2 female:male expression ratio was -1.2 for genes with male-biased expression and 0.8 for genes with female-biased expression. This indicates that there were more genes approaching male-specific expression than female-specific expression. The genes that showed sex-biased expression in each species are listed in Supplementary Information (Supplementary Tables 3–16).

To examine expression divergence over time, we parsed the genes with orthologues in every species and constructed a pairwise matrix of \log_2 female:male expression ratios. We compared expression within species (two strains of *D. simulans*), between species within the closely related melanogaster subgroup, and between all seven species (Fig. 2a–c). Similar pairwise matrices for quadruplicate replicates within each species were also plotted as a baseline measurement of technical noise and biological variability (Supplementary Fig. 2). All expression ratio plots were linear and showed increasing expression divergence with inferred genetic distance.

There was an especially clear relationship between sequence and expression divergence. Neighbour-joining trees of expression divergence (from the pairwise expression ratios between each species; $1 - \text{Pearson's } r$; Supplementary Fig. 3), or by sequence divergence^{9,11} have the same topology (Fig. 2d). Expression divergence tightly correlated with time (Fig. 2e, $r^2 = 0.96$), which may provide a useful tool in molecular phylogenetics.

Although the whole-genome trends in expression divergence were both obvious and clear, at the gene level, the magnitude of expression

divergence was modest. Only 384 orthologue pairs (0.3%) showed significant female-biased expression in one species and significant male-biased expression in another. Switches between highly female-biased expression and highly male-biased expression were never observed (Fig. 2c). Extensive (20%) categorical changes in sex-bias class, especially for genes with male-biased expression, were previously reported between *D. melanogaster* and *D. simulans*^{12,13}. We observed a categorical change in sex-biased expression in 12% of the orthologues between these two species, but the changes were dominated by low magnitude changes between modest sex-biased expression and non-sex-biased categories. These values are highly sensitive to arbitrary significance-level cut-offs; however, it was clear in exploratory plots of expression ratios that genes with male-biased expression showed greater expression divergence (Fig. 2b, c). Plots of expression ratio standard deviations against average expression ratio (Fig. 3a) also showed a clear excess of variable expression among orthologues with male-biased expression ($P < 10^{-8}$, chi-squared test). Thus, male-biased expression contributes heavily to overall expression divergence.

To determine if particular types of genes show greater or lesser expression divergence we analysed Gene Ontology¹⁴ (GO) terms. Unsurprisingly, genes annotated as ‘unknown function’ are significantly over-represented ($P < 10^{-8}$, Fisher’s exact test) among genes with variable expression. Genes with ‘transcriptional regulation’ annotations were under-represented in the same gene set ($P < 10^{-4}$, Fisher’s exact test), suggesting that genes involved in transcription regulation are under constraint. Similar constrained expression of transcriptional regulators was observed in a study of metamorphosis in the melanogaster subgroup⁵.

Just as changes in DNA sequence can have consequences ranging from deleterious to neutral to advantageous¹⁵, changes in gene

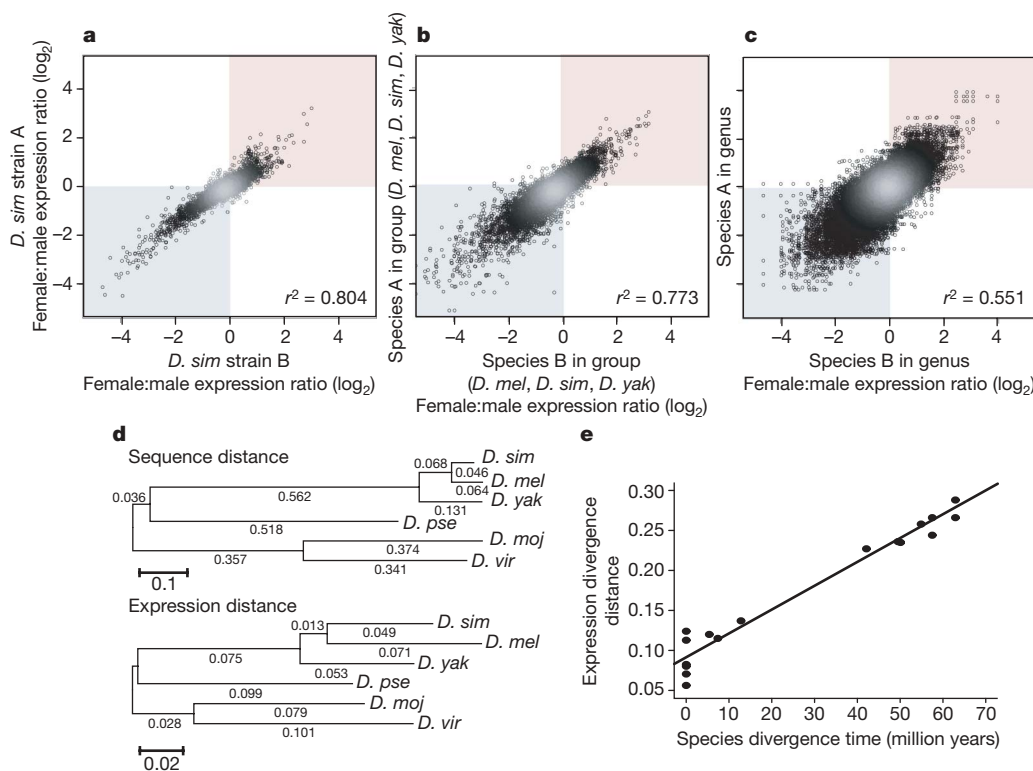


Figure 2 | Expression divergence among common orthologues.

Female:male expression ratios (\log_2) for orthologue pairs, plotted against each other: **a**, two different *D. simulans* strains; **b**, the melanogaster subgroup (*D. melanogaster*, *D. simulans* and *D. yakuba*); **c**, all seven *Drosophila* species. All the density (grey for high, black for low) scatter plots include every 1:1 pair of common orthologues for which both have an expression value. In **b** and **c**, the species A and B designation is arbitrary, but A is assigned to the species in the pair most closely related to

D. melanogaster. **d**, Neighbour-joining trees with branch lengths inferred using sequence distance (genomic mutation distance¹¹) and the expression distance ($1 - \text{Pearson's } r$) for all pairs of species except the pairs between the *D. ananassae* outlier and other species (Supplementary Fig. 3). **e**, Expression distance values plotted against estimated divergence time¹¹ for all possible species pairs and replicates within species. Quadruplicate replicates within each species were used at a time of 0 million years.

expression should have variable effects, owing to underlying mutations in transcription factors, *cis*-regulatory sites and post-transcriptional regulators, and the resulting variance will be subject to drift and selection^{2,3,5,13,16–18}. We were able to distinguish expression differences between species well enough to show a linear relationship with time at the full-transcriptome level, but does this apply to individual genes?

To determine if there is a common set of orthologues that can tolerate variable expression (that can be thought of as the thematic equivalent of a synonymous codon substitution), we asked if expression divergence between orthologues within the melanogaster subgroup correlates with the expression divergence between more distantly related species. We found no significant correlation between orthologue expression divergence between groups of species ($r^2 = 0.08$, Fig. 3b). Genes with greater expression divergence in the melanogaster subgroup and the remaining species are different. Thus, although overall expression divergence shows a clock-like behaviour (reflecting mutation accumulation in a neutral model, or an adaptive speed limit in a selection model), different individual genes contribute to this global expression divergence in different amounts. This suggests that there is not a common set of genes that tolerate large drifts in sex-biased expression ratios.

To analyse further the orthologues with the most divergent expression, we selected orthologues with the greatest expression divergence (s.d. > 0.5) and subjected them to cluster analysis with species-order fixed (Fig. 3c). Strikingly, even those genes with the most variable expression were organized into well-defined clusters. Each of the clusters was subsequently analysed to look for patterns of change. We observed three distinct cluster types revealing expression divergence between lineages, aberrant expression in a single species, and unpatterned variability (Fig. 3c, d). For example, cluster 'A' shows higher male-biased expression in just the melanogaster

subgroup (*D. melanogaster*, *D. simulans* and *D. yakuba*); cluster 'B' shows increased male-biased expression in *D. pseudoobscura* only; and cluster 'C' shows no evidence for a phylogenetic trend. Briefly, among the 5% of common orthologues with the most variable expression, 52% exhibited lineage-specific, 22% species-specific and only 25% unpatterned expression variability.

Having only a few sequenced genomes seriously hinders the study of genes that are species- or lineage-specific (species-restricted). We took advantage of the species-specific array design to determine the contribution of common orthologues and species-restricted genes to overall sex-biased expression patterns (Fig. 4a, b). Female-biased expression was over-represented ($P < 10^{-2}$, chi-squared test) among common orthologues in four of the seven species, whereas male-biased expression was always under-represented. The pattern was reversed among the species-restricted genes. Female-biased expression of species-restricted genes was less prevalent in all species except *D. virilis*, and male-biased expression was more prevalent in each of the species examined. Female-biased expression was also under-represented among paralogues (Supplementary Fig. 4). Similar results were obtained using TBLASTN methods to detect genes that had diverged to obscure orthology (Supplementary Fig. 5). These suggest that genes with male-biased expression have higher effective birth and extinction rates.

We also asked if sex-bias and expression divergence correlate with sequence divergence among orthologues. If similar selective pressure acts on both protein-coding capacity and expression at a given locus, then they should correlate. However, protein-coding capacity and expression divergence need not be tightly coupled. For example, high expression divergence can result from changes in upstream transcription factors or the *cis*-regulatory sites that they bind¹⁹.

Synonymous (K_S) and non-synonymous substitution rates (K_A) in protein-coding genes were used to examine sequence divergence²⁰.

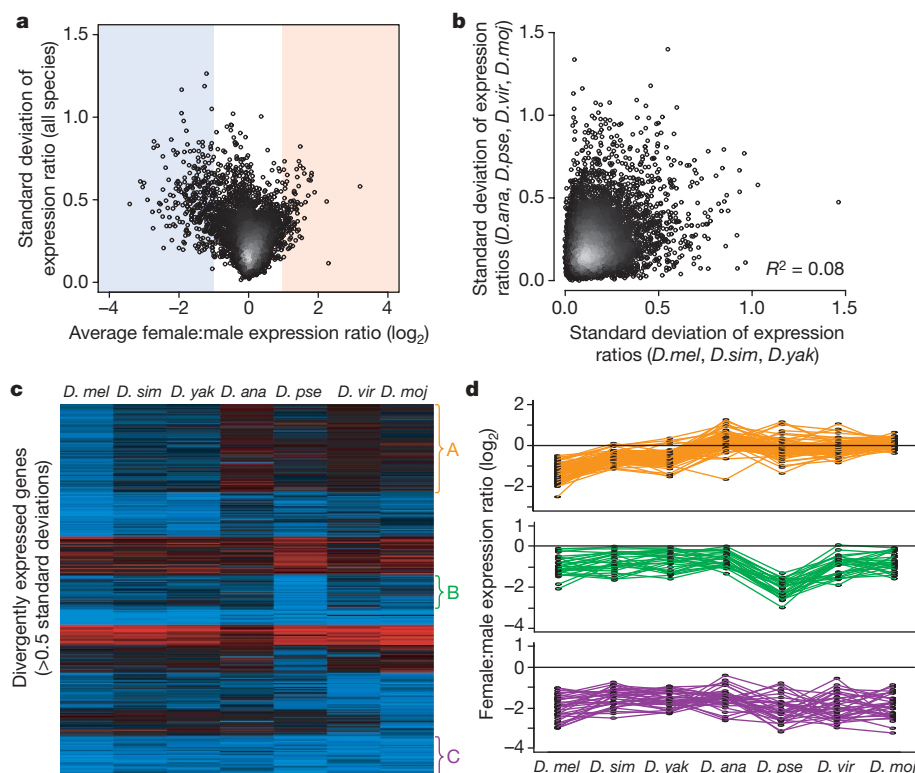


Figure 3 | Expression divergence within and between species and groups. **a**, Average female:male expression ratios for common orthologues plotted against expression divergence (expression ratio standard deviations between 7 species) for the same orthologues. **b**, Expression ratio standard deviations among members of the melanogaster subgroup (*D. melanogaster*, *D. simulans* and *D. yakuba*) plotted against standard deviations among the

other four species (*D. ananassae*, *D. pseudoobscura*, *D. virilis* and *D. mojavensis*). **c**, K-means clustering ($K = 10$, species-order fixed) of expression ratios where s.d. > 0.5. Female-biased (red), male-biased (blue) and non-biased (black) expression is indicated. **d**, Examples of gene clusters that are indicated on the Eisengram (**c**). Species (x axis) and \log_2 female:male expression ratio (y axis) of common orthologues are shown.

Multiple substitutions occur at a given site between distantly related species (for example, *D. melanogaster* and *D. mojavensis*) making K_A/K_S ratios much less reliable, and therefore K_A/K_S ratios were used only within the melanogaster subgroup (Fig. 4c, d). Genes with male-biased expression were expected to show higher K_A/K_S ratios¹⁰. Indeed, common orthologues with male-biased expression had K_A/K_S values within the melanogaster subgroup (0.129), more than two times those of common orthologues with female-biased expression (0.061). Interestingly, common orthologues with non-biased expression showed intermediate K_A/K_S values. We observed a strong correlation between expression and sequence divergence among the genes showing the greatest expression divergence (Fig. 4c), as

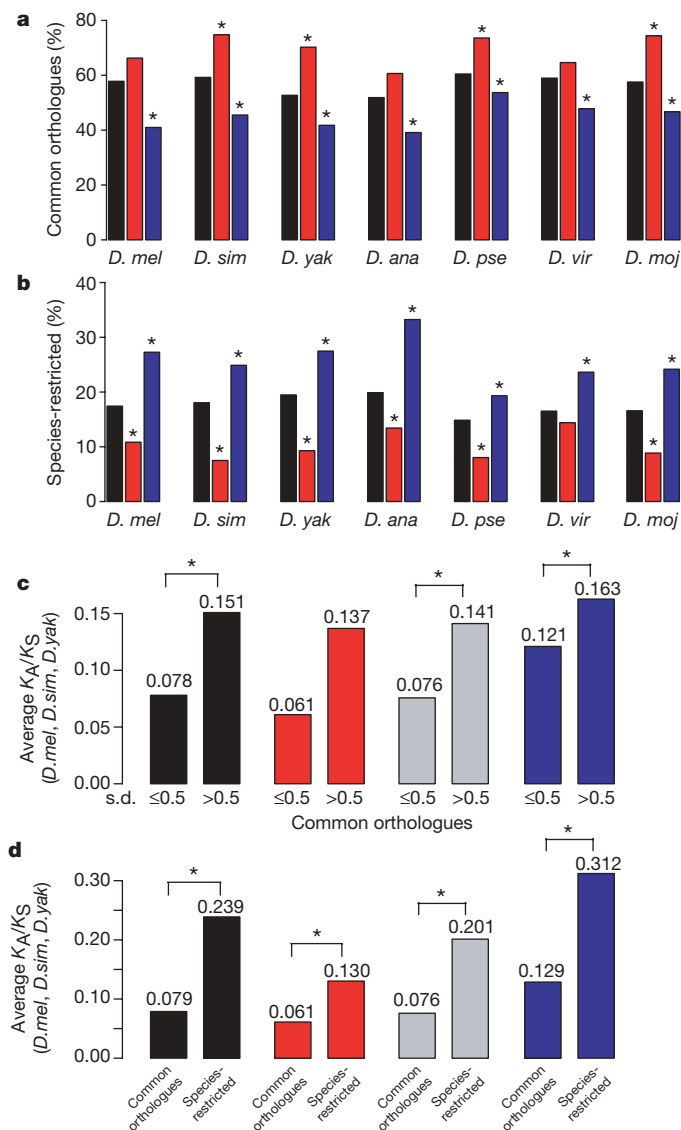


Figure 4 | Relationship between sex-biased expression, gene content and sequence divergence. Gene content and expression of common orthologues (a) and species-restricted (b) genes. The percentages of all genes (black) and with female (red) or male (blue)-biased expression are shown. Significant differences ($P < 10^{-2}$, chi-squared test) between sex-biased classes and total genes are indicated (asterisks). See Supplementary Fig. 5 for paralogs. Average K_A/K_S ratios within the melanogaster subgroup for common orthologues with high or low expression-ratio s.d. (c) and for all common orthologues or species-restricted genes (d). Bars are colour-coded as in a, with the addition of grey bars, which represent non-biased expression. Significant differences ($P < 10^{-2}$, Mann–Whitney test) between common orthologues with constrained expression and variable expression, or between common orthologues and species-restricted genes are indicated (asterisks).

has also been seen in mammals²¹. Additionally, species-restricted genes had higher sequence-divergence than common orthologues for all expression categories (Fig. 4d), as has been seen in vertebrates²². Perhaps expression divergence, gene turn-over, sex-bias and sequence divergence of individual genes are often coupled to the same selective forces.

The contrasting divergence and turnover patterns of genes with male-biased expression relative to those with female-biased expression is somewhat surprising. Reproduction is the function of a couple, not an individual; therefore co-evolution of reproductive traits is expected to occur. For example, selection for sperm tail length in *Drosophila* males is coupled to selection for length of the seminal receptacle in females²³. There are a number of possible explanations. There may be greater *de novo* generation of genes with male-biased expression as a result of simple sequence requirements for core promoter generation²⁴ and extremely high levels of RNA polymerase in spermatocytes²⁵. This combination might result in excessive transcription of intragenic regions²⁶. A few of these new genes with male-biased expression might be functional, but most of these ‘*de novo*’ genes would be expected to rapidly degenerate. Alternatively, genes required for oogenesis may be more constrained because of pleiotropy or the under-representation of paralogues with partially overlapping functions. Many *D. melanogaster* genes required for female fertility are also required for organismal viability²⁷, and genes with clear multiple functions, such as those encoding ribosomal proteins, are overexpressed in ovaries relative to testes²⁸. Finally, male–male competition might be particularly strong²⁹. The addition of more sequenced genomes will provide ample opportunities to explore these questions further.

METHODS SUMMARY

Flies. Species were grown on standard media (Tucson *Drosophila* Stock Center). We isolated messenger RNA from adult females and males grown at 22 °C (5–7 days post eclosion), and labelled and hybridized using standard methods.

Arrays. Oligonucleotide arrays of 50-mers (NimbleGen Systems) were designed against draft assemblies and *ab initio* annotations we contributed to the gene model reconciliation⁹ (Supplementary Table 2). *D. melanogaster* 60-mer expression array (NimbleGen Design ID 2005-10-17_Dmel4_60mer_exp) designed on the basis of Flybase annotation V4.2 was used for *D. melanogaster* hybridizations. For this report, we remapped all array elements to current consensus gene models⁹. Our expression results and conclusions were similar using the original models. Because low-magnitude expression divergence is difficult to distinguish from noise, we performed at least quadruplicate replicates for each species and only channels passing a stringent quality control regimen were used in the final analysis (72 channels total). Full platform descriptions and data are available at the GEO under accession GSE6640.

For each gene, \log_2 intensities for female and male expression were compared by non-parametric two-sample Mann–Whitney tests to generate the significance of sex-biased expression ($P \leq 0.01$) and ratios of each gene were calculated as the average probeset intensity in female channels divided by the intensity in male channels. Common orthologues are present in all 7 species and species-restricted genes are present in at least one species, but absent in ≥ 1 species.

Full Methods and any associated references are available in the online version of the paper at www.nature.com/nature.

Received 9 July; accepted 28 September 2007.

1. Denver, D. R. *et al.* The transcriptional consequences of mutation and natural selection in *Caenorhabditis elegans*. *Nature Genet.* **37**, 544–548 (2005).
2. Jordan, I. K., Marino-Ramirez, L. & Koonin, E. V. Evolutionary significance of gene expression divergence. *Gene* **345**, 119–126 (2005).
3. Khaitovich, P., Enard, W., Lachmann, M. & Paabo, S. Evolution of primate gene expression. *Nature Rev. Genet.* **7**, 693–702 (2006).
4. Rifkin, S. A., Houle, D., Kim, J. & White, K. P. A mutation accumulation assay reveals a broad capacity for rapid evolution of gene expression. *Nature* **438**, 220–223 (2005).
5. Rifkin, S. A., Kim, J. & White, K. P. Evolution of gene expression in the *Drosophila melanogaster* subgroup. *Nature Genet.* **33**, 138–144 (2003).
6. Powell, J. R. *Progress and Prospects in Evolutionary Biology: The Drosophila Model* (Oxford Univ. Press, Oxford, 1997).
7. Adams, M. D. *et al.* The genome sequence of *Drosophila melanogaster*. *Science* **287**, 2185–2195 (2000).

8. Richards, S. *et al.* Comparative genome sequencing of *Drosophila pseudoobscura*: chromosomal, gene, and *cis*-element evolution. *Genome Res.* **15**, 1–18 (2005).
9. *Drosophila* 12 Genomes Consortium. Evolution of genes and genomes in the *Drosophila* phylogeny. *Nature* doi:10.1038/nature06341 (this issue).
10. Ellegren, H. & Parsch, J. The evolution of sex-biased genes and sex-biased gene expression. *Nature Rev. Genet.* **8**, 689–698 (2007).
11. Tamura, K., Subramanian, S. & Kumar, S. Temporal patterns of fruit fly (*Drosophila*) evolution revealed by mutation clocks. *Mol. Biol. Evol.* **21**, 36–44 (2004).
12. Nuzhdin, S. V., Wayne, M. L., Harmon, K. L. & McIntyre, L. M. Common pattern of evolution of gene expression level and protein sequence in *Drosophila*. *Mol. Biol. Evol.* **21**, 1308–1317 (2004).
13. Ranz, J. M., Castillo-Davis, C. I., Meiklejohn, C. D. & Hartl, D. L. Sex-dependent gene expression and evolution of the *Drosophila* transcriptome. *Science* **300**, 1742–1745 (2003).
14. Harris, M. A. *et al.* The Gene Ontology (GO) database and informatics resource. *Nucleic Acids Res.* **32**, D258–D261 (2004).
15. Ohta, T. & Gillespie, J. H. Development of neutral and nearly neutral theories. *Theor. Popul. Biol.* **49**, 128–142 (1996).
16. Hsieh, W. P., Chu, T. M., Wolfinger, R. D. & Gibson, G. Mixed-model reanalysis of primate data suggests tissue and species biases in oligonucleotide-based gene expression profiles. *Genetics* **165**, 747–757 (2003).
17. Khaitovich, P., Paabo, S. & Weiss, G. Toward a neutral evolutionary model of gene expression. *Genetics* **170**, 929–939 (2005).
18. Lemos, B., Meiklejohn, C. D., Caceres, M. & Hartl, D. L. Rates of divergence in gene expression profiles of primates, mice, and flies: stabilizing selection and variability among functional categories. *Evolution Int. J. Org. Evolution* **59**, 126–137 (2005).
19. Wray, G. A. The evolutionary significance of *cis*-regulatory mutations. *Nature Rev. Genet.* **8**, 206–216 (2007).
20. Li, W. H. Unbiased estimation of the rates of synonymous and nonsynonymous substitution. *J. Mol. Evol.* **36**, 96–99 (1993).
21. Khaitovich, P. *et al.* Parallel patterns of evolution in the genomes and transcriptomes of humans and chimpanzees. *Science* **309**, 1850–1854 (2005).
22. Subramanian, S. & Kumar, S. Gene expression intensity shapes evolutionary rates of the proteins encoded by the vertebrate genome. *Genetics* **168**, 373–381 (2004).
23. Miller, G. T. & Pitnick, S. Sperm-female coevolution in *Drosophila*. *Science* **298**, 1230–1233 (2002).
24. FitzGerald, P. C., Sturgill, D., Shyakhtenko, A., Oliver, B. & Vinson, C. Comparative genomics of *Drosophila* and human core promoters. *Genome Biol.* **7**, R53 (2006).
25. Schmidt, E. E. & Schibler, U. High accumulation of components of the RNA polymerase II transcription machinery in rodent spermatids. *Development* **121**, 2373–2383 (1995).
26. Struhl, K. Transcriptional noise and the fidelity of initiation by RNA polymerase II. *Nature Struct. Mol. Biol.* **14**, 103–105 (2007).
27. Perrimon, N., Mohler, D., Engstrom, L. & Mahowald, A. P. X-linked female-sterile loci in *Drosophila melanogaster*. *Genetics* **113**, 695–712 (1986).
28. Parisi, M. *et al.* A survey of ovary-, testis-, and soma-biased gene expression in *Drosophila melanogaster* adults. *Genome Biol.* **5**, R40 (2004).
29. Singh, S. R., Singh, B. N. & Hoenigsberg, H. F. Female remating, sperm competition and sexual selection in *Drosophila*. *Genet. Mol. Res.* **1**, 178–215 (2002).

Supplementary Information is linked to the online version of the paper at www.nature.com/nature.

Acknowledgements We thank the *Drosophila* Comparative Genome Sequencing and Analysis Consortium for access to the assembly, alignment and annotation of the 12 sequenced *Drosophila* genomes, S. Davis for valuable technical advice, and K. P. White, C. Vinson, A. Clark, M. Lynch and members of the Oliver laboratory for helpful discussion and comments on the manuscript. We are supported by the Intramural Research Program of the NIH, NIDDK, except S.K. who is supported by the NIH Extramural Program.

Author Information Reprints and permissions information is available at www.nature.com/reprints. Correspondence and requests for materials should be addressed to Y.Z. (yuzhang@mail.nih.gov) and B.O. (oliver@helix.nih.gov).

METHODS

Flies. Stocks (Tucson Drosophila Stock Center) of *D. simulans* (14021-0251.198 and 14021-0251.011), *D. yakuba* (14021-0261.01), *D. ananassae* (14024-0371.13), *D. pseudoobscura* (14011-0121.94), *D. mojavensis* (15081-1352.22) and *D. virilis* (15010-1051.87) were grown on standard cornmeal media (Tucson Drosophila Stock Center), with the exception of *D. pseudoobscura*, *D. mojavensis* and *D. virilis*, which were grown on Banana-Opuntia media (Tucson Drosophila Stock Center).

Arrays. Oligonucleotide 50-mer arrays (NimbleGen Systems) were designed on the basis of draft or versioned genomic assemblies of six *Drosophila* species (*D. simulans* assembly: PCAP assembly for white501, GSC, Wash U, 01 December 04; *D. yakuba* assembly: GSC (WashU), 07 April 2004. *D. ananassae* assembly: Arachne Assembler, Agencourt, 06 December 2004; *D. pseudoobscura* assembly: v. 1.03 from FlyBase, December 2004; *D. mojavensis* assembly: Arachne Assembler, Agencourt, 06 December 2004; *D. virilis* assembly: Arachne Assembler, Agencourt, 29 October 2004). An average of 10 array probes were selected without bias with respect to position within each of our OLIV gene models. The OLIV set includes both high- and low-confidence models, which included non-overlapping draft EIS gene models based on *D. melanogaster* orthology (M. Eisen laboratory, v1.0, Feb 2005), *ab initio* GeneID³⁰ predictions using the *D. melanogaster* training set, FlyBase³¹ genes and expressed sequence tag sequence from GenBank³². Array probes were remapped to the final genome assemblies and gene predictions GLEANR⁹ by BLAT V25x1 (ref. 33). Only probes uniquely and perfectly matched to both annotation and assembly were used for final analysis.

Hybridization was according to the manufacturer's instructions (NimbleGen Systems), except that hybridization was done in custom-made chambers. Arrays were scanned on an Axon GenePix 4000B (Molecular Devices Corporation) and data were captured using NimbleScan 2.1 (NimbleGen Systems). For each species, at least four hybridizations, including technical (dye-flipped) replicates for each of two discrete samples (biological replicates) were performed. Extra hybridizations were performed for a different *D. simulans* strain (14021-0251.011).

Data handling. We used a multi-step quality control pipeline. Hybridization channels were retained when experimental intensities were >1 s.d. above mean on-spot background (from non-*Drosophila* control elements) and the inter-quartile ranges of log₂ intensities were >1. Passed channels were normalized using variance stabilization normalization³⁴. Signal variability between replicate channels was then tested by calculating the inter-quartile range of the relative log expression values for each channel against a virtual reference (the median value in all replicate channels for each array element). The channels with inter-quartile ranges of the relative log expression values greater than one were rejected. Passed channels were re-normalized by variance stabilization normalization from the raw data. This approach does not over-normalize the data while assuring that hybridization intensity is consistent between replicate channels.

For each gene, log₂ intensities from female-sample single channels and male-sample single channels were compared by non-parametric two-sample Mann-Whitney tests to generate a significance measure. Ratios were then calculated as the average probeset intensity in female channels divided by the average probeset intensity in male channels for each gene. *P* values were false-discovery-rate-corrected³⁵. The cut-off for sex-biased expression we used was

false-discovery-rate-adjusted $P \leq 0.01$. Expression was called 'below background' when the average probeset intensity was less than the average intensity of negative controls (probes targeting four *Arabidopsis* genes and two yeast genes) in both sexes.

Orthology calls are as described⁹. Common orthologues represent orthologues present in all 7 species and species-restricted genes are present in one species, but absent in ≥ 1 species. Paralogues are excluded from most of the data analysis. Multiple sequence alignments of orthologues were imported using the seqinR package³⁶. K_A/K_S estimates adjusted for differences in transition and transversion rates were calculated from these alignments²⁰. Average K_A/K_S of common orthologues were calculated from all possible K_A/K_S values between the melanogaster subgroup, then median K_A/K_S values were calculated for each category of genes with different sex-biased expression and genes with different expression divergence.

DNA sequence divergence and expression divergence ($1 - \text{Pearson's } r$ between the sex-biased expression ratio of two species) between each species pair was calculated. DNA sequence divergence was presented using genomic mutation distance by the method described previously¹¹. Neighbour-joining trees were then inferred using DNA sequence divergence and expression distance from six species separately in MEGA4 (ref. 37). The common orthologues with most variable expression among species (s.d. > 0.5) were K-means clustered with 10 nodes using the euclidean similarity metric in Cluster 3.0/Tree-View³⁸.

D. melanogaster v.4.3 and *D. pseudoobscura* v.2.0 sequence and annotation from FlyBase were used as queries against the final genome assemblies⁹ of all other six species by TBLASTN³⁹.

Unless otherwise noted all data handling was performed in BioConductor⁴⁰.

30. Parra, G., Blanco, E. & Guigo, R. GeneID in *Drosophila*. *Genome Res.* **10**, 511–515 (2000).
31. Grumbling, G. & Strelets, V. FlyBase: anatomical data, images and queries. *Nucleic Acids Res.* **34**, D484–D488 (2006).
32. Benson, D. A., Karsch-Mizrachi, I., Lipman, D. J., Ostell, J. & Wheeler, D. L. GenBank. *Nucleic Acids Res.* **34**, D16–D20 (2006).
33. Kent, W. J. BLAT—the BLAST-like alignment tool. *Genome Res.* **12**, 656–664 (2002).
34. Huber, W., von Heydebreck, A., Sultmann, H., Poustka, A. & Vingron, M. Variance stabilization applied to microarray data calibration and to the quantification of differential expression. *Bioinformatics* **18** (Suppl 1), S96–S104 (2002).
35. Benjamini, Y. & Hochberg, Y. Controlling the false discovery rate: a practical and powerful approach to multiple testing. *J. Roy. Statist. Soc. Ser. B. Methodological* **57**, 289–300 (1995).
36. Charif, D. & Lobry, J. R. in *Structural approaches to sequence evolution: Molecules, networks, populations* (eds Bastolla, U. M.P., Roman, H. E. and Vendruscolo, M.) (2006).
37. Tamura, K., Dudley, J., Nei, M. & Kumar, S. MEGA4: Molecular Evolutionary Genetics Analysis (MEGA) Software Version 4.0. *Mol. Biol. Evol.* **24**, 1596–1599 (2007).
38. de Hoon, M. J., Imoto, S., Nolan, J. & Miyano, S. Open source clustering software. *Bioinformatics* **20**, 1453–1454 (2004).
39. Altschul, S. F., Gish, W., Miller, W., Myers, E. W. & Lipman, D. J. Basic local alignment search tool. *J. Mol. Biol.* **215**, 403–410 (1990).
40. Gentleman, R. C. et al. Bioconductor: open software development for computational biology and bioinformatics. *Genome Biol.* **5**, R80 (2004).

LETTERS

Demasculinization of X chromosomes in the *Drosophila* genus

David Sturgill^{1*}, Yu Zhang^{1*}, Michael Parisi^{1†} & Brian Oliver¹

X chromosomes evolve differently from autosomes, but general governing principles have not emerged¹. For example, genes with male-biased expression are under-represented on the X chromosome of *D. melanogaster*², but are randomly distributed in the genome of *Anopheles gambiae*³. In direct global profiling experiments using species-specific microarrays, we find a nearly identical paucity of genes with male-biased expression on *D. melanogaster*, *D. simulans*, *D. yakuba*, *D. ananassae*, *D. virilis* and *D. mojavensis* X chromosomes. We observe the same under-representation on the neo-X of *D. pseudoobscura*. It has been suggested that precocious meiotic silencing of the X chromosome accounts for reduced X chromosome male-biased expression in nematodes⁴, mammals⁵ and *Drosophila*⁶. We show that X chromosome genes with male-biased expression are under-represented in somatic cells and in mitotic male germ cells. These data are incompatible with simple X chromosome inactivation models. Using expression profiling and comparative sequence analysis, we show that selective gene extinction on the X chromosome, creation of new genes on autosomes and changed genomic location of existing genes contribute to the unusual X chromosome gene content.

Several models have been advanced to explain the peculiar gene content on X chromosomes, which can be divided into those driven by gene-by-gene or chromosome-wide selective pressures^{1,7}. Antagonistic selection is a popular gene-by-gene model. Females and males are under different selective pressures and deploy the genome differently such that genes and expression states advantageous for one sex can be disadvantageous to the other. This is expected to have a profound influence on X chromosomes because hemizyosity and immediate selection of recessive alleles in males should be masculinizing, whereas the increased residency time of X chromosomes in females and immediate selection of dominant alleles should be a counteracting force. A popular chromosome-wide model suggests that X chromosome inactivation during spermatogenesis is responsible for the reduced number of X chromosome genes with male-biased expression. The X chromosome is precociously condensed, and thus silenced, in preparation for male meiosis, owing to the absence of a homologous pairing partner.

Before addressing particular models, we asked if X chromosome sex-biased expression patterns were consistent across the genus. We determined female:male expression ratios on species-specific microarrays⁸, normalized sex bias across species, and parsed the expression data by chromosome arm (Fig. 1a, and Supplementary Fig. 1). Homologous linkage groups in the *Drosophila* genus are referred to as 'Muller's elements' to standardize discordant species-specific chromosome nomenclature⁹. Muller A is part of the X chromosome in all the species examined. Muller A genes with male-biased expression were under-represented relative to autosomes in each of the seven species (30–43% less than expected,

$P < 10^{-4}$ by chi-squared test; Supplementary Table 1). No other chromosome arms showed a genus-wide significant departure from a random distribution, although we did observe a modest over-representation of genes with male-biased expression on Muller B ($P < 10^{-2}$ by chi-squared test) in *D. melanogaster*, *D. simulans*, *D. ananassae* and *D. mojavensis*. Therefore, a dearth of genes with male-biased expression on the X chromosome is characteristic of the genus.

Formally, reduced male-biased expression could be due to an historical accident on the Muller A element rather than a property of the X chromosome itself. This is directly testable owing to the chromosome arrangement in *D. pseudoobscura*, in which the ancestral autosome, Muller D, fused to the X chromosome ~8–12 million years ago¹⁰. The neo-X chromosome (Fig. 1a) also showed a strong under-representation of male-biased expression (37% of the expected random distribution, $P < 10^{-4}$ by chi-squared test). The consistent under-representation of genes with male-biased expression on the *D. pseudoobscura* neo-X and on the ancestral X chromosomes, suggests that the effect of linkage on male-biased expression is a property of X chromosomes and that it takes less than 12 million years to reach a stereotypical depleted status.

Important predictions of the X chromosome inactivation model for reduced male-biased expression are readily testable: Expression of all X chromosome genes should be reduced, and X chromosome deficits in male-biased expression should be restricted to late spermatocytes. There was no global reduction in X chromosome gene expression in males (Fig. 1b), suggesting that global inactivation in spermatocytes does not disrupt the over-all balance of gene expression at the organismal level. These data are also consistent with genus-wide high-fidelity X chromosome dosage compensation in both the male soma and germline as observed in *D. melanogaster*¹¹. The paucity of X chromosome genes with male-biased expression seems due to reduced numbers of genes with overt male-biased expression, not a chromosome-wide effect. Although these data do not support the X chromosome inactivation model, they are also based on whole-animal expression profiles that greatly dilute late spermatocyte expression.

If male-biased expression from X chromosomes is reduced owing to a germline-specific event, then there should be no similar reduction in the soma. Most orthologues show sex-biased expression in all tested species⁸. Therefore, we estimated somatic sex-biased expression by computationally removing orthologues with testis-biased expression in *D. melanogaster* (1,569 genes). We observed significant under-representation ($P < 10^{-4}$ by chi-squared test) of X chromosome genes with putative somatic male-biased expression in five of the seven species (Fig. 1c). This included the *D. pseudoobscura* neo-X chromosome. We also re-analysed non-gonadal *D. melanogaster* expression data (Fig. 2a)². Whereas the number of genes

¹Laboratory of Cellular and Developmental Biology, National Institute of Diabetes and Digestive and Kidney Diseases, National Institutes of Health, Department of Health and Human Services, Bethesda Maryland 20892, USA. [†]Present address: Department of Biology, University of Pennsylvania, Pennsylvania 19104, USA.

*These authors contributed equally to this work.

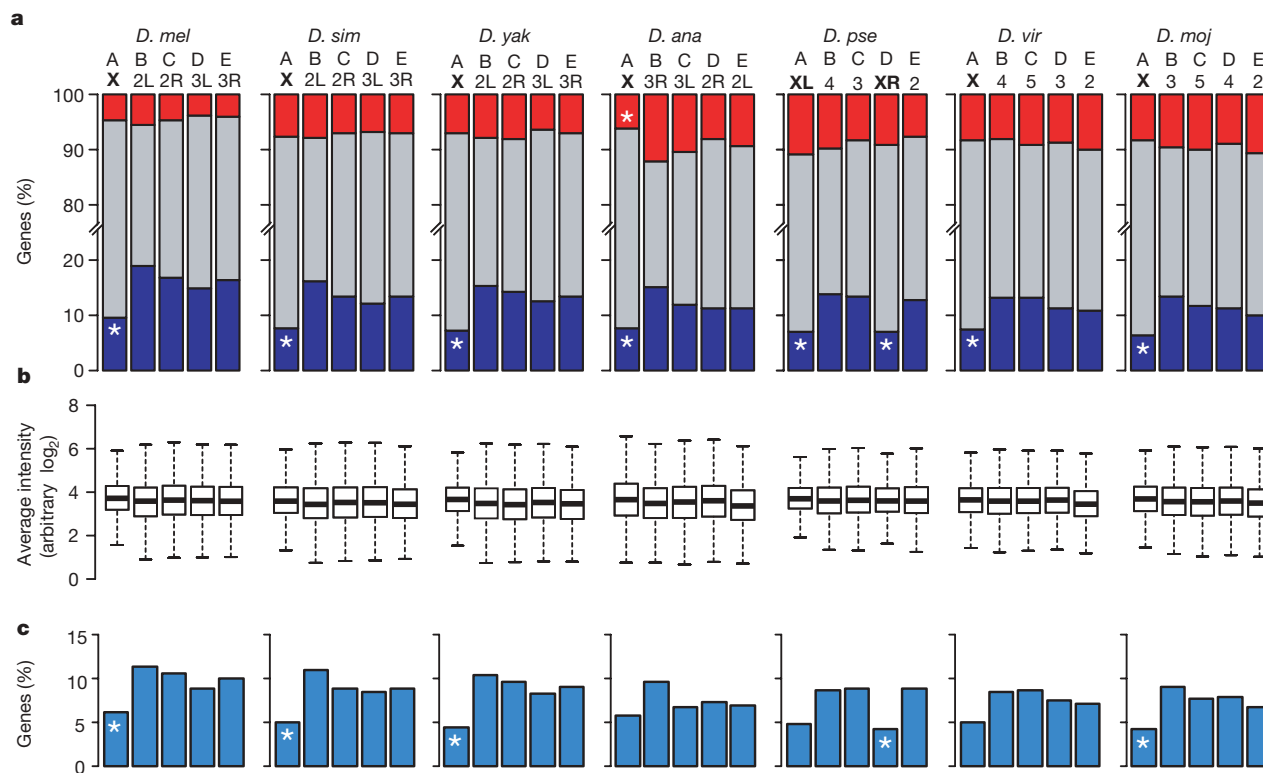


Figure 1 | Genes that show sex-biased expression, on chromosome arms.

a, Percentage of genes with female-biased (red), non-biased (grey) and male-biased (blue) expression on chromosome arms. Muller's elements and arms are indicated (X chromosomes in bold). Significant under-representation from a random distribution of genes in an expression class (chi-squared test) is noted (* $P < 10^{-4}$). The top 20% of differentially expressed genes (by ranked P values) are assigned a sex-biased expression class. **b**, Box plots of

average hybridization intensities for males by chromosome arm. Twenty-fifth to seventy-fifth percentiles (boxes), medians (lines in boxes) and ranges (whiskers) are indicated. **c**, As in **a**, but with genes with predicted testis-biased expression removed. *D. melanogaster*, *D. mel*; *D. simulans*, *D. sim*; *D. yakuba*, *D. yak*; *D. ananassae*, *D. ana*; *D. pseudoobscura*, *D. pse*; *D. virilis*, *D. vir*; *D. mojavensis*, *D. moj*.

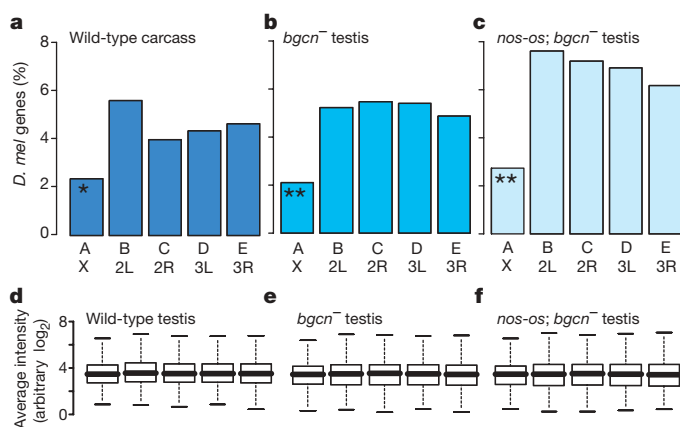


Figure 2 | Male-biased expression not subject to X chromosome inactivation.

a–c, Percentage of *D. melanogaster* genes with male-biased expression. Significant under-representation as in Fig. 1 is noted (* $P < 10^{-2}$; ** $P < 10^{-4}$). **a**, Non-gonadal soma (gonadectomized carcasses)². **b**, **c**, Testis from mutants with mitotically active germline tumours¹². Male-biased expression was determined by present calls in wild-type and mutant testis and absent calls in wild-type ovary expression profiles¹³ from FlyMine²⁰. Testis from *bgn*[−] males (primary spermatocyte-biased; **b**) accumulates mitotically active cysts of interconnected germ cells, whereas testis from males overexpressing *os* (*nos-os*) in a *bgn*[−] background (male germline stem-cell-biased; **c**) accumulates mitotically active germ cells that undergo complete cytokinesis¹². **d–f**, Box plots of average intensities (arbitrary scale) across hybridizations for wild-type (**d**), *bgn*[−] (**e**), or *nos-os*; *bgn*[−] (**f**) testis separated by chromosome arm. Twenty-fifth to seventy-fifth percentiles (boxes), medians (lines in boxes) and ranges (whiskers) are indicated.

with male-biased expression is much lower in the non-gonadal soma, we observed clear under-representation of X chromosome genes with male-biased expression ($P < 10^{-2}$), as previously observed².

To test the X chromosome inactivation model more directly, we used testis expression data from *D. melanogaster* mutants blocked during primary spermatocyte amplification¹². Testes from these mutants accumulate vast numbers of mitotic germ cells. We used independently profiled ovary samples as a reference¹³. X chromosome genes with testis-biased expression were under-represented in these mutant profiles ($P < 10^{-4}$ by chi-squared test, Fig. 2b, c). Additionally, there was no evidence for global reduction in the expression of all X chromosome genes in either wild-type or mutant testis (Fig. 2d–f). These data suggest that the X chromosome is a poor location for germline male-biased expression before X chromosome inactivation, which occurs in late post-mitotic spermatocytes⁶. X chromosome inactivation may be too late to affect most X chromosome transcript levels. We suggest that the paucity of X chromosome genes with male-biased expression in *Drosophila* is due to selection at the gene level, not global chromatin status.

Regardless of the thematic model, there are a limited number of physical mechanisms for achieving the observed under-representation of X chromosome genes with male-biased expression^{2,14}. We explored whether X chromosome genes with male-biased expression convert expression class, preferentially move to autosomes, are preferentially lost, or fail to arise on X chromosomes, using the *D. pseudoobscura* neo-X chromosome as a well-controlled natural experiment. We inferred the expression pattern of the ancestral Muller D of *D. pseudoobscura* before translocation to the X chromosome by using expression data from six phylogenetically flanking species. The extant expression pattern was directly

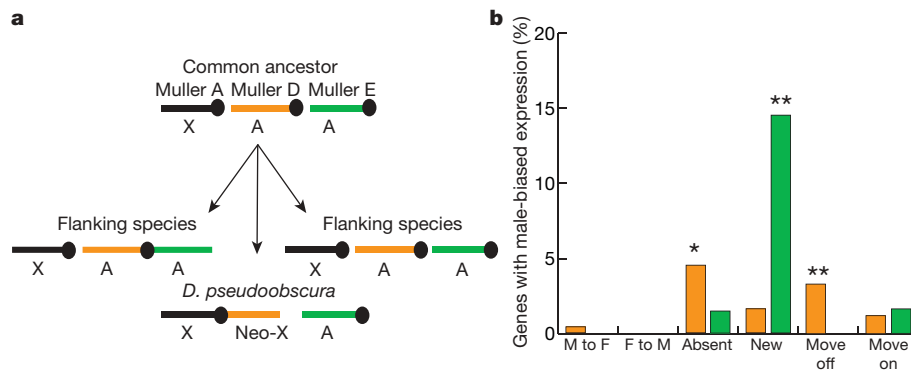


Figure 3 | The neo-X chromosome. **a**, *D. pseudoobscura* neo-X chromosome formation cartoon. Muller A, D and E are attached to different centromeres (filled circles) in *D. pseudoobscura* relative to flanking species. **b**, Bar plot showing changes to *D. pseudoobscura* Muller D neo-X chromosome (orange) and Muller E autosomal arm (green), based on the predicted expression pattern of the ancestral autosomes. Categories are: switches in sex-biased expression (F, female-biased; M, male-biased), not found

determined. In the other species, Muller D and Muller E are arms of the same chromosome or are individual chromosomes. Muller E provided a reference for the analysis (Fig. 3a, Supplementary Tables 3, 4, and Supplementary Fig. 2).

Of the 242 Muller D genes with ancestral or extant male-biased expression (Fig. 3b) that can be unambiguously assigned linkage and expression patterns, 216 (89%) remain in place on the neo-X chromosome. Only one gene on the neo-X chromosome switched from male-biased expression to female-biased expression. Although this particular gene *monkey king* (*mkg-p*) has undergone an interesting functional radiation, and sex-bias change on the neo-X chromosome is not significantly different from Muller E (no switches). Thus, there is no overt evidence that expression changes are responsible for under-representation of genes with male-biased expression on X chromosomes.

We found that 5% of genes with male-biased expression on the ancestral autosome had been lost from the genome of *D. pseudoobscura*, whereas only 1% of ancestral genes with male-biased expression were lost from Muller E ($P < 0.05$ by chi-squared test). Only 2% of genes with male-biased expression on the neo-X chromosome were unique to *D. pseudoobscura*, whereas 15% of the Muller E genes with male-biased expression in *D. pseudoobscura* are unique. The relative excess of new genes with male-biased expression on the autosome is highly significant ($P < 10^{-4}$ by chi-squared test). Determining if a gene is absent or new rather than highly diverged is difficult. However, exploration of genus-wide gene content using relaxed alignment instead of the consensus gene models indicates that many of these genes are likely to be completely absent rather than highly diverged (Supplementary Fig. 3). We also found clear evidence that non-synonymous substitutions (K_A) relative to synonymous substitution (K_S) rates are higher for X chromosome genes with male-biased expression than for those on autosomes (Supplementary Fig. 4). These data suggest that there is net loss of genes with male-biased expression from the X chromosome (as well as more subtle changes to sequence) and that functions lost from the X chromosome may be replaced by new gene formation on autosomes.

Analysis of gene transposition showed a net movement of genes with male-biased expression off the neo-X chromosome, with 3% of ancestral genes with male-biased expression moving to autosomes and no genes with male-biased expression moving from Muller E ($P < 10^{-4}$ by chi-squared test). Male-biased expression was always maintained in the new location. There was no significant difference between the neo-X and Muller E with respect to newly arriving genes, because 1% of ancestral genes with male-biased expression moved to

(absent), only found in *D. pseudoobscura* (new), and genes moving from (move off) and to (move on) the indicated arm. Significant differences (chi-squared test) between Muller D and Muller E are noted (** $P < 10^{-4}$; * $P < 0.05$). The ancestral condition of the neo-X chromosome was inferred by examining chromosome linkage and expression on homologous arms in species that diverged from the *Drosophila* lineage before and after *D. pseudoobscura*.

the neo-X chromosome and 2% moved to Muller E. These data clearly support the idea that movement of genes with male-biased expression to autosomes promotes long-term survival of those genes. Gene loss, gain and movement unambiguously accounted for 13% of the loss of male-biased expression from the neo-X chromosome and 73% of the gain of male-biased expression on Muller E (Supplementary Table 5). If these unambiguous results reflect the changes that we are unable to trace, then gene loss, gain and movement are the dominant mechanisms for depleting male-biased expression on the X chromosome relative to autosomes.

Our data strongly support the idea that the X chromosome has an unusual distribution of genes with male-biased expression^{4,5,16–18}. Although there is compelling evidence that precocious X chromosome inactivation occurs in at least some species, and that this may contribute to the reduced density of genes with male-biased expression on X chromosomes^{4,5}, our data indicate that this is not a major contributor to the pattern in the *Drosophila* genus. We suggest that the dominant mechanisms for achieving this under-representation are preferential extinction of X chromosome genes and formation of new autosomal genes with male-biased expression², along with movement of genes with male-biased expression from the X chromosome¹⁴. Somewhat surprisingly, altered gene expression does not seem to be a major contributor.

METHODS SUMMARY

Array data sources. Expression data for sex-sorted whole adults of the seven *Drosophila* species⁸ are from GEO¹⁹ (GSE6640). Data for *D. melanogaster* gonadectomized male and female carcass on the FlyGEM platform were published previously², GEO (GSE442). Affymetrix data for *bgn*[−] and UAS-*os*, *bgn*[−]/*nos-Gal4*-VP16, *bgn*[−] mutant testes expression¹² were obtained from GEO (GSE4188, GDS2228) and wild-type ovary data were obtained from FlyMine²⁰ release v.8.0.

Sequence analysis. *D. melanogaster* annotation v.4.3 (ref. 21) and Comparative Analysis Freeze 1 (CAF1) assemblies²² were used throughout. Orthology relationships between the seven species including orthologue, paralogue and no-homologue were assigned to consensus gene predictions²². Gene content changes were also determined by comparing *D. melanogaster* amino acid sequence against six-frame translated genomic DNA of each species by BLAST tblastn²³.

For gene loss and translocation, the ancestral state of the lost/moved gene was inferred by the consensus expression class and chromosome linkage for each gene. For the *D. pseudoobscura* neo-X chromosome (Muller D) and autosomal Muller E, gene gain/loss/movement was manually counted gene-by-gene. The ancestral gene content of this arm was inferred by phylogeny using genes present in species that diverged before (*D. virilis* and *D. mojavensis*) and after (*D. ananassae* and the melanogaster subgroup) the *melanogaster/obscura* group split. The ancestral state refers to the chromosome linkage and expression class of genes at the origin of this node in a rooted phylogenetic tree.

Full Methods and any associated references are available in the online version of the paper at www.nature.com/nature.

Received 9 September; accepted 28 September 2007.

- Vicoso, B. & Charlesworth, B. Evolution on the X chromosome: unusual patterns and processes. *Nature Rev. Genet.* **7**, 645–653 (2006).
- Parisi, M. *et al.* Paucity of genes on the *Drosophila* X chromosome showing male-biased expression. *Science* **299**, 697–700 (2003).
- Hahn, M. W. & Lanzaro, G. C. Female-biased gene expression in the malaria mosquito *Anopheles gambiae*. *Curr. Biol.* **15**, R192–R193 (2005).
- Bean, C. J., Schaner, C. E. & Kelly, W. G. Meiotic pairing and imprinted X chromatin assembly in *Caenorhabditis elegans*. *Nature Genet.* **36**, 100–105 (2004).
- Khil, P. P., Smirnova, N. A., Romanienko, P. J. & Camerini-Otero, R. D. The mouse X chromosome is enriched for sex-biased genes not subject to selection by meiotic sex chromosome inactivation. *Nature Genet.* **36**, 642–646 (2004).
- Wu, C. I. & Xu, E. Y. Sexual antagonism and X inactivation—the SAXI hypothesis. *Trends Genet.* **19**, 243–247 (2003).
- Ellegren, H. & Parsch, J. The evolution of sex-biased genes and sex-biased gene expression. *Nature Rev. Genet.* **8**, 689–698 (2007).
- Zhang, Y. *et al.* Constraint and turnover in sex-biased gene expression in the genus *Drosophila*. doi:10.1038/nature06323 (this issue).
- Ashburner, M., Golic, K. G. & Hawley, R. S. *Drosophila: A Laboratory Handbook* (Cold Spring Harbor Laboratory Press, Cold Spring Harbor NY, 2004).
- Richards, S. *et al.* Comparative genome sequencing of *Drosophila pseudoobscura*: chromosomal, gene, and *cis*-element evolution. *Genome Res.* **15**, 1–18 (2005).
- Gupta, V. *et al.* Global analysis of X-chromosome dosage compensation. *J. Biol.* **5**, 3 (2006).
- Terry, N. A., Tulina, N., Matunis, E. & DiNardo, S. Novel regulators revealed by profiling *Drosophila* testis stem cells within their niche. *Dev. Biol.* **294**, 246–257 (2006).
- Chintapalli, V. R., Wang, J. & Dow, J. A. Using FlyAtlas to identify better *Drosophila melanogaster* models of human disease. *Nature Genet.* **39**, 715–720 (2007).
- Betran, E., Thornton, K. & Long, M. Retroposed new genes out of the X in *Drosophila*. *Genome Res.* **12**, 1854–1859 (2002).
- Wang, W., Yu, H. & Long, M. Duplication–degeneration as a mechanism of gene fission and the origin of new genes in *Drosophila* species. *Nature Genet.* **36**, 523–527 (2004).
- Ranz, J. M., Castillo-Davis, C. I., Meiklejohn, C. D. & Hartl, D. L. Sex-dependent gene expression and evolution of the *Drosophila* transcriptome. *Science* **300**, 1742–1745 (2003).
- Reinke, V. *et al.* A global profile of germline gene expression in *C. elegans*. *Mol. Cell* **6**, 605–616 (2000).
- Wang, P. J., McCarrey, J. R., Yang, F. & Page, D. C. An abundance of X-linked genes expressed in spermatogonia. *Nature Genet.* **27**, 422–426 (2001).
- Edgar, R., Domrachev, M. & Lash, A. E. Gene Expression Omnibus: NCBI gene expression and hybridization array data repository. *Nucleic Acids Res.* **30**, 207–210 (2002).
- Lyne, R. *et al.* FlyMine: An integrated database for *Drosophila* and *Anopheles* genomics. *Genome Biol.* **8**, R129 (2007).
- Grumbling, G. & Strelets, V. FlyBase: anatomical data, images and queries. *Nucleic Acids Res.* **34**, D484–D488 (2006).
- Drosophila* 12 Genomes Consortium. Evolution of genes and genomes of the *Drosophila* phylogeny. doi:10.1038/nature06341 (this issue).
- Altschul, S. F., Gish, W., Miller, W., Myers, E. W. & Lipman, D. J. Basic local alignment search tool. *J. Mol. Biol.* **215**, 403–410 (1990).

Supplementary Information is linked to the online version of the paper at www.nature.com/nature.

Acknowledgements We thank the *Drosophila* 12 Genomes Consortium for access to the assembly, alignment and annotation of the 12 sequenced *Drosophila* genomes, S. Davis for valuable technical advice, and C. Vinson, A. Clark and members of the B. Oliver laboratory for helpful discussion and comments on the manuscript. We are supported by the Intramural Research Program of the NIH, NIDDK.

Author Information Reprints and permissions information is available at www.nature.com/reprints. Correspondence and requests for materials should be addressed to D.S. (davidsturgill@niddk.nih.gov) and B.O. (oliver@helix.nih.gov).

METHODS

Expression data for whole adults of the seven *Drosophila* species were generated with custom-designed oligonucleotide arrays (NimbleGen Systems). Array design, sample preparation and labelling, and data handling were as described⁸. Data for *D. melanogaster* gonadectomized male and female carcass² were re-analysed from raw intensity; these data were re-normalized by within-slide print-tip loess normalization, followed by between-slide quantile normalization using Bioconductor²⁴. Differential expression was then called in the same manner as the custom Nimblegen arrays, using Mann–Whitney tests with false-discovery rate correction. For Affymetrix data, we used ‘present’ and ‘absent’ calls to determine sex-bias. Intensity data were used directly from GEO without additional normalization, and averaged over replicates. Data were remapped to match DrosGenome2 to DrosGenome1 identifiers by Affymetrix.

‘Gained genes’ were defined as genes present in only one species (Supplementary Fig. 2). ‘Lost genes’ are genes absent from only one. ‘Moved genes’ are those that are present in all seven species, but with different chromosome linkage in at least one species. For gene loss and translocation, the ancestral state of the lost/moved gene is inferred by the consensus expression class and chromosome linkage for each gene. Genes with different arm linkage, owing to a large pericentric inversion in the *D. yakuba* lineage²¹, were not counted as translocations.

We also calculated content changes independent of gene prediction in the newly sequenced species. We performed a comparison of *D. melanogaster* amino acid sequence against six-frame translated genomic DNA of each species via BLAST tblastn²³. BLAST results were parsed and hits tiled together using BioPerl²⁵. *D. melanogaster* genes were called ‘absent’ in the other species if there was no hit below an *E*-value cut-off (10^{-3} and 10^{-17} are shown in Supplementary Fig. 3).

For the *D. pseudoobscura* neo-X chromosome (Muller D) and autosomal Muller E, gene gain/loss/movement was manually counted gene-by-gene. The ancestral gene content of this arm was inferred by phylogeny, using genes present in species that diverged before (*D. virilis* and *D. mojavensis*) and after (*D. ananassae* and the *melanogaster* subgroup) the *melanogaster/obscura* group split. The ancestral state refers to the chromosome linkage and expression class of genes at the origin of this node in a rooted phylogenetic tree^{21,22}. For both Muller D and E, we filtered genes that are linked to these arms in any species. These were then filtered to include those that are Muller D- or Muller E- linked in at least one species downstream and one species upstream, or in *D. pseudoobscura* itself. Then genes with male-biased expression in at least one species are filtered. Each remaining gene was then manually assigned a putative ancestral expression class and arm location and post neo-X chromosome fate that considered the entire *Drosophila* lineage. There are cases involving species on the ‘edge’ of the tree that could not be resolved by this approach. For example, a gene that is Muller B-linked in *D. mojavensis/D. virilis* (on the edge of the rooted tree), but Muller D-linked in every other species would not be counted, because it is not possible to discriminate the direction of translocation. Our approach includes only unambiguous cases (Supplementary Tables 2–4).

Multiple sequence alignments of orthologues were imported using the seqinR package²⁶. K_A/K_S estimates adjusted for differences in transition and transversion rates were calculated from these alignments²⁷.

All computation was performed in the R/Bioconductor environment²⁴.

24. Gentleman, R. C. *et al.* Bioconductor: open software development for computational biology and bioinformatics. *Genome Biol.* **5**, R80 (2004).
25. Stajich, J. E. *et al.* The Bioperl toolkit: Perl modules for the life sciences. *Genome Res.* **12**, 1611–1618 (2002).
26. Charif, D., Thioulouse, J., Lobry, J. R. & Perriere, G. Online synonymous codon usage analyses with the ade4 and seqinR packages. *Bioinformatics* **21**, 545–547 (2005).
27. Li, W. H. Unbiased estimation of the rates of synonymous and nonsynonymous substitution. *J. Mol. Evol.* **36**, 96–99 (1993).

Maternal nodal and zebrafish embryogenesis

Arising from: A. V. Gore *et al.* *Nature* **438**, 1030–1035 (2005).

In fish and amphibians, the dorsal axis is specified by the asymmetric localization of maternally provided components of the Wnt signaling pathway^{1,2}. Gore *et al.*³ suggest that the Nodal signal Squint (Sqt) is required as a maternally provided dorsal determinant in zebrafish. Here we test their proposal and show that the maternal activities of *sqt* and the related Nodal gene *cyclops* (*cyc*) are not required for dorsoventral patterning.

Sqt and Cyc induce mesoderm and endoderm^{1,4}. Embryos without zygotic *sqt* and *cyc* (*Zcyc;Zsqt*) lack all endoderm and most mesoderm⁵. Gore *et al.*³ suggest that maternal Sqt might also act as a dorsal determinant, because injection of antisense *sqt* morpholinos into unfertilized eggs induced dorsal defects³. However, we point out two potential caveats in their study. First, Gore *et al.*³ do not provide evidence that their approach eliminates maternal *sqt*. In particular, two morpholinos were designed to prevent *sqt* pre-messenger RNA splicing, even though there is little, if any, evidence that maternal pre-mRNAs are deposited in the egg and spliced after oviposition. Second, regardless of its effect on maternal *sqt*, the morpholino approach of Gore *et al.* also blocks zygotic *sqt* activity. Hence, these experiments did not specifically test the requirement for maternal *sqt*.

We first determined whether fully spliced *sqt* mRNA is present in ovaries and unfertilized eggs. Polymerase chain reaction with reverse transcription (RT-PCR) detected abundant spliced *sqt* mRNA, consistent with its cytoplasmic localization⁶ (Fig. 1a). Because we performed the reverse transcription with not only oligo(dT) but also gene-specific primers, our analysis would have detected unspliced *sqt* RNA regardless of its polyadenylation state. The presence of spliced *sqt* mRNA in early embryos demonstrates that splice-blocking morpholinos cannot fully block maternal *sqt* activity, if they have any effect at all.

To test conclusively the requirement for maternal *sqt*, one needs to generate embryos from *sqt* homozygous mutant mothers and wild-type fathers. We investigated whether the *sqt*^{cz35} allele lacks

Sqt activity. Sequencing of genomic DNA confirmed that *sqt*^{cz35} contains a 1,848-base-pair (bp) insertion (Fig. 1c)⁵. Homozygous *sqt*^{cz35} embryos contained no detectable *sqt* mRNA at the 8-cell stage (Fig. 1b). In the late blastula, all *sqt* RNA detectable in mutants contained the 1.8-kilobase insertion, which introduces numerous stop codons in all reading frames (data not shown). Hence, *sqt*^{cz35} mutants have strongly reduced levels of *sqt* mRNA, and the mutant allele cannot generate wild-type Sqt protein. The presence of an in-frame AUG codon 3' to the insertion indicated that *sqt*^{cz35} might produce an amino-terminally truncated Sqt protein (T-Sqt), which would lack a signal sequence. This would require the ribosome to bypass 41 upstream AUGs or the initiation of transcription within the insertion itself (Fig. 1c). Although it is unlikely that T-Sqt is produced, we tested its activity. Injection of mRNA encoding T-Sqt did not induce phenotypic abnormalities (Fig. 1d–f). Hence, all available evidence indicates that *sqt*^{cz35} completely eliminates Sqt activity, whereas the splice-site morpholinos³ cannot eliminate the function of spliced maternal *sqt* mRNA.

Maternal-zygotic and zygotic *sqt*^{cz35} and *sqt*^{hi975} (a retroviral insertional allele) mutants have similar phenotypes^{7,8}. To investigate a requirement for maternal Sqt, we generated embryos lacking

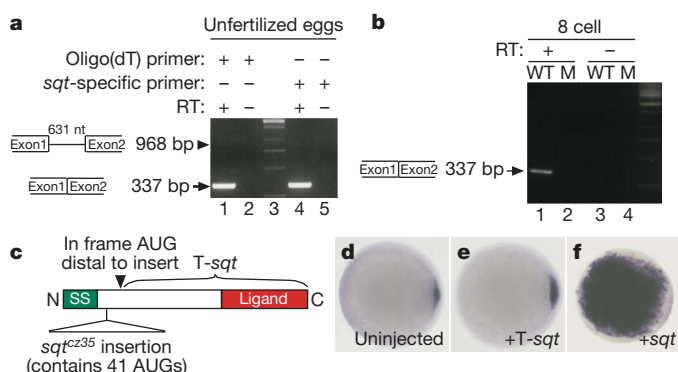


Figure 1 | Splicing and disruption of *sqt* RNA. **a**, Primers flanking the first intron of the *sqt* gene detected only spliced RNA (337 bp spliced versus 968 bp unspliced) in complementary DNA prepared from total RNA of unfertilized eggs. Gene-specific primers (lanes 4 and 5) and oligo(dT) primers (lanes 1 and 2) were used, so that non-polyadenylated, unspliced *sqt* RNA could be detected. RT, reverse transcriptase. **b**, *sqt* mRNA is detected in wild-type (WT) embryos (lane 1) but not *MZsqt*^{cz35} mutants (M) (lane 2) at the 8-cell stage. **c**, Schematic of Sqt protein, showing signal sequence (SS), prodomain (white), and mature ligand domain (red). The *sqt*^{cz35} insertion, and the N-terminally truncated putative product of *sqt*^{cz35} (T-Sqt) are indicated. **d–f**, Embryos injected with 50 pg of wild-type *sqt* mRNA have ectopic *gsc* expression (**f**), but injection of 150 pg of T-Sqt (**e**) has no effect. Additional supporting data and details of methods are available from the authors at <http://www.mcb.harvard.edu/Schier/BennettBCASuppl07.pdf>.

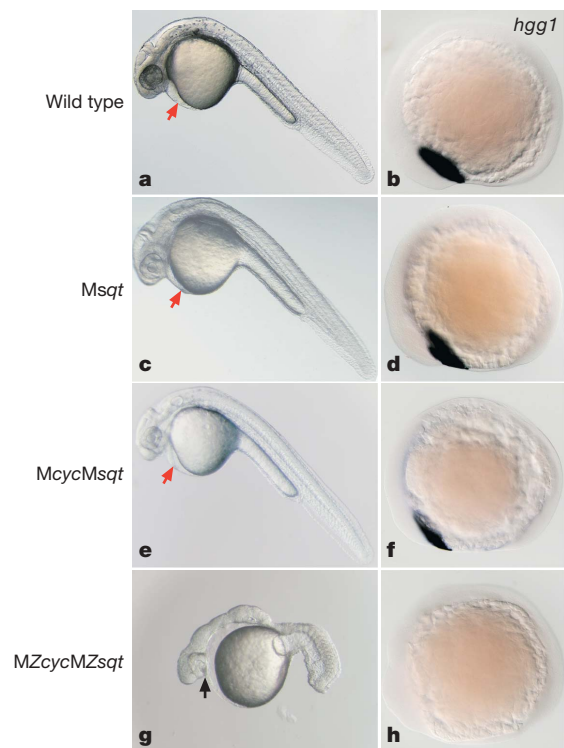


Figure 2 | The maternal Nodal genes *cyclops* and *squint* are not required for dorsal axis specification. **a, c, e, g**, Lateral views of live embryos 28 h post-fertilization. Genotypes are indicated on the left. *Msqt* and *Mcyc;Msqt* embryos appear phenotypically normal. The hatching gland, an anterior dorsal mesoderm derivative, is marked by red arrows. *MZcyc;MZsqt* embryos lack endoderm and head and trunk mesoderm but retain anterior neuroectoderm, including a cyclopic eye (black arrow), similar to *Zcyc;Zsqt*⁵ and *MZoeip*¹⁰ mutants. **b, d, f, h**, Expression of *hgg1*, a marker for anterior dorsal mesoderm, detected by whole-mount *in situ* hybridization in 10-somite-stage embryos (lateral view). We used *cyc*^{m294}, a mutation thought to eliminate all Cyc activity¹². Additional supporting data and details of methods are available from the authors at <http://www.mcb.harvard.edu/Schier/BennettBCASuppl07.pdf>.

maternal but not zygotic *sqt*, by crossing *sqt* homozygous mutant females and wild-type males. Maternal *sqt* mutants (*Msqt*) were viable and phenotypically normal (Fig. 2c). Analysis of markers expressed in axial, paraxial, intermediate, and lateral mesoderm did not detect any defects in *Msqt* embryos (Fig. 2d).

To determine whether maternal *sqt* acts redundantly with maternal *cyc*, we analysed *Mcyc;Msqt* embryos. *Mcyc;Msqt* embryos generated by germline replacement⁹ were viable and phenotypically normal (Fig. 2e). Hence, complete elimination of maternal Nodal signals does not affect zebrafish embryogenesis. To eliminate all early Nodal activity, we generated *MZcyc;MZsqt* embryos. These mutants developed dorsal derivatives such as the anterior neuroectoderm and appeared identical to *Zcyc;Zsqt* embryos and to *MZoepl*¹⁰ mutants, which lack the Nodal co-receptor (Fig. 2g).

These results cannot exclude potential contributions by maternal *cyc* or *sqt* under very particular genetic or environmental conditions^{8,11}, but we have shown that maternal *cyc* and *sqt* are not required for dorsal axis specification or for any other aspect of embryogenesis. We propose that Nodal signals act primarily as zygotic inducers of mesendoderm.

James T. Bennett^{1,2}, Heather L. Stickney³, Wen-Yee Choi^{1,2,4}, Brian Ciruna^{1,2,5,6}, William S. Talbot³ & Alexander F. Schier^{1,2,4}

¹Developmental Genetics Program, Skirball Institute of Biomolecular Medicine, New York University School of Medicine, New York, New York 10016, USA.

²Department of Cell Biology, New York University School of Medicine, New York, New York 10016, USA.

³Department of Developmental Biology, Stanford University, Stanford, California 94305, USA.

⁴Department of Molecular and Cellular Biology, Harvard Stem Cell Institute, Center for Brain Science, Broad Institute, Harvard University,

Cambridge, Massachusetts 02138, USA.

e-mail: schier@fas.harvard.edu

⁵Department of Molecular and Medical Genetics, University of Toronto, Toronto, Ontario M5G 1L7, Canada.

⁶The Program in Developmental and Stem Cell Biology, The Hospital for Sick Children, Toronto, Ontario M5G 1L7, Canada.

Received 25 September 2006; accepted 21 August 2007.

- Schier, A. F. & Talbot, W. S. Molecular genetics of axis formation in zebrafish. *Annu. Rev. Genet.* **39**, 561–613 (2005).
- Heasman, J. Patterning the early *Xenopus* embryo. *Development* **133**, 1205–1217 (2006).
- Gore, A. V. *et al.* The zebrafish dorsal axis is apparent at the four-cell stage. *Nature* **438**, 1030–1035 (2005).
- Schier, A. F. Nodal signaling in vertebrate development. *Annu. Rev. Cell Dev. Biol.* **19**, 589–621 (2003).
- Feldman, B. *et al.* Zebrafish organizer development and germ-layer formation require nodal-related signals. *Nature* **395**, 181–185 (1998).
- Gore, A. V. & Sampath, K. Localization of transcripts of the zebrafish morphogen Squint is dependent on egg activation and the microtubule cytoskeleton. *Mech. Dev.* **112**, 153–156 (2002).
- Aoki, T. O. *et al.* Regulation of nodal signalling and mesendoderm formation by TARAM-A, a TGFβ-related type I receptor. *Dev. Biol.* **241**, 273–288 (2002).
- Pei, W., Williams, P. H., Clark, M. D., Stemple, D. L. & Feldman, B. Environmental and genetic modifiers of squint penetrance during zebrafish embryogenesis. *Dev. Biol.* **308**, 368–378 (2007).
- Ciruna, B. *et al.* Production of maternal-zygotic mutant zebrafish by germ-line replacement. *Proc. Natl Acad. Sci. USA* **99**, 14919–14924 (2002).
- Gritsman, K. *et al.* The EGF-CFC protein one-eyed pinhead is essential for nodal signaling. *Cell* **97**, 121–132 (1999).
- Sirotkin, H. I., Dougan, S. T., Schier, A. F. & Talbot, W. S. *bozozok* and *squint* act in parallel to specify dorsal mesoderm and anterior neuroectoderm in zebrafish. *Development* **127**, 2583–2592 (2000).
- Sampath, K. *et al.* Induction of the zebrafish ventral brain and floorplate requires *cyclops/nodal* signalling. *Nature* **395**, 185–189 (1998).

doi:10.1038/nature06314

Gore et al. reply

Replying to: J. T. Bennett *et al.* *Nature* **450**, doi: 10.1038/nature06314 (2007).

We presented several lines of evidence indicating that dorso–ventral asymmetry is apparent in zebrafish embryos by cleavage stages¹, one of which showed that injection of three different morpholino oligonucleotides targeting three different *squint* (*sqt*) sequences cause severe disruption in dorsal structures. We concluded that the dorsal axis is evident by the 4-cell stage, and suggested that maternal Sqt and associated factors may function in zebrafish dorsal-axis formation¹. Bennett *et al.* challenge our results obtained with morpholino oligonucleotides because they do not find a comparable defect in maternal and zygotic *sqt* mutants².

How could these differences be explained? Antisense RNAs targeting short sequences can have off-target effects. One of the three morpholinos we used¹ was a previously described *sqt* ATG morpholino³, whereas the other two were directed against splice junctions. Eggs or embryos injected with control morpholinos did not manifest the same phenotypes. All three *sqt* morpholinos, when injected into fertilized embryos, recapitulated the milder-mutant phenotypes^{4,5}, which argues against off-target effects. Although all three morpholinos might have off-target effects that produce the same phenotype by chance, this explanation is unlikely.

Bennett *et al.* also raise a concern related to our *sqt* splice-junction morpholinos. They contend that there is little evidence for maternal pre-messenger RNAs in eggs, and therefore that they cannot be targeted by splice-junction morpholinos. However, for several maternal transcripts in *Xenopus*, a pool of unprocessed RNA is present in eggs and early embryos^{6–8}. Bennett *et al.* use primers spanning one of the

sqt introns and do not detect unspliced Sqt RNA in ovaries, early embryos, or at the peak of zygotic *sqt* expression^{4,9–11}. In further control experiments (Fig. 1), we consistently detect unspliced and spliced *sqt* RNA in zebrafish ovaries, eggs and early embryos, using primers for both *sqt* introns (ref. 12, and Fig. 1a–c). Furthermore, we detect aberrantly spliced and unspliced *sqt* RNA at the 8-cell stage (before zygotic *sqt* expression) on injection of *sqt* splice-junction morpholinos, but not of control morpholinos (Fig. 1c). Therefore, our use of splice-junction morpholinos to block maternal *sqt* function cannot be excluded as a valid approach.

It is also possible that the mutant used for genetic analysis may not behave as expected. The *sqt* insertion mutations are incompletely penetrant, sensitive to environmental conditions, genetic backgrounds and the age of the mother, and homozygous mutant embryos frequently survive to adulthood^{5,13,14}. So the *sqt* alleles may not be complete nulls. Some maternal zygotic *sqt*^{cz35} (*MZsqt*^{cz35}) embryos manifest dorso–anterior deficiencies¹⁴, similar to our findings after *sqt* morpholino injection.

Bennett *et al.* contend that the *sqt* alleles must be null because the insertions should prevent translation of the Sqt protein. However, some RNAs have functions independent of the protein they encode: for instance, in *Xenopus*, removal of VegT transcripts disrupts the cytoskeleton at the vegetal cortex and prevents formation of germinal granules¹⁵. We find that *sqt* RNA is present in *MZsqt* mutant embryos (Fig. 1d), and could perform a non-coding function. A priori considerations aside, to determine the loss-of-function phenotype

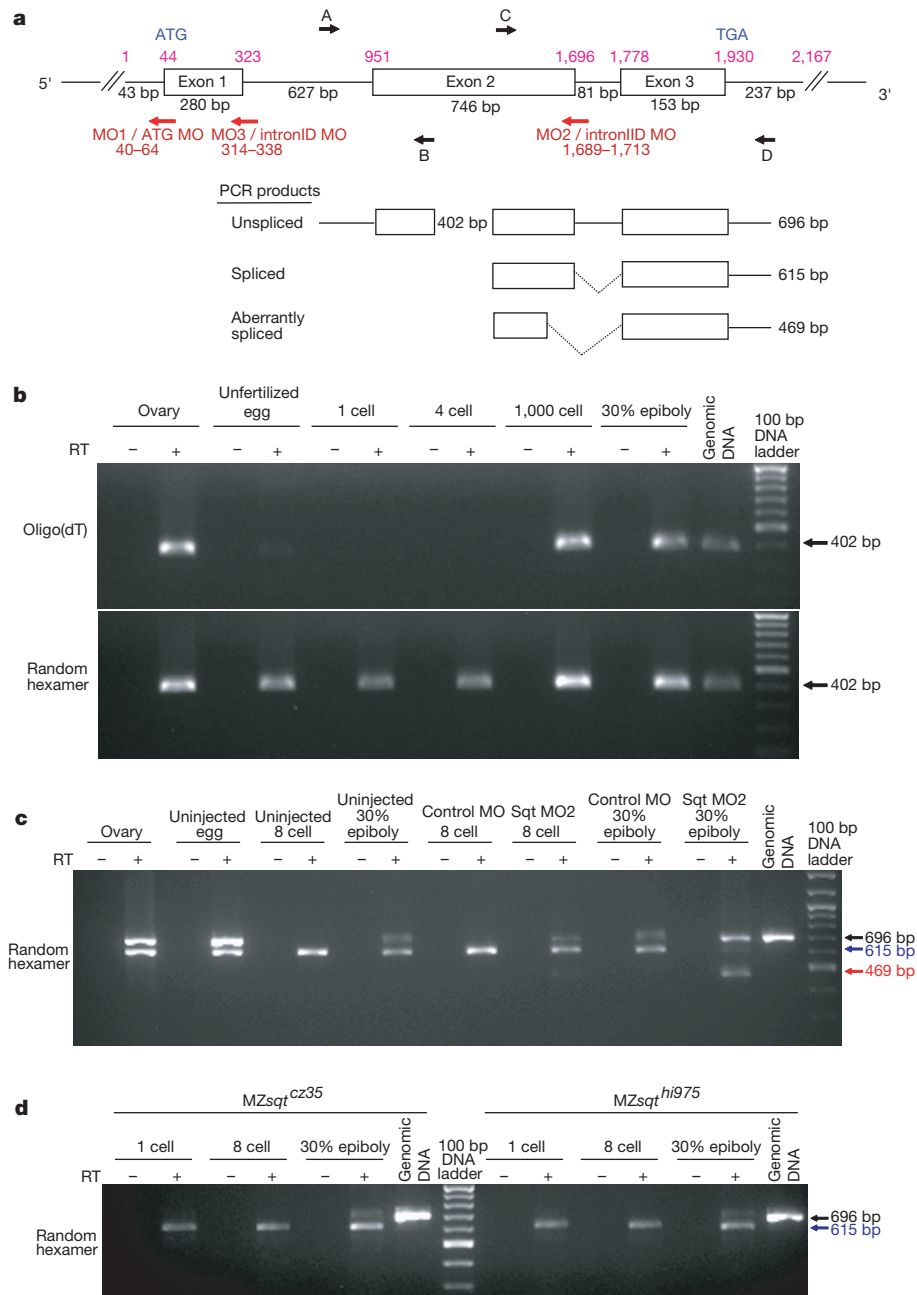


Figure 1 | Unspliced *sqt* RNA is present in zebrafish ovaries, eggs and embryos. **a**, The *squint* locus and polymerase chain reaction (PCR) products. Red arrows, target sites for the *sqt* morpholinos. Black arrows, position of PCR primers. Primer pair AB amplifies part of intron I and exon II; primer pair CD spans intron II. Numbers in pink indicate nucleotide positions based on Vega v28 (http://vega.sanger.ac.uk/Danio_rerio/exonview?transcript=OTTDART00000026522;db=core). **b**, Reverse transcription (RT)-PCRs for unspliced *sqt* intron I. Oligo(dT) or random hexamer-primed complementary DNAs synthesized from wild-type zebrafish RNAs was used in PCRs with primer pair AB. A 402-bp unspliced intron I product is detected in random-hexamer p(dN)₆-primed RT-PCRs at all stages. RT-PCRs on oligo(dT)-primed cDNA using the same primers detect the 402-bp unspliced product strongly in ovary, 1,000-cell and 30% epiboly samples, but poorly in unfertilized eggs. Unspliced *sqt* RNA is not detected in oligo(dT)-primed cDNA from cleavage-stage embryos. No product is detected in RT controls for all stages. **c**, RT-PCRs for unspliced *sqt* intron II. Random hexamer-primed cDNA synthesized from wild-type zebrafish RNAs was used in PCRs with primer pair CD. A 696-bp unspliced intron II product is detected strongly in whole ovary and unfertilized eggs.

The unspliced intron II product diminishes by the 8-cell stage and is detected again at 30% epiboly at the peak of zygotic *sqt* expression. Unfertilized eggs were injected with control or *sqt* morpholinos (MOs) and fertilized *in vitro* using sperm from wild-type male zebrafish. Only spliced *sqt* product (615 bp) is detected in uninjected or control MO-injected embryos at the 8-cell stage, when for *sqt* MO2-injected embryos, unspliced intron II containing *sqt* RNA is still detectable, with an aberrantly spliced *sqt* RNA species (469 bp). At 30% epiboly, both the 696-bp and the 469-bp products are enriched in *sqt* MO2-injected embryos. The aberrant *sqt* splice product should generate truncated Sqt protein lacking the carboxy-terminal 98 amino acids, which include six of seven conserved cysteine residues in the Sqt mature domain. No product is detected in RT controls. **d**, RT-PCRs for *sqt* transcripts in MZsqt mutant embryos. Random hexamer-primed cDNA from 1-cell, 8-cell and 30% epiboly MZsqt mutant^{5,13,14} embryos was used in PCRs with primer pair CD. Spliced *sqt* product (blue arrow) is detected in embryos from both MZsqt mutant alleles^{5,13,14}. Unspliced *sqt* product (black arrow) is detected at the 30% epiboly embryonic stage. No product is detected in RT controls. S. Lim provided these data. Further details (for example, on the RT-PCR method) are available from the authors.

definitively, a deletion that completely removes the *sqt* locus is required.

We therefore stand by our original conclusions¹. Although the mutant analysis by Bennett *et al.*² disagrees with our results, we believe that further investigation is necessary to understand precisely how maternal Sqt functions.

Aniket V. Gore^{1,†}, Albert Cheong^{1,†}, Patrick C. Gilligan¹ & Karuna Sampath^{1,2,3}

¹Vertebrate Development Group, Temasek Life Sciences Laboratory, 1 Research Link, National University of Singapore, 117604 Singapore.

²School of Biological Sciences, Nanyang Technological University, 60 Nanyang Drive, 637551 Singapore.

³Department of Biological Sciences, National University of Singapore, 117543 Singapore.

e-mail: karuna@tll.org.sg

†Present addresses: Unit on Vertebrate Organogenesis, Laboratory of Molecular Genetics, The National Institute of Child Health and Human Development, National Institutes of Health, Bethesda, Maryland 20892, USA (A.V.G.); Cell Culture Process Development, Lonza Biologics, 228 Bath Road, Slough, Berkshire, SL1 4DX, UK (A.C.).

1. Gore, A. V. *et al.* The zebrafish dorsal axis is apparent at the four-cell stage. *Nature* **438**, 1030–1035 (2005).
2. Bennett, J. T. *et al.* Maternal nodal and zebrafish embryogenesis. *Nature* **450**, 10.1038/nature06314 (2007).
3. Feldman, B. & Stemple, D. L. Morpholino phenocopies of *sqt*, *oep*, and *ntl* mutations. *Genesis* **30**, 175–177 (2001).

4. Feldman, B. *et al.* Zebrafish organizer development and germ-layer formation require nodal-related signals. *Nature* **395**, 181–185 (1998).
5. Aoki, T. O. *et al.* Regulation of nodal signalling and mesendoderm formation by TARAM-A, a TGF β -related type I receptor. *Dev. Biol.* **241**, 273–288 (2002).
6. Simon, R., Wu, L. & Richter, J. D. Cytoplasmic polyadenylation of activin receptor mRNA and the control of pattern formation in *Xenopus* development. *Dev. Biol.* **179**, 239–250 (1996).
7. Pandur, P. D., Sullivan, S. A. & Moody, S. A. Multiple maternal influences on dorsal-ventral fate of *Xenopus* animal blastomeres. *Dev. Dyn.* **225**, 581–587 (2002).
8. Vasudevan, S., Seli, E. & Steitz, J. A. Metazoan oocyte and early embryo development program: a progression through translation regulatory cascades. *Genes Dev.* **20**, 138–146 (2006).
9. Rebagliati, M. R., Toyama, R., Fricke, C., Haffter, P. & Dawid, I. B. Zebrafish nodal-related genes are implicated in axial patterning and establishing left-right asymmetry. *Dev. Biol.* **199**, 261–272 (1998).
10. Dougan, S. T., Warga, R. M., Kane, D. A., Schier, A. F. & Talbot, W. S. The role of the zebrafish nodal-related genes *squint* and *cyclops* in patterning of mesendoderm. *Development* **130**, 1837–1851 (2003).
11. Erter, C. E., Solnica-Krezel, L. & Wright, C. V. Zebrafish nodal-related 2 encodes an early mesendodermal inducer signaling from the extraembryonic yolk syncytial layer. *Dev. Biol.* **204**, 361–372 (1998).
12. Gore, A. V. *Localized Molecules and the Establishment of Polarity in Zebrafish*. PhD thesis, National Univ. Singapore (2006).
13. Pei, W., Williams, P. H., Clark, M. D., Stemple, D. L. & Feldman, B. Environmental and genetic modifiers of *squint* penetrance during zebrafish embryogenesis. *Dev. Biol.* **309**, 245–258 (2007).
14. Hagos, E. G., Fan, X. & Dougan, S. T. The role of maternal Activin-like signals in zebrafish embryos. *Dev. Biol.* **308**, 368–378; doi:10.1016/j.ydbio.2007.07.010 (2007).
15. Kloc, M. *et al.* Potential structural role of non-coding and coding RNAs in the organization of the cytoskeleton at the vegetal cortex of *Xenopus* oocytes. *Development* **132**, 3445–3457 (2005).

doi:10.1038/nature06315

Evolution of animal personalities

Arising from: M. Wolf, G. S. van Doorn, O. Leimar & F. J. Weissing *Nature* **447**, 581–584 (2007).

Wolf *et al.*¹ propose a model to explain the existence of animal personalities, consistent with behavioural differences among individuals in various contexts^{2–4}—their explanation is counter-intuitive and cogent. However, all models have their limits, and the particular life-history requirements of this one may be unclear. Here we analyse their model and clarify its organismal scope.

Under some conditions, Wolf *et al.*¹ find consistent behavioural differences between individuals that reproduce early in life and those that delay reproduction to explore their habitats instead to enhance future reproduction. Non-explorers that reproduce early in life later become bold and aggressive, whereas exploratory individuals with greater future reproductive potential are shy and unaggressive. These differences are caused by asset protection⁵ where individuals with greater future fitness take fewer risks that would jeopardize that fitness.

Asset protection, however, is a negative feedback process that, given time, makes individuals more alike, not less. In Clark's original asset protection paper⁵, many decisions are made over an animal's lifespan. Over time, individuals tend towards similar behaviour, despite any initial differences in assets, because those with assets take few risks and acquire little new fitness. Those without high assets take more risks and (unless they die trying) acquire new fitness assets that become worth protecting.

If, in the model of Wolf *et al.*, individuals experience many hawk–dove encounters, successful hawks would eventually accumulate enough fitness for playing dove to become their optimal behaviour. Given time to accrue new assets, behavioural types would converge. Two particular conditions that could prevent this convergence are: animals with very short lives might not have time to change their assets sufficiently to cause changes in behaviour; and early life-history choices can have such large fitness consequences that subsequent bold and aggressive behaviour has relatively little influence on assets. Notably, these conditions do not seem to fit the maintenance of stable personalities in long-lived organisms such as humans.

The model of Wolf *et al.* requires bold/aggressive contexts not to dominate one another in fitness consequences, otherwise the negative feedback of asset protection will apply at this smaller scale (Supplementary Fig. 2 of ref. 1: in the square in which behavioural correlations could evolve, there is a wedge-shaped region without

correlation between the hawk–dove and predator games). We reproduced their model and found that, in this region, thorough explorers are less aggressive than non-explorers, but no one is bold. Without the hawk–dove game, explorers would be shy and non-explorers bold, but when the hawk–dove game has sufficiently higher fitness consequences than the boldness game, all individuals are shy to eliminate the risk of dying before the fitness windfall from the hawk–dove game. This is the asset-protection principle, working on the scale of the low-fitness behavioural contexts, producing behavioural inconsistency, unless the contexts do not dominate one another.

An alternative way of explaining behavioural consistency and correlations is through positive (not negative) feedback. For example, if thorough explorers gain assets (energy, size, knowledge) that improve their abilities to escape predators or to win fights, then we might find positive correlations between exploration, boldness and aggressiveness. Additional behaviour would positively feed back on state, maintaining differences in assets and behavioural types. What is needed next is a unified modelling framework in which both negative and positive state feedback, as well as other mechanisms, can be compared.

Richard McElreath¹, Barney Luttbeg², Sean P. Fogarty², Tomas Brodin² & Andrew Sih²

¹Department of Anthropology, University of California, Davis, California 95616, USA.

²Department of Environmental Science and Policy, University of California, Davis, California 95616, USA.

e-mail: btluttbeg@ucdavis.edu

Received 26 June; accepted 3 September 2007.

1. Wolf, M., van Doorn, G. S., Leimar, O. & Weissing, F. J. Life-history trade-offs favour the evolution of animal personalities. *Nature* **447**, 581–584 (2007).
2. Gosling, S. D. From mice to men: what can we learn about personality from animal research? *Psychol. Bull.* **127**, 45–86 (2001).
3. Sih, A., Bell, A. M., Johnson, J. C. & Ziemba, R. E. Behavioral syndromes: an integrative overview. *Q. Rev. Biol.* **79**, 241–277 (2004).
4. Sih, A., Bell, A. & Johnson, J. C. Behavioral syndromes: an ecological and evolutionary overview. *Trends Ecol. Evol.* **19**, 372–378 (2004).
5. Clark, C. W. Antipredator behavior and the asset-protection principle. *Behav. Ecol.* **5**, 159–170 (1994).

doi:10.1038/nature06326

Wolf *et al.* reply

Replying to: R. McElreath, B. Luttbeg, S. P. Fogarty, T. Brodin & A. Sih *Nature* **450**, doi: 10.1038/nature06326 (2007).

The evolution of animal personalities is still poorly understood. The emergence of consistent individual differences is relatively easy to envisage when initial differences in behaviour are reinforced by positive feedback mechanisms. Such reinforcement might act through learning or training, or through behaviour-induced changes in an individual's condition¹ or environment². However, positive feedback is not required. We showed that, even without such feedback, differences in fitness expectations result in consistent differences in risk-taking behaviour³. This was illustrated by a model that, for simplicity, considers a short life history. McElreath *et al.*⁴ argue that our results extend to long-lived organisms only under specific conditions. Although we agree that the full scope and limitations of our model

still have to be mapped out, we believe that our arguments are also relevant to long-lived organisms.

Our theory is based on the principle of asset protection⁵: the more an individual stands to lose, the more cautiously it should behave. McElreath *et al.*⁴ argue that asset protection entails a negative feedback that tends to erode individual differences. This may indeed be the case if large assets can be accumulated by risky behaviour: risk-proneness while accumulating assets would then be followed by risk-aversion while protecting the acquired assets. However, the analysis of McElreath *et al.* is incomplete for at least two reasons.

First, not all payoffs should be considered as assets. Payoffs can be either spent immediately in current reproduction or invested into

future reproductive potential. Only the latter, resulting in an increase in future reproductive value⁶, corresponds to assets. Consequently, when the payoffs of risky games only affect immediate reproduction, no asset accumulation takes place and there is no negative feedback eroding individual differences. There might even be positive feedbacks, enhancing individual differences, if risky payoffs tend to be immediate whereas non-risky payoffs tend to increase the future reproductive value.

Second, McElreath *et al.* extrapolate our model to long-lived organisms in a one-sided manner. They assume that differences in assets due to life-history decisions only occur once in an individual's lifetime whereas the number and importance of risky games increases with life expectancy. There are certainly examples where an individual's fate is governed by a single life-history switch. Yet, such 'career decisions'⁷ are typically associated with long-lasting fitness consequences that are not eroded by everyday risky behaviour. More commonly, however, life-history decisions (such as thorough or superficial exploration) have to be taken repeatedly throughout an individual's life. As a consequence, assets are not only eroded but can also be built up.

In conclusion, the potential of negative feedback to erode individual differences is substantially smaller than McElreath *et al.* suggest. We therefore maintain that asset protection furthers the understanding of animal personalities in both short- and long-lived organisms. Yet, there are certainly situations in which negative feedbacks as described by McElreath *et al.* are important. In such situations, a switch might occur from a risk-prone to a risk-averse personality. Indeed, personalities are not always stable from the cradle to the grave. Take our own species, where young individuals with a risky lifestyle become more cautious later in life (when assets are at stake). Similarly, hover wasps switch from risk-prone to risk-averse

behaviour once they are close enough to the breeding position⁸. Our theory accounts for such switches associated with asset accumulation and it produces testable predictions for their occurrence. Hence, even in the presence of negative feedbacks, the principle of asset protection is crucial for understanding animal personalities.

Max Wolf¹, G. Sander van Doorn², Olof Leimar³ & Franz J. Weissing¹

¹Theoretical Biology Group, Centre for Ecological and Evolutionary Studies, University of Groningen, Kerklaan 30, 9751 NN Haren, The Netherlands.

²Santa Fe Institute, 1399 Hyde Park Road, Santa Fe, New Mexico 87501, USA.

³Department of Zoology, Stockholm University, SE-106 91 Stockholm, Sweden.

e-mail: f.j.weissing@rug.nl

1. Rands, S. A., Cowlishaw, G., Pettifor, R. A., Rowcliffe, J. M. & Johnstone, R. A. Spontaneous emergence of leaders and followers in foraging pairs. *Nature* **423**, 432–434 (2003).
2. Hemelrijk, C. K. & Wantia, J. Individual variation by self-organisation. *Neurosci. Biobehav. Rev.* **29**, 125–136 (2005).
3. Wolf, M., van Doorn, G. S., Leimar, O. & Weissing, F. J. Life-history trade-offs favour the evolution of animal personalities. *Nature* **447**, 581–584 (2007).
4. McElreath, R., Luttbeg, B., Fogarty, S. P., Brodin, T. & Sih, A. Evolution of animal personalities. *Nature* **450**, doi: 10.1038/nature06326 (2007).
5. Clark, C. W. Antipredator behavior and the asset-protection principle. *Behav. Ecol.* **5**, 159–170 (1994).
6. Williams, G. C. Natural selection, the costs of reproduction, and a refinement of Lack's principle. *Am. Nat.* **100**, 687–690 (1966).
7. Ens, B. J., Weissing, F. J. & Drent, R. H. The despotic distribution and deferred maturity: two sides of the same coin. *Am. Nat.* **146**, 625–650 (1995).
8. Field, J., Cronin, A. & Bridge, C. Future fitness and helping in social queues. *Nature* **441**, 214–217 (2006).

doi:10.1038/nature06327

The remarkable metal-catalysed olefin metathesis reaction

Amir H. Hoveyda¹ & Adil R. Zhugralin¹

Catalytic olefin metathesis—through which pairs of C=C bonds are reorganized—transforms simple molecules to those that are complex and precious. This class of reactions has noticeably enriched chemical synthesis, which is the art of preparing scarce molecules with highly desirable properties (for example, medicinal agents or polymeric materials). Research in the past two decades has yielded structurally well-defined catalysts for olefin metathesis that are used to synthesize an array of molecules with unprecedented efficiency. Nonetheless, the full potential of olefin metathesis will be realized only when additional catalysts are discovered that are truly practical and afford exceptional selectivity for a significantly broader range of reactions.

To appreciate the importance of catalytic olefin metathesis, we must consider the power of chemical synthesis. The ability to prepare molecules is crucial to advances in medicine, biology and materials science¹. Chemical synthesis challenges and expands our understanding of the fundamental principles of reactivity and selectivity, and gives us the opportunity to examine special molecules that were previously non-existent or available in such small quantities that a study was not feasible—for example, anticancer epothilones^{2,3} and anti-hepatitis C agent **43** (see below). A recent remark by the director of the National Institutes of Health is apropos: “One interesting result of the NIH Roadmap development process came when we surveyed scientists to find out what the stumbling blocks for biological sciences were. The number one stumbling block turned out to be synthetic organic chemistry”⁴.

For synthetic chemistry to provide its full impact, certain advances must first be realized. One crucial area is catalyst discovery. Catalytic processes represent a degree of efficiency superior to those that require one or more equivalents of a reagent (ideally, one mole per cent catalyst or less should be used). Of particular significance is the identification of effective catalysts that are readily available, easy to handle, reliable, and promote transformations at high selectivity with a broad range of substrates with minimal waste generation. Catalytic olefin metathesis^{5–10} is a ground-breaking advance that has significantly enhanced the power of chemical synthesis, and is likely to continue to do so.

Olefin metathesis and its importance

Olefin metathesis (‘metathesis’ from the Greek meaning ‘change of position, transposition’) reorganizes the carbon atoms of two C=C bonds (olefins or alkenes), generating two new ones; it promotes unique skeletal rearrangements, and is significant for several reasons. First, some olefins are easy to prepare and others require more effort to access. Terminal and some disubstituted alkenes are prepared

with relative ease; tri- or tetrasubstituted olefins, on the other hand, present a challenge owing to higher levels of steric hindrance and complications associated with controlling *cis* and *trans* (or *E* and *Z*) selectivity. Olefin metathesis allows facile access from the easily prepared olefins to those that are cumbersome to access. Efficient and stereoselective synthesis of the more substituted olefins is an important and largely unsolved problem in synthesis. Second, olefin metathesis reactions either do not generate a by-product or only produce one, such as ethylene, which can be removed by evaporation¹¹. Third, chemists routinely use olefins to interconvert molecules. Olefins are useful largely because they present the better of two worlds: stability and reactivity. Olefins are stable—they are typically stored indefinitely without decomposition. And yet, olefins contain a π -bond that is sufficiently reactive to be used in a wide range of transformations.

The repertoire of olefin metathesis catalysts. Olefin metathesis may be classified into three categories: cross, ring-closing and ring-opening metathesis (Fig. 1)¹². Cross metathesis is the most pedagogically relevant version¹³. As shown in Fig. 1, with an appropriate catalyst, C₁=C₂ and C₃=C₄ can be transposed into C₁=C₃ and C₂=C₄. It is perhaps difficult to see, at first glance, why one set of olefins would be favoured; this is a key issue, as all olefin metathesis reactions are in principle reversible. The possibility that products might be re-converted to the starting materials dictates that chemists must design reactions that avoid back-tracking.

Another type, thus far the most widely used, is ring-closing metathesis (Fig. 1)¹⁴. Here, two terminal alkenes react with the catalyst to generate a cyclic olefin, releasing a smaller olefin (C₂=C₄ in Fig. 1). Ring-closing metathesis reactions can proceed to completion partly because volatile by-products are removed, trumping a reverse process.

Finally, there is ring-opening metathesis¹⁵ (Fig. 1), through which a cyclic olefin reacts with a linear (acyclic) olefin, generating an

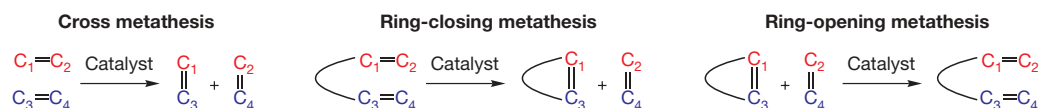


Figure 1 | Different types of olefin metathesis. Cross metathesis, ring-closing metathesis and ring-opening metathesis: each represents a different type of reaction and furnishes a different kind of product.

¹Department of Chemistry, Merkert Chemistry Center, Boston College, Chestnut Hill, Massachusetts 02467, USA.

acyclic diene. The driving force is the release of strain¹⁶ in ring structures; this also ensures minimal reaction back to the cyclic compound. Reactions that involve cross metathesis are mechanistically more complex, and controlling such transformations can be difficult (versus ring-closing). To promote cross metathesis, the catalyst must fuse together two different cross partners; otherwise, homodimerization predominates. Such complications do not occur in ring-closing metathesis where an intramolecular process is often preferred over an intermolecular one (unless strained and entropically disfavoured rings are sought¹⁷).

Catalysts that make it possible. Some of the olefin metathesis catalysts that are widely used and have served as the basis for a range of other systems are shown in Fig. 2. Centre-stage is a molybdenum (Mo; ref. 18) or a ruthenium (Ru; ref. 19) atom. The Mo=C or Ru=C double bonds (a Mo alkylidene or a Ru carbene) serve as points of contact between the catalyst and olefins. As we will see, the metal centres are crucial to the properties of these catalysts. Although complexes of other metals (such as tungsten^{18,20,21}, rhenium²² and osmium²³) promote olefin metathesis, these exhibit lower stability and/or reactivity, and have not been as extensively investigated. Development of such catalysts, however, is a compelling future objective, because—similar to Mo and Ru systems—additional metal complexes are likely to provide unique or complementary reactivity and/or selectivity profiles.

Mo catalyst **1**²⁴, prepared and handled under inert atmosphere, is generally more active than Ru catalysts **2**^{25–28} and **3**²⁹ (Fig. 2), which are stable to air and moisture. The activity of Mo and Ru catalysts are, to a large degree, complementary¹⁸. Ru catalysts may be used with substrates that carry an alcohol, a carboxylic acid, or an aldehyde, but can be rendered inactive in the presence of structurally exposed amines³⁰ and phosphines³¹; the reverse holds for Mo catalysts¹⁸. Metal complexes **1–3**, as well as a number of Ru-based derivatives^{32–34}, are commercially available.

Mo and Ru catalysts **4–6**^{35–37} (Fig. 2) are chiral. Handedness, or chirality, is an attribute of many molecules of life; polypeptides, nucleic acids, carbohydrates, and numerous naturally occurring molecules that exhibit biological activity exist as a single enantiomer and consist of enantiomerically pure smaller units. A critical objective of modern chemistry is the development of catalysts³⁸ that

promote the formation of chiral molecules of high enantiomeric purity (ideally >98% purity) from readily available and inexpensive achiral ones³⁹. Catalysts **4–6** initiate reactions that favour formation of one enantiomer. Thus far, Mo-based chiral catalysts, one of which is commercially available³⁵, promote ring-closing metathesis with higher enantioselectivities for a wider range of substrates^{18,36,40}; both classes are effective in enantioselective ring-opening/cross metathesis, affording carbo-^{37,41} and heterocyclic products^{42,43} (see below). The development of chiral olefin metathesis catalysts is less advanced than that of the achiral variants, and many important discoveries remain to be made. For instance, there are no effective chiral catalysts for enantioselective cross metathesis⁴¹.

Catalytic ring-closing metathesis

A general pathway⁴⁴ illustrating how such transformations proceed is shown in Fig. 3A. All olefin metathesis reactions involve association of the metal with an olefin substrate^{45–47}. It is in this crucial interaction that one significant difference between Mo- and Ru-based catalysts presents itself. A high-oxidation-state Mo centre (+6) is a Lewis acid that chelates with a Lewis basic olefin; in contrast, in Ru catalysts, it is the alkene substrate that serves primarily as a π Lewis acid^{48,49}.

Overall, the catalytic cycle (Fig. 3A) consists of an initiation phase (generation of the active complex) and a propagation phase (the active complex promotes additional cycles). Catalysis commences by a cross metathesis between an active carbene or alkylidene (M=C) and one of the two olefins of the substrate (**i**) to generate a metallacyclobutane (**ii**)^{50,51}. The metallacyclobutane might revert to **i** and M=C (pathway a) or the other two bonds of the ring might be ruptured, furnishing **iii**, where the metal (M) is within the substrate (pathway b). Formation of another metallacyclobutane (**iv**) and its disintegration furnishes cyclic product **v** and M=C₃ (**vi**), which is the metal-bearing agent serving as the catalyst. What typically drives reactions is that the cyclic product (**v**) does not easily react with the active catalyst (M=C₃) to cause ring-opening metathesis.

The identity of the intermediates in the catalytic cycle is well understood⁵²; it is, however, often unclear whether it is catalyst–substrate association (**i** and **vii** first chelate with the metal centre of M=C before conversion to **ii** or **viii**), formation of the metallacyclobutane^{50,53} or its cleavage that is the irreversible, product- or

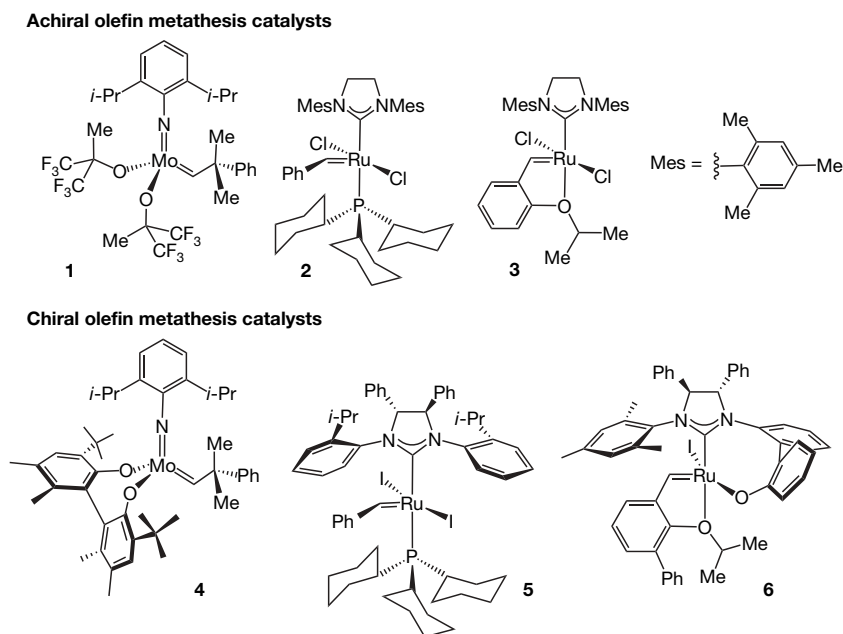


Figure 2 | Representative olefin metathesis catalysts. Catalysts **1–3** (top) are among the most commonly used achiral catalysts. Catalysts **4–6** (bottom) are chiral, and can react at different rates with two enantiomers of a substrate (kinetic resolution) or can convert an achiral molecule to a chiral one with preference for one of the two enantiomers (asymmetric synthesis). Mo-based catalysts **1** and **4** are air sensitive but generally more active than air-stable Ru-based catalysts **2**, **3** and **5**, **6**, respectively.

rate-determining step (Fig. 3A). It is a daunting task to predict a 'most effective catalyst' or to design—in the true definition of the word—one: what differentiates a selective process from one that is non-selective is a mere 2–2.5 kcal mol⁻¹ difference in activation barriers (for example, rotation around the C–C bond of ethane requires only ~3 kcal mol⁻¹), and seemingly insignificant alterations in the substrate structure or conditions can change the energetics of the catalytic cycle (which step is rate-determining)⁵⁴. These considerations indicate that seeking a truly 'general catalyst' is likely to be futile—different classes of substrates may require a different 'optimal' catalyst. Chemists address such challenges through invention of a class of catalysts (as opposed to one compound) that are easily modified to achieve maximum reactivity and/or selectivity. The more readily modifiable a catalyst class, the larger the number of available catalysts, and the better the odds of obtaining more desirable results¹⁸.

There is little doubt that ring-closing metathesis has elevated the art and science of chemical synthesis^{55,56}. Two ring-closing metathesis reactions that have been carried out for the synthesis of the large rings of two natural products are shown in Fig. 3B. The linear chain of **7**, with Lewis-basic and potentially catalyst-deactivating oxygen- and nitrogen-containing groups, is converted to the 14-membered

ring lactam **8** by catalyst **1**⁵⁷. In two additional steps, the product of ring-closing metathesis (**8**) is transformed to antifungal and anti-influenza agent fluvirucin B₁⁵⁸. The volatile ethylene (H₂C=CH₂) is the by-product.

It is easy to appreciate the power of catalysis when one considers the alternative pathways—exits on a reaction highway either avoided or traversed reversibly. The challenge in any ring-closing is that a cross metathesis, such as generation of **9** (Fig. 1), represents a competitive route; the catalyst must be sufficiently active to reverse this 'wrong turn'. The two C=C bonds in **7** are not identical: one is the more accessible and reactive monosubstituted alkene. Formation of **9** is therefore of particular concern, since it arises from coupling of two molecules of **7** by a reaction of the less hindered olefins. How is it, then, that **8** can be prepared in 92% yield? The key lies in the reversibility of olefin metathesis. Substantial amounts of **9** are indeed formed, but catalyst **1** reverts **9** to **7**. Macrocyclic **8**, on the other hand, does not undergo further reaction (ring-opening); the central olefin of **9** is less hindered than the olefin in **8** (trisubstituted). The success of the seemingly straightforward closure of **7** to afford **8** involves several nuances. Efficient synthesis of the large ring depends on striking a balance among cross metathesis, a process that delivers the undesired coupling of two substrate molecules, ring-closing

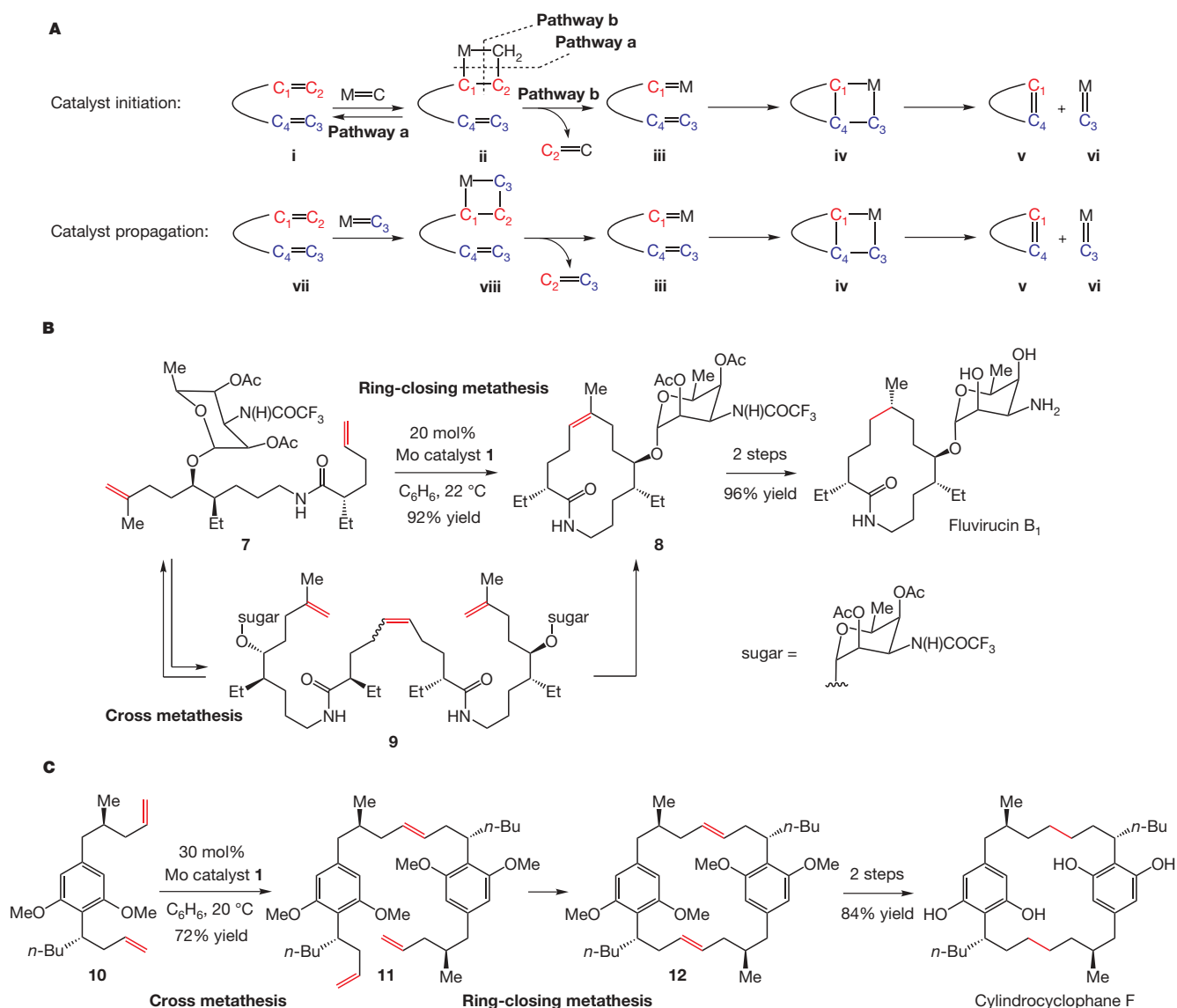


Figure 3 | The general mechanism for ring-closing olefin metathesis. This mechanism involves the intermediacy of metallacyclobutanes (**A**); also shown are two examples (**B** and **C**) that illustrate the power of catalytic ring-closing metathesis in the total synthesis of biologically active natural products (M = Mo or Ru). In both cases, the reversible nature of cross metathesis is critical to efficient synthesis of the desired macrocycles.

metathesis, a reaction that affords the desired product, and a ring-opening metathesis pathway that would dismantle the desired cyclic compound.

Another revealing example is the 'stitching' of two molecules of **10** to access 22-membered ring **12** en route to the cytotoxic agent cylindrocyclophane F (Fig. 3C)⁵⁹. The homodimerization of **10** must transpire in the desired fashion, as the two olefins within each molecule of **10** are different. The coupling can occur in two ways: head-to-head or head-to-tail, and the head-to-tail is needed for the subsequent ring-closing metathesis that affords **12**. The successful synthesis of **12** is not due to preferable formation of **11** over the alternative head-to-head product—it is because ring-closing metathesis of **11** is more favoured. Detailed investigations reveal that the head-to-head product is generated but is converted back to **10**, which undergoes coupling to generate **11**. The reversible nature of olefin metathesis proves crucial again.

In the case of **8**, the olefin, generated through olefin metathesis, is erased by palladium-catalysed hydrogenation to establish the distal methyl-bearing stereogenic centre. To untrained eyes, fluvirucin B₁ or cylindrocyclophane F are structures that do not contain an olefin within their macrocycle, and the idea of using olefin metathesis to access these molecules may not be evoked. When a synthetic chemist contemplates a target from the perspective of olefin metathesis, she must choose, among various possibilities, where to place an olefin in the precursor substrate, all signs of which may subsequently be erased. In designing a route, she commits to a strategy that predicates the identity of the bonds that realize their union. The chemist makes a move, one that affects the others that will follow^{1,60}.

The total synthesis presented in Fig. 4 is based on the insight that the architecture of longithorone A can be born through coupling of two (nearly identical) smaller building blocks **16** and **19**⁶¹.

Cyclizations of **13** and **17**, providing the 15-membered rings of **15** and **18** (Fig. 4) are catalysed by Ru complex **14**⁶², an earlier version of **2** (Fig. 1). These ring-closing reactions involve an alkyne in processes referred to as enyne metathesis^{63–65}. Products **15** and **18** are transformed to **16** and **19** such that these unsaturated macrocycles can be directed to participate in two separate Diels-Alder additions, courtesy of enyne metathesis products. The protagonists in the first act are identified in red: the 1,3-diene of **19** (red) reacts with the olefin of **16** (red) to join the two pieces while generating a cyclohexene (red). This is followed by another cycloaddition between the 1,3-diene (blue) and an olefin (blue) that resides within **16**.

Catalytic ring-opening and cross metathesis reactions

A general scheme illustrating the mechanism of ring-opening metathesis is depicted in Fig. 5. A cyclic olefin (**ix**) joins with a catalyst (M=C) to generate a metallacyclobutane (**x**), which may collapse to furnish a metal-containing intermediate **xi**. Acyclic **xi** can react with another acyclic olefin (C₃=C₄ versus cyclic olefin **x**) to yield another metallacyclobutane (**xii**). Rupture of **xii** furnishes the final product (**xiii**) and affords the active catalyst (**xiv**), which propagates additional cycles. The second olefin metathesis sequence, involving conversion of **xi** to **xiii**, constitutes a cross metathesis, and hence the concatenation of events that converts **ix** to **xiii** is referred to as ring-opening/cross metathesis. If the cyclic olefin proves more reactive than the cross partner, or if a cross partner (for example, C₃=C₄) is absent, **xi** can react with another molecule of **ix**. The resulting M=C transforms another **ix** and soon the active species romps through the substrate molecules, generating polymeric products. Such a process is referred to, appropriately, as ROMP (ring-opening metathesis polymerization). Alternatively, if the cross partner is more reactive (versus cyclic olefin), the major product arises from homo-coupling

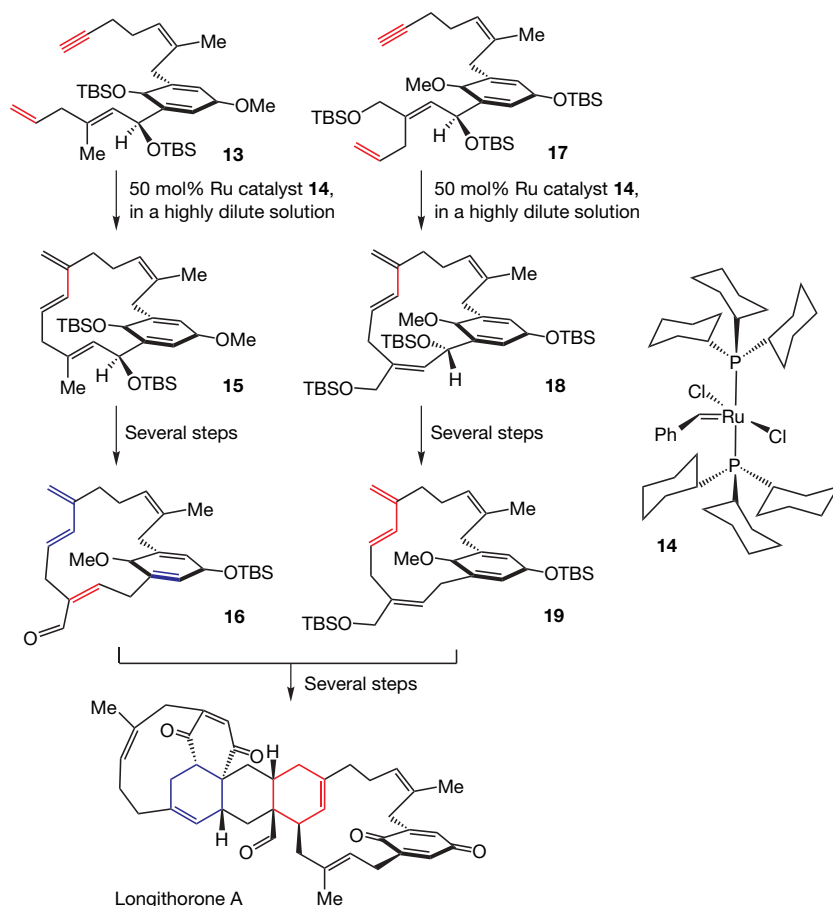


Figure 4 | A concise synthesis of longithorone A. This synthesis involves coupling of segments **16** and **19**, both of which were prepared by ring-closing enyne metathesis reactions of **13** and **17**, respectively. TBS (*t*-butyldimethylsilyl) is a common protecting group that masks alcohols.

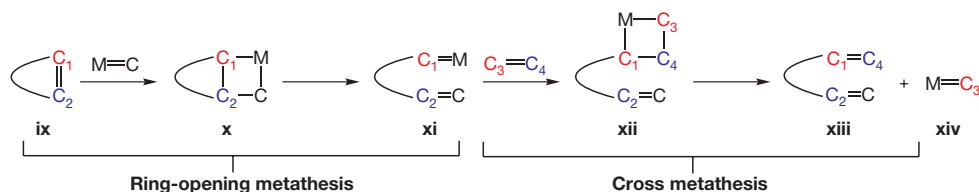


Figure 5 | General mechanism for catalytic ring-opening/cross metathesis. Ring-opening metathesis is initiated by the rupture of a cyclic C–C double bond (olefin) by a catalyst ($M=C$). This affords a new alkylidene (**xi**), which undergoes cross metathesis with another olefin to furnish the final product (**xiii**).

(cross metathesis). To achieve high yields of ring-opening/cross metathesis, the catalyst must react with the two substrates in the proper sequence with high precision. Such considerations pose demanding challenges in catalyst development. One recent approach involves catalysts that bear a stereogenic metal centre (for example, **6** in Fig. 2 and **49** below), leading to the intermediacy of two diastereomeric metal-carbene intermediates ($M=C$), each reacting preferentially with the cyclic olefin or the acyclic cross partner^{42,66}.

Small cyclic alkenes are strained¹⁶—they contain a substantial amount of energy that can be released on rupture (up to $\sim 55 \text{ kcal mol}^{-1}$; $\sim 2 \text{ kcal mol}^{-1}$ difference between two pathways means $\sim 97\%$ selectivity). Strain energies have been exploited to promote ring-opening/cross metathesis reactions^{15,42}. Two examples are presented in Fig. 6. In a total synthesis of cytotoxic agent bistramide **A**⁶⁷, cyclopropene **20** participates in a catalytic ring-opening/cross metathesis with acyclic

olefin **21** to yield **22**. In a subsequent cross transformation, the more accessible alkene of **22** (blue) is set up to react with another acyclic olefin (**23**) to furnish **24** (and gaseous ethylene as by-product). Two olefin metathesis reactions are therefore used to stitch three molecules—**20**, **21** and **23**—together, and, in short order, a complex molecule that constitutes a significant portion of bistramide **A** is fabricated.

In an enantioselective total synthesis of baconipyronone **C**⁶⁸, a siphonariid (isolated from false limpets, *Siphonaria baconi*) metabolite (Fig. 6), the plane of symmetry within achiral **25** is removed through a ring-opening/cross metathesis with styrene promoted by chiral catalyst **6** (Fig. 2), yielding heterocycle **26** with $\sim 95\%$ selectivity (89% enantiomeric excess). After conversion of **26** to **27**, another sequence involves conversion of **27** to **30** via **28** and **29**. A ring-closing olefin metathesis, this time promoted by achiral catalyst **3** (Fig. 2), furnishes allylic alcohol **30** en route to the target.

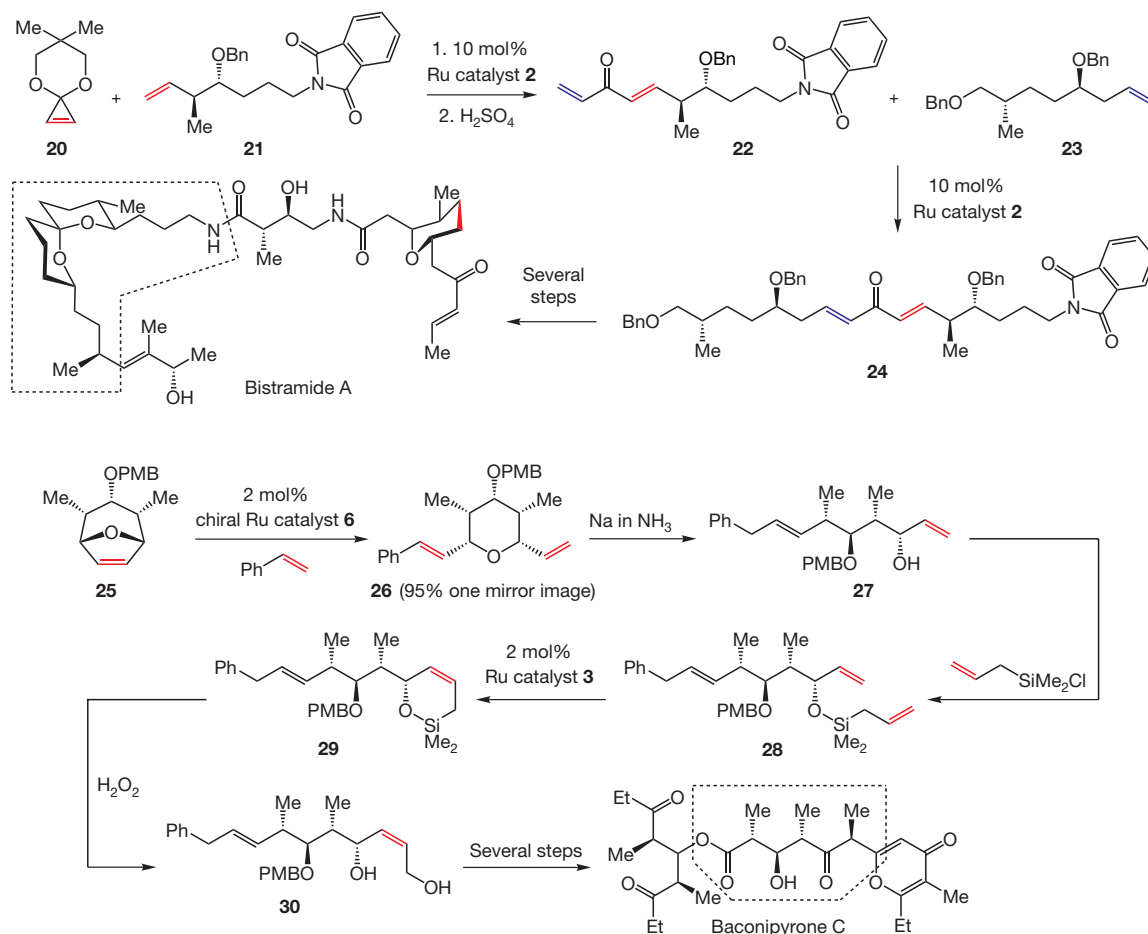


Figure 6 | Catalytic ring-opening/cross metathesis provides uniquely efficient pathways for synthesis of biologically active natural products. In the total synthesis of bistramide **A**, a Ru-catalysed ring-opening cross metathesis is followed by another cross metathesis to furnish **24**. In the total synthesis of baconipyronone **C**, a chiral Ru catalyst converts achiral **25** to pyran **26** with strong preference (95%) for one enantiomer. Bn (benzyl) and PMB (*p*-methoxybenzyl) are protecting groups that prevent alcohols from undergoing reaction. Dashed boxes represent segments of the target molecules prepared through catalytic olefin metathesis.

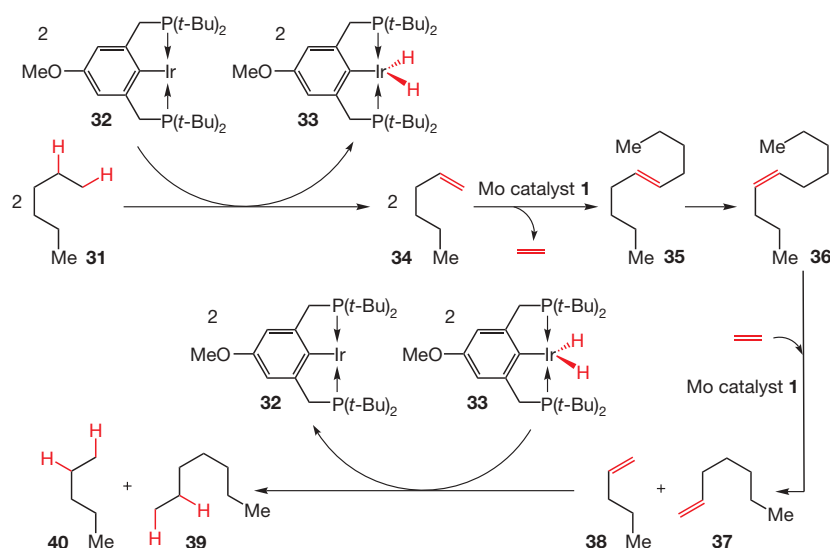


Figure 7 | Catalytic C–H activation is coupled with catalytic olefin metathesis for a net ‘alkane metathesis’ process.

Thus far, we have considered how, after ring-closing, ring-opening/cross or cross metathesis, olefins within the product might be masked by a subsequent reaction. The sequence in Fig. 7 illustrates a transformation that takes this ‘vanishing act’ to another level: although catalytic olefin metathesis is involved, neither the products nor the starting materials contain an olefin⁶⁹. The alkenes needed are obtained in the course of the transformation by iridium-based catalyst **32**, which converts two equivalents of the saturated hydrocarbon (alkane) **31** to two of alkene **34** by C–H activation⁷⁰; this process transforms **32** to iridium-dihydride **33**. Mo catalyst **1** (Fig. 1), present in the mixture, waiting for olefins to become available, connects with two molecules of **34** and transforms them to **35** and ethylene (cross metathesis). Alkene **35** can revert back to **34** after cross metathesis with ethylene, or, alternatively, its alkene may undergo isomerization to generate **36**, in a reaction that is also catalysed by iridium complex **32**. Alkene **36** participates in a Mo-catalysed cross metathesis with ethylene to produce two new terminal alkenes **37** and **38**, which can be converted to alkanes **39** and **40** by iridium-dihydride **33**, delivering back the hydrogens it borrowed from **31** to the olefins of **37** and **38**. The last reaction leads to re-formation of **32** from **33**, which moves on to afford alkene **34** and initiate additional cycles. One feature of this molecular choreography is that the sizeable iridium dihydride **33** deposits its two hydrogens on the terminal alkenes of **37** and **38** but not on the more hindered internal olefins of **35** or **36**. On the other hand, if **33** adds

its hydrogen atoms to the olefin in **34**, substrate **30** is generated again and the catalytic cycle begins anew.

With a two-catalyst approach for alkane cross metathesis, will it be feasible to design a catalytic alkane ring-closing metathesis? In cases where a cycloalkane is desired, such a direct process could be more efficient than a two-step, alkene ring-closing metathesis/hydrogenation sequence. An inherent advantage of catalytic olefin metathesis is, however, the range of useful possibilities that the rich chemistry of olefins offers. Nevertheless, such considerations have led to the development of tandem catalytic reactions carried out in a single vessel, promoted by one catalyst and involving olefin metathesis reactions; Ru-catalysed olefin metathesis/hydrogenation and olefin metathesis/olefin isomerization are representative examples⁷¹.

Catalytic olefin metathesis and a better quality of life

Through a select few examples (there are many more^{55,72–76}), we have seen how catalytic olefin metathesis has allowed chemists to synthesize medically relevant agents in entirely new ways. The utility of this class of reactions extends beyond small-scale laboratory preparation. A catalytic ring-closing metathesis promoted by catalyst **42**⁷⁷, a precursor to **3** (Fig. 2), has been used by scientists at Boehringer-Ingelheim to prepare multi-kilogram quantities of **43** (Fig. 8), a complex molecule that is precursor to a potent anti-hepatitis C agent^{78–80}.

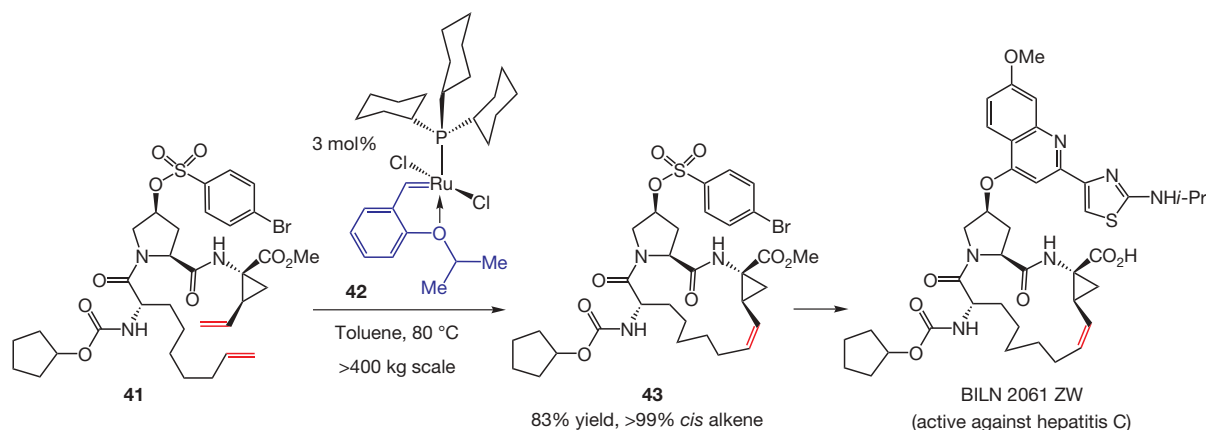


Figure 8 | Catalytic olefin metathesis has been used in the large-scale preparation of pharmaceutical candidates. An example is the potent hepatitis C protease inhibitor BILN 2061 ZW developed by Boehringer-Ingelheim. Macrocyclic intermediate **43** has been prepared in multi-kilogram quantities as a single C=C (olefin) isomer with high efficiency.

The influence of olefin metathesis has spread beyond biological chemistry⁸¹. Large-scale preparation of common organic feedstock chemicals and polymers is one area that has been affected. Polymers can be produced under mild conditions with commercial catalysts through ROMP processes. Commercially produced ROMP polymers include polyoctenamer (Vestener), polynorbornene (Norsorex) and polydicyclopentadiene⁸² (polyDCPD, Metathene, Metton, Pentam, Prometa, Telene). Fully hydrogenated analogues of some of these polymers are available as well; Zeonex is a saturated ROMP polymer of substituted polynorbornene.

Perhaps the most widely commercialized ROMP polymer is polydicyclopentadiene, which is prepared from *endo*-dicyclopentadiene—a by-product in naphtha crackers⁸³. Various ‘ill-defined’ olefin metathesis catalysts are used to manufacture polydicyclopentadiene. For example, in a process that affords Telene, tetrakis(tridodecylammonium)octa-molybdate serves as a precatalyst along with the activating mixture that consists of EtAlCl₂, SiCl₄ and propanol. A crucial advantage of well-defined Ru-based catalysts is their high degree of polymerization, an attribute that allows for removal of the odour that emanates from the un-reacted dicyclopentadiene monomer in polydicyclopentadiene⁸². Polydicyclopentadiene is easily castable and mouldable by reaction injection moulding technology; moreover, owing to its durability and resistance to corrosion, polydicyclopentadiene has found a wide range of applications in heavy machinery manufacturing (for example, agricultural equipment).

Although numerous polymers are used in the manufacturing of high-end sporting and recreational goods, day-to-day items, medical instruments and electronics, and have applications in optics, access to other ROMP polymers requires development of more efficient and ‘smarter’ catalysts. Within this context, Chen has devised an approach to the synthesis of alternating copolymers that is based on differential reactivity of diastereomeric carbene intermediates in ROMP processes⁶⁶. These transformations are promoted by complex **49**, which bears a stereogenic Ru centre (hence the involvement of stereoisomeric carbenes). Cyclooctene is thus co-polymerized with norbornene to afford an alternating copolymer, whereas copolymerization of these monomers under standard protocols delivers only a random copolymer. Chen’s method is proof-of-principle; future

research is required to address the need for active catalysts that yield a variety of alternating ROMP copolymers.

Block copolymers are poised to have a significant impact on nanotechnology. One approach to effective synthesis of these macromolecules involves ROMP processes promoted by rapidly initiating olefin metathesis catalysts. A new application for block copolymers, disclosed by General Electric, involves an inorganic-organic block copolymer of polynorbornene-decaborane as a single-source ceramic precursor, which was prepared by co-polymerization of norbornene with 6-(norbornenyl)decaborane^{84,85}. This copolymer was subsequently converted to nanostructured boron carbonitride and mesoporous boron nitride. In another development, Nuckolls has shown that a functionalized Ru-metal surface may catalyse olefin metathesis⁸⁶. Thus, ROMP on such a surface could furnish conducting polyene nanowires.

The robustness of the ROMP polymers, and of the catalytic processes used to prepare them, has allowed the ROMP reaction to be incorporated into manufacturing methods. For example, olefin metathesis has been used in the design of self-healing materials⁸⁷. Cracks, resulting from wear and tear, that appear in structural polymers can be made ‘self-healing’ by incorporation of small vesicles of dicyclopentadiene monomer, a highly effective ROMP substrate, within the material in question, together with small amounts of an olefin metathesis catalyst. If microcracking occurs, vesicles of monomer interact with the catalyst to elicit fast polymerization, resulting in formation of a robust polydicyclopentadiene plug in the place of the crack.

Challenges that lie ahead

Many critical discoveries in catalytic olefin metathesis remain to be made. One area relates to the development of more robust yet active catalysts that are easily prepared and provide exceptional control of stereochemistry. Discovery of catalysts that allow for control of olefin stereoselectivity to obtain the thermodynamically less favoured *cis* disubstituted olefins, or those that promote formation of *E* or *Z* trisubstituted alkenes, is a significant challenge, and would constitute a major contribution to olefin metathesis. Identification of chiral catalysts that furnish high enantioselectivity for a range of substrates

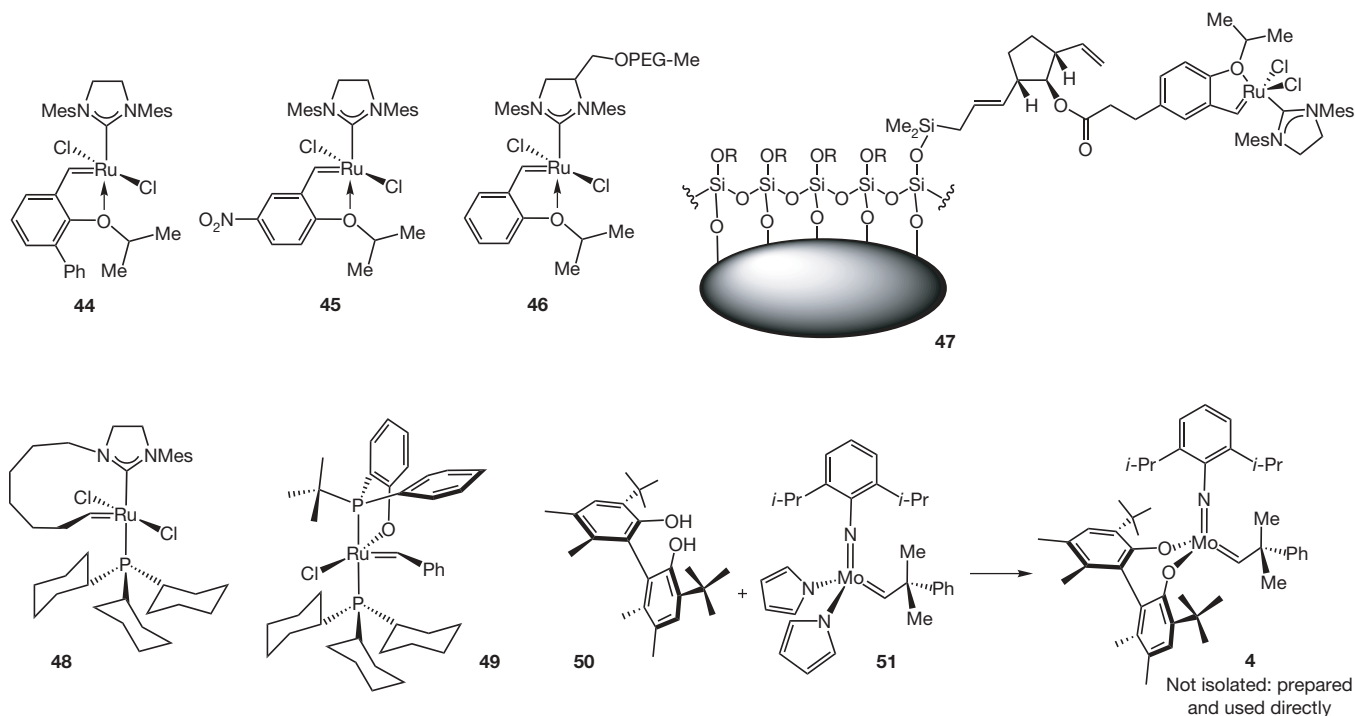


Figure 9 | More recent and modified variants of Ru-based olefin metathesis catalysts **44–49** and an easier way to access a range of chiral Mo catalysts. PEG, poly(ethyleneglycol).

and reaction classes, such as enantioselective cross metathesis or enyne metathesis, are exciting problems that are yet to be addressed.

Although many of the transformations presented above furnish desirable products, the amount of catalyst required for an efficient, cost-effective process is too high. In certain cases, as much as 50 mol% (half the amount of the substrate) of a catalyst is needed (for example, Fig. 4); but even a 3% loading is considered excessive for a 'real-world' industrial process (for example, Fig. 8). High loadings are often the result of less than optimal catalyst lifetimes. Catalyst efficiency is, therefore, about more than simply faster rates, or high turnover frequency—it is crucial that high turnover numbers are achieved. Discovery of active and selective catalysts that are more robust will require a detailed understanding of often unexpected and abstruse deactivation pathways⁸⁸.

Removal of trace metal impurities from olefin metathesis products is another complication of note, particularly in cases where compounds will be used in clinical trials. This brings us to the need for catalysts that can be easily recovered and re-used; effective catalysts bound to polymeric surfaces can minimize impurity levels and are economically attractive^{89,90}. In many olefin metathesis reactions that involve formation of large rings, high-dilution conditions are required, rendering the use of such processes difficult and prohibitively expensive in larger industrial-scale conditions. Catalysts designed to discourage competitive homodimerization of two substrate molecules (versus cyclization of one substrate molecule) are therefore needed.

With better catalysts, the currently untapped power of olefin metathesis will give rise to increasingly exciting applications. New-generation catalysts with improved properties are beginning to emerge. Notable examples are modified Ru catalysts **44**⁹¹ and **45**⁹² (Fig. 9), which can in some cases furnish faster reactions than the parent complex **3** (but, at times, this comes at the cost of lower catalyst stability), or those that can be used to catalyse reactions in water (**46**)⁹³. Ru catalysts have been attached to sol-gel glass surfaces to give 'tablets' (**47**); when the tablets are placed in solution, reaction with substrates causes catalyst release, leading to efficient reactions⁹⁴. The tablets can be removed simply with a pair of tweezers (no filtration and washing) and re-used up to 20 times. Catalyst **48** has been used to synthesize cyclic polymers by procedures that do not require linear precursors⁹⁵. The unique features of complex **49**, which, similar to **6**, contains a Ru stereogenic centre, have already been discussed⁶⁶. An important area of research involves development of highly reactive, but sensitive, catalysts by user-friendly *in situ* preparation methods that begin with relatively easy-to-handle precursors (**50** and **51** to give chiral Mo catalyst **4**)⁹⁶.

Nature presents us with a range of architectures that are diverse in size, complexity and function. Chemical synthesis—accessing molecules revealed to us by our imagination—is crucial to our ability to produce compounds that are not found in nature, but are perhaps equally as enriching. Catalytic olefin metathesis is a component of making such dreams come true. There is, however, far more that we cannot do. The little that we can do is in need of substantial improvement. To consider catalytic olefin metathesis, or chemical synthesis, a consummated field would be akin to suggesting to Henry Ford that his model T was the be-all and end-all as far as automobiles are concerned.

1. Corey, E. J. The logic of chemical synthesis: Multistep synthesis of complex carbogenic molecules (Nobel Lecture). *Angew. Chem. Int. Edn Engl.* **30**, 455–465 (1991).
2. Meng, D. *et al.* Total synthesis of epothilones A and B. *J. Am. Chem. Soc.* **119**, 10073–10092 (1997).
3. Nicolaou, K. C. *et al.* Synthesis of epothilones A and B in solid and solution phase. *Nature* **387**, 268–272 (1997).
4. Morrissey, S. R. NIH director has steered agency through congressional inquiries and penalty budget increases with bold actions to position agency for future. *Chem. Eng. News* **84** (27), 12–17 (2006).
5. Katz, T. J. & McGinnis, J. The mechanism of the olefin metathesis reaction. *J. Am. Chem. Soc.* **97**, 1592–1593 (1975).

6. Casey, C. P. & Burkhardt, T. J. Reactions of (diphenylcarbene)pentacarbonyltungsten(0) with alkenes. Role of metal-carbene complexes in cyclopropanation and olefin metathesis reactions. *J. Am. Chem. Soc.* **96**, 7808–7809 (1974).
7. Grubbs, R. H., Carr, D. D., Hopkin, C. & Burk, P. L. Consideration of the mechanism of the metal catalyzed olefin metathesis reaction. *J. Am. Chem. Soc.* **98**, 3478–3483 (1976).
8. Schrock, R. R. Multiple metal-carbon bonds for catalytic metathesis reactions (Nobel Lecture). *Angew. Chem. Int. Edn* **45**, 3748–3759 (2006).
9. Grubbs, R. H. Olefin metathesis molecules for the preparation of molecules and materials (Nobel Lecture). *Angew. Chem. Int. Edn* **45**, 3760–3765 (2006).
10. Chauvin, Y. Olefin metathesis: The early days (Nobel Lecture). *Angew. Chem. Int. Edn* **45**, 3740–3747 (2006).
11. Trost, B. M. The atom economy — a search for synthetic efficiency. *Science* **254**, 1471–1478 (1991).
12. Grubbs, R. H. (ed.) *Handbook of Metathesis* (Wiley-VCH, Weinheim, 2003).
13. Connon, S. J. & Blechert, S. Recent developments in olefin cross metathesis. *Angew. Chem. Int. Edn* **42**, 1900–1923 (2003).
14. Han, S.-Y. & Chang, S. in *Handbook of Metathesis* Vol. 2 (ed. Grubbs, R. H.) 5–127 (Wiley-VCH, Weinheim, 2003).
15. Schrader, T. O. & Snapper, M. L. in *Handbook of Metathesis* Vol. 2 (ed. Grubbs, R. H.) 205–237 (Wiley-VCH, Weinheim, 2003).
16. Wiberg, K. B. The concept of strain in organic chemistry. *Angew. Chem. Int. Edn Engl.* **25**, 312–322 (1986).
17. Conrad, J. C. *et al.* Oligomers as intermediates in ring-closing metathesis. *J. Am. Chem. Soc.* **129**, 1024–1025 (2007).
18. Schrock, R. R. & Hoveyda, A. H. Molybdenum and tungsten imido alkylidene complexes as efficient olefin metathesis catalysts. *Angew. Chem. Int. Edn* **42**, 4592–4633 (2003).
19. Nguyen, S. T. & Trnka, T. M. in *Handbook of Metathesis* Vol. 1 (ed. Grubbs, R. H.) 61–85 (Wiley-VCH, Weinheim, 2003).
20. Schrock, R. R. High oxidation state multiple metal-carbon bonds. *Chem. Rev.* **102**, 145–179 (2002).
21. Katz, T. J. in *Handbook of Metathesis* Vol. 1 (ed. Grubbs, R. H.) 47–60 (Wiley-VCH, Weinheim, 2003).
22. Toreki, R. & Schrock, R. R. A well-defined rhenium(VII) olefin metathesis catalyst. *J. Am. Chem. Soc.* **112**, 2448–2449 (1990).
23. Castarlenas, R., Esteruelas, M. A. & Onate, E. N-heterocyclic carbene-osmium complexes for olefin metathesis reactions. *Organometallics* **24**, 4343–4346 (2005).
24. Schrock, R. R. *et al.* Synthesis of molybdenum imido alkylidene complexes and some reactions involving acyclic olefins. *J. Am. Chem. Soc.* **112**, 3875–3886 (1990).
25. Scholl, M., Ding, S., Lee, C. W. & Grubbs, R. H. Synthesis and activity of a new generation of ruthenium-based olefin metathesis catalysts coordinated with 1,3-dimesityl-4,5-dihydroimidazol-2-ylidene ligands. *Org. Lett.* **1**, 953–956 (1999).
26. Weskamp, T., Schattenmann, W. C., Speglar, M. & Herrmann, W. A. A novel class of ruthenium catalysts for olefin metathesis. *Angew. Chem. Int. Edn Engl* **37**, 2490–2493 (1995).
27. Huang, J., Stevens, E. D., Nolan, S. P. & Petersen, J. L. Olefin metathesis — active ruthenium complexes bearing nucleophilic carbene ligand. *J. Am. Chem. Soc.* **121**, 2674–2678 (1999).
28. Halback, T. S. *et al.* Novel ruthenium-based metathesis catalysts containing electron-withdrawing ligands: synthesis, immobilization, and reactivity. *J. Org. Chem.* **70**, 4687–4694 (2005).
29. Garber, S. B., Kingsbury, J. S., Gray, B. L. & Hoveyda, A. H. Efficient and recyclable monomeric and dendritic Ru-based metathesis catalysts. *J. Am. Chem. Soc.* **122**, 8168–8179 (2000).
30. Cortez, G. A., Schrock, R. R. & Hoveyda, A. H. Efficient enantioselective synthesis of piperidines through catalytic asymmetric ring-opening/cross-metathesis reactions. *Angew. Chem. Int. Edn* **46**, 4534–4538 (2007).
31. Slinn, C. A. *et al.* Synthesis of unprotected and borane-protected phosphines using Ru- and Mo-based olefin metathesis catalysts. *Org. Biomol. Chem.* **1**, 3820–3825 (2003).
32. Jafarpour, L., Schanz, H.-J., Stevens, E. D. & Nolan, S. P. Indenylidene-imidazolidene complexes of ruthenium as ring-closing metathesis catalysts. *Organometallics* **18**, 5416–5419 (1999).
33. Barbasiewicz, M. *et al.* Probing of the ligand anatomy: Effects of the chelating alkoxy ligand modifications on the structure and catalytic activity of ruthenium carbene complexes. *Adv. Synth. Catal.* **349**, 193–203 (2007).
34. Stewart, I. C. *et al.* Highly efficient ruthenium catalysts for the formation of tetrasubstituted olefins via ring-closing metathesis. *Org. Lett.* **9**, 1589–1592 (2007).
35. Alexander, J. B., La, D. S., Cefalo, D. S., Hoveyda, A. H. & Schrock, R. R. Catalytic enantioselective ring-closing metathesis by a chiral biphen-Mo complex. *J. Am. Chem. Soc.* **120**, 4041–4042 (1998).
36. Funk, T. W., Berlin, J. M. & Grubbs, R. H. Highly active chiral ruthenium catalysts for asymmetric ring-closing olefin metathesis. *J. Am. Chem. Soc.* **128**, 1840–1846 (2006).
37. Van Veldhuizen, J. J., Campbell, J. E., Giudici, R. E. & Hoveyda, A. H. A readily available chiral Ag-based N-heterocyclic carbene complex for use in efficient and highly enantioselective Ru-catalyzed olefin metathesis and Cu-catalyzed allylic alkylation reactions. *J. Am. Chem. Soc.* **127**, 6877–6882 (2005).
38. Thayer, A. Chiral catalysts. *Chem. Eng. News* **83**, 40–48 (2005).

39. Jacobsen, E. N., Pfaltz, A. & Yamamoto, H. (eds) *Comprehensive Asymmetric Catalysis* (Springer, Berlin, 1999).
40. Hoveyda, A. H. in *Handbook of Metathesis* Vol. 2 (ed. Grubbs, R. H.) 128–150 (Wiley-VCH, Weinheim, 2003).
41. Berlin, J. M., Goldberg, S. D. & Grubbs, R. H. Highly active chiral ruthenium catalysts for asymmetric cross- and ring-opening cross-metathesis. *Angew. Chem. Int. Edn* **45**, 7591–7595 (2006).
42. Giudici, R. E. & Hoveyda, A. H. Directed catalytic asymmetric olefin metathesis. Selectivity control by enoate and ynoate groups in Ru-catalyzed asymmetric ring-opening/cross-metathesis. *J. Am. Chem. Soc.* **129**, 3824–3825 (2007).
43. Cortez, G. A., Baxter, C. A., Schrock, R. R. & Hoveyda, A. H. Comparison of Ru- and Mo-based chiral olefin metathesis catalysts. Complementarity in asymmetric ring-opening/cross-metathesis reactions of oxa- and azabicycles. *Org. Lett.* **9**, 2871–2874 (2007).
44. Hérisson, J.-L. & Chauvin, Y. Catalyse de transformation des oléfines par les complexes du tungstène. II. Télomérisation des oléfines cycliques en présence d'oléfines acycliques. *Makromol. Chem.* **141**, 161–176 (1971).
45. Tallarico, J. A., Bonitatibus, P. J. Jr & Snapper, M. L. Ring-opening metathesis. A ruthenium catalyst caught in the act. *J. Am. Chem. Soc.* **119**, 7157–7158 (1997).
46. Anderson, D. R., Hickstein, D. D., O'Leary, D. J. & Grubbs, R. H. Model compounds of ruthenium-alkene intermediates in olefin metathesis reactions. *J. Am. Chem. Soc.* **128**, 8386–8387 (2006).
47. Poater, A., Solans-Monfort, X., Clot, E., Copèret, C. & Eisenstein, O. Understanding d⁰-olefin metathesis catalysts: Which metal? Which ligands? *J. Am. Chem. Soc.* **129**, 8207–8216 (2007).
48. Sanford, M. S., Love, J. A. & Grubbs, R. H. Mechanism and activity of ruthenium olefin metathesis catalysts. *J. Am. Chem. Soc.* **123**, 6543–6554 (2001).
49. McGuinness, D. S. & Cavell, K. J. Zerovalent palladium and nickel complexes of heterocyclic carbenes: Oxidative addition of organic halides, carbon-carbon coupling processes, and Heck reaction. *Organometallics* **18**, 1596–1605 (1999).
50. Romero, P. E. & Piers, W. E. Direct observation of a 14-electron ruthenacyclobutane relevant to olefin metathesis. *J. Am. Chem. Soc.* **127**, 5032–5033 (2005).
51. Tsang, W. C. P. et al. Alkylidene and metallacyclic complexes of tungsten that contain a chiral biphenoxide ligand. Asymmetric ring-closing metathesis, and mechanistic investigations. *J. Am. Chem. Soc.* **125**, 2652–2666 (2003).
52. Aldhart, C. & Chen, P. Mechanism and activity of ruthenium olefin metathesis catalysts: The role of ligands and substrates from a theoretical perspective. *J. Am. Chem. Soc.* **126**, 3496–3510 (2004).
53. Tsang, W. C. P. et al. Investigations of reactions between chiral molybdenum imido alkylidene complexes and ethylene: Observation of unsolvated base-free methylene complexes, metalacyclobutane and metalacyclopentane complexes, and molybdenum (IV) olefin complexes. *Organometallics* **23**, 1997–2007 (2004).
54. Hoveyda, A. H. in *Handbook of Combinatorial Chemistry* Vol. 2 (eds Nicolaou, K. C., Hanks, R. & Hartwig, W.) 991–1016 (Wiley-VCH, Weinheim, 2003).
55. Nicolaou, K. C., Bulger, P. G. & Sarlah, D. Metathesis reactions in total synthesis. *Angew. Chem. Int. Edn* **44**, 4490–4527 (2005).
56. Gradillas, A. & Perez-Castells, J. Macrocyclization by ring-closing metathesis in total synthesis of natural products: Reaction conditions and limitation. *Angew. Chem. Int. Edn* **45**, 6086–6101 (2006).
57. Deiters, A. & Martin, S. F. Synthesis of oxygen- and nitrogen-containing heterocycles by ring-closing metathesis. *Chem. Rev.* **104**, 2199–2238 (2004).
58. Xu, Z. et al. Applications of Zr-catalyzed carbomagnesation and Mo-catalyzed macrocyclic ring-closing metathesis in asymmetric synthesis. Enantioselective total synthesis of Sch 38516 (fluvirucin B₁). *J. Am. Chem. Soc.* **119**, 10302–10316 (1997).
59. Smith, A. B. III, Adams, C. M., Kozmin, S. A. & Paone, D. V. Total synthesis of (–)-cylindrocyclophanes A and F exploiting the reversible nature of olefin cross metathesis reaction. *J. Am. Chem. Soc.* **123**, 5925–5937 (2001).
60. Nicolaou, K. C. & Sorensen, E. J. in *Classics in Total Synthesis* 1–19 (Wiley-VCH, Weinheim, 1996).
61. Layton, M. E., Morales, C. A. & Shair, M. D. Biomimetic synthesis of (–)-longithorone A. *J. Am. Chem. Soc.* **124**, 773–775 (2002).
62. Schwab, P., Grubbs, R. H. & Ziller, J. W. Synthesis and application of RuCl₂(=CHR')(PR₃)₂: The influence of the alkylidene moiety on metathesis activity. *J. Am. Chem. Soc.* **118**, 100–110 (1995).
63. Katz, T. J., Lee, S. J., Nair, M. & Savage, E. B. Reactivities of metal carbenes towards alkenes and alkynes. *J. Am. Chem. Soc.* **102**, 7942–7944 (1980).
64. Katz, T. J., Savage, E. B., Lee, S. J. & Nair, M. Induction of olefin metathesis by acetylenes. *J. Am. Chem. Soc.* **102**, 7940–7942 (1980).
65. Diver, S. T. & Giessert, S. J. Enyne metathesis (enyne bond reorganization). *Chem. Rev.* **104**, 1317–1382 (2004).
66. Bornand, M. & Chen, P. Mechanism-based design of a ROMP catalyst for sequence-selective copolymerization. *Angew. Chem. Int. Edn* **44**, 7909–7911 (2005).
67. Statsuk, A. V., Liu, D. & Kozmin, S. A. Synthesis of bistramide A. *J. Am. Chem. Soc.* **126**, 9546–9547 (2004).
68. Gillingham, D. G. & Hoveyda, A. H. Chiral N-heterocyclic carbenes in natural product synthesis: Application of Ru-catalyzed asymmetric ring-opening/cross-metathesis and Cu-catalyzed allylic alkylation to total synthesis of baconipyrene C. *Angew. Chem. Int. Edn* **46**, 3860–3864 (2007).
69. Goldman, A. S. et al. Catalytic alkane metathesis by tandem alkane dehydrogenation-olefin metathesis. *Science* **312**, 257–261 (2006).
70. Labinger, J. A. & Bercaw, J. E. Understanding and exploiting C–H bond activation. *Nature* **417**, 507–514 (2002).
71. Dragutan, V. & Dragutan, I. A resourceful new strategy in organic synthesis: Tandem and stepwise metathesis/non-metathesis catalytic processes. *J. Organomet. Chem.* **681**, 5129–5147 (2006).
72. Nickel, A. et al. Total synthesis of ingenol. *J. Am. Chem. Soc.* **126**, 16300–16301 (2004).
73. Wipf, P. & Spencer, S. R. Asymmetric total synthesis of tuberstemonine, dihydrotuberstemonine, and 13-epituberstemonine. *J. Am. Chem. Soc.* **127**, 225–235 (2004).
74. Kinderman, S. S. et al. Aminopalladation of alkoxyallenes applied in the synthesis of an enantiopure 1-ethylquinolizidine frog alkaloid. *J. Am. Chem. Soc.* **126**, 4100–4101 (2004).
75. Kuramochi, A., Usuda, H., Yamatsugu, K., Kanai, M. & Shibasaki, M. Total synthesis of (±)-garsubellin A. *J. Am. Chem. Soc.* **127**, 14200–14201 (2005).
76. Kummer, D. A., Brennen, J. B. & Martin, S. F. Application of a domino intramolecular enyne metathesis/cross-metathesis reaction to the total synthesis of (+)-8-*epi*-xanthatin. *Org. Lett.* **7**, 4621–4623 (2005).
77. Kingsbury, J. S., Harrity, J. P. A., Bonitatebus, P. J. Jr & Hoveyda, A. H. A recyclable Ru-based metathesis catalyst. *J. Am. Chem. Soc.* **121**, 791–799 (1999).
78. Nicola, T., Brenner, M., Donsbach, K. & Kreye, P. First scale-up to production scale of a ring closing metathesis reaction forming a 15-membered macrocycle as a precursor of an active pharmaceutical ingredient. *Org. Proc. Res. Dev.* **9**, 513–515 (2005).
79. Poirer, M. et al. RCM of tripeptide dienes containing a chiral vinylcyclopropane moiety: Impact of different Ru-based catalysts on the stereochemical integrity of the macrocyclic products. *J. Org. Chem.* **70**, 10765–10773 (2005).
80. Yee, N. K. et al. Efficient large-scale synthesis of BILN 2061, a potent HCV protease inhibitor, by a convergent approach based on ring-closing metathesis. *J. Org. Chem.* **71**, 7133–7145 (2006).
81. Streck, R. Economic and ecological aspects in applied olefin metathesis. *J. Mol. Catal.* **76**, 359–372 (1992).
82. Mol, J. C. Industrial applications of olefin metathesis. *J. Mol. Catal. A* **213**, 39–45 (2004).
83. Johnson, H. F. Jr. (Standard Oil Development Co.) Cyclopentadiene. US patent 2636054 (1953).
84. Malenfant, P. R. L., Wan, J., Taylor, S. T. & Manoharan, M. Self-assembly of an organic-inorganic block copolymer for nano-ordered ceramics. *Nature Nanotechnol.* **2**, 43–46 (2007).
85. Wei, X., Carroll, P. J. & Sneddon, L. G. New routes to organodecaborane polymers via ruthenium-catalyzed ring-open metathesis polymerization. *Organometallics* **23**, 163–165 (2004).
86. Tulevski, G. S., Myers, M. B., Hybertsen, M. S., Steigerwald, M. L. & Nuckolls, C. Formation of catalytic metal-molecule surface. *Science* **309**, 591–594 (2005).
87. White, S. R. et al. Autonomic healing of polymer composites. *Nature* **409**, 794–797 (2001).
88. Hong, S. H., Wenzel, A. G., Salguero, T. T., Day, M. W. & Grubbs, R. H. Decomposition of ruthenium olefin metathesis catalysts. *J. Am. Chem. Soc.* **127**, 7961–7968 (2007).
89. De Vos, D. E., Vankelecom, I. F. J. & Jacobs, P. A. *Chiral Catalyst Immobilization and Recycling* (VCH-Wiley, Weinheim, 2000).
90. Kingsbury, J. S. & Hoveyda, A. H. in *Polymeric Materials in Organic Synthesis and Catalysis* (ed. Buchmeiser, M. R.) 467–502 (VCH-Wiley, Weinheim, 2003).
91. Wakamatsu, H. & Blechert, S. A new highly efficient ruthenium catalyst. *Angew. Chem. Int. Edn* **41**, 2403–2405 (2002).
92. Grela, K., Harutyunyan, S. & Michrowska, A. A highly efficient ruthenium catalyst for metathesis reactions. *Angew. Chem. Int. Edn* **41**, 4038–4040 (2002).
93. Hong, S. H. & Grubbs, R. H. Highly active water-soluble olefin metathesis catalyst. *J. Am. Chem. Soc.* **128**, 3508–3509 (2006).
94. Kingsbury, J. S. et al. Immobilization of olefin metathesis catalysts on monolithic sol-gel: Practical, efficient, and easily recyclable catalysts for organic and combinatorial synthesis. *Angew. Chem. Int. Edn* **40**, 4251–4256 (2001).
95. Bielawski, C. W., Benitez, D. & Grubbs, R. H. An “endless” route to cyclic polymers. *Science* **297**, 2041–2044 (2006).
96. Hock, A. S., Schrock, R. R. & Hoveyda, A. H. Dipyrrolyl precursors to bisalkoxide molybdenum olefin metathesis catalysts. *J. Am. Chem. Soc.* **128**, 16373–16375 (2006).

Acknowledgements Research in our laboratories regarding the development of catalysts for olefin metathesis has been funded by the US National Science Foundation and the US National Institutes of Health, Institute of General Medical Sciences.

Author Information Reprints and permissions information is available at www.nature.com/reprints. Correspondence should be addressed to A.H.H. (amir.hoveyda@bc.edu).

ARTICLES

Hedgehog regulates smoothened activity by inducing a conformational switch

Yun Zhao^{1*}, Chao Tong^{1*†} & Jin Jiang^{1,2}

Hedgehog (HH) morphogen is essential for metazoan development. The seven-transmembrane protein smoothened (SMO) transduces the HH signal across the plasma membrane, but how SMO is activated remains poorly understood. In *Drosophila melanogaster*, HH induces phosphorylation at multiple Ser/Thr residues in the SMO carboxy-terminal cytoplasmic tail, leading to its cell surface accumulation and activation. Here we provide evidence that phosphorylation activates SMO by inducing a conformational switch. This occurs by antagonizing multiple Arg clusters in the SMO cytoplasmic tail. The Arg clusters inhibit SMO by blocking its cell surface expression and keeping it in an inactive conformation that is maintained by intramolecular electrostatic interactions. HH-induced phosphorylation disrupts the interaction, and induces a conformational switch and dimerization of SMO cytoplasmic tails, which is essential for pathway activation. Increasing the number of mutations in the Arg clusters progressively activates SMO. Hence, by employing multiple Arg clusters as inhibitory elements counteracted by differential phosphorylation, SMO acts as a rheostat to translate graded HH signals into distinct responses.

The HH morphogen controls many key development processes, with different thresholds specifying distinct outcomes^{1–4}. In *Drosophila* wing discs, HH proteins secreted by posterior (P) compartment cells move into the anterior (A) compartment to form a local concentration gradient^{5,6}. Low levels of HH suffice to induce the expression of *decapentaplegic* (*dpp*), whereas high levels are required to induce *patched* (*ptc*) and *engrailed* (*en*) (Supplementary Fig. 1)^{7–9}.

The reception system for HH consists of a twelve-transmembrane protein, PTC, as the HH receptor and a seven-transmembrane protein smoothened (SMO) as the signal transducer^{10–13}. In *Drosophila*, HH binding to PTC abrogates its inhibition on SMO and induces extensive phosphorylation of the SMO cytoplasmic tail by protein kinase A (PKA) and casein kinase I (CKI), leading to SMO cell surface accumulation and activation^{14–17}. How phosphorylation promotes SMO cell surface accumulation is not understood. In addition, phosphorylation may regulate SMO activity through mechanism(s) other than controlling its cell surface abundance.

Regulation of SMO by multiple Arg clusters

Our previous study indicates that phosphorylation may regulate SMO cell surface abundance by either preventing its endocytosis and/or promoting its recycling¹⁵. To investigate further how SMO cell surface expression is regulated, we generated a set of C-terminally truncated SMO variants and examined their subcellular localization using a cell-based assay (Fig. 1). Deletion up to amino acid 818 did not significantly change SMO subcellular distribution; however, further deletions resulted in progressively increased cell surface expression (Fig. 1a, c), implying that multiple negative regulatory elements exist between amino acids 661–818.

SMO Δ C710 exhibits consistently higher cell surface expression than SMO Δ C730 (Fig. 1c), indicating that amino acids 710–730 may harbour a negative element(s). Ala-scan mutagenesis, which substituted multiple residues to Ala, identified the Arg residues in RRTQRRR as critical for preventing SMO cell surface accumulation (Fig. 1b, c; data not shown). Interestingly, multiple Arg clusters,

arbitrarily named R1 to R4, are located between amino acids 661–818, a region critical for blocking SMO cell surface accumulation (Fig. 1d). We therefore introduced into the full-length SMO Arg to Ala (RA) mutations in individual, or combinations of, Arg clusters. SMO variants with one Arg cluster mutated did not exhibit significant change in their cell surface expression; however, mutating two or more Arg clusters caused a gradual increase in SMO cell surface expression (Fig. 1d–f; data not shown), suggesting that multiple Arg clusters cooperate to restrict SMO cell surface accumulation.

To determine whether the Arg clusters negatively regulate SMO activity, SMO variants with one or more mutated Arg clusters were expressed in wing discs using the *MS1096 Gal4* driver. SMO variants with one mutated Arg cluster exhibited low levels of basal activity similar to that of wild-type SMO, as is evident from the ectopic expression of *dpp* but not *ptc* and *en* (Fig. 2a–c). However, SMO variants with two or more mutated Arg clusters exhibited a progressive increase in their constitutive signalling activities (Fig. 2d–i). Thus, SMO activity is inversely correlated with the number of functional Arg clusters. We also mutated several Arg clusters in the membrane-proximal region of the SMO cytoplasmic tail and observed no effect on SMO cell surface expression and activity (Supplementary Fig. 2). Hence, the Arg clusters between amino acids 661–818 are specifically involved in SMO autoinhibition.

Phosphorylation counteracts the Arg motifs

Increasing the number of phosphorylation-mimetic mutations in PKA/CKI sites resulted in a graded increase in SMO cell surface level and activity¹⁵, which phenocopies the effect of increasing the number of RA mutations, indicating that phosphorylation may activate SMO by antagonizing the Arg motifs. Consistently, an internal deletion that removes both the phosphorylation and Arg clusters (SMO Δ 661–818) results in high levels of SMO cell surface expression and activity (Figs 1a, c and 2j).

It is intriguing that the Arg clusters are situated adjacent to the PKA/CKI phosphorylation clusters (Fig. 1d). In fact, R1, R2 and R4

¹Department of Developmental Biology, and ²Department of Pharmacology, University of Texas Southwestern Medical Center, Dallas, Texas 75390, USA. †Present address: Department of Molecular and Human Genetics, Baylor College of Medicine, Houston, Texas 77030, USA.

*These authors contributed equally to this work.

are part of the PKA phosphorylation consensus site, R/KRXS. The juxtaposition of the Arg and phosphorylation clusters may allow precise control of SMO activity because phosphorylation at

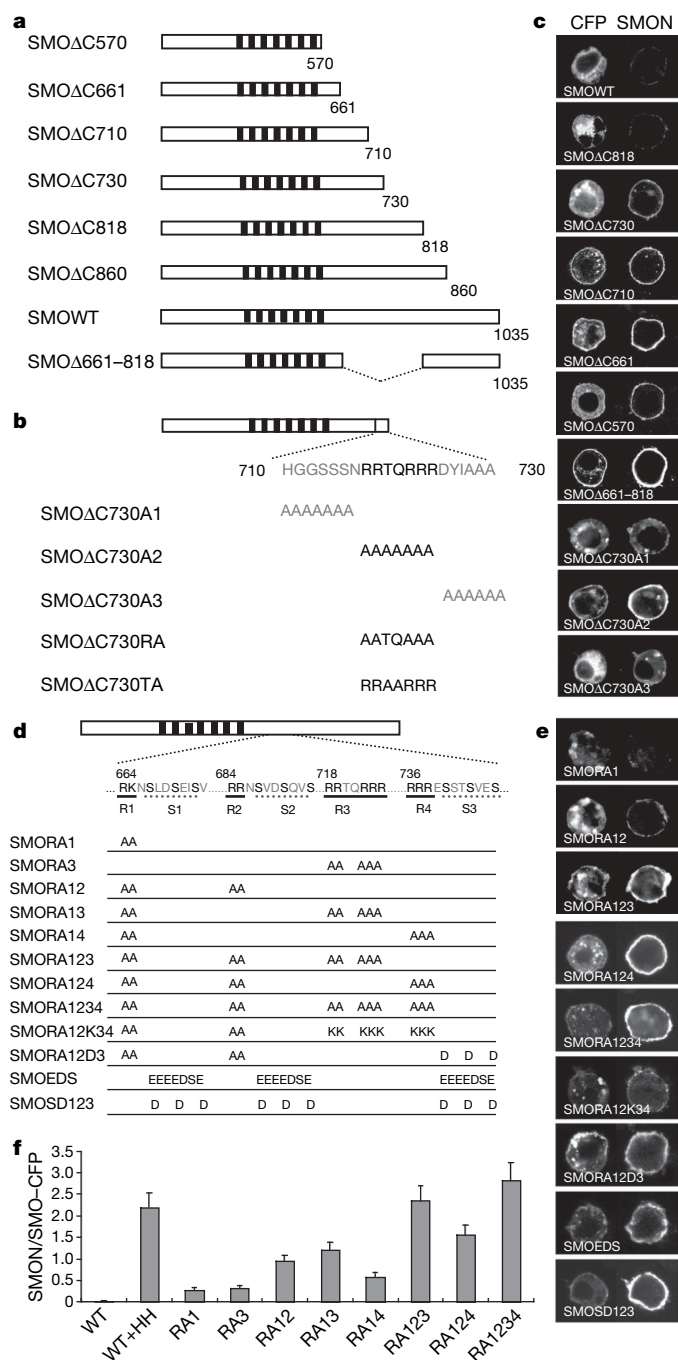


Figure 1 | Regulation of SMO cell surface expression by multiple Arg clusters. **a**, SMO deletion mutants with CFP (not shown) fused to their C termini. Filled boxes indicate the transmembrane domains. **b**, Ala-scan mutagenesis of SMOΔC730 with the last 20 amino acids and corresponding substitutions shown underneath. **c**, **e**, Cell surface expression of the indicated SMO mutants. S2 cells were transfected with the indicated CFP-tagged SMO constructs, followed by immunostaining with anti-SMON antibody before membrane permeabilization¹⁵. The SMON column indicates cell surface staining, whereas the CFP column indicates the total protein distribution. SMOΔ730RA and SMOΔ730TA behaved like SMOΔ710 and SMOΔ730, respectively (data not shown). **d**, A schematic drawing of a full-length SMO with the sequences of the four Arg clusters (R1–R4) and three phosphorylation clusters (S1–S3) shown underneath. SMO variants with the indicated substitutions are listed. **f**, Ratio of cell surface level (SMON signal) to total level (CFP signal) of protein for wild-type and indicated mutant forms of SMO. For SMO variants, $n = 20$; error bars, 1 s.d.

individual clusters may only neutralize the negative influence of adjacent Arg clusters. To test this, we constructed SMOA12D3 and found it behaved like SMORA124 (Fig. 1d, e; compare Fig. 2l with 2h), suggesting that phosphorylation at S3 (Fig. 1d) neutralizes the negative effect of R4.

Because Arg carries positive charge whereas phosphorylation brings in negative charge, phosphorylation may antagonize the Arg clusters by neutralizing their positive charges. In support of this model, we found that R3 and R4 can be functionally substituted by Lys, because SMORA12K34 behaved like SMORA12 rather than SMORA1234 (Fig. 1d, e, 2k). Furthermore, SMOEDS, which has three PKA/CKI phosphorylation clusters replaced by a stretch of acidic amino acids (Fig. 1d), exhibited high levels of cell surface expression and signalling activity similar to the phosphorylation-mimetic SMO variant, SMOSD123 (Fig. 1d, e, 2m; ref. 15), suggesting that the exact sequence composition of the phosphorylation clusters is not critical, but rather the negative charges they carry are important.

HH induces increased proximity of SMO cytoplasmic tails

Although SMO activity correlates with its cell surface levels, HH may induce SMO activation through additional mechanism(s) such as dimerization and/or conformational change^{18,19}. To test these possibilities,

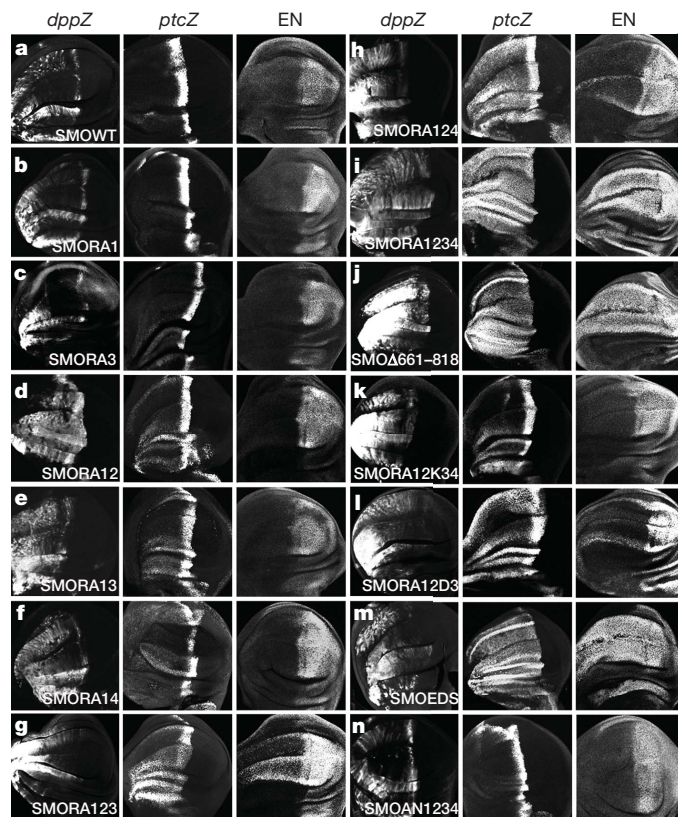


Figure 2 | In vivo activities of SMO variants. **a–n**, Wing discs expressing the indicated SMO variants from *MS1096* were immunostained to show the expression of *dpp-lacZ* (*dppZ*), *ptc-lacZ* (*ptcZ*) and *EN*. *dppZ*, *ptcZ* and *en* are induced by low, intermediate and high levels of HH, respectively. The levels of SMO activity inversely correlate with the number of intact Arg clusters (**b–i**). An internal deletion removing amino acids 661–818 resulted in high levels of constitutive SMO activity (**j**). SMORA12K34 (**k**) has similar activity to SMORA12 (compare to **d**). SMORA12D3 (**l**) exhibited constitutive activity similar to that of SMORA124 (**h**). **m**, Substitution of the three PKA/CKI phosphorylation clusters with acidic clusters led to high constitutive activity similar to that of SMOSD123 (ref. 15). **n**, SMOAN1234 (see Fig. 4a) did not exhibit higher basal activity than SMOWT (compare to **a**).

we employed fluorescence resonance energy transfer (FRET) analysis, which measures the transfer of energy between yellow fluorescent protein (YFP) and cyan fluorescent protein (CFP) as a function of distance²⁰. We initially constructed two pairs of tagged SMO with CFP/YFP either fused to the C terminus (SMO-CFP^C/SMO-YFP^C) or inserted at an amino-terminal position (SMO-CFP^N/SMO-YFP^N) of SMO (Fig. 3a, b; Supplementary Fig. 3). As controls, we constructed CFP/YFP-tagged forms of frizzled 2 (FZ2) and RAB5.

Consistent with a previous finding that FZ family members form constitutive dimers/oligomers²¹, we observed high FRET between FZ2-CFP^C/FZ2-YFP^C ($17.3 \pm 1.9\%$) or FZ2-CFP^N/FZ2-YFP^N ($12.6 \pm 1.1\%$) in S2 cells (Fig. 3c, d). Under similar conditions, FRET between SMO-CFP^N/SMO-YFP^N (referred to as FRET^N) was $14.1 \pm 1.4\%$ (Fig. 3c), whereas FRET between SMO-CFP^C/SMO-YFP^C (FRET^C) was $5.7 \pm 1.3\%$ (Fig. 3d). HH stimulation significantly increased FRET^C to $21.7 \pm 1.5\%$ (Fig. 3d), but only modestly increased FRET^N (Fig. 3c). FRET between control pairs (SMO/FZ2 or SMO/RAB5) was $\leq 1.0\%$ (Fig. 3c, d). In addition, CFP- and YFP-tagged SMO colocalized whereas SMO-CFP barely overlapped

with FZ2-YFP (Supplementary Fig. 4). Even in S2 cells stimulated with HH, in which SMO accumulated on the cell surface and overlapped with FZ2, FRET between SMO/FZ2 remained low (Fig. 3c, d, and Supplementary Fig. 4). Furthermore, over fourfold changes in SMO signal intensity did not significantly affect FRET^C (Supplementary Fig. 5).

In wing discs, FRET^N was high in both A and P compartments regardless of HH (Fig. 3e), whereas FRET^C in A-compartment cells distant from the A/P boundary was relatively low but increased significantly in P-compartment cells and in A-compartment cells exposed to HH or lacking PTC (Fig. 3f; Supplementary Figs 6–7a). The high basal FRET^N suggests that SMO forms a constitutive dimer/oligomer (dimer is used hereafter for simplicity), as is the case for the FZ family. Constitutive SMO dimerization was confirmed by immunoprecipitation assays (Supplementary Figs 8 and 9). SMO dimerization is likely to be mediated by SMON, which includes the N-terminal extracellular domain and transmembrane helices, because SMON-CFP^N and SMON-YFP^N colocalized and produced high basal FRET (Fig. 3c).

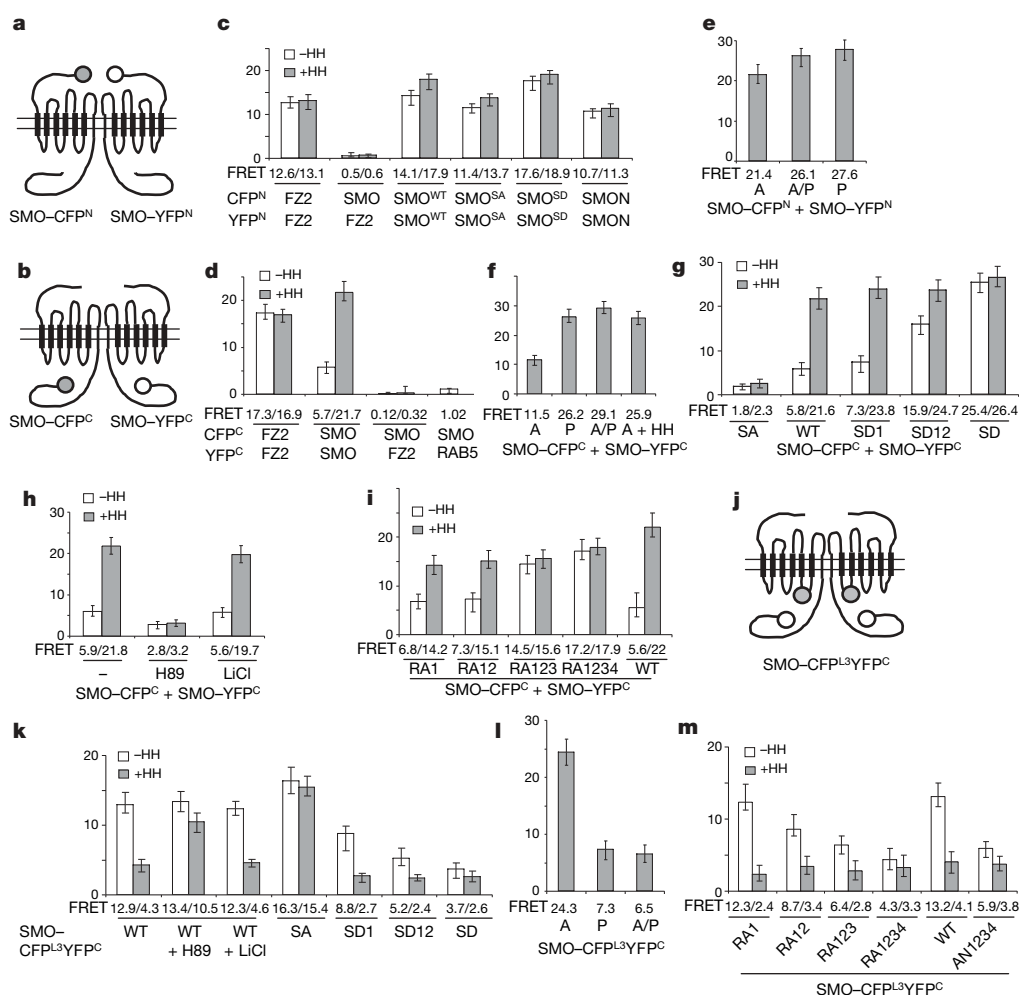


Figure 3 | Regulation of both conformation and proximity of SMO cytoplasmic tails. **a, b, j,** Cartoons of SMO-CFP^N/SMO-YFP^N (**a**), SMO-CFP^C/SMO-YFP^C (**b**), and SMO-CFP^{L3}/SMO-YFP^{L3} (**j**). The filled and open circles indicate CFP and YFP, respectively. **c, d, g–i, k, m,** FRET efficiency (y axis and numbers below bars) from the indicated CFP/YFP-tagged constructs in S2 cells treated with or without HH-conditioned medium, and with or without PKA inhibitor H89 or GSK3 inhibitor LiCl (mean \pm s.d., $n \geq 10$). SMO^{SA} has three PKA sites mutated to Ala, whereas SMO^{SD1}, SMO^{SD12} and SMO^{SD} have PKA and CKI sites in one, two and three phosphorylation clusters converted to Asp, respectively (**c, g, k**; ref. 15). SMON lacks a cytoplasmic tail (**c**). RA1, RA12, RA123 and RA1234 have one, two, three and four Arg clusters mutated to Ala, respectively (**i, m**; see

Fig. 1d). AN1234 has four C-terminal acidic clusters mutated to Ala (**m**; see Fig. 4a). HH increased FRET^C between SMO-CFP^C/SMO-YFP^C (**d**) and decreased FRET^{L3C} from SMO-CFP^{L3}/SMO-YFP^{L3} (**k**), both of which were blocked by the SA mutations (**g**) or H89 but not by LiCl (**h, k**). Phospho-mimetic or RA mutations progressively increased basal FRET^C (**g, i**) whereas they gradually decreased FRET^{L3C} (**k, m**). **e, f, l,** FRET efficiency between SMO-CFP^N/SMO-YFP^N (**e**), SMO-CFP^C/SMO-YFP^C (**f**), or from SMO-CFP^{L3}/SMO-YFP^{L3} (**l**) expressed in wing discs (mean \pm s.d., $n \geq 5$). A, A-compartment cells away from the A/P boundary; P, P-compartment cells; A/P, A-compartment cells adjacent to the A/P boundary; A + HH, A-compartment cells expressing UAS-HH.

The low basal but high HH-induced FRET^C suggests that the two SMO cytoplasmic tails within a dimer are separated from each other but HH signalling increases their proximity. To investigate whether increased proximity is accompanied by a conformational change, we generated a doubly tagged SMO (SMO–CFP^{L3}YFP^C) with CFP inserted into the third intracellular loop (L3) and YFP fused to the C terminus (Fig. 3j; Supplementary Fig. 3). SMO–CFP^{L3}YFP^C responded to HH and possessed signalling activity (Supplementary Figs 10, 11). In S2 cells, basal FRET from SMO–CFP^{L3}YFP^C (referred to as FRET^{L3C}) was $12.9 \pm 1.2\%$ but dropped to $4.3 \pm 0.8\%$ after HH treatment (Fig. 3k; Supplementary Fig. 11). In wing discs, FRET^{L3C} was $24.3 \pm 2.1\%$ in A-compartment cells distant from the A/P boundary, but dropped to $6.5 \pm 1.5\%$ in A-compartment cells near the A/P boundary or to $7.3 \pm 1.6\%$ in P-compartment cells (Fig. 3l; Supplementary Fig. 12). FRET^{L3C} also reduced to $5.9 \pm 1.2\%$ in A-compartment *ptc* mutant clones (Supplementary Fig. 7b). The high basal FRET^{L3C} is probably due to close proximity between the C terminus and L3 of the same SMO molecule (Supplementary Fig. 13). These results suggest that SMO adopts a closed inactive conformation with its C terminus in close proximity to L3, in quiescent cells. HH promotes SMO to adopt an open active conformation in which its C terminus moves away from L3 but closer to the C terminus of its binding partner.

Phosphorylation regulates SMO conformation

To determine if conformational change and increased proximity of SMO cytoplasmic tails is regulated by phosphorylation, we mutated three PKA sites (Ser 667, Ser 687 and Ser 740) to Ala (SA) or substituted them and adjacent CKI sites with Asp (SD123 or SD for simplicity)¹⁵. The HH-induced increase in FRET^C or decrease in FRET^{L3C} was blocked by the SA mutation as well as a PKA inhibitor H89 (Fig. 3g, h, k), whereas the SD123 substitution resulted in high basal FRET^C but low basal FRET^{L3C} (Fig. 3g, k). In contrast, neither the basal nor the HH-induced FRET^N was significantly affected by the SA or SD123 mutation (Fig. 3c), suggesting that constitutive SMO dimerization is not regulated by phosphorylation, but conformational change and increased proximity of SMO cytoplasmic tails are triggered by phosphorylation. Mutating multiple Arg clusters also resulted in high basal FRET^C but low basal FRET^{L3C} (Fig. 3i, m), suggesting that the Arg motifs keep SMO cytoplasmic tails in a closed inactive conformation.

To assess direct physical interaction between SMO cytoplasmic tails and its regulation by phosphorylation, we applied the CytoTrap yeast two-hybrid assay (Methods Summary). Wild-type SMO cytoplasmic tail (SMOC^{WT}) failed to self-associate, whereas phosphomimetic SMO cytoplasmic tail (SMOC^{SD}) could self-associate and also interact weakly with SMO^{WT} (Supplementary Fig. 14), indicating that phosphorylation of the SMO cytoplasmic tail may promote self-association.

Our previous study suggests that graded SMO activities are governed by SMO phosphorylation levels¹⁵. To determine if increasing SMO phosphorylation could induce gradual changes in SMO conformation, we compared FRET^C and FRET^{L3C} for several phosphorylation-mimetic forms of SMO. SMO^{SD1}, SMO^{SD12} and SMO^{SD} contain Ser to Asp substitution in one, two and three phosphorylation clusters, respectively, and exhibit progressively higher levels of basal activity¹⁵. Interestingly, they also exhibited a progressive increase in basal FRET^C (Fig. 3g) and gradual decrease in basal FRET^{L3C} (Fig. 3k). Furthermore, FRET^C progressively increased, whereas FRET^{L3C} gradually decreased, when increasingly more Arg clusters were mutated (Fig. 3i, m). Thus, increasing SMO phosphorylation seems to induce progressive changes in SMO conformation by antagonizing the Arg clusters. SMO may adopt a series of conformational states determined by its phosphorylation levels. Alternatively, SMO may switch in equilibrium between two distinct conformational states: a closed inactive conformation and an open

active conformation; phosphorylation increases the probability for individual SMO to adopt the open active conformation.

Arg clusters mediate intramolecular interaction

To determine how Arg clusters keep SMO in a closed inactive conformation, we tested the possibility that they might be involved in intramolecular interactions. A glutathione S-transferase (GST) fusion protein (GST–SMO656–755) that contains the SMO region between amino acids 656–755 (referred to hereafter as SAID for SMO auto-inhibitory domain) was tested for interaction with a set of C-terminal fragments, and a minimal SAID interacting fragment (NT860) was identified that contains the C-terminal region between amino acids 860–1035 (Supplementary Fig. 15). SAID–NT860 interaction was diminished by PKA/CKI phosphorylation as well as RA or SD123 mutations (Fig. 4b, c), and the binding affinity gradually decreased with more phosphorylation or Arg clusters mutated (Fig. 4d). The importance of Arg clusters in the SAID–NT860 interaction indicates that the association may be mediated by electrostatic interactions. Indeed, mutating several acidic clusters in the C-terminal half of NT860 gradually diminished the SAID–NT860 interaction (Fig. 4a, e).

The electrostatic interaction between NT860 and SAID may result in a folding back of the SMO cytoplasmic tail to form a closed conformation (Fig. 4f). Consistently, mutating the acidic clusters (SMOAN1234) resulted in decreased basal FRET^{L3C} (Fig. 3m). However, unlike RA mutations, which not only caused conformational change but also promoted SMO cell surface accumulation, SMOAN1234 exhibited little if any cell surface expression and did not exhibit high levels of constitutive activity (Fig. 2n), indicating that both cell surface accumulation and conformational change may be critical for SMO activity.

Clustering of the SMO cytoplasmic tail activates the HH pathway

To assess the biological significance of SMO dimerization, we analysed two SMO mutants with point mutations in the N-terminal extracellular domain: SMO^{IA3} is encoded by a hypomorphic allele such that Cys 90 is substituted to Ser; and SMO^{F11} is encoded by a strong allele that changes Cys 155 to Tyr (ref. 22). Both mutations reduced basal as well as HH-induced FRET^N and FRET^C, with SMO^{F11} exhibiting more severe defects (Supplementary Fig. 16). Immunoprecipitation assays indicated that SMO^{IA3} and SMO^{F11} failed to dimerize with SMO^{WT} (Supplementary Fig. 17a). Unlike SMO^{WT}, neither SMO^{IA3} nor SMO^{F11} was phosphorylated in response to HH (Supplementary Fig. 17b). In addition, both SMO^{IA3} and SMO^{F11} lost HH-induced activity (Fig. 5a).

If loss of SMO activity was due to compromised dimerization, restoring dimerization to these mutants should rescue their activities. To test this, we developed an inducible dimerization system by taking advantage of the observation that the mammalian receptor tyrosine kinase EphB2 forms a hetero-tetramer with its ligand ephrin B2 (EB2; also known as Efnb2) to trigger bidirectional signalling²³. Accordingly, we constructed EB2–SMO chimaeric proteins in which the extracellular domain of EB2 was inserted into the SMO N-terminal extracellular domain (Supplementary Fig. 3). When expressed in cl-8 cells, EB2–SMO^{IA3} and EB2–SMO^{F11} failed to be activated by HH-conditioned medium; however, they were activated when cells were exposed to the soluble pre-clustered EphB2 extracellular domain, EphB2–Fc (Fig. 5a). In addition, FRET^C between mutant pairs of EB2–SMO–CFP^C/EB2–SMO–YFP^C increased significantly in response to EphB2–Fc but not HH (Fig. 5b).

To determine if dimerization of the SMO cytoplasmic tail suffices to activate the HH pathway, we constructed EB2–SMO cytoplasmic-tail chimaeric proteins in which the intracellular domain of EB2 was replaced by the wild-type (EB2–SMOC^{WT}), phosphorylation-deficient (EB2–SMOC^{SA}), or phosphorylation-mimetic (EB2–SMOC^{SD}) SMO cytoplasmic tail (Fig. 5e, and Supplementary Fig. 3). In both cl-8 cells and wing discs, EB2–SMOC^{WT} exhibited low

basal activity but was markedly stimulated by EphB2 (Fig. 5c, f). Furthermore, EB2-SMOC^{WT} activated the HH pathway independent of endogenous SMO (Supplementary Fig. 18). EB2-SMOC^{WT} also induced FU phosphorylation in response to EphB2-Fc (Supplementary Fig. 19a). In addition, FRET between EB2-SMOC^{WT}-CFP^C/EB2-SMOC^{WT}-YFP^C increased significantly in response to EphB2-Fc (Fig. 5d).

EB2-SMOC^{SA} did not significantly activate any HH target genes even after clustering by EphB2 (Fig. 5c, f). PKA-site mutation may lock the cytoplasmic tails in a closed inactive conformation that prevents their association. Consistent with this model, FRET between EB2-SMOC^{SA}-CFP^C/EB2-SMOC^{SA}-YFP^C remained low after EphB2-Fc treatment (Fig. 5d). EphB2-Fc treatment induced phosphorylation of EB2-SMOC, which was abolished by the SA mutation and H89 (Supplementary Fig. 19b), suggesting that EphB2/EB2-induced clustering of SMO cytoplasmic tails promoted their phosphorylation and close proximity, leading to HH pathway activation.

EB2-SMOC^{SD} exhibited high basal activity, yet its activity was further enhanced by EphB2 (Fig. 5c, f). In addition, FRET between EB2-SMOC^{SD}-CFP^C/EB2-SMOC^{SD}-YFP^C increased after EphB2-Fc treatment (Fig. 5d). Thus, even though 'phosphorylated' SMO cytoplasmic tails may adopt an open conformation that allows them to interact more avidly, as suggested by their high basal FRET^C (Fig. 5d), EphB2/EB2-induced clustering further increased their proximity, leading to enhanced pathway activation. These results further underscore the importance of close proximity between SMO cytoplasmic tails for pathway activation.

Regulation of mammalian SMO

In response to SHH and PTC inactivation, mammalian SMO (Smo) translocates to primary cilia, which is thought to trigger pathway activation^{24–26}. To determine if SHH may also regulate Smo

conformation, we constructed C- or N-terminally CFP/YFP-tagged Smo or a doubly tagged Smo with CFP inserted into the second intracellular loop (L2) and YFP fused to the C terminus (Supplementary Fig. 20a). All tagged forms exhibited activities similar to that of the untagged wild-type form (Supplementary Fig. 20b). Like *Drosophila* SMO, Smo also exhibited high basal FRET^N and low basal FRET^C; however, SHH as well as an oncogenic mutation (A1)²⁷ induced significant increases in FRET^C (Supplementary Fig. 20c, d). In addition, both SHH and the A1 mutation reduced FRET from Smo-CFP^{L2}-YFP^C (FRET^{L2C}; Supplementary Fig. 20e), indicating that Smo may also exist as a constitutive dimer and that SHH induces a conformational change, leading to increased proximity of Smo cytoplasmic tails. Interestingly, induced clustering of full-length Smo through the ephrin B2/EphB2 system also triggered pathway activation; however, unlike *Drosophila* SMO, clustering of Smo cytoplasmic tails failed to activate the pathway (Supplementary Fig. 21). It is possible that other intracellular domains such as L3 may be essential for inducing the active conformation of Smo and/or recruiting the intracellular signalling complex because point mutations in L3 inactivate Smo²⁸.

Vertebrate SMO proteins contain multiple conserved clusters of basic residues in their cytoplasmic tails, including a long stretch of Arg/Lys residues in the central region (Supplementary Fig. 22a). Interestingly, mutating this long stretch of Arg/Lys residues to Ala resulted in constitutive activity of Smo, increased FRET^C and decreased FRET^{L2C} (Supplementary Fig. 22b–e), indicating that Smo may employ an Arg/Lys cluster to regulate its conformation and activity.

Discussion

The prevalent view regarding SMO regulation is that SMO is activated as a result of subcellular compartmentation^{14,15,24–26,29}. Here we

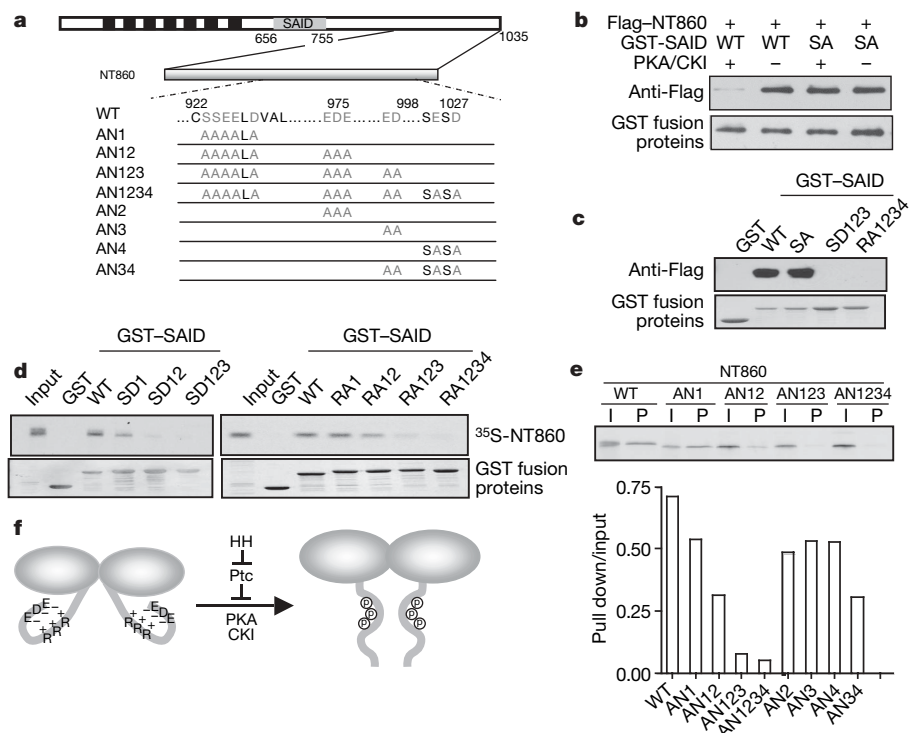


Figure 4 | The Arg clusters mediate intramolecular electrostatic interaction. **a**, Diagram of SMO with the SAID indicated by a grey box, and NT860 with indicated substitutions. **b**, GST pull-down assay using GST-SAID and S2 cell extracts expressing the indicated Flag-tagged SMO C-terminal fragments. **c**, **d**, GST pull-down experiments using wild-type or the indicated mutant GST-SAID and S2 cell extracts expressing Flag-tagged NT860 (**c**) or *in vitro* translated ³⁵S-labelled NT860 (**d**). **e**, Autoradiography

(upper panel) and quantification (lower panel) of a GST pull-down assay using GST-SAID and *in vitro* translated ³⁵S-labelled wild-type (WT) or mutant (AN) NT860. I, input; P, pulled-down protein. The binding affinity was indicated by the ratio of pulled-down protein (pull down) to input. **f**, A model for regulating SMO conformation by multiple Arg clusters and HH-induced phosphorylation; see text for detail.

provide substantial evidence that SMO activity is also regulated by a conformational switch. In particular, we identified an autoinhibitory domain (SAID) in the *Drosophila* SMO cytoplasmic tail, containing multiple Arg clusters that keep SMO in a closed inactive conformation through intracellular electrostatic interaction (Fig. 4f). HH-induced phosphorylation disrupts such interaction and triggers a conformational switch and increased proximity of SMO cytoplasmic tails, which may further promote recruitment and interaction of intracellular signalling complexes^{30–33}. Our results also indicate that the Arg clusters may promote endocytosis and degradation of SMO, whereas multiple phosphorylation events neutralize the negative effect of the Arg clusters either by inhibiting endocytosis and/or promoting recycling of SMO.

A striking feature of the SAID domain is that it contains multiple regulatory modules each of which consists of an Arg cluster linked to

a phosphorylation cluster. The pairing of positive and negative regulatory elements may offer precise regulation, because phosphorylation at a given cluster may only neutralize adjacent negative element(s), leading to an incremental change in SMO activity. We propose that increasing phosphorylation gradually neutralizes the negative effect of multiple Arg clusters, leading to a progressive increase in SMO cell surface expression and activity (Supplementary Fig. 23). Thus, by employing multiple Arg clusters as inhibitory elements that are counteracted by differential phosphorylation, SMO acts as a rheostat to translate graded HH signals into distinct responses.

METHODS SUMMARY

*smo*³ and *ptc*^{1W} are strong alleles of *smo* and *ptc*, respectively (<http://flybase.bio.indiana.edu/>). *MS1096*, *ptc-Gal4*, *dpp-lacZ*, *UAS-smo-CFP^C/UAS-smo-YFP^C* and their mutant derivatives have been described¹⁵. *Drosophila smo* and mouse *Smo* constructs were generated using the *pUAST* and *pGE* vectors, respectively. Amino acid substitutions were generated using PCR-based mutagenesis. Fly transformants were generated by standard P-element mediated transformation. Multiple independent transgenic lines were tested for activity. Immunostaining was carried out as described³⁴. S2 and cl-8 cells were cultured as described^{35,36}. Treatment of transfected cells with HHN-conditioned medium and *ptc-luc* reporter assays were carried out as described³². Cell surface staining was carried out as described¹⁵. NIH-3T3 cells were cultured in DMEM medium. Mammalian reporter assays were performed essentially as described²⁷. For GST pull-down assays, S2 cell lysates or reticulocytes with *in vitro* translated ³⁵S-labelled proteins were incubated with GST fusion proteins absorbed on glutathione beads. Proteins bound to the beads were separated on SDS-PAGE, followed by western blot or autoradiography. Immunoprecipitation and western blot analysis were carried out using standard protocols. Yeast two-hybrid assays were carried out using Stratagene's CytoTrap system according to the manufacturer's instructions. For FRET analysis, a Zeiss LSM510 confocal microscope was used. CFP was excited at 458 nm wavelength and the emission was collected through a BP 480–520 nm filter. YFP was excited at 514 nm wavelength and the emission was collected through a BP 535–590 nm filter. CFP signal was obtained once before (BP) and once after (AP) photobleaching YFP using the full power of the 514 nm laser line for 1–2 min at the top half of each cell or selected disc area, leaving the bottom as an internal control. The intensity change of CFP was analysed using the Metamorph software (Universal Imaging). The efficiency of FRET was calculated using the formula: $\text{FRET\%} = [(\text{CFP}_{\text{AP}} - \text{CFP}_{\text{BP}})/\text{CFP}_{\text{AP}}] \times 100$.

Full Methods and any associated references are available in the online version of the paper at www.nature.com/nature.

Received 4 June; accepted 7 September 2007.

Published online 24 October 2007.

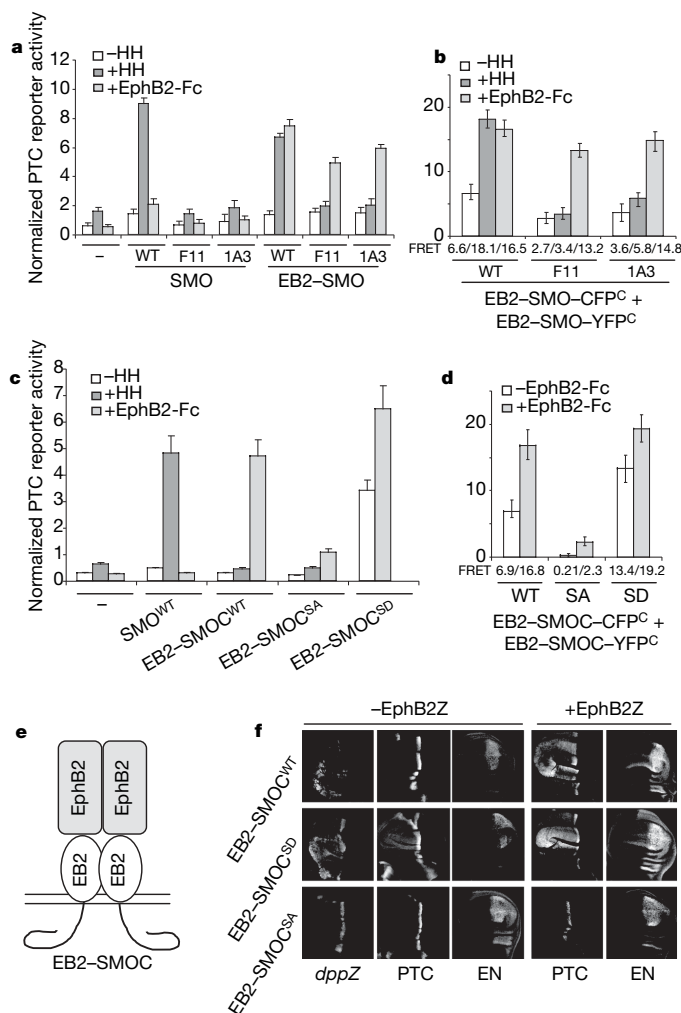


Figure 5 | Clustering of SMO cytoplasmic tails triggers HH pathway activation. **a, c,** The *ptc-luc* reporter assay in cl-8 cells transfected with the indicated SMO expression constructs and treated with or without HH-conditioned medium or EphB2-Fc. Error bars, 1 s.d. (triplicate wells). **b, d,** FRET between wild-type or mutant pairs of EB2-SMO-CFP^C/EB2-SMO-YFP^C (**b**) or EB2-SMO-CFP^C/EB2-SMO-YFP^C (**d**) expressed in S2 cells treated with or without HH-conditioned medium or EphB2-Fc (mean \pm s.d., $n \geq 10$). **e,** Cartoon of the EB2-SMO-CFP complex. **f,** Wing discs expressing the indicated SMO constructs with or without EphB2Z under the control of the *MS1096 Gal4* driver were immunostained to show the expression of *dpp-lacZ* (*dppZ*), PTC and EN. Of note, EB2-SMO^{SD} exhibited higher basal activity than EB2-SMO^{WT} because it induced higher levels of ectopic *dppZ* and also induced ectopic albeit low levels of *ptc*. When coexpressed with EphB2Z, both EB2-SMO^{WT} and EB2-SMO^{SD} ectopically activated high levels of *ptc* and low levels of *en*. In contrast, EB2-SMO^{SA} failed to activate any HH target genes.

- Ingham, P. W. & McMahon, A. P. Hedgehog signaling in animal development: paradigms and principles. *Genes Dev.* **15**, 3059–3087 (2001).
- Heemskerk, J. & DiNardo, S. *Drosophila* hedgehog acts as a morphogen in cellular patterning. *Cell* **76**, 449–460 (1994).
- Roelink, H. *et al.* Floor plate and motor neuron induction by different concentrations of the amino-terminal cleavage product of sonic hedgehog autoproteolysis. *Cell* **81**, 445–455 (1995).
- Riddle, R. D., Johnson, R. L., Laufer, E. & Tabin, C. *Sonic hedgehog* mediates the polarizing activity of the ZPA. *Cell* **75**, 1401–1416 (1993).
- Hooper, J. E. & Scott, M. P. Communicating with Hedgehogs. *Nature Rev. Mol. Cell Biol.* **6**, 306–317 (2005).
- Jia, J. & Jiang, J. Decoding the Hedgehog signal in animal development. *Cell. Mol. Life Sci.* **63**, 1249–1265 (2006).
- Basler, K. & Struhl, G. Compartment boundaries and the control of *Drosophila* limb pattern by *hedgehog* protein. *Nature* **368**, 208–214 (1994).
- Tabata, T. & Kornberg, T. B. Hedgehog is a signaling protein with a key role in patterning *Drosophila* imaginal discs. *Cell* **76**, 89–102 (1994).
- Strigini, M. & Cohen, S. M. A Hedgehog activity gradient contributes to AP axial patterning of the *Drosophila* wing. *Development* **124**, 4697–4705 (1997).
- van-den-Heuvel, M. & Ingham, P. W. *smoothed* encodes a receptor-like serpentine protein required for *hedgehog* signalling. *Nature* **382**, 547–551 (1996).
- Alcedo, J., Ayzenzon, M., Von Ohlen, T., Noll, M. & Hooper, J. E. The *Drosophila smoothed* gene encodes a seven-pass membrane protein, a putative receptor for the Hedgehog signal. *Cell* **86**, 221–232 (1996).
- Chen, Y. & Struhl, G. Dual roles for Patched in sequestering and transducing Hedgehog. *Cell* **87**, 553–563 (1996).
- Stone, D. M. *et al.* The tumour-suppressor gene *patched* encodes a candidate receptor for Sonic hedgehog. *Nature* **384**, 129–134 (1996).

14. Deneff, N., Neubuser, D., Perez, L. & Cohen, S. M. Hedgehog induces opposite changes in turnover and subcellular localization of patched and smoothened. *Cell* **102**, 521–531 (2000).
15. Jia, J., Tong, C., Wang, B., Luo, L. & Jiang, J. Hedgehog signalling activity of smoothened requires phosphorylation by protein kinase A and casein kinase I. *Nature* **432**, 1045–1050 (2004).
16. Zhang, C., Williams, E. H., Guo, Y., Lum, L. & Beachy, P. A. Extensive phosphorylation of Smoothened in Hedgehog pathway activation. *Proc. Natl Acad. Sci. USA* **101**, 17900–17907 (2004).
17. Apionishev, S., Katanayeva, N. M., Marks, S. A., Kalderon, D. & Tomlinson, A. *Drosophila* Smoothened phosphorylation sites essential for Hedgehog signal transduction. *Nature Cell Biol.* **7**, 86–92 (2005).
18. Schlessinger, J. Cell signaling by receptor tyrosine kinases. *Cell* **103**, 211–225 (2000).
19. Bourne, H. R. How receptors talk to trimeric G proteins. *Curr. Opin. Cell Biol.* **9**, 134–142 (1997).
20. Centonze, V. E., Sun, M., Masuda, A., Gerritsen, H. & Herman, B. Fluorescence resonance energy transfer imaging microscopy. *Methods Enzymol.* **360**, 542–560 (2003).
21. Kaykas, A. *et al.* Mutant Frizzled 4 associated with vitreoretinopathy traps wild-type Frizzled in the endoplasmic reticulum by oligomerization. *Nature Cell Biol.* **6**, 52–58 (2004).
22. Nakano, Y. *et al.* Functional domains and sub-cellular distribution of the Hedgehog transducing protein Smoothened in *Drosophila*. *Mech. Dev.* **121**, 507–518 (2004).
23. Himanen, J. P. & Nikolov, D. B. Eph signaling: a structural view. *Trends Neurosci.* **26**, 46–51 (2003).
24. Huangfu, D. & Anderson, K. V. Signaling from Smo to Ci/Gli: conservation and divergence of Hedgehog pathways from *Drosophila* to vertebrates. *Development* **133**, 3–14 (2006).
25. Corbit, K. C. *et al.* Vertebrate Smoothened functions at the primary cilium. *Nature* **437**, 1018–1021 (2005).
26. Rohatgi, R., Milenkovic, L. & Scott, M. P. Patched1 regulates hedgehog signaling at the primary cilium. *Science* **317**, 372–376 (2007).
27. Taipale, J. *et al.* Effects of oncogenic mutations in Smoothened and Patched can be reversed by cyclopamine. *Nature* **406**, 1005–1009 (2000).
28. Varjosalo, M., Li, S. P. & Taipale, J. Divergence of hedgehog signal transduction mechanism between *Drosophila* and mammals. *Dev. Cell* **10**, 177–186 (2006).
29. Zhu, A. J., Zheng, L., Suyama, K. & Scott, M. P. Altered localization of *Drosophila* Smoothened protein activates Hedgehog signal transduction. *Genes Dev.* **17**, 1240–1252 (2003).
30. Jia, J., Tong, C. & Jiang, J. Smoothened transduces Hedgehog signal by physically interacting with Costal2/Fused complex through its C-terminal tail. *Genes Dev.* **17**, 2709–2720 (2003).
31. Ruel, L., Rodriguez, R., Gallet, A., Lavenant-Staccini, L. & Therond, P. P. Stability and association of Smoothened, Costal2 and Fused with Cubitus interruptus are regulated by Hedgehog. *Nature Cell Biol.* **5**, 907–913 (2003).
32. Lum, L. *et al.* Hedgehog signal transduction via Smoothened association with a cytoplasmic complex scaffolded by the atypical kinesin, Costal-2. *Mol. Cell* **12**, 1261–1274 (2003).
33. Ogden, S. K. *et al.* Identification of a functional interaction between the transmembrane protein Smoothened and the kinesin-related protein Costal2. *Curr. Biol.* **13**, 1998–2003 (2003).
34. Jiang, J. & Struhl, G. Protein kinase A and Hedgehog signalling in *Drosophila* limb development. *Cell* **80**, 563–572 (1995).
35. Zhang, W. *et al.* Hedgehog-regulated costal2-kinase complexes control phosphorylation and proteolytic processing of cubitus interruptus. *Dev. Cell* **8**, 267–278 (2005).
36. van Leeuwen, F., Harryman Samos, C. & Nusse, R. Biological activity of soluble wingless protein in cultured *Drosophila* imaginal disc cells. *Nature* **368**, 342–344 (1994).
37. Dravis, C. *et al.* Bidirectional signaling mediated by ephrin-B2 and EphB2 controls urorectal development. *Dev. Biol.* **271**, 272–290 (2004).

Supplementary Information is linked to the online version of the paper at www.nature.com/nature.

Acknowledgements We thank B. Wang and S. Thet for technical assistance, L. Zhang for assistance with yeast two-hybrid experiments, Q. Shi for help with Smo constructs, M. Chumley, L. Lum, P. Beachy, I. Guerrero and DSHB for reagents, and K. Wharton and H. Kramer for comments. Y.Z. was supported by a National Scientist Development Grant from the American Heart Association. J.J. was supported by grants from the National Institutes of Health, the Leukemia & Lymphoma Society Scholar Program, and the Robert A. Welch Foundation. J.J. is a Eugene McDermott Endowed Scholar of Biomedical Science at UTSW.

Author Contributions Y.Z. and C.T. participated in the design, execution and analysis of experiments, and the preparation of the manuscript. Y.Z. conducted and analysed all the FRET experiments. C.T. identified the Arg clusters. J.J. participated in the design and analysis of experiments and writing the manuscript.

Author Information Reprints and permissions information is available at www.nature.com/reprints. Correspondence and requests for materials should be addressed to J.J. (jin.jiang@utsouthwestern.edu).

METHODS

Constructs and transgenes. SMO C-terminal deletion constructs were generated by PCR amplification of the corresponding coding sequences, followed by subcloning into a *pUAST* vector containing CFP coding sequence so that the CFP was fused to the C terminus of each SMO deletion mutant. For Ala-scan mutagenesis and F11, 1A3, RA, SA and SD mutations, substitutions were generated by PCR-based site-directed mutagenesis. For *UAS-Smo-CFP^{L3}YFP^C*, the CFP coding sequence was inserted between SMO amino acids 451–452, and YFP was fused to the C terminus. To construct mutant forms of SMO–CFP^C/YFP^C or SMO–CFP^{L3}YFP^C, the corresponding mutant sequences were swapped by using a unique *SpeI* site in the seventh transmembrane domain. To construct wild-type or mutant forms of SMO–CFP^N/YFP^N, CFP/YFP was inserted in frame into a unique *SfiI* site near the N-terminal region. To construct EB2–SMOC chimaeric proteins, the intracellular domain of EB2 was replaced by wild-type or mutant forms of the SMO cytoplasmic tail (amino acids 556–1035). To construct EB2–SMO^{WT}, EB2–SMO^{F11} and EB2–SMO^{A11}, the extracellular domain of EB2 was fused to SMO sequence encoding amino acids 33–1035. EphB2Z contains a full-length EphB2 fused to β -galactosidase to facilitate oligomerization³⁷. To generate GST–SMO fusion constructs, *smo* complementary DNA fragments encoding amino acids 656–755 with wild-type sequence or point mutations were amplified by PCR and inserted between *NotI* and *EcoRI* sites in the *pGEX4T-2* vector. To generate Flag-tagged SMO C-terminal fragments such as SMO–NT860, the corresponding cDNA fragments were amplified by PCR and subcloned to a *pUAST-Flag* vector. To construct Smo–CFP^C/YFP^C, CFP/YFP was fused in frame to the Smo C terminus. To construct Smo–CFP^N/YFP^N, CFP/YFP was inserted in frame after amino acid 31. To construct Smo–CFP^{L2}YFP^C, the CFP coding sequence was inserted between Smo residues 355 and 356, and YFP was fused in frame to the C terminus. For EB2–Smo, the extracellular domain of EB2 was fused N-terminally to the full-length Smo. For EB2–SmoC, the intracellular domain of EB2 was replaced by the Smo cytoplasmic tail (amino acids 544–793). Multiple independent transgenic lines were tested for each construct. *MS1096*, *ptc-gal4*, *dpp-lacZ*, *UAS-smo-CFP^C/YFP^C* and their mutant derivative have been described¹⁵.

Cell culture, immunoprecipitation, GST pull-down, western blot, immunostaining and luciferase reporter assay. S2 and cl-8 cells were cultured as described^{35,36}. Transfection was carried out using the Calcium Phosphate Transfection Kit (Specialty Media). HH-condition medium treatment was carried out as described³². Immunoprecipitation and western blot analysis were

carried out using standard protocols. For cell surface staining, transfected cells were fixed with 4% paraformaldehyde and incubated with primary antibody in PBS for 30 min at room temperature, followed by incubation with secondary antibody in PBT. For GST pull-down assays, GST fusion proteins absorbed on glutathione beads were washed three times with ice-cold PBS containing 1% NP40. Cell lysates from S2 cells expressing tagged SMO C-terminal fragments or reticulocytes with *in vitro* translated ³⁵S-labelled SMO C-terminal fragments were then added and the mixtures were incubated at 4 °C for 1 h with occasional mixing. Proteins bound to the beads were washed five times with PBS plus 1% NP40 before separation on SDS–PAGE, followed by western blot or autoradiography. For EphB2-Fc treatment, EphB2-Fc chimaera (R&D Systems) and goat anti-human IgG Fc (Jackson ImmunoResearch Labs) were mixed for 4 h at 4 °C before being added into cultured cells. NIH-3T3 cells were cultured in DMEM containing 10% bovine calf serum and antibiotics penicillin/streptomycin at 5% CO₂ in a humidified incubator. Transfection of NIH-3T3 cells was carried out using FuGENE6 (Roche). Briefly, after transfection for 2 days, cell culture medium was changed to DMEM with 0.5% bovine calf serum with or without recombinant mouse SHHN (R&D Systems). Mammalian reporter assays were performed essentially as described²⁷. Immunostaining of imaginal discs was carried out as described³⁴. Antibodies used in this study were: rabbit anti- β Gal (Cappel), mouse anti-PTC (from I. Guerrero), mouse anti-EN (DSHB), rabbit and mouse anti-Flag (Sigma), mouse anti-SMON (DSHB) and mouse anti-Myc (Santa Cruz).

FRET analysis using confocal microscopy. For FRET analysis of cultured cells, CFP- and YFP-tagged constructs were transfected into S2 cells together with an *ub-Gal4* expression vector¹⁵. Transfected cells were treated with or without HH-conditioned medium. For maximal HH signalling strength, a *UAS-HH* expression construct was also included in the transfection³². Cells were washed with PBS, fixed with 4% formaldehyde for 20 min, and mounted on slides in 80% glycerol. For FRET analysis of wing discs, *smo* transgenes were expressed with *MS1096* (for analysis of A- or P-compartment cells) or *ptc-Gal4* (for analysis of A-compartment cells near the A/P boundary). Late third instar wing discs were fixed with 4% formaldehyde and mounted on slides in 80% glycerol. Fluorescence signals were acquired with the $\times 100$ objective of a Zeiss LSM510 confocal microscope. Each data set was based on 10–15 individual cells. In each cell, four to five regions of interest in photobleached area were selected for analysis.

Yeast two-hybrid assay. The prey and bait plasmids were constructed using the C-terminal fragment of SMO (amino acids 641–1035).

High-resolution structure prediction and the crystallographic phase problem

Bin Qian^{1*}, Srivatsan Raman^{1*}, Rhiju Das^{1*}, Philip Bradley¹, Airlie J. McCoy², Randy J. Read² & David Baker¹

The energy-based refinement of low-resolution protein structure models to atomic-level accuracy is a major challenge for computational structural biology. Here we describe a new approach to refining protein structure models that focuses sampling in regions most likely to contain errors while allowing the whole structure to relax in a physically realistic all-atom force field. In applications to models produced using nuclear magnetic resonance data and to comparative models based on distant structural homologues, the method can significantly improve the accuracy of the structures in terms of both the backbone conformations and the placement of core side chains. Furthermore, the resulting models satisfy a particularly stringent test: they provide significantly better solutions to the X-ray crystallographic phase problem in molecular replacement trials. Finally, we show that all-atom refinement can produce *de novo* protein structure predictions that reach the high accuracy required for molecular replacement without any experimental phase information and in the absence of templates suitable for molecular replacement from the Protein Data Bank. These results suggest that the combination of high-resolution structure prediction with state-of-the-art phasing tools may be unexpectedly powerful in phasing crystallographic data for which molecular replacement is hindered by the absence of sufficiently accurate previous models.

High-resolution prediction of protein structures from their amino acid sequences and the refinement of low-resolution protein structure models to produce more accurate structures are long-standing challenges in computational structural biology¹. The refinement problem has become particularly important in recent years, as the continued increase in the number of experimentally determined protein structures, together with the explosion of genome sequence information, has made it possible to produce comparative models of a large number of protein structures with wide utility². Ideally, these models would consistently approach the resolution offered by X-ray crystallography, enabling precise drug design and a deeper understanding of catalysis and binding. Accurate high-resolution models can, in principle, be achieved by searching for the lowest energy structure given the sequence of the protein. However, despite progress³, the large number of degrees of freedom in a protein chain and the ruggedness of the energy landscape produced by strong atomic repulsion at short distances greatly complicate this search for sequences lacking close homologues of known structure.

An important application for predicted structures is to help solve the X-ray crystallographic phase problem^{4,5}. Converting X-ray diffraction data into electron density maps of proteins requires the inference of phases associated with each diffraction peak. Although phase estimates can be obtained through the preparation of heavy atom derivatives, the problem can be solved without additional experimental information by the technique of molecular replacement^{4,5} given a structure model that has high structural similarity (better than 1.5 Å root-mean-squared (r.m.s.) deviation) to the crystallized protein over a large fraction of the molecule. As an example of the stringency of this condition, models of protein structures derived from nuclear magnetic resonance (NMR) data typically do not give good molecular replacement models for crystallographic data on the same proteins⁶. Perhaps the most successful approach to molecular replacement is the use of previous crystal structures of highly

sequence-similar (>40%) templates as search models. In cases of lower sequence similarity, structure prediction tools can frequently help build comparative models that give better molecular replacement solutions; however, the success rate drops rapidly as the template sequence identity falls below 30%^{4,5}. In cases where structurally similar experimental models are not available, *ab initio* phasing techniques have had some success for targets with simple folds of high symmetry^{7,8} or with new structures that have been rationally designed from first principles⁹, but *ab initio* phasing of diffraction data for natural globular proteins remains an unsolved problem.

In this study, we present a new energy-based rebuilding-and-refinement method that consistently improves models derived from NMR, from sequence-distant templates, and from *de novo* folding methods. The final models include high-resolution features not present in the starting models, including the packing of core side chains. Bringing together these results from all-atom structure prediction with state-of-the-art algorithms for molecular replacement and automated rebuilding^{10–12}, we show that distant-template-based and *de novo* models can reach the accuracy required to solve the X-ray crystallographic phase problem.

Targeted rebuilding-and-refinement protocol

We have developed a new approach for refining protein models that combines the targeting of aggressive sampling to regions most likely to be in error with powerful global optimization techniques. The new protocol is outlined in Fig. 1a. The first step of this protocol is the energy-based optimization of an input ensemble of models using the previously described Rosetta all-atom refinement method. This method combines Monte Carlo minimization with side-chain remodelling to relieve inter-atomic clashes and to optimize side-chain packing and hydrogen bonding, as encoded by an all-atom force field^{13,14}. Briefly, in each Monte Carlo move, a random perturbation to the protein backbone torsion angles is followed by discrete

¹University of Washington, Department of Biochemistry and Howard Hughes Medical Institute, Box 357350, Seattle 98195, USA. ²Department of Haematology, University of Cambridge, Cambridge Institute for Medical Research, Wellcome Trust/MRC Building, Hills Road, Cambridge CB2 0XY, UK.

*These authors contributed equally to this work.

optimization of the side-chain conformations^{14,15}, which allows efficient crossing of side-chain torsional barriers. Then, quasi-Newton optimization of the side-chain and backbone torsion angles is carried out before the decision on whether to accept the move. Because of the final minimization, each point on the landscape is mapped to the closest local minimum, flattening energy barriers¹⁶. Although making it possible to recognize near-native predictions based on their low energies^{1,13}, this all-atom refinement alone does not consistently produce significant improvements in model quality (Supplementary Fig. 1).

The second step in the new protocol is the identification of regions of variation in the ensemble of refined models. We have found a marked correlation between the extent of variation in the coordinates of a residue in the refined structures and the deviation of the coordinates of the residue in the refined models from the native structure. An example is shown in Fig. 1b, c: positions exhibiting small variance across the models are usually quite close to the correct structure, whereas positions for which the variance is large often deviate considerably from the native structure. This correlation arises from the relatively short range of the force field and the energy gap between the native structure and the models: because the energy of the entire system is roughly equal to the sum of its parts, for most portions of the protein, the correct conformation will be lower in energy than non-native conformations. Regions of the protein that can access the native conformation are likely to converge on this conformation and thus exhibit less variation, whereas locally incorrect conformations are likely to be spread throughout the landscape and exhibit more variation. We observe this correlation for many different proteins in both the cartesian coordinates and the internal torsion angles; a related principle has recently been used in the Pcons method for assessing protein models¹⁷.

The third step in the new protocol targets aggressive sampling to the regions most likely to be in error. A fragment-based segment rebuilding method (see Supplementary Material) is used to rebuild completely regions of models with relatively high variation in the model population. Because the precise regions that are incorrect cannot be identified unambiguously, we carry out many independent

calculations in which different segments in the higher variation regions are randomly selected for complete rebuilding. The partially rebuilt models are then subjected to the Rosetta all-atom refinement protocol described above^{13,14}. In the segment rebuilding process, side chains are initially represented as soft interaction centres and the connectivity of the chain is temporarily broken, thus permitting the traversal of much larger barriers than those crossed by all-atom refinement alone.

As indicated in Fig. 1a, if the lowest energy refined structures have not converged, the rebuilding-and-refinement protocol is applied iteratively using a selection process inspired by natural evolution to guide convergence on the global minimum. At each iteration, a subset of models that are low in energy yet structurally diverse is chosen to seed the next round; the regions to be rebuilt are determined on the basis of the backbone variation in the selected population. Bringing together ideas from tabu search¹⁸ and conformational space annealing¹⁹, the selection process alternates between the propagation of a structurally diverse population into the next round (diversification) and focusing in on the lowest energy regions of the energy landscape explored thus far (intensification). The lowest energy models after ten iterations are selected as the final predictions. As illustrated in Fig. 1d, models with progressively lower energies and more native-like structures can be obtained with increasing number of iterations; results on a number of refinement problems are summarized in Supplementary Fig. 2.

Improving NMR models

As a first test of the new rebuilding-and-refinement method, we sought to improve the accuracy of protein structure models derived from moderate-resolution NMR experiments. NMR is an important method for determining structures of proteins at atomic resolution that has the advantage of not requiring crystals. In some cases, however, NMR models can contain errors due to either insufficient data or ambiguities in interpretation of the input NMR spectra²⁰. We applied the method outlined in Fig. 1a to ten ensembles of NMR models deposited in the Protein Data Bank (PDB) for which independently determined high-resolution X-ray crystal structures

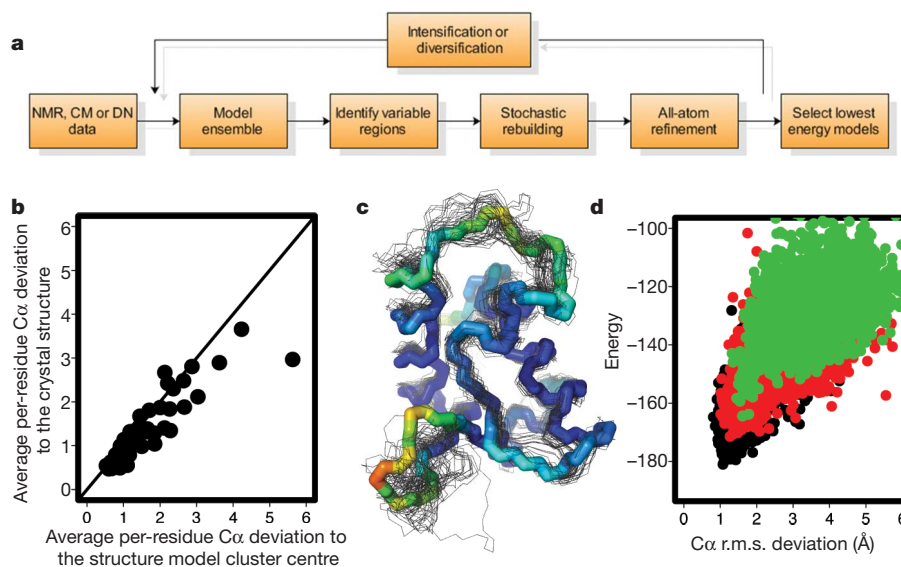


Figure 1 | Overview of the rebuilding-and-refinement method. **a**, Schematic diagram of the rebuilding-and-refinement method applied to structures from NMR, from comparative modelling (CM) and from *de novo* (DN) modelling approaches. **b**, Strong correlation between the per-residue backbone conformation variation in the model ensemble and the deviation from the native structure for target T0199 from the sixth critical assessment of structure prediction (CASP6). **c**, Superposition of the native structure of CASP6 target T0199 with 50 low-energy all-atom refined models. The native structure backbone is shown as a thick line, and the models are shown as

thinner lines. Residues in the native structure are coloured by the average per-residue C α r.m.s. deviation to the native from 4.5 Å (red) to 0.5 Å (blue). **d**, Iterative rebuilding and refinement yields low-energy native-like models. The energy and the C α r.m.s. deviation of models generated during three iterations of the loop-relax protocol are displayed for iteration 1 (green), iteration 4 (red) and iteration 7 (black). The Rosetta all-atom energy includes the enthalpy plus the solvation contribution to the entropy but not the configurational entropy.

provide tests of model accuracy^{21,22}. Regions with high variation in initial all-atom refined ensembles were stochastically rebuilt as well as regions assessed as poorly packed (see Methods) to allow for possible over-convergence of the initial NMR ensemble in regions with incorrect constraints.

In eight of the ten cases, the lowest energy refined model was closer to the crystal structure than any member of the starting NMR ensemble (typically 20 members) in terms of backbone agreement, as assessed by GDT-HA (geometric distance test (high accuracy))²³. Comparison of the best of five lowest energy refined models to the NMR ensemble indicates improvement in backbone accuracy and core packing in all cases (see Table 1 and Supplementary Figs 3 and 4). In addition, the quality of the lowest energy models was consistently better than the starting NMR models in terms of clash score, number of rotamer outliers and number of backbone (Ramachandran) outliers, as assessed by the MolProbity server (Supplementary Table 2)²⁴. Four examples of this energy-based structural improvement are shown in Fig. 2a–d. It should be noted that no NMR data were included in these rebuilding-and-refinement tests; judicious use of experimental NMR information to focus all-atom refinement (for example, using inferential structure determination²²) could yield still better results.

As noted above, NMR structures often do not give good molecular replacement models for crystallographic data⁶, and we hypothesized that the all-atom refined models would yield better solutions. Indeed, we found such improvement in molecular replacement scores for all eight cases in which diffraction data were publicly available (Table 1), using the sensitive and widely used Phaser software¹⁰. Furthermore,

using phases from the molecular replacement trial with the highest translation function Z-score, electron density maps were generated and in seven of the eight cases the widely used ARP/wARP¹¹ or RESOLVE¹² automatic map tracing programs could build the majority of the residues with no human intervention (Table 1). An example of the improvement in density is shown in Fig. 3a, b. These results suggest that all-atom rebuilding and refinement may be a powerful supplement to existing strategies of trial-and-error trimming of NMR ensembles to improve molecular replacement solutions for crystallographic data⁶.

Improved blind predictions based on templates

As a further challenging test, we used the new energy-based rebuilding-and-refinement method to make blind structure predictions for 26 proteins with lengths less than 200 residues that had distant homologues (sequence identity lower than 30%) with known structure during the seventh Critical Assessment of Techniques for Protein Structure Prediction (CASP7). Ensembles of starting models based on different alignments to one or more of these distant homologues were generated as described in the Supplementary Information, and the rebuilding-and-refinement protocol was carried out with several rounds of iteration to explore more broadly conformational space (Fig. 1a). Five representative low-energy structures from the final population were submitted to the CASP organizers. For 18 of the 26 cases, at least one of these 5 models was closer to the correct structure than the closest homologous structure in the PDB, as assessed by the GDT-HA score²⁵. Marked improvement was observed in seven cases, with a 10–30% increase in this measure of model quality (see Table 1).

Table 1 | Improvement of model accuracy and molecular replacement by a rebuilding and refinement protocol

	X-ray structure	Starting model*	Length (n)†	Sequence identity to best template (%)‡	GDT-HA§		TFZ in molecular replacement		Auto-traced residues (backbone, side chain)¶	
					Best template	Refined model	Best template	Refined model	Best template	Refined model
NMR	1hb6	2abd	86	N/A	0.58	0.79	4.1	11.3	12, 0	80, 80
	1who	1bmw	94	N/A	0.59	0.68	5.7	8.3	25, 12	47, 44
	1gnu	1kot	119	N/A	0.64	0.73	6.6	10.6	62, 53	82, 78
	1a19	1ab7	89 (2)	N/A	0.63	0.78	3.7	8.8	31, 20	48, 37
							4.5	12.5	14, 0	44, 35
	1fvk	1a24	189 (2)	N/A	0.49	0.69	3.4	6.9	66, 50	97, 91
							4.3	12.4	55, 43	85, 68
	1mzl	1afh	93	N/A	0.60	0.66	4.6	5.1	36, 29	58, 44
	1tvq	1xpw	143	N/A	0.63	0.74	4.3	6.7	15, 6	103, 86
	2snm	2sob	97	N/A	0.45	0.48	3.8	4.8	17, 16	43, 37
CM										
	2hhz (T0331)	1ty9A	149	14.5	0.49	0.58	5.4	8.8	28, 24	68, 63
	2hr2 (T0368)	2c21C	158 (6)	14.8	0.57	0.67	6.0	5.4	37, 37	20, 14
	2hq7 (T0380)	2fhqA	145 (2)	25.4	0.58	0.69	4.4	6.6	47, 23	92, 83
							4.6	14.2	30, 17	60, 59
	2ib0 (T0385)	1jgcB	170 (2)	7.8	0.62	0.69	5.1	7.9	63, 37	56, 56
							5.8	15.5	50, 2	52, 52
	2hi0 (T0329_D2)	1rqIA	92 (2)	8.8	0.52	0.67		N/A#		N/A#
	2hcf (T0330_D2)	1lvhB	75	14.1	0.51	0.65		N/A#		N/A#
	2hi6 (T0357)**	1aco	132	8.4	0.45	0.52		N/A**		N/A**
DN	2hh6 (T0283)	2b2j	112	3.6	0.22	0.64	5.4	9.0	26, 12	112, 112

* PDB accession numbers for the closest previously known template (comparative modelling (CM) and *de novo* modelling (DN)) or for the NMR structure.

† Length of sequence in crystal structure (number of monomers in asymmetric unit, n).

‡ Number of sequence-identical residues across regions structurally aligned within 4 Å³⁴ divided by the length of the shorter sequence.

§ Fraction of residues in model superimposable on crystal structure with high accuracy (see Supplementary Information and ref. 23). This value is the average of four numbers: the numbers of residues aligned between model and experimental structure within 0.5 Å, within 1 Å, within 2 Å and within 4 Å. For the CM cases, GDT-HA was determined for the residues structurally aligned between the native structure and the closest template. For the NMR cases, the GDT-HA comparison presented for the best template is between the first member of the deposited NMR structural ensemble and the crystal structure.

|| Z-score of Phaser log-likelihood translation function for molecular replacement solution. For CM and DN cases, molecular replacement for the best template was carried out using a mixed-model based on the best possible structural alignment between the native structure and template structure⁴; no such alignment was carried out for the refined model, however. The TFZ scores for the next best model submitted by all other CASP7 predictors were 5.4 (T0331), 6.0 (T0368), 4.4 (T0380), 5.1 (T0385) and 6.9 (T0283). For NMR cases, the presented results are from molecular replacement with the full deposited NMR ensemble and from each of the lowest energy 25 refined models (see also Supplementary Table 1). In the NMR cases, the best-TFZ structure from the deposited ensemble (see Supplementary Table 1) typically gave slightly worse results in subsequent automatic tracing than using the full ensemble, as expected⁶. In cases with multiple monomers present in the asymmetric unit, Z-scores for each monomer are presented, except for T0368, for which decreasing TFZ scores for molecular replacement of additional monomers after the first one indicated the solutions to be ambiguous.

¶ Number of automatically traced residues starting with molecular replacement phases given by Phaser that match the deposited crystal structure within 2 Å. In all cases, tracing and refinement was carried out with the ARP/wARP¹¹ and RESOLVE¹² programs, with the better results from the two programs presented.

Predicted model is for the smaller of two domains present in the crystal structure and is thus not sufficient for molecular replacement.

☆ Structure factors not deposited in the PDB.

** Solved by NMR spectroscopy.

This is a particularly notable result because improving on the best template structure has been a long standing challenge for comparative modelling—owing to the high dimensionality of conformational space, there are many more ways to degrade a reasonably accurate model than to improve it. Superpositions of the closest homologous structure, the submitted refined models and the native structure for cases with the greatest improvement are shown in Fig. 2e–h. The improvement in the refined structures is evident even in core secondary structural elements.

Out of the seven high-resolution predictions, there were four targets for which diffraction data were available and the modelled sequence constituted the entire crystallized construct, enabling tests of molecular replacement. In each of these cases, we found that the best previous templates in the PDB failed to produce clear-cut molecular replacement solutions (Phaser Z-scores greater than 7), even after using knowledge of structurally alignable regions and a side-chain truncation approach to trim back the search models to their most accurate atoms⁴. Other template-based models submitted to CASP7, based on methods that typically did not use aggressive all-atom refinement, gave similarly low molecular replacement scores (Table 1). For three of the four cases, however, the refined models that we submitted for CASP7 gave significantly better molecular replacement solutions than the best template (Table 1). For these targets, the maps produced by combining phases from the blindly predicted model with the experimental diffraction amplitudes were of sufficient quality to permit the automatic chain-tracing program RESOLVE¹² to build a large fraction of each structure with high accuracy (Table 1). An example of the marked improvement in electron density on using the refined models is shown in Fig. 3c, d.

Ab initio phasing by ab initio modelling

To the best of our knowledge, a *de novo* structure prediction for a natural protein with an asymmetric, globular fold has never been used successfully for molecular replacement. However, the accuracy

of *de novo* prediction methods has been improving rapidly. In particular, the use of all-atom refinement to follow low-resolution modelling by the Rosetta *de novo* modelling method¹³ led to several blind predictions in CASP7 for proteins of all- α , all- β and $\alpha+\beta$ secondary structure classes that placed most of the backbone elements and core side chains with high accuracy (see Fig. 4a–c)²⁵. This progress in *de novo* modelling, along with the successes above with refined NMR and template-based models, encouraged us to attempt molecular replacement with an exceptional prediction for the 112-residue α -helical CASP7 target T0283.

The best of five models for T0283 blindly predicted without the use of templates matched the subsequently released crystal structure (2hh6²⁶) with a C α r.m.s. deviation of 1.4 Å over 90 residues (Fig. 4c). The closest previously known fold in the PDB, identified from structure superpositions by CASP7 assessors (2b2j²⁷), was significantly different from the T0283 crystal structure, aligning 70 residues with a C α r.m.s. deviation of 3.1 Å (note also the poor GDT-HA score in Table 1).

After truncating the Rosetta prediction to a consensus core (residues 10 to 88, for which four of the five submitted models coincided to within 2.5 Å C α r.m.s. deviation), molecular replacement by Phaser showed clear features for the omitted amino- and carboxy-terminal helices (see Supplementary Fig. 5 and caption). Starting from this molecular replacement solution, the ARP/wARP software was able to complete the structure automatically, tracing all 112 residues correctly. The final result (Fig. 4d) is in excellent agreement with the structure deposited in the PDB, which used phases experimentally derived by selenium single-wavelength anomalous dispersion, with an r.m.s. deviation of 0.13 Å for all 112 C α atoms. In contrast, attempts to solve the structure by molecular replacement with the closest existing ‘template’ 2b2j failed to produce a clear-cut phasing solution (Table 1), even when knowledge of the optimal superposition was used to trim this search model back to the 70 residues that aligned best to the actual structure. It will be of great interest to investigate whether this result can be generalized to rapidly phase diffraction data for proteins of new folds.

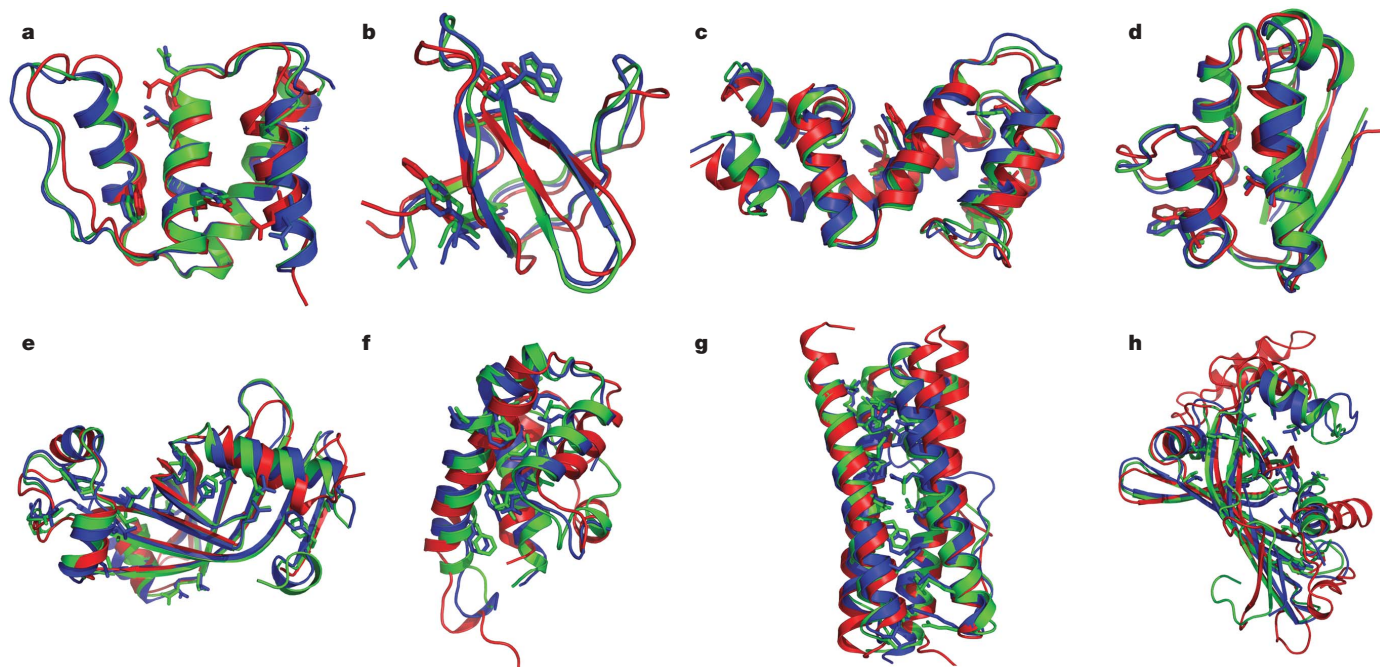


Figure 2 | Improvement in model accuracy produced by rebuilding and refinement. a–d, NMR refinement tests displaying superpositions of the crystal structure (blue), model 1 of the NMR ensemble (red) and the lowest energy all-atom refined model (green) for four NMR refinement test cases (a, acyl CoA binding protein, 2abd; b, SH3 domain of ABL tyrosine kinase, 1awo; c, guanine nucleotide binding protein, 1ezy; d, barstar, 1ab7). e–h, Blind

predictions produced by comparative modelling, displaying superpositions of the native structure (blue), the best template in the PDB (red) and the best of our five submitted models (green) for four CASP7 targets (e, T0380; f, T0385; g, T0330 domain 2; h, T0331). A subset of the core side chains is shown in stick representation to illustrate the accuracy of core packing. Figures were prepared in PyMOL (Delano Scientific, Palo Alto, California).

Improving model accuracy and molecular replacement

The results described here show that an all-atom rebuilding-and-refinement protocol can produce protein structure models of high accuracy. The iterative protocol outlined in Fig. 1a brings together the individually quite powerful global optimization ideas underlying Monte Carlo minimization¹⁶, tabu search¹⁸ and conformational space annealing¹⁹ while targeting aggressive sampling to regions most likely to be incorrect. The substantial improvements achieved in prediction quality—in several cases enabling molecular replacement phasing of X-ray diffraction data—suggest that structure prediction has matured considerably. Nevertheless, we emphasize that there is still considerable room for improvement: our high-resolution rebuilding-and-refinement protocol does not always improve starting models, and T0283 is the only CASP7 target predicted *de novo* for which the models were accurate enough for molecular replacement. We look forward to advances in both the energy function, notably the addition of configurational entropy, and in conformational sampling. The significant energy gap between the refined models and the refined crystal structure¹³ for most of the cases studied here suggests that sampling is still the primary bottleneck for high-accuracy all-atom structure prediction.

At present, the Protein Structure Initiative lists hundreds of proteins with lengths less than 200 residues that have been crystallized but not yet solved. Publication of diffraction data sets that have not yielded to experimental phasing could catalyse the development of new hybrid prediction/phasing algorithms, much like the blind CASP trials have accelerated progress in the field of structure

prediction. With continuing advances in high-resolution structure prediction, in molecular replacement tools, and in the interface between these two fields, we expect that *in silico* phasing will become an increasingly important component of the crystallographer's toolkit.

In the present study, aggressive all-atom refinement was carried out in the absence of any experimental information. The incorporation of experimental data into the rebuilding-and-refinement protocol could help overcome the current shortcomings in both the energy function and conformational sampling and allow more consistent high-resolution structural inference. In practical applications to molecular replacement trials, the diffraction data do not need to be set aside as a stringent *post facto* test of model accuracy, as was carried out in this study. Diffraction data without phases would be useful in screening larger numbers of trial structures for molecular replacement or in complementing the physical energy terms with diffraction-data-derived likelihood scores²⁸ during rebuilding and refinement. Weak phase information, for example based on anomalous scattering from intrinsic sulphur atoms²⁹, could also be exploited, for instance by using an initial molecular replacement model to locate the anomalous scatterer sites¹⁰. Although not used in the present study, NMR chemical shift, nuclear Overhauser effect, and residual dipolar coupling data can help to pinpoint regions of the models to rebuild and regions to constrain during all-atom refinement. On a larger scale, mass spectrometry techniques coupled with hydrogen/deuterium exchange³⁰, chemical cross-linking³¹ and radical footprinting³² show great promise for providing high-throughput, residue-level information that may rapidly constrain structure prediction and, in the absence of crystallographic data, help validate models. We anticipate that the combination of high-resolution modelling with limited experimental structural data will

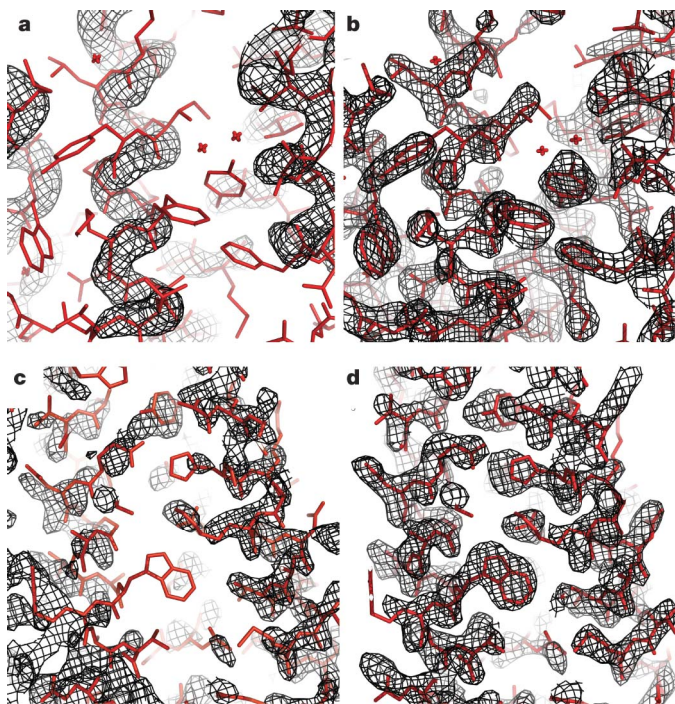


Figure 3 | Improvement in electron density using models from rebuilding and refinement in molecular replacement searches. Examples are presented for the NMR structure of acyl CoA binding protein 2abd (a, b) and CASP7 comparative modelling target T0385 (c and d). Black mesh represents electron density ($2mF_o - DF$; 1.5σ contour) using experimental structure factors and phases from molecular replacement with the starting model (a and c) or the refined model (b and d). The coordinates deposited in the PDB, determined using experimental phase information, are shown in stick representation. Note that the 'refinement' applied to the models refers to the all-atom energy-based protocol (see Fig. 2 and text) and not to refinement against the diffraction data. The accurate modelling of side chains by Rosetta was critical for the illustrated map improvement; molecular replacement trials gave significantly better solutions if the Rosetta-predicted side chains were retained rather than truncated.

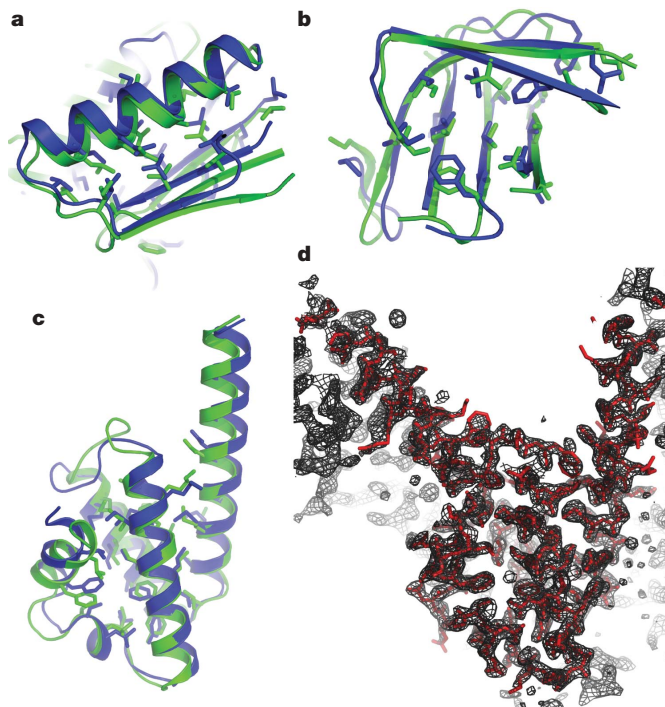


Figure 4 | Ab initio phasing by ab initio modelling. a–c, Superpositions of blind Rosetta *de novo* structure predictions (green) and the subsequently released crystal structures (blue) for CASP7 targets T0354 (a), domain 3 of T0316 (b) and T0283 (c). Buried side chains and backbone-aligned residues are displayed. d, Electron density map ($2mF_o - DF$; 2σ contour) produced by automatic refinement of the molecular replacement solution obtained from the T0283 structure prediction (black mesh; 1σ contour) agrees with the coordinates deposited in the PDB (red), solved with experimental phase information. The electron density map immediately after molecular replacement is shown in Supplementary Fig. 5.

become an increasingly powerful approach for characterizing the structures of biological macromolecules and complexes in the years to come.

METHODS SUMMARY

Models produced using NMR data, comparative modelling and *de novo* structure prediction were refined using the targeted rebuilding-and-refinement protocol introduced in this paper. To assess accuracy, the resulting models were compared to high-resolution crystal structures by the GDT-HA (geometric distance test (high accuracy)) score^{24,33}, the average percentage of C α atoms agreeing within 0.5, 1.0, 2.0 and 4.0 Å. As a final test of accuracy and of practical utility, models were screened for suitability in phase estimation for crystallographic diffraction data using the Phaser molecular replacement software¹⁰. The widely used ARP/wARP¹¹ and RESOLVE¹² programs were then used to refine automatically the electron density maps and build density-constrained protein coordinates.

Full Methods and any associated references are available in the online version of the paper at www.nature.com/nature.

Received 8 May; accepted 13 September 2007.

Published online 14 October 2007.

- Misura, K. M. & Baker, D. Progress and challenges in high-resolution refinement of protein structure models. *Proteins* **59**, 15–29 (2005).
- Pieper, U. *et al.* MODBASE: a database of annotated comparative protein structure models and associated resources. *Nucleic Acids Res.* **34**, D291–D295 (2006).
- Moult, J. A decade of CASP: progress, bottlenecks and prognosis in protein structure prediction. *Curr. Opin. Struct. Biol.* **15**, 285–289 (2005).
- Schwarzenbacher, R., Godzik, A., Grzechnik, S. K. & Jaroszewski, L. The importance of alignment accuracy for molecular replacement. *Acta Crystallogr. D* **60**, 1229–1236 (2004).
- Giorgetti, A., Raimondo, D., Miele, A. E. & Tramontano, A. Evaluating the usefulness of protein structure models for molecular replacement. *Bioinformatics* **21** (suppl. 2), ii72–ii76 (2005).
- Chen, Y. W., Dodson, E. J. & Kleywegt, G. J. Does NMR mean “not for molecular replacement”? Using NMR-based search models to solve protein crystal structures. *Structure* **8**, R213–R220 (2000).
- Strop, P., Brzustowicz, M. R. & Brunger, A. T. *Ab initio* molecular-replacement phasing for symmetric helical membrane proteins. *Acta Crystallogr. D* **63**, 188–196 (2007).
- Rossmann, M. G. *Ab initio* phase determination and phase extension using non-crystallographic symmetry. *Curr. Opin. Struct. Biol.* **5**, 650–655 (1995).
- Kuhlman, B. *et al.* Design of a novel globular protein fold with atomic-level accuracy. *Science* **302**, 1364–1368 (2003).
- McCoy, A. J. *et al.* Phaser crystallographic software. *J. Appl. Crystallogr.* **40**, 658–674 (2007).
- Perrakis, A., Morris, R. & Lamzin, V. S. Automated protein model building combined with iterative structure refinement. *Nature Struct. Biol.* **6**, 458–463 (1999).
- Terwilliger, T. C. Automated main-chain model building by template matching and iterative fragment extension. *Acta Crystallogr. D* **59**, 38–44 (2003).
- Bradley, P., Misura, K. M. & Baker, D. Toward high-resolution *de novo* structure prediction for small proteins. *Science* **309**, 1868–1871 (2005).
- Rohl, C. A., Strauss, C. E., Misura, K. M. & Baker, D. Protein structure prediction using Rosetta. *Methods Enzymol.* **383**, 66–93 (2004).
- Leaver-Fay, A., Kuhlman, B. & Snoeyink, J. Rotamer-pair energy calculations using a Trie data structure. In *Algorithms in Bioinformatics* (eds Casadio, R. & Myers, G.) 389 (Springer, Berlin, 2005).
- Wales, D. J. & Scheraga, H. A. Global optimization of clusters, crystals, and biomolecules. *Science* **285**, 1368–1372 (1999).
- Wallner, B. & Elofsson, A. Identification of correct regions in protein models using structural, alignment, and consensus information. *Protein Sci.* **15**, 900–913 (2006).
- Glover, F. & Laguna, M. *Tabu Search* (Kluwer, Norwell, Massachusetts, 1997).
- Lee, J., Liwo, A. & Scheraga, H. A. Energy-based *de novo* protein folding by conformational space annealing and an off-lattice united-residue force field: application to the 10–55 fragment of staphylococcal protein A and to apo calbindin D9K. *Proc. Natl Acad. Sci. USA* **96**, 2025–2030 (1999).
- Doreleijers, J. F., Rullmann, J. A. & Kaptein, R. Quality assessment of NMR structures: a statistical survey. *J. Mol. Biol.* **281**, 149–164 (1998).
- Grishaev, A. & Bax, A. An empirical backbone-backbone hydrogen-bonding potential in proteins and its applications to NMR structure refinement and validation. *J. Am. Chem. Soc.* **126**, 7281–7292 (2004).
- Rieping, W., Habeck, M. & Nilges, M. Inferential structure determination. *Science* **309**, 303–306 (2005).
- Zemla, A. LGA: A method for finding 3D similarities in protein structures. *Nucleic Acids Res.* **31**, 3370–3374 (2003).
- Lovell, S. C. *et al.* Structure validation by C α geometry: ϕ , ψ and C β deviation. *Proteins* **50**, 437–450 (2003).
- Das, R. *et al.* Structure prediction for CASP7 targets using extensive all-atom refinement with Rosetta@home. *Proteins* doi:10.1002/prot.21636 (25 September 2007).
- Berman, H., Henrick, K., Nakamura, H. & Markley, J. L. The worldwide Protein Data Bank (wwPDB): ensuring a single, uniform archive of PDB data. *Nucleic Acids Res.* **35**, D301–D303 (2007).
- Andrade, S. L., Dickmanns, A., Ficner, R. & Einsle, O. Crystal structure of the archaeal ammonium transporter Amt-1 from *Archaeoglobus fulgidus*. *Proc. Natl Acad. Sci. USA* **102**, 14994–14999 (2005).
- Pannu, N. S. & Read, R. J. Improved structure refinement through maximum likelihood. *Acta Crystallogr. A* **52**, 659–668 (1996).
- Dauter, Z. New approaches to high-throughput phasing. *Curr. Opin. Struct. Biol.* **12**, 674–678 (2002).
- Englander, J. J. *et al.* Protein structure change studied by hydrogen-deuterium exchange, functional labeling, and mass spectrometry. *Proc. Natl Acad. Sci. USA* **100**, 7057–7062 (2003).
- Young, M. M. *et al.* High throughput protein fold identification by using experimental constraints derived from intramolecular cross-links and mass spectrometry. *Proc. Natl Acad. Sci. USA* **97**, 5802–5806 (2000).
- Takamoto, K. & Chance, M. R. Radiolytic protein footprinting with mass spectrometry to probe the structure of macromolecular complexes. *Annu. Rev. Biophys. Biomol. Struct.* **35**, 251–276 (2006).
- Zhang, Y. & Skolnick, J. TM-align: a protein structure alignment algorithm based on the TM-score. *Nucleic Acids Res.* **33**, 2302–2309 (2005).
- Ortiz, A. R., Strauss, C. E. & Olmea, O. MAMMOTH (matching molecular models obtained from theory): an automated method for model comparison. *Protein Sci.* **11**, 2606–2621 (2002).

Supplementary Information is linked to the online version of the paper at www.nature.com/nature.

Acknowledgements We thank Rosetta@home participants for contributing computing power that made testing of many new ideas possible; the DOE INCITE program for access to Blue Gene/L at Argonne National Laboratory and the IBM Blue Gene Watson supercomputers; and the NCSA, SDSC and Argonne National Laboratory supercomputer centres for computer time and help with porting Rosetta to Blue Gene. We thank D. Kim and K. Laidig for developing the computational infrastructure underlying Rosetta@home; J. Abendroth for help with RESOLVE and ARP/wARP software; M. Kennedy of NESG for the NMR structure coordinates of protein 1xpw and for help with the molecular replacement calculations; and J. Abendroth, J. Bosch, J. Havranek and C. Wang for comments on the manuscript. We also thank the CASP organizers and contributing structural biologists for providing an invaluable test set for new structure refinement methods. This work was funded by the National Institute of General Medical Sciences, National Institutes of Health (to D.B.), the Wellcome Trust, UK (to R.J.R.), the Howard Hughes Medical Institute (D.B.), a Leukemia and Lymphoma Society Career Development fellowship (to B.Q.), and a Jane Coffin Childs fellowship (to R.D.).

Author Contributions B.Q., S.R. and R.D. contributed equally to this work. Structure predictions for NMR-based, comparative-model-based and *de novo* predictions were carried out by S.R., B.Q. and R.D. respectively, with advice and software from D.B. and P.B. Phasing trials were performed by R.J.R., B.Q., S.R. and R.D., with advice from R.J.R. and A.J.M. All authors discussed results and commented on the manuscript.

Author Information Rosetta software and source code are available to academic users free of charge at <http://www.rosettacommons.org/software/>. Reprints and permissions information is available at www.nature.com/reprints. Correspondence and requests for materials should be addressed to D.B. (dabaker@u.washington.edu).

METHODS

We present detailed descriptions of six methods discussed in the main text: (1) rebuilding-and-refinement protocol; (2) identification of regions to rebuild from the NMR structure ensemble; (3) preparation of blind predictions; (4) metrics for comparing models with crystal structures; (5) screening of models for suitability for molecular replacement; (6) assessing model quality with MolProbity.

Rebuilding-and-refinement protocol. We describe below the three key steps of the rebuilding-and-refinement protocol: segment rebuilding, all-atom refinement and iterative evolution.

For the first of these three steps, we used a new segment rebuilding protocol to rebuild regions with high structural variation in the model population, as these regions are often incorrect (see, for example, Fig. 1b). Because of uncertainties in the precise locations of incorrect regions, the portions of the model to be rebuilt were chosen stochastically from the regions with high variance at the beginning of each simulation. Up to 90% of all the separate regions were rebuilt in a given run—this allows for compensatory changes in interacting segments to occur.

The coordinates in the region to be rebuilt were generated using the Rosetta fragment-insertion-based *de novo* folding protocol³⁶. After each fragment insertion, the decision to accept or reject was made according to the standard Metropolis criterion based on the total energy of the system. To maintain the connectivity of the protein chain, cyclic coordinate descent (CCD)³⁷ was used to close the chain break at a stochastically selected position of the region rebuilt. The rebuilding process was divided into ten stages. At each successive stage, an increasing chain-break score (a penalty to the deviation of the peptide bond length at the chain break from the ideal peptide bond length) was applied. In each of the first five stages, the number of fragment insertion trials was ten times the number of residues in the region being rebuilt. In a fragment insertion trial, randomly chosen nine-residue, three-residue, or one-residue fragments were inserted into randomly chosen positions in the region being rebuilt, and the Metropolis Monte Carlo criterion was used to accept or reject the newly inserted fragment based on the Rosetta low-resolution energy function¹⁴. In each of the five last stages, in addition to the fragment insertion trials, we also performed cyclic-coordinate-descent-based backbone torsion angle moves (CCD moves) in which the cyclic coordinate descent solution was calculated and the backbone torsion angles for five randomly picked positions in the region being rebuilt were modified according to the CCD solution.

If after the ten rebuilding stages described above any chain break remained larger than 0.2 Å, the region to be rebuilt was expanded by one residue on both sides. The above fragment insertion and chain-break closing process was repeated using a harmonic tether to the starting values of the torsion angles in the newly included regions (which may fall into regions with low variance in the starting population) and another stochastically selected chain-break position. The regions to be rebuilt were allowed to expand by up to five residues upstream and downstream of the original starting and ending positions, until chain closure was achieved. This procedure was usually sufficient to ensure the recovery of a continuous peptide chain. In very rare cases where the chain could not be closed in a rebuilt region, it was merged with an adjacent region to be rebuilt along with the fixed portion of the model between these two regions and the rebuilding process was repeated. With the added flexibility of a larger region being rebuilt, the peptide chain could essentially always be closed. Variable regions at the chain termini were rebuilt using the fragment insertion-based *de novo* protocol without steps for chain-break closure.

The segment rebuilding protocol is implemented in the 'loop_relax' subroutine in the freely available Rosetta source code.

The segment rebuilding protocol described above aggressively employs fragment insertion moves to sample a broad range of conformations. The all-atom refinement protocol—the second key step of the rebuilding-and-refinement protocol—then searches for local minima in the vicinity of the structures produced by segment rebuilding using a detailed all-atom force-field.

The Rosetta all-atom energy function is largely dominated by short-range interactions⁹, primarily Lennard–Jones interactions, orientation-dependent hydrogen bonding, and the Lazaridis–Karplus implicit solvation model³⁸. The torsional states of backbone and side chains are evaluated using knowledge-based potentials derived from amino-acid-specific Ramachandran maps and the rotamer probabilities and χ angle standard deviations in the backbone-dependent rotamer library developed by ref. 39.

During all-atom refinement, all the backbone and side-chain atoms in the protein are explicitly represented. The bond lengths and angles are kept fixed at ideal values⁴⁰, and the polypeptide chain is described in internal coordinates (the backbone and side-chain torsion angles). A single move in the all-atom refinement protocol consists of the following steps: (1) one of the several types of perturbations to the backbone torsion angles described below; (2) greedy

optimization of the side-chain rotamer conformations ('rotamer trials'⁴¹) for the new backbone conformation; (3) minimization of the energy with respect to either the backbone degrees of freedom only (first half of refinement procedure) or backbone and side-chain degrees of freedom (second half of refinement procedure) using the Davidson–Fletcher–Powell (DFP) algorithm. The convergence criterion for exiting this quasi-Newton minimization was decreased from 10^{-3} to 10^{-5} during the course of refinement to enable more complete minimization in the final stages of refinement. (4) The compound move (steps 1–3) is accepted or rejected according to the Metropolis Monte Carlo criterion. These compound moves extend the Monte Carlo minimization procedure found to be quite powerful in previous studies⁴² by incorporating discrete optimization of side-chain conformations; this allows energy-directed barrier hopping at the level of the side chains.

The following backbone perturbations are used at step (1) in the Monte Carlo minimization move described above and in a previous reference¹⁴. The 'small' and 'shear' moves are small perturbations of the backbone at five to ten randomly chosen positions. In small moves, ϕ and ψ are perturbed randomly by up to 1° in helix or strand regions or 1.5° in loop regions. In shear moves, ϕ is perturbed randomly by up to 2° in helix or strand regions or 3° in loop regions and the preceding ψ is perturbed by the same amount of degrees in the opposite direction to produce a compensatory shear motion in the peptide plane. The 'wobble' and 'crank' moves involve insertion of fragments and are more aggressively perturbing than the small and shear moves¹⁴. For both of these move types, the fragment set³⁶ is filtered to exclude those which cause a mean square deviation in the coordinates of the downstream atoms of more than 60 Å and one of the remaining fragments is chosen randomly for insertion. In wobble moves, the torsion angles belonging to the three residues immediately following the site of the one- or three-residue fragment insertion are varied to minimize the downstream perturbation still further. In crank moves, one residue is varied immediately after the insertion site, and three more residues at a site spaced by 6–20 residues from the fragment insertion site; this produces a 'crankshaft'-like movement of the intervening portion of the chain. 'Small-wobble' moves involve an initial 10–20° random change in the torsion angles of a single residue, followed by minimization of the perturbation over the three adjacent residues. The minimization of the perturbation in the wobble and crank moves is carried out using the fast gradient-based algorithm described previously¹⁴. After all five move types, the side chains are optimized and the energy is minimized as described in the preceding paragraph.

The all-atom refinement protocol is divided into three stages. The first is ramp-up. The ramp-up stage consists of sets of ten small and shear moves preceded by combinatorial optimization of the side-chain rotamer conformations. The weight on the repulsive part of the Lennard–Jones potential is progressively increased from 0.05 to 1.0 over eight such move sets. The gradual ramping up of the repulsive weight facilitates a smooth rearrangement of the side chains with small perturbations of the backbone and ensures a reasonably well-packed low-energy model before the more aggressive second stage. This second stage is the aggressive sampling stage: alternating wobble, small-wobble and crank compound Monte Carlo minimization moves are carried out; the total number of attempts for each move type is equal to the number of residues in the protein. A full combinatorial search over side-chain rotamer conformations is carried out after every 25 attempts of each type of move. The more aggressive nature of the moves used at this stage allows the traversal of modest energy barriers. The convergence tolerance for the DFP minimization is set to 10^{-4} . The third stage is the fine optimization stage: alternating small and shear moves are carried out, again for a total number of attempts equal to the number of residues in the protein. The more subtle backbone conformation changes brought about by these moves assist convergence on a relatively low-energy local minimum. The convergence tolerance for minimization is set to 10^{-5} . After these three stages, a final minimization with respect to all degrees of freedom is carried out with a convergence tolerance of 10^{-6} .

The refinement protocol described above is implemented in the 'fullatom_relax' subroutine in Rosetta; the CPU cost is about 20 min for a 100-residue protein on an Intel Pentium IV 1.6 GHz processor.

The challenge in refinement is to focus sampling on the lowest energy regions of the energy landscape identified up to that point while maintaining a broad enough search to avoid converging on a local energy minimum. Towards this end, we developed a protocol that balances intensification of the search in low-energy regions with diversification to maintain subpopulations exploring alternative energy minima. The approach—the third key step of the rebuilding-and-refinement protocol; that is, ensemble evolution by alternate cycles of diversification and intensification—adopts the idea of explicit control of the search intensity from tabu search¹⁸, and is a generalization of the conformational space annealing (CSA) technique, which has achieved success in a broad range of optimization problems¹⁹.

In both the intensification and diversification steps, an input population of 200 models was clustered using the method described in ref. 13 to identify distinct populations of structures. The clustering threshold was chosen such that the largest cluster contained 10% of the models. For each cluster, ten models were selected (if there were fewer than 10 models in a cluster, all were selected) and each model was subjected to nine independent segment rebuilding plus all-atom refinement runs initialized with different random number seeds.

In the diversification stages (iterations 1, 3, 5, 7 and 9), the models in the parent population were kept in their original cluster assignment. A newly generated model was assigned to the closest cluster if the root-mean-squared deviation over alpha carbons (C_{α} r.m.s. deviation) between this model and the closest cluster member was less than the current diversity threshold (see below), and the highest energy member of the cluster was thrown away. If the r.m.s. deviation between a newly generated model and its closest cluster member was higher than the current diversity threshold, then the model with the highest energy in the current parent population was thrown away, and the newly generated model formed a cluster of its own. This is analogous to speciation in natural evolution. As a model is discarded for each new model added, the population size stayed unchanged. The diversification step favours a broad exploration of the conformational space by maintaining the distinct populations of clusters: there is competition for low energy within but not between clusters. Combined with the initial clustering step, it ensures that the new population will not be dominated by overly closely related structures, which could result in premature convergence away from the global minimum.

In the intensification stages (iterations 2, 4, 6, 8 and 10), all but the lowest energy 10% of the entire population (parents plus offspring) is discarded to bring the population back to a size of 200. The remaining models from the parent population keep their original cluster assignment. A newly generated model was assigned to the closest remaining cluster if the r.m.s. deviation between this model and the closest cluster member was lower than the current diversity threshold; otherwise it formed a new cluster of its own. This stage differs from the diversification stage in that the energy-based selection is carried out across all clusters and hence higher energy clusters can be eliminated completely. This stage allows more thorough exploration of the most promising (lowest energy) regions of the energy landscape explored thus far.

The diversity threshold used to maintain distinct populations and to guide the spawning of new populations was reduced at each iteration to allow gradual convergence on the global energy minimum. The starting value was the clustering threshold in the original population, and this was reduced by 0.1 Å at each iteration. This annealing of the diversity threshold was introduced in the CSA strategy¹⁹.

The new parent population generated by the diversification or intensification procedures was used to seed the next generation, and nine independent segment rebuilding plus all-atom refinement calculations were again carried out for each parent. After ten iterations, the low energy models were clustered and the lowest energy models in the largest five clusters were selected as the final predictions. The overall iterative procedure took approximately 2,000 CPU hours per target. For molecular replacement efforts, this computational effort would probably be significantly reduced if phasing trials with diffraction data are used to screen models.

Identification of regions to rebuild from the NMR structure ensemble. The test cases for NMR refinement were chosen to be proteins representing different fold topologies for which an NMR structure and a high-resolution crystal structure (with structure factors deposited in PDB) existed. These were chosen from the data sets used by refs 21 and 43.

For investigations of refinement of NMR structures, we rebuilt two sets of regions. The first are regions that vary within the NMR ensemble. As in the comparative modelling case, we have observed that regions that vary within the NMR ensemble are likely to be the regions that are most different from a high-resolution crystal structure. These are most likely loops that are either inherently dynamic in the NMR structure or loops that are held in place with insufficient restraints. (Applying all-atom refinement to the NMR ensembles gave essentially the same list of variable regions (data not shown).)

The second set of regions are segments that are internally consistent within the NMR ensemble but systematically under-packed. To estimate packing we used a recently developed packing metric (W. Sheffler, personal communication) based on the relative accessible surface areas of groups of atoms. For each buried atom, we compute the largest sphere tangent to that atom which can fit into empty space within the protein. A group composed of all atoms within 5 Å of the centre is defined for each sphere. For each group of atoms, accessible surface (SASA) to small and large spherical probes (radii 0.9 Å and 2 Å, respectively) is computed; given that a ball of atoms has a certain area accessible to a large sphere, less-accessible area to a small sphere indicates better packing. A summary percentile score is computed on the basis of a reference set of crystal

structures, approximating the fraction of native proteins which are better packed than the scored structure.

Preparation of blind predictions. The initial set of template-based models was obtained from the 3D-Jury server⁴⁴ and subjected to all-atom refinement using the Rosetta all-atom energy function. Up to ten templates from which the very lowest energy models were derived were used as the candidate templates. Alignment ensembles between the candidate templates and the target sequence were parametrically generated using the K*Sync alignment method⁴⁵. The alignment ensemble was turned into a model ensemble by placing the sequence of the query onto the backbone of the parent based on each alignment. Missing densities from the insertion and deletion regions of the alignment were modelled using the segment modelling protocol described in the 'rebuilding-and-refinement protocol' section. The full-chain models were then subjected to the all-atom refinement procedure as described in the same section, constrained by a set of C_{α} - C_{α} distance constraints, described next.

The C_{α} - C_{α} distance constraints were generated from the 3D-Jury⁴⁴ template-based models with the lowest Rosetta all-atom energies after all-atom refinement. A C_{α} - C_{α} pair was used to derive constraints only when the associated distance was less than 8 Å in more than 80% of the selected constraint-generating models. Upper and lower bounds for each of these pairs were determined by padding the highest and lowest of these distances by one standard deviation of the C_{α} - C_{α} distance distribution function, as described in ref. 46. For computational efficiency, we further trimmed down the number of constraint pairs by eliminating neighbouring pairs separated by one or two residues. During all-atom refinement, a penalty is applied when the C_{α} - C_{α} distances in the model exceed the upper or lower limit of the corresponding constraints. If a distance exceeds the upper or lower constraint limit by d (in Å), then the penalty E_c is d^2 when $d < 0.5$ Å, and $(d - 0.25)$ when $d \geq 0.5$ Å. The resulting ensemble of low-energy comparative models became the inputs to further rounds of rebuilding-and-refinement (Fig. 1a).

For targets without clear templates identified by the 3D-Jury server⁴⁴, the full chain was fully modelled by fragment assembly starting from an extended chain, followed by the all-atom refinement procedure described above. The convergence of the Rosetta *de novo* prediction protocol can differ significantly for different sequence representatives of a given fold^{13,47}. For T0283, one of seven tested sequence homologues gave exceptionally well converged low-energy models that, after sequence mapping, allowed structure prediction for the target sequence with the rebuilding-and-refinement protocol^{13,25}.

About 100,000 all-atom refined models were generated for each modelling target, requiring approximately 100,000 CPU hours. As noted above, for molecular replacement efforts, this computational effort would probably be significantly reduced if phasing trials with diffraction data are used to screen models; as the predicted models used in this manuscript were prepared as blind predictions for CASP7, such diffraction data were not available at the time of modelling.

Metrics for comparing models with crystal structures. As has been discussed previously, no metric for comparing structure models with the crystal structures is perfect⁴⁸. In this work, we used three different structural metrics for model quality assessment. The C_{α} r.m.s. deviation is a widely used metric for structure comparison, but it can be distorted by large deviations in a small number of residues, especially at the termini or in long surface loops. The GDT-HA (geometric distance test (high accuracy)) score is the average percentage of C_{α} s in the model within 0.5, 1.0, 2.0, and 4.0 Å of the corresponding C_{α} coordinates in the crystal structure; we used TMalign³³ to align the structures. This metric is less sensitive than the full-chain r.m.s. deviation to deviations in poorly ordered termini and long loops, and was used in the CASP7 template-based modelling assessment.

The core residue all-atom r.m.s. deviation describes the accuracy of both the backbone and side-chain conformation prediction. We used this metric in the evaluation of NMR refinement because it can be applied to both the starting (NMR ensemble) and ending (Rosetta refined) models. In template-based modelling, this metric is not practical as the template usually does not have the same amino acid sequence as the target to be modelled.

In addition, successful molecular replacement using the predicted structure can be regarded as a stringent test for model quality assessment, as suggested in ref. 49.

Screening of models for suitability for molecular replacement. Searching for molecular replacement solutions involves applying rigid-body transformations along the six rotational and translational degrees of freedom. We carried out this search with the Phaser software, which is described in ref. 10 and references therein. For completeness, the algorithms are briefly summarized here. Phaser uses likelihood functions to judge how well molecular replacement models agree with the measured diffraction data after they have been first rotated and then also translated. Brute-force likelihood calculations over grids of orientations and

positions are computationally expensive, so fast-fourier-transform-based approximations are used to compute sets of possible solutions, which are rescored with the full likelihood targets. By using a tree-search-with-pruning strategy, almost all solutions that would be found with a full six-dimensional search are found, but with a much lower computational cost. As well, this strategy allows effective searches for multiple copies, in crystals with more than one molecule in the asymmetric unit. For each molecule to be placed, a rotation search is first carried out. A translation search is then carried out for each plausible orientation. All plausible rotation/translation solutions are checked for packing in the lattice, and solutions that pack successfully are subjected to rigid body refinement. If more than one copy is present, all plausible partial solutions are fixed in turn while carrying out rotation and translation searches for subsequent copies. In molecular replacement trials with Phaser, the clearest indication of success comes from high values of the Z-score (number of standard deviations above the mean), computed by comparing the log-likelihood-gain (LLG) for the peak with LLG scores for a random sample of search points.

For molecular replacement in each of the NMR modelling cases, we evaluated the combined NMR ensemble as a potential search model and compared these results to trials with the 25 lowest energy Rosetta models from rebuilding and refinement (Table 1). Furthermore, we have carried out molecular replacement trials with each of the members of the deposited NMR ensemble individually, with results given in Supplementary Table 1. Finally, for an actual search for a good molecular replacement solution, a larger set of models from rebuilding and refinement can be screened rapidly. We thus extended the search to the 1,000 lowest energy models from Rosetta rebuilding and refinement and the results, notably improved, are presented in Supplementary Table 1.

For molecular replacement in comparative modelling cases, we prepared search models from the best existing templates and from our comparative modelling predictions. For the best templates, we followed the 'mixed model' protocol described in ref. 4 for optimizing molecular replacement. Furthermore, on the basis of the 3DPAIR⁵⁰ structure alignment between the native structure and the best template structure, the template structure was trimmed to contain only the structurally alignable regions. Then the native sequence was threaded onto the backbone of the corresponding template structure, while retaining the side-chain coordinates of the identical residues between the template and native sequences. Non-identical side chains longer than serine were mutated to serine, followed by Rosetta side-chain packing protocol⁵¹ to model the mutated serine and the shorter non-identical side chains, while keeping the identical side-chain conformation fixed. To prepare search models for these predictions, we superimposed 100 low-energy models from the final round of refinement, and defined the model that has the lowest average r.m.s. deviation to the rest of the models as the reference model. Then we calculated the average per-atom distance D_a between each of the superimposed models and the reference model. The Rosetta temperature factor is calculated as $T_e = 8\pi^2 D_a^2/3$ for each atom and inserted to the B-factor column of the refined model files. The Rosetta temperature factor is intended to represent the uncertainty in the final refined models after extensive refinement in the Rosetta all-atom force field. As suggested earlier¹⁹, by using the B-factor effectively to smear each atom over its possible

positions, the correlation of the modelled electron density with the true electron density can be maximized.

For the *de novo* modelling case, target T0283, search models for molecular replacement were trimmed according to residues for which there was consensus among submitted models. Supplementary Fig. 5 gives a more detailed description and illustration of the molecular replacement solution.

Assessing model quality with MolProbity. For the investigations of refinement of NMR models, we used the MolProbity software²⁴ to investigate the quality of the refined models versus that of the starting NMR ensemble. For purposes of comparison, we chose the lowest energy refined model and the first member of the deposited NMR structure. Supplementary Table 2 shows the clash score, number of rotamer outliers and number of Ramachandran outliers of the NMR and refined models. The refined models consistently have better model quality than the starting NMR structure based on these metrics.

36. Simons, K. T., Kooperberg, C., Huang, E. & Baker, D. Assembly of protein tertiary structures from fragments with similar local sequences using simulated annealing and Bayesian scoring functions. *J. Mol. Biol.* **268**, 209–225 (1997).
37. Canutescu, A. A. & Dunbrack, R. L. Jr. Cyclic coordinate descent: A robotics algorithm for protein loop closure. *Protein Sci.* **12**, 963–972 (2003).
38. Lazaridis, T. & Karplus, M. Effective energy function for proteins in solution. *Proteins* **35**, 133–152 (1999).
39. Dunbrack, R. L. Jr & Cohen, F. E. Bayesian statistical analysis of protein side-chain rotamer preferences. *Protein Sci.* **6**, 1661–1681 (1997).
40. Engh, R. A. & Huber, R. Accurate bond and angle parameters for X-ray protein structure refinement. *Acta Crystallogr. A* **47**, 392–400 (1991).
41. Wang, C., Schueler-Furman, O. & Baker, D. Improved side-chain modeling for protein-protein docking. *Protein Sci.* **14**, 1328–1339 (2005).
42. Li, Z. & Scheraga, H. A. Monte Carlo-minimization approach to the multiple-minima problem in protein folding. *Proc. Natl Acad. Sci. USA* **84**, 6611–6615 (1987).
43. Garbuzynskiy, S. O., Melnik, B. S., Lobanov, M. Y., Finkelstein, A. V. & Galzitskaya, O. V. Comparison of X-ray and NMR structures: is there a systematic difference in residue contacts between X-ray- and NMR-resolved protein structures? *Proteins* **60**, 139–147 (2005).
44. Ginalski, K., Elofsson, A., Fischer, D. & Rychlewski, L. 3D-Jury: a simple approach to improve protein structure predictions. *Bioinformatics* **19**, 1015–1018 (2003).
45. Chivian, D. & Baker, D. Homology modeling using parametric alignment ensemble generation with consensus and energy-based model selection. *Nucleic Acids Res.* **34**, e112 (2006).
46. Sali, A. & Blundell, T. L. Comparative protein modelling by satisfaction of spatial restraints. *J. Mol. Biol.* **234**, 779–815 (1993).
47. Bonneau, R., Strauss, C. E. & Baker, D. Improving the performance of Rosetta using multiple sequence alignment information and global measures of hydrophobic core formation. *Proteins* **43**, 1–11 (2001).
48. Moulton, J., Fidelis, K., Rost, B., Hubbard, T. & Tramontano, A. Critical assessment of methods of protein structure prediction (CASP)–round 6. *Proteins* **61** (suppl. 7), 3–7 (2005).
49. Petsko, G. A. The grail problem. *Genome Biol.* **1**, COMMENT002 (2000).
50. Plewczynski, D., Pas, J., Von Grotthuss, M. & Rychlewski, L. Comparison of proteins based on segments structural similarity. *Acta Biochim. Pol.* **51**, 161–172 (2004).
51. Kuhlman, B. & Baker, D. Native protein sequences are close to optimal for their structures. *Proc. Natl Acad. Sci. USA* **97**, 10383–10388 (2000).

Modulation of Saturn's radio clock by solar wind speed

Philippe Zarka¹, Laurent Lamy¹, Baptiste Cecconi¹, Renée Prangé¹ & Helmut O. Rucker²

The internal rotation rates of the giant planets can be estimated by cloud motions, but such an approach is not very precise because absolute wind speeds are not known a priori and depend on latitude¹: periodicities in the radio emissions, thought to be tied to the internal planetary magnetic field, are used instead^{2–5}. Saturn, despite an apparently axisymmetric magnetic field⁶, emits kilometre-wavelength (radio) photons from auroral sources. This emission is modulated at a period initially identified as 10 h 39 min 24 ± 7 s, and this has been adopted as Saturn's rotation period³. Subsequent observations^{7,8}, however, revealed that this period varies by ±6 min on a timescale of several months to years. Here we report that the kilometric radiation period varies systematically by ±1% with a characteristic timescale of 20–30 days. Here we show that these fluctuations are correlated with solar wind speed at Saturn, meaning that Saturn's radio clock is controlled, at least in part, by conditions external to the planet's magnetosphere. No correlation is found with the solar wind density, dynamic pressure or magnetic field; the solar wind speed therefore has a special function. We also show that the long-term fluctuations are simply an average of the short-term ones, and therefore the long-term variations are probably also driven by changes in the solar wind.

Low-frequency magnetospheric radio emissions have been used until now to measure the rotation of giant planets because they are produced by keV electrons moving along planetary magnetic field lines that are presumed to rotate with the planet's interior⁹. These emissions are anisotropic; that is, they are preferentially directed in a hollow conical beam aligned with the direction of the local magnetic field¹⁰. Combined with the rotation of the usually non-axisymmetric planetary magnetic field¹¹, these properties lead to a rotational modulation of the observed intensity of the emission. At Saturn, the intense auroral kilometric radiation (SKR) was found in the Voyager era to be strongly modulated at a period $P_{\text{SKR}} = 10 \text{ h } 39 \text{ min } 24 \pm 7 \text{ s}$, which is close to that observed for atmospheric cloud features³. However, Saturn's magnetic field is very nearly axisymmetric, and the auroral sources are not co-rotating with the planet; rather, they are fixed in local time^{12,13}. This makes it difficult to understand the strong SKR modulation without appeal to the existence of a magnetic anomaly that escaped detection by magnetometers on the Pioneer and Voyager spacecraft^{14–16}. The uncertainty of ±7 s on $P_{\text{SKR}} = 10 \text{ h } 39 \text{ min } 24 \text{ s}$ was thought to be limited only by the available time span (nine months), under the implicit assumption of a constant rotation period. However, 24 years later, the SKR period measured by the radio experiment on board Cassini⁸ is $P_{\text{SKR}} = 10 \text{ h } 45 \text{ min } 45 \pm 36 \text{ s}$. The difference of more than 6 min cannot be due to a change in Saturn's rotation rate, owing to the large inertia of the planet. Ulysses⁷ and Cassini^{8,17} radio measurements actually showed that P_{SKR} continuously varies over the long term (several months to years), with ~1% relative amplitude.

Two models were proposed to explain these variations. The first¹⁸ invoked an external cause, with nonrandom fluctuations in the solar wind speed at Saturn causing SKR source displacement in local time, leading to an apparent radio period that is different from the planet's true rotation period. The other¹⁹ invoked an internal cause, namely mass injection from Enceladus in the magnetosphere's plasma disk and a variable electrodynamic coupling between this disk and Saturn's ionosphere.

Standard techniques for harmonic signal analysis, such as Fourier transform, require a 100-period window to provide 1% accuracy, and thus permit only long-term variations to be addressed¹⁷. Taking advantage of Cassini's quasi-continuous radio observations, we developed a method to address faster fluctuations. By integrating the received flux over the range 100–400 kHz, where most of the SKR power is emitted, we obtained a time series of SKR power in which one broad peak was observed for each rotation of Saturn (see Supplementary Figs 1 and 2). This time series is displayed in Fig. 1 in a format that reveals variations in the phase of SKR peaks relative to a fixed reference period. In addition to the previously noted long-term variation¹⁷, we see quasi-periodic oscillations of the SKR phase—and thus of the SKR period—on a timescale of 20–30 days. Smoothing the SKR time series and cross-correlating consecutive peaks (as described in Supplementary Figs 1–3) allowed us to estimate P_{SKR} with an accuracy of ±2 min (0.3%) at timescales down to ~1 week. Results are displayed in Fig. 2a over the 1,186-day interval studied (2003 June 30 to 2006 September 27). Ubiquitous fluctuations of ~2% peak-to-peak amplitude are detected on a timescale of 20–30 days, superimposed on the long-term trend measured by previous authors¹⁷.

What is the origin of these variations? A timescale of 20–30 days is characteristic of variations in the solar wind at Saturn, already known to control the SKR intensity and power^{20,21}, as can be seen in Fig. 1. However, the duration of Cassini's orbits around Saturn has also varied between 18 and 30 days since mid-2004. Orbital parameters such as the planetocentric distance and latitude of the spacecraft affect observations of SKR: decreasing distance increases SKR signal strength, and hence detectability, and changes in latitude influence SKR visibility as a result of the change in the geometry of observation, SKR being emitted from high-latitude sources in conical patterns centred on the local magnetic field^{9,10,13}. Thus, Fig. 2a includes the fluctuations in the solar wind speed ballistically projected to Saturn; variations of spacecraft range and latitude are displayed in Fig. 2b. In Fig. 2c we compare the Fourier power spectrum of the fluctuations of P_{SKR} over the entire interval studied with those of the solar wind speed, spacecraft distance and latitude. Peaks appear in P_{SKR} fluctuations at ~21.5, 23.0 and 25.5 days. The last of these coincides with the same peak in solar wind speed fluctuations. Spacecraft latitude peaks with an 18–19-day period. We simulated possible beatings between solar-wind-induced and orbit-induced variations by the product

¹Laboratoire d'Études Spatiales et d'Instrumentation en Astrophysique, Observatoire de Paris, Centre National de la Recherche Scientifique, Université Pierre et Marie Curie, Université Paris Diderot, 92190 Meudon, France. ²Space Research Institute, Austrian Academy of Sciences, A-8042 Graz, Austria.

(versus time) of the solar wind speed multiplied by the spacecraft latitude. The spectrum of this quantity shows main peaks at ~ 20.0 , 21.5, 24.0 and 26.5 days, all in the same range as—and some of them matching—main peaks in P_{SKR} . Study of subintervals from our data set confirms these results: within the interval day of the year (DOY) 2004 = 415–670 (DOY = 1.0 corresponds to 2004 January 1 at 0 h UT), where both distance and latitude are regularly modulated, strong P_{SKR} peaks precisely match peaks in solar wind speed, spacecraft latitude variations, and their product; in the interval between DOY 280 and 620, after Cassini's Saturn orbit insertion, the main peak of both P_{SKR} and the solar wind speed is at about 22 days. Both solar wind speed and orbit-dependent viewing geometry therefore seem to contribute to observed variations in the SKR period.

For better quantification of the influence of the solar wind, we analysed separately the interval before Cassini's Saturn orbit insertion (left of the dotted vertical line in Fig. 2a), over which the SKR viewing geometry remained fixed with no expected influence of orbital parameters on SKR visibility. We found a linear correlation²² coefficient $C > 40\%$ between P_{SKR} and the solar wind speed (Fig. 3a). For comparison, the well-known correlation between SKR power and solar wind speed gives here a similar coefficient $C = 44\%$. The probability of obtaining $C > 40\%$ with two random data sets of the same length as in Fig. 3a is $\sim 10^{-7}$; the correlation found is therefore highly significant. A similar study of other subintervals leads to correlation coefficients of up to $+70\%$ between P_{SKR} and the solar wind speed (for example, within the interval between DOY 640 and 760, where the spacecraft's latitude remained fixed and near zero). The lack of a perfect phase relationship ($C \approx 100\%$) comes from the inevitable inaccuracies in the ballistic projection of the solar wind to Saturn (never exceeding ± 4 days^{23,24}), time-variable solar activity (for example coronal mass ejections) causing azimuthal variations in the structure of the solar wind²⁵, and details of the interaction between the solar wind and Saturn's magnetosphere (the solar wind might function as a

trigger, efficient only when energy has previously been stored in the magnetosphere, so that SKR peaks may sometimes be 'missing').

The correlation found above between short-term (< 1 month) fluctuations in Saturn's radio period and variations in the solar wind speed indicates an external origin for P_{SKR} variations. As we did not find any significant correlation between P_{SKR} and other solar wind parameters such as density, dynamic pressure (Fig. 3b) or magnetic field, its speed must have a special function. This result validates the assumptions of the model¹⁸ proposed to explain these variations in terms of SKR source displacement in local time caused by fluctuations in the solar wind speed. An additional internal cause¹⁹ is not excluded, which could be another reason for not finding a one-to-one correlation between P_{SKR} and the solar wind speed.

When averaging P_{SKR} fluctuations over > 1 month, one obtains the long-term fluctuations already noted by previous authors¹⁷, which are therefore merely an average of the short-term ones (Fig. 1). The long-term variations could therefore also be driven by changes in the solar wind. In the long term, there does indeed seem to be a relationship between the solar wind speed and P_{SKR} : the slow overall decrease

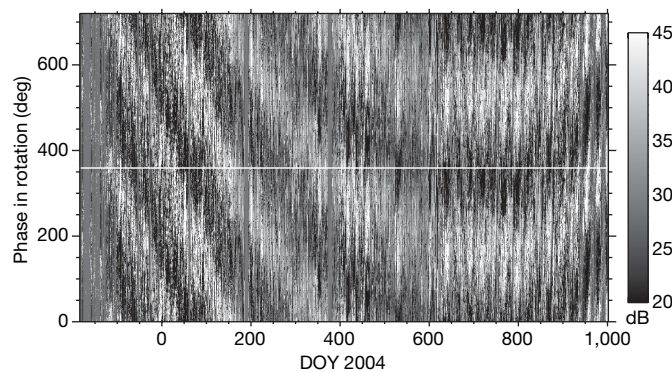


Figure 1 | Evidence of short-term variations in P_{SKR} and their relation to long-term variations. The SKR power–time series (derived as explained in Supplementary Figs 1 and 2) is displayed here over the 3.25-year interval studied, in a format similar to that of Fig. 1 in ref. 17. Variations in SKR power during consecutive rotations are plotted as consecutive vertical lines with a power scale in grey levels, using an assumed fixed period of 10 h 48 min. Time is in day of the year (DOY) 2004. Data gaps are displayed in flat grey (major ones are before DOY -137 and at about DOY 191 ± 4 and 377 ± 5). Each rotation is plotted twice for clarity, separated by the white horizontal line. The origin of phases—and thus the absolute phase—is arbitrary. Previous authors¹⁷ noted that the fact that the SKR peak wanders with variable slope over the time interval means that a fixed period does not organize the SKR modulation well. We see here the same long-term behaviour. In addition, the quality of our data processing (see the legend to Supplementary Fig. 1a) reveals quasi-periodic oscillations of the SKR period on a timescale of 20–30 days. Those are especially clear after DOY 400, where the long-term drift is small and fewer data gaps are present. The amplitude of these fluctuations is large ($\sim 2\%$ peak to peak), and their long-term averaging results in the slow, smaller-amplitude ($< 1\%$ peak to peak over the studied interval) variation of P_{SKR} noted by previous authors.

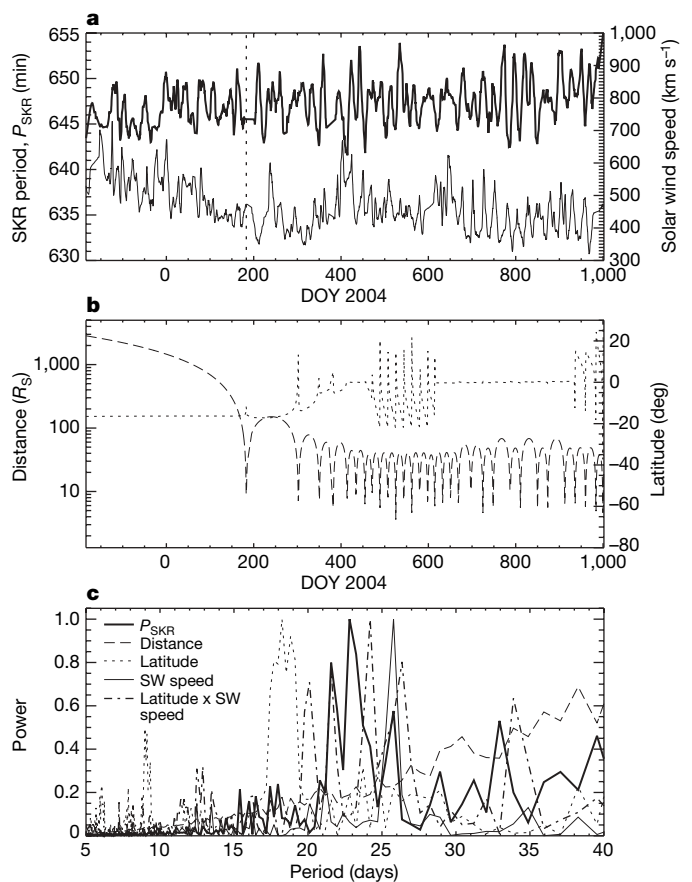


Figure 2 | 'Short-term' variations in P_{SKR} compared with solar wind speed at Saturn and with variations in orbital parameters of Cassini. The same 3.25-year interval as in Fig. 1 is shown. **a**, Variations in P_{SKR} (heavy line; left scale) obtained as explained in the text and in Supplementary Figs 1–3. The solar wind speed plotted below (light line; right scale), measured by the ACE and WIND spacecraft near the Earth's orbit (<http://omniweb.gsfc.nasa.gov/>) and projected to Saturn, shows similar fluctuations on a timescale of 20–30 days. Solar wind projection includes ballistic radial projection from ~ 1 to 10 AU, plus a delay compensating for the longitude difference between Earth and Saturn. The dotted vertical line indicates Cassini's Saturn orbit insertion. **b**, Cassini orbital parameters: distance to Saturn (dashed; left scale; $1 R_S = 1$ Saturn radius = 60,300 km) and latitude (dotted; right scale). **c**, Fourier power spectrum of the fluctuations of all the above quantities, plus the quantity (latitude \times solar wind speed) which provides a simple way of simulating beating between latitudes (and thus visibility of the radio emission) and variations in the solar wind (SW) speed.

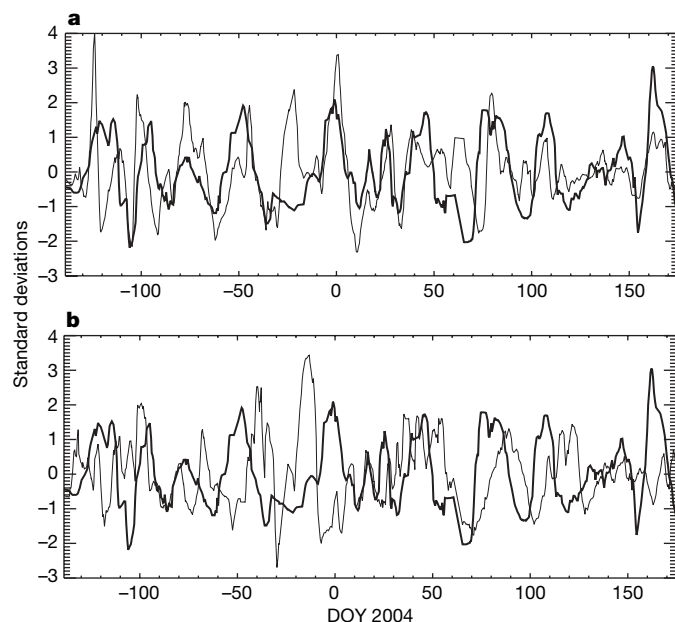


Figure 3 | Comparison of SKR period variations with solar wind speed and dynamic pressure at Saturn. In the time interval before Saturn orbit insertion shown here, the spacecraft latitude remains quasi-constant and its distance to Saturn steadily decreases; no influence of orbital parameters on SKR visibility is therefore expected. This interval is therefore best suited to searching for a correlation between P_{SKR} variations (heavy lines) and the solar wind parameters (light lines), not polluted by other variabilities. For a better comparison of their fluctuations on a timescale shorter than ~ 1 month, the two displayed quantities have been detrended (by subtraction of a running average over ~ 2 months) and normalized by their respective standard deviations. **a**, Correlation between P_{SKR} and solar wind speed. Except for two ~ 10 -day intervals, near DOY -25 and $+65$, the correlation is high, with a linear correlation coefficient $C \geq +0.4$ (see the text). In the two main 'anomalous' intervals mentioned above, a few data gaps exist in Cassini SKR data, and the solar wind speed may have been contaminated by the effect of coronal mass ejections, whose ballistic projection leads to overestimated values whenever the point at which the solar wind is measured *in situ* (here, by ACE or WIND spacecraft) and the target of the projection (Saturn) are not radially aligned^{23–25}. **b**, Correlation between P_{SKR} and solar wind dynamic (ram) pressure. Correlation is low, with $C \approx -0.1$.

in the solar wind speed from $\sim 550 \text{ km s}^{-1}$ to $\sim 400 \text{ km s}^{-1}$ in Fig. 2a seems to be anticorrelated with the trend of P_{SKR} increasing from $<646 \text{ min}$ to $>649 \text{ min}$.

Long-term variations similar to those of P_{SKR} have been found to affect Saturn's azimuthal magnetic field component^{26–28} and possibly also the electron density in the inner magnetosphere¹⁹ and the position of the magnetopause²⁹. Short-term fluctuations are very difficult to address for these quantities because they are measured *in situ* by Cassini during a small fraction of each orbit. Their dependence on fluctuations in the solar wind remains to be investigated. If variations in P_{SKR} are indeed caused by SKR source displacement in local time¹⁸, then the use of Cassini's instantaneous radio imaging capability³⁰ for monitoring motions of the SKR source should permit their deconvolution from P_{SKR} measurements, thus permitting a more accurate determination of Saturn's true (internal) rotation rate.

Received 24 January; accepted 10 September 2007.

- Sanchez-Lavega, A. How long is the day on Saturn? *Science* **307**, 1223–1224 (2005).
- Higgins, C. A., Carr, T. D., Reyes, F., Greenman, W. B. & Lebo, G. R. A redefinition of Jupiter's rotation period. *J. Geophys. Res.* **102**, 22033–22041 (1997).
- Desch, M. D. & Kaiser, M. L. Voyager measurement of the rotation period of Saturn's magnetic field. *Geophys. Res. Lett.* **8**, 253–256 (1981).
- Desch, M. D., Connerney, J. E. P. & Kaiser, M. L. The rotation period of Uranus. *Nature* **322**, 42–43 (1986).

- Lecacheux, A., Zarka, P., Desch, M. D. & Evans, D. R. The sidereal rotation period of Neptune. *Geophys. Res. Lett.* **20**, 2711–2714 (1993).
- Connerney, J. E. P., Ness, N. F. & Acuña, M. H. Zonal harmonic model of Saturn's magnetic field from Voyager 1 and 2 observations. *Nature* **298**, 44–46 (1982).
- Galopeau, P. H. M. & Lecacheux, A. Variations in Saturn's radio rotation period measured at kilometer wavelengths. *J. Geophys. Res.* **105**, 13089–13101 (2000).
- Gurnett, D. A. et al. Radio and plasma wave observations at Saturn from Cassini's approach and first orbit. *Science* **307**, 1255–1259 (2005).
- Zarka, P. Auroral radio emissions at the outer planets: Observations and theories. *J. Geophys. Res.* **103**, 20159–20194 (1998).
- Zarka, P. in *Planetary Radio Emissions II* (eds Rucker, H. O., Bauer, S. J. & Pedersen, B. M.) 327–342 (Austrian Acad. Sci. Press, Vienna, 1988).
- Ness, N. F. in *Planetary Radio Emissions II* (eds Rucker, H. O., Bauer, S. J. & Pedersen, B. M.) 3–13 (Austrian Acad. Sci. Press, Vienna, 1988).
- Warwick, J. W. et al. Planetary radio astronomy observations from Voyager 1 near Saturn. *Science* **212**, 239–243 (1981).
- Galopeau, P. H. M., Zarka, P. & Le Quéau, D. Source location of Saturn's kilometric radiation: The Kelvin–Helmholtz instability hypothesis. *J. Geophys. Res.* **100**, 26397–26410 (1995).
- Galopeau, P., Ortega-Molina, A. & Zarka, P. Evidence of Saturn's magnetic field anomaly from SKR high-frequency limit. *J. Geophys. Res.* **96**, 14129–14140 (1991).
- Connerney, J. E. P. & Desch, M. D. Comment on: 'Evidence of Saturn's magnetic field anomaly from SKR high-frequency limit' by Galopeau et al. *J. Geophys. Res.* **97**, 8713–8717 (1992).
- Galopeau, P. & Zarka, P. Reply to the Comment on: 'Evidence of Saturn's magnetic field anomaly from SKR high-frequency limit' by Connerney & Desch. *J. Geophys. Res.* **97**, 12291–12297 (1992).
- Kurth, W. S., Lecacheux, A., Averkamp, T. F., Groene, J. B. & Gurnett, D. A. A Saturnian longitude system based on a variable kilometric radiation period. *Geophys. Res. Lett.* **34**, L02201, doi:10.1029/2006GL028336 (2007).
- Cecconi, B. & Zarka, P. Model of a variable radio period for Saturn. *J. Geophys. Res.* **110**, A12203, doi:10.1029/2005JA011085 (2005).
- Gurnett, D. A. et al. The variable rotation period of the inner region of Saturn's plasma disk. *Science* **316**, 442–445 (2007); published online 22 March 2007.
- Desch, M. D. Evidence for solar wind control of Saturn radio emission. *J. Geophys. Res.* **87**, 4549–4554 (1982).
- Desch, M. D. & Rucker, H. O. The relationship between Saturn kilometric radiation and the solar wind. *J. Geophys. Res.* **88**, 8999–9006 (1983).
- Bevington, P. R. & Robinson, D. K. *Data Reduction and Error Analysis for the Physical Sciences* 2nd edn 198–200 (McGraw-Hill, New York, 1992).
- Tao, C., Kataoka, R., Fukunishi, H., Takahashi, Y. & Yokoyama, T. Magnetic field variations in the Jovian magnetotail induced by solar wind dynamic pressure enhancements. *J. Geophys. Res.* **110**, A11208, doi:10.1029/2004JA010959 (2005).
- Prangé, R. et al. An interplanetary shock traced by planetary auroral storms from the Sun to Saturn. *Nature* **432**, 78–81 (2004).
- Hanlon, P. G. et al. On the evolution of the solar wind between 1 and 5 AU at the time of the Cassini Jupiter flyby: Multispacecraft observations of interplanetary coronal mass ejections including the formation of a merged interaction region. *J. Geophys. Res.* **109**, A09S03, doi:10.1029/2003JA010112 (2004).
- Espinosa, S. E., Southwood, D. J. & Dougherty, M. K. How can Saturn impose its rotation period in a noncorotating magnetosphere? *J. Geophys. Res.* **108**, 1086, doi:10.1029/2001JA005084 (2003).
- Cowley, S. W. H. et al. Cassini observations of planetary-period magnetic field oscillations in Saturn's magnetosphere: Doppler shifts and phase motion. *Geophys. Res. Lett.* **33**, L07104, doi:10.1029/2005GL025522 (2006).
- Southwood, D. J., Dougherty, M. K. & Kivelson, M. G. Time variability in Saturn's magnetic rotation. Presented at American Geophysical Union Fall Meeting 2006 abstract P52A-08 (2006).
- Clarke, K. E. et al. Cassini observations of planetary-period oscillations of Saturn's magnetopause. *Geophys. Res. Lett.* **33**, L23104, doi:10.1029/2006GL027821 (2006).
- Cecconi, B., Zarka, P. & Kurth, W. S. in *Planetary Radio Emissions VI* (eds Rucker, H. O., Kurth, W. S. & Mann, G.) 37–49 (Austrian Acad. Sci. Press, Vienna, 2006).

Supplementary Information is linked to the online version of the paper at www.nature.com/nature.

Acknowledgements We thank D. Southwood for a seminar at Meudon Observatory; F. Mottez, S. Hess and J.-M. Griessmeier for early inputs; B. Kurth for comments on the manuscript; D. Pelat for advice on the statistical analysis; Cassini Radio and Plasma Wave Science (RPWS) engineers at the University of Iowa and the Laboratoire d'Études Spatiales et d'Instrumentation en Astrophysique for support on instrumental questions and ephemeris; and N. Letourneur for processing RPWS data. The French co-authors acknowledge support from the Centre National d'Études Spatiales.

Author Contributions P.Z., L.L., B.C. and R.P. contributed equally to this work. H.O.R. contributed to the projection of solar wind data. P.Z. wrote the paper. All authors discussed the results and commented on the manuscript.

Author Information Reprints and permissions information is available at www.nature.com/reprints. Correspondence and requests for materials should be addressed to P.Z. (philippe.zarka@obspm.fr).

LETTERS

Cavity QED with a Bose–Einstein condensate

Ferdinand Brennecke¹, Tobias Donner¹, Stephan Ritter¹, Thomas Bourdel², Michael Köhl³ & Tilman Esslinger¹

Cavity quantum electrodynamics (cavity QED) describes the coherent interaction between matter and an electromagnetic field confined within a resonator structure, and is providing a useful platform for developing concepts in quantum information processing¹. By using high-quality resonators, a strong coupling regime can be reached experimentally in which atoms coherently exchange a photon with a single light-field mode many times before dissipation sets in. This has led to fundamental studies with both microwave^{2,3} and optical resonators⁴. To meet the challenges posed by quantum state engineering⁵ and quantum information processing, recent experiments have focused on laser cooling and trapping of atoms inside an optical cavity^{6–8}. However, the tremendous degree of control over atomic gases achieved with Bose–Einstein condensation⁹ has so far not been used for cavity QED. Here we achieve the strong coupling of a Bose–Einstein condensate to the quantized field of an ultrahigh-finesse optical cavity and present a measurement of its eigenenergy spectrum. This is a conceptually new regime of cavity QED, in which all atoms occupy a single mode of a matter-wave field and couple identically to the light field, sharing a single excitation. This opens possibilities ranging from quantum communication^{10–12} to a wealth of new phenomena that can be expected in the many-body physics of quantum gases with cavity-mediated interactions^{13,14}.

The coherent coupling of a single two-level atom with one mode of the quantized light field leads to a splitting of the energy eigenstates of the combined system and is described by the Jaynes–Cummings model¹⁵. For the experimental realization the strong coupling regime has to be reached, where the maximum coupling strength g_0 between atom and light field is larger than both the amplitude decay rate of the excited state γ and that of the intracavity field κ . In the case of a thermal ensemble of atoms coupled to a cavity mode, the individual, position-dependent coupling for each atom has to be taken into account.

To capture the physics of a Bose–Einstein condensate (BEC) coupled to the quantized field of a cavity, we consider N atoms occupying a single wavefunction. Because the atoms are in the same motional quantum state, the coupling g to the cavity mode is identical for all atoms. Moreover, bosonic stimulation into the macroscopically populated ground state should largely reduce the scattering of atoms into higher momentum states during the coherent evolution. This situation is therefore well described by the Tavis–Cummings model¹⁶, where N two-level atoms are assumed to identically couple to a single field mode. A single cavity photon resonantly interacting with the atoms then leads to a collective coupling of $g\sqrt{N}$.

A key characteristic of the coupled BEC–cavity system is its eigenenergy spectrum, which we map out with a single excitation present. An ensemble of thermal atoms does not fulfill the requirement of identical coupling, but it shows a similar energy spectrum, which can be modelled by the Tavis–Cummings hamiltonian with an effective collective coupling¹⁷. In previous measurements^{18,19} and also in a very recent report²⁰, these eigenenergies have been measured for thermal atoms coupled to a cavity. Aside from the sensitivity of the spectrum

to the precise spatial distribution of the atoms, the differences between a BEC and a thermal cloud, or between a BEC and a Mott insulator, should also be accessible through the fluctuations of the coupling, that is, in the width of the resonances²¹.

First experiments bringing together BEC physics and cavities concentrated on correlation measurements using single atom counting²², studied cavity enhanced superradiance of a BEC in a ring cavity²³, observed nonlinear and heating effects for ultracold atoms in an ultrahigh-finesse cavity^{24,25} and achieved very high control over the condensate position within an ultrahigh-finesse cavity using atom chip technology²⁰.

To create a BEC inside an ultrahigh-finesse optical cavity we have modified our previous set-up²⁶. The experiment uses a magnetic trap 36 mm above the cavity, where we prepare 3.5×10^6 ⁸⁷Rb atoms in the $|F, m_F\rangle = |1, -1\rangle$ state with a small condensate fraction present. The atoms are then loaded into the dipole potential of a vertically oriented standing wave, formed by two counter-propagating laser beams. By varying the frequency difference δ between the upwards and the downwards propagating wave, the standing-wave pattern, and with it the confined atoms, move downwards at a velocity $v = \lambda\delta/2$, where λ is the wavelength of the trapping laser^{8,27}. Because of continuous evaporative cooling during the transport, the number of atoms arriving in the cavity is reduced to typically 8.4×10^5 atoms with a small condensate fraction present. During the 100 ms of transport a small magnetic field is applied to provide a quantization axis and the sample remains highly spin-polarized in the $|1, -1\rangle$ state. However, owing to off-resonant scattering in the transport beams, a small fraction of the atoms undergoes transitions into the $|F = 2\rangle$ hyperfine state manifold.

At the position of the cavity mode, the atoms are loaded into a crossed-beam dipole trap formed by one of the transport beams and an additional, horizontal dipole beam with a waist radius of $w_x = w_z = 27 \mu\text{m}$ (see Fig. 1). A final stage of evaporative cooling is performed by suitably lowering the laser power to final trapping frequencies $(\omega_x, \omega_y, \omega_z) = 2\pi \times (290, 43, 277)$ Hz, ending up with an almost pure condensate of 2.2×10^5 atoms.

The ultrahigh-finesse cavity has a length of 176 μm and consists of symmetric mirrors with a 75 mm radius of curvature, resulting in a mode waist radius of 25 μm . A slight birefringence splits the resonance frequency of the empty cavity for the two orthogonal, principal polarization axes by 1.7 MHz. With the relevant cavity QED parameters $(g_0, \kappa, \gamma) = 2\pi \times (10.6, 1.3, 3.0)$ MHz, the system is in the strong coupling regime. The length of the cavity is actively stabilized using a laser at 830 nm (ref. 26). The intracavity intensity of the stabilization light gives rise to an additional dipole potential of $2.4E_{\text{rec}}$, with the recoil energy defined as $E_{\text{rec}} = \hbar^2/(2m\lambda^2)$, where m is the mass of the atom. The chemical potential $\mu = 1.8E_{\text{rec}}$ of 2.2×10^5 trapped atoms is comparable to the depth of this one-dimensional lattice, so that long-range phase coherence is well established in the atomic gas. The 1/e lifetime of the atoms in the combined trap was measured to be 2.8 s.

¹Institute for Quantum Electronics, ETH Zürich, 8093 Zürich, Switzerland. ²Laboratoire Charles Fabry, Institut d'Optique, Campus Polytechnique, RD 128, F91127 Palaiseau cedex, France. ³Cavendish Laboratory, University of Cambridge, Cambridge CB3 0HE, UK.

To find the eigenenergies of the coupled BEC–cavity system for a single excitation, we perform transmission spectroscopy with a weak, linearly polarized probe laser of frequency ω_p . To this end, the resonance frequency of the empty cavity is stabilized to a frequency ω_c , which in general is detuned by a variable frequency $\Delta_c = \omega_c - \omega_a$ with respect to the frequency ω_a of the $|F=1\rangle \rightarrow |F'=2\rangle$ transition of the D₂ line of ⁸⁷Rb. The transmission of the probe laser through the cavity is monitored as a function of its detuning $\Delta_p = \omega_p - \omega_a$ (see Fig. 2). The two orthogonal circular polarizations of the transmitted light are separated and detected with single-photon counting modules. The overall detection efficiency for an intracavity photon is 5%. To probe the system in the weak excitation limit, the probe laser intensity is adjusted such that the mean intracavity photon number is always below the critical photon number $n_0 = \gamma^2/(2g_0^2) = 0.04$. A magnetic field of 0.1 G, oriented parallel (within 10%) to the cavity axis provides a quantization axis.

From individual recordings of the cavity transmission as shown in Fig. 2 we map out the low-excitation spectrum of the coupled system as a function of Δ_c (see Fig. 3). After resonant excitation we do not detect an influence on the BEC in absorption imaging for large atom numbers (see Fig. 1). For small BECs of the order of 5,000 atoms we observe a loss of 50% of the atoms after resonant probing. The normal mode splitting at $\Delta_c = 0$ amounts to 7 GHz for σ^+ polarization, which results in a collective cooperativity of $C = Ng^2/(2\kappa\gamma) = 1.6 \times 10^6$. The splitting for the σ^- component is smaller, because the dipole matrix elements for transitions starting in $|1, -1\rangle$ driven by this polarization are smaller than those for σ^+ .

A striking feature of the energy spectrum in Fig. 3 is a second avoided crossing at probe frequencies resonant with the bare atomic transitions $|F=2\rangle \rightarrow |F'=1, 2, 3\rangle$. It is caused by the presence of atoms in the $|F=2\rangle$ hyperfine ground state. This avoided crossing

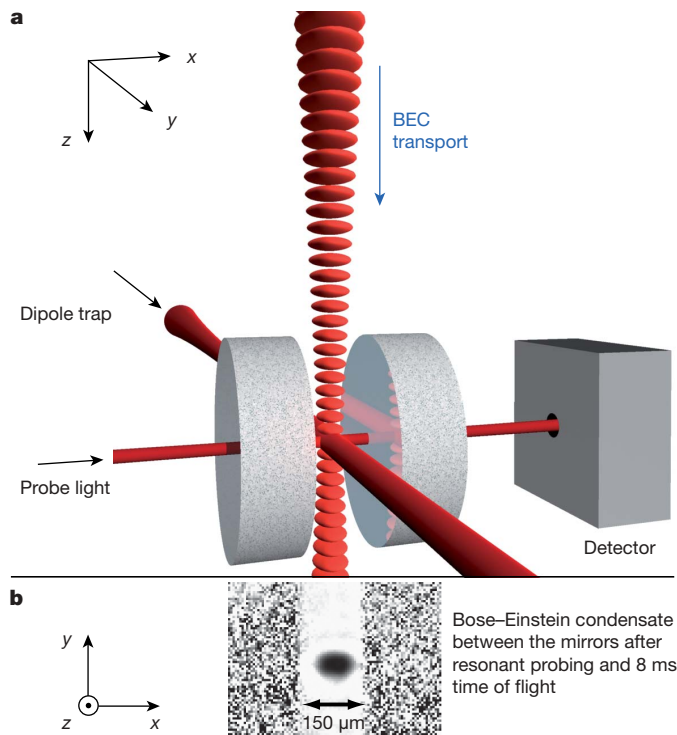


Figure 1 | Experimental situation. **a**, 36 mm above the cavity, 3.5×10^6 ultracold atoms are loaded into the dipole potential of a vertically oriented one-dimensional optical lattice. This trumpet-shaped standing wave has its waist inside the ultrahigh-finesse cavity and is composed of two counter-propagating laser beams. A translation of the lattice transports the atoms into the cavity mode. There, they are loaded into a crossed-beam dipole trap formed by a focused beam oriented along the y axis and one of the transport beams. **b**, Almost pure condensates with 2.2×10^5 atoms are obtained.

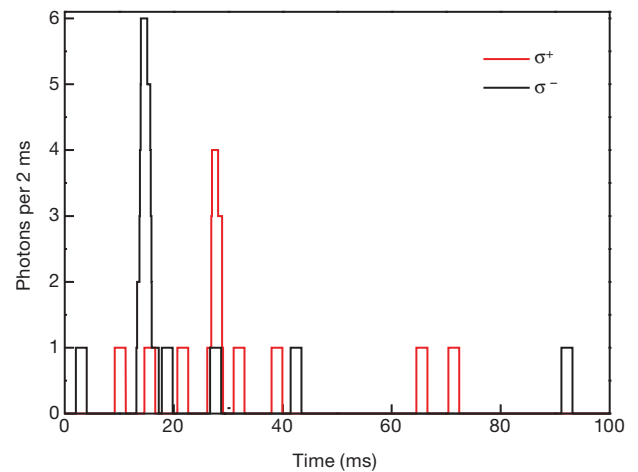


Figure 2 | Cavity transmission for the σ^+ and σ^- polarization component. The probe laser frequency is scanned at a speed of 25 MHz ms^{-1} while the cavity detuning is fixed. The original transmission data, recorded with a resolution of $0.4 \mu\text{s}$, is averaged over 2 ms using a sliding average. A single peak for each polarization can clearly be distinguished from the background of about 60 dark counts per second.

is located at a cavity detuning where the eigenenergy branch of the BEC–cavity system with no atoms in $|F=2\rangle$ would intersect the energy lines of the atomic transitions $|F=2\rangle \rightarrow |F'=1, 2, 3\rangle$. Accordingly, the avoided crossing is shifted by approximately $Ng^2/\Delta_p = 2\pi \times 1.8 \text{ GHz}$ with respect to the intersection of the empty cavity resonance with the bare atomic transition frequencies. From a theoretical analysis (see Methods), we find the size of the $|F=2\rangle$ minority component to be 1.7% of the total number of atoms.

Our near-planar cavity supports higher-order transverse modes equally spaced by 18.5 GHz, which is of the order of the collective coupling $g\sqrt{N}$ in our system. In general, the presence of one additional mode with the same coupling but detuned from the TEM_{00}

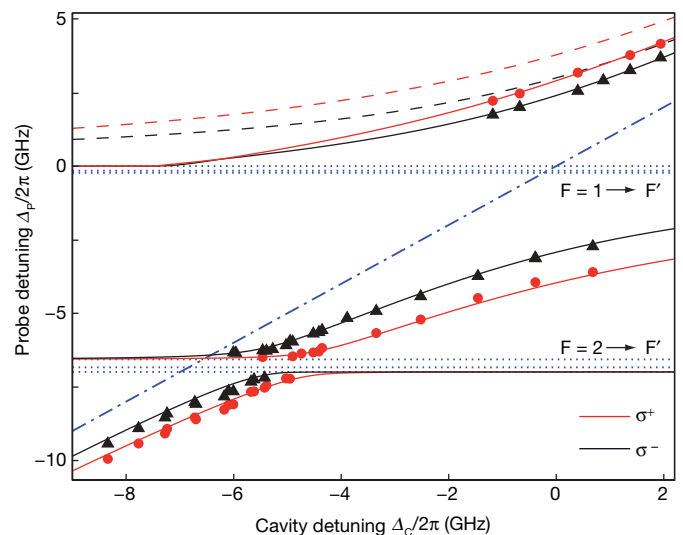


Figure 3 | Energy spectrum of the coupled BEC–cavity system. The data points are measured detunings of resonances for σ^+ (red circles) and σ^- (black triangles) polarized light. Each data point is the average of three measurements with an uncertainty of about 25 MHz. The solid lines are the result of a theoretical model (see Methods). Bare atomic resonances are shown as dotted lines, whereas the empty cavity resonance of the TEM_{00} mode is plotted as a dashed-dotted line. Note the asymmetry in the splitting at $\Delta_c = 0$ caused by the influence of higher-order transverse modes. Neglecting this influence, the eigenenergies shown by the dashed lines would be expected where the free parameters were adjusted to fit the spectrum for $\Delta_p < 0$.

mode by Δ_c would shift the resonance frequencies at $\Delta_c = 0$ to first order by $Ng^2/(2\Delta_c)$. In our system, this results in a clearly visible change of the energy spectrum with respect to a system with a single cavity mode only (see dashed lines in Fig. 3). This can be seen as a variant of the “superstrong coupling regime”²⁸, in which the coupling between atoms and the light field is of the order of the free spectral range of the cavity.

We describe the BEC–cavity system in a fully quantized theoretical model (see Methods), which yields the eigenenergies of the coupled system. Good agreement between the measured data and the model is found (see Fig. 3) for 154,000 atoms in the $|1, -1\rangle$ state and for 2,700 atoms distributed over the Zeeman sublevels of the $|F = 2\rangle$ state, with the majority in $|2, -1\rangle$. The substantial influence of the higher-order transverse modes is modelled for simplicity by the coupling of the BEC to one additional effective cavity mode.

To test the square-root dependence of the normal mode splitting on the number of atoms in the BEC, a second measurement was conducted. We set the cavity frequency to $\Delta_c = 0$ and record the detuning of the lower coupled state from the bare atomic resonance $|F = 1\rangle \rightarrow |F' = 2\rangle$ as a function of the number of atoms as displayed in Fig. 4. The atom number was varied between 2,500 and 200,000, determined from separately taken absorption images with an estimated statistical error of $\pm 10\%$; possible systematic shifts are estimated to be within $\pm 7\%$. The dependence of $|\Delta_p|$ on the number of atoms is well described by a square root, as expected from the Tavis–Cummings model (dashed lines). However, for a weakly interacting BEC the size of the atomic cloud—and thus the spatial overlap with the cavity mode—depends on the atom number. Our more detailed model, which includes this effect, as well as the influence of higher-order cavity modes, yields maximum single-atom couplings of $g_{\sigma^+} = 2\pi \times (14.4 \pm 0.3)$ MHz and $g_{\sigma^-} = 2\pi \times (11.3 \pm 0.2)$ MHz for the two polarization components (solid lines). The ratio of these two couplings is 1.27 ± 0.03 and agrees with the ratio of 1.29 that is obtained from the effective Clebsch–Gordan coefficients for the σ^+ and σ^- transitions starting in state $|1, -1\rangle$.

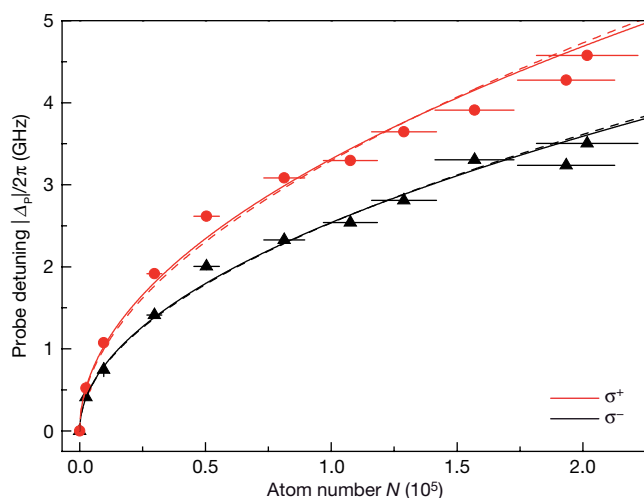


Figure 4 | Shift of the lower resonance of the coupled BEC–cavity system from the bare atomic resonance. The cavity was locked at $\Delta_c = 0$. σ^+ and σ^- polarization are shown as red circles and black triangles, respectively. Each data point is the average of three measurements. The atom number was determined separately from absorption images with an assumed error of $\pm 10\%$; the vertical error bars are too small to be resolved. The dashed lines are fits of the square root dependence on the atom number, as predicted by the Tavis–Cummings model. The solid lines are fits of a more detailed theoretical model (see Methods) resulting in maximum coupling rates $g_{\sigma^+} = 2\pi \times (14.4 \pm 0.3)$ MHz and $g_{\sigma^-} = 2\pi \times (11.3 \pm 0.2)$ MHz. The ratio of the two coupling rates of 1.27 ± 0.03 agrees with the expected ratio of 1.29 of the corresponding Clebsch–Gordan coefficients.

The coupling of a single mode of a matter-wave field to a single cavity mode opens a route to new experiments. It facilitates the manipulation and study of statistical properties of quantum-degenerate matter-wave fields by a quantized optical field, or even the generation of entanglement between these two fields^{21,29}. The detection of single atoms falling through the cavity has already been demonstrated with this set-up²². In principle, the detection of small impurity components embedded in a large BEC presented here can also be extended to single atoms. This is an important step towards the realization of schemes aiming at the cooling of qubits immersed in a large BEC³⁰.

METHODS SUMMARY

Optical transport. The transport of the atoms into the cavity is accomplished in $T = 100$ ms with a maximum acceleration of $a = 22.4 \text{ m s}^{-2}$. The standing wave used to transport the atoms has its waist $(w_x, w_y) = (25, 50) \mu\text{m}$ centred inside the cavity and is locked to a ^{133}Cs resonance at a wavelength of 852 nm. The intensity and frequency of each beam are precisely controlled by acousto-optical modulators, which are driven by two phase-locked, homebuilt direct digital synthesis generators. The frequency difference δ between the two counter-propagating waves follows $\delta(t) = [1 - \cos(2\pi t/T)]\delta_{\text{max}}/2$, with a maximum detuning of $\delta_{\text{max}} = 1,670$ kHz. With the maximally available power of 76 mW per beam the trap depth at the position of the magnetic trap is 1.1 μK . During transport, the power in the laser beams is kept constant until the intensity at the position of the atoms has increased by a factor of ten. Subsequently, this intensity is kept constant.

Theoretical model. To gain understanding of the presented measurements we have developed a fully quantized theoretical description of the coupled BEC–cavity system. Our model includes all Zeeman sublevels in the $5^2S_{1/2}$ and $5^2P_{3/2}$ state manifolds of ^{87}Rb and both orthogonal polarizations of the TEM_{00} cavity mode. For simplicity, the effect of higher-order transverse cavity modes is modelled by the effective coupling to one additional mode which is detuned from the TEM_{00} mode by $\Delta_c = 2\pi \times 18.5$ GHz. The free parameters of the model are the coupling strength between this effective mode and the BEC and the population of the several ground states in the condensate. Good agreement with the measured energy spectrum is found for the ground-state population given in the main text and a coupling between BEC and effective cavity mode that is $r = 1.2$ times the coupling to the TEM_{00} mode.

Full Methods and any associated references are available in the online version of the paper at www.nature.com/nature.

Received 21 June; accepted 20 July 2007.

- van Enk, S. J., Kimble, H. J. & Mabuchi, H. Quantum information processing in cavity-QED. *Quantum Inform. Process.* **3**, 75–90 (2004).
- Raimond, J. M., Brune, M. & Haroche, S. Colloquium: manipulating quantum entanglement with atoms and photons in a cavity. *Rev. Mod. Phys.* **73**, 565–582 (2001).
- Walther, H. Quantum phenomena of single atoms. *Adv. Chem. Phys.* **122**, 167–197 (2002).
- Kimble, H. J. Strong interactions of single atoms and photons in cavity QED. *Phys. Scr.* **T76**, 127–137 (1998).
- Mabuchi, H. & Doherty, A. C. Cavity quantum electrodynamics: coherence in context. *Science* **298**, 1372–1377 (2002).
- Boozer, A. D., Boca, A., Miller, R., Northup, T. E. & Kimble, H. J. Cooling to the ground state of axial motion for one atom strongly coupled to an optical cavity. *Phys. Rev. Lett.* **97**, 083602 (2006).
- Nußmann, S. *et al.* Vacuum-stimulated cooling of single atoms in three dimensions. *Nature Phys.* **1**, 122–125 (2005).
- Sauer, J. A., Fortier, K. M., Chang, M. S., Hamley, C. D. & Chapman, M. S. Cavity QED with optically transported atoms. *Phys. Rev. A* **69**, 051804 (2004).
- Anderson, M. H., Ensher, J. R., Matthews, M. R., Wieman, C. E. & Cornell, E. A. Observation of Bose–Einstein condensation in a dilute atomic vapor. *Science* **269**, 198–201 (1995).
- Pellizzari, T., Gardiner, S. A., Cirac, J. I. & Zoller, P. Decoherence, continuous observation, and quantum computing: a cavity QED model. *Phys. Rev. Lett.* **75**, 3788–3791 (1995).
- Duan, L.-M., Lukin, M. D., Cirac, J. I. & Zoller, P. Long-distance quantum communication with atomic ensembles and linear optics. *Nature* **414**, 413–418 (2001).
- Cirac, J. I., Zoller, P., Kimble, H. J. & Mabuchi, H. Quantum state transfer and entanglement distribution among distant nodes in a quantum network. *Phys. Rev. Lett.* **78**, 3221–3224 (1997).
- Horak, P., Barnett, S. M. & Ritsch, H. Coherent dynamics of Bose–Einstein condensates in high-finesse optical cavities. *Phys. Rev. A* **61**, 033609 (2000).

14. Lewenstein, M. *et al.* Travelling to exotic places with ultracold atoms. In *Atomic Physics 20* Vol. 869 of *XX International Conference on Atomic Physics (ICAP) 2006* 201–211 (American Institute of Physics, New York, 2006).
15. Jaynes, E. & Cummings, F. Comparison of quantum and semiclassical radiation theories with application to the beam maser. *Proc. IEEE* **51**, 89–109 (1963).
16. Tavis, M. & Cummings, F. W. Exact solution for an n-molecule radiation-field hamiltonian. *Phys. Rev.* **170**, 379–384 (1968).
17. Leslie, S., Shenvi, N., Brown, K. R., Stamper Kurn, D. M. & Whaley, K. B. Transmission spectrum of an optical cavity containing N atoms. *Phys. Rev. A* **69**, 043805 (2004).
18. Raizen, M. G., Thompson, R. J., Brecha, R. J., Kimble, H. J. & Carmichael, H. J. Normal-mode splitting and linewidth averaging for two-state atoms in an optical cavity. *Phys. Rev. Lett.* **63**, 240–243 (1989).
19. Tuchman, A. K. *et al.* Normal-mode splitting with large collective cooperativity. *Phys. Rev. A* **74**, 053821 (2006).
20. Colombe, Y. *et al.* Strong atom-field coupling for Bose-Einstein condensates in an optical cavity on a chip. Preprint at (<http://arxiv.org/abs/0706.1390>) (2007).
21. Mekhov, I. B., Maschler, C. & Ritsch, H. Probing quantum phases of ultracold atoms in optical lattices by transmission spectra in cavity quantum electrodynamics. *Nature Phys.* **3**, 319–323 (2007).
22. Öttl, A., Ritter, S., Köhl, M. & Esslinger, T. Correlations and counting statistics of an atom laser. *Phys. Rev. Lett.* **95**, 090404 (2005).
23. Slama, S., Bux, S., Krenz, G., Zimmermann, C. & Courteille, P. W. Superradiant Rayleigh scattering and collective atomic recoil lasing in a ring cavity. *Phys. Rev. Lett.* **98**, 053603 (2007).
24. Murch, K. W., Moore, K. L., Gupta, S. & Stamper Kurn, D. M. Measurement of intracavity quantum fluctuations of light using an atomic fluctuation bolometer. Preprint at (<http://arxiv.org/abs/0706.1005>) (2007).
25. Gupta, S., Moore, K. L., Murch, K. W. & Stamper Kurn, D. M. Cavity nonlinear optics at low photon numbers from collective atomic motion. Preprint at (<http://arxiv.org/abs/0706.1052>) (2007).
26. Öttl, A., Ritter, S., Köhl, M. & Esslinger, T. Hybrid apparatus for Bose-Einstein condensation and cavity quantum electrodynamics: Single atom detection in quantum degenerate gases. *Rev. Sci. Instrum.* **77**, 063118 (2006).
27. Kuhr, S. *et al.* Deterministic delivery of a single atom. *Science* **293**, 278–280 (2001).
28. Meiser, D. & Meystre, P. Superstrong coupling regime of cavity quantum electrodynamics. *Phys. Rev. A* **74**, 065801 (2006).
29. Moore, M. G., Zobay, O. & Meystre, P. Quantum optics of a Bose-Einstein condensate coupled to a quantized light field. *Phys. Rev. A* **60**, 1491–1506 (1999).
30. Daley, A. J., Fedichev, P. O. & Zoller, P. Single-atom cooling by superfluid immersion: a nondestructive method for qubits. *Phys. Rev. A* **69**, 022306 (2004).

Acknowledgements We thank A. Öttl for early contributions to the experiment, R. Jördens and A. Frank for developing the direct digital synthesis generators used for the optical transport, H. Ritsch and A. Imamoglu for discussions and OLAQUI and QSIT for funding. T.B. acknowledges funding by an EU Marie Curie fellowship.

Author Information Reprints and permissions information is available at www.nature.com/reprints. The authors declare no competing financial interests. Correspondence and requests for materials should be addressed to T.E. (esslinger@phys.ethz.ch).

METHODS

To characterize the coupled BEC–cavity system theoretically, we start with the second-quantized hamiltonian describing the matter–light interaction in the electric-dipole and rotating-wave approximation²⁹. We take all hyperfine states including their Zeeman sublevels in the $5^2S_{1/2}$ and $5^2P_{3/2}$ state manifolds of ^{87}Rb into account and describe the cavity degrees of freedom by two orthogonal linear polarizations of the TEM_{00} mode. We choose the quantization axis, experimentally provided by a small magnetic field, to be oriented parallel to the cavity axis. The near-planar cavity supports higher-order transverse modes equally spaced by $\Delta_t = 2\pi \times 18.5$ GHz. To incorporate the coupling to all higher-order transverse modes we include one additional effective cavity mode in our model with its resonance frequency shifted by Δ_t with respect to that of the TEM_{00} mode.

Considering only one spatial atomic mode for the ground-state manifold and another one for the excited-state manifold, the hamiltonian of the uncoupled system reads

$$\hat{H}_0 = \sum_i \hbar\omega_{g_i} \hat{g}_i^\dagger \hat{g}_i + \sum_j \hbar\omega_{e_j} \hat{e}_j^\dagger \hat{e}_j + \sum_{k=0}^1 \sum_{p=\rightarrow, \uparrow} \hbar\omega_k \hat{a}_{k,p}^\dagger \hat{a}_{k,p}$$

where the indices i and j label the states $5^2S_{1/2} |F, m_F\rangle$ and $5^2P_{3/2} |F', m_{F'}\rangle$, respectively. The operators \hat{g}_i^\dagger (or \hat{g}_i) and \hat{e}_j^\dagger (or \hat{e}_j) create (or annihilate) an atom in the mode of the corresponding ground and excited states with frequencies ω_{g_i} and ω_{e_j} . The operators $\hat{a}_{k,p}^\dagger$ (or $\hat{a}_{k,p}$) create (or annihilate) a photon with energy $\hbar\omega_k$ and linear polarization p in the cavity mode k , where $k = 0, 1$ labels the TEM_{00} mode and the additional effective cavity mode, respectively.

The coupling between the BEC and the cavity is described by the interaction hamiltonian

$$\hat{H}_{\text{int}} = -i\hbar \sum_{k=0}^1 \sum_{p=\rightarrow, \uparrow} \sum_{i,j} g_{ij}^{k,p} \hat{e}_j^\dagger \hat{a}_{k,p} \hat{g}_i + \text{h.c.}$$

where $g_{ij}^{k,p}$ denotes the coupling strength for the transition $i \rightarrow j$ driven by the cavity mode k with polarization p , and h.c. is the hermitian conjugate. For the TEM_{00} mode the coupling strength $g_{ij}^{0,p}$ depends on the dipole matrix element \mathcal{D}_{ij}^p for the transition $i \rightarrow j$ driven by the polarization p , the mode volume V_0 , and the overlap \mathcal{U}_0 between the two spatial atomic modes and the TEM_{00} mode:

$$g_{ij}^{0,p} = \mathcal{D}_{ij}^p \sqrt{\frac{\hbar\omega_0}{2\epsilon_0 V_0}} \mathcal{U}_0$$

We numerically calculated the ground state of the Gross–Pitaevskii equation in the potential formed by the dipole trap and the cavity stabilization light for $N = 2 \times 10^5$ atoms, and found the spatial overlap between BEC and TEM_{00} mode to be $\mathcal{U}_0 = 0.63$. Because of the position uncertainty of the BEC relative to the cavity mode, the overlap might deviate by up to 20% from this value. The repulsive interaction between the atoms leads to a slight decrease in \mathcal{U}_0 with increasing atom number, which was found numerically to follow $\mathcal{U}_0(N) = \sqrt{0.5(1 - 0.0017N^{0.34})}$. For the coupling strength to the additional effective cavity mode we assume $g_{ij}^{1,p} = r g_{ij}^{0,p}$, with r being a free parameter.

The initial atomic population of the several ground states i given by the free parameters N_i is relevant for the form of the energy spectrum of the coupled BEC–cavity system. To find the energy spectrum in the weak excitation limit we can restrict the analysis to states containing a single excitation. These are the states $|1_{k,p}; N_1, \dots, N_8; 0\rangle$, where one photon with polarization p is present in the mode k and all atoms are in the ground-state manifold, and also all possible states $|0_{k,p}; N_1, \dots, N_i - 1, \dots, N_8; 1_j\rangle$, where no photon is present and one atom was transferred from the ground state i to the excited state j . Diagonalization of the hamiltonian $\hat{H} = \hat{H}_0 + \hat{H}_{\text{int}}$ in the truncated Hilbert space spanned by these states yields the eigenspectrum of the coupled system as a function of the cavity detuning Δ_c . The relevant transition energies with respect to the energy of the initial ground state are plotted in Fig. 3.

The detuning of the lower resonance branch at $\Delta_c = 0$ is a function of the atom number and given by

$$|A_p| = \mathcal{U}_0(N) g_{\sigma^\pm} \sqrt{N} + \frac{(\mathcal{U}_0(N) r g_{\sigma^\pm})^2 N}{2\Delta_t} + \mathcal{O}(1/\Delta_t^2)$$

Fitting this dependence to the data in Fig. 4 yields the maximum coupling strengths g_{σ^\pm} for the two polarization components σ^\pm .

LETTERS

Strong atom–field coupling for Bose–Einstein condensates in an optical cavity on a chip

Yves Colombe^{1*}, Tilo Steinmetz^{1,2*}, Guilhem Dubois¹, Felix Linke^{1†}, David Hunger² & Jakob Reichel¹

An optical cavity enhances the interaction between atoms and light, and the rate of coherent atom–photon coupling can be made larger than all decoherence rates of the system. For single atoms, this ‘strong coupling regime’ of cavity quantum electrodynamics^{1,2} has been the subject of many experimental advances. Efforts have been made to control the coupling rate by trapping^{3,4} the atom and cooling^{5,6} it towards the motional ground state; the latter has been achieved in one dimension so far⁵. For systems of many atoms, the three-dimensional ground state of motion is routinely achieved⁷ in atomic Bose–Einstein condensates (BECs). Although experiments combining BECs and optical cavities have been reported recently^{8,9}, coupling BECs to cavities that are in the strong-coupling regime for single atoms has remained an elusive goal. Here we report such an experiment, made possible by combining a fibre-based cavity¹⁰ with atom-chip technology¹¹. This enables single-atom cavity quantum electrodynamics experiments with a simplified set-up and realizes the situation of many atoms in a cavity, each of which is identically and strongly coupled to the cavity mode¹². Moreover, the BEC can be positioned deterministically anywhere within the cavity and localized entirely within a single antinode of the standing-wave cavity field; we demonstrate that this gives rise to a controlled, tunable coupling rate. We study the heating rate caused by a cavity transmission measurement as a function of the coupling rate and find no measurable heating for strongly coupled BECs. The spectrum of the coupled atoms–cavity system, which we map out over a wide range of atom numbers and cavity–atom detunings, shows vacuum Rabi splittings exceeding 20 gigahertz, as well as an unpredicted additional splitting, which we attribute to the atomic hyperfine structure. We anticipate that the system will be suitable as a light–matter quantum interface for quantum information¹³.

The interaction of an ensemble of N atoms with a single mode of radiation has been a recurrent theme in quantum optics at least since the work of Dicke¹⁴, who showed that under certain conditions the atoms interact with the radiation collectively, giving rise to new effects such as superradiance. Recently, collective interactions with weak fields, with and without a cavity, have become a focus of theoretical and experimental investigations, especially since it became clear that they can turn the ensemble into a quantum memory^{13,15}. Such a memory would become a key element for processing quantum information^{13,16} if realized with near-unit conversion efficiency and long storage time. The figure of merit determining the probability of converting an atomic excitation into a cavity photon (a ‘memory qubit’ into a ‘flying qubit’) is the collective cooperativity $C_N = g_N^2 / (2\kappa\gamma)$, where g_N is the collective coupling strength¹⁷ between the ensemble and the field, 2κ is the cavity photon decay rate and 2γ the atomic spontaneous emission rate. (Up to a factor of order 1, C_N is the single-pass optical depth of the atomic sample multiplied by the cavity finesse \mathcal{F} .) For weak excitation, to which

we restrict ourselves throughout this Letter, $g_N = \sqrt{N}g_1$, where $\bar{g}_1^2 = \int \frac{\rho(\mathbf{r})}{N} |g_1(\mathbf{r})|^2 d\mathbf{r}$, $g_1(\mathbf{r})$ is the position-dependent single-atom coupling strength and $\rho(\mathbf{r})$ is the atomic density distribution: the ensemble couples to the mode as a single ‘superatom’ with a coupling strength increased by \sqrt{N} . In the strong-coupling regime $g_N > \kappa, \gamma$, which is realized in our cavity even for $N = 1$, the atomic ensemble oscillates between its ground state and a symmetric excited state where a single excitation is shared by all the atoms.

The coupled atoms–cavity system has dressed states of energies

$$E_{\pm} = \hbar\omega_A + \frac{\hbar}{2} \left(\Delta_C \pm \sqrt{\Delta_C^2 + 4g_N^2} \right) \quad (1)$$

where $\Delta_C = \omega_C - \omega_A$, ω_C and ω_A being the cavity and atom resonance frequencies. When the cavity is tuned to atomic resonance ($\Delta_C = 0$), these states are separated by the vacuum Rabi frequency^{1,2} $2g_N$. The collective interaction and \sqrt{N} scaling are not a consequence of atomic quantum statistics, but apply to thermal and quantum degenerate bosons and fermions, and even to non-identical particles having the same transition moment^{2,18}, for a wide range of conditions in which interparticle correlations in the initial atomic state are negligible (see Supplementary Information). Nevertheless, the spatial coherence, fundamentally lowest kinetic energy and smallest size of a BEC influence its interaction with light, and make it the most desirable atomic state in many situations of conceptual and practical interest: the BEC makes it possible to maximize the coupling and avoid decoherence effects associated with spatial inhomogeneities and with atomic motion¹⁵. In the free-space case, some of these aspects have been shown in detail for the case of superradiance, where reduced Doppler broadening in the condensate increased the coherence time by a factor of 30 over a thermal cloud at the transition temperature, making the effect observable only in the BEC¹⁹.

Here we take advantage of the fact that the BEC has the smallest possible position spread in a given trap. This allows us to load the BEC into a single site of a far-detuned intracavity optical lattice. By choosing the lattice site, we achieve well-defined, maximized atom–field coupling in the standing-wave cavity field, where the local coupling varies as $g_1(x, r_{\perp}) = g_0 \cos(2\pi x / \lambda_C) \exp(-r_{\perp}^2 / w^2)$ (here x and r_{\perp} are respectively the longitudinal and transverse atomic coordinates, and w and $\lambda_C = 2\pi c / \omega_C$ are respectively the mode radius and wavelength). This is an important improvement for applications such as the quantum memory. Furthermore, BEC–cavity quantum electrodynamics (QED) experiments such as ours and a simultaneous similar one¹² can be used to study BECs in the regime of very small atom numbers where the mean-field approximation breaks down, and may allow observation of effects such as a predicted slight modification of the refractive index of the atomic sample close to the BEC transition²⁰, and differences between quantum phases in

¹Laboratoire Kastler Brossel, ENS/UPMC-Paris 6/CNRS, 24 rue Lhomond, 75005 Paris, France. ²Max-Planck-Institut für Quantenoptik/LMU, Schellingstr. 4, 80799 München, Germany. [†]Present address: BMW Group, Abt. Instrumentierung und Displays, Knorrstr. 147, D-80788 München, Germany.

*These authors contributed equally to this work.

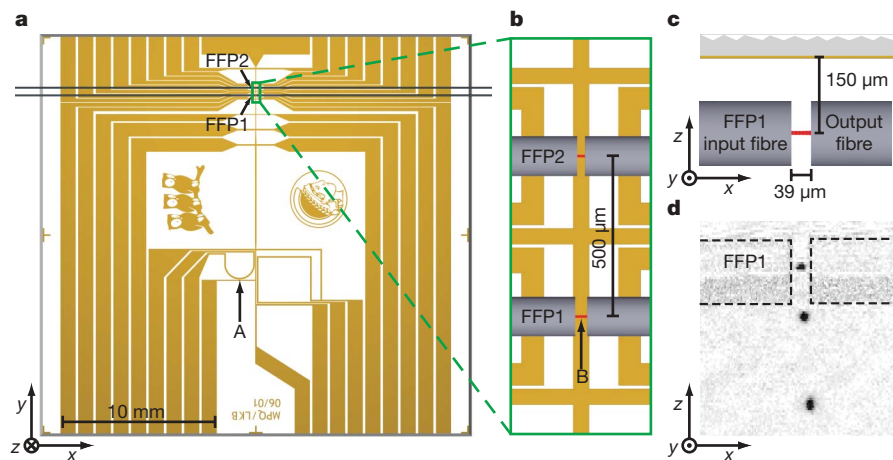


Figure 1 | Experimental set-up. **a**, Layout of the atom chip. “A” indicates the location of the first magnetic trap, loaded from a magneto-optical trap. **b**, Close-up view of the two fibre Fabry–Perot (FFP) optical cavities that are mounted on the chip. Cavity modes are drawn to scale in red. The BEC is produced in a magnetic trap and positioned in the FFP1 mode (‘B’).

transmission spectra of cavities containing a degenerate gas in an optical lattice²¹.

We have developed a novel type of fibre-based Fabry–Perot (FFP) cavity^{10,22}, which achieves large single-atom peak coupling rates g_0 through reduced mode volume and high mirror curvature (see Methods), without the difficulties associated with evanescent fields in microtoroidal²³ or microsphere cavities. The set-up is shown in Fig. 1. The combination ($g_0 = 2\pi \times 215$ MHz, $\kappa = 2\pi \times 53$ MHz, $\gamma = 2\pi \times 3$ MHz) places our cavity in the single-atom strong coupling regime, and leads to a high single-atom cooperativity $C_0 = 145$. Despite its finesse, which is an order of magnitude below that of standard cavities used in cavity QED, the performance data of our cavity are comparable or superior to most of those, while all the dynamics occurs on a faster timescale. Two laser beams are coupled into the cavity through the input fibre—a weak tunable probe beam

(frequency ω_L), and an optional far-detuned beam at $\lambda_D = 830.6$ nm used to form a one-dimensional optical lattice along the cavity axis. Using a combination of chip currents and external magnetic fields, a BEC or cold thermal cloud of ^{87}Rb atoms in the $|F=2, m_F=2\rangle$ ground state is prepared inside the cavity, and then positioned anywhere within the cavity mode. The slow axis of the magnetic trap can be oriented along the cavity axis x or perpendicular to it along y . Atom–field interaction is studied either directly in this trap, or after switching on the far-detuned lattice to increase the confinement and gain control over the coupling rate. For magnetic trapping and also for weak lattices, we are able to observe an intact BEC after its interaction with the cavity field (Fig. 1d). For lattices with trapping frequency above $\nu_x \approx 20$ kHz, technical fluctuations in the lattice potential³, possibly due to laser intensity noise, heat up the condensate.

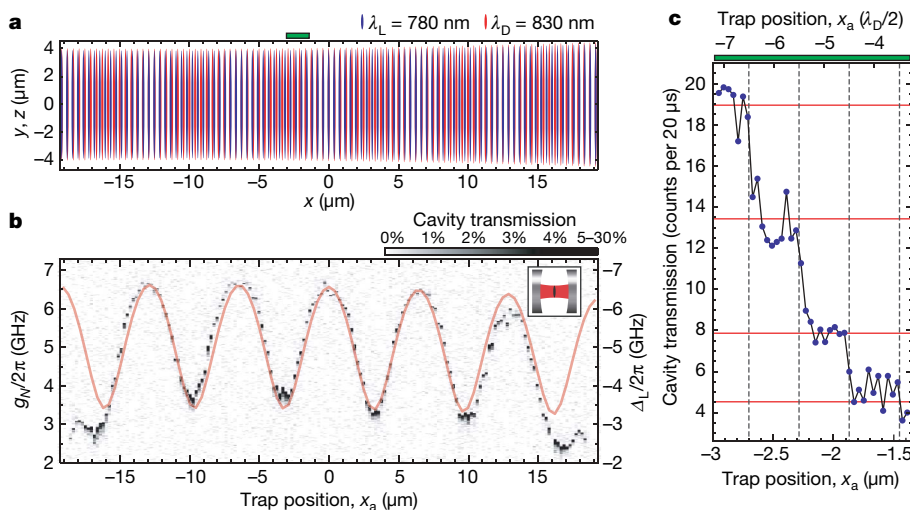


Figure 2 | Control of the coupling along the resonator axis. The BEC is brought to a position x_a on the cavity axis, and loaded into the optical lattice. **a**, The probe laser ($\lambda_L = 780.2$ nm) and optical lattice ($\lambda_D = 830.6$ nm) standing waves in the cavity have a variable overlap with 6.4 μm period. The green bar (top) indicates the region of the measurement in **c**. **b**, The loaded atoms show a strongly modulated coupling 3.4 GHz $\leq g_N(x_a)/2\pi \leq 6.6$ GHz, depending on the local overlap between lattice and probe field. The rapid decrease of g_N at the extremities of the mode is probably due to atom loss caused by collisions with the mirrors. The pictogram inset shows the orientation of the magnetic trap relative to the cavity mode. Probe intensity

corresponds to a mean intracavity photon number for a resonant cavity without atoms of $n_{\text{res}} \approx 5.5 \times 10^{-2}$. (Here and in the following experiments, we have checked that intensity-dependent peak shifts are negligible.) Maximum transmission in the figure corresponds to an intracavity photon number $n \approx 1.1 \times 10^{-2}$. **c**, The transmission of the cavity, probed at $\Delta_L = \Delta_C = 2\pi \times -100$ GHz with position increments $\delta x_a = 40$ nm, exhibits well-separated steps owing to the loading into successive single lattice sites. Vertical lines indicate the intensity minima of the optical lattice. Horizontal lines are expected transmission values with atoms localized in successive single lattice sites. Probe intensity: $n_{\text{res}} \approx 3.3 \times 10^{-2}$.

In the following, we describe three experiments that explore the main aspects of atoms–field interaction in our system. First, we study the position dependence of $g_N(x)$ and show that a full control is achieved. Second, we observe the dependence of g_N on atom number, and map out the energies of the dressed states. Finally, we investigate the heating of a condensate by the intracavity field.

To study the position dependence of $g_N(x)$, we start by placing a BEC containing $N \approx 1,000$ atoms at a position x_a on the cavity axis in a magnetic trap oriented along y ($\nu_{x,z} = 2.7$ kHz, $\nu_y = 230$ Hz, bias field $B_y \approx 1$ G). We then ramp up a tight optical lattice with trapping frequencies $\nu_x = 50$ kHz, $\nu_{y,z} = 2.4$ kHz. The loaded atoms are now strongly confined in the combined trap, even though no longer Bose-condensed owing to the technical heating. As the lattice and the probed cavity mode have different wavelengths λ_D and λ_L , their overlap is modulated with a period $\lambda_D \lambda_L / 2(\lambda_D - \lambda_L) = 6.4 \mu\text{m}$ (Fig. 2a). We measure $g_N(x_a)$ by sweeping the probe laser detuning $\Delta_L = \omega_L - \omega_A = 2\pi \times (+1 \dots -13)$ GHz in 50 ms, with cavity detuning $\Delta_C = \omega_C - \omega_A = 0$. A transmission peak occurs at $|\Delta_L| = g_N$ when the lower dressed state is excited. Figure 2b shows the result for x_a values spanning the full cavity length. We are able to reproduce the observed $g_N(x_a)$ by calculating the coupling of a gaussian cloud centred on a single lattice site. The corresponding fit (red line on Fig. 2b) using the cloud diameter $2\sigma_x$ as a free parameter gives the value $2\sigma_x = 130$ nm, from which we deduce $2\sigma_y = 2.7 \mu\text{m}$, $2\sigma_z = 1.8 \mu\text{m}$ based on the known ratio of the trapping frequencies and assuming thermal equilibrium ($T = 4.4 \mu\text{K}$). This fit gives a good indication of σ_x , but does not prove single-site loading because a similar fit is obtained when considering several clouds in adjacent sites, each with $2\sigma_x = 130$ nm.

To demonstrate unambiguously the transfer into a single lattice site, we measure the transmission as a function of x_a in the dispersive regime, $\Delta_L = \Delta_C = 2\pi \times -100$ GHz, where it depends on the atoms-induced cavity resonance shift $\delta\omega_C = g_N^2/\Delta_L$. If and only if single-site loading is achieved, transmission should change in steps between x_a values corresponding to adjacent lattice sites. We use reduced increments $\delta x_a = 40$ nm, a BEC with $N \approx 600$ and a magnetic trap with $\nu_{x,z} = 4$ kHz, $\nu_y = 230$ Hz. Using analytical formulas²⁴ for the one-dimensional/three-dimensional crossover regime applying to this BEC, we find a central radial diameter $2\sigma_{x,z} = 2 \times 1.37\sigma_{ho} = 330$ nm, where σ_{ho} is the harmonic-oscillator ground state radius. This BEC is loaded into a lattice with $\nu_x = 100$ kHz, $\nu_{y,z} = 4.8$ kHz (destroying the condensate, but producing stronger confinement along x), and the magnetic potential switched off. Figure 2c shows the transmission of the cavity. Each point is averaged over two experimental runs. Well-separated plateaus are observed, corresponding to discrete values of g_N in good agreement with the calculated transmissions for ensembles localized in a single lattice site with diameter $2\sigma_x = 100$ nm (horizontal lines). This experiment shows the deterministic transfer of the atom cloud into successively addressed single sites of the lattice, each of which is differently coupled to the cavity.

A crucial feature of the collective coupling is its scaling with atom number. Early strong-coupling cavity QED experiments measured this in an atomic-beam apparatus with fluctuations both in N and in the atomic spatial positions²⁵. In our experiment, a BEC or a strongly confined cold thermal cloud minimize position fluctuations and N remains fixed (as long as the interaction time is short enough to induce no significant losses, which is fulfilled here). We vary N by forced evaporation, which produces BECs for $N < 3,000$. The transmission is measured at $\Delta_C = 0$ while sweeping the probe laser, $\Delta_L = 2\pi \times (0 \dots \pm 13)$ GHz. N is determined independently by absorption imaging (which underestimates the number of atoms, see Methods). We can either perform the measurement after transferring the atoms into a combined trap (same parameters as Fig. 2b), or directly in the magnetic trap, without an optical lattice. The combined trap destroys BECs, but increases the coupling when loading large thermal clouds; BECs confined in the magnetic trap alone remain intact after the measurement. The small, but measurable,

difference shown in Fig. 3a between the BEC (circles) and thermal cloud (greyscale) spectra is in accord with what is expected from the different density distributions (see Methods). The vacuum Rabi splitting reaches $2g_N = 2\pi \times 24$ GHz for $N \approx 7,000$, corresponding to $C_N = 4.4 \times 10^5$. For $N < 1,000$, the dressed state frequencies E_{\pm}/\hbar have the expected $\pm\sqrt{N}g_1$ dependence, with $g_1 \approx 2\pi \times 200$ MHz. The slower increase of the coupling for higher N in the thermal cloud spectrum is due to the growing size of the sample. The anticrossing for $N \approx 2,000$ can be understood qualitatively on the reasonable assumption that a few atoms are in the $|F=1\rangle$ ground state. Atoms in $|F=2\rangle$ have transitions to the upper and lower dressed states at frequencies $\omega_A \pm g_N$, whereas $|F=1\rangle$ atoms have a transition at $\omega_A + \Delta_{\text{HFS}}$, $\Delta_{\text{HFS}} = 2\pi \times 6.8$ GHz being the ground state hyperfine splitting of ^{87}Rb . An anticrossing appears when the transition frequencies coincide at $g_N = \Delta_{\text{HFS}}$. However, this simple model, as well as the model used in ref. 12, cannot explain why the anticrossing occurs at larger detuning $\Delta_L \approx 2\pi \times 8.5$ GHz (see Supplementary Information). A complete understanding of this effect requires further investigation.

Figure 3b shows a measurement of the complete dressed-state spectrum (equation (1)). Conditions are as in Fig. 3a, but now $N \approx 750$ is held constant and Δ_C is varied. Again, the observed resonances are in good agreement with the expected eigenfrequencies

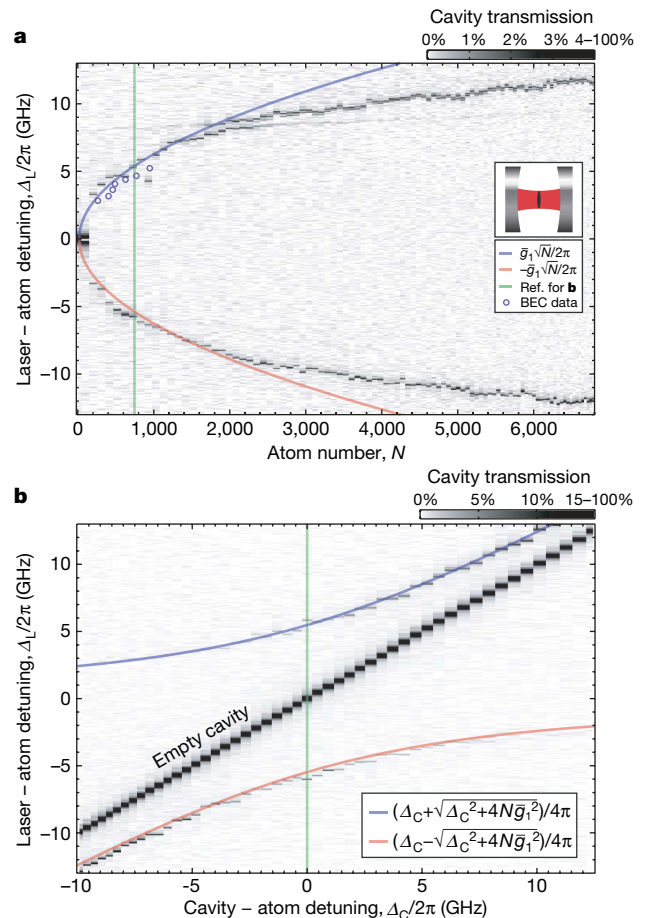


Figure 3 | Map of the energies of the dressed states. **a**, N is varied for $\Delta_C = 0$. Greyscale spectra were taken on non-condensed atoms, circles were measured with BECs. The blue and red curves are the expected resonances at $\Delta_L = \pm\sqrt{N}g_1$, where g_1 is fitted to the non-condensed data for $N < 1,000$. Inset, the pictogram shows the orientation of the trap. **b**, Δ_C is varied for constant $N \approx 750$; the empty cavity transmission ($N = 0$) is also recorded and superimposed for reference. The green lines indicate experimental runs in **a** and **b** with common parameters $N = 750$, $\Delta_C = 0$. Probe intensity: $n_{\text{res}} \approx 1.7 \times 10^{-1}$ (**a**) and $n_{\text{res}} \approx 1.5 \times 10^{-1}$ (**b**), leading to $n \approx 2.9 \times 10^{-2}$ (**a**) and $n \approx 5.5 \times 10^{-2}$ (**b**) with atoms, at transmission peak.

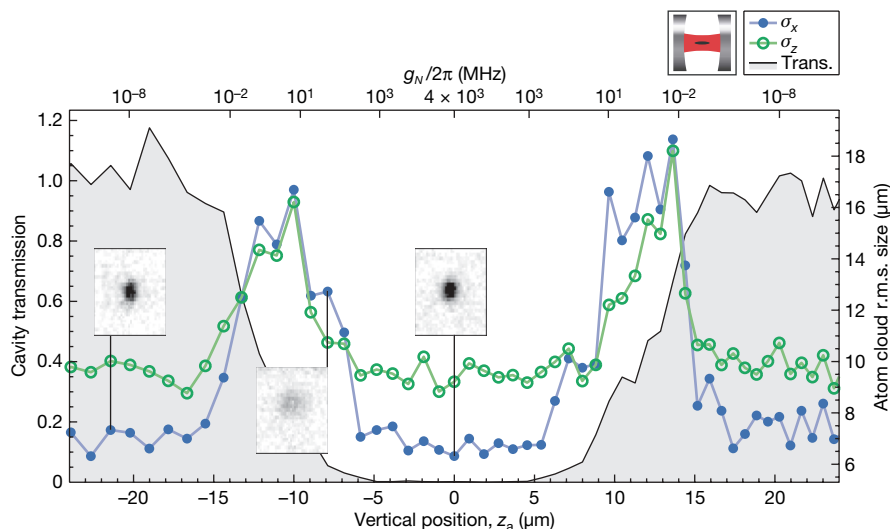


Figure 4 | Cavity-induced heating of the BEC at different transverse positions for $\Delta_L = \Delta_C = 0$. The pictogram at top right shows the orientation of the trap. g_N is varied by positioning the BEC at different heights z_a relative to the cavity axis. The BEC causes a drop in the cavity transmission (line with shading under) when it is sufficiently coupled to the mode. The r.m.s. size

along x (filled circles) and z (open circles) of the atom cloud after a 2.8 ms TOF shows two heating peaks when the BEC is positioned such that $g_N \approx 2\pi \times 10$ MHz, and no detectable heating for large coupling ($g_N > 2\pi \times 1$ GHz). Insets, examples of TOF images.

E_{\pm}/\hbar plotted for $\bar{g}_1 = 2\pi \times 200$ MHz. For large cavity detunings $|\Delta_C| \gg g_N$, the dressed states of the system evolve towards the uncoupled states $|g; N-1; e; 1; n=0\rangle$, where a single excitation is shared by all the atoms, and $|g; N; e; 0; n=1\rangle$, for which the cavity contains a photon. (Here $|g\rangle$ and $|e\rangle$ are respectively the atomic ground and excited states, and n is the intracavity photon number.)

Finally, we measure the heating of a BEC caused by the intracavity field. To minimize technical heating, we use a purely magnetic trap ($\nu_x = 230$ Hz, $\nu_{y,z} = 2.0$ kHz). The BEC contains $N \approx 800$ atoms, and we use $n_{\text{res}} \approx 3.9 \times 10^{-3}$, $\Delta_L = \Delta_C = 0$, and an interaction time of 10 ms. The BEC remains intact after the interaction with no measurable loss or heating if we maximize the coupling by positioning it on the cavity axis. We can vary the coupling by positioning the BEC at different heights z_a relative to the centre of the mode. Figure 4 shows that the cavity transmission quickly drops to zero as the coupling increases, because the strongly coupled system is no longer resonant for $\Delta_L = \Delta_C = 0$. (Note that the probe light is then mostly reflected from the non-resonant cavity, not scattered by the atoms.) The heating rate of the condensate is measured using time-of-flight imaging after the interaction (Fig. 4). It exhibits two peaks corresponding to measurements where g_N is high enough for the atoms to be excited, but still low enough to allow a non-zero intracavity field. In these regions the BEC is destroyed after the interaction, whereas it is left unaffected for $|z_a| > 18 \mu\text{m}$ and $|z_a| < 5 \mu\text{m}$, corresponding to $g_N < 2\pi \times 10^{-3}$ MHz and $g_N > 2\pi \times 10^3$ MHz. g_N is calculated from z_a and the measured N , averaging over the standing wave. The observed heating rate can be accounted for with a simple momentum-diffusion model^{26,27} (see Supplementary Information). This model predicts a peak heating rate about twice the observed value of ~ 400 cycles s^{-1} per atom, which is a satisfactory agreement given the uncertainty of our atom number calibration. For maximum coupling, the model yields a heating rate of 3×10^{-2} cycles s^{-1} per atom, which means that the whole BEC scatters an average of 0.24 photons during the interaction time.

In the experiments reported here, the small size of BECs was essential to produce an atomic ensemble with an extremely large, well-controlled, and homogeneous coupling rate. Although the quantum degeneracy appears to leave no trace in the interaction with photons, our system is well-suited to directly study BEC atom statistics⁸. The cavity should allow quantum non-demolition measurement of the BEC atom number²⁸, and can be used as a single-atom detector

with high quantum efficiency. Such a detector is sensitive to the internal atomic state and therefore highly suitable for use as a qubit detector. In the regime of atomic ensembles, compared to quantum light-matter interface experiments using non-condensed atoms in a cavity¹⁶, the BEC additionally offers collisional interaction between atoms that can reach large, well-defined values and can be used as a resource²⁹. Proposals exist, for example, to use Raman transitions for transferring a small, exactly known number N_e of BEC atoms into a different internal state³⁰. With the addition of a transverse laser beam, the cavity could be used to convert such state into a N_e -photon Fock state. Another, more technical advantage is the inherent fibre coupling of our cavities. We expect all of these properties to become important in future experiments.

METHODS SUMMARY

Our set-up features two FFP cavities mounted on an atom chip with $150 \mu\text{m}$ distance between their optical axes and the chip surface (Fig. 1). Both cavities are tunable independently over a full spectral range with piezoelectric actuators. Cavity FFP1 used in the experiments has length $d = 38.6 \mu\text{m}$, waist radius $w_0 = 3.9 \mu\text{m}$, finesse $\mathcal{F} = 37,000$ and field decay rate $\kappa = \pi c / (2\mathcal{F}d) = 2\pi \times 53$ MHz. The calculated maximum single-atom coupling rate is $g_0 = 2\pi \times 215$ MHz, yielding a resonant saturation photon number $n_0 = \gamma^2 / (2g_0^2) \approx 1 \times 10^{-4}$. The transmitted probe and lattice beams are separated after the output fibre, and the probe beam is detected with a photon-counting avalanche photodiode. The probe laser can be swept continuously over a range $\Delta_L = \omega_L - \omega_A = \pm 2\pi \times 15$ GHz, where ω_A is the frequency of the $5S_{1/2}[F=2] \rightarrow 5P_{3/2}[F'=3]$ transition of ^{87}Rb at $\lambda_A = 780.2$ nm. BEC preparation is similar to our previous work. Absorption imaging inside and below the cavity is used for temperature and atom number measurements. Several effects lead to an underestimation of N in these images; atom numbers extracted from the cavity QED measurements by using calculated \bar{g}_1 values are systematically higher by about a factor of 2.

Full Methods and any associated references are available in the online version of the paper at www.nature.com/nature.

Received 1 June; accepted 26 September 2007.

- Kimble, H. J. Strong interactions of single atoms and photons in cavity QED. *Phys. Scr.* **T76**, 127–137 (1998).
- Haroche, S. & Raimond, J.-M. *Exploring the Quantum: Atoms, Cavities and Photons* (Oxford Univ. Press, Oxford, UK, 2006).
- Ye, J., Vernooij, D. W. & Kimble, H. J. Trapping of single atoms in cavity QED. *Phys. Rev. Lett.* **83**, 4987–4990 (1999).
- Pinkse, P. W. H., Fischer, T., Maunz, P. & Rempe, G. Trapping an atom with single photons. *Nature* **404**, 365–368 (2000).

5. Boozer, A. D., Boca, A., Miller, R., Northup, T. E. & Kimble, H. J. Cooling to the ground state of axial motion for one atom strongly coupled to an optical cavity. *Phys. Rev. Lett.* **97**, 083602 (2006).
6. Maunz, P. *et al.* Cavity cooling of a single atom. *Nature* **428**, 50–52 (2004).
7. Anglin, J. R. & Ketterle, W. Bose–Einstein condensation of atomic gases. *Nature* **416**, 211–218 (2002).
8. Öttl, A., Ritter, S., Köhl, M. & Esslinger, T. Correlations and counting statistics of an atom laser. *Phys. Rev. Lett.* **95**, 090404 (2005).
9. Slama, S., Bux, S., Krenz, C., Zimmermann, C. & Courteille, P. W. Superradiant Rayleigh scattering and collective atomic recoil lasing in a ring cavity. *Phys. Rev. Lett.* **98**, 053603 (2007).
10. Steinmetz, T. *et al.* A stable fiber-based Fabry–Perot cavity. *Appl. Phys. Lett.* **89**, 111110 (2006).
11. Fortágh, J. & Zimmermann, C. Magnetic microtraps for ultracold atoms. *Rev. Mod. Phys.* **79**, 235–289 (2007).
12. Brennecke, F. *et al.* Cavity QED with a Bose–Einstein condensate. *Nature* doi:10.1038/nature06120 (this issue).
13. Duan, L. M., Lukin, M. D., Cirac, J. I. & Zoller, P. Long-distance quantum communication with atomic ensembles and linear optics. *Nature* **414**, 413–418 (2001).
14. Dicke, R. H. Coherence in spontaneous radiation processes. *Phys. Rev.* **93**, 99–110 (1954).
15. Sherson, J., Julsgaard, B. & Polzik, E. S. Deterministic atom–light quantum interface. *Adv. At. Mol. Opt. Phys.* **54**, 81–130 (2006).
16. Simon, J., Tanji, H., Thompson, J. K. & Vuletic, V. Interfacing collective atomic excitations and single photons. *Phys. Rev. Lett.* **98**, 183601 (2007).
17. Tavis, M. & Cummings, F. W. Approximate solutions for an N-molecule–radiation-field Hamiltonian. *Phys. Rev.* **188**, 692–695 (1969).
18. Ketterle, W. & Inouye, S. Does matter wave amplification work for fermions? *Phys. Rev. Lett.* **86**, 4203–4206 (2001).
19. Inouye, S. *et al.* Superradiant Rayleigh scattering from a Bose–Einstein condensate. *Science* **285**, 571–574 (1999).
20. Morice, O., Castin, Y. & Dalibard, J. Refractive index of a dilute Bose gas. *Phys. Rev. A* **51**, 3896–3901 (1995).
21. Mekhov, I. B., Maschler, C. & Ritsch, H. Probing quantum phases of ultracold atoms in optical lattices by transmission spectra in cavity quantum electrodynamics. *Nature Phys.* **3**, 319–323 (2007).
22. Treutlein, P. *et al.* Quantum information processing in optical lattices and magnetic microtraps. *Fortschr. Phys.* **54**, 702–718 (2006).
23. Aoki, T. *et al.* Observation of strong coupling between one atom and a monolithic microresonator. *Nature* **443**, 671–674 (2006).
24. Gerbier, F. Quasi-1D Bose–Einstein condensates in the dimensional crossover regime. *Europhys. Lett.* **66**, 771–777 (2004).
25. Thompson, R. J., Rempe, G. & Kimble, H. J. Observation of normal-mode splitting for an atom in an optical cavity. *Phys. Rev. Lett.* **68**, 1132–1135 (1992).
26. Fischer, T., Maunz, P., Puppe, T., Pinkse, P. W. H. & Rempe, G. Collective light forces on atoms in a high-finesse cavity. *N. J. Phys.* **3**, 11 (2001).
27. Murch, K. W., Moore, K. L., Gupta, S. & Stamper-Kurn, D. M. Measurement of intracavity quantum fluctuations of light using an atomic fluctuation bolometer. Preprint at (<http://arxiv.org/abs/0706.1005>) (2007).
28. Lye, J. E., Hope, J. J. & Close, J. D. Nondestructive dynamic detectors for Bose–Einstein condensates. *Phys. Rev. A* **67**, 043609 (2003).
29. Greiner, M., Mandel, O., Hänsch, T. W. & Bloch, I. Collapse and revival of the matter wave field of a Bose–Einstein condensate. *Nature* **419**, 51–54 (2002).
30. Mohring, B. *et al.* Extracting atoms on demand with lasers. *Phys. Rev. A* **71**, 053601 (2005).

Supplementary Information is linked to the online version of the paper at www.nature.com/nature.

Acknowledgements We thank J. Hare and F. Orucevic for support in producing the fibre mirror surfaces, and F. Gerbier for the calculation of condensate size in the crossover regime. We acknowledge discussions with Y. Castin and J. Dalibard about atom–light interaction in BECs, as well as with T. W. Hänsch, I. Cirac, P. Treutlein and R. Long. This work was supported by a European Young Investigator Award (EURYI), a Chaire d'Excellence of the French Ministry for Research, and by the EU ('Atom Chips' Research Training Network and 'SCALA' Integrated Programme). The Atom Chip team at Laboratoire Kastler Brossel is part of the Institut Francilien de Recherche sur les Atomes Froids (IFRAF).

Author Information Reprints and permissions information is available at www.nature.com/reprints. Correspondence and requests for materials should be addressed to J.R. (jakob.reichel@ens.fr).

METHODS

FFP cavity. For a two-level atom in a symmetric Fabry–Perot cavity (mirror distance d and radius of curvature r), $g_0 = \sqrt{\frac{3\lambda^2 \mathcal{F}}{\pi^2 w_0^2 d}} = \sqrt{\frac{6\lambda c \mathcal{F}}{\pi d \sqrt{2dr - d^2}}}$ and $C_0 = \frac{3\lambda^2 \mathcal{F}}{\pi^2 w_0^2} = \frac{6\lambda \mathcal{F}}{\pi^2 \sqrt{2dr - d^2}}$, where w_0 is the mode waist radius (which depends on the mirror distance and curvature) and $\mathcal{F} \approx \frac{\pi}{T+L}$ is the cavity finesse, which depends solely on the intensity transmission T and loss L of each mirror, but not on geometry. The second expression for C_0 shows that short cavities with strongly curved mirrors lead to high cooperativity. In our FFP cavity¹⁰, the concave mirror surfaces are realized on the cleaved surfaces of two optical fibre tips facing each other (Fig. 1b, c). With this type of cavity, the optical axis can approach the chip surface to half a fibre diameter, and maximum coupling is achieved by placing the atoms in the gap between the mirrors, so that their distance from any material surface remains in the many-micrometre range, where long coherent trapping times have been demonstrated. In the second-generation FFP fabrication method used here, a laser surface machining process is used to shape the mirror surfaces, which has allowed us to achieve a finesse of $\mathcal{F} = 37,000$ for the cavity used here, and should ultimately enable $\mathcal{F} = 150,000$ (for mirrors where transmission equals total loss), based on the measured surface roughness. Additionally, this method can produce very small radii of curvature. The FFP1 cavity used here has an asymmetric geometry with radii $r_1 = 450 \mu\text{m}$ and $r_2 = 150 \mu\text{m}$ (measured by atomic force microscopy), and uses a single-mode (SM) fibre on the input side, while a multi-mode (MM) output fibre on the output side assures high outcoupling efficiency (Fig. 1c). There is a splitting between modes of orthogonal linear polarization, which is 540 MHz between the TEM₀₀ modes in our cavity. This allows us to adjust probe beam polarization to one particular linear polarization. However, owing to the direct fibre coupling, we are currently unable to determine the axis of this polarization in the y - z plane. The cavity length $d = 38.6 \mu\text{m}$ (longitudinal mode number $n = 99$) is confirmed by two-frequency transmission measurements, and the waist radius $w_0 = 3.9 \mu\text{m}$ is inferred from this d and the mirror curvatures. These parameters lead to the g_0 value quoted in the main text. With a Rayleigh length of about $60 \mu\text{m}$, the cavity mode is quasi-cylindrical: the variation of the beam radius $w(x)$ is 12%. (In the fit of Fig. 2b, this variation is taken into account.) The resonance linewidth 2κ is measured with two frequency-stabilized lasers. The transmission of each cavity mirror is $T = 31 \pm 2$ p.p.m. as determined from a reference substrate coated in the same batch as the fibres. From this value and the measured finesse, we infer per-mirror intensity losses $L = 56$ p.p.m. The measured intensity transmission from before the input of the SM fibre to after the output of the MM fibre is 0.094 for a resonant cavity. Comparison to the calculated transmission of the cavity $\left(\frac{T}{T+L}\right)^2 = 0.126$ indicates that the combined losses of coupling into the SM fibre, mode-matching into the cavity, and from the cavity to the MM fibre are 0.253, a low value. The cavity length is actively stabilized to compensate for thermal drifts of $\sim 1,500$ linewidths. The locking scheme uses a correction signal from FFP2 which is locked on a resonance and subjected to the same thermal perturbations as FFP1; residual drifts of a few linewidths are corrected using an error signal derived from the 830 nm lattice beam.

Atom chip and BEC production. The cavity subassembly is glued onto an atom chip, which forms the top wall of a commercial glass cell³¹. Sealed fibre feed-throughs are formed simply by two slits machined into opposite walls of the cell,

which are filled with vacuum-compatible epoxy glue once the fibres are in place. Base pressure in the cell is 3×10^{-10} hPa, comparable to the pressure in similar cells without cavities. As in our previous work³², we use a mirror-magneto-optical trap (MOT) to precool ⁸⁷Rb atoms. To avoid obscuring of MOT beams by the cavity subassembly, the horizontal MOT beams are parallel to the x axis and there is a distance of 11 mm along y between the MOT (position A in Fig. 1a) and cavity centres. After optical pumping to the $|F = 2, m_F = 2\rangle$ state and initial magnetic trapping near the MOT location and magnetic transport (which combines a wire guide¹¹ and an external quadrupole field), the atoms are further cooled by forced radio-frequency evaporation in a ‘dimple’ trap³² (formed by a wire cross with currents 3 A and 300 mA) between the chip surface and the cavity mode at position B (Fig. 1b); the BEC is produced $17 \mu\text{m}$ above the mode axis. Alternatively, in some experiments, we use surface evaporation^{33,34} near one of the fibre endfaces, as we found that this increases atom number stability for small condensates. The trap geometry is prolate (cigar-shaped); by ramping wire currents we can align its long axis parallel or perpendicular to the cavity axis³⁵, as required in a particular experiment. Absorption imaging inside and above the cavity is possible with a probe beam in the y - z plane, which subtends an angle of 30° with the chip surface and is reflected by the dielectric coating on the chip before its passage through the cavity (Fig. 1d). This reflection limits the achievable purity of the desired circular polarization; furthermore, camera noise in conjunction with the magnification of about 4 forces us to use a relatively high imaging beam intensity that causes some saturation. We have not attempted to correct these effects, all of which lead to an underestimation of N . Atom numbers extracted from the cavity QED measurements by using calculated \bar{g}_1 values are systematically higher by about a factor of 2.

BEC coupling strength. In Fig. 3a the circles show the coupling strength g_N for BECs held in a magnetic trap ($\nu_{x,z} = 2.7$ kHz, $\nu_y = 230$ Hz, bias field $B_y \approx 1$ G), with atom numbers N ranging from 260 to 950. g_N is reduced by a factor of about 0.86 (mean value over the seven measurements) with respect to the values measured for thermal samples in the combined trap (same trap parameters as in Fig. 2b). The expected reduction in g_N is calculated using the density distributions of the BECs in the one-dimensional/three-dimensional crossover regime²⁴ and the density distribution of thermal clouds at $4.4 \mu\text{K}$, as obtained from the fit in Fig. 2b. This assumes that the final temperature of the sample is independent of N when loading BECs. We find a reduction by a factor 0.83 (mean value), in good agreement with the measured value. For these measurements a very weak probe beam is used, $n_{\text{res}} = 6.3 \times 10^{-4}$, in order to leave the condensate unaffected. For each of the seven data points, we average over four identical experimental runs to obtain a clear transmission signal.

31. Du, S. W. *et al.* Atom-chip Bose–Einstein condensation in a portable vacuum cell. *Phys. Rev. A* **70**, 053606 (2004).
32. Hänsel, W., Hommelhoff, P., Hänsch, T. W. & Reichel, J. Bose–Einstein condensation on a microelectronic chip. *Nature* **413**, 498–501 (2001).
33. Reichel, J., Hänsel, W. & Hänsch, T. W. Atomic micromanipulation with magnetic surface traps. *Phys. Rev. Lett.* **83**, 3398–3401 (1999).
34. Harber, D. M., McGuirk, J. M., Obrecht, J. M. & Cornell, E. A. Thermally induced losses in ultra-cold atoms magnetically trapped near room-temperature surfaces. *J. Low Temp. Phys.* **133**, 229–238 (2003).
35. Reichel, J. Microchip traps and Bose–Einstein condensation. *Appl. Phys. B* **74**, 469–487 (2002).

Stability of organic carbon in deep soil layers controlled by fresh carbon supply

Sébastien Fontaine¹, Sébastien Barot², Pierre Barré³, Nadia Bdioui¹, Bruno Mary⁴ & Cornelia Rumpel³

The world's soils store more carbon than is present in biomass and in the atmosphere¹. Little is known, however, about the factors controlling the stability of soil organic carbon stocks^{2–4} and the response of the soil carbon pool to climate change remains uncertain^{5,6}. We investigated the stability of carbon in deep soil layers in one soil profile by combining physical and chemical characterization of organic carbon, soil incubations and radiocarbon dating. Here we show that the supply of fresh plant-derived carbon to the subsoil (0.6–0.8 m depth) stimulated the microbial mineralization of $2,567 \pm 226$ -year-old carbon. Our results support the previously suggested idea⁷ that in the absence of fresh organic carbon, an essential source of energy for soil microbes, the stability of organic carbon in deep soil layers is maintained. We propose that a lack of supply of fresh carbon may prevent the decomposition of the organic carbon pool in deep soil layers in response to future changes in temperature. Any change in land use and agricultural practice that increases the distribution of fresh carbon along the soil profile^{1,8,9} could however stimulate the loss of ancient buried carbon.

The soil reservoir of organic carbon corresponds to 615 Gt C in the top 0.2 m layer and 2,344 Gt C at depths of up to 3 m, which is more than biomass and atmospheric CO₂ combined¹. The mean residence time (MRT) of soil organic carbon (SOC) increases strongly with depth, reaching values of 2,000–10,000 yr in deep soil layers (>0.2 m)^{2–4}. However, little is known about the factors controlling the stability of carbon in deep soil layers. Improved knowledge of these factors is essential to determine whether this pool of carbon will react to global change and accelerate the increase in atmospheric CO₂.

We investigated the stability of carbon in deep soil layers in a soil profile located within the research observatory on grasslands set up by the French National Institute for Agricultural Research in 2003 (Massif Central, France). This site has been under grassland for >50 yr, and was covered with forests of chestnut and hornbeam 2,000 yr ago¹⁰. Radiocarbon (¹⁴C) dating suggests that SOC stored in deep layers is derived from these old forests (Table 1). SOC content declines with depth, but $77 \pm 1\%$ (mean \pm s.e.m.) of the soil reservoir of carbon is below 0.2 m (Supplementary Table 1). The soil is a drained Cambisol developed from granitic rock. Cambisols, which are relatively rich in deep C and cover 10% of the terrestrial surface, are the second most widespread soil type of the world after Leptosols, which are poor in deep C¹¹.

It has been widely demonstrated that the chemical nature of organic compounds may control the intensity of decomposer activities and rates of degradation. To test whether the stability of deep C is due to its inherent chemical structure, soil samples from the surface layer (0–0.2 m) and a deeper layer (0.6–0.8 m) were collected. ¹⁴C content was measured to date SOC and determine its MRT using a model of flux (Methods). The chemical composition of SOC in the

two layers was analysed by ¹³C CPMAS (cross polarization with magic-angle spinning) NMR (nuclear magnetic resonance) and by FTIR (Fourier transform infrared) spectroscopy to determine whether changes in MRT with depth may result from a shift in the chemical composition of SOC.

The ¹⁴C content of SOC declined with depth, from $100.2 \pm 0.4\%$ of modern carbon (MC%) in the surface layer to 77.9 ± 0.3 MC% in the subsoil. The ¹⁴C dating and the calculation of MRT of SOC both gave consistent results (Table 1). The surface layer was dominated by young fast-cycling carbon (320 ± 27 yr) whereas the subsoil was dominated by ancient slow-cycling carbon ($2,560 \pm 74$ yr), often referred to as the passive fraction of SOC¹². This result indicates that the decomposition of SOC is strongly reduced at depth.

These differences in MRT were not mirrored by changes in the chemical composition of SOC. Figure 1 shows that the ¹³C CPMAS NMR spectra of both layers were similar. They were characterized by dominant signals in the O-alkyl C region, which are generally assigned to amide C of proteins and to C2, C3, C5 of polysaccharides¹³. The resonance centred in the alkyl C region indicated the

Table 1 | Properties of the two soil layers

Property	Layer depth 0–0.2 m	Layer depth 0.6–0.8 m
pH	6.1 ± 0.1	6.7 ± 0
Clay (%)	27 ± 1	34 ± 1
Clay minerals*	70 ± 2	65 ± 1
Kaolinite	25 ± 1	26 ± 2
HIV	5 ± 1	9 ± 1
Illite		
Oxides	27 ± 0.1	36 ± 0.1
Fe (g kg ⁻¹)	6.5 ± 0.2	7.6 ± 0.0
Al (g kg ⁻¹)		
SOC content (g C kg ⁻¹)	32 ± 1	23.3 ± 0.5
SOC bound to minerals (% of total)	50 ± 0.5	58 ± 1
SOC $\delta^{13}\text{C}$ (‰)	-27.4 ± 0.4	-25.9 ± 0.4
SOC ¹⁴ C content (MC%)	100.2 ± 0.4	77.9 ± 0.3
SOC ¹⁴ C-age (yr BP)	Modern	$2,007 \pm 31$
SOC MRT (yr)	320 ± 27	$2,560 \pm 74$
Root (g C kg ⁻¹)	3.9 ± 0.5	0.008 ± 0.002
Root production of fresh litter† (g C kg ⁻¹ yr ⁻¹)	4.3 ± 0.6	0.009 ± 0.002
POM content (>200 µm; g C kg ⁻¹)	1.8 ± 0.7	0.016 ± 0.05
POM ¹⁴ C content (MC%)	ND	109 ± 2.8
POM MRT (yr)	ND	$6.4 \pm 4.1\ddagger$
Microbial biomass (mg C kg ⁻¹)	853 ± 11	193 ± 22

Soil properties, clay mineralogy, iron (Fe) and aluminium (Al) oxides, ¹⁴C content, ¹⁴C age and mean residence time (MRT) of soil organic carbon (SOC) and particulate organic matter (POM). Values are given as mean \pm s.e.m. ($n = 3$ for all analyses except ¹⁴C analysis of SOC and POM, $n = 2$). MC%, percentage of modern carbon; HIV, hydroxy-interlayer vermiculite; ND, not determined.

* Relative peak area of diffractograms in %.

† Root production of fresh litter was calculated as (root density)/(root MRT). Root MRT (0.9 yr) was calculated for the same grassland exposed to ¹³C labelled CO₂ (ref. 28).

‡ The model yielded two possible MRT, 6.4 ± 4.1 yr and 101 ± 35 yr, but the latter was excluded as it was inconsistent with the MRT calculated as (POM content)/(POM input flux) (Supplementary Data 2).

¹INRA, UR 874 Agronomie, 234 Avenue du Brézet, 63100 Clermont-Ferrand, France. ²IRD, UMR 137, 32 Avenue H. Varagnat, 93143 Bondy, France. ³BIOEMCO, UMR 7618, CNRS-INRA-ENS-Paris 6, Bâtiment EGER, Aile B, 78820 Thiverval-Grignon, France. ⁴INRA, UR 1158 Agronomie, Rue Fernand Christ, 02007 Laon, France.

presence of methyl C in long chain aliphatic compounds, derived from lipids¹³. Both soil layers showed signals in the aromatic region of the spectra (C substituted aryl C, and O substituted aryl C), indicative of C derived from lignin and charcoal. The only significant difference, but not quantitatively important, was a higher contribution of C substituted aryl C in the subsoil ($10 \pm 0.0\%$) than in the soil surface ($8.7 \pm 0.4\%$) ($P < 0.02$, Supplementary Table 2). The FTIR spectra also indicated that the SOC chemical composition does not change markedly with depth (Supplementary Data 1), suggesting that the stability of SOC in the subsoil is not due to the chemical structure of SOC itself.

The deep carbon may persist because it is bound to soil minerals and exists in forms that decomposers cannot access^{14,15}. Table 1 shows that the proportion of SOC bound to minerals increased slightly with depth, from $50 \pm 0.5\%$ for the surface layer to $58 \pm 1\%$ for the subsoil. Could this 8% change explain the shift in MRT of SOC with depth? We used a simple model (Supplementary Method 1) to show that the only way to simulate the shift in MRT of SOC with depth is to assume a large change in the type of organo-mineral associations, that is, organo-mineral complexes at depth must be ten times more stable than in the surface. This assumption is not supported by our results. Table 1 shows that clay mineralogy, which was dominated by kaolinite, did not change markedly with depth. Fe and Al oxides and oxyhydroxides, which play a role in the preservation of SOC, increased with depth (Fe $\times 1.3$, Al $\times 1.2$), but not to the extent imposed by our model ($\times 10$). Thus, the stability of SOC in the subsoil cannot entirely be ascribed to SOC fixation on minerals.

The slow SOC decomposition at depth could result from inappropriate conditions for microbes, such as a lack of oxygen. To test whether the overall conditions found at depth allow microbial activities, we determined MRT of particulate organic matter (POM > 200 μm). If microbial activities are possible, the small pool of root litter should be quickly recycled and dominated by recent C. This was confirmed by the results, as the MRT of POM in the deep layer was 6.4 ± 4.1 yr, in sharp contrast with SOC (Table 1).

Under these circumstances, how can deep SOC escape from microbial degradation? A new theory of SOC dynamics⁷ has proposed that the slow SOC turnover at depth results from scarcity of fresh C (plant litter and exudates). Based on many empirical results^{16–20}, this theory assumes that soil humus is the result of the

long-term accumulation of biochemically recalcitrant compounds having low energy content. Near the soil surface, microbes are able to decompose these compounds with their enzymes because they use fresh C as source of energy. In deep soil layers, however, fresh-C inputs by plants are extremely low (for example, fresh-litter deposition by roots was 478 times lower in our subsoil than in the surface layer; Table 1). Under these conditions, the theory predicts that acquisition of energy from recalcitrant compounds cannot sustain microbial activity, and soil decomposition is strongly reduced. This prediction can be experimentally tested: if the theory is right, then the delivery of fresh C to the subsoil should activate mineralization of ancient C.

To test this theory, we incubated soil sampled from the deep layer (0.6–0.8 m) with cellulose, which is the main component of plant litter. We used a novel technique based on dual labelling of cellulose (¹³C, ¹⁴C) in order to trace decomposition of cellulose C and SOC, and to determine the mean age of SOC mineralized by microbes (Methods). Soil without cellulose was also incubated as a control.

Incubation of control soil released CO₂ (Fig. 2a), indicating that there were metabolically active microbes in the subsoil and that a fraction of deep C was degraded. The ¹⁴C dating of CO₂ produced during the incubation showed that microbes in the control soils mostly decomposed recent organic matter (Table 2). Nevertheless, it is likely that decomposers mineralized a small amount of old C together with recent plant litter because the ¹⁴C content of respired CO₂ was lower than that of actual atmospheric CO₂ (~ 105 MC%).

The addition of cellulose stimulated microbial respiration and growth, demonstrating that microbes were limited by energy

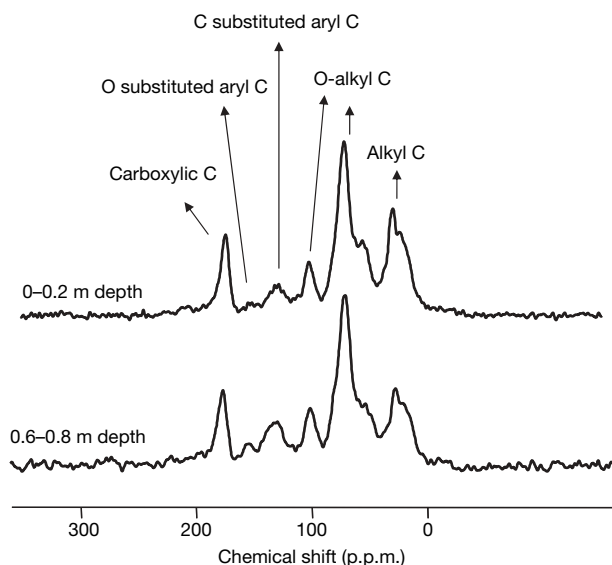


Figure 1 | ¹³C CPMAS NMR spectra of soil carbon for the two soil layers. The chemical shift regions 0–45 p.p.m., 45–110 p.p.m., 110–140 p.p.m., 140–160 p.p.m. and 160–220 p.p.m. were referred to respectively as alkyl C, O-alkyl C, C substituted aryl C, O substituted aryl C and carboxylic C.

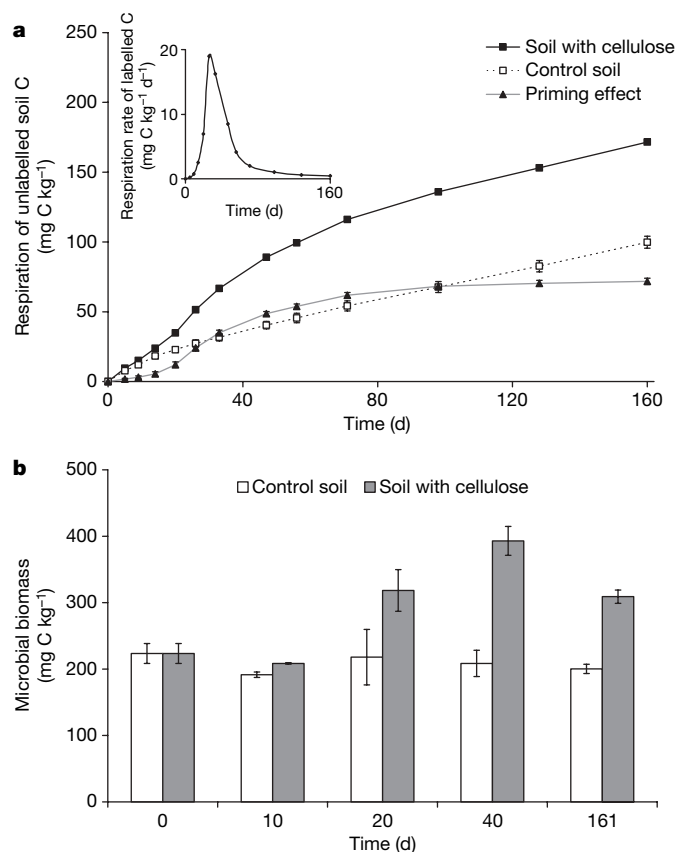


Figure 2 | Effect of cellulose supply on respiration and biomass of microbes of the deep layer. **a**, **b**, Cumulative respiration of unlabelled soil carbon (**a**) and total microbial biomass (**b**). The difference in soil carbon respiration between control and cellulose-amended soil represents the priming effect. Inset, respiration rate of labelled cellulose. The decrease in respiration after day 26 indicates the exhaustion of cellulose. Values are given as mean \pm s.e.m. ($n = 3$).

Table 2 | Properties of unlabelled soil C released during incubation

	Quantity (mg C kg ⁻¹)	¹⁴ C activity (MC%)	¹⁴ C age (yr BP)
Control soil	100 ± 4	97 ± 1.4	222 (+119/–117)
Soil with cellulose	172 ± 3	85 ± 1.6	1,329 (+154/–152)
Priming effect	72 ± 2	73 ± 2	2,567 (+226/–219)

Quantity, ¹⁴C activity and ¹⁴C age of unlabelled soil C released as CO₂ by the control, the soil with cellulose and the priming effect during the 161 days of incubation of the subsoil. Values are given as mean ± s.e.m. (n = 3). Standard errors of ¹⁴C age are asymmetric owing to the exponential decay of ¹⁴C.

(Fig. 2). The stimulation of decomposers induced a significant ($P < 0.001$, analysis of variance, ANOVA) increase in production of unlabelled soil-originated CO₂, an effect known as priming^{16–20}. It has been previously proposed that the priming effect may result from decomposition of recalcitrant old SOC by stimulated microbes. However, this hypothesis has not been demonstrated^{7,16}. Here, we show that the ¹⁴C content of the CO₂ derived from SOC decreased significantly ($P < 0.01$, ANOVA) after cellulose supply, demonstrating that cellulose-stimulated decomposers degraded very old C (Table 2). Calculations indicated that the pool of carbon decomposed by the priming effect was $2,567 \pm 226$ yr old.

Both the total microbial biomass and the priming effect significantly decreased ($P < 0.01$, ANOVA) with the exhaustion of cellulose (Fig. 2). Thus, although decomposers are able to decompose ancient C, the acquisition of energy from such substrate is not sufficient to sustain long-term biological activity. Mechanistically, this suggests that the energy required to break down the recalcitrant SOC (for example, extracellular enzyme production) is higher than the energy supplied by the catabolism of such substrate. As a result, the long-term activity of decomposer populations depends on a permanent supply of fresh C (ref. 7).

The addition of cellulose, at a rate representing about one-quarter of the annual fresh litter C deposition into the surface layer by plant roots (Table 1), led to the mineralization of 72 ± 2 mg C per kg soil of old SOC (Table 2). If this cellulose supply and the resulting priming effect were repeated each year, we calculated that, under laboratory conditions, the MRT of SOC in the subsoil would be $23,300/72 = 324$ yr, which is very close to the MRT found in the surface layer (Table 1).

The present results show that the stability of SOC in the studied deep layer reflects a lack of fresh C for microbes. We cannot be certain that the limitation by fresh C detected here, with this deep soil, will also be the dominant control of SOC stability in other deep soils. We therefore encourage research in other soils to quantify the relative role of mechanisms studied here at global scale. However, given that the breakdown of SOC is limited by the availability of fresh C in most soils^{16–20}, and that the low fresh-C availability at depth relies on a fundamental property of ecosystems (plants live and incorporate most of their litter at the surface), our results can probably be generalized to many well-drained deep soils. They cannot apply to waterlogged peat soils, because decomposition there is primarily constrained by a lack of oxygen.

Our results have several implications. First, they suggest that biological and physical processes that bury recalcitrant SOC below the deposits of fresh C protect it from decomposition and allow C storage over millennia (Supplementary Fig. 1). This mechanism provides an interesting alternative to current approaches that involve short-term storage of carbon in vulnerable compartments (plant biomass, surface SOC)²¹. Second, our incubation results suggest that, even under favourable conditions of temperature and moisture for microbial activities, SOC from the deep soil does not provide enough energy to sustain active microbial populations and thereby the production of enzymes. The existence of this energetic barrier could reduce or cancel the effect of future changes in temperature on the decomposition of this large pool of deep C, in contradiction to the predicted effect based on the temperature-induced acceleration of enzymatic reactions²². Last, our results show that deep SOC decomposition may

be reactivated. Changes in land use and agricultural practices (for example, deep ploughing versus conservation tillage, use of drought-resistant crops with deep root systems) that increase the distribution of fresh C at depth^{18,9} could stimulate loss of this ancient buried carbon.

METHODS SUMMARY

Characterization of the soil profile. Three independent soil samples were collected in layers of 0.2 m down to the depth at which unweathered parent material was encountered. Organic C and bulk density were measured in each layer to determine SOC content and storage. We studied the stability of deep SOC by focusing on two contrasted layers, that is 0–0.2 m and 0.6–0.8 m. A subsample of intact soil was used for the determination of POM²³, the remainder was sieved. The sieved soil was used to determine pH, clay content, total nitrogen, microbial C (ref. 24), age and MRT of SOC, chemical and physical composition of SOC, and to conduct the incubation.

Soil analyses. ¹⁴C content of SOC and POM (>200 µm) was measured by liquid scintillation counting. The ¹⁴C age was calculated with the Libby half-life. To determine the MRT of SOC and POM, we used the measured ¹⁴C content to constrain a flux model²⁵. The chemical composition of SOC was then analysed by CPMAS NMR ¹³C and by FTIR spectroscopy (Supplementary Data 1). The amount of C bound to soil minerals was estimated by the demineralization technique²⁶. Clay mineralogy was determined by X-ray diffraction of oriented samples. Iron and aluminium oxides and oxyhydroxides were estimated by the dithionite-citrate-bicarbonate method²⁷.

Incubation experiment. Fresh sieved soils were incubated at 20 °C and at a water potential of –100 kPa for 161 days. Dual-labelled cellulose ($\delta^{13}\text{C} = 1,860\text{‰}$, ¹⁴C activity = 2 MC%) was mixed with half of the incubated soils, 1 g cellulose C per kg of soil. The other half without cellulose (control soils) was also mixed to apply the same disturbance. The CO₂ evolved was trapped in NaOH and measured by continuous flow colorimetry. ¹³C and ¹⁴C content of CO₂ was analysed after precipitating the carbonates with excess BaCl₂. ¹³C and ¹⁴C analysis of carbonates was carried out by IRMS (isotope ratio mass spectrometry) and AMS (accelerator mass spectrometry), respectively.

Full Methods and any associated references are available in the online version of the paper at www.nature.com/nature.

Received 5 February; accepted 13 September 2007.

1. Jobbágy, E. G. & Jackson, R. B. The vertical distribution of soil organic carbon and its relation to climate and vegetation. *Ecol. Appl.* **10**, 423–436 (2000).
2. Martel, Y. A. & Paul, E. A. The use of radiocarbon dating of organic matter in the study of soil genesis. *Soil Sci. Soc. Am. Proc.* **38**, 501–506 (1974).
3. Rumpel, C., Kögel-Knabner, I. & Bruhn, F. Vertical distribution, age, and chemical composition of organic carbon in two forest soils of different pedogenesis. *Org. Geochem.* **33**, 1131–1142 (2002).
4. Schöning, I. & Kögel-Knabner, I. Chemical composition of young and old carbon pools throughout Cambisol and Luvisol profiles under forests. *Soil Biol. Biochem.* **38**, 2411–2424 (2006).
5. Luo, Y., Wan, S., Hui, D. & Wallace, L. L. Acclimatization of soil respiration to warming in a tall grass prairie. *Nature* **413**, 622–624 (2001).
6. Bellamy, P. H., Loveland, P. J., Bradley, R. I., Lark, R. M. & Kirk, G. J. D. Carbon losses from all soils across England and Wales 1978–2003. *Nature* **437**, 245–247 (2005).
7. Fontaine, S. & Barot, S. Size and functional diversity of microbe populations control plant persistence and long-term soil carbon accumulation. *Ecol. Lett.* **7**, 1075–1087 (2005).
8. Hurd, E. A. Phenotype and drought tolerance in wheat. *Agric. Meteorol.* **14**, 39–55 (1974).
9. Lal, R. Soil carbon sequestration impacts on global climate change and food security. *Science* **304**, 1623–1627 (2004).
10. Boivin, P. et al. *Volcanologie de la Chaîne des Puys* (Parc naturel régional de la chaîne des Puys, Clermont Ferrand, 2004).
11. FAO-Unesco. *Soil Map of the World (1:5,000 000)* (Unesco, Paris, 1974).
12. Jenkinson, D. S., Harkness, D. D., Vance, E. D., Adams, D. E. & Harrison, A. F. Calculating net primary production and annual input of organic matter to soil from the amount and radiocarbon content of soil organic matter. *Soil Biol. Biochem.* **24**, 295–308 (1992).
13. Kögel-Knabner, I. ¹³C and ¹⁵N NMR spectroscopy as a tool in soil organic matter studies. *Geoderma* **80**, 243–270 (1997).
14. Baldock, J. A. & Skjemstad, J. O. Role of the matrix and minerals in protecting natural organic materials against biological attack. *Org. Geochem.* **31**, 697–710 (2000).
15. Wattel-Koekkoek, E. J. W., Buurman, P., van der Plicht, J., Wattel, E. & van Breemen, N. Mean residence time of soil organic matter associated with kaolinite and smectite. *Eur. J. Soil Sci.* **54**, 269–278 (2003).
16. Kuzyakov, Y., Friedel, J. K. & Stahr, K. Review of mechanisms and quantification of priming effects. *Soil Biol. Biochem.* **32**, 1485–1498 (2000).

17. Cheng, W., Johnson, D. W. & Fu, S. Rhizosphere effects on decomposition: Controls of plant species, phenology, and fertilisation. *Soil Sci. Soc. Am. J.* **67**, 1418–1427 (2003).
18. Fontaine, S., Bardoux, G., Abbadie, L. & Mariotti, A. Carbon input to soil may decrease soil carbon content. *Ecol. Lett.* **7**, 314–320 (2004).
19. Malosso, E., English, L., Hopkins, D. W. & O'Donnell, A. G. Use of ^{13}C -labelled plant materials and ergosterol, PLFA and NLFA analyses to investigate organic matter decomposition in Antarctic soil. *Soil Biol. Biochem.* **36**, 165–175 (2003).
20. Carney, K. M., Hungate, B. A., Drake, B. G. & Megonigal, J. P. Altered soil microbial community at elevated CO_2 leads to loss of soil carbon. *Proc. Natl Acad. Sci. USA* **104**, 4990–4995 (2007).
21. Ciais, P. *et al.* Europe-wide reduction in primary productivity caused by the heat and drought in 2003. *Nature* **437**, 529–533 (2005).
22. Davidson, E. A. & Janssens, I. A. Temperature sensitivity of soil carbon decomposition and feedbacks to climate change. *Nature* **440**, 165–173 (2006).
23. Loiseau, P. & Soussana, J. F. Elevated $[\text{CO}_2]$, temperature increase and N supply effects on the turnover of below-ground carbon in a temperate grassland ecosystem. *Plant Soil* **210**, 233–247 (1999).
24. Vance, E. D., Brookes, P. C. & Jenkinson, D. S. An extraction method for measuring soil microbial biomass C. *Soil Biol. Biochem.* **19**, 703–707 (1987).
25. Hsieh, Y.-P. Radiocarbon signatures of turnover rates in active soil organic carbon pools. *Soil Sci. Soc. Am. J.* **57**, 1020–1022 (1993).
26. Eusterhues, K., Rumpel, C., Kleber, M. & Kögel-Knabner, I. Stabilisation of soil organic matter by interactions with minerals as revealed by mineral dissolution and oxidative degradation. *Org. Geochem.* **34**, 591–1600 (2003).
27. Mehra, O. P. & Jackson, M. L. Iron oxide removal from soils and clays by dithionite-citrate system buffered with sodium bicarbonate. *Clays Clay Miner.* **32**, 557–563 (1960).
28. Klumpp, K., Soussana, J. F. & Falcimagne, R. Effects of past and current disturbance on carbon cycling in grassland mesocosms. *Agric. Ecosyst. Environ.* **121**, 59–73 (2007).

Supplementary Information is linked to the online version of the paper at www.nature.com/nature.

Acknowledgements We thank S. Révaillot, J. Messaoud, S. Millon, G. Alavoine and O. Delfosse for assistance during the incubation and for chemical and isotopic analysis. We thank J.-F. Soussana, J. Bloor, R. Hakkenberg, P. Loiseau, V. Maire, A. Chabbi and K. Klumpp for critical comments on the manuscript. The Lehrstuhl für Bodenkunde, TU München, is acknowledged for providing the NMR spectrometer. The Hydrasa Laboratory (University of Poitiers) is acknowledged for providing the X-ray diffractometer. This work was financially supported by the INRA Ecology Department, the MED (GESSOL) and the ANR (BIOMOS and C Profond).

Author Contributions S.F. conceived and designed this study; C.R. performed NMR and FTIR analyses; P.B. performed clay mineralogy analyses; B.M. performed ^{13}C analyses; N.B. and S.F. jointly conducted the incubation; S.F. wrote the manuscript; S.B. commented on the manuscript, the modelling and the statistical analyses; and all authors took part in the interpretation of the results.

Author Information Reprints and permissions information is available at www.nature.com/reprints. Correspondence and requests for materials should be addressed to S.F. (fontaine@clermont.inra.fr).

METHODS

Characterization of the soil profile. Three soil samples were collected at a distance of 1–2 m from each other, and in layers of 0.2 m down to the depth at which unweathered parent material was encountered (1 m) (Supplementary Fig. 1). Each replicate was analysed separately. Organic C and bulk density were measured for each horizon to determine SOC content and storage at each depth. We studied the deep SOC stability by focusing on two contrasted layers, that is, 0–0.2 m and 0.6–0.8 m. A subsample of intact soil was used for the determination of POM²³, the remainder was sieved (2 mm) and visible plant residues were removed (sieved soil). After this treatment, POM (>200 µm), soluble C and microbial C accounted for less than 4.5% of total C in both soil layers, indicating that the remaining C is dominated by humified SOC. The sieved soil was used to determine pH, clay content, total nitrogen, microbial C²⁴, age and MRT of SOC, chemical and physical composition of SOC, and to conduct the incubation experiment. All the analyses were made in three replicates per soil layer except ¹⁴C analysis of SOC and POM that were made in two replicates per soil layer.

Chemical characterization of soil carbon. Soils were treated with 10% HF to concentrate organic C and to remove paramagnetic compounds²⁹. Solid-state ¹³C NMR spectra were obtained on a Bruker DSX-200 NMR spectrometer. CPMAS was applied at 6.8 kHz. Solid-state ¹³C NMR signal was recorded as free induction decay and Fourier-transformed to yield a NMR spectrum.

¹⁴C dating and estimation of the mean residence time of soil carbon. Soils were treated with dilute HCl before ¹⁴C measurements to remove eventual traces of carbonates. ¹⁴C content of SOC and POM, measured by liquid scintillation counting at the Centre de Datation par le Radiocarbène (France), is expressed in percentage of modern carbon (MC%), which is the percentage deviation from ¹⁴C/¹²C ratio of oxalic acid in 1950³⁰. Fast cycling C (turnover time, years–centuries) has value >100 MC% because it has incorporated a significant proportion of ¹⁴C emitted by nuclear bomb testing. Before weapons testing, atmospheric ¹⁴C was approximately 100 MC%. Slow-cycling C (turnover time, millennia) has value <100 MC% because of radioactive decay of ¹⁴C. The ¹⁴C age was calculated with the Libby half-life (5,568 yr) and expressed in years before present (yr BP). To determine the MRT of SOC and POM, we used the measured ¹⁴C content to constrain a flux model²⁵. The ¹⁴C content of SOC was modelled as:

$$A_{\text{SOC}}^{14}(t) = \frac{\sum_{i=b}^p [M_i e^{-(p-i)/\text{MRT}} \times A_i^{14} e^{-(p-i)\lambda}]}{\sum_{i=b}^p M_i e^{-(p-i)/\text{MRT}}}$$

where M_i is the amount of new SOC input to the soil in year i , MRT the mean residence time of SOC, p the year when the soil sample is taken, b the year when the simulation starts, A_i^{14} the ¹⁴C activity in the atmosphere of year i and λ the ¹⁴C decay rate (1/8,268). See Supplementary Method 2 for more details.

Carbon bound to soil minerals. Soils were treated with 10% HF to remove mineral material and release mineral-associated carbon. The carbon lost upon the demineralization procedure is assumed to represent the carbon bound to soil minerals²⁶.

Clay mineralogy, content of iron and aluminium oxides. Clay mineralogy was determined by X-ray diffraction (XRD) of oriented samples. The diffractograms, shown in Supplementary Fig. 2, were obtained with a Phillips diffractometer using Cu radiation. Peak areas of the clay minerals were measured and reported in percentages of total peak area to compare the (semiquantitative) XRD diffractograms. Iron and aluminium oxides and oxyhydroxides were estimated by the dithionite-citrate-bicarbonate method²⁷.

Incubation experiment. Experimental units consisted of 60 g (oven-dried basis) samples of fresh sieved soils placed in 500 ml flasks and incubated at 20 °C for 161 days. The moisture content of the soil was adjusted to a water potential of –100 kPa with a nutrient solution (NH₄NO₃, KH₂PO₄). After 15 days of pre-incubation, 1 g cellulose C per kg soil of dual-labelled cellulose (¹³C = 1,860‰, ¹⁴C activity = 2 MC%) was mixed with half of the incubated soils. The other half without cellulose (control soils) was also mixed to apply the same disturbance. The CO₂ evolved was trapped in NaOH and was measured by continuous flow colorimetry. ¹³C-CO₂ was analysed by an elemental analyser coupled to a mass spectrometer after precipitating the carbonates with excess BaCl₂ and filtration. Microbial C and ¹³C were determined by the fumigation-extraction technique²⁴. Measurements of ¹⁴C-CO₂ were conducted on a separate set of flasks. In this set, the NaOH solutions taken at each sampling date were kept under free CO₂ atmosphere until the end of incubation. These samples were then pooled together to produce a single sample which received BaCl₂. ¹⁴C analysis of carbonates and cellulose was carried out by AMS (Radiocarbon Laboratory of Poznań, Poland).

Calculations. The ¹⁴C content of CO₂ emitted in the control soil was transformed into age BP using the Libby half-life of ¹⁴C. Measurement of the ¹⁴C content of total CO₂ emitted in soils with cellulose does not allow for the calculation of the age of SOC released as CO₂ because of the two sources of carbon (cellulose, SOC). We circumvented this problem using dual labelling of cellulose. The ¹³C labelling of cellulose allowed the separation of soil C (R_S) and cellulose (R_C) respiration (mg C CO₂ per kg soil) using mass balance equations:

$$R_S A_S + R_C A_C = R_T A_T$$

$$R_S + R_C = R_T$$

where A_S is the ¹³C abundance (dimensionless) of soil carbon, A_C the ¹³C abundance of cellulose, R_T the total CO₂ emitted by soil with cellulose and A_T its ¹³C abundance.

Then, we calculated the ¹⁴C content (expressed in MC%) of SOC released as CO₂ (A_S^{14}) with the equation

$$R_S A_S^{14} + R_C A_C^{14} = R_T A_T^{14}$$

where A_C^{14} is the ¹⁴C content of cellulose and A_T^{14} the ¹⁴C content of the total CO₂ emitted by soil with cellulose. A_S^{14} was converted into age BP using the Libby half-life of ¹⁴C.

The priming effect (PE, mg C CO₂ per kg soil) induced by the addition of cellulose was calculated as:

$$\text{PE} = (R_S \text{ soil with cellulose}) - (R_S \text{ control soil})$$

We calculated the ¹⁴C content of the pool of SOC decomposed via the priming effect (A_{pe}^{14}) as

$$A_{\text{pe}}^{14} = \frac{(R_S \text{ soil with cellulose}) A_S^{14} - (R_S \text{ control soil}) A_{S0}^{14}}{\text{PE}}$$

where A_{S0}^{14} is the ¹⁴C content of CO₂ emitted in the control soil. A_{pe}^{14} was converted into age BP as previously described.

29. Schmidt, M. W. I., Knicker, H., Hatcher, P. G. & Kögel-Knabner, I. Improvement of ¹³C and ¹⁵N CPMAS NMR spectra of bulk soils, particle size fractions and organic material by treatment with hydrofluoric acid (10%). *Eur. J. Soil Sci.* **48**, 319–328 (1997).
30. Stuiver, M. & Polach, H. A. Discussion—reporting of ¹⁴C data. *Radiocarbon* **19**, 355–363 (1977).

Detection of stratospheric ozone intrusions by windprofiler radars

W. K. Hocking¹, T. Carey-Smith^{1,2}, D. W. Tarasick², P. S. Argall¹, K. Strong³, Y. Rochon², I. Zawadzki⁴ & P. A. Taylor⁵

Stratospheric ozone attenuates harmful ultraviolet radiation and protects the Earth's biosphere¹. Ozone is also of fundamental importance for the chemistry of the lowermost part of the atmosphere, the troposphere^{1–8}. At ground level, ozone is an important by-product of anthropogenic pollution⁷, damaging forests and crops^{5,6}, and negatively affecting human health⁹. Ozone is critical to the chemical and thermal balance of the troposphere¹⁰ because, via the formation of hydroxyl radicals, it controls the capacity of tropospheric air to oxidize and remove other pollutants¹. Moreover, ozone is an important greenhouse gas, particularly in the upper troposphere¹. Although photochemistry in the lower troposphere is the major source of tropospheric ozone^{2,7,11}, the stratosphere–troposphere transport of ozone^{12–19} is important to the overall climatology, budget and long-term trends of tropospheric ozone^{3,4,8,12}. Stratospheric intrusion events, however, are still poorly understood. Here we introduce the use of modern windprofiler radars^{20–22} to assist in such transport investigations. By hourly monitoring the radar-derived tropopause height^{23–25} in combination with a series of frequent ozonesonde balloon launches, we find numerous intrusions of ozone from the

stratosphere into the troposphere in southeastern Canada. On some occasions, ozone is dispersed at altitudes of two to four kilometres, but on other occasions it reaches the ground, where it can dominate the ozone density variability. We observe rapid changes in radar tropopause height immediately preceding these intrusion events. Such changes therefore serve as a valuable diagnostic for the occurrence of ozone intrusion events. Our studies emphasize the impact that stratospheric ozone can have on tropospheric ozone, and show that windprofiler data can be used to infer the possibility of ozone intrusions, as well as better represent tropopause motions in association with stratosphere–troposphere transport.

Ozone enters the troposphere from the stratosphere as part of the Brewer–Dobson circulation¹³, through episodic events, but details of the process are not well known. In this work, we observed a number of such events, using a unique combination of windprofiler radars, frequent ozonesonde launches and computer modelling. Windprofiler radars at two locations were used to provide tropopause heights and vector winds as a function of time, at a resolution of typically one hour, as described in the Methods Summary and illustrated in Fig. 1a.

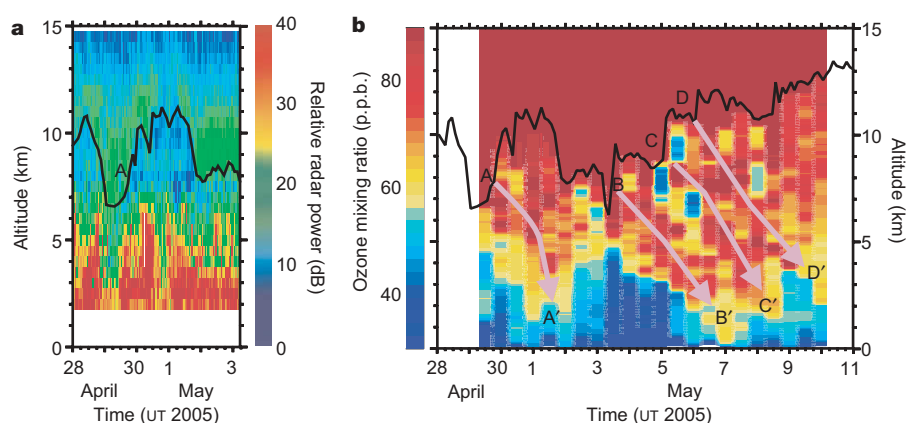


Figure 1 | Simultaneous radar and ozonesonde measurements from the Montreal Campaign of April–May 2005. **a**, Altitude–time intensity plot of backscattered radar power observed with the McGill windprofiler radar, expressed as relative power in decibels. Absolute maximum values of backscattered powers occurred in the lower atmosphere, but a secondary maximum appeared in the altitude region between 6 and 14 km. The lower edge (region of largest local power gradient as a function of height) of this secondary maximum (green in the figure) is shown as a black line. This represents the height of the tropopause, as has been shown in a variety of studies^{23–25}. Radar data were recorded from 28 April to 11 May, but only a subset of the radar data are shown. **b**, Ozone densities (measured in parts per

billion) are plotted as a function of height and time for the period 29 April to 10 May. Each vertical column of coloured boxes represents a different launch. The tropopause height as determined by the radar is marked as the solid black line at 6–14 km altitude. Regions of rapid tropopause ascent are labelled as A, B, C and D. Stratospheric ozone intrusion trajectories are highlighted approximately by the hand-drawn pink arrows (A–A', B–B', C–C', D–D'), although these should only be taken as a guide, because the detailed trajectories are complicated by dispersive processes, by the presence of pre-existing tropospheric ozone, and, in cases C and D, by the close proximity of the two jumps (making their effects hard to separate).

¹Department of Physics and Astronomy, University of Western Ontario, London, Ontario, N6A 3K7 Canada. ²Environment Canada, 4905 Dufferin Street, Downsview, Ontario, M3H 5T4 Canada. ³Department of Physics, University of Toronto, 60 St George Street, Toronto, Ontario, M5S 1A7 Canada. ⁴Department of Atmospheric and Oceanic Sciences, McGill University, 805 Sherbrooke Street W., Montreal, Quebec, H3A 2K6 Canada. ⁵Department of Earth and Space Science and Engineering, York University, 4700 Keele Street, Toronto, Ontario, M3J 1P3 Canada.

The radars used were located at Montreal, Quebec (45.4°N, 73.9°W), and Walsingham, Ontario (42.6°N, 80.6°W). They had steerable beams with one-way beam half-power half-widths of 2.1°, which could be pointed vertically, or at 10.9° off-vertical in various azimuthal directions. The radio frequencies used were 52.00 MHz (Montreal) and 44.50 MHz (Walsingham). The vertical resolution was 500 m in each case.

Ozonesonde balloons were released close to the radars, and profiles of ozone concentration, temperature, humidity, pressure, wind speed and wind direction were obtained at intervals of typically 8–12 hours. In the Montreal case, the launches were made at the Canadian Space Agency Head Office in St Hubert, Quebec, while the radar was located on the MacDonald campus of McGill University, about 45 km away. At Walsingham, launches took place at the radar site. Studies were carried out in five campaigns, each about two weeks long. These simultaneous measurements of radar tropopause heights, together with dynamical parameters, ozone and water-vapour content, were supplemented by calculations using a three-dimensional dynamical lagrangian particle dispersion and tracking model of ozone transport, called FLEXPART^{26–29}, which used regional meteorological analyses of the Canadian operational weather forecast Global Environmental Multiscale (GEM) model³⁰ as input. More specifics can be found in the Methods Summary, and in the Supplementary Information. The results of our study demonstrate the capability of windprofilers to be used to understand ozone intrusions better.

The balloons used in the study carried EN-SCI model 2Z-ECC ozonesondes equipped with Global Positioning System (GPS) receivers and Vaisala RS80 radiosondes. The vertical resolution was about 100 m, and ozone measurement accuracy was about 5%. Over a hundred launches were carried out in five campaigns. Water vapour content was also measured by the ozonesondes, and low water vapour content in the middle troposphere, typically less than 0.2 mb, associated with ozone peaks, was taken as partial evidence that the ozone enhancement had a stratospheric origin. Every campaign showed evidence of stratospheric ozone intrusions into the troposphere, but in the first campaign, high levels of radio interference prevented useful radar measurements. Our discussions will therefore focus on the subsequent four campaigns.

Figure 1b shows a height–time ozone-density plot from Montreal for April–May 2005, as well as the tropopause height taken from Fig. 1a. The tropopause height closely follows the height at which ozone density increases markedly. Excursions of stratospheric ozone density above the background values (typically dark blue in Fig. 1b) are our main interest here. ‘Background’ ozone is generally defined as tropospheric ozone that is more than seven days old and therefore of uncertain origin, and typical values^{2–4,11} are of the order of 20–40 p.p.b.

Three rapid ascents in tropopause height are labelled A, B and C, and a fourth, smaller one is labelled D. In each case there is evidence of ozone intrusion from the stratosphere. Case B is especially clear. In the other cases, the intrusion is less distinct, but increases are apparent in ground-level ozone density following the tropopause jumps. Jumps C and D occur close together, making separation of their effects harder, and the effect of event D seems delayed until after the campaign ended. Nevertheless, increases in low-altitude ozone densities are clearly associated with the tropopause jumps. In each case, decreased humidity served as an additional indicator that the air was stratospheric in origin. In case B–B', a noticeable increase in surface ozone was also observed at stations from Montreal back to the Great Lakes, 1,000 km to the west. Back-trajectory calculations and meteorological analyses indicated that a significant part of this ozone enhancement was stratospheric in origin. Ozone had entered the troposphere both above Montreal and as much as 1,000 km upstream to the west and northwest on 3 May, and the whole ozone enhancement moved downward and downstream as a layer. An initially upstream component reached the ground in Montreal on 7 May. Ground-level values at these stations before and after the two events of 30 April–2 May and 6–9 May to were typically 15 p.p.b. at night and 30 p.p.b. during the day, but during the event of 6–9 May were typically 30 p.p.b. (night-time) to 50 p.p.b. (daytime). Stratospheric ozone had a large impact on the surface ozone densities, even in a large city in which photochemical effects might have been expected to dominate.

Figure 2 shows an example from the Walsingham campaign of November 2005, which ran from 17 to 25 November (23 launches). The period of greatest interest is the time frame covering 23–25 November. An enhancement of ozone appeared at an altitude of about 5–6 km, briefly descended, and then rose again to about 8 km in altitude (Fig. 2b). This layer had low water vapour content (<0.2 mbar), suggestive of stratospheric origin, but otherwise did not seem strongly associated with the stratosphere.

However, the radar data did suggest a stratospheric link. The scattered power as a function of height and time is shown in Fig. 2a, with the radar-determined tropopause indicated. At about the same time that the ozone enhancement appeared, the radar-determined tropopause showed a rapid descent (point P in Fig. 2a). The tropopause temperature profiles determined from the radiosondes showed a correlated behaviour, with strong temperature inversions tracking the radar-determined tropopause. The trajectory of this enhancement is shown by the broken line. When the radar tropopause descended, it left a region of only weak scatter at the ‘normal’ tropopause height (marked Q on the figure). The tropopause jet stream showed a very wavelike structure, indicating strong nonlinear planetary wave

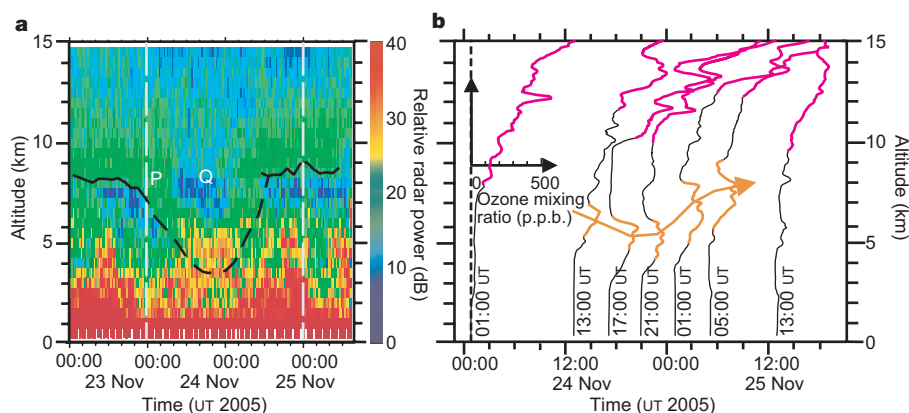


Figure 2 | Radar and ozone data recorded during the first campaign at Walsingham in November 2005. **a**, Altitude–time intensity plot of backscattered power during the campaign. The curved black broken line shows the radar-determined tropopause. The vertical grey broken lines show the start- and end-times of the period covering seven ozonesonde ascents of

interest. **b**, Successive ozone profiles for the seven ozonesonde launches. The upper, red sections of the profiles indicate the stratosphere, based on the World Meteorological Organization (WMO) definition of the tropopause (which by definition generally occurs above 500 mb), and the centre, orange sections emphasize the region of ozone of interest.

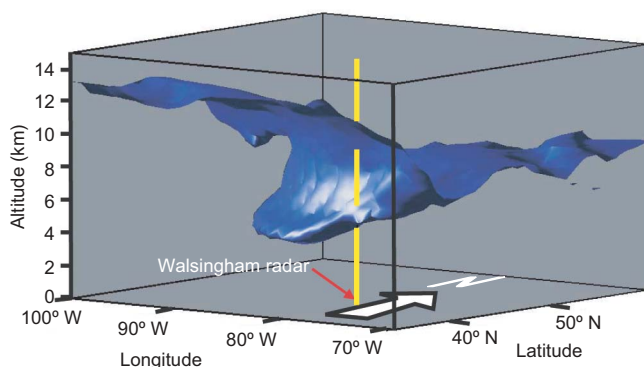


Figure 3 | Three-dimensional image of the 100 p.p.b. ozone surface during the event of 23–25 November 2005, as determined by the FLEXPART model. The time was specifically 24 November 2005 at 15:00 UT. The location of the Walsingham radar and radiosonde launch site is shown (vertical yellow line). The white arrow shows north.

activity in the lower stratosphere, as shown in maps provided by the Canadian Meteorological Centre (http://weatheroffice.gc.ca/analysis/index_e.html).

Figure 3 shows the results of a numerical simulation using FLEXPART. The model clearly indicates a deep influx of ozone from the stratosphere, resulting in a tongue of ozone penetrating to 4 km altitude, implying significant downward motion. The tongue of stratospheric air swept over the radar in such a way that its tip passed over the radar, producing the variation shown in Fig. 2b. Without the use of radar data, the stratospheric origin of this ozone tongue may well have been missed. In contrast to the Montreal case, in which the ozone reached the ground, the ozone in Fig. 3 appeared to mix with the surrounding air at 3–4 km.

Figure 4 shows the occurrence of all ozone intrusions during the four campaigns studied, shown placed end-to-end. Dark blue lines show occasions of strong intrusion, light blue represents weaker

intrusions, and black lines represent strong upward tropopause motions. Large positive vertical velocities can arise due to true tropopause jumps (as in Fig. 1b) and can also be produced by split tropopauses, as in Fig. 2. In the latter case, the tropopause-determination software follows the descending tropopause from point P until it becomes so low that it would not normally be considered a tropopause, and then finds the higher-level, weaker, tropopause (closer to point Q), producing an apparent jump in tropopause height. Both types of jumps will be considered collectively.

Every occurrence of definite ozone intrusion is associated with a level 2 or level 3 radar-tropopause excursion rate at, or just before, the intrusion, with the exceptions of events A, B, C and D. For cases C and D, the tropopause was only intermittently visible with the radar (this happens on occasion). Of the remaining 13 intrusions, 11 (that is, all except A and B), were associated with a level 2 or level 3 tropopause excursion. Even more telling, every level 2 or level 3 tropopause excursion was associated with some form of ozone intrusion. Hence, a level 2 or level 3 tropopause jump is a very strong predictor for ozone intrusion. No matter whether the jumps are real, or a consequence of a split tropopause or discontinuity, they serve as a valuable diagnostic. The ability to detect ozone intrusions in this way is an important capability, and a major result of our study. This is particularly true because windprofilers generally operate 24 hours per day, 365 days per year, so even when ozonesonde data are not available, windprofiler data can be used as a proxy for the possibility of ozone intrusions. This will be useful for air-quality forecasts, stratosphere–troposphere transport research, and general understanding of the ozone circulation, transport, and budget.

METHODS SUMMARY

The simultaneous and co-located use of windprofiler radars combined with frequent ozonesonde launches represents the key experimental aspect of this project. Windprofilers^{20–25} are radars that permit ground-based studies of the atmosphere from regions close to ground-level, to altitudes of 12 km and higher (depending on power output). A powerful transmitter initially emits repeated pulses of radio waves into the air, whereupon small portions of this signal are

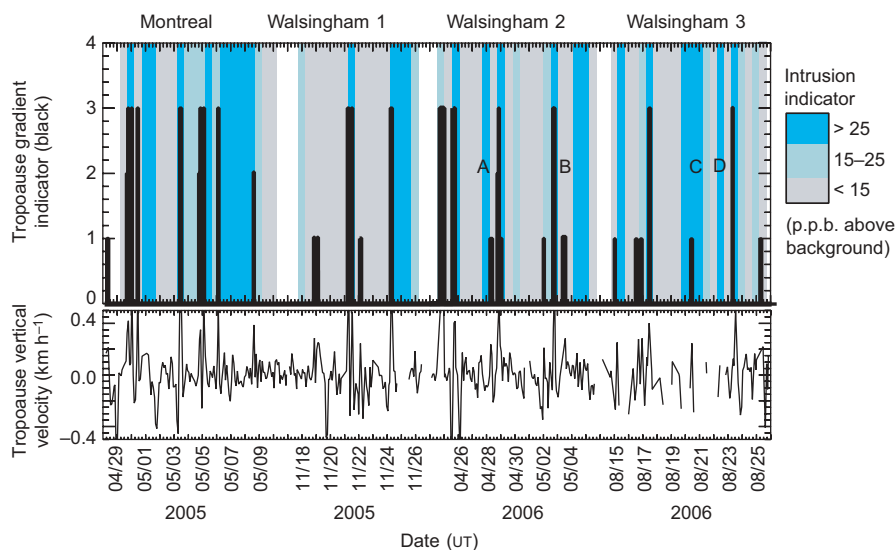


Figure 4 | Occurrence of ozone intrusions compared to radar-determined tropopause excursions. Dates for the campaigns are given as month/day. Dark-blue vertical bands represent occasions where a tropospheric ozone maximum occurred between 3 km altitude and the tropopause, and where this maximum exceeded the background value (that is, average of values before, after, above and below the maximum) by at least 25 p.p.b. A coincident local minimum in water vapour content was also required. This combination is taken as a strong indicator that a stratospheric intrusion had occurred, particularly if the layer showed evidence of descent. Light-blue shading indicates a weaker but nevertheless real intrusion, where in this case the excess of the local peak exceeded the background by 15–25 p.p.b. Grey

bands represent occasions when there was no significant tropospheric maximum, and white bands indicate times when no ozone data were available. The date of intrusion is set according to the time at which the intrusion left the stratosphere, and not the time of arrival at the ground. The lower panel shows the vertical velocity of the tropopause, as determined from the radar data. Tropopause excursion velocities have been classified into four categories using the tropopause gradient indicator; specifically: type 3 means $>0.4 \text{ km h}^{-1}$, type 2 means $>0.3 \text{ km h}^{-1}$, type 1 means $>0.2 \text{ km h}^{-1}$ and type 0 means $<0.2 \text{ km h}^{-1}$. These categories are plotted as black vertical lines in the upper graph.

returned to the radar antennas and recorded for analysis. Proper interpretation of these returned signals allows wind and turbulence strengths in the atmosphere to be measured, and in our case the height of the tropopause can also be found. The radars run continuously, allowing unprecedented monitoring of tropopause height. Ozone measurements were made using EN-SCI ozonesondes and ancillary equipment, including a ground station. The ozonesondes were accompanied by Vaisala RS-80 radiosondes for pressure, humidity and temperature measurements. On-board GPS receivers were used to track the the sonde positions and allow wind velocity determination. Typically either 800 g or 1,200 g balloons were used, filled with sufficient helium that they achieved an ascent rate of $3\text{--}5\text{ m s}^{-1}$. Experimental studies were supported by application of the FLEXPART²⁶ computer model, which permitted modelling of ozone movement. FLEXPART required hourly wind fields produced by a regional analysis model called GEM³⁰, run at $0.1375^\circ \times 0.1375^\circ$ resolution on a domain covering North America with 58 vertical levels to 10 hPa. Each FLEXPART run released 600,000 particles in the model domain, with those in the stratosphere initialized using an empirical relationship between potential vorticity and ozone concentration¹⁵. These were then advected using wind fields from GEM, and the resulting ozone field was output at $1^\circ \times 1^\circ \times 500\text{ m}$ resolution. Chemistry is not included in the model. FLEXPART has been extensively validated^{19,27–29}. Please see the Supplementary Information for further details.

Received 5 February; accepted 24 September 2007.

- World Meteorological Organization. *Scientific Assessment of Ozone Depletion 1998*. Global Ozone Research Monitoring Project Report 44 (WMO, Geneva, 1999).
- Altshuler, A. P. & Lefohn, A. S. Background ozone in the planetary boundary layer over the United States. *J. Air Waste Manage. Assoc.* **46**, 134–141 (1996).
- Lin, C.-Y. C., Jacob, D. J., Munger, J. W. & Fiore, A. M. Increasing background ozone in surface air over the United States. *Geophys. Res. Lett.* **27**, 3465–3468 (2000).
- Naja, M., Akimoto, H. & Staehelin, J. Ozone in background and photochemically aged air over central Europe: analysis of long-term ozonesonde data from Hohenpeissenberg and Payerne. *J. Geophys. Res.* **108** (D2), 4063, doi:10.1029/2002JD002477 (2003).
- Ashmore, M. R. Assessing the future global impacts of ozone on vegetation. *Plant Cell Environ.* **28**, 949–964 (2005).
- Wang, X. & Mauzerall, D. L. Characterizing distributions of surface ozone and its impact on grain production in China, Japan and South Korea: 1900 and 2020. *Atmos. Environ.* **38**, 4383–4402 (2004).
- Hogrefe, C. et al. Simulating changes in regional air pollution over the eastern United States due to changes in global and regional climate and emissions. *J. Geophys. Res.* **109**, D22301, doi:10.1029/2004JD004690 (2004).
- Stevenson, D. S. et al. Multimodel ensemble simulations of present-day and near future tropospheric ozone. *J. Geophys. Res.* **111**, doi:10.1029/2005JD006338 (2006).
- World Health Organization (WHO). *Health Aspects of Air Pollution with Particulate Matter, Ozone And Nitrogen Dioxide*. Report EUR/03/5042688 on a WHO working group (WHO Regional Office for Europe, Copenhagen, 2003); (<http://www.euro.who.int/document/e79097.pdf>).
- Lelieveld, J. & Dentener, F. J. What controls tropospheric ozone? *J. Geophys. Res.* **105** (D3), 3531–3552 (2000).
- Hirsch, A. I., Munger, J. W., Jacob, D. J., Horowitz, L. W. & Goldstein, A. H. Seasonal variation of the ozone production efficiency per unit NO_x at Harvard Forest, Massachusetts. *J. Geophys. Res.* **101**, 12659–12666 (1996).
- Tarasick, D. W., Fioletov, V. E., Wardle, D. I., Kerr, J. B. & Davies, J. Changes in the vertical distribution of ozone over Canada from ozonesondes: 1980–2001. *J. Geophys. Res.* **110**, doi:10.1029/2004JD004643 (2005).
- Holton, J. R. et al. Stratosphere-troposphere exchange. *Rev. Geophys.* **33**, 403–439 (1995).
- Stohl, A. et al. A new perspective on stratosphere-troposphere exchange. *Bull. Am. Meteorol. Soc.* **84**, 1565–1573 (2003).
- Stohl, A. et al. The influence of stratospheric intrusions on alpine ozone concentrations. *Atmos. Environ.* **34**, 1323–1354 (2000).
- Beekmann, M. et al. Regional and global tropopause fold occurrence and related ozone flux across the tropopause. *J. Atmos. Chem.* **28**, 29–44 (1997).
- Sprenger, M., Croci Maspoli, M. & Wernli, H. Tropopause folds and cross-tropopause exchange: A global investigation based upon ECMWF analyses for the time period March 2000 to February 2001. *J. Geophys. Res.* **108** (D12), 8518, doi:10.1029/2002JD002587 (2003).
- Wernli, H. & Bourqui, M. A Lagrangian 1-year climatology of (deep) cross-tropopause exchange in the extratropical Northern Hemisphere. *J. Geophys. Res.* **107** (D2), 4021, doi:10.1029/2001JD000812 (2002).
- Cooper, O. R. et al. Large upper tropospheric ozone enhancements above mid-latitude North America during summer: In situ evidence from the IONS and MOZIC ozone monitoring network. *J. Geophys. Res.* **111**, D24S05, doi:10.1029/2006JD007306 (2006).
- Roettger, J. & Larsen, M. F. in *Radar in Meteorology* (ed. Atlas, D.) 235–281 (American Meteorology Society, Boston, Massachusetts, 1990).
- Gage, K. S. in *Radar in Meteorology* (ed. Atlas, D.) 534–565 (American Meteorology Society, Boston, Massachusetts, 1990).
- Hocking, W. K. Recent advances in radar instrumentation and techniques for studies of the mesosphere, stratosphere and troposphere. *Radio Sci.* **32**, 2241–2270 (1997).
- Larsen, M. F. & Röttger, J. VHF and UHF Doppler radars as tools for synoptic research. *Bull. Am. Meteorol. Soc.* **63**, 996–1008 (1982).
- Hocking, W. K., Ruester, R. & Czechowsky, P. Absolute reflectivities and aspect sensitivities of VHF radio wave scatterers measured with the SOUSY radar. *J. Atmos. Terr. Phys.* **48**, 131–144 (1986).
- Gage, K. S. & Green, J. L. An objective technique for the determination of tropopause height from VHF radar observations. *J. Appl. Meteorol.* **21**, 1150–1154 (1982).
- Stohl, A., Forster, C., Frank, A., Seibert, P. & Wotawa, G. Technical note: The Lagrangian particle dispersion model FLEXPART version 6.2. *Atmos. Chem. Phys.* **5**, 2461–2474 (2005).
- Stohl, A., Hittenberger, M. & Wotawa, G. Validation of the Lagrangian particle dispersion model FLEXPART against large scale tracer experiment data. *Atmos. Environ.* **24**, 4245–4264 (1998).
- Stohl, A. et al. A replacement for simple back trajectory calculation in the interpretation of atmospheric trace substance measurements. *Atmos. Environ.* **36**, 4635–4648 (2002).
- Forster, C. et al. Lagrangian transport model forecasts and a transport climatology for the Intercontinental Transport and Chemical Transformation 2002 (ITCT 2K2) measurement campaign. *J. Geophys. Res.* **109**, D07S92, doi:10.1029/2003JD003589 (2004).
- Côté, J. et al. The operational CMC/MRB Global Environmental Multiscale (GEM) model. Part 1: design considerations and formulation. *Mon. Weath. Rev.* **126**, 1373–1395 (1998).

Supplementary Information is linked to the online version of the paper at www.nature.com/nature.

Acknowledgements This work was funded primarily by the Canadian Foundation for Climate and Atmospheric Science, and by the Natural Sciences and Engineering Research Council of Canada. We are grateful for logistical and financial support provided by Environment Canada. The McGill and Walsingham radars were installed with support from the Canada Innovation Foundation and Ontario Innovation Trust. Technical support was provided by G. Carey-Smith, J. Davies, T. Officer, M. van der Zanden and R. van der Zanden. We thank the CSA staff for making facilities at the Canadian Space Agency in Montreal available to us. Assistance and advice regarding the FLEXPART model was provided by O. Cooper, and advice and guidance from W. Komhyr at EN-SCI Corporation was also appreciated.

Author Contributions W.K.H. designed and built all the windprofiler radars used in the studies, and wrote all the on-line radar analysis software. He also originally proposed the concept of using the radars and ozone studies together to investigate stratosphere–troposphere transport, wrote the original proposal, and was the principal investigator on the grant used to obtain the data. T.C.-S. was a post-doctoral fellow on the project, and was responsible for all ozonesonde launches in regard to planning and implementation. He was also responsible for adaptation and implementation of the Flexpart model, and was responsible for data analysis after each flight. D.W.T. was the most experienced of the team in regard to ozone science, and was responsible for the direct supervision of T.C.-S. for significant parts of his tenure. He provided advice about ozonesonde launches and data interpretation, including initiating the use of FLEXPART and GEM to provide a four-dimensional view of the intrusion processes. P.S.A. is a research scientist who co-managed the ozonesonde programme, undertook much of the pre-campaign preparation work, and provided scientific direction during the experimental campaigns. K.S. operated the Toronto Atmospheric Observatory, which was used as a support facility to provide back-up data about the behaviour of various atmospheric chemical constituents. Y.R. supported T.C.-S. with advice. I.Z. and P.A.T., as principal investigators of various windprofiler projects, were responsible for the day-to-day running of the radars.

Author Information Reprints and permissions information is available at www.nature.com/reprints. Correspondence and requests for materials should be addressed to W.K.H. (whocking@uwo.ca).

Haemodynamics determined by a genetic programme govern asymmetric development of the aortic arch

Kenta Yashiro^{1,2,†}, Hidetaka Shiratori^{1,2} & Hiroshi Hamada^{1,2}

Laterality of the internal organs of vertebrates is determined by asymmetric Nodal signalling in the lateral plate mesoderm¹. A deficiency of such signalling results in heterotaxia syndrome, characterized by anomalous laterality of visceral organs and complex congenital heart conditions¹. *Pitx2*, the transcription factor induced by the Nodal signal, regulates left–right asymmetric morphogenesis^{1–4}. The cellular and molecular bases of asymmetric morphogenesis remain largely unknown, however. Here we show that ablation of unilateral *Pitx2* expression in mice impairs asymmetric remodelling of the branchial arch artery (BAA) system, resulting in randomized laterality of the aortic arch. *Pitx2*-positive cells were found not to contribute to asymmetrically remodelled arteries. Instead, *Pitx2* functions in the secondary heart field⁵ and induces a dynamic morphological change in the outflow tract of the heart, which results in the provision of an asymmetric blood supply to the sixth BAA. This uneven distribution of blood flow results in differential signalling by both the platelet-derived growth factor receptor and vascular endothelial growth factor receptor 2. The consequent stabilization of the left sixth BAA and regression of its right counterpart underlie left-sided formation of the aortic arch. Our results therefore indicate that haemodynamics, generated by a *Pitx2*-induced morphological change in the outflow tract, is responsible for the asymmetric remodelling of the great arteries.

To understand how the Nodal–*Pitx2* signalling pathway brings about asymmetric organ morphology, we studied the mechanism of situs-specific development of the aortic arch. Mutant mice (*Pitx2*^{ΔASE/ΔASE}) lacking the asymmetric enhancer (ASE) of *Pitx2* develop right isomerism⁶, which manifests in part as severe congenital heart conditions^{1,2,7}. The laterality of the aortic arch also seems to be randomized in these mice (Fig. 1a, Supplementary Fig. 1, and data not shown). The cardiovascular phenotype of *Pitx2*^{ΔASE/ΔASE} mice seemed similar to that of a *Pitx2c*^{−/−} mutant³, but re-evaluation of newborn *Pitx2*^{ΔASE/ΔASE} mice further revealed that laterality of the patent sixth BAA was randomized (whereas the fourth BAA remained normal) and was always concordant with that of the patent dorsal aorta (dAo). The correlation between the laterality of the sixth BAA and that of the dAo, together with the fact that the earliest event of asymmetric BAA remodelling is thought to be regression of the right sixth BAA^{8,9}, suggested that the situs of the aortic arch depends on which side the sixth BAA undergoes regression.

The arterial system is initially formed symmetrically, with subsequent asymmetric remodelling giving rise to the aortic arch^{9,10}. Thus, two regions, namely the right sixth BAA and the right dAo, undergo complete regression in the wild type (Fig. 1a). In *Pitx2*^{ΔASE/ΔASE} embryos, the symmetrical BAA system seems to form normally (Supplementary Fig. 2a). As in the *Pitx2c* mutant mice³, the migration and function of cardiac neural crest cells also seems to be

normal in *Pitx2*^{ΔASE/ΔASE} mice^{2,11,12}, given that they do not manifest persistent truncus arteriosus¹⁰ (Supplementary Fig. 2b). These observations suggested that the aortic arch anomaly in *Pitx2*^{ΔASE/ΔASE} mice is due to impaired BAA remodelling.

To determine the role of *Pitx2* in BAA remodelling, we next examined the contribution of *Pitx2*-positive cells to the developing BAA system. Unexpectedly, we did not detect any *Pitx2*-positive cells in or near the sixth BAA or dAo (Fig. 1b, d, and Supplementary Fig. 2c–e). As expected¹², *Pitx2*-positive cells were abundant in the secondary heart field, including the myocardium of the left wall of the outflow tract (OFT) (Fig. 1c). These results indicated that, although BAA remodelling requires *Pitx2*, it is not governed directly by *Pitx2*-positive cells, whereas morphogenesis of the OFT does involve such cells^{5,12}.

To determine whether unknown morphological features of the OFT contribute to asymmetric remodelling of the sixth BAA³, we examined OFT morphology at embryonic day (E)11.5 and E12.0 by optical projection tomography¹³. At E11.5, immediately before BAA remodelling, the OFT spiralled through 180° in wild-type embryos⁹ (Fig. 1e). In *Pitx2*^{ΔASE/ΔASE} mice, however, the OFT had failed to adopt the spiral structure and remained linear. This finding suggested that *Pitx2* is required for formation of the spiral structure of the OFT, which is probably responsible for the correct alignment of the ventricles with the great arteries. At E12.0, the spiral structure of the OFT undergoes a 90° rewinding as a result of a clockwise rotational movement of the arterial pole¹⁴ (Fig. 1f). This rotation shifts the entry point of the right sixth BAA towards the left, adjacent to the aorta (Fig. 1f). Simultaneously, the right sixth BAA undergoes a decrease in diameter and becomes longer than its left counterpart (Fig. 1f). In *Pitx2*^{ΔASE/ΔASE} embryos, however, this rotational movement fails to occur, and the sixth BAA remains bilaterally patent at E12.5 (Supplementary Fig. 3). These results suggested that the rotational movement of the arterial pole that takes place between E11.5 and E12.0 may be responsible for the right-side-specific regression of the sixth BAA in wild-type mice. Neither cell death nor cell growth seems to be the initial cue for BAA remodelling (Supplementary Fig. 4a–o, Supplementary Fig. 5a).

Rotation of the arterial pole renders the right sixth BAA longer and narrower than its left counterpart (Figs 1f and 2a), changes that would be expected to reduce the flow rate in the right vessel. Previous studies have suggested that haemodynamics may regulate morphogenesis of the aortic arch^{10,15}. Furthermore, echocardiography of the uterus¹⁶ revealed that blood flow in the left dAo was similar to that in the right dAo at E11.5 but was significantly greater during arterial remodelling at E12.0 in wild-type embryos, whereas blood flow in the dAo was bilaterally equal in *Pitx2*^{ΔASE/ΔASE} embryos at both developmental stages (Supplementary Fig. 6 and Supplementary Table 1). A decrease in or loss of blood flow in the right sixth BAA of wild-type embryos might therefore result in its regression. To test

¹Developmental Genetics Group, Graduate School of Frontier Biosciences, Osaka University, 1–3 Yamada-oka, Suita, Osaka 565-0871, Japan. ²CREST, Japan Science and Technology Corporation (JST), 1–3 Yamada-oka, Suita, Osaka 565-0871, Japan. [†]Present address: Translational Cardiovascular Therapeutics, William Harvey Research Institute, Barts and The London, Queen Mary's School of Medicine and Dentistry, University of London, Charterhouse Square, London EC1M 6BQ, UK

this hypothesis, we ligated the left sixth BAA immediately before the onset of remodelling; this did not affect heart beating (Fig. 2b, c, Supplementary Table 2 and Supplementary Movies 1–4). Ligated embryos were then cultured *in vitro* for 36 h before examination of arterial morphology (Fig. 2d–f). In control embryos, BAA remodelling occurred normally. However, in about half of the embryos with the left sixth BAA ligated, the right sixth BAA persisted, whereas the ligated left artery underwent complete regression in all cases. In the embryos in which the right sixth BAA remained patent, the diameter of the dAo was larger on the right side than on the left. Ligation induced ectopic apoptosis in the left sixth BAA (Supplementary Fig. 4p–u). These results indicate that blood flow is essential and sufficient for the persistent patency of the sixth BAA and dAo. In support of this notion, a decrease in heart rate induced by the

β -adrenergic antagonist propranolol resulted in bilateral sixth BAA regression in wild-type embryos (see below).

We next examined whether growth factor signalling might change during regression of the sixth BAA, as occurs with the regression of tumour vessels¹⁷. Among several signalling molecules examined, platelet-derived growth factor (PDGF)-A and vascular endothelial growth factor receptor 2 (VEGFR2) were found to be associated with remodelling of the sixth BAA (Fig. 3a–h). In wild-type embryos at E12.0, *Pdgfa* expression in the sixth BAA was maintained on the left side but decreased on the right (Fig. 3a–c). Furthermore, the level of phosphorylated VEGFR2 (pVEGFR2) in endothelial cells was decreased in the right sixth BAA near the OFT (Fig. 3g). In *Pitx2* ^{Δ ASE/ Δ ASE} embryos, however, *Pdgfa* (Fig. 3d–f) and pVEGFR2 (Fig. 3h) remained symmetrical. Conversely, in four of six embryos in

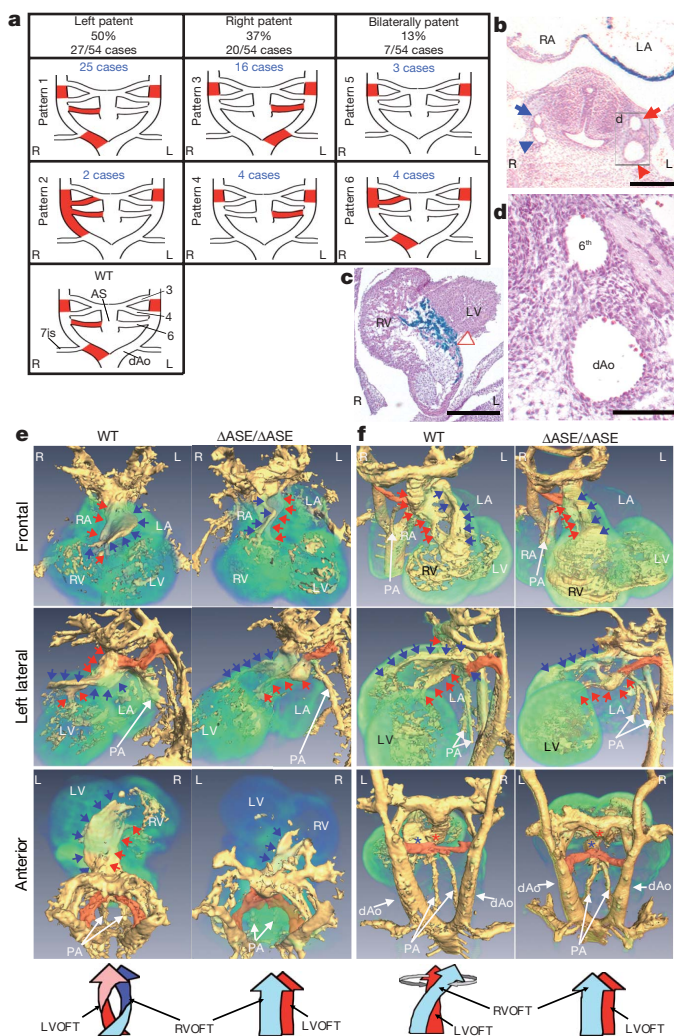


Figure 1 | Remodelling of the sixth BAA is governed in a non-cell-autonomous manner by left-side-specific *Pitx2*. **a**, Patterns of BAA remodelling in *Pitx2* ^{Δ ASE/ Δ ASE} embryos as represented by system morphology at E11.5. Red regions, complete regression; R, right; L, left; AS, aortic sac; 7is, seventh intersegmental artery; 3, 4 and 6 in wild-type (WT) indicate third, fourth and sixth BAA, respectively. **b–d**, Staining for *Pitx2*-positive cells around remodelled arteries (**b**, **d**) and outflow tract (**c**) in horizontal sections of E11.5 wild-type embryos. The boxed region in **b** is shown in **d**. The ventral side is at the top. Red and blue arrowheads, dAo; open arrowhead, *Pitx2*-positive cells; LA, left atrium; LV, left ventricle; RA, right atrium; RV, right ventricle. Scale bars, 250 μ m (**b**, **c**) or 100 μ m (**d**). **e**, **f**, Arterial pole rotation in WT embryos between E11.5 (**e**) and E12.0 (**f**). Blue arrows, right ventricular outflow tract (RVOFT), red arrows, left ventricular outflow tract (LVOFT); PA, pulmonary artery; blue asterisk, pulmonary trunk; red asterisk, aortic trunk.

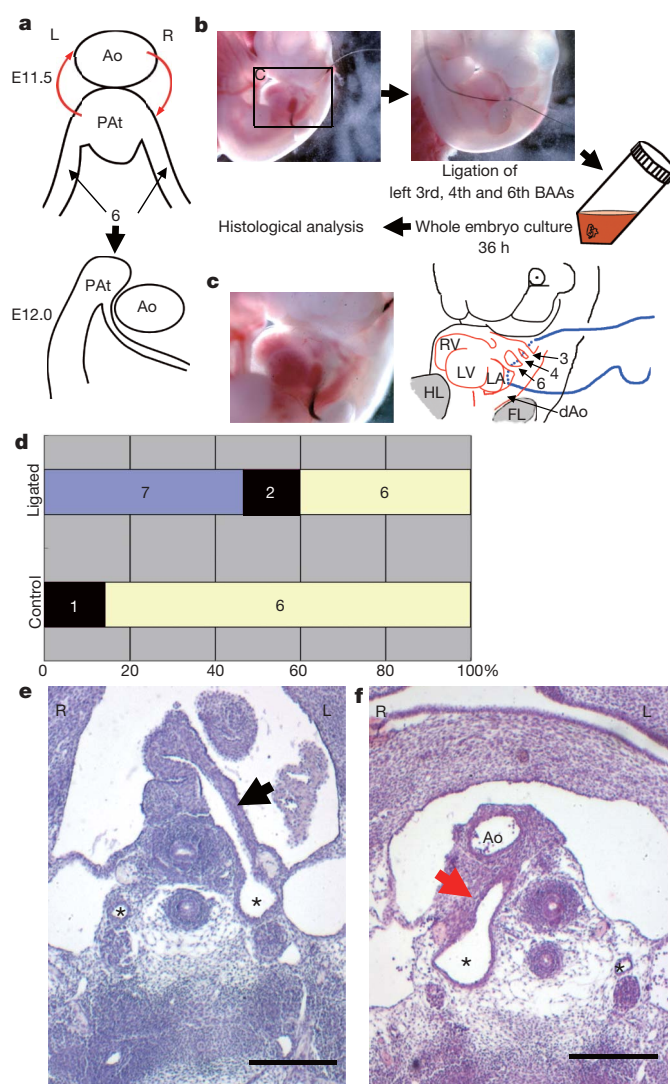


Figure 2 | Blood flow is essential and sufficient for persistent patency of the sixth BAA. **a**, Proposed mechanism for regression of the right sixth BAA. Ao, aorta; PA, pulmonary trunk; 6, sixth BAA. **b**, **c**, Experimental strategy to determine the effect of ligation of the sixth BAA on its right counterpart. HL, hindlimb bud; FL, forelimb bud; 3, 4 and 6 in the diagram indicate third, fourth and sixth BAA, respectively. **d**, Frequency of persistent patency of the right sixth BAA in embryos subjected, or not (control), to ligation of the left sixth at E11.0. The numbers of embryos showing each morphological pattern are indicated in the bar graph: blue, persistently patent; black, under regression; yellow, completely regressed. **e**, **f**, Haematoxylin/eosin staining of horizontal sections of cultured embryos either subjected to ligation of the left sixth BAA (**f**) or unligated (**e**). Ventral side is up. Black arrow, left sixth BAA; red arrow, right sixth BAA; asterisks, dAo. Scale bars, 250 μ m.

which the left sixth BAA had been ligated, the levels of *Pdgfa* and pVEGFR2 were decreased on the left side and maintained on the right side (Fig. 3i, j). These observations suggested that a differential blood supply results in asymmetry both in *Pdgfa* expression and in the amount of activated VEGFR2 in the sixth BAA, which is consistent with the higher rate of cell proliferation apparent in the left sixth BAA than in its right counterpart at E12.0 (Supplementary Fig. 5b).

To examine further the roles of PDGF and VEGF, we investigated the effects of chemical inhibitors of PDGF receptor (PDGFR) or VEGFR signalling on the patency of the sixth BAA in wild-type embryos. Although administration of a VEGFR tyrosine kinase inhibitor or PDGFR inhibitor (AG1296) alone to E11.0 embryos in culture had only small effects, administration of both together induced bilateral loss of the sixth BAA in most cases (Fig. 4a). Similarly, bilateral regression of the sixth BAA was induced by treatment with AG1433, which inhibits both PDGFR and VEGFR2 signalling at 10 μ M. The effects of these inhibitors were specific to the sixth BAA, given that the gross appearance of the embryo, heart and third and fourth BAAs were not affected (Supplementary Fig. 7a, b, Supplementary Videos 5–9, Supplementary Table 2, and data not shown). Although the molecular basis of this specificity is unknown,

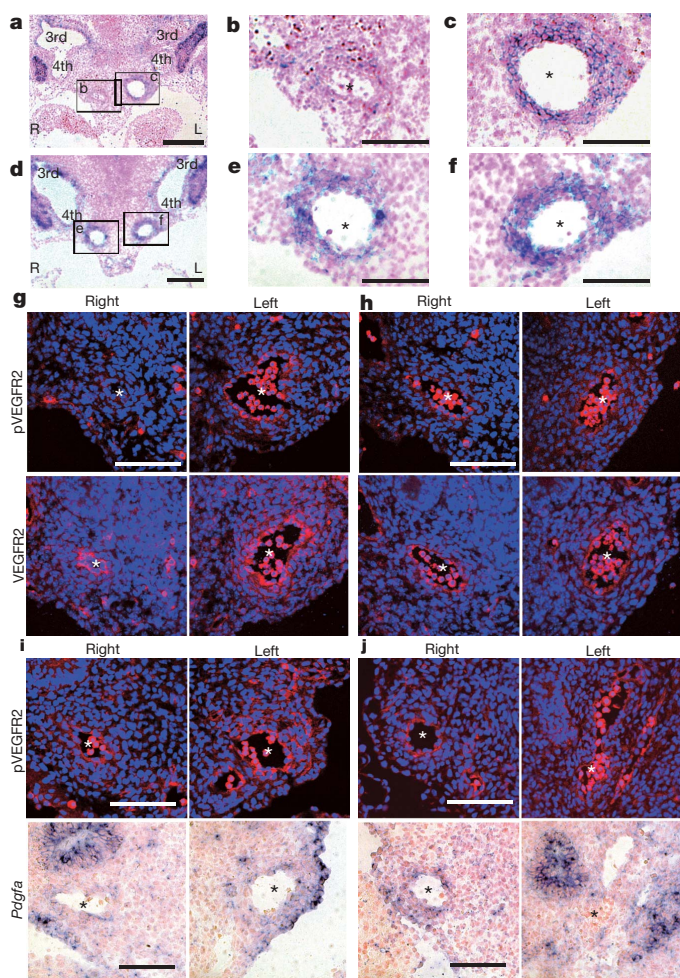


Figure 3 | Relation between blood supply and both the expression of *Pdgfa* and the level of activated VEGFR2 in the sixth BAA. a–f, Expression of *Pdgfa* in frontal sections of wild-type (a–c) or *Pitx2*^{ΔASE/ΔASE} (d–f) embryos at E12.0. Asterisks, sixth BAA. Scale bars, 250 μ m (a, d) or 100 μ m (b, c, e, f). g, h, Immunofluorescence analysis of VEGFR2 and pVEGFR2 of the sixth BAA (asterisks) in frontal sections of wild-type (g) or *Pitx2*^{ΔASE/ΔASE} (h) embryos at E12.0. VEGFR2 was symmetrical in both genotypes. Blue, nuclei. Scale bars, 100 μ m. i, j, pVEGFR2 and *Pdgfa* in frontal sections of wild-type embryos subjected (j) or not (i) to ligation of the left sixth BAA. VEGFR2 was not affected (data not shown) (j). Asterisks, sixth BAA. Scale bars, 100 μ m.

the sixth BAA has been suggested to possess different characteristics from the fourth¹⁸. Furthermore, our results are consistent with previous observations that mice deficient in PDGF or VEGF signalling manifest normal regression of the sixth BAA and a low frequency of right-sided aortic arch^{19,20}. Loss of both PDGFR and VEGFR signalling therefore seems to result in bilateral regression of the sixth BAA. Furthermore, expression of a *Vegfa* transgene, but not that of a *Pdgfa* transgene, in the smooth muscle cells of the great arteries prevented the right sixth BAA and dAo from undergoing complete regression (three of nine *Vegfa* transgene-positive embryos; Fig. 4b), although these vessels were hypoplastic or had collapsed, suggesting that the VEGF signal is sufficient to preserve the sixth BAA and dAo (Supplementary Discussion 1).

On the basis of our results, we propose a model for situs-specific BAA remodelling (Fig. 4c). First, the genetic programme, including the expression of *Pitx2*, induces a dynamic morphological change in the OFT, which in turn generates a differential distribution of blood flow. Blood flow in the left sixth BAA is sufficient to stimulate

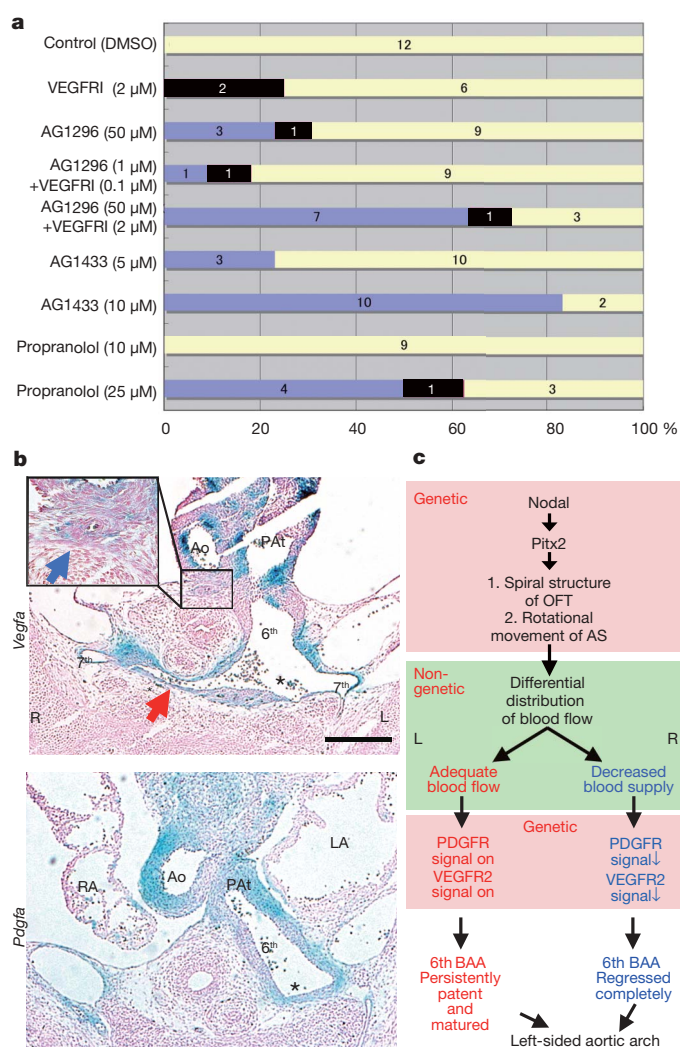


Figure 4 | Both PDGF and VEGF signals are required for persistent patency of the sixth BAA. a, Frequency of patency of the left sixth BAA in embryos cultured with or without inhibitors. DMSO, dimethylsulphoxide (vehicle); VEGFR1, VEGFR tyrosine kinase inhibitor. Blue columns, completely regressed; black columns, under regression; yellow columns, persistently patent. b, X-Gal staining of horizontal sections of E13.5 embryos harbouring an *SM22 α -Vegfa-IRES-lacZ* or *SM22 α -Pdgfa-IRES-lacZ* transgene. Asterisk, dAo; red arrow, unregressed right dAo; blue arrow, unregressed right sixth BAA. Ventral side is up. Scale bar, 250 μ m. c, Model for the conversion of genetic (leftness) information into asymmetric aortic arch morphogenesis. AS, aortic sac.

PDGFR and VEGFR2 signalling and the consequent maintenance of arterial structure, whereas the decreased blood flow in the right sixth BAA results in its regression. This sequence of events ensures that the aortic arch is established on the left side by E12.5.

Various mutant mice show a laterality defect of the aortic arch without a deficiency in the Nodal–Pitx2 signalling pathway^{8,19–23}. However, all such mutants manifest a combination of hypoplasia or aplasia of BAAs, malfunction or impaired migration of cardiac neural crest cells, and an OFT anomaly. The causes of the aortic arch anomaly in these animals might therefore differ from those of the anomaly in the *Pitx2*^{ΔASE/ΔASE} mutant, although the anomalies may share a common molecular mechanism to some extent.

The notion that blood flow is responsible for the laterality of the aortic arch is consistent with the aetiology of congenital heart diseases in humans (Supplementary Discussion 2). It remains unknown, however, how *Pitx2* governs the formation of the spiral septum and the subsequent rotation of the arterial pole. Further studies are therefore necessary to characterize the cellular and molecular mechanisms underlying the morphological changes of the OFT.

METHODS SUMMARY

Mice. The generation of *Pitx2*^{ΔASE/ΔASE} mutant mice², *Pitx2* 17-*Cre* transgenic mice², *Wnt1-Cre* transgenic mice¹¹ and *CAG-CAT-lacZ* reporter mice² was described previously.

Histological analyses. *In situ* hybridization, immunostaining and staining of sections with X-Gal (5-bromo-4-chloro-3-indolyl-β-D-galactopyranoside) were performed as described previously^{24,25}.

Optical projection tomography (OPT). OPT experiments were performed as described previously^{13,26}.

Whole-embryo culture. Whole-embryo culture was performed as described²⁴.

Cell lineage analysis. *Pitx2* 17-*Cre*, *Wnt1-Cre* or *CAG-CAT-lacZ* transgenes were introduced into *Pitx2*^{ΔASE/+} heterozygotes.

Full Methods and any associated references are available in the online version of the paper at www.nature.com/nature.

Received 22 March; accepted 13 September 2007.

1. Hamada, H., Meno, C., Watanabe, D. & Saijoh, Y. Establishment of vertebrate left–right asymmetry. *Nature Rev. Genet.* **3**, 103–113 (2002).
2. Shiratori, H., Yashiro, K., Shen, M. M. & Hamada, H. Conserved regulation and role of *Pitx2* in situs-specific morphogenesis of visceral organs. *Development* **133**, 3015–3025 (2006).
3. Liu, C. *et al.* *Pitx2c* patterns anterior myocardium and aortic arch vessels and is required for local cell movement into atrioventricular cushions. *Development* **129**, 5081–5091 (2002).
4. Liu, C. *et al.* Regulation of left–right asymmetry by thresholds of *Pitx2c* activity. *Development* **128**, 2039–2048 (2001).
5. Buckingham, M., Meilhac, S. & Zaffran, S. Building the mammalian heart from two sources of myocardial cells. *Nature Rev. Genet.* **6**, 826–835 (2005).
6. Shiratori, H. *et al.* Two-step regulation of left–right asymmetric expression of *pitx2*: Initiation by nodal signaling and maintenance by *Nkx2*. *Mol. Cell* **7**, 137–149 (2001).
7. Becker, A. & Anderson, R. in *Pathology of Congenital Heart Disease* (ed. Crawford, T.) 321–337 (Butterworths, London, 1981).
8. Yanagisawa, H. *et al.* Role of endothelin-1/endothelin—a receptor-mediated signaling pathway in the aortic arch patterning in mice. *J. Clin. Invest.* **102**, 22–33 (1998).

9. Hiruma, T., Nakajima, Y. & Nakamura, H. Development of pharyngeal arch arteries in early mouse embryo. *J. Anat.* **201**, 15–29 (2002).
10. Waldo, K. & Kirby, M. in *Living Morphogenesis of the Heart* (eds de la Cruz, M. & Markwald, R.) 187–217 (Birkhäuser, Boston, MA, 1998).
11. Jiang, X. *et al.* Fate of the mammalian cardiac neural crest. *Development* **127**, 1607–1616 (2000).
12. Ai, D. *et al.* *Pitx2* regulates cardiac left–right asymmetry by patterning second cardiac lineage-derived myocardium. *Dev. Biol.* **296**, 437–449 (2006).
13. Sharpe, J. *et al.* Optical projection tomography as a tool for 3D microscopy and gene expression studies. *Science* **296**, 541–545 (2002).
14. Bajolle, F. *et al.* Rotation of the myocardial wall of the outflow tract is implicated in the normal positioning of the great arteries. *Circ. Res.* **98**, 421–428 (2006).
15. Rychter, Z. Experimental morphology of the aortic arches and the heart loop in chick embryos. *Adv. Morphog.* **2**, 333–371 (1962).
16. Phoon, C. K., Aristizabal, O. & Turnbull, D. H. 40 MHz doppler characterization of umbilical and dorsal aortic blood flow in the early mouse embryo. *Ultrasound Med. Biol.* **26**, 1275–1283 (2000).
17. Carmeliet, P. Angiogenesis in health and disease. *Nature Med.* **9**, 653–660 (2003).
18. Gittenberger-de Groot, A. C., Azhar, M. & Molin, D. G. Transforming growth factor β–Smad2 signaling and aortic arch development. *Trends Cardiovasc. Med.* **16**, 1–6 (2006).
19. Tallquist, M. D. & Soriano, P. Cell autonomous requirement for PDGFRα in populations of cranial and cardiac neural crest cells. *Development* **130**, 507–518 (2003).
20. Stalmans, I. *et al.* Vegf: A modifier of the del22q11 (DiGeorge) syndrome? *Nature Med.* **9**, 173–182 (2003).
21. Abu-Issa, R. *et al.* Fgf8 is required for pharyngeal arch and cardiovascular development in the mouse. *Development* **129**, 4613–4625 (2002).
22. Phillips, H. M. *et al.* Vangl2 acts via RhoA signaling to regulate polarized cell movements during development of the proximal outflow tract. *Circ. Res.* **96**, 292–299 (2005).
23. Vitelli, F. *et al.* A genetic link between Tbx1 and fibroblast growth factor signaling. *Development* **129**, 4605–4611 (2002).
24. Yashiro, K. *et al.* Regulation of retinoic acid distribution is required for proximodistal patterning and outgrowth of the developing mouse limb. *Dev. Cell* **6**, 411–422 (2004).
25. Uehara, M. *et al.* CYP26A1 and CYP26C1 cooperatively regulate anterior–posterior patterning of the developing brain and the production of migratory cranial neural crest cells in the mouse. *Dev. Biol.* **302**, 399–411 (2007).
26. Takeuchi, J. K. *et al.* Tbx20 dose-dependently regulates transcription factor networks required for mouse heart and motoneuron development. *Development* **132**, 2463–2474 (2005).

Supplementary Information is linked to the online version of the paper at www.nature.com/nature.

Acknowledgements We thank S. Iseki, A. McMahon and H. Sucov for *Wnt1-Cre* mice; the staff of MRC Technology in Edinburgh for technical assistance with OPT; K. Yamashita for transgene construction; K. Mochida, S. Ohishi and Y. Ikawa for general technical assistance; Primetech Corp. for technical assistance with Vevo770; and P. Soriano, T. Kubo, K. Ozono, T. Sano, T. Matsusita, S. Kogaki and the cardiologists in the Department of Pediatrics, Osaka University Medical School, for advice. This work was supported by grants (to H.H.) from the Ministry of Education, Culture, Sports, Science, and Technology of Japan and by CREST.

Author Contributions Project planning was mainly performed by K.Y.; most of the experiments were carried out by K.Y. and the remaining experiments by H.S. and H.H.; the manuscript was written by K.Y. and H.H.

Author Information Reprints and permissions information is available at www.nature.com/reprints. Correspondence and requests for materials should be addressed to K.Y. (k.yashiro@qmul.ac.uk) or H.H. (hamada@fbs.osaka-u.ac.jp).

METHODS

Mice. The *SM22 α -Vegfa-IRES-lacZ* and *SM22 α -Pdgfa-IRES-lacZ* transgenes were constructed from mouse *Vegfa* or *Pdgfa* complementary DNAs (provided by S. Nishikawa and P. Soriano, respectively), an *IRES-lacZ* cassette and a 2.8-kilobase genomic DNA fragment including the promoter and enhancer of mouse *SM22 α* required for expression in smooth muscle cells of great arteries²⁷. The latter fragment was amplified by PCR with the primers 5'-GCCAGGACAGATGCAGGTAGGAGACTTTGG-3' and 5'-AGGAGAGTAGCTTCGGTGTCTGGGCTGGGG-3'.

Histological analyses. The assay of bromodeoxyuridine incorporation was performed as described previously²⁴; embryos were dissected and fixed 30 min after intraperitoneal injection of bromodeoxyuridine into pregnant mice. Immunostaining was performed with antibodies specific for cleaved caspase 3 (dilution 1:100; Cell Signalling), for VEGFR2 (dilution 1:100; Cell Signalling), for platelet-endothelial cell adhesion molecule (PECAM; dilution 1:20; Upstate Biotechnology) or for phosphorylated VEGFR2 (dilution 1:25; Spring Biosciences), as described previously²⁵. Antigen unmasking by autoclaving of sections for 10 min in 10 mM sodium citrate (pH 6.0) was performed before incubation with the antibodies against cleaved caspase 3 and VEGFR2, and Can Get Signal immunodetection solution B (Toyobo) was used for the detection of pVEGFR2. Immune complexes were detected with Alexa568-conjugated or Alexa488-conjugated secondary antibodies against rabbit or mouse immunoglobulin G (dilution 1:400; Molecular Probes) or with a peroxidase-based Vectastain kit (Vector). Nuclei were stained either with 4',6-diamidino-2-phenylindole (for immunofluorescence), nuclear fast red (for X-Gal staining and *in situ* hybridization), methyl green or haematoxylin (for staining with the peroxidase-based Vectastain kit). Images were obtained and analysed with a confocal microscope (LSM510 META; Carl Zeiss) and Axiophoto2 (Carl Zeiss).

Cell lineage analysis. *Pitx2* 17-*Cre*, *Wnt1-Cre* or *CAG-CAT-lacZ* transgenes were introduced into *Pitx2*^{ΔASE/+} heterozygotes. Analysis of the lineage distribution of neural crest cells or of *Pitx2*-positive cells of the left lateral plate mesoderm was performed as described previously². *Pitx2*-positive cells were localized with a *Cre* transgene driven by the ASE of *Pitx2* (*Pitx2* 17-*Cre*) and with a *Cre*-responsive *lacZ* transgene (*CAG-CAT-lacZ*)²; this approach would be expected to detect cells actively expressing *Pitx2* as well as those that had previously expressed *Pitx2*, given that the ASE is active from E8.0.

Treatment with chemical inhibitors. AG1296, AG1433 and VEGFR tyrosine kinase inhibitor were obtained from Calbiochem, and propranolol from Sigma. All were dissolved in dimethylsulphoxide (Sigma). Median inhibitory

concentrations provided by the manufacturer were 1.0 μ M for AG1296 (PDGFR), 5 μ M (PDGFR) and 9.4 μ M (VEGFR2) for AG1433, and 0.1 μ M for VEGFR tyrosine kinase inhibitor (VEGFR2). ICR mouse embryos dissected at E11.0 were cultured with vehicle alone or with inhibitors for 36 h (unless indicated otherwise), when they had developed to a stage equivalent to E12.5. Only well-developed embryos with a normal heartbeat were subjected to further analysis except propranolol. Embryos cultured in the presence of 25 μ M propranolol were always deformed, which might have resulted from extremely reduced peripheral circulation.

Ligation experiments. In the arterial ligation experiments, the third, fourth and sixth BAAs on the left side of E11.0 or E11.5 ICR embryos were carefully ligated with a suture needle (nylon monofilament 10-0, T4A10N10-25; Bear Medic) so as not to damage the great vessels and atrium. Control embryos were simply punctured near the left BAAs with the suture needle. For examination of arterial morphogenesis, E11.0 embryos were cultured for 36 h, when they had developed to the stage equivalent to E12.5. For analysis of *Pdgfa* expression and pVEGFR2 distribution, E11.5 embryos were cultured for 4–8 h. For evaluation of apoptosis, E11.0 embryos were cultured for 12 h. Only well-developed embryos with a normal heartbeat were subjected to further analysis.

Optical projection tomography (OPT). A Bioptronics OPT scanner 3001 was used for scanning (Bioptronics Microscopy, MRCT). Data were analysed with Amira v. 4.0 software (TGS)²⁶. Arterial morphology was revealed by whole-mount immunostaining with antibodies against PECAM, and heart morphology by autofluorescence of the embryo itself.

Echocardiography. Echocardiography of fetuses was performed as described previously¹⁶ with the use of a Vevo-770 imaging system, a Vevo Integrated Rail System and a Vevo Mouse Handling Table (VisualSonics). The probe was RMV-704. The rectal temperature of the dam was monitored continuously and maintained at 37 °C during measurements. Data obtained from embryos with bradycardia or tachycardia for the corresponding gestational age¹⁶ were discarded.

Video recording. Embryos cultured for 12–14 h were transferred to DMEM medium without phenol red (Sigma) at 37 °C and were immediately subjected to recording with a MAS30-SR1M adaptor (McCan Imaging) and a HandyCam DCR-SR300 (Sony). The resulting videos (MPEG2 format) were edited and changed to QuickTime movies with QuickTime Pro (Apple).

27. Li, L., Miano, J. M., Mercer, B. & Olson, E. N. Expression of the *SM22 α* promoter in transgenic mice provides evidence for distinct transcriptional regulatory programs in vascular and visceral smooth muscle cells. *J. Cell Biol.* **132**, 849–859 (1996).

An essential role for a CD36-related receptor in pheromone detection in *Drosophila*

Richard Benton^{1†}, Kirsten S. Vannice^{1†} & Leslie B. Vosshall¹

The CD36 family of transmembrane receptors is present across metazoans and has been implicated biochemically in lipid binding and transport¹. Several CD36 proteins function in the immune system as scavenger receptors for bacterial pathogens and seem to act as cofactors for Toll-like receptors by facilitating recognition of bacterially derived lipids^{2–4}. Here we show that a *Drosophila melanogaster* CD36 homologue, Sensory neuron membrane protein (SNMP), is expressed in a population of olfactory sensory neurons (OSNs) implicated in pheromone detection. SNMP is essential for the electrophysiological responses of OSNs expressing the receptor OR67d to (Z)-11-octadecenyl acetate (*cis*-vacenyl acetate, cVA), a volatile male-specific fatty-acid-derived pheromone that regulates sexual and social aggregation behaviours^{5–8}. SNMP is also required for the activation of the moth pheromone receptor HR13 by its lipid-derived pheromone ligand (Z)-11-hexadecenal⁹, but is dispensable for the responses of the conventional odorant receptor OR22a to its short hydrocarbon fruit ester ligands. Finally, we show that SNMP is required for responses of OR67d to cVA when ectopically expressed in OSNs not normally activated by pheromones. Because mammalian CD36 binds fatty acids¹⁰, we suggest that SNMP acts in concert with odorant receptors to capture pheromone molecules on the surface of olfactory dendrites. Our work identifies an unanticipated cofactor for odorant receptors that is likely to have a widespread role in insect pheromone detection. Moreover, these results

define a unifying model for CD36 function, coupling recognition of lipid-based extracellular ligands to signalling receptors in both pheromonal communication and pathogen recognition through the innate immune system.

Insect odorant receptors represent a novel class of polytopic membrane proteins unrelated to vertebrate G-protein-coupled chemosensory receptors^{11,12}. The functional insect odorant receptor is a heteromer of a ligand-binding subunit and the highly conserved OR83b co-receptor, which mediates transport to sensory cilia^{11,13–15}. Little is known about how this complex recognizes odours and evokes neuronal depolarization. To isolate novel components involved in insect olfactory detection, we used a bioinformatic approach to identify molecules that exhibit the same insect-specific orthology and olfactory-specific tissue expression as these receptors (Fig. 1). Two-thousand one-hundred and thirty-five *Drosophila* genes with insect-specific orthologues were identified by comparing the fruit fly (*Drosophila melanogaster*), mosquito (*Anopheles gambiae*) and eight non-insect genomes using the OrthoMCL algorithm (Fig. 1a)¹⁶. Broadly expressed genes were excluded by selecting only the 616 genes with fewer than two expressed sequence tags. We recovered all classes of known insect chemosensory genes, including odorant receptors, gustatory receptors, odorant and other chemosensory binding proteins, and putative odour-degrading enzymes (Fig. 1b and Supplementary Table 1). The remaining genes were classified on the basis of predicted protein domains (Fig. 1b and

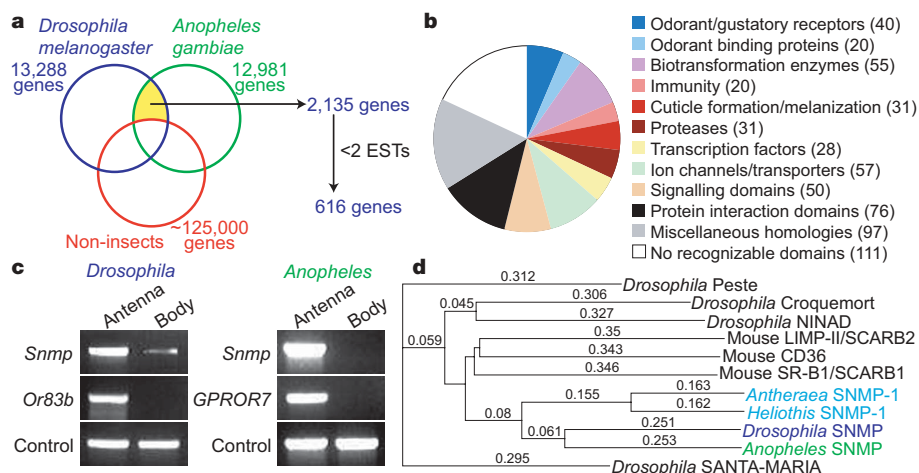


Figure 1 | A comparative genomics screen for olfactory molecules identifies *Drosophila* SNMP, a CD36-related receptor. **a**, Summary of bioinformatic screen. EST, expressed sequence tag. **b**, Pie chart of putative functions of genes retrieved from the screen. **c**, RT-PCR of *Snmp*

homologues in *Drosophila* and *Anopheles*. Control RT-PCR products: *Cam* (*Drosophila*) and *rps7* (*Anopheles*). **d**, Phylogenetic tree of insect SNMPs and related *Drosophila* and mammalian CD36 proteins. Values are uncorrected ('p') distance.

¹Laboratory of Neurogenetics and Behaviour, The Rockefeller University, 1230 York Avenue, Box 63, New York, New York 10065, USA. [†]Present addresses: Center for Integrative Genomics, Genopode Building, University of Lausanne, CH-1015 Lausanne, Switzerland (R.B.); Johns Hopkins Bloomberg School of Public Health, 615 North Wolfe Street, Baltimore, Maryland 21205, USA (K.S.V.).

Supplementary Table 1) and included many implicated in immunity and defence.

Three-hundred and thirty-nine uncharacterized genes were screened for selective expression in the antenna—the major olfactory organ of *Drosophila*—by reverse transcriptase–polymerase chain reaction (RT–PCR). Of these, we focus here on *Snmp*, an antennal-enriched gene related to the CD36 receptor family (Fig. 1c). The *Anopheles* homologue of *Snmp* was also antennal-specific (Fig. 1c), consistent with the previously described olfactory-specific expression pattern of the silk moth (*Antheraea polyphemus*) homologue *Snmp-1* (ref. 17). SNMPs form an insect-specific sub-group of the CD36 family (Fig. 1d), explaining how *Drosophila Snmp* emerged from our bioinformatic screen.

In the antenna, *Snmp* was found prominently expressed in a lateral-distal population of OSNs that co-express *Or83b* (Fig. 2b)^{11,13–15}, in non-neuronal support cells that surround these OSNs, and in support cells elsewhere in the antenna and chemosensory organs on the proboscis (Fig. 2b, and data not shown). Genetic labelling of SNMP-expressing OSNs with mouse CD8 fused to green fluorescent protein (CD8–GFP) revealed that these neurons target nine glomeruli in the antennal lobe (Fig. 2c)^{18,19}—DA1, VA1d, VA1l/m, DL3, DA4m, DA4l, DA2, DC3 and DC1—corresponding to those innervated by OSNs of the trichoid sensilla, which are involved in pheromone detection^{20,21}.

Using a peptide antibody, SNMP was found concentrated in trichoid sensory cilia, where it co-localized with OR83b (Fig. 2d), but only at very low levels in the cell bodies and axons (Fig. 2d, and data not shown), similar to moth SNMP-1 (ref. 17). We did not observe SNMP in non-trichoid OSNs, but it was expressed in support cells

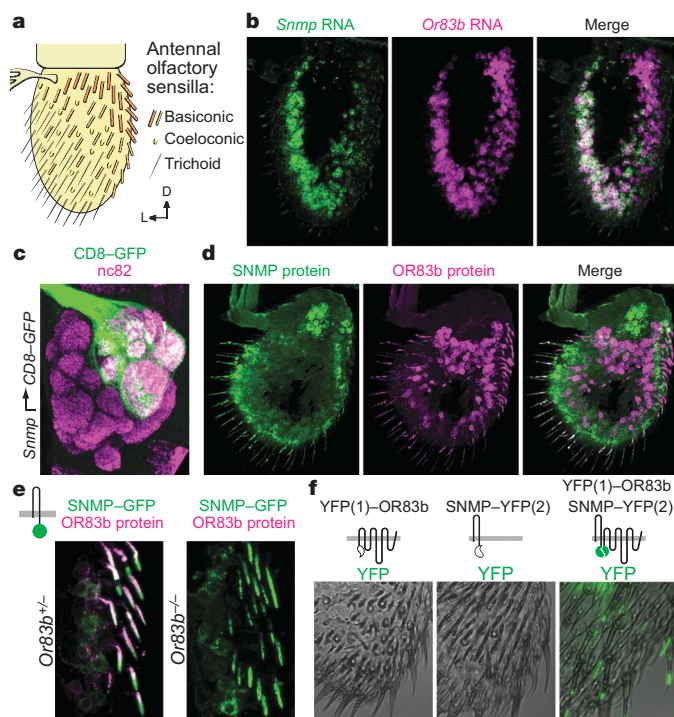


Figure 2 | SNMP localizes to sensory cilia of pheromone-sensitive OSNs. **a**, Olfactory sensilla distribution on the third antennal segment. Tissue orientation is always dorsal up, lateral left. **b**, RNA *in situ* hybridization of *Snmp* and *Or83b* on a wild-type antenna section. **c**, Immunostaining of CD8–GFP (anti-GFP) and neuropil (nc82) of a whole-mount brain of an *Snmp*-promoter-VP22–GAL4/UAS-CD8–GFP animal. **d**, Immunostaining of SNMP and OR83b on a wild-type antenna section. **e**, Immunostaining of SNMP–GFP (anti-GFP) and OR83b on antennal sections of control heterozygous (left) and homozygous (right) *Or83b*-null mutant animals. A model of SNMP–GFP is at the top left. **f**, Intrinsic YFP fluorescence in antennal sections of animals expressing YFP(1)–OR83b, SNMP–YFP(2) or both fusion proteins, as indicated. *Drosophila* genotypes are in Methods.

throughout the antenna (Fig. 2d). All anti-SNMP immunoreactivity was abolished in an *snmp*-null mutant (see below), confirming antibody specificity. Although the localization of SNMP in OSN cilia was similar to that of odorant receptors, it did not depend on OR83b when we expressed a functional SNMP–GFP fusion protein in OSNs innervating basiconic sensilla (Fig. 2e, and Supplementary Fig. 1). Therefore, SNMP ciliary trafficking is independent of both specific ligand-binding odorant receptors and OR83b. We examined whether SNMP might still contact odorant receptors in trichoid cilia by using the fluorescent protein fragment complementation assay¹¹. We generated and functionally verified SNMP and OR83b bearing complementary fragments of a yellow fluorescent protein (YFP) reporter (Fig. 2f and Supplementary Fig. 1). Reconstitution of the fluorescent YFP signal in sensory cilia was only observed when both fusion proteins were expressed (Fig. 2f). As the YFP fragments do not self-associate, this reconstitution could only result if SNMP and OR83b were brought into close proximity (<80 Å), providing evidence that SNMP is closely apposed to, although not necessarily directly interacting with, odorant receptors in the sensory compartment.

We generated null mutants in *Snmp* by gene targeting²² (Fig. 3a–d). *snmp* mutants are viable and fertile with no gross morphological or locomotor defects. We examined the function of SNMP in the sub-population of trichoid sensilla innervated by neurons expressing OR67d—the best-characterized *Drosophila* pheromone receptor that recognizes cVA^{8,21,23}. In *snmp* mutants, neither the expression of *Or67d* nor the ciliary localization of GFP–OR67d or OR83b was affected (Fig. 3c, e) and axonal projections of *snmp* mutant OR67d-expressing neurons to the antennal lobe were wild type (Fig. 3f). The expression of LUSH, an odorant-binding protein secreted by trichoid sensilla support cells into the lymph⁶ was normal (Fig. 3g). Thus *Snmp* is dispensable for the development of trichoid OSNs and support cells.

We investigated whether the responses of OR67d neurons to cVA stimulation were altered in *snmp* mutants. The relatively low

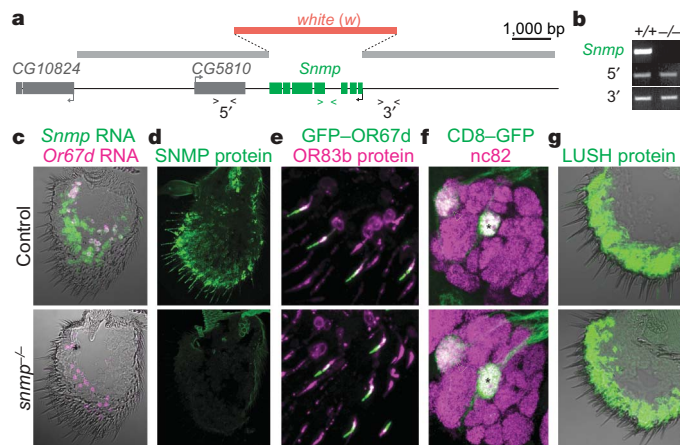


Figure 3 | Genetic analysis of *Snmp*. **a**, *Snmp* genomic locus and gene-targeting strategy. **b**, PCR confirmation of homozygous *snmp*-null mutant (*snmp*¹) using primer pairs indicated in **a**. **c**, RNA *in situ* hybridization of *Snmp* and *Or67d* in antennal sections of control heterozygous (*snmp*^{1/+}) or homozygous *snmp* mutant (*snmp*^{1/snmp}²) animals. **d**, Immunostaining of SNMP on antennal sections of control wild-type or homozygous *snmp* mutant (*snmp*^{1/snmp}²) animals. **e**, Immunostaining of GFP–OR67d (anti-GFP) and OR83b on antennal sections of control heterozygous or homozygous *snmp* mutant animals. **f**, Immunostaining of CD8–GFP-labelled OR67d-expressing axon termini (anti-GFP) and neuropil (nc82) on whole-mount brains of control heterozygous and homozygous *snmp* mutant animals. *Or67d*-GAL4 labels two glomeruli^{18,19}: DA1 (receives input from OR67d-expressing OSNs) and VA6 (black asterisk; receives input from OR82a-expressing OSNs), the latter originally interpreted by us as co-convergence¹⁹ but later shown to be due to ectopic expression of *Or67d*-GAL4 in OR82a neurons⁸. **g**, Immunostaining of LUSH on antennal sections of control wild-type or homozygous *snmp* mutant (*snmp*^{1/snmp}²) animals.

spontaneous activity of the OR67d neuron was observable as a sparse distribution of action potentials of uniform amplitude (Fig. 4a). On stimulation with cVA, wild-type neurons responded with a robust train of action potentials in a dose-dependent manner (Fig. 4a, b). *snmp* mutant neurons displayed no cVA-evoked electrophysiological responses at any concentration tested (Fig. 4a, b), but showed an increase in spontaneous activity (Fig. 4a). Both spontaneous and stimulus-evoked responses were fully restored by expression of the *Snmp* rescuing transgene in OR67d-expressing neurons (Fig. 4a, b, and Supplementary Fig. 2), but not by expression in support cells surrounding these neurons (Fig. 4a, b, and Supplementary Fig. 2). Expression of a distinct *Drosophila* CD36-related protein, NINAD, in OR67d-expressing neurons did not rescue electrophysiological defects of *snmp* mutants (data not shown). Thus, SNMP has an essential, cell-autonomous and specific function in OR67d-expressing neurons in mediating responses to cVA.

cVA detection is also dependent on LUSH and the OR67d/OR83b heteromeric receptor complex^{6,8,23} (data not shown), suggesting that SNMP acts with these proteins in a signalling pathway. In contrast to *snmp* mutants, however, loss of *lush*, *Or67d* or *Or83b* severely decreased spontaneous activity of these neurons (Fig. 4c, d)^{6,8}. Double-mutant analysis of this spontaneous activity phenotype revealed that *Snmp* is epistatic to *lush*, because OR67d-expressing neurons retained high levels of spontaneous activity in animals lacking both SNMP and LUSH (Fig. 4c, d). In contrast, *snmp Or83b* double mutants were, like *Or83b*, electrically silent (Fig. 4c, d). Although the mechanism by which spontaneous activity is regulated in *Drosophila* OSNs is unknown, our genetic analysis indicates that SNMP may act downstream of LUSH and upstream of, or in parallel with, odorant receptors in the generation of action potentials.

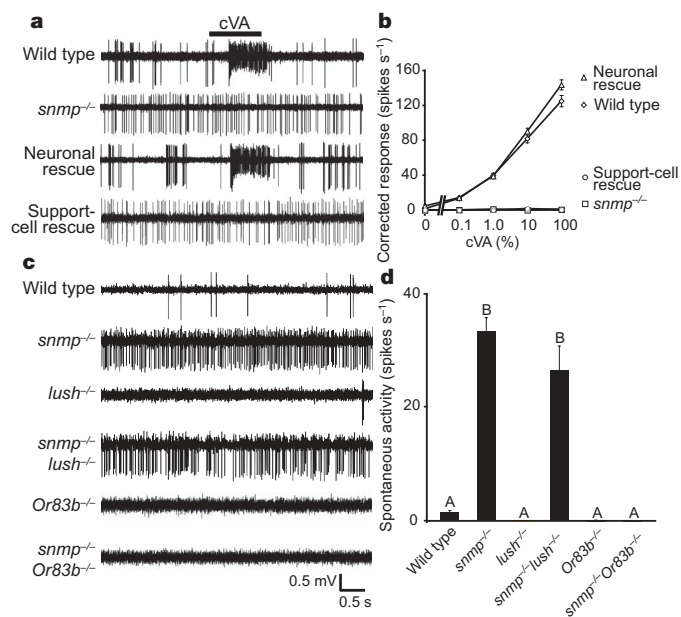


Figure 4 | SNMP mediates electrophysiological responses to cVA.

a, Representative traces of extracellular recordings of OR67d neurons stimulated with 10% cVA in wild-type, *snmp* mutant, neuronal rescue, and support-cell rescue animals. Bar above traces marks stimulus time (1 s). Traces are from female flies, but no significant sex-specific cVA responses are observed. **b**, Dose-response curves for cVA in the genotypes in **a**. Mean responses are plotted (\pm s.e.m.; $n = 39$ –47 sensilla; ≤ 4 sensilla per animal, mixed genders). *snmp* mutant and support-cell *Snmp* rescue are highly significantly different from wild-type and neuronal rescue animals at all concentrations of cVA (ANOVA; $P < 0.0001$). **c**, Representative traces of spontaneous activity in OR67d neurons in wild-type, *snmp* mutant, *lush* mutant, *snmp lush* double-mutant, *Or83b* mutant and *snmp Or83b* double mutant animals. **d**, Quantification of mean spontaneous activity in the genotypes in **c** (\pm s.e.m.; $n = 16$ –20, male flies). Bars labelled with different letters are highly significantly different (ANOVA; $P < 0.0001$).

To investigate the specificity of SNMP function, we ectopically expressed in OR67d neurons a second receptor, OR22a, which is responsive to fruit esters, such as ethyl butyrate and pentyl acetate²⁴. Although chemically related to cVA, OR22a ligands lack the long hydrophobic tail of this fatty-acid-derived pheromone (Fig. 5a). Ectopic expression of OR22a in wild-type OR67d-expressing neurons conferred responses to a panel of known OR22a ligands in addition to the endogenous cVA response (Fig. 5a, b), but not to a control odour, geranyl acetate, which activates neither OR67d nor OR22a (ref. 25). In *snmp* mutants, ectopic OR22a-dependent responses were unaffected, but all cVA responses were lost (Fig. 5a, b). The broad expression of SNMP in trichoid OSNs indicates that it might have a general function in pheromone detection. Because no other volatile pheromones have been identified in *Drosophila*, we tested whether SNMP is required for the activation of the moth (*Heliothis virescens*) pheromone receptor HR13 by (Z)-11-hexadecenal⁹, a component of the sex pheromone blend of this species. As previously observed, expression of HR13 in OR67d-expressing neurons conferred responsiveness to this pheromone⁸ (Fig. 5c, d). This response was almost completely abolished in *snmp* mutants and restored by transgenic rescue of *Snmp* (Fig. 5c, d). Together, these experiments reveal a specific and conserved function for SNMP in mediating pheromone-evoked neuronal activity. OR67d and HR13 share $<15\%$ amino acid identity and their ligands have chemically distinct head groups, suggesting that it is the fatty-acid-derived hydrocarbon tail common to these pheromones that necessitates SNMP.

Finally, we asked whether SNMP is required for the activation of OR67d by cVA in neurons not normally responsive to pheromones. We ectopically expressed OR67d in basiconic OSNs that lack the endogenous OR22a ligand-binding odorant receptor, but retain OR83b (ref. 24). All action potentials in these neurons can therefore be ascribed to OR67d/OR83b activity. *Or22a* mutant neurons expressing OR67d without SNMP exhibited spontaneous firing, but did not respond to cVA (Fig. 5e, f). In contrast, when OR67d was co-expressed with SNMP, significant responses to this pheromone were observed (Fig. 5e, f); compared to the responses of native OR67d neurons, the frequency of action potentials was lower and exhibited slower rise and decay rates (Fig. 5e, f). Such differences may be due to the absence in basiconic sensilla of LUSH or odour-degrading enzymes specialized to inactivate pheromone molecules²⁶.

Through a bioinformatic screen for insect olfactory transduction molecules, we have identified *Drosophila* SNMP as a CD36-related receptor broadly expressed in pheromone-sensing neurons, which is an essential co-factor for detection of the fatty-acid-derived pheromone cVA. As mammalian CD36 has an important biochemical function in binding and membrane translocation of fatty acids we suggest SNMP directly captures pheromone molecules on the surface of OSN cilia—possibly retrieving them from odorant-binding proteins in the extracellular milieu—and facilitates their transfer to the odorant-receptor–OR83b complex (Fig. 5g). A recent study showed OR67d ectopically expressed without SNMP could be activated by cVA when the pheromone was directly applied to the sensillar cuticle overlying the OSN²¹, indicating that pheromone receptors can be directly stimulated by ligand. When pheromones are presented in an air stream to the receptor in its native environment, however, SNMP (and odorant-binding proteins⁶) are essential. We suggest that the combination of molecular specializations of pheromone-sensing trichoid neurons together contribute to the sensitivity of these cells and that SNMP-related proteins function in the detection of many insect pheromones.

The mechanistic basis of CD36 ligand interactions and signalling is still poorly understood in any biological system. Our results have three important general implications. First, we show that SNMP has a specific role in the detection of fatty-acid-derived odour ligands. Because other CD36-related receptors are involved in binding and transport of lipid-based molecules, for example in the

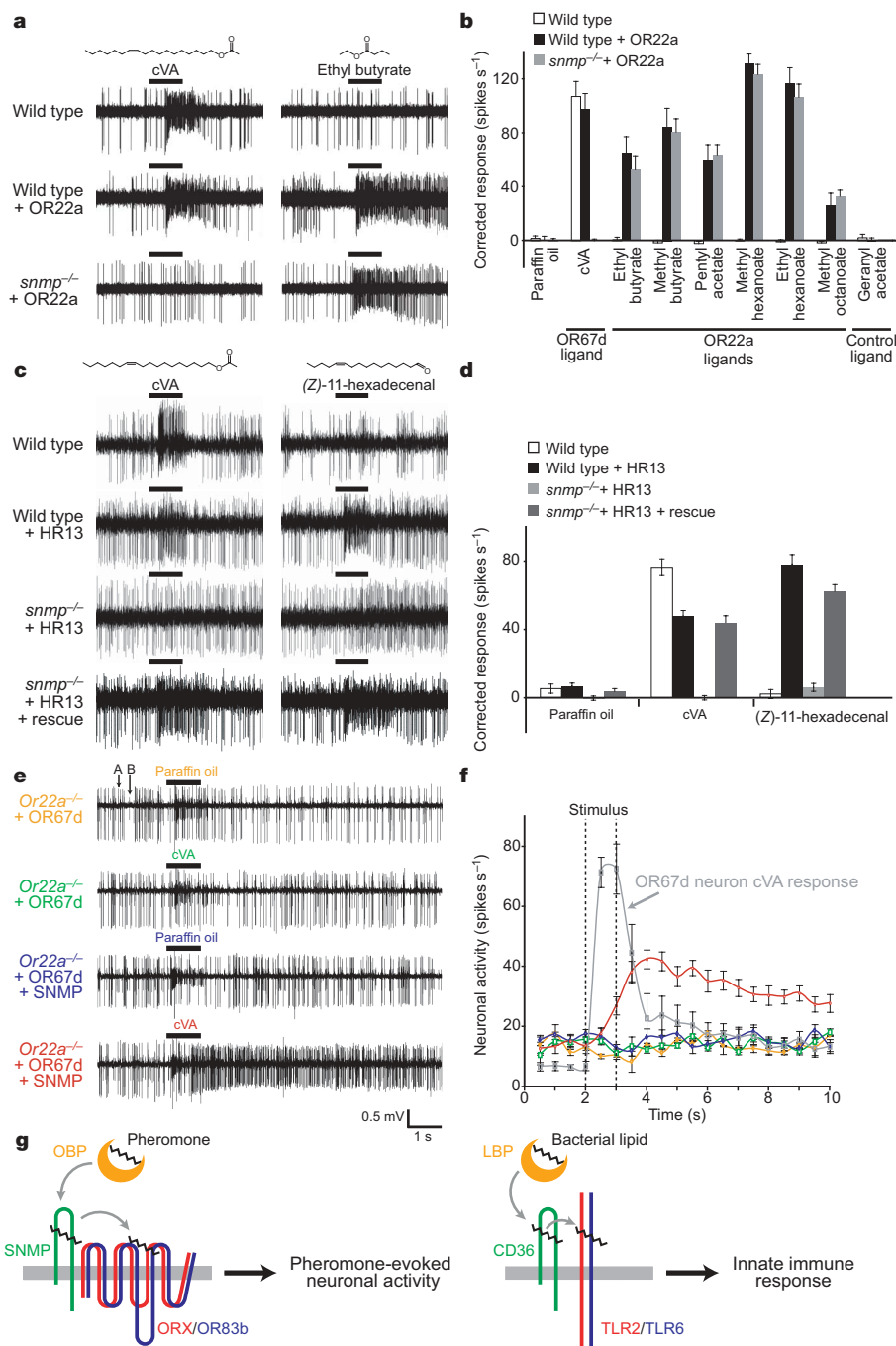


Figure 5 | SNMP is specifically required, and sufficient, for pheromone detection. **a**, Representative traces from OR67d neurons stimulated with 10% cVA or 10% ethyl butyrate in wild-type, wild-type + ectopic OR22a, or *snmp*-null mutant + ectopic OR22a animals. Bars above traces mark stimulus time (1 s). Structures of compounds are depicted at the top. **b**, Quantification of responses to cVA and OR22a ligands in the genotypes in **a**. Mean responses are plotted (\pm s.e.m.; $n = 16$, female flies). Responses of wild-type and *snmp*-mutant OR67d-expressing neurons ectopically expressing OR22a are highly significantly different for cVA (ANOVA; $P < 0.0001$) but not to any OR22a ligand (ANOVA; $P > 0.4149$). Geranyl acetate is a control odour that does not stimulate OR67d or OR22a. **c**, Representative traces from OR67d neurons stimulated with 10% cVA or 100% (Z)-11-hexadecenal in wild-type, wild-type + ectopic HR13, *snmp*-null mutant + ectopic HR13, or *snmp*-null mutant + ectopic HR13 + *Snmp* rescue animals. Bars above traces mark stimulus time (1 s). Structures of pheromones are depicted at the top. **d**, Quantification of responses to cVA and (Z)-11-hexadecenal in the genotypes in **c**. Mean responses are plotted (\pm s.e.m.; $n = 17$ –19, female flies). Responses to (Z)-11-hexadecenal of wild-type and *snmp*-mutant OR67d neurons ectopically expressing HR13 are highly significantly different (ANOVA; $P < 0.0001$). HR13-dependent responses to (Z)-11-hexadecenal of

Snmp rescue animals are highly significantly different from both wild-type and *snmp* mutant responses (ANOVA; $P < 0.0001$), indicating partial rescue. **e**, Representative traces from *Or22a* mutant neurons expressing OR67d alone or OR67d and SNMP, stimulated with control solvent paraffin oil or 100% cVA. Bars above traces mark stimulus time (1 s). OR22a neurons reside in basiconic sensilla with two neurons, visible as two distinct amplitudes (labelled A and B) of action potentials: responses of OR67d in *Or22a* mutant neurons are represented by the larger amplitude. The neuron with smaller amplitude action potentials responds to both control and cVA stimuli. **f**, Peristimulus time histograms for the genotype and stimulus combinations in **e**, using the same colour scheme. Endogenous OR67d neuron response to 100% cVA is in grey. Mean responses are plotted (\pm s.e.m.; $n = 9$ –12, mixed genders). The activity of *Or22a* mutant neurons expressing both OR67d and SNMP and stimulated with cVA is highly significantly different between time-points 3–9 s to *Or22a* mutant neurons expressing OR67d alone and/or when stimulated with paraffin oil (ANOVA; $P < 0.0001$). **g**, Model of mechanistic parallels between insect pheromone detection and bacterial pathogen detection. Extracellular LBPs (liposaccharide-binding proteins) may be functionally analogous to odorant-binding proteins (OBPs). ORX is any of the ligand-binding *Drosophila* pheromone receptors.

mammalian intestine¹, this protein family may represent specialized receptors for extracellular fatty ligands of diverse biological origin and function. Second, we show that SNMP acts in concert with other transmembrane odorant receptors in OSN cilia in mediating pheromone-evoked activity. Because CD36 was previously shown to act as a co-receptor for Toll-like receptors², we suggest that CD36-related proteins have obligate transmembrane partners in all their cellular roles.

Finally, our results reveal a molecular parallel in the mechanisms of intraspecific recognition through pheromone detection and pathogen recognition through the innate immune system (Fig. 5g). CD36 proteins in both invertebrates and vertebrates have been implicated in the recognition of specific lipid-derived products from bacterial cell walls, and coupling of this recognition through Toll-like receptors to initiate the innate immune response^{2–4}. Notably, mammalian CD36 has been proposed as a candidate fat taste receptor²⁷. Common molecular recognition mechanisms in immune and chemosensory systems may therefore be widespread.

METHODS SUMMARY

Bioinformatics. Insect-specific orthologues were identified using the OrthoMCL server (<http://orthomcl.cbil.upenn.edu/cgi-bin/OrthoMclWeb.cgi>)¹⁶. Gene targeting of *Snmp* was performed essentially as described¹³. Two null mutants, *snmp*¹ and *snmp*², arising from different starting insertions of the targeting construct were analysed.

Histology and immunocytochemistry. Two-colour *in situ* RNA hybridization¹⁹ and immunofluorescence on antennal sections or whole-mount brains^{11,13} were performed as described. A rabbit polyclonal antibody against SNMP was raised against the synthetic peptide TNPATNPATHHKMEHRERY and affinity-purified by Proteintech Group.

Electrophysiology and odorants. Extracellular recordings in single sensilla of 2–8-day-old flies were performed essentially as described¹³. High-purity odorants were obtained from Sigma-Aldrich, except cVA (purity ~99%) obtained from Pherobank.

Full Methods and any associated references are available in the online version of the paper at www.nature.com/nature.

Received 11 June; accepted 1 October 2007.

Published online 17 October 2007.

- Ge, Y. & Elghetany, M. T. CD36: a multiligand molecule. *Lab. Hematol.* **11**, 31–37 (2005).
- Hoebe, K. *et al.* CD36 is a sensor of diacylglycerides. *Nature* **433**, 523–527 (2005).
- Philips, J. A., Rubin, E. J. & Perrimon, N. *Drosophila* RNAi screen reveals CD36 family member required for mycobacterial infection. *Science* **309**, 1251–1253 (2005).
- Stuart, L. M. *et al.* Response to *Staphylococcus aureus* requires CD36-mediated phagocytosis triggered by the COOH-terminal cytoplasmic domain. *J. Cell Biol.* **170**, 477–485 (2005).
- Bartelt, R. J., Schaner, A. M. & Jackson, L. L. *cis*-Vaccenyl acetate as an aggregation pheromone in *Drosophila melanogaster*. *J. Chem. Ecol.* **11**, 1747–1756 (1985).
- Xu, P., Atkinson, R., Jones, D. N. & Smith, D. P. *Drosophila* OBP LUSH is required for activity of pheromone-sensitive neurons. *Neuron* **45**, 193–200 (2005).
- Ejima, A. *et al.* Generalization of courtship learning in *Drosophila* is mediated by *cis*-vaccenyl acetate. *Curr. Biol.* **17**, 599–605 (2007).
- Kurtovic, A., Widmer, A. & Dickson, B. J. A single class of olfactory neurons mediates behavioural responses to a *Drosophila* sex pheromone. *Nature* **446**, 542–546 (2007).
- Grosse-Wilde, E., Gohl, T., Bouche, E., Breer, H. & Krieger, J. Candidate pheromone receptors provide the basis for the response of distinct antennal neurons to pheromonal compounds. *Eur. J. Neurosci.* **25**, 2364–2373 (2007).

- Bonen, A. *et al.* Regulation of fatty acid transport by fatty acid translocase/CD36. *Proc. Nutr. Soc.* **63**, 245–249 (2004).
- Benton, R., Sachse, S., Michnick, S. W. & Vosshall, L. B. Atypical membrane topology and heteromeric function of *Drosophila* odorant receptors *in vivo*. *PLoS Biol.* **4**, e20 (2006).
- Wistrand, M., Kall, L. & Sonnhämmer, E. L. A general model of G protein-coupled receptor sequences and its application to detect remote homologs. *Protein Sci.* **15**, 509–521 (2006).
- Larsson, M. C. *et al.* *Or83b* encodes a broadly expressed odorant receptor essential for *Drosophila* olfaction. *Neuron* **43**, 703–714 (2004).
- Nakagawa, T., Sakurai, T., Nishioka, T. & Touhara, K. Insect sex-pheromone signals mediated by specific combinations of olfactory receptors. *Science* **307**, 1638–1642 (2005).
- Neuhaus, E. M. *et al.* Odorant receptor heterodimerization in the olfactory system of *Drosophila melanogaster*. *Nature Neurosci.* **8**, 15–17 (2005).
- Li, L., Stoekert, C. J. Jr & Roos, D. S. OrthoMCL: identification of ortholog groups for eukaryotic genomes. *Genome Res.* **13**, 2178–2189 (2003).
- Rogers, M. E., Sun, M., Lerner, M. R. & Vogt, R. G. *Snmp*-1, a novel membrane protein of olfactory neurons of the silk moth *Antheraea polyphemus* with homology to the CD36 family of membrane proteins. *J. Biol. Chem.* **272**, 14792–14799 (1997).
- Couto, A., Alenius, M. & Dickson, B. J. Molecular, anatomical, and functional organization of the *Drosophila* olfactory system. *Curr. Biol.* **15**, 1535–1547 (2005).
- Fishilevich, E. & Vosshall, L. B. Genetic and functional subdivision of the *Drosophila* antennal lobe. *Curr. Biol.* **15**, 1548–1553 (2005).
- Kaissling, K. E. Peripheral mechanisms of pheromone reception in moths. *Chem. Senses* **21**, 257–268 (1996).
- van der Goes van Naters, W. & Carlson, J. R. Receptors and neurons for fly odors in *Drosophila*. *Curr. Biol.* **17**, 606–612 (2007).
- Gong, W. J. & Golic, K. G. Ends-out, or replacement, gene targeting in *Drosophila*. *Proc. Natl Acad. Sci. USA* **100**, 2556–2561 (2003).
- Ha, T. S. & Smith, D. P. A pheromone receptor mediates 11-*cis*-vaccenyl acetate-induced responses in *Drosophila*. *J. Neurosci.* **26**, 8727–8733 (2006).
- Dobritsa, A. A., van der Goes van Naters, W., Warr, C. G., Steinbrecht, R. A. & Carlson, J. R. Integrating the molecular and cellular basis of odor coding in the *Drosophila* antenna. *Neuron* **37**, 827–841 (2003).
- Hallam, E. A. & Carlson, J. R. Coding of odors by a receptor repertoire. *Cell* **125**, 143–160 (2006).
- Ishida, Y. & Leal, W. S. Rapid inactivation of a moth pheromone. *Proc. Natl Acad. Sci. USA* **102**, 14075–14079 (2005).
- Laugerette, F. *et al.* CD36 involvement in orosensory detection of dietary lipids, spontaneous fat preference, and digestive secretions. *J. Clin. Invest.* **115**, 3177–3184 (2005).

Supplementary Information is linked to the online version of the paper at www.nature.com/nature.

Acknowledgements We thank R. Fenster and S. Katz for expert technical assistance; W. Jones for training in electrophysiology; M. Ditzgen for providing spike analysis software; P. Morozov of the Columbia Genome Centre and AMDeC Bioinformatics Core Facility for programming to permit batch retrieval of insect-specific orthologues and expressed sequence tags; E. Zdobnov for providing a *D. melanogaster*/*A. gambiae* orthologue data set; P. Howell and M. Q. Benedict of the CDC and MR4 for mosquitoes; D. Smith for reagents; B. Dickson for sharing unpublished fly reagents; S. Piccinotti for graphic design; R. Vogt for discussions; and M. Heiman, K. Lee, S. Martin, K. Scott and members of the Vosshall laboratory for comments on the manuscript. R.B. was supported by an EMBO Long-Term Fellowship and the Helen Hay Whitney Foundation. This work was supported by grants to L.B.V. from the NIH and the McKnight Endowment Fund for Neuroscience.

Author Contributions R.B. and K.S.V. performed the screen for olfactory genes. R.B. carried out all other experiments and analysed the data. R.B. and L.B.V. together designed the experiments, interpreted the results, produced the figures and wrote the paper.

Author Information Reprints and permissions information is available at www.nature.com/reprints. Correspondence and requests for materials should be addressed to L.B.V. (leslie@mail.rockefeller.edu).

METHODS

Bioinformatics. Insect-specific orthologues were identified using the OrthoMCL DB server (<http://orthomcl.cbil.upenn.edu/cgi-bin/OrthoMclWeb.cgi>)¹⁶, by comparing the predicted complete proteomes (in April 2004) of *Drosophila melanogaster*, *Anopheles gambiae*, *Homo sapiens*, *Mus musculus*, *Caenorhabditis elegans*, *Saccharomyces cerevisiae*, *Arabidopsis thaliana*, *Escherichia coli*, *Plasmodium falciparum* and *Plasmodium yoelii*. A supplementary data set of insect-specific orthologues was obtained from the *Anopheles gambiae* genome-sequencing project²⁸. Expressed sequence tag numbers for the corresponding *Drosophila* genes were downloaded from Flybase (<http://flybase.bio.indiana.edu/>) in June 2004. Protein sequences were manually curated using BLAST (<http://www.ncbi.nlm.nih.gov/BLAST/>) and SMART (<http://smart.embl-heidelberg.de>) servers. *Snmnp* was previously curated by Flybase/NCBI as CG7000-RA under accession number NM_142696. The best-fit phylogenetic tree in Fig. 1d was generated using the neighbour-joining algorithm in MacVector v9.0 with default parameters.

Molecular biology. Complementary DNA was synthesized from insect tissues using the Absolutely RNA Microprep Kit (Stratagene) and Superscript First-Strand Synthesis System (Invitrogen). Gene-specific primers for RT-PCR were designed using Primer3 (ref. 29) to amplify ~500 bp spanning at least one intron. All plasmid constructs were generated by amplification of the desired cDNA or genomic fragments with primers containing flanking restriction sites using the Expand High Fidelity PLUS PCR system (Roche) and Oregon-R antennal or appendage cDNA or genomic DNA as templates. PCR products were T:A cloned into pGEM-T Easy (Promega), sequenced and subcloned into appropriate vectors as detailed below: *Snmnp*-promoter-VP22-GAL4: the *Snmnp* 5.412 kb promoter region (nucleotides 16,998,115–16,992,704 in GenBank accession AE014297) was subcloned into pVP22-GAL4 (ref. 30). *lush*-promoter-GAL4: the *lush* 0.959 kb promoter region (nucleotides 19,599,310–19,598,352 in GenBank accession AE014296) was subcloned into pCaSpeR-AUG-GAL4 (ref. 30). *UAS-Snmnp*: full-length *Snmnp* open reading frame (GenBank accession NM_142696) was subcloned into pUAST (ref. 31). *UAS-Snmnp-GFP*: full-length *Snmnp* open reading frame without termination codon was subcloned 5' of *EGFP* (Clontech) in pUAST. *UAS-Snmnp-YFP(2)*: full-length *Snmnp* open reading frame without termination codon was subcloned upstream of DNA encoding a 10 amino acid linker [(GGGGS)₂] and a carboxy-terminal YFP fragment of YFP(2) in pUAST (ref. 11). *UAS-Or67d*: full-length open reading frame of *Or67d* was subcloned in pUAST. *UAS-GFP-Or67d*: full-length open reading frame of *Or67d* was subcloned 3' of *EGFP* (without termination codon) in pUAST. *Snmnp* targeting construct: 5' and 3' homologous arms (16,998,850–16,993,851 and 16,991,435–16,986,436 of GenBank accession AE014297, respectively) were subcloned to flank the *white* reporter gene in CMC105 (ref. 13). The gene structure in Fig. 3a was generated using GenePalette v1.2 (ref. 32).

Insect strains. *Drosophila* stocks were maintained on conventional cornmeal-agar-molasses medium under a 12 h light:12 h dark cycle at 25 °C. Wild-type Berlin (M. Heisenberg) was used for electrophysiological experiments and the wild-type Oregon-R strain was used for histology. Mutant alleles and transgenic lines used: *Or83b¹*, *Or83b²* (ref. 13), *lush¹* (ref. 33), *Or22a/b^{Ala}* (ref. 24), *Or67d-GAL4* (ref. 19), *Or83b-GAL4* (ref. 34), *Or22a-GAL4* (ref. 19), *UAS-YFP(1)-Or83b* (ref. 11), *UAS-CD8-GFP* (ref. 35), *UAS-Or22a* (ref. 13), *UAS-HR13* (ref. 8), *UAS-ninaD* (ref. 36), *70FLP,70I-Scel/Cyo* and *70FLP* (ref. 37).

Specific genotypes of flies in the figures are listed below. Figure 2e: *Or83b-GAL4/UAS-Snmnp-GFP;Or83b¹/+* (left) *Or83b-GAL4/UAS-Snmnp-GFP;Or83b¹/Or83b²* (right). Figure 2f: *Or67d-GAL4,UAS-YFP(1)-Or83b/+* (left), *Or67d-GAL4,UAS-Snmnp-YFP(2);snmnp¹/snmnp²* (centre), *Or67d-GAL4,UAS-YFP(1)-Or83b/UAS-Snmnp-YFP(2);snmnp¹,Or83b²/snmnp²,Or83b¹* (right). Figure 3e: *Or67d-GAL4/UAS-GFP-Or67d;snmnp¹/+* (top) *Or67d-GAL4/UAS-GFP-Or67d;snmnp¹/snmnp²* (bottom). Figure 3f: *Or67d-GAL4/UAS-CD8-GFP;snmnp¹/+* (top) *Or67d-GAL4/UAS-CD8-GFP;snmnp¹/snmnp²* (bottom). Figure 4a: *Or67d-GAL4/+; snmnp¹/snmnp²* (second trace) *Or67d-GAL4/UAS-Snmnp;snmnp¹/snmnp²* (third trace) *lush-GAL4/UAS-Snmnp;snmnp¹/snmnp²* (bottom trace). Figure 4c: *snmnp¹/snmnp²* (second trace) *lush¹/lush¹* (third trace) *lush¹,snmnp¹/lush¹,snmnp²* (fourth trace) *Or83b¹/Or83b²* (fifth trace) *snmnp¹,Or83b²/snmnp²,Or83b¹* (bottom trace). Figure 5a: *Or67d-GAL4/UAS-Or22a* (middle) *Or67d-GAL4/UAS-Or22a;snmnp¹/snmnp²* (bottom). Figure 5c: *Or67d-GAL4/UAS-HR13* (second trace) *Or67d-GAL4/UAS-HR13;snmnp¹/snmnp²* (third trace) *Or67d-GAL4,UAS-Snmnp/UAS-HR13;snmnp¹/snmnp²* (bottom trace). Figure 5e: *Or22a/b^{Ala}/Or22a/b^{Ala}*; *Or22a-GAL4,UAS-Or67d/+* (top two traces) *Or22a/b^{Ala}/Or22a/b^{Ala}*; *Or22a-GAL4,UAS-Or67d/UAS-Snmnp* (bottom two traces).

Adult mosquitoes (*Anopheles gambiae* G3 strain; MRA-112) were obtained from MR4 (www.mr4.org) through the Centers for Disease Control and Prevention.

Gene targeting screen. Gene targeting of *Snmnp* was performed essentially as described^{13,38}, using five independent insertions of the targeting construct.

From approximately 200,000 F₂ progeny, at least 6 null mutants were obtained, which were confirmed by PCR on genomic DNA preparations from homozygous mutant animals amplifying fragments corresponding to 16,990,010–16,990,525 (5') 16,992,709–16,993,129 (*Snmnp*) and 16,994,279–16,994,757 (3') in GenBank accession AE014297. Two of these, *snmnp¹* and *snmnp²*, arising from different starting insertions of the targeting construct, were retained for phenotypic analysis.

Histology and immunocytochemistry. Two-colour *in situ* RNA hybridization was performed essentially as described¹⁹ using *Or83b*-FITC, *Or67d*-DIG, and *Snmnp*-DIG or -FITC RNA probes. Immunofluorescence on antennal sections or whole-mount brains was performed as described^{11,13}. Primary antibodies: rabbit anti-OR83b EC2, 1:5,000 (ref. 13), rabbit anti-LUSH, 1:1,000 (ref. 33), mouse monoclonal nc82, 1:10 (R. Stocker), rabbit anti-GFP, 1:1,000 (Molecular Probes), mouse anti-GFP 1:500 (Molecular Probes). A rabbit polyclonal antibody against SNMP was raised against the synthetic peptide TNPATNPATHHKMEHRERY (corresponding to the C-terminal 19 amino acids), affinity-purified by Proteintech Group and used at 1:1,000. Secondary antibodies: Alexa488- and Cy3-conjugated anti-mouse IgG or anti-rabbit IgG 1:100 or 1:1,000 for whole-mount brains and antennal sections, respectively (Molecular Probes; Jackson ImmunoResearch). All microscopy was performed using a Zeiss LSM 510 Laser Scanning Confocal Microscope. For the Protein Fragment Complementation assay, the intrinsic fluorescence signal of reconstituted YFP was detected in fixed samples by excitation with an Argon Laser (excitation wavelength 488 nm) and collection of the emitted light with Band Pass filter 505–530.

Electrophysiology and odorants. Extracellular recordings in single sensilla of 2–8-day-old flies were performed essentially as described^{13,38,39}. Ten microlitres of odorant was added to a 6 mm filter paper disk (Whatman), which was placed inside a 1 ml tuberculin syringe (Becton, Dickinson and Company). A charcoal-filtered airflow (35 ml s⁻¹) was used to deliver odours to the preparation through a 10 ml serological pipette that was trimmed to remove the tapered tip, and the cut end positioned 15 mm away from the preparation. Half this airflow was diverted through the odour syringe during odour stimulation periods (1 s) under the control of the Syntech CS-55 Stimulus controller. cVA (purity ~99%) was obtained from Pherobank. Other odorants were obtained from Sigma-Aldrich at high purity. Chemical Abstracts Service (CAS) numbers: ethyl butyrate (105-54-4), methyl butyrate (623-42-7), pentyl acetate (628-63-7), methyl hexanoate (106-70-7), ethyl hexanoate (123-66-0), methyl octanoate (111-11-5), geranyl acetate (105-87-3), (Z)-11-hexadecenal (53939-28-9). Odorants were diluted to 10% in paraffin oil, except cVA, which was used at a range of dilutions (as indicated in the figures), methyl hexanoate and ethyl hexanoate, which were used at 1%, and (Z)-11-hexadecenal, which was used at 100%. Trichoid sensilla innervated by OR67d neurons are proximally distributed on the antenna and can be unambiguously identified by extracellular electrophysiological recordings of individual sensilla because they are unique in housing only a single OSN. We found that the onset of cVA responses varied slightly (usually <200 ms) between animals of the same genotype recorded on different days, most probably owing to small variations in the position of the odour delivery apparatus relative to the preparation. For quantification of responses, we therefore determined the time of onset of the response of a control wild-type sensillum to 100% cVA for each recording session. Corrected responses for all recordings in the same session were quantified by counting spikes in a 0.5 s window from this time point, subtracting the number of spontaneous spikes in a 0.5 s window before stimulation, and doubling the result to obtain spikes s⁻¹. Spontaneous activity was quantified by counting the spikes in a 5 s window without stimulus, and dividing by 5 to obtain spikes s⁻¹. Peristimulus time histograms (PSTHs) were generated by counting the numbers of spikes in 0.5 s bins from 2 s before 7 s after odour stimulation for each trial, using custom software written by M. Ditzgen in IDL. These values were then averaged across all trials. After verifying that responses were normally distributed, we compared all genotypes for a given experiment by ANOVA, with genotype as the main effect, and adjusted the alpha level for planned post-hoc means comparisons.

28. Zdobnov, E. M. et al. Comparative genome and proteome analysis of *Anopheles gambiae* and *Drosophila melanogaster*. *Science* **298**, 149–159 (2002).
29. Rozen, S. & Skaletsky, H. Primer3 on the WWW for general users and for biologist programmers. *Methods Mol. Biol.* **132**, 365–386 (2000).
30. Vosshall, L. B., Wong, A. M. & Axel, R. An olfactory sensory map in the fly brain. *Cell* **102**, 147–159 (2000).
31. Brand, A. H. & Perrimon, N. Targeted gene expression as a means of altering cell fates and generating dominant phenotypes. *Development* **118**, 401–415 (1993).
32. Rebeiz, M. & Posakony, J. W. GenePalette: a universal software tool for genome sequence visualization and analysis. *Dev. Biol.* **271**, 431–438 (2004).
33. Kim, M. S., Repp, A. & Smith, D. P. LUSH odorant-binding protein mediates chemosensory responses to alcohols in *Drosophila melanogaster*. *Genetics* **150**, 711–721 (1998).

34. Wang, J. W., Wong, A. M., Flores, J., Vosshall, L. B. & Axel, R. Two-photon calcium imaging reveals an odor-evoked map of activity in the fly brain. *Cell* **112**, 271–282 (2003).
35. Lee, T. & Luo, L. Mosaic analysis with a repressible cell marker for studies of gene function in neuronal morphogenesis. *Neuron* **22**, 451–461 (1999).
36. Kiefer, C., Sumser, E., Wernet, M. F. & Von Lintig, J. A class B scavenger receptor mediates the cellular uptake of carotenoids in *Drosophila*. *Proc. Natl Acad. Sci. USA* **99**, 10581–10586 (2002).
37. Rong, Y. S. *et al.* Targeted mutagenesis by homologous recombination in *D. melanogaster*. *Genes Dev.* **16**, 1568–1581 (2002).
38. Jones, W. D., Cayirlioglu, P., Kadow, I. G. & Vosshall, L. B. Two chemosensory receptors together mediate carbon dioxide detection in *Drosophila*. *Nature* **445**, 86–90 (2007).
39. de Bruyne, M., Clyne, P. J. & Carlson, J. R. Odor coding in a model olfactory organ: the *Drosophila* maxillary palp. *J. Neurosci.* **19**, 4520–4532 (1999).

LETTERS

Drosophila hygrosensation requires the TRP channels *water witch* and *nanchung*

Lei Liu¹, Yuhong Li¹, Runping Wang^{1,2}, Chong Yin³, Qian Dong^{1,2}, Huey Hing³, Changsoo Kim⁴ & Michael J. Welsh^{1,2}

The ability to detect variations in humidity is critical for many animals. Birds, reptiles and insects all show preferences for specific humidities that influence their mating, reproduction and geographic distribution^{1,2}. Because of their large surface area to volume ratio, insects are particularly sensitive to humidity, and its detection can influence their survival^{3–7}. Two types of hygroreceptors exist in insects: one responds to an increase (moist receptor) and the other to a reduction (dry receptor) in humidity^{4,6,8}. Although previous data indicated that mechanosensation might contribute to hygrosensation^{6,9}, the cellular basis of hygrosensation and the genes involved in detecting humidity remain unknown. To understand better the molecular bases of humidity sensing, we investigated several genes encoding channels associated with mechanosensation, thermosensing or water transport. Here we identify two *Drosophila melanogaster* transient receptor potential channels needed for sensing humidity: CG31284, named by us *water witch* (*wtrw*), which is required to detect moist air, and *nanchung* (*nan*), which is involved in detecting dry air. Neurons associated with specialized sensory hairs in the third segment of the antenna express these channels, and neurons expressing *wtrw* and *nan* project to central nervous system regions associated with mechanosensation. Construction of the hygrosensing system with opposing receptors may allow an organism to very sensitively detect changes in environmental humidity.

Previous work indicated that hygrosensing might involve mechanosensation. For example, mechanical deformation activated moist receptors and inhibited dry receptors in cricket and honeybee^{5,6}. In addition, hygroreceptor cells in the capitulum sensilla in cockroach responded to physical stresses⁹. Therefore, we screened genes from the transient receptor potential (TRP) and degenerin/epithelial Na⁺ channel (DEG/ENaC) families because members of both are involved in mechanosensation in species ranging from nematodes to mammals^{10,11}. We also tested several aquaporin genes because we thought their involvement in water transport might extend to moisture sensing. The *D. melanogaster* genome encodes 13 TRP, 24 DEG/ENaC and seven aquaporin genes^{12,13}.

We tested hygrosensing behaviour by placing flies between two tubes: air at ~100% humidity flowed into one and air at ~0% humidity flowed into the other¹. After five minutes, between 12% and 30% of wild-type flies distributed to the humid tube (Fig. 1a). We investigated eight TRP genes using available deficiencies and mutant lines (see footnote 1 in Supplementary Information)^{12,13}. Although deficiency lines only eliminate one of each TRP allele and reduce expression of many other genes in the deleted region, they are a useful tool for genetic screens¹⁴. Deficiencies covering two TRP genes, *nanchung* (*nan*)¹⁵ and CG31284, which we named '*water witch*' (*wtrw*; Supplementary Fig. 1) because of its role in detecting moisture, disrupted hygrosensing behaviour (Fig. 1a). The other TRP

genes, 11 DEG/ENaC, and five aquaporin genes studied either did not show a haploinsufficient phenotype and/or were shown by other studies to have no effect on hygrosensing behaviour (Supplementary Figs 2, 3, and Supplementary Information footnote 1).

To evaluate further *wtrw* and *nan*, we asked if they are expressed in structures that sense humidity. Although *Drosophila* hygrosensing involves the distal antenna, earlier work disagreed about the location of hygrosensing neurons; hygrosensing has been attributed to neurons innervating the arista¹ and to 3rd antennal segment neurons of coeloconic sensilla¹⁶. Consistent with a previous report¹, ablating either the 3rd segment and arista (bar B in Fig. 1a) or the arista alone (bar C) eliminated hygrosensing behaviour. Because removing the arista might damage the antenna, we also made a small cut in the 3rd segment (bar D)—an intervention that also disrupted the normal humidity preference. These data implicate function of the 3rd antennal segment, and potentially the arista in hygrosensing. We also used the *GH86* promoter to express tetanus neurotoxin light chain (*Clostridium* *TNT* in the *UAS-TNT-H* transgenic line). The *GH86* promoter drives expression in many 3rd but not 2nd antennal segment cells (Supplementary Fig. 2e), and *TNT-H* inactivates chemical synapses, but can also cause some general cellular toxicity¹⁷. Crossing *GH86-GAL4* and *UAS-TNT-H* lines disrupted moisture sensing (Fig. 1a). In contrast, when the promoter for *nompC*, encoding a mechanosensitive channel expressed in the 2nd antennal segment (Supplementary Fig. 2f), drove *TNT-H*, there was no effect. These and electrophysiological results (presented below) indicate that the 3rd antennal segment is the site of moisture sensing.

Figure 1b shows the *Drosophila* antenna. The 3rd segment contains three main morphologic types of multipored sensilla (basiconic, coeloconic and trichoid) with most containing two to four neurons^{18–20}. The *wtrw* and *nan* promoters each drove reporter gene expression in ~27–37 cells of the 3rd antennal segment (Fig. 1c). These promoters were also expressed in neurons in the 2nd antennal segment (data not shown). We obtained similar results using *in situ* hybridization (Supplementary Fig. 4a). The *nan* expression pattern was similar to the general arrangement of basiconic sensilla, although not to the distribution of specific subsets of large, thin or small basiconic sensilla^{18–20}. The distribution of *wtrw*-expressing neurons most resembled that of coeloconic sensilla¹⁸. *nan*-expressing neurons had a single long dendrite that seemed to extend into basiconic sensilla (Fig. 1d). In contrast, *wtrw*-expressing neurons had short dendrites (Fig. 1e); although we were not able to identify the associated sensilla, in some cases they seemed to sit near the base of small, thin sensilla that might represent coeloconic sensilla that have been associated with hygroreception¹⁶ (Supplementary Information footnote 2). Both *wtrw*- and *nan*-expressing neurons were also labelled by a neuron-specific antibody (22C10) (Fig. 1f, g), and *wtrw-GAL4/UAS-GFP* (green fluorescent protein) also showed some expression

¹Departments of Internal Medicine, ²Departments of Physiology and Biophysics, Howard Hughes Medical Institute, Roy J. and Lucille A. Carver College of Medicine, University of Iowa, Iowa City, Iowa 52242, USA. ³Department of Cell and Structure Biology, University of Illinois at Urbana-Champaign, Urbana, Illinois 61801, USA. ⁴Hormone Research Center, School of Biological Sciences and Technology, Chonnam National University, Gwangju 500-757, Korea.

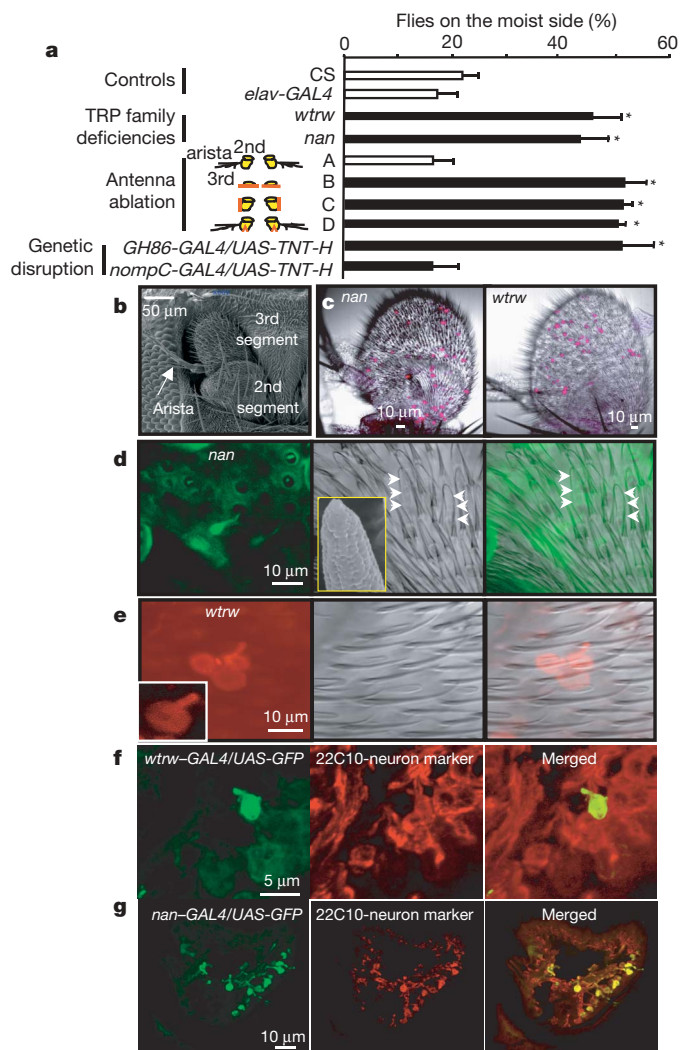


Figure 1 | Behavioural preference and expression of *wtrw* and *nan*.

a, Behavioural preference of flies to moist or dry air and expression of *nan* and *wtrw*. White bars represent an example of a control for a specific experiment, and black bars were tests. Additional controls and tested lines are shown in Supplementary Figs 2 and 3. Controls: *Canton S* (CS) and *elav-GAL4* lines ($N = 6$ and 9 , respectively; for behavioural tests, N indicates the number of trials). TRP family deficiency lines covering two TRP genes are shown: *nan* (Bloomington stock no. 3124, *Df(3L)fz-GF3b, p{wA^R}66E/TM6B, Tb¹ ca¹* and no. 3125, *Df(3L)fz-GS1a, p{wA^R}66E/TM3, Sb¹*) and *wtrw* (Bloomington stock no. 1883, *Df(3R)dsx5, Ubx^{bx-1} sr¹ e⁴/TM1* and no. 1898, *Df(3R)D7, Ubx¹ e⁴/TM1*) ($N = 17$ and 19 , respectively). Organ ablation involved no intervention (A), removing the entire 3rd segment and arista (B), removing the arista (C), or making a small cut in the 3rd segment (D), as indicated by the red lines ($N = 7, 6, 6$ and 6 , respectively). Genetic disruption was done by crossing either a *nompC-GAL4* line, which drives expression in the 2nd antennal segment, or a *GH86-GAL4* line, which expresses in the 3rd segment, to a *UAS-TNT-H* line ($N = 7$ and 11 , respectively). Statistical analysis for all studies used a one-way analysis of variance (ANOVA) with post-hoc multiple comparisons of Sidak. Asterisks indicate $P < 0.05$. For this panel and all other quantitative figures, data are means \pm s.e.m.

b–g, Expression pattern of *wtrw* and *nan*. **b**, Scanning electron photomicrograph showing *Drosophila* antenna. **c**, *nan-GAL4* (also called *F-GAL4*; ref. 15) and *wtrw-GAL4* driving *UAS-DsRed^{tracheus}* overlaid on a differential interference contrast (DIC) image of the 3rd segment of the antenna. The fluorescence images represent a stack of confocal sections. **d**, *nan-GAL4/UAS-GFP* line with fluorescence image in left panel, DIC image in middle, and overlay in the right panel. Dendrites of *nan*-expressing neurons at the base of and extending into a probable basiconic sensilla (white arrowheads). Inset shows scanning electron photomicrograph of a multi-pored basiconic sensilla. **e**, *wtrw-GAL4/UAS-CD8-GFP* neurons stained with anti-GFP-Alexa 555. Inset shows an additional example. **f**, **g**, *wtrw-GAL4/UAS-GFP* (**f**) or *nan-GAL4/UAS-GFP* (**g**) co-stained with neuron marker, 22C10. GFP channel, green; 22C10, red.

in non-neuronal cells (Supplementary Fig. 4). Their expression in the 3rd antennal segment and the behavioural screen implicated *wtrw* and *nan* in sensing humidity and suggested that distinct types of sensory neurons express these two TRP genes.

To test whether cells expressing *nan* and *wtrw* are involved in hygro-sensation, we used *nan* and *wtrw* promoters to drive either *TNT-H*, which suppresses synaptic transmission, or a temperature-sensitive *shibire* (*shi*), which blocks endocytosis and thereby neurotransmission at the non-permissive temperature (29°C). *TNT-H* and *shi* (at 29°C) both impaired hygro-sensing behaviour (Fig. 2, and Supplementary Fig. 2d), suggesting that cells expressing these genes contribute to humidity detection and that developmental changes did not cause the behavioural defect.

The *nan* deletion mutants, *nan^{36a}* and *nan^{dy5}* (ref. 15), failed to avoid high humidity. Because there are no available *wtrw* mutations, we targeted three different regions of *wtrw* transcripts with RNA interference (RNAi; Supplementary Fig. 5). Driving *wtrw^{RNAi}* expression with a promoter expressed in neurons (*elav-GAL4*) or a *wtrw* promoter (*wtrw-GAL4*), but not a *nan* or DEG/ENaC promoter (*ppk12-GAL4*) reduced the preference for dry air (Fig. 2, and Supplementary Fig. 2b). Thus, disrupting hygro-sensation required *wtrw^{RNAi}* expression in specific neuronal cells. As an independent method of inhibiting WTRW, we expressed a dominant-negative WTRW and found that it too impaired hygro-sensing behaviour

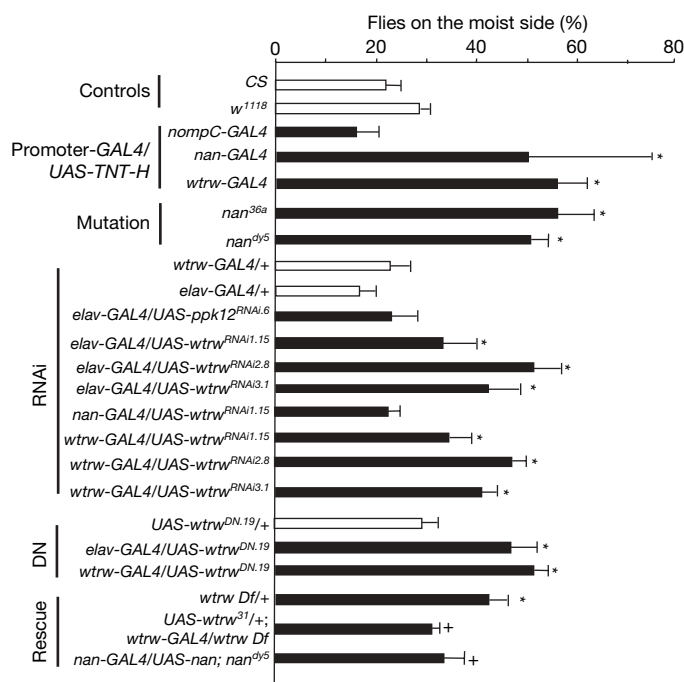


Figure 2 | Hygro-sensing behaviour of promoter-GAL4/UAS-TNT-H, mutant, RNAi and dominant-negative lines. Details are as described in the Fig. 1 legend. Controls: CS and *w¹¹¹⁸* ($N = 6$ and 16 , respectively). Promoter-GAL4/UAS-TNT-H lines: driving *UAS-TNT-H* with *nompC-GAL4* (as a control), *nan-GAL4* and *wtrw-GAL4* ($N = 6, 12$ and 15 , respectively). We obtained similar results with *TNT-E* (not shown). Mutations: homozygous *nan^{36a}* and *nan^{dy5}* ($N = 9$ and 6 , respectively; Supplementary Information footnote 6). RNAi: *wtrw-GAL4/+* and *elav-GAL4* are shown as controls with matched genetic backgrounds ($N = 11$ and 13 , respectively). *elav-GAL4*, *nan-GAL4* or *wtrw-GAL4* drove *ppk12^{RNAi}* and *wtrw^{RNAi}*, as indicated ($N = 12, 27, 10, 13, 9, 11, 14$ and 9 , respectively). DN: *UAS-wtrw^{DN.19/+}* is shown as a control ($N = 6$). *elav-GAL4* or *wtrw-GAL4* drove *UAS-wtrw^{DN.19/+}* ($N = 9$ and 10 , respectively). Rescue: *wtrw-GAL4* driving *UAS-wtrw³¹* was used to rescue the behavioural phenotype of the *wtrw* deficiency line (no. 1898, *Df(3R)D7, Ubx¹ e⁴/TM1*) ($N = 9$ and 10 , respectively). *nan-GAL4/UAS-nan* was used to rescue *nan^{dy5}* ($N = 12$). Asterisk indicates $P < 0.05$, compared to controls. Cross indicates $P < 0.05$, compared to appropriate *wtrw Df* (deficiency) and *nan^{dy5}* lines.

(Fig. 2), although we cannot exclude the possibility that the dominant-negative mutant protein inhibited related TRP channels. We rescued the hygrosensing defect in the *wtrw* deficiency and *nan*^{dy5} mutation lines by expressing wild-type *wtrw* and *nan*, respectively (Fig. 2). *nan*^{36a}, *wtrw*-GAL4/UAS-*wtrw*^{RNAi}, and *wtrw*-GAL4/UAS-*wtrw*^{DN.19} flies showed normal responses to odors in the T-maze used for humidity sensing (Supplementary Fig. 6; DN, dominant negative), and they distributed normally on a temperature gradient (15–30 °C, not shown). These results indicate that *wtrw* and *nan* have an important role in hygrosensing. An earlier report indicated that the TRP channel inactive (IAP) forms a complex with NAN and that both are required for normal hearing²¹. Therefore, we tested an *iav* mutant and found that it also altered hygrosensing (Supplementary Fig. 7).

To assess activity of hygrosensing neurons, we positioned an extracellular electrode at different locations in the 3rd antennal segment and recorded spiking activity evoked by dry and moist air (Fig. 3a). Some neurons responded to dry air and some to moist air (Fig. 3b), consistent with reports in several other insect species^{4,6–8}. Although

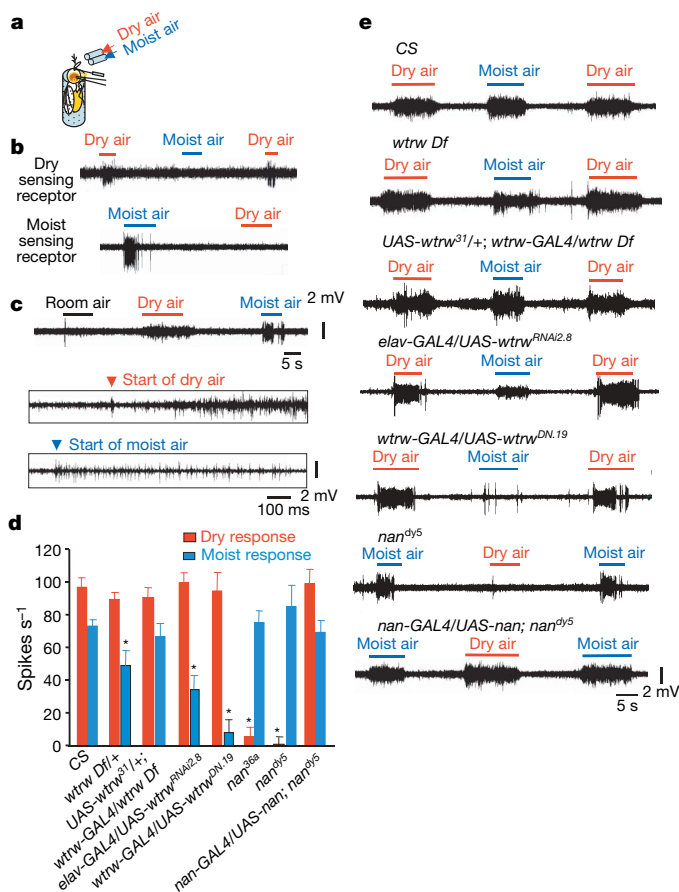


Figure 3 | Electrophysiologic response to dry and moist air. **a**, Diagram of recording method. A reference electrode was inserted into the eye, and a tungsten electrode was inserted into the 3rd antennal segment or at the base of 2nd segment. Dry or moist air was delivered to the antenna. **b**, Recording electrode placed in the 3rd antennal segment, and dry and moist air were delivered as indicated. **c**, Recording from an electrode positioned at the base of the 2nd antennal segment. Trace was from a *HS-GAL4/+* control fly. Dry air, moist air, or air at room humidity was delivered as indicated. Bottom panels show expanded examples of response to dry and moist air. **d**, Summary of electrophysiologic data. Spikes s⁻¹ indicates the maximum frequency during a 1 s recording during dry or moist air application. The number of flies tested was *N* = 13, 27, 11, 12, 12, 18, 11 and 9, respectively. **e**, Examples of responses to moist and dry air from CS, *wtrw* deficiency (*Df(3R)D7,Ubx¹e⁴/TM1*) crossed to *w¹¹¹⁸*, *wtrw* deficiency rescued with *wtrw*-GAL4/UAS-*wtrw*³¹, *elav-GAL4/UAS-wtrw*^{RNAi2.8}, *wtrw*-GAL4/UAS-*wtrw*^{DN.19}, homozygous *nan*^{dy5}, and *nan*^{dy5} rescued with *nan*-GAL4/UAS-*nan*.

we recorded at the base of the arista on many occasions, we could detect no response to changing humidity (Supplementary Information footnote 3). Thus, *Drosophila* possess distinct receptor cells for high and low humidity.

Our success rate in obtaining recordings from individual moisture-sensitive neurons was <10%, making this method unsuitable for quantifying the response of mutants. As an alternative approach, we recorded at the base of the 2nd antennal segment. Because all 3rd segment sensory neurons project through the 2nd segment to the brain, an electrode placed there should record most of the activity generated in the antenna. Both moist and dry air generated strong responses (Fig. 3c). Moist air initiated an immediate response that abated over 5–15 s. Dry air induced a slower increase in frequency over ~5 s. Ablating the arista had no acute effect, although with time, responses to moist and dry air disappeared, consistent with an injury (Supplementary Fig. 8).

The *wtrw* deficiency, RNAi and dominant-negative lines impaired the electrophysiological response to moist air, while leaving dry-air sensing unaffected (Fig. 3d, e). In contrast, *nan*^{dy5} and *nan*^{36a} mutants eliminated the response to dry air, yet left intact activity to moist air. Moreover, transgenic *wtrw* and *nan* expression rescued the defective responses of the *wtrw* deficiency and *nan*^{dy5}, respectively. These data identify distinct roles for *wtrw* and *nan*; one is involved in sensing moist air and the other in sensing dry air.

The fly central nervous system is segregated by specific modalities, with sensory neurons that detect specific stimuli projecting to the same primary brain centre, independent of their body position²². Thus, the central projection of a sensory neuron can suggest its modality. In several insects, the olfactory centre is in the antennal lobe, the primary centre for taste is located in the subesophageal ganglia, and the mechanosensory area is associated with the dorsal lobe (Fig. 4a)²². To obtain additional clues about the sensory modality involved in hygrosensing, we traced the central projections of *nan* and *wtrw* neurons. Because the dorsal lobe is not well defined in *Drosophila*, we first examined the projection pattern of *nompC*, a gene associated with mechanosensation in flies²³. This pattern showed that antennal nerve termini projected locally close to but not into the antennal lobe (Fig. 4b), a position associated with mechanosensory neurons in several other insects and called the antennal mechanosensory and motor centre (AMMC)²². The antennal nerve termini labelled in *nan*-GAL4/UAS-CD8-GFP and *wtrw*-GAL4/UAS-CD8-GFP (CD8 is a lymphocyte marker) lines projected to a brain region similar to that marked by *nompC*-GAL4/UAS-GFP (Fig. 4c, d). The patterns for *nan* and *wtrw* were also similar to projections reported in cockroach, in which hygrosensory axons lie at the margin of the antennal lobe²⁴. Although these studies cannot determine whether the *nan*- and *wtrw*-expressing neurons arose from the 3rd antennal segment or from other sites, such as Johnston's organ in the legs or 2nd antennal segments, they do indicate that these neurons did not project to the antennal lobe or subesophageal ganglia. In addition, when we labelled 3rd antennal segment neurons with a tracer (DiI) in *wtrw*-GAL4/UAS-GFP flies, we found nerve terminals in the AMMC region showing co-localization of DiI and GFP (Supplementary Fig. 9).

Our results raise interesting questions and speculations. How might these TRP channels sense humidity? The channels themselves probably do not directly sense humidity, because electrolyte-containing solutions are required on the extracellular surface for channel function. Rather, we speculate that they function as mechanosensors or thermosensors or modify the receptor's function. First, mechanical stimulation can activate hygrosensory cells in other insects (Supplementary Information footnotes 4 and 5)^{6,9}. Second, the appearance of their dendrites indicates *wtrw*-expressing neurons may be mechanosensory; mechanosensory neurons often have short dendrites that attach to the base of hairs via a dendritic sheath²⁵. Third, *wtrw*- and *nan*-expressing neurons project to brain regions associated with mechanosensory function²². Fourth, *wtrw* belongs to the TRPA subfamily, some of which are gated by temperature changes¹³.

What is the logic in constructing a sensory system comprised of two distinct sets of receptors and cells, one set that detects an increase and another that detects a decrease in an environmental signal? Our data indicate that both sensors are required; disrupting either the moist or the dry receptors impaired the behavioural response to humidity. Opposing receptors would create a system poised to respond to changes in either direction. In the hygrosensing system, this would allow flies to detect subtle differences in humidity with greater sensitivity than absolute values of humidity. Consistent with this idea, hygrosensing cells displayed minimal basal activity, but responded to humidity changes. This arrangement differs significantly from some senses, such as olfaction and gustation. However, hygrosensing may not be the only sensory system with this design. Thermosensation might share a similar organization, because distinct cells respond to heating and to cooling²⁶, and TRP channels with varying temperature sensitivity have been reported²⁷. The organization of humidity- and temperature-sensing systems may have evolved to allow organisms to identify environments between

extremes of a physical property, whereas in olfaction and gustation a ligand primarily attracts or repels an organism. Thus, construction of the hygrosensing system with opposing receptors may allow the organism to sensitively detect environmental humidity differences critical for mating and survival.

Finding TRP channels as the first candidate hygrosensors in any animal species paves the way to understand better this interesting sensory modality. It may also offer new approaches to elucidating the design of sensory systems.

METHODS SUMMARY

See Supplementary Information for detailed Methods and Materials.

Cloning *water witch* and generation of transgenic fly lines. *Water witch* (*wtrw*) was cloned by designed primer sets flanking the predicted CG31284 messenger RNA in Flybase (<http://flybase.bio.indiana.edu/>). A 2 kb genomic DNA sequence that was 5' to the translational start site of *wtrw* was cloned into a *GAL4* PTGAL vector and used to make transgenic flies. Transgenic RNAi flies were made using the SympUAST-w vector using *wtrw* sequence from 5' 206 to 804 bp (RNAi1), 2,258–2,359 (RNAi2) or 2,468–2,592 (RNAi3). To produce a WTRW dominant negative (DN)²⁸, we generated a transgene expressing the amino terminus of WTRW including the first predicted transmembrane domain using the pUAST vector. To rescue the effects of the *wtrw* deficiency, the full-length *wtrw* complementary DNA was cloned into the pUAST and pCaSpeR-hs-act vectors.

Behavioural assay. Hygrosensory behavioural assays were done on the basis of previously described methods, with some modification¹. Briefly, in a trial, 20–50 flies were introduced into a T-maze through an elevator. One tube received moist airflow with ~100% humidity and the other received dry air flow at ~0% humidity. Most of the flies had made a choice and stopped motion in 5 min.

Electrophysiological recording. We used an extracellular recording technique (see Fig. 3a for a diagram). Briefly, living female flies were placed into a cut plastic pipette tip, with the fly head protruding from the tip. Dry or moist air was blown from 10 mm in front of the fly head. A sharp tungsten electrode was placed in the 3rd segment of the antenna or at the base of the 2nd segment. A glass reference electrode filled with 0.1 M KCl was positioned in one eye. Voltage differences between the reference and recording electrodes were amplified by an Axopatch-1D (Axon Instruments). To analyse spike frequency, we used Clampfit 9.0 software (Axon Instruments). The amplitude threshold was set at 2.5 times the baseline noise level and the number of spikes was counted automatically.

Full Methods and any associated references are available in the online version of the paper at www.nature.com/nature.

Received 25 June; accepted 3 September 2007.

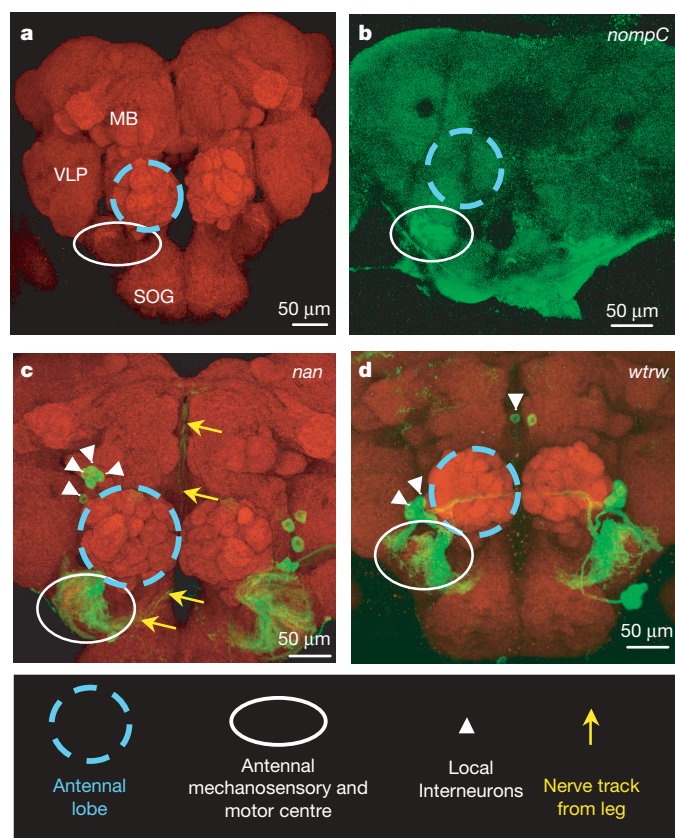


Figure 4 | Central nervous system projection pattern of *nompC-GAL4*, *nan-GAL4* and *wtrw-GAL4* driving *UAS-GFP*. Images show frontal view of the adult central nervous system; they are all stacks of confocal images. **a**, Brain labelled by nc82, a mouse monoclonal antibody that labels neuropil²⁹. The stereotypical glomeruli of the antennal lobe (blue dashed line), mushroom body (MB), subesophageal ganglia (SOG), and ventro-lateral procerebrum (VLP) are indicated. An area associated with mechanosensation, the AMMC (white oval), is also shown. **b**, *nompC-GAL4/UAS-GFP* showing the projection pattern in brain. Note the varicosities of the axon termini within the AMMC. **c**, *nan-GAL4/UAS-mCD8-GFP* showing a view of whole brain, with nc82 staining in red. Yellow arrows indicate nerve tract from chordotonal organ in the leg (Supplementary Information footnote 7). White arrowheads indicate local interneurons that may be involved in other functions¹⁹. Note that the GFP-labelled (green) projections remain locally in the AMMC. **d**, *wtrw-GAL4/UAS-mCD8-GFP* co-stained with nc82. Note projections around the antennal lobe in the AMMC. Although it seems that some of the *wtrw*-expressing interneurons might have projected into the AMMC, this was not the case when we examined individual confocal sections. We have examined many samples to assess this.

1. Sayeed, O. & Benzer, S. Behavioral genetics of thermosensation and hygrosensation in *Drosophila*. *Proc. Natl Acad. Sci. USA* **93**, 6079–6084 (1996).
2. Shelford, V. E. A comparison of the responses of animals in gradient of environmental factors with particular reference to the method of reaction of representatives of the various groups from protozoa to mammals. *Science* **48**, 225–230 (1918).
3. Altner, H., Sass, H. & Altner, I. Relationship between structure and function of antennal chemo-, hygro-, and thermoreceptive sensilla in *Periplaneta americana*. *Cell Tissue Res.* **176**, 389–405 (1977).
4. Tichy, H. Hygro- and thermoreceptive triad in antennal sensillum of the stick insect, *Carausius morosus*. *J. Comp. Physiol.* **132**, 149–152 (1979).
5. Yokohari, F. The coelocapitular sensillum, an antennal hygro- and thermoreceptive sensillum of the honey bee, *Apis mellifera* L. *Cell Tissue Res.* **233**, 355–365 (1983).
6. Itoh, T., Yokohari, F. & Tominaga, Y. Two types of antennal hygro- and thermoreceptive sensilla of the cricket, *Gryllus bimaculatus* (De Geer). *Zoolog. Sci.* **1**, 533–543 (1984).
7. Iwasaki, M., Itoh, T., Yokohari, F. & Tominaga, Y. Identification of antennal hygroreceptive sensillum and other sensilla of the firefly, *Luciola cruciata*. *Zoolog. Sci.* **12**, 725–732 (1995).
8. Yokohari, F. & Tateda, H. Moist and dry hygroreceptors for relative humidity of the cockroach, *Periplaneta americana* L. *J. Comp. Physiol.* **106**, 137–152 (1976).
9. Yokohari, F. Hygroreceptor mechanism in the antenna of the cockroach *Periplaneta*. *J. Comp. Physiol.* **124**, 53–60 (1978).
10. Welsh, M. J., Price, M. P. & Xie, J. Biochemical basis of touch perception: mechanosensory function of degenerin/epithelial Na⁺ channels. *J. Biol. Chem.* **277**, 2369–2372 (2002).
11. Clapham, D. E. TRP channels as cellular sensors. *Nature* **426**, 517–524 (2003).
12. Littleton, J. T. & Ganetzky, B. Ion channels and synaptic organization: analysis of the *Drosophila* genome. *Neuron* **26**, 35–43 (2000).
13. Montell, C. *Drosophila* TRP channels. *Pflugers Arch.* **451**, 19–28 (2005).
14. Desbordes, S. C., Chandraratna, D. & Sanson, B. A screen for genes regulating the wingless gradient in *Drosophila* embryos. *Genetics* **170**, 749–766 (2005).

15. Kim, J. *et al.* A TRPV family ion channel required for hearing in *Drosophila*. *Nature* **424**, 81–84 (2003).
16. Yao, C. A., Ignell, R. & Carlson, J. R. Chemosensory coding by neurons in the coeloconic sensilla of the *Drosophila* antenna. *J. Neurosci.* **25**, 8359–8367 (2005).
17. Sweeney, S. T., Broadie, K., Keane, J., Niemann, H. & O’Kane, C. J. Targeted expression of tetanus toxin light chain in *Drosophila* specifically eliminates synaptic transmission and causes behavioral defects. *Neuron* **14**, 341–351 (1995).
18. Shanbhag, S. R., Muller, B. & Steinbrecht, R. A. Atlas of olfactory organs of *Drosophila melanogaster*. 1. Types, external organization, innervation and distribution of olfactory sensilla. *Int. J. Insect Morphol. Embryol.* **28**, 377–397 (1999).
19. Stocker, R. F. *Drosophila* as a focus in olfactory research: mapping of olfactory sensilla by fine structure, odor specificity, odorant receptor expression, and central connectivity. *Microsc. Res. Tech.* **55**, 284–296 (2001).
20. de Bruyne, M., Foster, K. & Carlson, J. R. Odor coding in the *Drosophila* antenna. *Neuron* **30**, 537–552 (2001).
21. Gong, Z. *et al.* Two interdependent TRPV channel subunits, inactive and Nanchung, mediate hearing in *Drosophila*. *J. Neurosci.* **24**, 9059–9066 (2004).
22. Homberg, U., Christensen, T. A. & Hildebrand, J. G. Structure and function of the deutocerebrum in insects. *Annu. Rev. Entomol.* **34**, 477–501 (1989).
23. Walker, R. G., Willingham, A. T. & Zuker, C. S. A *Drosophila* mechanosensory transduction channel. *Science* **287**, 2229–2234 (2000).
24. Nishikawa, M., Yokohari, F. & Ishibashi, T. Central projections of the antennal cold receptor neurons and hygroreceptor neurons of the cockroach *Periplaneta americana*. *J. Comp. Neurol.* **361**, 165–176 (1995).
25. Keil, T. A. Functional morphology of insect mechanoreceptors. *Microsc. Res. Tech.* **39**, 506–531 (1997).
26. Liu, L., Yermolaieva, O., Johnson, W. A., Abboud, F. M. & Welsh, M. J. Identification and function of thermosensory neurons in *Drosophila* larvae. *Nature Neurosci.* **6**, 267–273 (2003).
27. Dhaka, A., Viswanath, V. & Patapoutian, A. Trp ion channels and temperature sensation. *Annu. Rev. Neurosci.* **29**, 135–161 (2006).
28. Niemeyer, B. A. Structure–function analysis of TRPV channels. *Naunyn Schmiedeberg Arch. Pharmacol.* **371**, 285–294 (2005).
29. Rein, K., Zockler, M. & Heisenberg, M. A quantitative three-dimensional model of the *Drosophila* optic lobes. *Curr. Biol.* **9**, 93–96 (1999).

Supplementary Information is linked to the online version of the paper at www.nature.com/nature.

Acknowledgements We thank T. O. Moninger for help with scanning electron microscopy, Y. Ben-Shahar for discussions, and K. Knudtson and the University of Iowa DNA Core Facility for assistance with sequencing, oligonucleotide synthesis and real-time PCR experiments. Supported in part by an NRL grant (C.K.). M.J.W. is an Investigator of the HHMI.

Author Contributions L.L. was responsible for molecular cloning, behavioural tests, extracellular electrophysiology, statistical analysis and preparation of the manuscript. Y.L. performed molecular cloning, transgenic generation, fly genetics and *in situ* hybridization. R.W. and Q.D. did *in vitro* wtrw cDNA expression and electrophysiology (data not shown in manuscript). C.Y. and H.H. were responsible for immunohistochemistry of wtrw and nan promoter expression in the brain. C.K. provided nan mutant, promoter and rescue flies. M.J.W. supervised the work and wrote the manuscript.

Author Information Reprints and permissions information is available at www.nature.com/reprints. Correspondence and requests for materials should be addressed to M.J.W. (michael-welsh@uiowa.edu).

METHODS

Fly maintenance and stocks. *Drosophila* stocks were reared on standard corn-meal-agar-molasses medium at constant 25 °C with a 12 h light and 12 h dark cycle. The *GH86-GAL4* line was a gift from G. Heimbeck. *UAS-TNT-H* was a gift from C. J. O'Kane. *UAS-shi^{ts1}* was a gift from T. Kitamoto. *Pyr³* and *pyr³;Ge^d* were gifts from J. Kim. All the deficiency lines for TRP and aquaporin genes and *elav-GAL4* lines were obtained from the Bloomington Stock Center. The deleted chromosomal regions in these deficiency lines were based on Flybase and the Stock Center's database information.

Cloning water witch and generation of transgenic fly lines. We found that the DNA sequences of introns and exons were the same as those predicted for CG31284. The protein-coding sequence for *wtrw* was 2,958 bp. *yw^{67c23}* strains were used for transgenic injections. P-element-mediated transformation and subsequent fly crossings were performed following standard techniques. A 2 kb genomic DNA sequence that was 5' to the translational start site of *wtrw* was amplified by PCR from genomic DNA purified from wild-type adult flies. This 2 kb DNA sequence should contain most of the promoter activity of *wtrw* and was cloned into a *GAL4* PTGAL vector (a gift from D. F. Eberl). We generated several independent P-element-mediated transgenics from this PTGAL vector. We studied *UAS-wtrw^{RNAi1.15}* and *UAS-wtrw^{RNAi1.19}* on the X chromosome and *UAS-wtrw^{RNAi1.3}*, *UAS-wtrw^{RNAi2.8}*, *UAS-wtrw^{RNAi3.1}* on the 2nd or 3rd chromosome. To produce a WTRW dominant negative (DN)²⁸, we generated a transgene expressing the N terminus of WTRW including the first predicted transmembrane domain (predicted protein size is 653 amino acids) using the pUAST vector. We studied *UAS-wtrw^{DN.19}* on the 2nd chromosome.

To rescue the effects of the *wtrw* deficiency, the full-length *wtrw* cDNA was cloned into the pUAST and pCaSpeR-hs-act vectors (GenBank accession number: U60735). *UAS-wtrw³¹* inserted on the 2nd chromosome. Because the pCaSpeR-hs-act vector has a heat shock 70 promoter in front of the inserted cDNA, it will express *wtrw* mRNA after heat shock in the transgenic line. To express the *hs-wtrw²²* transgene (located on the 3rd chromosome), we placed the flies in a 37 °C incubator for 3 h a day for 3 days.

Immunohistochemistry. Adult heads were dissected from the progenies of *wtrw-GAL4/UAS-mCD8-GFP* and *nan-GAL4/UAS-mCD8-GFP* crosses. Adult heads were sectioned following a previously described protocol³⁰. Anti-GFP rabbit polyclonal serum (1:5,000, Invitrogen, Molecular Probes) and the monoclonal antibody 22C10 (1:500, Developmental Studies Hybridoma Bank, University of Iowa) were used. Alexa Fluor 488 goat anti-rabbit IgG (1:1,000, Invitrogen, Molecular Probes) and cyanine 3 (Cy3)-conjugated goat anti-mouse

IgG (1:500, Jackson ImmunoResearch) were used as secondary antibodies. The staining was observed with a confocal microscope (BioRad).

Behavioural assay. At the point when flies had made a decision regarding preference of humid or dry air, the elevator was raised, so that flies could not change sides. We then counted the number of flies on each side and calculated the percentage on the moist side. For each genotype, we performed 6–27 such trials. To determine the average percentage of flies on the moist side, we calculated the mean and s.e.m. for the trials. Between 12% and 30% of our wild-type flies distributed to the moist side, a percentage point higher than a previous report¹. This difference might have been due to different genetic backgrounds or other laboratory variables. To reduce variability, we avoided experiments in bad weather conditions and between 11:00 and 16:00, because flies were generally less active at those times.

Electrophysiological recording. Data were recorded using p-Clamp7.0 software; the sampling interval was 100 μs.

To deliver moist or dry air, a single source of air at a constant flow rate was switched to pass through either a stone aerator in a water-filled flask or an aerator in a flask filled with drierite beads. It then emerged from tubes positioned 10 mm in front of the fly's head. We measured relative humidity and temperature with a digital humidity and temperature meter (Control Company). Experiments were performed at room temperature, and no temperature changes were detected with interventions, suggesting the temperature changes were less than 0.1 °C. To test the effect of airflow alone, we did experiments on days when the relative humidity was ~20%, because the relative humidity of the compressed air source was ~20%. We used the same tubing setup but left the aerators out of the water and the drierite beads. We observed no response to the airflow alone.

Confocal imaging. To investigate the peripheral expression pattern and central projections of various genes, we used their promoters to generate promoter-*GAL4* lines and crossed them to *UAS-CD8-GFP* (encoding a fusion protein between mouse lymphocyte marker CD8 and GFP that marks cell surface membranes and is concentrated in neuronal processes). Antenna or dissected adult brain was fixed in 4% paraformaldehyde in PBS for 30 min. Then, they were stained with rabbit anti-GFP-Alexa 555 (Invitrogen) to detect *mCD8-GFP*; nc82—a mouse monoclonal antibody that labels neuropil²⁹—or fluorescence of the GFP-based fluorophore was viewed directly. Confocal images were obtained with an LSM 510 META NLO (BioRad).

30. Wolff, T. in *Drosophila Protocols* (eds Sullivan, W., Ashburner, M. & Hawley, R. S.) 229–234 (Cold Spring Harbor Laboratory, Cold Spring Harbor, New York, 2000).

Roquin represses autoimmunity by limiting inducible T-cell co-stimulator messenger RNA

Di Yu¹, Andy Hee-Meng Tan², Xin Hu¹, Vicki Athanasopoulos^{1,3}, Nicholas Simpson¹, Diego G. Silva¹, Andreas Hutloff⁴, Keith M. Giles⁵, Peter J. Leedman^{5,6}, Kong Peng Lam², Christopher C. Goodnow^{1,7*} & Carola G. Vinuesa^{1*}

Immune responses are normally targeted against microbial pathogens and not self-antigens by mechanisms that are only partly understood. Here we define a newly discovered pathway that prevents autoimmunity by limiting the levels on T lymphocytes of a co-stimulatory receptor, the inducible T-cell co-stimulator (ICOS). In *sanroque* mice homozygous for an M199R mutation in the ROQ domain of Roquin (also known as Rc3h1)¹, increased Icos expression on T cells causes the accumulation of lymphocytes that is associated with a lupus-like autoimmune syndrome. Roquin normally limits Icos expression by promoting the degradation of *Icos* messenger RNA. A conserved segment in the unusually long *ICOS* 3' untranslated mRNA is essential for regulation by Roquin. This segment comprises a 47-base-pair minimal region complementary to T-cell-expressed microRNAs including miR-101, the repressive activity of which is disrupted by base-pair inversions predicted to abrogate miR-101 binding. These findings illuminate a critical post-transcriptional pathway within T cells that regulates lymphocyte accumulation and autoimmunity, and highlights the therapeutic potential of partially antagonising the ICOS pathway.

A two-signal mechanism regulates T-cell responses in secondary lymphoid tissues^{2–4}, whereby T-cell receptor engagement by antigen-major histocompatibility complex on an antigen-presenting cell (APC) only triggers T-cell accumulation and effector functions when a second co-stimulatory receptor on the T cell, CD28, is simultaneously engaged by B7 proteins that are induced on the APC on exposure to microbes. ICOS, a CD28 paralogue, can provide co-stimulation for T-cell responses in the absence of CD28 and is critical for follicular helper T (T_{FH}) cell survival, germinal centre reactions and generation of B-cell memory^{5–15}. The ligand for ICOS (ICOSL), unlike B7, is expressed constitutively on many APCs in the absence of microbe components, raising a paradox about how autoimmunity is avoided in the face of this second co-stimulatory system.

The *sanroque* M199R mutation in *Rc3h1* (*Rc3h1*^{san/san}) causes lupus associated with lymphadenopathy, splenomegaly and accumulation of T cells expressing increased Icos levels¹. To test the contribution of increased Icos expression to the pathology of *Rc3h1*^{san/san} mice, the *Icos* gene dosage was halved by interbreeding with *Icos* knockout mice. CD4⁺ T cells from *Rc3h1*^{san/san} *Icos*^{+/-} mice expressed 70% less Icos than cells from *Rc3h1*^{san/san} *Icos*^{+/+} mice, although this was still double that of wild-type mice (Fig. 1a and Supplementary Fig. 2). Partial correction of Icos overexpression in *Rc3h1*^{san/san} *Icos*^{+/-} mice was accompanied by a parallel reduction of

lymphadenopathy, splenomegaly, total T- and B-cell numbers, T_{FH} cell expansion and germinal-centre B-cell numbers in *sanroque* mice (Fig. 1b–e and Supplementary Fig. 3a, b). This effect is unlikely to reflect a nonspecific reduction in co-stimulation because halving the gene dose of *Cd28* in *sanroque* mice using a similar strategy did not reduce spleen nor lymph node size (Supplementary Fig. 4a, b). Furthermore, the severity of the lymphadenopathy correlated closely with the levels of Icos expressed on naive T cells across the different groups of genetically manipulated mice (Supplementary Fig. 4c). These results indicate that Icos overexpression caused by Roquin (M199R) is an essential contributor to the lupus phenotype, and demonstrate that tight regulation of Icos expression by Roquin is crucial to prevent T- and B-cell accumulation.

Because ectopic expression of Roquin in CD4⁺ T cells reduces endogenous Icos protein expression¹, we tested whether it regulated endogenous *Icos* mRNA abundance by overexpressing Roquin in stimulated EL4 T cells. In cells expressing wild-type Roquin, the quantity of *Icos* mRNA was halved compared to cells transfected with empty vector, whereas Roquin(M199R) was a less potent repressor of *Icos* mRNA (Fig. 2a). Manual annotation of *ICOS* mRNA by a BLAST search of the expressed-sequence-tag database revealed a remarkably long ~2,000 base pair (bp) 3' untranslated region (UTR) containing six highly conserved segments (Fig. 2b and Supplementary Table 1). To test the role of the *ICOS* 3' UTR, Roquin was expressed in NIH3T3 cells using the pR-IRES-GFP retroviral vector together with a pR-IRES-CD4 retroviral vector expressing either full-length human *ICOS* complementary DNA (*ICOS*^{FL}) or human *ICOS* complementary DNA lacking the 3' UTR (*ICOS*^{Δ3'UTR}; Fig. 2c, d). Although human *ICOS* expressed from *ICOS*^{FL} was strongly repressed in green fluorescent protein (GFP)⁺ cells co-expressing wild-type Roquin, there was negligible repression when human *ICOS* was expressed from *ICOS*^{Δ3'UTR} (Fig. 2e). Using GFP to determine relative Roquin levels in individual cells, repression of human *ICOS* expression by wild-type Roquin was shown to be dose-dependent (Fig. 2f and Supplementary Fig. 5).

We took advantage of the *ICOS* retroviral vector, which constitutively expresses a single bicistronic mRNA encoding *ICOS* and human CD4 (Fig. 2d), to confirm that the *ICOS* 3' UTR was the target of Roquin's repressive effect on the transcript. Provided *ICOS* 3' UTR sequences were present within the bicistronic mRNA, wild-type Roquin caused a dose-dependent repression of human CD4 expression (Fig. 2g; Supplementary Fig. 6). Notably, Roquin(M199R) was a less-efficient repressor of human *ICOS*

¹Division of Immunology and Genetics, John Curtin School of Medical Research, The Australian National University, Canberra, 2601, Australia. ²Laboratory of Molecular and Cellular Immunology, Biomedical Sciences Institute, Agency for Science, Technology and Research (A*STAR), Singapore 138673, Singapore. ³ARC Centre for the Molecular Genetics of Development, Australian National University, Canberra, 2601, Australia. ⁴Molecular Immunology, Robert Koch-Institute, 13353, Berlin, Germany. ⁵Laboratory for Cancer Medicine, The University of Western Australia Centre for Medical Research, Western Australian Institute for Medical Research, Perth, 6000, Australia. ⁶School of Medicine and Pharmacology, The University of Western Australia, Perth, 6000, Australia. ⁷Australian Phenomics Facility, Canberra, 2601, Australia.

*These authors contributed equally to this work.

expression (Supplementary Fig. 7), indicating that the *sanroque* mutation reduces but does not abolish this activity of Roquin.

To demonstrate that this mechanism operates in mouse primary T cells expressing endogenous Roquin, *ICOS^{FL}*, *ICOS^{Δ3'UTR}* or the 3' UTR alone of human *ICOS* (*ICOS^{3'UTR}*) were inserted into the pR-IRES-GFP vector (Fig. 2d). Mean GFP levels were higher in *sanroque* CD4⁺ T cells compared to wild-type CD4⁺ T cells transduced with constructs containing the *ICOS* 3' UTR, regardless of the presence or absence of the *ICOS* coding region (Fig. 2h). In contrast, the *sanroque* mutation did not affect GFP levels from the construct lacking the 3' UTR (*ICOS^{Δ3'UTR}*, Fig. 2h).

Given the regulatory role of 3' UTRs in mRNA stability and Roquin's localization to cytoplasmic stress granules¹, from which some mRNAs are transported to processing bodies where mRNA degradation occurs¹⁶, we next asked if *ICOS* mRNA is localized to stress granules and if its stability is regulated by Roquin. We visualized human *ICOS* mRNA in transduced cells using the MS2 plasmid expression system (Supplementary Fig. 8) and found *ICOS^{FL}* mRNA localized within stress granules and processing bodies (Fig. 3a, b). The rate of *Icos* mRNA decay was measured in stimulated EL4 cells transfected with Roquin or empty vector after inhibiting transcription. Roquin overexpression shortened the half-life of endogenous *Icos* mRNA to 46% of the empty vector control (Fig. 3c).

To identify the *cis*-acting regulatory elements within the *ICOS* 3' UTR that mediate Roquin's action, we introduced three human *ICOS* 3' UTR fragments of similar size—3' UTR-F1, 3' UTR-F2 and 3' UTR-F3, each containing at least one conserved region (Fig. 2c)—into the pR-IRES-CD4 vector (Fig. 2d) and measured the effect of co-expressing Roquin (Fig. 3d). Wild-type Roquin did not repress expression of human *CD4* mRNA containing either 3' UTR-F1 or 3' UTR-F2, but significantly reduced expression of human *CD4* mRNA containing 3' UTR-F3. This activity of 3' UTR-F3 was diminished by the M199R mutation. The inhibitory effect of the 3' UTR-F3 on mRNA abundance was confirmed by real-time polymerase chain reaction (PCR) measurements in sorted cells (Fig. 3e). In cells transduced with 3' UTR-F3-CD4, but not

control cells with 3' UTR-F1-CD4 or empty human CD4 vector (not shown), sorted GFP^{hi} cells expressing exogenous wild-type Roquin had 70% less human *CD4* mRNA than GFP^{int} control cells in the same culture (Fig. 3e).

Although AU-rich elements are the best characterized *cis*-acting elements for mRNA degradation¹⁷, there is no typical AU-rich element within *ICOS* 3' UTR-F3. Recent work has shown that microRNAs (miRNAs), a class of small non-coding RNAs of 20–22 nucleotides, base-pair with *cis*-regulatory sites within the 3' UTRs of target mRNAs and mediate post-transcriptional repression of gene expression¹⁸. *In silico* analysis of *ICOS* 3' UTR-F3 using MiRanda^{18–20} revealed several putative miRNA target sites (Supplementary Fig. 9a, b). MicroRNA target region one (MTR1), a 47 bp region containing target sequences for miR-101, 103/107 and 338, and miRNA target region two (MTR2), a 47 bp region containing the target sequence for miR-149, were subcloned into the pR-IRES-CD4 retroviral vector (Fig. 2d). MTR1 but not MTR2 was able to mediate repression of human *CD4* expression by wild-type Roquin but not by Roquin (M199R) (Fig. 4a).

Because miR-101 is expressed in NIH3T3 cells and mouse T lymphocytes²¹, we tested whether complementarity between MTR1 and miR-101 is required for repression by determining the activity of a mutant construct (MTR1^{Mut}) containing a two-nucleotide inversion within a region of MTR1 that is perfectly complementary to the so-called 'seed' of miR-101 (Fig. 4b). Complete pairing within the seed sequence is essential for miRNA recognition of its target sequence^{22,23}. Mismatches within the seed region inhibited MTR1-mediated repression of human *CD4* expression by Roquin (Fig. 4b). Ectopic expression of miR-101 precursor in EL4 cells reduced endogenous *Icos* mRNA levels (Fig. 4c). Consistent with a role in repressing *ICOS*, we found that miR-101 is differentially expressed in human naive, memory and T_{FH} CD4⁺ cells (Fig. 4d), and inversely correlates to *ICOS* expression in these subsets^{24,25}, with the highest levels found in naive (*ICOS^{neg}*) cells, intermediate levels in memory cells (*ICOS^{int}*) and lowest levels in T_{FH} cells (*ICOS^{high}*) (Fig. 4d). The levels of miR-101 and its primary miRNA transcript were higher in

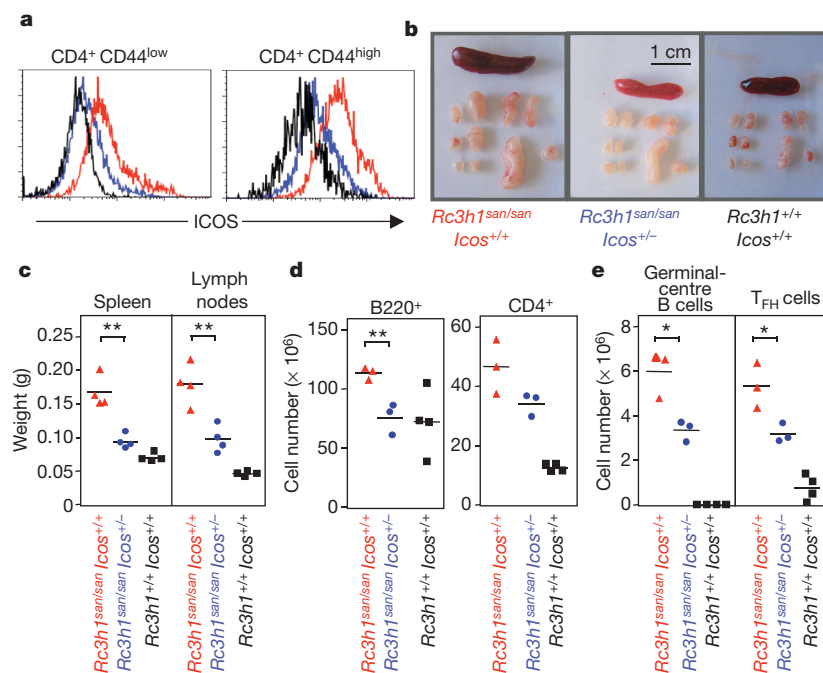


Figure 1 | Overexpression of *Icos* contributes to autoimmunity in *sanroque* (*Rc3h1^{san/san}*) mice. **a, *Icos* expression on naive (CD44^{low}, left) and antigen-experienced (CD44^{high}, right) splenic CD4⁺ T cells from 8-week-old C57BL × CBA H-2^{kk} mice with the indicated genotypes. **b**, Spleen (top) and lymph nodes (bottom) from representative mice. **c**, Weights of spleen and**

combined lymph nodes. **d**, Total numbers of B cells (B220⁺) and CD4⁺ T cells from spleens in **c**. **e**, Total numbers of germinal-centre B cells and T_{FH} cells from spleens in **c**. Each symbol represents one mouse. The lines show arithmetic means. Significant differences by Student's *t*-test are marked by asterisks: one asterisk, *P* < 0.05; two asterisks, *P* < 0.01.

sanroque naive CD4⁺ T cells than in the wild type (Supplementary Fig. 10), indicating that the M199R mutation of Roquin does not dysregulate *Icos* mRNA by means of a loss of miR-101 expression. The paradoxical increase in miR-101 indicates a compensatory upregulation. MiR-103 and miR-338 are both also predicted to recognize MTR1; ectopic expression of the miR-103 precursor, but not the miR-338 precursor, also reduced endogenous *Icos* mRNA levels (Supplementary Fig. 11). It is thus possible that several miRNAs act together regulate *Icos* mRNA decay.

We next asked whether defective miR-101-mediated repression could explain increased expression of other genes in *sanroque* T cells¹. Messenger RNA levels of neuropilin 1, important for the formation

of an 'immunological synapse' between T cells and dendritic cells²⁶, are increased in *sanroque* naive CD4⁺ T cells, and neuropilin 1 is a predicted target of miR-101 (Supplementary Fig. 12a, b). Overexpression of wild-type Roquin in EL4 T cells reduced neuropilin 1 mRNA compared to cells transfected with the empty vector. In contrast, Roquin(M199R) increased the levels of neuropilin 1 mRNA (Supplementary Fig. 12c). As shown for *Icos*, ectopic expression of miR-101 also reduced endogenous neuropilin 1 mRNA levels (Supplementary Fig. 12d).

The findings reported here demonstrate a newly discovered mRNA regulatory pathway, the partial failure of which leads to autoimmunity. Autoimmune lymphocyte accumulation in mice homozygous

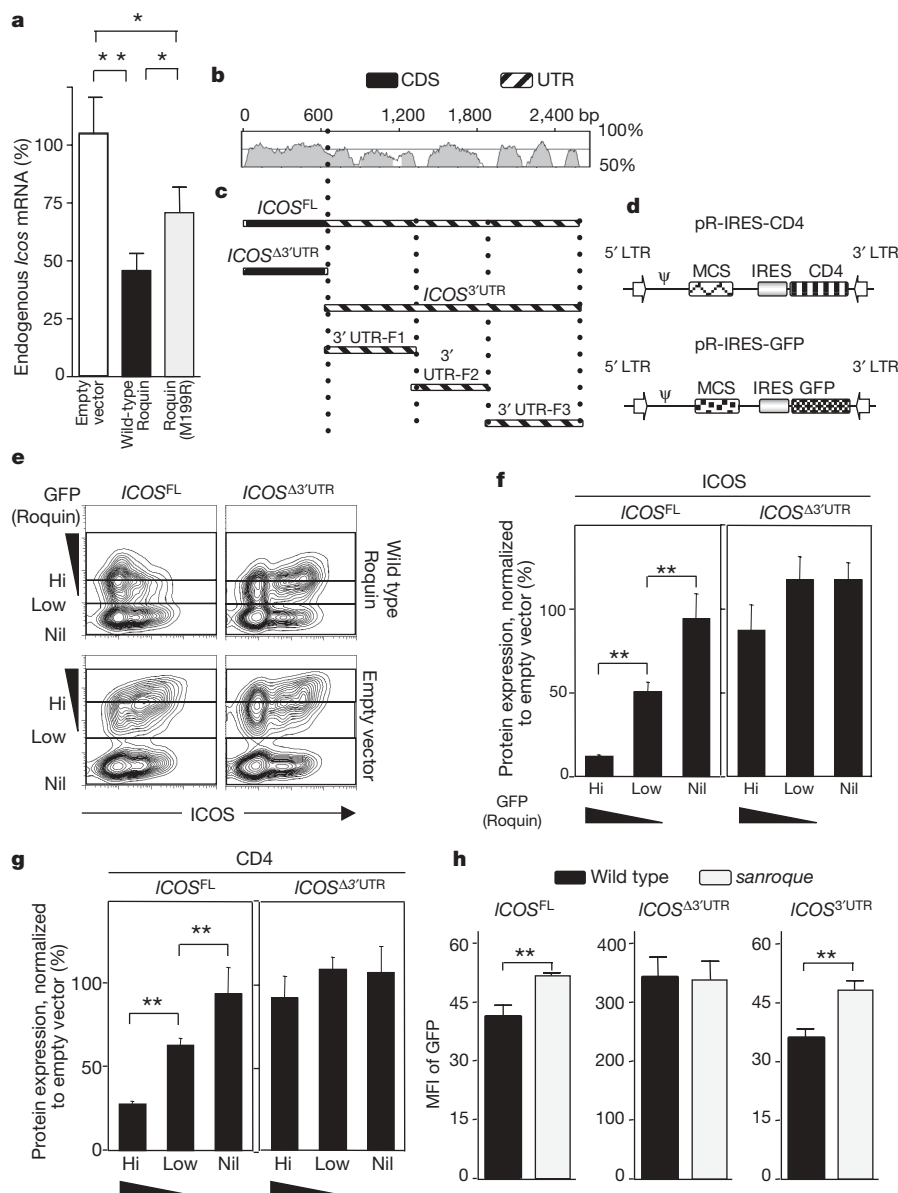


Figure 2 | Roquin represses ICOS through sequences in the *ICOS* mRNA 3' UTR. **a**, Endogenous *Icos* mRNA measured by real-time PCR with reverse transcription (RT-PCR) in EL4 cells transfected with empty vector, wild-type Roquin or Roquin(M199R) and then stimulated with anti-CD3ε plus anti-CD28. The level of *Icos* mRNA in cells transfected with empty vector was assigned 100%. **b**, Conservation between full-length human and mouse *Icos* cDNA. Shaded areas represent conserved regions with more than 70% homology in 100 bp. CDS, coding sequence. **c**, The human *ICOS* cDNA fragments used. **d**, Schematic maps for retroviral vectors. CD4, human tailless CD4 cDNA; IRES, internal ribosome entry sequence; LTR, long terminal repeat; Ψ, packaging signal; MCS, multiple cloning site. **e**, Flow cytometric

plots showing GFP and human ICOS expression on NIH3T3 cells transduced with the indicated *ICOS* vectors plus either Roquin or the empty (GFP-only) vector. The boxes show the gates used to define the GFP^{hi}, GFP^{low} and GFP^{nil} populations. **f**, **g**, Mean fluorescent intensity (MFI) of human ICOS (**f**) and human CD4 (**g**) in the populations gated in **e**. Repression of ICOS and CD4 was quantified as explained in Supplementary Fig. 5. **h**, Activated CD4⁺ *sanroque* CD45.2 and wild-type CD45.1 cells were transduced with retroviruses packaged from pR-IRES-GFP vectors expressing human *ICOS* cDNA fragments, and GFP MFI was quantified. Data shown represent mean values ± s.d., with *n* = 3. Significant differences by Student's *t*-test are marked by asterisks: one asterisk, *P* < 0.05; two asterisks, *P* < 0.01.

for Roquin(M199R) results at least in part from failure to repress expression of the co-stimulatory molecule ICOS, particularly on naive T cells. ICOS expression is normally tightly regulated post-transcriptionally by a mechanism that involves a conserved miRNA binding sequence within the 3' UTR. Whether Roquin binds directly to its target mRNAs and/or to the complementary miRNAs is not

known. Roquin contains a potential RNA-binding CCCH domain and localizes within stress granules, in close association with processing bodies, leading us to speculate that Roquin forms part of a multi-protein complex within stress granules that directs certain mRNAs, including ICOS, to the route of miRNA-mediated decay in processing bodies. There are precedents for proteins that regulate miRNA-mediated repression by directing localization of target mRNAs to specific cytoplasmic compartments²⁷. Notably, a number of human and mouse autoantibodies target key elements of the RNA

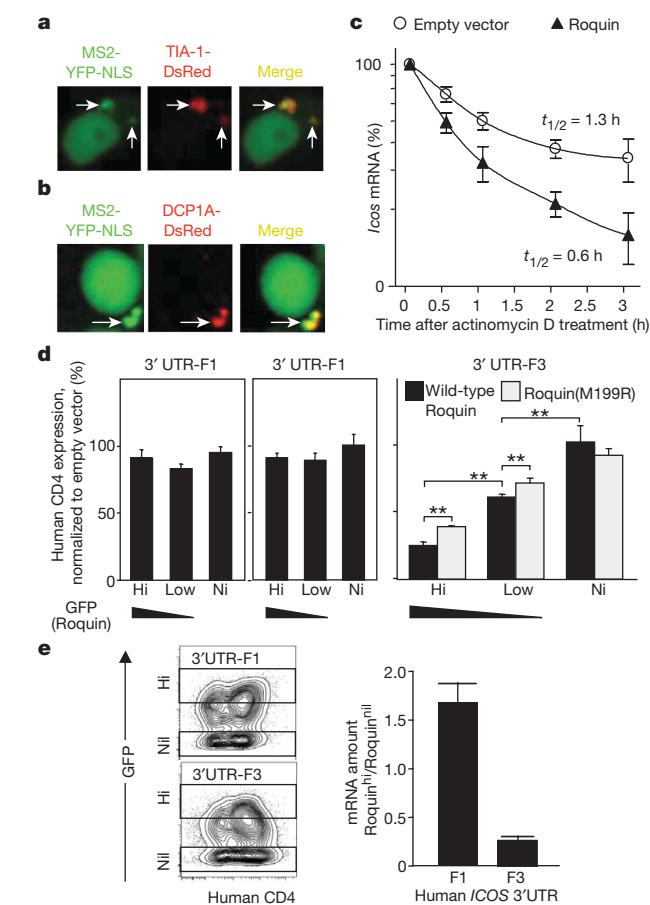


Figure 3 | Identification of the minimal region within ICOS 3' UTR containing cis-acting elements for Roquin control of ICOS mRNA abundance. **a, b,** Intracellular localization of human ICOS mRNA in 293T cells co-transfected with plasmids expressing ICOS^{FL} (pR-ICOS^{FL}-MS2 binding site₍₂₄₎-IRES-CD4), TIA-1-DsRed (**a**, a stress granule marker) or DCP1a-DsRed (**b**, a processing-body marker), and MS2-YFP-NLS. Green fluorescence shows the localization of ICOS transcripts bound to MS2-YFP-NLS protein. Arrows indicate stress granules (**a**) and processing-bodies (**b**). **c,** ICOS mRNA levels in activated EL4 cells transfected with Roquin or empty vector, treated with actinomycin D for the times indicated. Endogenous ICOS mRNA levels were measured using real-time RT-PCR and normalized to Actb. The amount of ICOS mRNA at time 0 h was assigned 100%. Trendlines (Graphpad Prism) were fitted to predict the indicated mRNA half-lives. Data shown are mean values ± s.d. with *n* = 3. **d,** MFI of human CD4 in NIH3T3 cells co-transduced with vectors expressing ICOS 3' UTR-F1, -F2 or -F3 upstream of IRES-CD4, and vectors expressing either wild-type Roquin or Roquin(M199R) upstream of IRES-GFP. Data shown are mean values ± s.d. with *n* = 3. Statistically significant differences are marked by asterisks: Student's *t*-test, two asterisks, *P* < 0.01. **e,** Human CD4 mRNA levels in NIH3T3 cells co-transduced with bicistronic retroviral vectors containing ICOS 3' UTR-F1- or 3' UTR-F3-CD4 and Roquin-GFP. GFP^{hi} and GFP^{nil} populations were FACS-sorted using the gates shown in the contour plots (left), and total RNA was isolated. The bar graph shows relative human CD4 mRNA in Roquin^{high} (GFP^{hi}) cells compared to Roquin^{nil} (GFP^{nil}) cells. The small increase in human CD4 mRNA in ICOS 3' UTR-F1 cells expressing Roquin was also observed in GFP^{hi} cells expressing empty vector (not shown), indicating that this effect is not due to Roquin, but probably reflects enrichment for cell cycling among double-transduced cells. Data shown represent mean values ± s.d. with *n* = 4 different primer pairs designed to amplify different regions of CD4 cDNA.

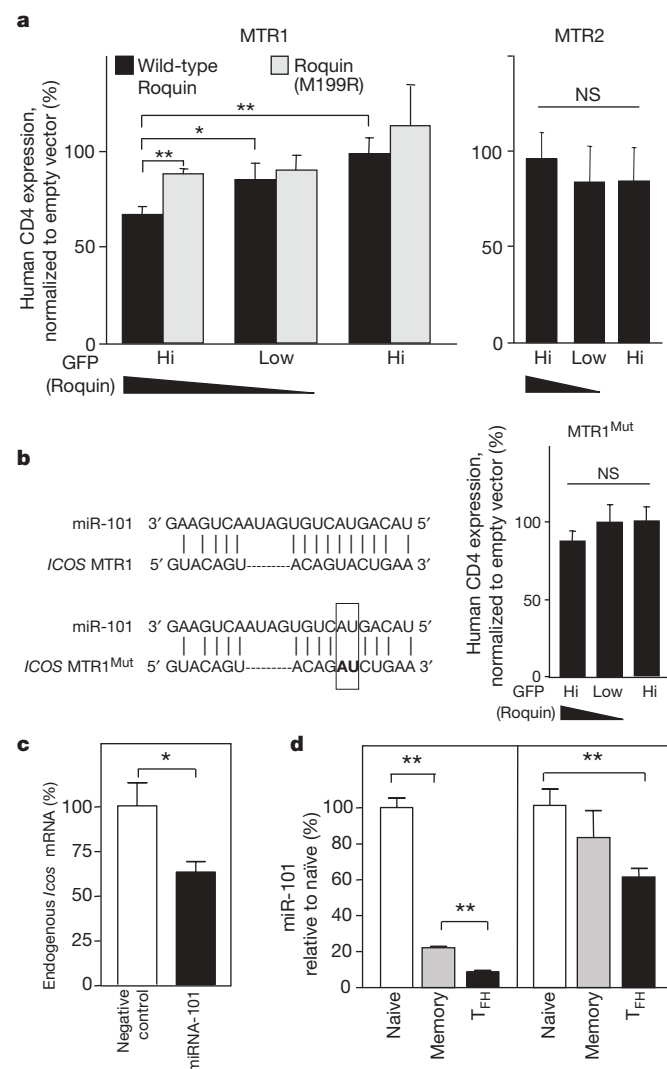


Figure 4 | A miRNA target site mediates the regulation of ICOS mRNA by Roquin. **a,** MFI of CD4 assessed by flow cytometry in NIH3T3 cells retrovirally co-transduced with vectors expressing MTR1 or MTR2 upstream of IRES-CD4, and wild-type Roquin or Roquin(M199R) upstream of IRES-GFP. **b,** The human miR-101 binding site within ICOS 3' UTR, as predicted by miRanda. MTR1^{Mut} was constructed by reversing two adjacent nucleotides (box) in the predicted 'seed' sequence within MTR1. The bar graph shows the MFI of CD4 in NIH3T3 cells transduced with wild-type Roquin (GFP) and MTR1^{Mut} (human CD4) analysed as described in **a**. **c,** Endogenous ICOS mRNA levels assessed by real-time RT-PCR in EL4 cells transfected with miRNA precursor negative control and human miR-101 precursor for 24 h. The level of ICOS mRNA in cells transfected with miRNA precursor negative control was assigned 100%. **d,** Levels of mature miRNA-101 in human naive (CD4⁺CD45RO⁻CXCR5⁻ICOS^{int}), memory (CD4⁺CD45RO⁺CXCR5⁻low⁻ICOS^{int}) and T_{FH} (CD4⁺CD45RO⁺CXCR5^{high}ICOS^{high}) CD4⁺ cells sorted from tonsil were quantified using TaqMan miRNA assays. Data shown are mean values ± s.d. with *n* = 3. Each panel represents a separate experiment from different individuals. Statistically significant differences are marked by asterisks: Student's *t*-test, one asterisk, *P* < 0.05; two asterisks, *P* < 0.01; NS, no significant difference.

interference machinery, including argonaute proteins and Dicer²⁸. It is intriguing that stress granules and their other components, notably TIA-1 (T-cell restricted intracellular antigen-1) are more prominent in primed T cells²⁹. Taken together, this raises the possibility that dysfunction of the machinery for RNA decay and interference lies at the core of the pathogenesis of autoimmune diseases. The findings here demonstrate a unique mechanism to prevent autoimmunity by limiting T-cell receptivity to co-stimulation. This contrasts with, and probably complements, the mechanisms that control expression on APCs of B7 co-stimulatory ligands for CD28. The marked effect of quantitative shifts in ICOS expression demonstrated here highlights the potential for treating autoimmunity in some individuals by partial antagonism of ICOS–ICOSL interaction.

METHODS SUMMARY

Mice. Sanroque C57BL/6 H-2^{bb} mice were used for *in vitro* experiments, and C57BL × CBA H-2^{kk} mice were used for *in vivo* experiments and crosses with *Icos*^{−/−} and *Cd28*^{−/−} mice. All animal procedures were approved by the Australian National University Animal Ethics and Experimentation Committee. **Cells, retroviruses, transduction and transfection.** Fragments of human ICOS cDNA were amplified from the BC028210 cDNA clone and were inserted into retroviral vectors. Retroviral supernatants were harvested from packaging Phoenix cells transfected with individual retroviral constructs. NIH3T3 cells and primary CD4⁺ T cells were transduced by retroviruses by spinoculation. Roquin cDNA was subcloned into pcDNA3.1/CT-GFP TOPO TA fusion vector, which was used to transfect EL4 cells. MicroRNA precursors and the negative control (Ambion's negative control 1) were transfected into EL4 cells using the siPORT NeoFX. Plasmids expressing the ICOS^{FL} (pR-ICOS^{FL}-MS2 binding site₍₂₄₎-IRES-CD4), TIA-1-DsRed or DCP1A-DsRed, and MS2–YFP–NLS (nuclear localization signal) were co-transfected into 293T cells.

Flow cytometry and immunofluorescence. Flow cytometry and immunofluorescence were performed as described¹.

Real-time PCR with reverse transcription. Complementary DNA expression was determined with the ABI Prism 7900 sequence-detection system and SYBR Green reagents. The amount of mRNA was expressed relative to that of β-actin (*Actb*) or *Ube2d2* and expressed as 2^{−ΔC_T} (see Methods). For miRNA assessment, human naive, memory and T_{FH} CD4⁺ cell subsets were sorted from tonsil, and RNA was isolated using the mirVana miRNA isolation kit. Mature miRNA levels were quantified using the TaqMan miRNA assay.

Computational methods. Human (BC028210) and mouse (AK030827) ICOS nucleotide sequences were aligned using LAGAN (limited area global alignment of nucleotides)³⁰. MicroRNA target sequences within *Icos* mRNA were predicted using the MiRanda software¹⁹.

Full Methods and any associated references are available in the online version of the paper at www.nature.com/nature.

Received 30 June; accepted 11 September 2007.

- Vinuesa, C. G. *et al.* A RING-type ubiquitin ligase family member required to repress follicular helper T cells and autoimmunity. *Nature* **435**, 452–458 (2005).
- Matzinger, P. Tolerance, danger, and the extended family. *Annu. Rev. Immunol.* **12**, 991–1045 (1994).
- Janeway, C. A. Jr & Bottomly, K. Signals and signs for lymphocyte responses. *Cell* **76**, 275–285 (1994).
- Lafferty, K. J., Andrus, L. & Prowse, S. J. Role of lymphokine and antigen in the control of specific T cell responses. *Immunol. Rev.* **51**, 279–314 (1980).
- Suh, W. K. *et al.* The inducible costimulator plays the major costimulatory role in humoral immune responses in the absence of CD28. *J. Immunol.* **172**, 5917–5923 (2004).
- Nurieva, R. *et al.* T-cell tolerance or function is determined by combinatorial costimulatory signals. *EMBO J.* **25**, 2623–2633 (2006).

- Bossaller, L. *et al.* ICOS deficiency is associated with a severe reduction of CXCR5⁺CD4 germinal center Th cells. *J. Immunol.* **177**, 4927–4932 (2006).
- Akiba, H. *et al.* The role of ICOS in the CXCR5⁺ follicular B helper T cell maintenance *in vivo*. *J. Immunol.* **175**, 2340–2348 (2005).
- Dong, C. *et al.* ICOS co-stimulatory receptor is essential for T-cell activation and function. *Nature* **409**, 97–101 (2001).
- Dong, C., Temann, U. A. & Flavell, R. A. Cutting edge: critical role of inducible costimulator in germinal center reactions. *J. Immunol.* **166**, 3659–3662 (2001).
- McAdam, A. J. *et al.* ICOS is critical for CD40-mediated antibody class switching. *Nature* **409**, 102–105 (2001).
- Tafari, A. *et al.* ICOS is essential for effective T-helper-cell responses. *Nature* **409**, 105–109 (2001).
- Grimbacher, B. *et al.* Homozygous loss of ICOS is associated with adult-onset common variable immunodeficiency. *Nature Immunol.* **4**, 261–268 (2003).
- Mak, T. W. *et al.* Costimulation through the inducible costimulator ligand is essential for both T helper and B cell functions in T cell-dependent B cell responses. *Nature Immunol.* **4**, 765–772 (2003).
- Wong, S. C., Oh, E., Ng, C. H. & Lam, K. P. Impaired germinal center formation and recall T-cell-dependent immune responses in mice lacking the costimulatory ligand B7–H2. *Blood* **102**, 1381–1388 (2003).
- Newbury, S. F., Muhlemann, O. & Stoecklin, G. Turnover in the Alps: an mRNA perspective. Workshops on mechanisms and regulation of mRNA turnover. *EMBO Rep.* **7**, 143–148 (2006).
- Barreau, C., Paillard, L. & Osborne, H. B. AU-rich elements and associated factors: are there unifying principles? *Nucleic Acids Res.* **33**, 7138–7150 (2005).
- Rajewsky, N. MicroRNA target predictions in animals. *Nature Genet.* **38** (Suppl), S8–S13 (2006).
- John, B. *et al.* Human MicroRNA targets. *PLoS Biol.* **2**, e363 (2004).
- Sethupathy, P., Megraw, M. & Hatzigeorgiou, A. G. A guide through present computational approaches for the identification of mammalian microRNA targets. *Nature Methods* **3**, 881–886 (2006).
- Monticelli, S. *et al.* MicroRNA profiling of the murine hematopoietic system. *Genome Biol.* **6**, R71 (2005).
- Jackson, R. J. & Standart, N. How do microRNAs regulate gene expression? *Sci. STKE* **2007**, re1 (2007).
- Lim, L. P. *et al.* Microarray analysis shows that some microRNAs downregulate large numbers of target mRNAs. *Nature* **433**, 769–773 (2005).
- Yoshinaga, S. K. *et al.* T-cell co-stimulation through B7RP-1 and ICOS. *Nature* **402**, 827–832 (1999).
- Hutloff, A. *et al.* ICOS is an inducible T-cell co-stimulator structurally and functionally related to CD28. *Nature* **397**, 263–266 (1999).
- Tordjman, R. *et al.* A neuronal receptor, neuropilin-1, is essential for the initiation of the primary immune response. *Nature Immunol.* **3**, 477–482 (2002).
- Bhattacharyya, S. N., Habermacher, R., Martine, U., Closs, E. I. & Filipowicz, W. Relief of microRNA-mediated translational repression in human cells subjected to stress. *Cell* **125**, 1111–1124 (2006).
- Jakymiw, A. *et al.* Autoimmune targeting of key components of RNA interference. *Arthritis Res. Ther.* **8**, R87 (2006).
- Scheu, S. Activation of the integrated stress response during T helper cell differentiation. *Nature Immunol.* **7**, 644–651 (2006).
- Brudno, M. *et al.* LAGAN and Multi-LAGAN: efficient tools for large-scale multiple alignment of genomic DNA. *Genome Res.* **13**, 721–731 (2003).

Supplementary Information is linked to the online version of the paper at www.nature.com/nature. A summary figure is also included.

Acknowledgements We thank R. Parker and J. Liu for the MS2–YFP–NLS plasmids; R. Kroczeck and Millennium Pharmaceuticals for *Icos*^{−/−} mice; Q.-J. Li, M. Davis and C.-Z. Chen for advice with the miRNA experiments; and the ACRF Biomolecular Resource Facility for real-time RT–PCR. This work was supported by the NHMRC, and by a Senior Viertel Medical Research Fellowship to C.G.V.

Author Contributions D.Y., C.C.G. and C.G.V. designed the study; D.Y., A.H.T. and X.H. performed experiments and analyzed the data; V.A., N.S., K.M.G. and D.G.S. helped with experiments; A.H., P.J.L. and K.P.L. provided expertise and advice; and D.Y., C.C.G. and C.G.V. wrote the manuscript.

Author Information Reprints and permissions information is available at www.nature.com/reprints. Correspondence and requests for materials should be addressed to C.G.V. (carola.vinuesa@anu.edu.au).

METHODS

Mice. *sanroque* C57BL/6 H-2^{bb} mice were used for *in vivo* experiments; for *in vitro* experiments and crosses to *Icos*^{-/-} and *Cd28*^{-/-} mice, the test and control littermates were a mixed C57BL/6, B10.BR and CBA background. All mice were housed in specific pathogen-free conditions in the Australian Phenomics Facility.

Cells, retroviruses, transduction and transfection. NIH3T3 cells were grown in DMEM medium supplemented with 10% FCS and antibiotics. Various fragments of human *ICOS* cDNA were amplified by PCR from the BC028210 cDNA clone and were inserted into retroviral vectors. Primer sequences are available on request. Retroviral supernatants were harvested from packaging Phoenix cells transfected with individual retroviral constructs. NIH3T3 cells and primary CD4⁺ T cells were transduced by retroviruses by spinoculation.

EL4 cells were grown in RPMI medium supplemented with 10% FCS and antibiotics. *Roquin* cDNA was subcloned into the pcDNA3.1/CT-GFP TOPO TA fusion vector (Invitrogen), which was then used to transfect EL4 cells.

MicroRNA precursors and the negative control (number 1) were purchased from Ambion and transfected into EL4 cells using the siPORT NeoFX (Ambion).

293T cells were grown in DMEM medium supplemented with 10% FCS and antibiotics. Plasmids expressing the *ICOS*^{FL} (pR-*ICOS*^{FL}-MS2 binding site₍₂₄₎-IRES-CD4), TIA-1-DsRed or DCP1a-DsRed, and MS2-YFP-NLS were co-transfected into 293T cells.

Real-time PCR with reverse transcription. RNA was isolated using TRIzol reagent (Invitrogen) and reverse-transcribed with oligo(dT) using Superscript II RT enzyme (Invitrogen). Complementary DNA expression was determined with the ABI Prism 7900 sequence-detection system and SYBR Green reagents (PE Biosystems). Primer sequences are available on request. Fluorescence signals were measured over 40 PCR cycles, and the cycle at which signals crossed a threshold set within the logarithmic phase (C_T) was recorded. The C_T for the target gene was subtracted from the C_T for *Actb* or *Ube2d2* (ΔC_T). The relative amount of mRNA was calculated as $2^{-\Delta C_T}$.

To measure levels of individual mature miRNAs, human naive, memory and T_{FH} CD4⁺ cell subsets were sorted from tonsil using a FACSaria (Becton Dickinson) and RNA was isolated using the mirVana miRNA Isolation Kit (Ambion). Mature miRNA levels were quantified using the TaqMan miRNA assay (Applied Biosystems).

Activation of EL4 cells and primary CD4⁺ cells. To assess endogenous *Icos* mRNA levels in EL4 cells, these were first transfected with empty vector, wild-type Roquin or Roquin(M199R) and were then stimulated with plate-bound anti-CD3 ϵ (1 $\mu\text{g ml}^{-1}$) plus anti-CD28 (4 $\mu\text{g ml}^{-1}$) for 16 h. For experiments assessing *Icos* mRNA decay in EL4 cells, these cells were transfected with Roquin or empty vector, stimulated with plate-bound anti-CD3 ϵ (1 $\mu\text{g ml}^{-1}$) plus anti-CD28 (4 $\mu\text{g ml}^{-1}$) for 6 h and treated with transcriptional inhibition reagent actinomycin D (10 $\mu\text{g ml}^{-1}$) for the times indicated.

For transduction of primary T cells, CD4⁺ T cells were magnetically isolated from spleen and lymph nodes of *sanroque* (CD45.2) and wild-type C57BL/6 (congenic, CD45.1) mice. Wild-type and *sanroque* CD4⁺ cells were co-cultured and stimulated with plate-bound anti-CD3 ϵ (2 $\mu\text{g ml}^{-1}$) plus anti-CD28 (5 $\mu\text{g ml}^{-1}$) for 24 h before transduction with retroviruses packaged from pR-IRES-GFP vector inserted with *ICOS* cDNA fragments as indicated.

Computational and statistical methods. The human *ICOS* nucleotide sequence (BC028210) was aligned with mouse *Icos* nucleotide sequence (AK030827) using pairwise alignment software LAGAN³⁰ through the VISTA server (<http://genome.lbl.gov/vista/index.shtml>).

For assessment of mRNA decay after treatment with actinomycin D, trendlines were fitted using the Graphpad Prism software; these were used to predicted mRNA half-lives.

MicroRNA target sequences within *Icos* and neuropilin 1 (*Nrp1*) mRNAs were predicted by the MiRanda software¹⁹.

LETTERS

An epigenetic activation role of Piwi and a Piwi-associated piRNA in *Drosophila melanogaster*

Hang Yin^{1,2} & Haifan Lin^{1,2}

Heterochromatin, representing the silenced state of transcription, consists largely of transposon-enriched and highly repetitive sequences. Implicated in heterochromatin formation and transcriptional silencing in *Drosophila* are Piwi (P-element induced wimpy testis)^{1,2} and repeat-associated small interfering RNAs (rasiRNAs)^{3–5}. Despite this, the role of Piwi in rasiRNA expression and heterochromatic silencing remains unknown. Here we report the identification and characterization of 12,903 Piwi-interacting RNAs (piRNAs) in *Drosophila*, showing that rasiRNAs represent a subset of piRNAs. We also show that Piwi promotes euchromatic histone modifications and piRNA transcription in subtelomeric heterochromatin (also known as telomere-associated sequence, or TAS), on the right arm of chromosome 3 (3R-TAS). Piwi binds to 3R-TAS and a piRNA uniquely mapped to 3R-TAS (3R-TAS1 piRNA). In *piwi* mutants, 3R-TAS loses euchromatic histone modifications yet accumulates heterochromatic histone modifications and Heterochromatin Protein 1a (HP1a). Furthermore, the expression of both the 3R-TAS1 piRNA and a *white* reporter gene in 3R-TAS becomes suppressed. A P element inserted 128 base pairs downstream of the 3R-TAS1 piRNA coding sequence restores the euchromatic histone modifications of 3R-TAS and the expression of 3R-TAS1 piRNA in *piwi* mutants, as well as partly rescuing their defects in germline stem-cell maintenance. These observations suggest that Piwi promotes the euchromatic character of 3R-TAS heterochromatin and its transcriptional activity, opposite to the known roles of Piwi and the RNA-mediated interference pathway in epigenetic silencing. This activating function is probably achieved through interaction with at least 3R-TAS1 piRNA and is essential for germline stem-cell maintenance.

Non-coding small RNAs in the nucleus have been proposed to provide a sequence-specific interface between a DNA sequence and its epigenetic state, presumably by their base-pairing with genomic DNA or nascent RNA^{6,7}. Recent studies in the fission yeast have indicated that RNA-interference (RNAi)-mediated heterochromatin assembly occurs by means of a self-enforcing loop mechanism^{8–10}. A central player of this loop is the RITS (RNAi-induced initiation of transcriptional gene silencing) complex, which contains a chromodomain-containing protein (Chp1), Argonaute 1 (Ago1), Tas3, and siRNAs^{9–12}. Ago1 confers the sequence specificity by binding to siRNAs and recruits other chromatin proteins to initiate the heterochromatinization⁹. Despite this progress, the role of non-coding small RNAs in epigenetic regulation in higher organisms remains largely unexplored.

To examine this role, we focus on Piwi and its interacting piRNAs in *Drosophila*. Piwi is an Ago/Piwi protein that was initially identified to be essential for stem-cell self-renewal¹³. Subsequently, it was implicated in heterochromatin formation, transposon silencing, and clustering of multiple copies of transgenes through the RNAi-mediated

pathway^{1–3,14–16}. Piwi interacts with piRNAs^{3–5}, bears RNA cleavage activity⁴, and may participate in an ‘amplification cycle’ that accelerates piRNA biogenesis^{5,17}.

To identify Piwi-interacting piRNAs systematically, we conducted immunoprecipitation to purify the Myc-Piwi complex from ovaries of adult flies carrying a fully functional *myc-piwi* transgene (Supplementary Fig. 1a)¹⁸. Small RNAs ranging from 18 to 32 nucleotides (nt) in length were specifically precipitated with the Myc-Piwi complex (Fig. 1a, in which 24–26-nt RNAs are visible). We recovered 19,048 candidate small RNA clones with perfect matches in the *Drosophila melanogaster* genome, which represent 13,299 unique Piwi-associated small RNAs. Of these, about 8.7% match known non-coding RNAs (Supplementary Fig. 1b). The remaining 12,903 small RNAs are Piwi-associated piRNAs, which show a gaussian distribution in size and have a peak at 24–26 nt (Fig. 1b). Of these, 55.2% contain U as the first 5′ nucleotide, a bias similar to that in mammalian piRNAs, whereas the second 5′ nucleotide shows a strong bias against U (Fig. 1c). A total of 10,792 piRNAs can be mapped to the assembled genome (Fig. 1d and Supplementary Figs 1c–4). Of these, 7,651 (59.3%) are mapped to transposons (9.7% of the assembled genome), especially LTR (long terminal repeat) and LINE (long interspersed nuclear element) types of retrotransposon (Fig. 1d). In contrast, Piwi-associated piRNAs are underrepresented in gene-coding sequences, intergenic regions, and simple or low-complexity repeats. Along chromosomes, Piwi-associated piRNAs are highly enriched in pericentromeric regions and subtelomeric regions, which contain a high density of transposons (Supplementary Figs 1c–4). These results are consistent with recent findings that Piwi subfamily proteins bind to transposon-derived piRNAs^{3–5,17} and echo the role of Piwi in the epigenetic regulation of transposons and tandem transgenes^{1–3,16}.

To investigate the potential function of Piwi and its interacting piRNAs in epigenetic regulation, we focused on the 20-nt 3R-TAS1 piRNA, which is uniquely mapped to 3R-TAS (Fig. 2a). We chose this piRNA for five reasons: first, TAS is genetically well characterized heterochromatin crucial for telomere function and genome integrity^{19,20}; second, TASs share structural similarity between eukaryotes, implicating their functional conservation²¹; third, 3R-TAS is composed of tandem repeats highly homologous to LTR regions of the *Invader4* retrotransposon (Supplementary Fig. 5), providing an opportunity to study the role of retrotransposon-originated piRNAs; fourth, 3R-TAS1 piRNA is uniquely mapped to 3R-TAS (Supplementary Fig. 5), which allows us to establish a one-to-one functional relationship between a specific piRNA and its genomic sequence; and last, we previously identified a P-element insertional mutation, *P{w⁺,ry⁺}A4-4*, inserted 128 base pairs (bp) downstream of the 3R-TAS1 piRNA coding sequence (Fig. 2a), as the strongest suppressor of *piwi* for its germline stem-cell phenotype²². One copy

¹Department of Cell Biology, Duke University Medical School, Durham, North Carolina 27710, USA. ²Yale Stem Cell Center and Department of Cell Biology, Yale University School of Medicine, New Haven, Connecticut 06509, USA.

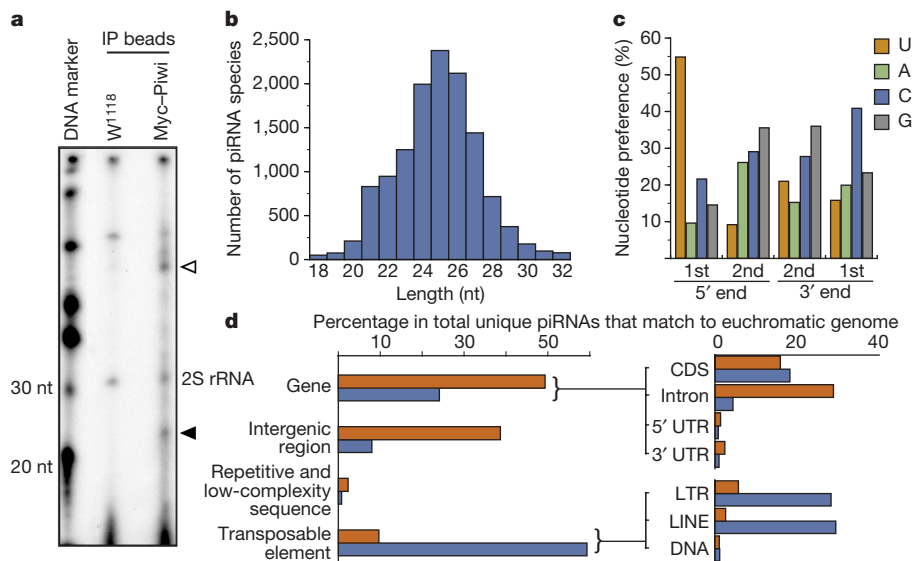


Figure 1 | Identification and characterization of Piwi-associated piRNAs. **a**, Small RNAs of 24–26 nt (arrow) and about 80 nt (open arrowhead) are specifically precipitated together with Myc-Piwi. IP, immunoprecipitation. **b**, Size distribution of Piwi-associated piRNAs. **c**, Nucleotide preference at 5'

and 3' ends of Piwi-associated piRNAs. **d**, Percentages of Piwi-associated piRNAs in various annotated genomic regions. Orange, expected number; blue, cloned number. CDS, protein coding sequence; UTR, untranslated region.

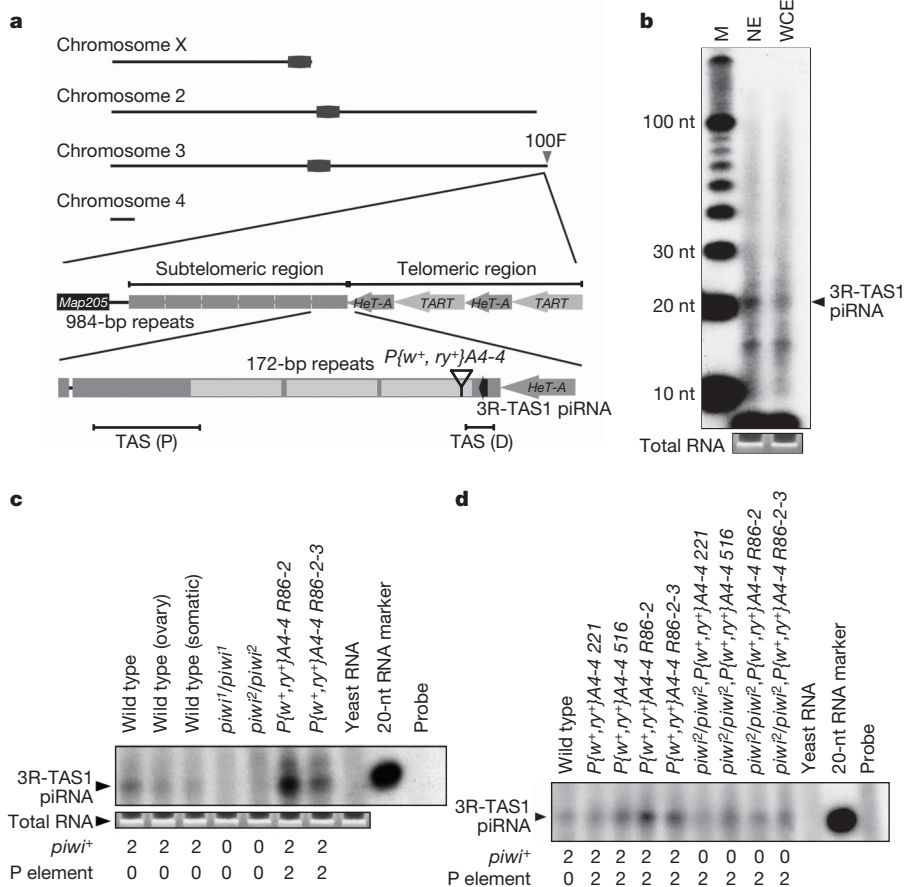


Figure 2 | The expression of 3R-TAS1 piRNA is Piwi-dependent and correlates with germline stem-cell maintenance. **a**, The organization of 3R-TAS. The black arrow indicates the position and direction of the unique mapped 3R-TAS1 piRNA. 100F is the polytene band name; this band contains the chromosome 3 right-arm TAS and telomere. **b**, RNase protection assay showing that the 3R-TAS1 piRNA can protect a 597-bp antisense probe that spans the piRNA coding region and covers 386–982 nt of the 984-bp repeat unit in the antisense direction. The 3R-TAS1 piRNA is relatively enriched in nuclear extracts (NE) over whole-cell extracts (WCE).

M, 10-bp DNA marker. **c**, RNase protection assay showing that 3R-TAS1 piRNA is expressed in the wild-type adult fly, in both ovarian and extra-ovarian cells. Its expression is markedly decreased in $piwi^1$ and $piwi^2$ mutants and is drastically increased by the $P\{w^+, ry^+\}A4-4$ insertion (four separately maintained lines, namely 221, 516, R86-2 and R86-2-3, were checked). All lanes were loaded with equal amounts of total RNA. The copy number of $piwi$ and $P\{w^+, ry^+\}A4-4$ is noted at the bottom for **c** and **d**. **d**, $P\{w^+, ry^+\}A4-4$ restores expression of the 3R-TAS1 piRNA in $piwi$ mutants. All lanes were loaded with equal amounts of total RNA.

of the $P\{w^+, ry^+\}A4-4$ allele restores germline stem cells in about 70% of the homozygous $piwi^2$ mutant females²². This suggests an important role for 3R-TAS in germline stem-cell maintenance that probably resides in niche cells where Piwi functions¹⁸.

We first used electrophoretic mobility-shift assays to confirm that Piwi binds directly to 3R-TAS1 piRNA (Supplementary Results and Supplementary Fig. 6). We then examined 3R-TAS1 piRNA expression, which was detected in wild-type cells in both the germline and soma and was enriched in nuclei, suggesting its nuclear function (Fig. 2b, c). However, it is not detectable in $piwi$ mutants, suggesting that Piwi is required for its transcription and/or its processing/stability.

To distinguish between these two possibilities, we first examined whether $P\{w^+, ry^+\}A4-4$ affects 3R-TAS1 piRNA expression. We reasoned that $P\{w^+, ry^+\}A4-4$, being a 20-kilobase (kb) euchromatic sequence inserted at the heterochromatic 3R-TAS1 piRNA locus, is more likely to affect the local chromatin state and transcription of 3R-TAS1 than its processing and/or stability. As expected, this piRNA is significantly overexpressed in $P\{w^+, ry^+\}A4-4$ flies (Fig. 2c, d). In precise excision revertants, its expression level is reduced to that in the wild type (Supplementary Fig. 7a), indicating that the P-element insertion is the cause of its overexpression. Moreover, $P\{w^+, ry^+\}A4-4$ rescues its expression in $piwi$ mutants (Fig. 2d). These observations favour a role for Piwi in regulating the transcription of its precursor. The function of Piwi in its processing or stability, if any, must be redundant and thus can be replaced by Ago3 and/or Aubergine in $piwi$ mutants.

$P\{w^+, ry^+\}A4-4$ rescues both 3R-TAS1 piRNA expression and germline stem-cell function in $piwi$ mutants, suggesting the involvement of the 3R-TAS1 piRNA and potentially other piRNAs from 3R-TAS for germline stem-cell maintenance. To assess the range of the $P\{w^+, ry^+\}A4-4$ effect in 3R-TAS, we examined the expression of two piRNAs closest to $P\{w^+, ry^+\}A4-4$ and 3R-TAS1 piRNA: the TAS2 piRNA on the centromeric side, only 54 bp from $P\{w^+, ry^+\}A4-4$, and the HeT-A1 piRNA mapped to the HeT-A retrotransposon on the telomeric side. Because neither piRNA is unique to 3R-TAS, our nuclease protection assays reflect the effects of $P\{w^+, ry^+\}A4-4$ on the total cellular levels of these piRNAs; only the total cellular level is functionally relevant. The TAS2 and HeT-A1 piRNAs are expressed at similar levels in the wild-type and $piwi$ mutant flies, either with or without $P\{w^+, ry^+\}A4-4$ (Supplementary Fig. 7b, c). This suggests that, even if $P\{w^+, ry^+\}A4-4$ has a *cis* effect on the transcription of these piRNAs from 3R-TAS, this effect is insignificant on their cellular levels and therefore should not have a functional impact. 3R-TAS1 piRNA therefore provides a unique opportunity to assess the *cis* effect of $P\{w^+, ry^+\}A4-4$ on 3R-TAS and its effect on germline stem-cell maintenance.

To further confirm the effect of P-element insertion on the expression of its nearby piRNA, we examined the expression of the 2R-42AB-B1 piRNA uniquely mapped to the 42AB region (piRNA cluster 17; Supplementary Table 1 and Supplementary Fig. 7d). Like that of 3R-TAS1 piRNA, the expression of the 2R-42AB-B1 piRNA is markedly decreased in $piwi$ mutants. However, a P-element insertion 170 bp downstream of the 2R-42AB-B1 piRNA-coding region

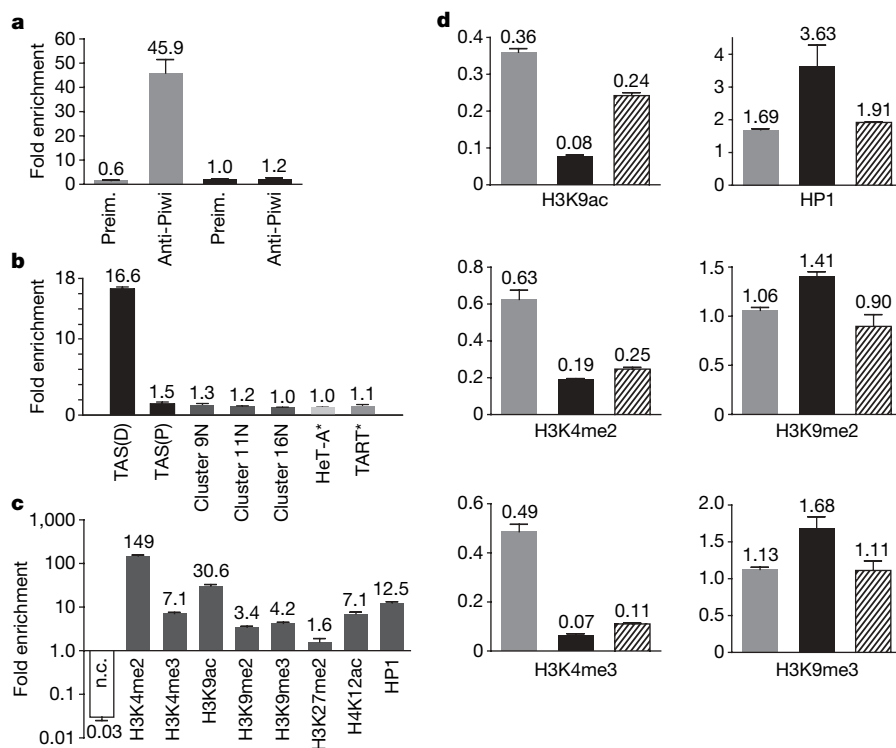


Figure 3 | Piwi protein is associated with 3R-TAS and is required for its euchromatic state. **a**, ChIP by anti-Piwi antibody or preimmune serum (preim.) in wild-type and $piwi$ mutant followed by quantitative PCR reveals that Piwi is strongly associated with the 73-bp TAS(D) region. The relative enrichment is calculated by normalizing the quantity of 3R-TAS genomic DNA against the quantity of *Rp49* genomic DNA. Grey columns, ry^{506} ; black columns, $piwi^2/piwi^2;ry^{506}$. **b**, ChIP by anti-Myc antibody in wild-type and $myc-piwi$ transgenic flies shows that Myc-Piwi is specifically associated with the TAS(D) region but not with three regions 2–10 kb near (N) the representative piRNA clusters (no. 9, no. 11 and no. 16), or non-telomeric HeT-A and TART homologous regions on chromosome 4, or even TAS(P). The relative enrichment is the ratio of the enrichment in $myc-piwi$ flies to

that in w^{1118} flies. **c**, ChIP reveals that TAS(D) has both euchromatic and heterochromatic histone modifications. Relative enrichment was calculated by normalizing the quantity of TAS(D) DNA co-precipitated by various antibodies against that of control without antibody. n.c., negative control, containing no DNA, for quantitative PCR. **d**, Association of modified histones H3K4me2, H3K4me3, H3K9ac, H3K9me2, H3K9me3 and HP1 with TAS(D) was assayed by ChIP and quantitative PCR. The relative enrichment of modified histones was calculated by normalizing the quantity of TAS(D) DNA against the quantity of *Actin5C*. Grey columns, ry^{506} ; black columns, $piwi^2/piwi^2;ry^{506}$; hatched columns, $piwi^2/piwi^2;ry^{506};P\{w^+, ry^+\}A4-4$. Each individual experiment was repeated at least three times. Error bars indicate s.d.

decreases rather than increases the expression of this piRNA. Thus, P-element insertions at different sites exert divergent effects on the expression of their nearby piRNAs.

We then investigated whether the positive role of Piwi in regulating 3R-TAS1 piRNA expression is due to its direct effect on the epigenetic state of 3R-TAS. We first examined whether Piwi directly localizes to 3R-TAS(D), a 73-bp region spanning the 3R-TAS1 piRNA-coding sequence (D here stands for distal; Fig. 2a), by Piwi-chromatin immunoprecipitation (ChIP). Piwi is associated with the TAS repeats at a level 46-fold that of the housekeeping gene *Rp49* (Fig. 3a). This specific association is further confirmed by Myc–Piwi ChIP with an anti-Myc antibody. Myc–Piwi is enriched in TAS(D) 16.6-fold over an intergenic region on chromosome 2 (Fig. 3b), and 11.4-fold and 11.5-fold over the *succinate dehydrogenase B* and *actin88F* genes, respectively (Supplementary Fig. 8). In contrast, Piwi is not associated with any of the five piRNA-poor genomic regions examined, or even with a proximal 3R-TAS sequence (TAS(P)) only 387bp away (Figs 2a and 3b, and Supplementary Fig. 8). Piwi is therefore strongly associated with TAS(D), which transcribes the 3R-TAS1 piRNA.

We then characterized the epigenetic states of 3R-TAS(D) by ChIP. In wild-type flies, 3R-TAS(D) is associated with both euchromatic modification markers (H3K4me2, H3K4me3 and H3K9ac, the last of these being a transcriptional marker) and heterochromatic modification markers (H3K9me2, H3K9me3, H4K12ac and HP1), suggesting that 3R-TAS(D) might be under dynamic equilibrium between euchromatic transcription and heterochromatic silencing (Fig. 3c). Although Piwi has a global function in heterochromatic silencing (Supplementary Results and Supplementary Fig. 9), it has the opposite effect on 3R-TAS(D). In *piwi* mutants, TAS(D)-associated H3K9ac, H3K4me2 and H3K4me3 levels are decreased 4.5-fold, 3.3-fold and 7.0-fold, respectively (Fig. 3c). In contrast, TAS(D)-associated HP1, H3K9me2 and H3K9me3 are enriched 2.2-fold, 1.3-fold and 1.5-fold, respectively. Similarly, in the 172-bp repeat region, levels of the three euchromatic markers were decreased more than in the 73-bp region, HP1 was enriched 10.3-fold, even though H3K9me2 and H3K9me3 levels were decreased by 31% and 41%, respectively (Supplementary Fig. 10). These histone modification profiles are consistent with our finding that 3R-TAS1 piRNA is expressed in the wild-type fly but not in *piwi* mutants, indicating that Piwi promotes the euchromatic feature of TAS(D) chromatin.

To further test the positive epigenetic role of Piwi towards TAS(D), we examined the histone modification profile of this region in

*piwi*²/*piwi*²; *P*{*w*⁺,*ry*⁺}*A4-4*/+ flies, in which 3R-TAS1 piRNA expression is restored. Indeed, we found that the euchromatic feature of TAS(D) is significantly restored (Fig. 3d). In comparison with the *piwi*² mutant, the TAS-associated H3K9ac in *piwi*²; *P*{*w*⁺,*ry*⁺}*A4-4* flies is increased 3.1-fold, reaching about 70% of the wild-type level. Correspondingly, TAS-associated HP1, H3K9me2 and H3K9me3 levels are decreased to those of the wild type. This significant restoring effect of *P*{*w*⁺,*ry*⁺}*A4-4* is unlikely to be due to other cryptic effects of *P*{*w*⁺,*ry*⁺}*A4-4* itself, because the same sequence inserted into other genomic sites does not suppress the *piwi* mutant phenotype²². Instead, it is likely that the insertion of *P*{*w*⁺,*ry*⁺}*A4-4*, as a 20-kb unique sequence, may affect heterochromatinization in 3R-TAS. *P*{*w*⁺,*ry*⁺}*A4-4* therefore rescues the germline stem-cell phenotype of the *piwi* mutant by restoring the euchromatic feature of 3R-TAS and the transcription of 3R-TAS1 piRNA.

The positive epigenetic role of Piwi in TAS(D) is also demonstrated by the expression of a reporter gene, *white*, in *P*{*w*⁺,*ry*⁺}*A4-4* insertion. This *white* gene exhibits a typical telomere position effect (Fig. 4), suggesting that TAS is under heterochromatic influence²³. Expectedly, loss of *piwi* function enhances telomere position effect in a dosage-sensitive manner, opposite to the known suppression effects of Polycomb group proteins (Fig. 4a)^{24,25}. In *P*{*w*⁺,*ry*⁺}*A4-4* stocks, the *white* gene was variably expressed in different ommatidia in *piwi*⁺/*piwi*⁺ flies, with an overall orange eye colour with spotty red ommatidia in the posterior region. In *piwi*⁺/*piwi*² flies, the eye colour becomes lighter. In *piwi*²/*piwi*² flies, the eye colour turns completely white in most ommatidia, leaving the posterior red ommatidia apparently unaffected by the *piwi* dosage. This indicates that *piwi* is required for the expression of *white* inserted in 3R-TAS. Eye pigment assay shows that *white* is expressed in *piwi*² homozygotes at a level 5.0–7.8-fold lower than in *piwi*² heterozygotes (Fig. 4b). Because *piwi* does not affect the expression level of the endogenous *white* gene on the X chromosome (Fig. 4b), *piwi* is probably required for the expression of the *white* reporter gene by promoting the active epigenetic state of 3R-TAS.

The above findings reveal the complexity of small RNA-mediated epigenetic regulation, namely that Piwi can exert opposite effects on different genomic regions. piRNAs may have a function in guiding Piwi to the target sites, yet the opposite effects of Piwi at different target sites might be mediated by the local chromatin context, which would render the selective binding of the Piwi–piRNA complex to different partners such as HP1a or JmJC domain-containing histone demethylases²⁶. The activating effect of Piwi, 3R-TAS1 piRNA

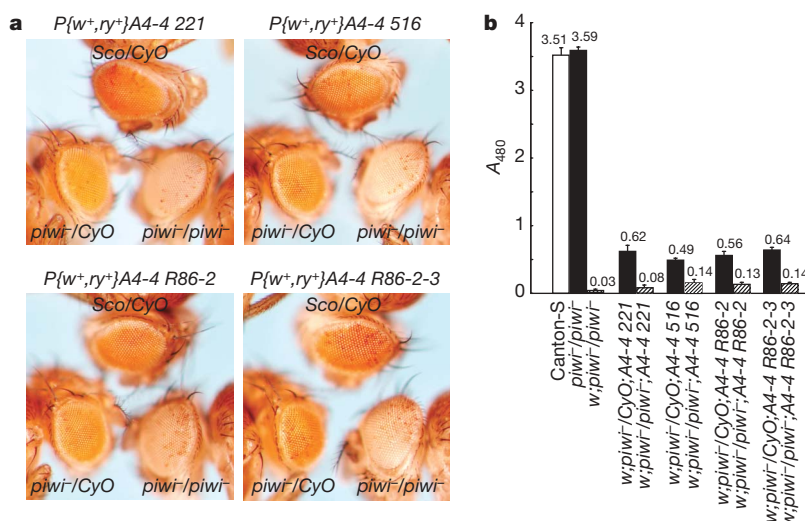


Figure 4 | *piwi* is an enhancer of telomere position effect. **a**, The eye colours of four independently maintained *w*¹¹¹⁸; *P*{*w*⁺,*ry*⁺}*A4-4* strains (211, 516, R86-2 and R86-2-3) in wild-type, heterozygous and homozygous *piwi*² backgrounds. **b**, Levels of eye pigmentation in Canton-S, *piwi*²/*piwi*²,

w; *piwi*²/*piwi*² and *w*¹¹¹⁸; *P*{*w*⁺,*ry*⁺}*A4-4* strains (211, 516, R86-2 and R86-2-3) in both heterozygous and homozygous *piwi*² backgrounds. Error bars indicate s.d.

and possibly other piRNAs in 3R-TAS can be explained by a heterochromatin/euchromatin counterbalance model in which the repetitive nature of 3R-TAS by default is a substrate for heterochromatinization. The heterochromatic state could be established and maintained by the Polycomb group proteins or an RNAi pathway mediated by Ago proteins, or yet another mechanism. However, the association of Piwi with 3R-TAS by means of the 3R-TAS1 piRNA or $P\{w^+, ry^+\}A4-4$ insertion as a roughly 20-kb unique sequence counteracts the heterochromatinization (Supplementary Discussion and Supplementary Fig. 11). Our finding that Piwi is required for the epigenetic activation of the subtelomeric region starts to reveal a mechanism underlying epigenetic regulation and stem-cell maintenance.

METHODS SUMMARY

piRNA cloning, mapping and annotation. Myc-Piwi ribonucleoprotein complexes were immunoprecipitated from adult ovarian tissues with monoclonal anti-Myc antibody (9E10). Total RNA was prepared by using TRIzol. Small RNAs were gel-purified, cloned and sequenced as described²⁷. Cloned small RNAs were mapped to the *D. melanogaster* genome assembly, version 5.1. Functional annotation was performed by in-house Perl scripts aiding BioPerl modules and Ensembl API.

RNase protection assay. PCR-amplified template DNAs were cloned into the pGEM-T vector (Promega). High-specific-activity probes were generated by *in vitro* transcription with the MaxiScript T7/Sp6 kit (Ambion) and [α -³²P]UTP. TRIzol-extracted RNA (20 µg) was hybridized overnight with 2×10^5 c.p.m. of radioactive probe at 42 °C. Unpaired RNA was digested by an RNaseA/RNaseT1 mixture.

Chromatin immunoprecipitation and quantitative PCR. Nuclei from adult flies were isolated and crosslinked with 0.1% formaldehyde. Chromatin was fragmented by sonication in RIPA buffer. Antibodies were incubated overnight with nuclear extracts at 4 °C. Bead-bound DNA was eluted, reverse-crosslinked and precipitated. Quantitative PCR was conducted on a Roche LightCycler 2.0 system with the LightCycler DNA Master SYBR Green I. Sequences of primers are provided in Methods. Normalized enrichment values were calculated with a standard formula.

Full Methods and any associated references are available in the online version of the paper at www.nature.com/nature.

Received 28 May; accepted 17 September 2007.

Published online 21 October 2007.

1. Pal-Bhadra, M., Bhadra, U. & Birchler, J. A. RNAi related mechanisms affect both transcriptional and posttranscriptional transgene silencing in *Drosophila*. *Mol. Cell* **9**, 315–327 (2002).
2. Pal-Bhadra, M. *et al.* Heterochromatic silencing and HP1 localization in *Drosophila* are dependent on the RNAi machinery. *Science* **303**, 669–672 (2004).
3. Vagin, V. V. *et al.* A distinct small RNA pathway silences selfish genetic elements in the germline. *Science* **313**, 320–324 (2006).
4. Saito, K. *et al.* Specific association of Piwi with rasiRNAs derived from retrotransposon and heterochromatic regions in the *Drosophila* genome. *Genes Dev.* **20**, 2214–2222 (2006).
5. Brennecke, J. *et al.* Discrete small RNA-generating loci as master regulators of transposon activity in *Drosophila*. *Cell* **128**, 1089–1103 (2007).
6. Wassenaar, M. The role of the RNAi machinery in heterochromatin formation. *Cell* **122**, 13–16 (2005).
7. Grewal, S. I. & Jia, S. Heterochromatin revisited. *Nature Rev. Genet.* **8**, 35–46 (2007).
8. Volpe, T. A. *et al.* Regulation of heterochromatic silencing and histone H3 lysine-9 methylation by RNAi. *Science* **297**, 1833–1837 (2002).

9. Noma, K. *et al.* RITS acts in cis to promote RNA interference-mediated transcriptional and post-transcriptional silencing. *Nature Genet.* **36**, 1174–1180 (2004).
10. Sugiyama, T., Cam, H., Verdel, A., Moazed, D. & Grewal, S. I. RNA-dependent RNA polymerase is an essential component of a self-enforcing loop coupling heterochromatin assembly to siRNA production. *Proc. Natl Acad. Sci. USA* **102**, 152–157 (2005).
11. Motamedi, M. R. *et al.* Two RNAi complexes, RITS and RDRC, physically interact and localize to noncoding centromeric RNAs. *Cell* **119**, 789–802 (2004).
12. Verdel, A. *et al.* RNAi-mediated targeting of heterochromatin by the RITS complex. *Science* **303**, 672–676 (2004).
13. Cox, D. N. *et al.* A novel class of evolutionarily conserved genes defined by piwi are essential for stem cell self-renewal. *Genes Dev.* **12**, 3715–3727 (1998).
14. Kalmykova, A. I., Klenov, M. S. & Gvozdev, V. A. Argonaute protein PIWI controls mobilization of retrotransposons in the *Drosophila* male germline. *Nucleic Acids Res.* **33**, 2052–2059 (2005).
15. Grimaud, C. *et al.* RNAi components are required for nuclear clustering of Polycomb group response elements. *Cell* **124**, 957–971 (2006).
16. Pelisson, A., Sarot, E., Payen-Groschene, G. & Bucheton, A. A novel repeat-associated small interfering RNA-mediated silencing pathway downregulates sense *gypsy* transcripts in the somatic cells of the *Drosophila* ovary. *J. Virol.* **81**, 1951–1960 (2006).
17. Gunawardane, L. S. *et al.* A slicer-mediated mechanism for repeat-associated siRNA 5' end formation in *Drosophila*. *Science* **315**, 1587–1590 (2007).
18. Cox, D. N., Chao, A. & Lin, H. *piwi* encodes a nucleoplasmic factor whose activity modulates the number and division rate of germline stem cells. *Development* **127**, 503–514 (2000).
19. Mason, J. M., Ransom, J. & Konev, A. Y. A deficiency screen for dominant suppressors of telomeric silencing in *Drosophila*. *Genetics* **168**, 1353–1370 (2004).
20. Biessmann, H. *et al.* Two distinct domains in *Drosophila melanogaster* telomeres. *Genetics* **171**, 1767–1777 (2005).
21. Pryde, F. E., Gorham, H. C. & Louis, E. J. Chromosome ends: all the same under their caps. *Curr. Opin. Genet. Dev.* **7**, 822–828 (1997).
22. Smulders-Srinivasan, T. K. & Lin, H. Screens for *piwi* suppressors in *Drosophila* identify dosage-dependent regulators of germline stem cell division. *Genetics* **165**, 1971–1991 (2003).
23. Hazelrigg, T., Levis, R. & Rubin, G. M. Transformation of white locus DNA in *Drosophila*: dosage compensation, zeste interaction, and position effects. *Cell* **36**, 469–481 (1984).
24. Boivin, A., Gally, C., Netter, S., Anxolabehere, D. & Ronsseray, S. Telomeric associated sequences of *Drosophila* recruit polycomb-group proteins *in vivo* and can induce pairing-sensitive repression. *Genetics* **164**, 195–208 (2003).
25. Cryderman, D. E., Morris, E. J., Biessmann, H., Elgin, S. C. & Wallrath, L. L. Silencing at *Drosophila* telomeres: nuclear organization and chromatin structure play critical roles. *EMBO J.* **18**, 3724–3735 (1999).
26. Zofall, M. & Grewal, S. I. Swi6/HP1 Recruits a JmjC domain protein to facilitate transcription of heterochromatic repeats. *Mol. Cell* **22**, 681–692 (2006).
27. Ambros, V. & Lee, R. C. Identification of microRNAs and other tiny noncoding RNAs by cDNA cloning. *Methods Mol. Biol.* **265**, 131–158 (2004).

Supplementary Information is linked to the online version of the paper at www.nature.com/nature.

Acknowledgements We thank L. Rusche for discussions and help with quantitative PCR; S. Sweeney for RNase protection assays for TAS2 piRNA, HeT-A1 piRNA and 2R-42AB-B1 piRNA; R. Levis for $w^{1118}; P\{w^+, ry^+\}A4-4$ stocks; and S. Elgin, T. Hsieh, E. Beyret, H. Megosh, S. Findley, M. Nolde and V. Ganguraju for comments on the manuscript. This study was supported by the NIH and the Mathers Foundation.

Author Contributions H.Y. contributed to project design, all experimental work, data analysis and manuscript preparation. H.L. contributed to project design, data analysis and manuscript preparation.

Author Information The Piwi-associated piRNA sequences have been deposited in the NCBI Gene Expression Omnibus with the accession number GSE9138. Reprints and permissions information is available at www.nature.com/reprints. Correspondence and requests for materials should be addressed to H.L. (haifan.lin@yale.edu).

METHODS

Drosophila stocks and cultures. All fly stocks were maintained at 20 °C. For the immunoprecipitation assay, a Myc–Piwi transgenic strain (G38-1A) and w^{1118} flies were used. For the RNase protection assay, w^{1118} , $w^{1118};piwi^1/piwi^1$, $w^{1118};piwi^2/piwi^2$, $w^{1118};P\{w^+,ry^+\}A4-4,ry^{506}(221|516|R86-2|R86-2\#3)$ and $w^{1118};piwi^2/piwi^2;P\{w^+,ry^+\}A4-4,ry^{506}(221|516|R86-2|R86-2\#3)$ flies were used. For the ChIP assay, $w^{1118};ry^{506}$, $w^{1118};piwi^2/piwi^2;ry^{506}$, $w^{1118};piwi^2/piwi^2;P\{w^+,ry^+\}A4-4(221),ry^{506}/+,ry^{506}$ and G38-1A flies were used. For global analysis of histone PTMs, w^{1118} and $w^{1118};piwi^2/piwi^2$ flies were used. For the telomere position effect assay and the fly eye pigmentation assay, Canton-S, $piwi^2/piwi^2$, $w^{1118};piwi^2/piwi^2$, $w^{1118};Sco/CyO;P\{w^+,ry^+\}A4-4,ry^{506}(221|516|R86-2|R86-2\#3)$, $w^{1118};piwi^2/CyO;P\{w^+,ry^+\}A4-4,ry^{506}(221|516|R86-2|R86-2\#3)$ and $w^{1118};piwi^2/piwi^2;P\{w^+,ry^+\}A4-4,ry^{506}(221|516|R86-2|R86-2\#3)$ flies were used.

Immunoprecipitation assay and cloning of piRNAs. Adult ovaries (100 pairs) were homogenized in an equal volume of ovary lysis buffer (20 mM HEPES pH 7.5, 100 mM KCl, 5 mM MgCl₂, 0.1% SDS, 0.1% sodium deoxycholate, 1% Triton X-100, 1 mM dithiothreitol, 0.2 mM phenylmethylsulphonyl fluoride, 1 × Complete Mini, EDTA free Proteinase Inhibitor cocktail (Roche), 0.5 unit μl^{-1} RNAaseOUT (Invitrogen), 5% glycerol). Anti-Myc monoclonal antibody (9E10; Developmental Studies Hybridoma Bank at the University of Iowa) was added at 1:10 dilution to the precleared ovary lysate and incubated for 2 h at 4 °C. Protein G–Sepharose 4B beads were added and incubated for a further 1 h at 4 °C. Bead-bound RNAs were extracted with TRIzol (Invitrogen) and precipitated in the presence of 50 $\mu\text{g ml}^{-1}$ GlycoBlue (Ambion). The co-precipitated RNA was 5' labelled with [γ -³²P]ATP by T4 polynucleotide kinase (NEB), purified on a Sephadex G-25 fine RNA spin column (Roche) and separated by 15% denaturing PAGE for detection. A PCR-amplified small RNA library (1 μg) was directly sequenced with a large-scale pyrosequencing method (454 Life Sciences).

Genome mapping and annotation of cloned small RNAs. Cloned small RNAs were mapped to both the *D. melanogaster* genome assembly, version 5.1, and annotated sequence databases to infer the likely genome origins. The mapping was performed with a standalone NCBI BLAST program (<http://www.ncbi.nlm.nih.gov/BLAST/download.shtml>), with sensitive parameters to identify perfect matches of short query sequences (no mismatch, insertion or deletion is allowed). In-house Perl scripts aiding BioPerl modules (<http://www.bioperl.org>) and Ensembl API (http://www.ensembl.org/info/software/core/core_tutorial.html) were used to automate the mapping, annotation and analysis procedure. A home-made non-coding RNA database was built by combining the available databases with batch-fetched entries with appropriate feature keys from Ensembl. The sequences and annotations of transposons and repetitive sequences in *Drosophila melanogaster* genome assembly, version 5.1, were identified by a standalone RepeatMasker program with a sensitive filter (<http://www.repeatmasker.org>).

A piRNA was annotated to a specific type of genomic sequence only if the sequence covered the full length of the piRNA. A piRNA cluster was defined as a genomic region containing more than 100 piRNA mapped sequences and not having any piRNA mapped sequence in the upstream 5-kb region or the downstream 5-kb region. The borders of a piRNA cluster were defined by the first nucleotide of the farthest upstream piRNA and the last nucleotide of the farthest downstream piRNA.

Chromatin immunoprecipitation and quantitative PCR. Nuclear extract was incubated at 4 °C for 2 h separately with the following antibodies: anti-Piwi (generated in the Lin laboratory against Piwi C-terminal peptide), 1:100 dilution; preimmune of anti-Piwi, 1:10 dilution; anti-Myc monoclonal antibody (9E10; Developmental Studies Hybridoma Bank, University of Iowa), 1:10 dilution; anti-dimethyl-histone3 K4 (Upstate), 1:100 dilution; anti-trimethyl-histone3 K4 (Upstate), 1:100 dilution; anti-dimethyl-histone3 K9 (Upstate), 1:50 dilution; anti-trimethyl-histone3 K9 (Upstate), 1:50 dilution; anti-acetyl-histone3 K9 (Upstate), 1:100 dilution; anti-acetyl-histone4 K12 (Upstate), 1:100

dilution; anti-dimethyl-histone3 K27 (Upstate), 1:50; and anti-HP1 (Covance), 1:50 dilution. Salmon-sperm DNA (50 μl)/Protein A/G-agarose beads (Upstate) was added and samples were incubated at 4 °C for 1 h. After washing, cross-linking was reversed at 65 °C overnight. DNA was purified from the beads by phenol/chloroform extraction and ethanol precipitation.

The following primer sets were used for quantitative PCR: for the TAS(D) region, 5'-gtgtctcatcattcttattcag-3' (forward) and 5'-tggtcgtgtgatcgttacttg-3' (reverse); for a 169-bp fragment of the 172-bp repeat region, 5'-gatcttcttaccattcttcttcaac-3' (forward) and 5'-cggcagaggcagcaaac-3' (reverse); for a 345-bp region in the proximal end of the 3R-TAS repeat, 5'-caaccaatcgacctt-3' (forward) and 5'-gtgacgattaatacgaacttacaac-3' (reverse); for an 81-bp region about 2 kb upstream of the piRNA cluster no. 9, 5'-aatgacgagcagcagcgcaa-3' (forward) and 5'-cctcaatgttagatgtgagtgactt-3' (reverse); for an 86-bp region about 8 kb downstream of the piRNA cluster no. 11, 5'-gctcaagagtcctccagacaggtt-3' (forward) and 5'-gcagtgatggtggtgaggtt-3' (reverse); for a 128-bp region about 10 kb downstream of the piRNA cluster no. 16, 5'-agggttatgctaggttcttattgctgc-3' (forward) and 5'-ggaacgaataaacaatgggtgcaaca-3' (reverse); for a 164-bp non-telomeric HeT-A homologous region on chromosome 4, 5'-agtcgatgttaattccattccg-3' (forward) and 5'-tgggttactgttccattgtgc-3' (reverse); for 129-bp non-telomeric TART homologous region on chromosome 4, 5'-tcaacatacgcagacgacct-3' (forward) and 5'-agcattactgagataccaccatt-3' (reverse); for a 97-bp region in the *Rp49* gene, 5'-tcgagtgtaactgcgttagtccgt-3' (forward) and 5'-gccatttggcgaaactttcacagga-3' (reverse); for a 224-bp intergenic region [2R:11,327,115..11,327,338], 5'-ttgggagcagggaaggatg-3' (forward) and 5'-aaggaggagaatggaaggagatggtat-3' (reverse); for a 165-bp region in the *Succinate Dehydrogenase B* gene (*SDHB*), 5'-ccaggaaccaggtgagtgagtg-3' (forward) and 5'-gcgtgcttatctgtggcgtttatc-3' (reverse); for a 187-bp region in the *Actin88F* gene, 5'-aagctctcaaggcagcaaccg-3' (forward) and 5'-aatggccatgaaggatgagcacc-3' (reverse); for 334-bp region in the *Actin5C* gene, 5'-tgcccagcggacaggtgat-3' (forward) and 5'-tggaaggtggacagcgaagc-3' (reverse). Using a standard formula, the quantities of target genomic regions precipitated by different antibodies were normalized against those of *Rp49*, the 2R intergenic region, *Actin5C*, *SDHB* and *Actin88F*. This ratio was further normalized against those from input DNA (without ChIP). The relative quantities of the TAS(D) region precipitated by different antibodies in Fig. 3c were normalized against the quantity of TAS(D) region precipitated by naked beads without any antibody. The difference in amplification efficiency between the various primer sets was determined by standard curves and was taken into account in the normalization calculation. The average values and standard deviations of the relative enrichments were used to compare the association of Piwi in different genomic regions and the histone modification profiles of the TAS region in different genotypes.

Drosophila eye pigmentation assay. Fifty 5–8-day-old fly heads were homogenized in 400 μl of acidified methanol (0.1% HCl in methanol) and vortex-mixed for 30 min at room temperature. After centrifugation for 5 min, 20 μl of 0.5% H₂O₂ was added to the supernatant. After centrifugation for 10 min, the absorbance at 480 nm was measured. Samples for each genotype were repeated three times. The average absorbance and standard deviations were used to quantify eye colours.

Electrophoretic mobility-shift assay. Piwi full-length complementary DNA with a 5' Myc tag sequence was cloned into the pBlueScript KS vector (Stratagene). Myc–Piwi protein was translated *in vitro* with a TNT T7 Coupled Wheat Germ Extract System (Promega) and standard procedures. Mock *in vitro* translation was performed without pBS-KS:myc–piwi DNA template. Increasing amounts of concentrated Myc–Piwi and mock *in vitro* translation reactions were incubated at room temperature for 30 min with 5 fmol (about 10⁴ c.p.m.) of 5' end-labelled 3R-TAS1 piRNA probe or 3R-TAS1 piRNA probe with the 5' U replaced with C, in the presence or absence of different amounts of unlabelled RNA oligonucleotides (10 and 50 fmol). The binding was done in 1 × binding buffer (20 mM HEPES pH 7.5, 150 mM NaCl, 2 mM MgCl₂, 1 mM dithiothreitol, 10% glycerol, 15 nM yeast tRNA).

JHDM1B/FBXL10 is a nucleolar protein that represses transcription of ribosomal RNA genes

David Frescas¹, Daniele Guardavaccaro¹, Florian Bassermann¹, Ryo Koyama-Nasu¹ & Michele Pagano¹

JHDM1B is an evolutionarily conserved and ubiquitously expressed member of the JHDM (JmjC-domain-containing histone demethylase) family^{1–3}. Because it contains an F-box motif, this protein is also known as FBXL10 (ref. 4). With the use of a genome-wide RNAi screen, the JHDM1B worm orthologue (T26A5.5) was identified as a gene that regulates growth⁵. In the mouse, four independent screens have identified JHDM1B as a putative tumour suppressor by retroviral insertion analysis^{6–9}. Here we identify human JHDM1B as a nucleolar protein and show that JHDM1B preferentially binds the transcribed region of ribosomal DNA to repress the transcription of ribosomal RNA genes. We also show that repression of ribosomal RNA genes by JHDM1B is dependent on its JmjC domain, which is necessary for the specific demethylation of trimethylated lysine 4 on histone H3 in the nucleolus. In agreement with the notion that ribosomal RNA synthesis and cell growth are coupled processes, we show a JmjC-domain-dependent negative effect of JHDM1B on cell size and cell proliferation. Because aberrant ribosome biogenesis and the disruption of epigenetic control mechanisms contribute to cellular transformation, these results, together with the low levels of JHDM1B expression found in aggressive brain tumours, suggest a role for JHDM1B in cancer development.

To begin assessing the biological function of JHDM1B, we investigated its cellular localization by using indirect immunofluorescence analysis. The results presented in Fig. 1a and Supplementary Fig. 1a show the localization of endogenous JHDM1B to the nucleolus of human cell lines (HeLa and T98G) and non-immortalized, non-transformed fibroblasts (IMR90). The nucleolar localization was confirmed by simultaneous staining with the nucleolar protein nucleophosmin/B23. Knockdown of JHDM1B by short interfering RNA (siRNA) eliminated this nucleolar signal, demonstrating the specificity of the immunostaining (Fig. 1a). JHDM1B has a putative and evolutionarily conserved nucleolar localization signal (NoLS) (Supplementary Fig. 1b). Comparison between wild-type JHDM1B and a mutant lacking the NoLS (JHDM1B(NoLS)) revealed the requirement of this basic amino-acid motif in the targeting of JHDM1B to the nucleolus (Fig. 1b). Disruption of other domains by point mutation or deletion failed to disrupt the localization of JHDM1B to the nucleolar compartment (Supplementary Fig. 2). Last, green fluorescent protein (GFP)-tagged JHDM1B localized to the nucleolus of living HeLa cells (Supplementary Fig. 3). Taken together, these data show that JHDM1B is a nucleolar protein, and its subcellular localization is dependent on the presence of a NoLS motif.

The nucleolar localization of JHDM1B, together with the presence of a CXXC zinc-finger DNA-binding domain, suggested that this protein might bind ribosomal DNA. During mitosis, rDNA-binding proteins, such as RNA polymerase I (pol I) and the pol I transcription factor UBF (upstream binding factor), remain associated with

chromosomes and display discrete foci at nucleolar organizing regions (NORs)¹⁰, which mark transcriptionally competent nucleation points for nucleoli from the previous interphase. JHDM1B localized together with UBF at NORs in mitotic cells (Supplementary Figs 4 and 5). Moreover, JHDM1B continued to localize to the nucleolar compartment after pretreatment with Triton X-100 (Supplementary Fig. 6), similar to UBF¹¹, suggesting stable association with rDNA.

To confirm the binding of JHDM1B to rDNA and to obtain a high-resolution map for this binding, we performed chromatin immunoprecipitation (ChIP) assays followed by quantitative real-time polymerase chain reaction (PCR) using primer pair sets that span the entire human rDNA repeat¹². Mapping of JHDM1B binding throughout the rDNA locus showed that JHDM1B bound mainly to the transcribed region of rDNA, with particular enrichment at 8 kilobases (kb) (Fig. 1c–e). The specificity of the binding to rDNA was confirmed by the lack of JHDM1B enrichment on the *glyceraldehyde-3-phosphate dehydrogenase* (GAPDH) promoter and by the fact that a DNA-binding mutant, JHDM1B(CXXC), failed to bind to the 8-kb region (Fig. 1e, f). CXXC zinc-finger domains specifically recognize and bind unmethylated CpG-rich regions¹³. This binding was confirmed *in vitro* for JHDM1B¹⁴. CpG-island prediction by the bioinformatics program cpGplot (<http://www.ebi.ac.uk/emboss/cpgplot>) and previously reported biochemical studies¹⁵ show enrichment of CpG-rich regions in rDNA over the transcribed region of rDNA (Supplementary Fig. 7), where JHDM1B binds. Thus, JHDM1B binds across the transcriptionally competent region of the rDNA repeat, with particular affinity for regions containing elevated CpG frequency.

To determine whether JHDM1B has a function in regulating rDNA transcription *in vivo*, we measured the levels of the 45S pre-ribosomal RNA by quantitative reverse transcriptase-mediated PCR (qRT-PCR). Silencing of JHDM1B by siRNA resulted in a significant increase in the expression of pre-rRNA compared with control siRNA (Fig. 2a), suggesting that JHDM1B is a repressor of rDNA transcription. Accordingly, we observed that cells expressing exogenous JHDM1B displayed a marked decrease in pre-rRNA synthesis compared with mock-transfected cells (Fig. 2b).

To investigate the domains required for JHDM1B-mediated repression of rRNA *in vivo*, we measured pre-rRNA levels in cells expressing JHDM1B mutants. Loss of the PHD finger or the F-box domain resulted in continued repression by JHDM1B, whereas loss of the NoLS or the CXXC zinc-finger blocked this transcriptional repression (Fig. 2b). We also found that the JmjC histone demethylase domain was required for the transcriptional repression of rDNA by JHDM1B (Fig. 2b). Moreover, a significant portion of cells expressing JHDM1B also failed to incorporate BrUTP within the nucleolus in a JmjC-domain-dependent manner (Fig. 2c). Taken together, these data show that JHDM1B represses rDNA transcription. This

¹Department of Pathology, NYU Cancer Institute, New York University School of Medicine, 550 First Avenue, New York, New York 10016, USA.

repression requires the NoLS motif (to allow nucleolar localization) and the CXXC zinc-finger domain (to bind DNA). In addition, the repressive activity of JHDM1B required its JmjC domain.

To investigate the requirement for the JmjC domain, we addressed previous studies showing that JHDM1A demethylates dimethylated lysine 36 on histone 3 (H3K36me₂) by means of this motif¹. We conducted an immunofluorescence analysis in HeLa cells transfected with constructs encoding JHDM1A or JHDM1B by using an antibody against H3K36me₂, and we found that forced expression of JHDM1A significantly decreased the levels of H3K36me₂, as reported previously¹, whereas JHDM1B had no effect (Supplementary Fig. 8). JHDM1B was also unable to produce any significant changes in the methylation status of H3K36me₃, H3K9me₃, H3K27me₃ or H3K4me₂ (Supplementary Fig. 9). In contrast, JHDM1B overexpression resulted in a significant decrease in H3K4me₃ levels, and this decrease required the presence of the JmjC domain (Fig. 3a, b). The specific reduction of H3K4me₃ levels by JHDM1B was confirmed by immunoblotting (Fig. 3c, d). Last, incubation of core histones with immunopurified JHDM1B confirmed *in vitro* the ability of JHDM1B

to demethylate H3K4me₃ (Supplementary Fig. 10). Taken together, these results demonstrate that JHDM1B is a histone demethylase that catalyses the demethylation of H3K4me₃. This finding is significant because active rRNA genes are reported to display active, euchromatic features that include H3K4me₃ (refs 16, 17).

Because the decrease in global H3K4me₃ levels was probably due to leakage of exogenous JHDM1B into the nucleoplasm, we investigated whether local changes in H3K4 trimethylation levels occur on rDNA by using an anti-H3K4me₃ antibody in ChIP analysis. Downregulation of JHDM1B resulted in an increase in H3K4me₃ on rDNA, particularly in the promoter region (42.9 kb) (Fig. 3e). Accordingly, we found a significant decrease in the levels of H3K4me₃ at the rDNA locus in cells ectopically expressing JHDM1B (Fig. 3f).

Interestingly, ectopic expression of JHDM1B decreased the occupancy of UBF at rDNA regions previously reported to be enriched for the protein¹² (Fig. 3g). Similarly, JHDM1B expression decreased the amount of chromatin-bound UBF in a JmjC-dependent manner, whereas depletion of JHDM1B increased the binding of UBF to chromatin (Supplementary Figs 11 and 12).

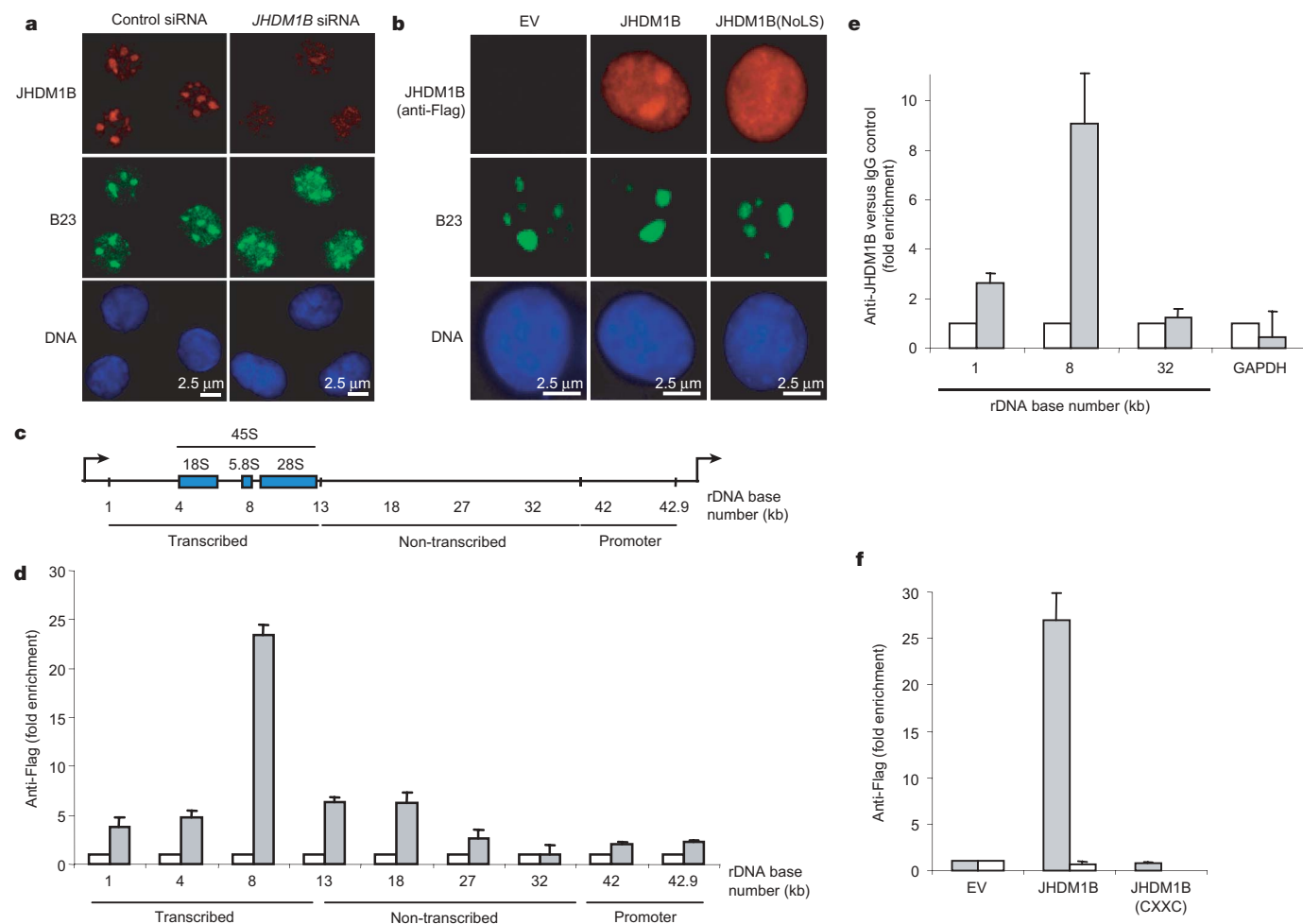


Figure 1 | JHDM1B localizes to the nucleolus and associates with rDNA.

a, Indirect immunofluorescence analysis of endogenous JHDM1B in HeLa cells treated with control siRNA oligonucleotides or oligonucleotides targeting *JHDM1B* mRNA. Cells were stained with antibodies against JHDM1B and nucleophosmin/B23 and DAPI (to visualize DNA), as indicated. **b**, Indirect immunofluorescence analysis of HeLa cells transfected with an empty vector (EV) or constructs encoding Flag-tagged JHDM1B or JHDM1B(NoLS), as indicated. Cells were stained with an anti-Flag antibody, an antibody against B23 and DAPI. **c**, Schematic representation of a single human rDNA repeat. **d**, JHDM1B binds across the transcriptionally competent region of rDNA. Enrichment of rDNA obtained with anti-Flag antibody as determined by ChIP analysis using chromatin prepared from

HeLa cells transfected with Flag-EV (open columns) or a construct encoding Flag-tagged JHDM1B (filled columns). DNA binding was quantified by real-time PCR with primer sets at indicated regions along the rDNA. The value given for the amount of PCR product present in EV-transfected cells was set at 1. **e**, Analysis of endogenous JHDM1B enrichment on rDNA and the *GAPDH* promoter by ChIP from chromatin of HeLa cells. JHDM1B enrichment (filled columns) was quantified by real-time PCR with the indicated primer sets. The value given for the amount of PCR product present from ChIP with control IgG (anti-haemagglutinin; open columns) was set as 1. **f**, ChIP experiment for enrichment of rDNA at 8 kb (filled columns) and the *GAPDH* promoter (open columns) was performed as in **d**. All error bars represent s.d. ($n = 3$).

Because the synthesis of rRNAs and cell growth are coupled processes¹⁸, we investigated whether JHDM1B affected cell size and cell proliferation. Forward scatter analysis showed that HeLa cells exogenously expressing JHDM1B were significantly smaller than control or JHDM1B(JmjC)-expressing cells (Fig. 4a). This effect also required the NoLS and the CXXC zinc-finger domains but not the PHD domain (Supplementary Fig. 13). Cells expressing JHDM1B also incorporated about 40% less bromodeoxyuridine (BrdU) than control cells, reflecting a smaller population of cells in S phase (Fig. 4b). Conversely, cells in which JHDM1B was silenced were significantly larger than control cells and showed a 1.67-fold increase in BrdU incorporation (Fig. 4c,d). Accordingly, JHDM1B-depleted cells proliferated at a faster rate than control HeLa cells (Fig. 4e). Taken together, these data suggest that JHDM1B-mediated modulation of rRNA gene expression influences cell growth and proliferation. Interestingly, under conditions in which rRNA production has been shown to decrease, such as during serum deprivation¹⁹, the

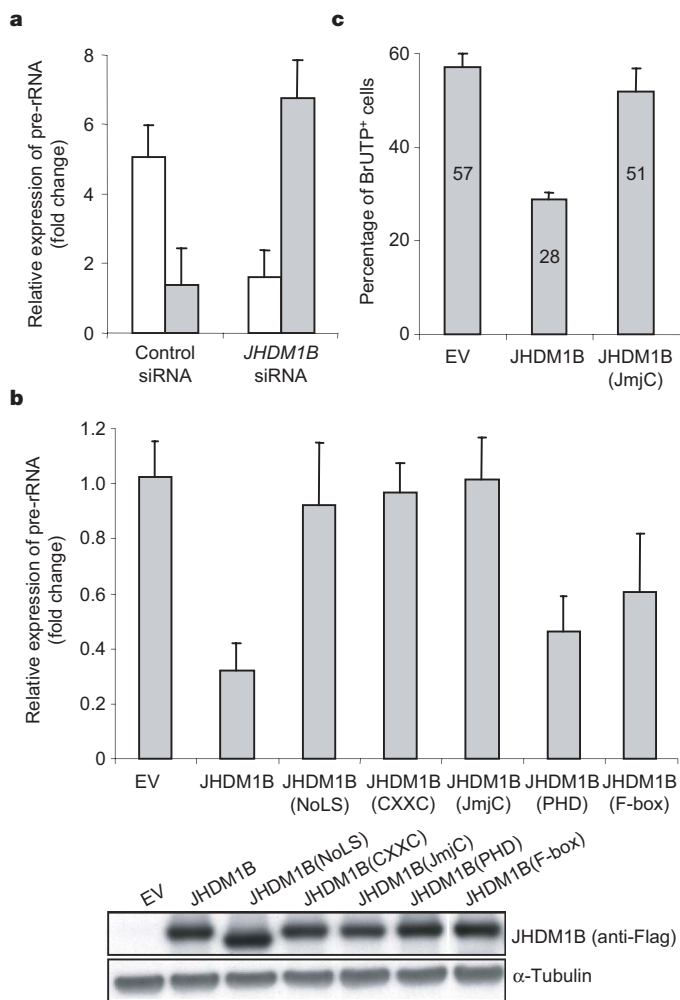


Figure 2 | JHDM1B represses transcription of rRNA genes via the JmjC domain. **a**, qRT-PCR analysis of pre-rRNA (filled columns) and JHDM1B mRNA (open columns) from HeLa cells transfected with siRNA targeting JHDM1B compared with control. The value given for the amount of pre-rRNA PCR product present in control cells was set as 1. The value given for the amount of JHDM1B PCR product present in control cells was set at 5. **b**, Top: qRT-PCR analysis of pre-rRNA in HeLa cells retrovirally infected with an empty vector (EV) or constructs encoding wild-type JHDM1B or the indicated mutants. The value given for the amount of pre-rRNA present in empty vector (EV) transfected cells was set as 1. Bottom: expression of JHDM1B proteins, as analysed by immunoblotting (α -tubulin was used as a loading control). **c**, Graphical representation of BrUTP incorporation in the nucleolus of HeLa cells transfected with EV or constructs encoding JHDM1B or JHDM1B(JmjC). All error bars represent s.d. ($n = 3$).

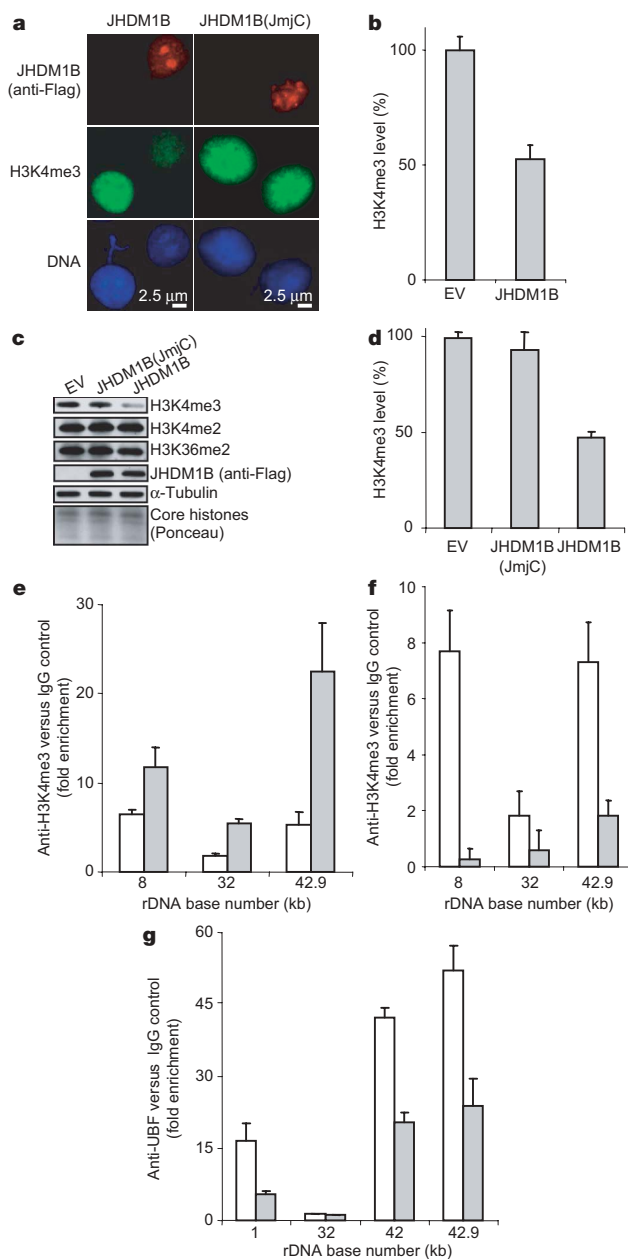


Figure 3 | JHDM1B demethylates H3K4me3 on the rDNA locus. **a**, Indirect immunofluorescence analysis of H3K4me3 levels in HeLa cells transfected with vectors encoding JHDM1B or JHDM1B(JmjC). Cells were stained with antibodies against Flag and H3K4me3, and with DAPI, as indicated. **b**, Quantification of three experiments performed as in **a**. The value given for H3K4me3 present in EV-transfected cells was set at 100%. Error bars represent s.d. ($n = 3$). **c**, Levels of methylated histone H3 in HeLa cells infected with an empty retrovirus (EV) or with retroviruses encoding JHDM1B or JHDM1B(JmjC) and analysed by immunoblotting with antibodies against the indicated proteins. The bottom panel shows core histones stained with Ponceau red. **d**, Densitometric quantification of three experiments performed as in **c**. The value given for H3K4me3 present in EV-transfected cells was set at 100%. Error bars represent s.d. ($n = 3$). **e**, HeLa cells were transfected with control siRNA (open columns) or JHDM1B siRNA (filled columns) oligonucleotides, and ChIPs were performed as in Fig. 1e. **f**, Analysis of H3K4me3 enrichment on rDNA, quantified as in **e**, using chromatin from 293T cells transfected with Flag-EV (open columns) or a construct encoding Flag-JHDM1B (filled columns). **g**, JHDM1B expression induces the dissociation of UBF from rDNA. Analysis of UBF enrichment on rDNA, quantified as in **e**, using chromatin from HeLa cells transfected with empty vector (open columns) or a construct encoding Flag-JHDM1B (filled columns). Error bars in **e-g** represent s.d. ($n = 3$).

amount of chromatin-bound JHDM1B increased, whereas serum re-addition transiently abolished this binding (Supplementary Fig. 14), suggesting that the binding of JHDM1B to rDNA is regulated by mitogens.

Actively proliferating cells transcribe high levels of rDNA and often show an increase in nucleolar number¹⁸. Whereas about 60% of HeLa cells possessed five or six nucleoli, cells ectopically expressing JHDM1B had a substantial nucleolar contraction, with most JHDM1B-positive cells possessing three or fewer nucleoli per cell (Fig. 4f). Consistent with the inability of JHDM1B(JmjC) and JHDM1B(NoLS) to repress rRNA expression was the observation that these mutants were unable to induce nucleolar contraction

(Fig. 4f). Knockdown of JHDM1B resulted in the generation of nuclei with disorganized nucleoli; the number of nucleoli in *JHDM1B* siRNA-treated cells exceeded seven per nucleus (Figs 1a and 4g, and Supplementary Fig. 15).

A recent study has established a NOR-based index as a marker for grading and staging astrocytic lesions of the brain²⁰. The number of NORs was found to rise in parallel with the grade, stage and proliferative state of the tumour. To investigate a potential involvement of JHDM1B in human cancer, we searched the Oncomine and the NIH-GEO online databases for differential *JHDM1B* expression in normal versus tumorigenic tissues^{21,22}. Expression of *JHDM1B*, but not that of *JHDM1A*, was significantly decreased in the most common and the most aggressive of the primary brain tumours, glioblastoma multiform (GBM), relative to normal brain tissue (Fig. 4h and Supplementary Fig. 16). This decrease in *JHDM1B* expression was correlated with brain tumour type and tumour grade (Fig. 4i). Taken together, these results suggest that the decreased expression of *JHDM1B* might contribute to the increased cell growth/proliferation and the number of NORs in GBM tumours, possibly resulting from aberrant regulation of rRNA expression.

Thus, we show here that JHDM1B localizes to the nucleolus and provides a fundamental function for silencing rRNA genes in a manner dependent on its JmjC domain. Our findings suggest that this activity involves the demethylation of H3K4me3 at the rDNA locus, although we cannot exclude additional nucleolar, non-histone targets. Ribosome biogenesis is a highly coordinated process that ensures proper cell growth and proliferation by supporting the synthesis of proteins. Deregulation of this process has been linked to multiple forms of human disease, including cancer. Our study provides critical insight into the role of aberrant ribosome biogenesis and epigenetic mechanisms to cellular transformation. We propose JHDM1B as an addition to the list of tumour suppressors, such as p53 and pRb, that negatively regulate rRNA gene expression¹⁸.

METHODS SUMMARY

RNA interference. HeLa cells were transfected by using HiPerFect transfection reagent (Qiagen), in accordance with the manufacturer's protocol, with either a single siRNA oligonucleotide (5'-AGGCAAGUUUAAACCUCAUG-3') or a pool of four siRNA oligonucleotides (5'-GCAUAAGGUCACUGAUCUU-3', 5'-GACCUCAGCUGGACCAUAUU-3', 5'-GGGAGUCGAUCUUUAUGAUU-3' and 5'-CAGCAUAGACGGCUUCUCUUU-3') targeting human JHDM1B (Dharmacon). Direct comparison of the pool of oligonucleotides and the single oligonucleotide (which was not present in the pool) showed identical results.

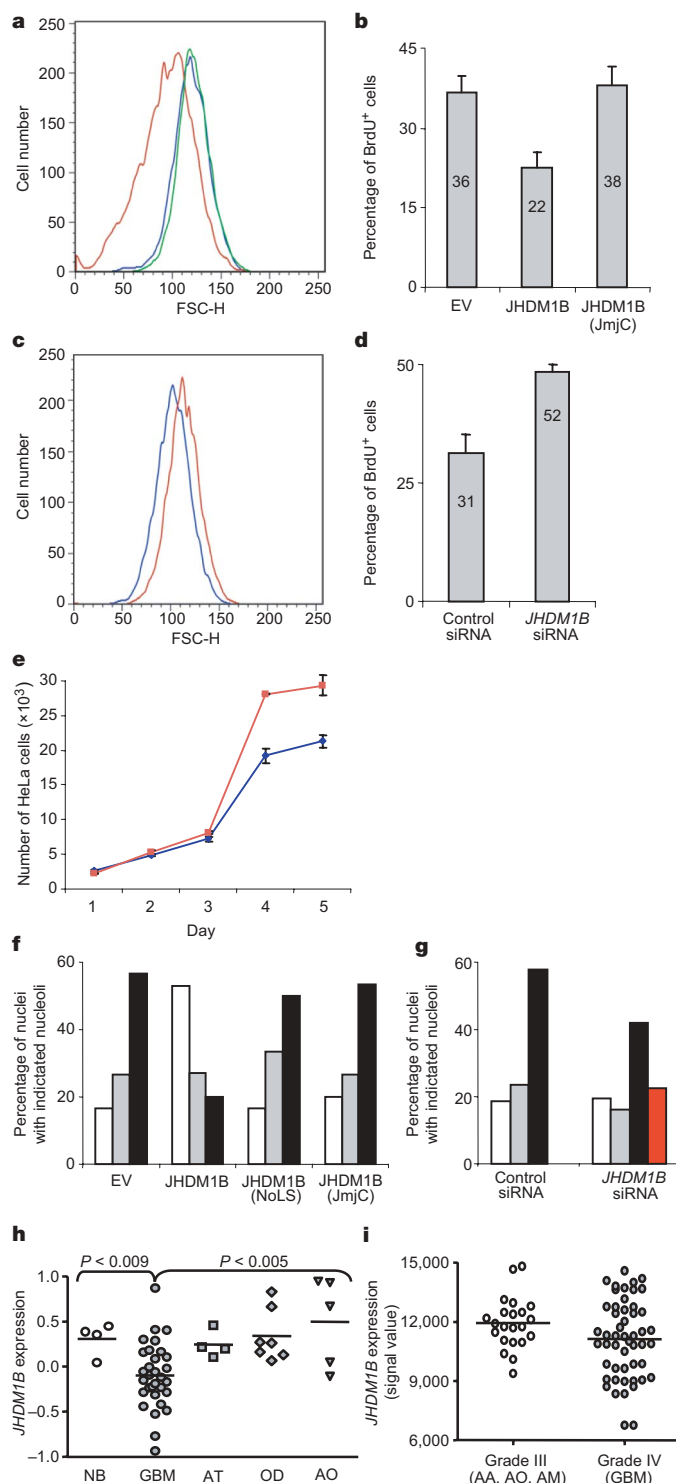


Figure 4 | JHDM1B inhibits cell growth and proliferation. **a**, Cell size was determined by fluorescence-activated cell sorting (FACS; forward scatter) in HeLa cells retrovirally infected with empty vector (blue) or constructs encoding wild-type JHDM1B (red) or JHDM1B(JmjC) (green), as indicated. **b**, Percentage of BrdU-positive HeLa cells transfected with EV or constructs encoding Flag-tagged JHDM1B or JHDM1B(JmjC). **c**, Cell size was determined by FACS (forward scatter) in HeLa cells transfected with control siRNA (blue) or *JHDM1B* siRNA (red) oligonucleotides. **d**, Percentage of BrdU-positive HeLa cells transfected as indicated. **e**, Proliferation of HeLa cells (transfected with control siRNA (blue) or *JHDM1B* siRNA (red) oligonucleotides) over a five-day period. **f**, Analysis of the number of nucleoli (determined by immunofluorescence with anti-B23 antibody) in HeLa cells transfected with EV or with constructs encoding Flag-tagged JHDM1B or the indicated JHDM1B mutants. White columns, three or fewer nucleoli; grey columns, four nucleoli; black columns, five or six nucleoli. **g**, Experiment performed as in **f** except that siRNA oligonucleotides against JHDM1B were compared with the control. White columns, three or fewer nucleoli; grey columns, four nucleoli; black columns, five or six nucleoli; red column, seven or more nucleoli. **h**, Data from ref. 21 (provided by Oncomine) reanalysed to show expression levels of *JHDM1B* in normal brain (NB), glioblastomas multiform (GBM), astrocytic tumours (AT), oligodendrogliomas (OD) and anaplastic oligoastrocytomas (AO). **i**, Data from ref. 22 (provided by NIH-GEO) reanalysed to show expression levels of *JHDM1B* in grade III and grade IV brain tumours (AA, anaplastic astrocytoma; AM, anaplastic mixed oligoastrocytoma). $P < 0.040$; $t = 1.770$. Where present, error bars represent s.d. ($n = 3$).

Transcription analysis by qRT-PCR. RNA was extracted with the use of the RNeasy kit (Qiagen), and reverse transcriptions were performed as described previously¹². qRT-PCR analysis was performed in accordance with standard procedures with SYBR Green mix (Bio-Rad). Primer sequences used to detect pre-rRNA and the housekeeping gene *ARPP P0* were as reported¹². The primer pairs used for the quantification of pre-rRNA recognize the 5' external transcribed spacer (5' ETS), and because the 5' ETS is processed rapidly during transcription, it accurately reflects the rate of RNA pol I transcription¹². The sequences used for JHDM1B were 5'-GAGGAGAAGAAGAAGGTGAAG-3' and 5'-TTGATGGGCTGCTGGTTC-3'.

Indirect immunofluorescence. Cells were plated and cultured on chambered glass tissue-culture slides (BD Falcon) with complete medium. For immunofluorescence, cells were washed in PBS, fixed and permeabilized in 100% methanol at -20 °C for 10 min, and then incubated with the primary antibodies for 1 h at 25 °C in 0.5% Tween 20 in PBS (0.5% TBST). Slides were washed three times in 0.5% TBST for 5 min and incubated with secondary antibodies, diluted 1:1,000. 4',6-Diamidino-2-phenylindole (DAPI; Molecular Probes) was included to reveal nuclei. Slides were washed in PBS and subsequently mounted with Aqua Poly/Mount (Polysciences). Images were acquired with a Nikon Eclipse E800 fluorescence deconvolution microscope. For pre-extraction, cells were rinsed in PBS and incubated in 0.5% Triton X-100 for 5 min on ice followed by methanol fixation at -20 °C, permeabilization, and the immunofluorescence procedure described above. Fluorescence quantification was determined with ImageJ software (NIH).

Full Methods and any associated references are available in the online version of the paper at www.nature.com/nature.

Received 15 August; accepted 13 September 2007.

1. Tsukada, Y. *et al.* Histone demethylation by a family of JmjC domain-containing proteins. *Nature* **439**, 811–816 (2006).
2. Klose, R. J., Kallin, E. M. & Zhang, Y. JmjC-domain-containing proteins and histone demethylation. *Nature Rev. Genet.* **7**, 715–727 (2006).
3. Shi, Y. & Whetstone, J. R. Dynamic regulation of histone lysine methylation by demethylases. *Mol. Cell* **25**, 1–14 (2007).
4. Jin, J. *et al.* Systematic analysis and nomenclature of mammalian F-box proteins. *Genes Dev.* **18**, 2573–2580 (2004).
5. Pothof, J. *et al.* Identification of genes that protect the *C. elegans* genome against mutations by genome-wide RNAi. *Genes Dev.* **17**, 443–448 (2003).
6. Li, J. *et al.* Leukaemia disease genes: large-scale cloning and pathway predictions. *Nature Genet.* **23**, 348–353 (1999).
7. Suzuki, T. *et al.* New genes involved in cancer identified by retroviral tagging. *Nature Genet.* **32**, 166–174 (2002).
8. Suzuki, T., Minehata, K., Akagi, K., Jenkins, N. A. & Copeland, N. G. Tumor suppressor gene identification using retroviral insertional mutagenesis in Blm-deficient mice. *EMBO J.* **25**, 3422–3431 (2006).
9. Hwang, H. C. *et al.* Identification of oncogenes collaborating with p27^{Kip1} loss by insertional mutagenesis and high-throughput insertion site analysis. *Proc. Natl Acad. Sci. USA* **99**, 11293–11298 (2002).
10. Dousset, T. *et al.* Initiation of nucleolar assembly is independent of RNA polymerase I transcription. *Mol. Biol. Cell* **11**, 2705–2717 (2000).
11. Daniely, Y., Dimitrova, D. D. & Borowiec, J. A. Stress-dependent nucleolin mobilization mediated by p53–nucleolin complex formation. *Mol. Cell. Biol.* **22**, 6014–6022 (2002).
12. Grandori, C. *et al.* c-Myc binds to human ribosomal DNA and stimulates transcription of rRNA genes by RNA polymerase I. *Nature Cell Biol.* **7**, 311–318 (2005).
13. Voo, K. S., Carlone, D. L., Jacobsen, B. M., Flodin, A. & Skalknik, D. G. Cloning of a mammalian transcriptional activator that binds unmethylated CpG motifs and shares a CXXC domain with DNA methyltransferase, human trithorax, and methyl-CpG binding domain protein 1. *Mol. Cell. Biol.* **20**, 2108–2121 (2000).
14. Koyama-Nasu, R., David, G. & Tanese, N. The F-box protein Fbl10 is a novel transcriptional repressor of c-Jun. *Nature Cell Biol.* **9**, 1074–1080 (2007).
15. Brock, G. J. & Bird, A. Mosaic methylation of the repeat unit of the human ribosomal RNA genes. *Hum. Mol. Genet.* **6**, 451–456 (1997).
16. Earley, K. *et al.* Erasure of histone acetylation by *Arabidopsis* HDA6 mediates large-scale gene silencing in nucleolar dominance. *Genes Dev.* **20**, 1283–1293 (2006).
17. Preuss, S. & Pikaard, C. S. rRNA gene silencing and nucleolar dominance: Insights into a chromosome-scale epigenetic on/off switch. *Biochim. Biophys. Acta.* **1769**, 383–392 (2007).
18. Ruggero, D. & Pandolfi, P. P. Does the ribosome translate cancer? *Nature Rev. Cancer* **3**, 179–192 (2003).
19. Zhao, J., Yuan, X., Frodin, M. & Grummt, I. ERK-dependent phosphorylation of the transcription initiation factor TIF-IA is required for RNA polymerase I transcription and cell growth. *Mol. Cell* **11**, 405–413 (2003).
20. Bukhari, M. H., Hashmi, I., Naeem, S., Abro, A. K. & Chaudhry, N. A. Use of AgNOR index in grading and differential diagnosis of astrocytic lesions of brain. *Pak. J. Med. Sci.* **23**, 206–210 (2007).
21. Bredel, M. *et al.* Functional network analysis reveals extended gliomagenesis pathway maps and three novel MYC-interacting genes in human gliomas. *Cancer Res.* **65**, 8679–8689 (2005).
22. Freije, W. A. *et al.* Gene expression profiling of gliomas strongly predicts survival. *Cancer Res.* **64**, 6503–6510 (2004).

Supplementary Information is linked to the online version of the paper at www.nature.com/nature.

Acknowledgements We thank D. Reinberg, R. Santoro, J. Skaar and J. Wysocka for suggestions and/or critically reading the manuscript; L. Busino for helping with qRT-PCR analysis; and J. Wysocka and G. David for reagents. D.F. is grateful to A. Nans. M.P. is grateful to T. M. Thor for continuous support. This work was supported by an Emerald Foundation grant to D.G., a Fellowship from the American-Italian Cancer Foundation to D.G., a fellowship from the German Research Foundation to F.B., a Bernard B. Levine Foundation award to R.K.-N., and grants from the NIH to M.P.

Author Contributions D.F. performed all experiments, contributed to their planning and co-wrote the manuscript. D.G. contributed to the planning of experiments and discussing and interpreting results. F.B. conducted the fluorescence-activated cell sorting analysis. R.K.-N. generated JHDM1B mutants. M.P. coordinated the study and co-wrote the manuscript. All authors discussed the results and commented on the manuscript.

Author Information Reprints and permissions information is available at www.nature.com/reprints. Correspondence and requests for materials should be addressed to M.P. (michele.pagano@nyumc.org).

METHODS

Cell culture. HeLa, T98G, 293T, GP-293 and IMR90 cells were cultured as described previously^{23,24}.

Antibodies. A polyclonal antibody against JHDM1B was generated by immunizing rabbits with a peptide containing amino-acid residues 800–1000 of human JHDM1B. Rabbit polyclonal antibodies were as follows: anti-Flag (F7425; Sigma), anti-haemagglutinin (anti-HA) (71-5500; Zymed), anti-di-methyl H3K36 (07-274; Upstate), anti-di-methyl H3K4 (07-030; Upstate), anti-tri-methyl H3K4 (05-745; Upstate), anti-tri-methyl H3K9 (07-523; Upstate), anti-tri-methyl H3K27 (07-449; Upstate), anti-tri-methyl H3K36 (ab9050; Abcam), anti-Alexa Fluor 568 (A11036; Molecular Probes) and anti-phospho-H3 (Ser 10) (06-570; Upstate). Mouse monoclonal antibodies were as follows: anti-M2 Flag (F3165; Sigma), anti-nucleophosmin (32-5200; Zymed), anti-UBF (sc-13125; Santa Cruz Biotechnology), anti- α -tubulin (32-2500; Zymed), anti-JHDM1B (H00084678-M09; Abnova), anti-GFP (A-11121; Molecular Probes), anti-BrdU (347580 (7580); BD) and anti-Alexa Fluor 488 (A21121; Molecular Probes).

Chromatin immunoprecipitations. ChIP assays were conducted as described previously²³. The polyclonal antibody against JHDM1B was used for ChIP analysis of endogenous JHDM1B. anti-HA or anti-GFP antibodies were used as controls. Primer sequences for rDNA were as reported¹². *GAPDH* sequences were: 5'-TCCACCACCCTGTTGCTGTA-3' and 5'-ACCACAGTCCATGCC-ATCAC-3'.

Cell proliferation and FACS analysis. HeLa cells were transfected with siRNA oligonucleotides for two consecutive days, as described in the Methods Summary. At 48 h after the second transfection, an 80% confluent dish was trypsinized, split into five dishes and retransfected with siRNA oligonucleotides, in accordance with the long-term gene-silencing technique from the manufacturer (Qiagen). Cells were collected daily for five days and analysed by standard counting methods. FACS and forward scatter analysis were conducted as described previously^{23–25}.

Solubilized chromatin purification. Purification of solubilized chromatin fractions was performed as described previously²⁶.

BrdU and BrUTP incorporation. BrdU incorporation was performed as described previously²⁷. For BrUTP incorporation, BrUTP (Molecular Probes) was added to a FuGENE 6 and 20-mM HEPES mixture (1:10) to a final concentration of 1 mM for 15 min at 25 °C, as described by Roche Molecular Biochemicals. During this short period, BrUTP specifically highlights transcriptionally active nucleoli, and no BrUTP incorporation is observed outside the nucleoli^{28,29}. Slides were washed in PBS and the BrUTP–FuGENE 6 mixture was added to cells. Cells were incubated at 4 °C for 15 min, washed briefly in PBS and then incubated at 37 °C in culture medium for 5 min. Cells were processed for immunofluorescence analysis, as stated above, and an anti-BrdU antibody was used for detection. The BrdU and nucleolar-BrUTP-positive cells were analysed with standard counting methods.

Data mining. Gene expression data on *JHDM1A* and *JHDM1B* were retrieved from the Oncomine website (<http://www.oncomine.org>) and the National Institutes of Health (NIH) Gene expression omnibus (GEO) (<http://www.ncbi.nlm.nih.gov/geo/>). Data from two brain cancer studies were used

for statistical calculations. Bredel *et al.*²¹ includes analysis of 50 human gliomas of various histogenesis with the use of cDNA microarrays. Data were reanalysed in GraphPad software to show expression levels of *JHDM1B* and *JHDM1A*. Additional details of the study, including the pathological and clinical data, are available at Oncomine or on the *Cancer Research* journal website. Data from the second study were from an analysis of grade III and IV gliomas of various histological types²². These data were gathered as part of the NIH Neuroscience Microarray Consortium (<http://arrayconsortium.tgen.org>). Data were acquired and reanalysed with a signal value threshold of 15,000, using GraphPad software to show expression levels of *JHDM1B* and to determine *P* and one-tailed *t*-test values.

In vitro histone demethylation assay. *In vitro* demethylation assays were conducted as described previously³⁰. In brief, core histones were incubated with Flag-immunopurified JHDM1B from 293T cells in demethylation buffer (50 mM Tris-HCl pH 8.0, 50 mM KCl, 10 mM MgCl₂, 1 mM α -oxoglutarate, 40 mM FeSO₄, 2 mM ascorbic acid) at 37 °C. Core histones (2 μ g) were incubated for 30 min with Flag-immunopurified JHDM1B in a volume of 30 μ l. Reaction mixtures were analysed by western blotting. Quantification by densitometry was performed with ImageJ (NIH) software.

FRAP (fluorescence recovery after photobleaching) analysis. HeLa cells were plated, transfected with *JHDM1B-pEGFP-N1* (Clontech Laboratories) by FuGENE 6 (Roche) and observed in LabTek II chambers (Nalgene). Selective photobleaching of the nucleolus was conducted on an LSM 510 microscope (Zeiss) with laser excitation at 488 nm for GFP and a 63 \times , 1.2 numerical aperture, oil-immersion objective, as described previously³¹. JHDM1B–GFP fluorescence for each image in the sequence was determined with ImageJ software (NIH).

23. Busino, L. *et al.* SCFFbx13 controls the oscillation of the circadian clock by directing the degradation of cryptochrome proteins. *Science* **316**, 900–904 (2007).
24. Dorrello, N. V. *et al.* S6K1- and β TRCP-mediated degradation of PDCD4 promotes protein translation and cell growth. *Science* **314**, 467–471 (2006).
25. Amador, V., Ge, S., Santamaria, P. G., Guardavaccaro, D. & Pagano, M. APC/C^{Cdc20} controls the ubiquitin-mediated degradation of p21 in prometaphase. *Mol. Cell* **27**, 462–473 (2007).
26. Groisman, R. *et al.* The ubiquitin ligase activity in the DDB2 and CSA complexes is differentially regulated by the COP9 signalosome in response to DNA damage. *Cell* **113**, 357–367 (2003).
27. Bashir, T., Dorrello, N. V., Amador, V., Guardavaccaro, D. & Pagano, M. Control of the SCF^{Skp2-Cks1} ubiquitin ligase by the APC/C^{Cdh1} ubiquitin ligase. *Nature* **428**, 190–193 (2004).
28. Leung, A. K. *et al.* Quantitative kinetic analysis of nucleolar breakdown and reassembly during mitosis in live human cells. *J. Cell Biol.* **166**, 787–800 (2004).
29. Arabi, A. *et al.* c-Myc associates with ribosomal DNA and activates RNA polymerase I transcription. *Nature Cell Biol.* **7**, 303–310 (2005).
30. Cloos, P. A. *et al.* The putative oncogene GASC1 demethylates tri- and dimethylated lysine 9 on histone H3. *Nature* **442**, 307–311 (2006).
31. Frescas, D., Mavrikakis, M., Lorenz, H., Delotto, R. & Lippincott-Schwartz, J. The secretory membrane system in the *Drosophila* syncytial blastoderm embryo exists as functionally compartmentalized units around individual nuclei. *J. Cell Biol.* **173**, 219–230 (2006).

naturejobs

**JOBS OF
THE WEEK**

Job mobility is a key trait for anyone pursuing a career in science. A willingness to switch disciplines, change labs, relocate to a different country or move between the worlds of academia and business can be crucial to success. But for many, that last transition can prove to be fairly problematic.

In Britain, for example, biomedical scientists face several barriers should they consider moving from academia to industry, according to a report from the Academy of Medical Sciences (www.acmedsci.ac.uk). The problem is fuelled in part by fears among academics that a move into business will rob them of some autonomy and divorce them from academic networks. This in turn is caused by a lack of information — both about what life in business is like and about the opportunities that exist in the industrial sector. Among the solutions to this information gap, the report suggests organizing introductory programmes to allow academics to gain industrial experience, and an increase in 'industry open days' at universities.

The importance of these sectors getting to know one another better is emphasized by the Science, Technology and Industry Scoreboard released by the Organisation for Economic Co-operation and Development (OECD) last month. This shows that 3.9 million people in OECD countries were working in research and development in 2005. Of these, a significant proportion were in the business sector: 80% in the United States, 66% in Japan and 50% in the European Union. And in China, the number of researchers working in the business sector has risen by 15% per year for the past five years.

But the OECD figures also reveal that flexibility and mobility between disciplines and across borders are growing in importance. There were five times more scientific papers with international co-authors in 2005 compared with 1985. This globalization of science means that young researchers have greater opportunities. It offers them broader scope for finding their favoured living conditions and ideal collaborations — as long as they have the wherewithal to make the move.

Gene Russo, acting editor of *Naturejobs*

CONTACTS

Acting Editor: Gene Russo

European Head Office, London

The Macmillan Building,
4 Crinan Street,
London N1 9XW, UK
Tel: +44 (0) 20 7843 4961
Fax: +44 (0) 20 7843 4996
e-mail: naturejobs@nature.com

European Sales Manager:

Andy Douglas (4975)
e-mail: a.douglas@nature.com
**Business Development
Manager:**
Amelie Pequignot (4974)
e-mail: a.pequignot@nature.com

Natureevents:

Claudia Paulsen Young
(+44 (0) 20 7014 4015)
e-mail: c.paulsenyoung@nature.com

France/Switzerland/Belgium:

Muriel Lestringuez (4994)

Southwest UK/RoW:

Nils Moeller (4953)

Scandinavia/Spain/Portugal/Italy:

Evelina Rubio-Hakansson (4973)

Northeast UK/Ireland:

Matthew Ward (+44 (0) 20 7014 4059)

North Germany/The Netherlands:

Reya Silao (4970)

South Germany/Austria:

Hildi Rowland (+44 (0) 20 7014 4084)

Advertising Production Manager:

Stephen Russell
To send materials use London
address above.
Tel: +44 (0) 20 7843 4816
Fax: +44 (0) 20 7843 4996
e-mail: naturejobs@nature.com
Naturejobs web development:
Tom Hancock

Naturejobs online production:

Jasmine Myer
US Head Office, New York
75 Varick Street, 9th Floor,
New York, NY 10013-1917
Tel: +1 800 989 7718
Fax: +1 800 989 7103
e-mail: naturejobs@natureny.com

US Sales Manager:

Peter Bless

Japan Head Office, Tokyo

Chiyoda Building,
2-37 Ichigayatamachi,
Shinjuku-ku, Tokyo 162-0843
Tel: +81 3 3267 8751
Fax: +81 3 3267 8746

Asia-Pacific Sales Manager:

Ayako Watanabe
Tel: +81-3-3267-8765
e-mail: a.watanabe@natureasia.com

MOVERS

Alan Bernstein, executive director, Global HIV Vaccine Enterprise, Seattle, Washington



2000–07: President, Canadian Institutes of Health Research, Toronto, Canada
1994–2000: Director of research, Samuel Lunenfeld Research Institute of Mount Sinai Hospital; professor of molecular & medical genetics, University of Toronto
1984–1994 Head of molecular and developmental biology, Samuel Lunenfeld Institute

Alan Bernstein made sure he would never be pigeonholed into one discipline — a move that enabled the would-be physicist to make his mark in the biomedical sciences.

As an undergraduate in maths and physics at the University of Toronto, he stumbled across the medical biophysics department. There he met Harold Johns, discoverer of cobalt-60 radiation therapy for cancer, who lured him into the burgeoning field of medical biophysics.

For his PhD, Bernstein worked on mice with defective blood-cell production before realizing that he wanted a solid background in genetics. “Genetics is to biology what mathematics is to physics,” he says. But, he admits, he had no idea that a revolution in biology was imminent.

In London as a postdoc, Bernstein worked on retroviruses at the Imperial Cancer Research Fund. An experiment he did there provided genetic evidence of the first retroviral oncogene, dubbed *src*. Back in Toronto, he determined how the Friend leukaemia virus affects the ability to form new blood cells. His was one of the first labs both to clone a retrovirus and to exploit it as a vector to deliver genes to cells.

In 1984, Bernstein was asked to head the division of cancer research at the newly formed Samuel Lunenfeld Research Institute at Mount Sinai Hospital in Toronto. Instead, he chose to lead the institute's division of molecular and developmental biology, a field he expected would be hot. He spent the next 15 years, including time as Lunenfeld's director, demonstrating how oncogenes control developmental processes.

“Unlike many scientists, Alan doesn't have a comfort zone,” says long-time colleague Janet Rossant, researcher at the Hospital for Sick Children in Toronto. “He's always looking for new scientific directions.” As inaugural president of the Canadian Institutes of Health Research, Bernstein built a US\$1-billion budget combining molecular biology and social-science research agendas.

In January, Bernstein will become the first executive director of the \$750-million Global HIV Vaccine Enterprise, sponsored by the Bill & Melinda Gates Foundation. He takes on the directorship at a crucial time. Merck recently announced that it was dropping the development of what had been considered the most promising HIV vaccine candidate to date. Bernstein believes the way forward is to develop creative routes for collaborations by the vaccine enterprise, scientists and companies in the field. “No group can do this alone,” says Rossant. ■

Virginia Gewin

NETWORKS & SUPPORT

Latin American challenges

Young Latin American biomedical scientists seeking postdoctoral positions abroad face significant funding challenges. True, top graduates from developing countries can often obtain fellowships to work abroad from their countries' national research councils or equivalent organizations. But the stipends are usually lower than those offered by prestigious programmes such as the European Molecular Biology Organization, NATO or the US National Academies. And those three programmes do not accept applications from Latin American citizens.

Fortunately, a few highly selective international programmes fund Latin American citizens. Two examples are the Human Frontier Science Program (HFSP) and the Pew Latin American Fellows Program, both coordinated by Nobel laureate Torsten Wiesel, president emeritus at Rockefeller University, New York. These not only support postdoctoral training but also help young scientists return home.

The difficult transition from postdoc to independent investigator is well known. It can be especially hard for scientists returning to developing countries, where doing research can be frustrating. In Brazil, for example, they face a long wait for reagents that

often cost more than twice the price of those ordered in the United States. Just bringing in scientific equipment and reagents can be a nightmare (S. K. Rehen *Nature* **428**, 601; 2004).

As developing countries are short of money, support from programmes such as the HFSP or Pew can make a world of difference. Pew provides funds for equipment and supplies to set up a laboratory in the country of origin. The HFSP emphasizes interdisciplinary research and focuses on young researchers' careers, offering competitive awards after they return home.

Science in Latin America has grown vigorously in the past decade. The Latin American share of the world's scientific publications increased from 1.8% in 1991–95 to 3.4% in 1999–2003 (M. Hermes-Lima *et al. IUBMB Life* **4**, 199–210; 2007). But its visibility is low, indicating a need to increase the quality of science in general and biomedical sciences in particular. Supporting the initial phases of independent careers is crucial, not only for competitiveness but to prevent a brain drain. ■

Fernanda De Felice is a postdoctoral fellow at Northwestern University in Evanston, Illinois, and an assistant professor at the Federal University of Rio de Janeiro, Brazil.

POSTDOC JOURNAL

Meet my lab minion

There comes a point in your academic career when you can employ minions to do menial lab work for you. Sadly, I have yet to reach that point. When I need someone to spend most of their working hours sitting in a magnetically shielded laboratory, coaxing the ancient magnetic signals from three-billion-year-old South African lavas, there's only one person that I can delegate the task to: me. Unfortunately, it's not just a matter of placing my samples in a fancy machine and instantly getting the data I want; every sample has to be measured a dozen times or more, as I attempt to destabilize unwanted overprints with ever-stronger blasts of heat or artificial magnetic fields.

Weeks of repetitive measurements might not sound that intellectually stimulating. But I actually enjoy getting my hands dirty in the lab — I take great satisfaction from the thought that I'm personally uncovering long-buried clues about southern Africa's geological history. Besides, I'm not simply repeating my PhD research. I'm using an unfamiliar machine to analyse ancient lavas with magnetic quirks and subtleties quite different from the much younger sediments I've studied before. Even now, I'm still learning the tricks of my scientific trade, and gaining the broader experience necessary to supervise my future minions effectively, should I ever be given any. ■

Chris Rowan is a postdoctoral student in the geology department at the University of Johannesburg, South Africa.

A hand and honour

Keeping pace with the human race.

Brenda Cooper

John Justice stretched up, fingers scraping at cool morning air, then bent down, cupping his calves, the nanskin registering his fingertips as data points: pressure, heat, sweat, angle.

The hum of the crowd, the band's drums and wind instruments, and even the race announcer seemed far, far away. He already knew what medals felt like. Before his turn in the never-ending war, his men's relay team won gold in London.

Last month, he'd killed the world record for the 10,000-metre run, coming in at just over 24 minutes. No medal for that. Twenty or so news stories, a political cartoon or two, and a combination of joy and bitterness sticking so deep in his gut he threw up all over the course when he was done.

Today, his race would be one-on-one against the man whose record still stood even after John beat it. Hsui Smith, an improbably tall Chinese-American who held the world record in the 10,000 metres. Who would still hold the official record, even after today.

Discrimination was a bitch. Change was tested for like steroids.

John nearly jumped as his coach, Nicolai, placed his metal hand on the small of his back. "Don't think about it. Just run. Run for all of us."

It was nearly time. "I'll win," he nodded at Nicolai, forcing a smile, staring into the shorter, blockier man's deep brown eyes. Nic's naked hope made him clap the man on the back. "I know it matters."

Nicolai headed for the finish line. As the noise and movement swallowed Nic, John muttered, "Damned exhibition." He had always yearned to be the fastest man in the world. The best that war-wounded John could become for child-John was the fastest un-man.

Kim Moon waited for him on the way to the starting blocks, looking more like a debutante than an engineer-medic, her figure slim and curvy in a one-piece shorts outfit. She reached up and hugged him. "Good luck."

He didn't have to fake a smile for her. "It's all your fault."

"They're your legs," she retorted. "The best I've ever made."

One of her customers had new hands and feet with built in temperature controls, and had climbed Everest and K2. After an artificial hand replaced one eaten by frostbite, the climber had made news by chopping

off the functioning hand for another of Kim's sculptures.

Without Kim, he would have walked, and run, but never raced. She was all the magic of maths and engineering held together with heart. He leaned down and kissed her forehead, savouring her honey-suckle scent.

As John approached the starting blocks, Hsui stood up from a hamstring stretch and extended a hand. John took it. Where he'd expected to see challenge in the notoriously cocky runner's eyes, he swore he saw fear. His nerves screamed at it. "Why did you agree to this?"



Hsui shook John's hand, replying softly, "My brother lost a hand in the war." He let go and turned to his starting blocks.

"Thank you," John said to his back.

John swept Hsui's fears, and his own, into a deep breath and puffed them out, relaxing his cheeks. He rocked a bit, setting his calves, running a quick mental skip across the sensors in his skin, checking the breeze, temperature and humidity. He struggled to close his ears as the announcer droned on. Kim's legs — his — wouldn't win by themselves. He mentally shrank the world to a bubble around him, and the long slender corridor of space on the track in front of him.

The starting gun swept him forward, following Hsui.

He fell in right behind, body straight, arms pumping.

No need to pass. Yet.

He let the first round of the track go, calibrating, bidding time. His legs were all he had, he'd refused changes to his lungs and circulatory system, wanting some purity. Important not to overrun his breath.

He was about to pass the fastest human ever. The fastest pure human. He threw the thought away. A break in stride or a stumble could steal the race. Counting and breathing and moving. Just the track under him and the narrow corridor, the wind on his teeth. Breath and wind and stride and arms.

His head turned a little, as if the force of Hsui's run called it. Hsui didn't return John's darting glance, just kept going, head up. Surging. To match him, John told his legs to give more, asked his heart to keep up.

Breath and wind and spine and floor. Data instead of Hsui's desperate face.

Another turn around the track, a matched pair.

The image of two feet crossing at the same time raced through John's head. An honourable outcome. Except he was a racer. The sound of Hsui's breath fell to behind John's shoulder. The finish line blurred under him.

Nic's arms encircled him. Kim leapt up on Nic's back. Nic grabbed her under the knees, boosting her like a child. She looked down, her joy at the win overtaken by a crease in her brow. "Why so slow?"

He shook his head, unsure how to explain it. "I'll be right back." Hsui jogged well past him now, sweat dripping down his back.

John caught him. "I hope your brother is proud of you."

Hsui winced. "He went back to the war. They put him in special ops 'cause his hand-eye coordination was so much better than anyone else's." He looked away. "After his enhancements his hand was steadier than anybody else's."

Hsui had lost face to honour a brother with no more change than a hand? A man who had done well for himself? Hsui continued. "He's dead. They gave him a purple heart." He turned, and without so much as a smile, the fastest man in the world walked away from the fastest un-man in the world.

Brenda Cooper is a futurist, a writer and the chief information officer for the City of Kirkland, Washington. Her latest novel is *The Silver Ship and the Sea* from Tor Books.